

# **Advanced precursor design for atomic layer deposition and chemical vapour deposition of gold metal**

by

**Matthew Bertram Edward Griffiths**

A thesis submitted to the Faculty of Graduate and Postdoctoral Affairs in partial fulfillment of the requirements for the degree of

Doctor of Philosophy

In

Chemistry

Carleton University

Ottawa, Ontario

© 2020

Matthew Bertram Edward Griffiths

This thesis is dedicated to my family

# Abstract

This thesis first outlines the current state-of-the-art of gold CVD and ALD precursors based on their precursor figures of merit ( $\sigma$ ) which was a concept developed in this research program. Then, this thesis demonstrates the ability to control the structure of deposited nanoparticles by CVD, using a combination of thermogravimetric analysis (TGA), scanning electron microscopy (SEM), and X-ray photoelectron spectroscopy (XPS) to elucidate the mechanism of growth. This represents one of the first gold CVD studies to rationally design a precursor that would deposit anisotropic nanostructures. This thesis then describes the first gold ALD process ( $\text{PMe}_3\text{AuMe}_3$ ). Then, a new process using this same precursor and hydrogen plasma was developed and the surface mechanism of this new ALD process was investigated using a combination of *in-situ* reflection absorption infrared spectroscopy (RAIRS), XPS, and quadrupole mass spectrometry (QMS). This mechanistic study provides insight on the kinetics of Me and  $\text{PMe}_3$  ligand desorption from the surface and re-defines the upper limit of the Au ALD process. In order to improve on the existing state-of-the-art of gold precursors, this thesis then describes a systematic gold(I) precursor design. Using a combination of TGA, differential scanning calorimetry (DSC), x-ray crystallography, and density functional theory (DFT), we delineate why certain ligands work well for gold(I) and we develop the precursor figure of merit ( $\sigma$ ) in this chapter. With a knowledge of the design factors that make a good precursor from the standpoint of thermolysis, this thesis then describes a study where the rate of CVD of various gold(I) precursors is compared by *in situ* monitoring using a combination of quartz crystal microbalance (QCM) and quadrupole mass spectrometry (QMS). This study culminates in a new idea in the field of ALD: the rational design of a kinetically limited ALD process. We then show that the kinetic implications of steric bulk that are ubiquitous in solution-phase synthetic chemistry can also be exploited in the fields of CVD and ALD. Finally, this thesis describes a study where an alkylgold(I) NHC self-limiting precursor is rationally designed. A family of these types of precursors is presented, and the self-limiting capability of these precursors is demonstrated using our *in-situ* QCM/QMS monitoring apparatus. We then show that highly conductive and high-purity gold thin films can be deposited with one of these new precursors, and the film's purity (>99% by XPS) and resistivity (4.2  $\mu\Omega$  cm) rival the current state of the art of Au ALD films. Altogether, this thesis demonstrates that the rational design of deposition precursors is essential to the advancement of the fields of CVD and ALD not only for the development of new processes, but also because of the importance of the precursor on growth morphology. Being able to tailor a compound for a specific thin film material is important not only for gold thin films, but also for the rest of the periodic table, as well as new materials that have not yet been synthesized.

## Preface

This preface provides full bibliographical details for each article included in this thesis, as well as whether the article is reproduced in whole or in part. Use of copyrighted material is likewise acknowledged here. When citing material from this thesis, please cite the article relevant to the chapter, if the chapter is based on a publication.

Pursuant to the *Integrated Thesis Policy* of Carleton University, the supervisor (Dr. Seán T. Barry) and the “student” (Matthew B. E. Griffiths) confirm that the student was fully involved in setting up and conducting the research, obtaining data and analyzing results, as well as preparing and writing the material presented in the co-authored article(s) integrated in the thesis. Additionally, the supervisor confirms the information provided by the student in this preface.

## Chapter 2

**Matthew B. E. Griffiths\***, Peter G. Gordon, Zachary S. Dubrawski, and Seán T. Barry, *Literature review and figure of merit analysis of gold CVD and ALD precursors*, 2020

This literature review would not have been completed if not for the help of Peter G. Gordon and Zachary S. Dubrawski. Matthew B. E. Griffiths researched, extracted data from literature, tabulated, performed figure of merit analysis of the precursors, and wrote the manuscript. Peter G. Gordon and Zachary S. Dubrawski canvassed, categorized, and summarized literature on gold CVD and ALD precursors during the preliminary stages of writing the review. Seán T. Barry supervised MBEG, PGG, and ZSD.

## Chapter 3

**Matthew B. E. Griffiths\***, Sara E. Koponen, David J. Mandia, Jennifer F. McLeod, Jason P. Coyle, Jeffrey J. Sims, Javier B. Giorgi, Eric R. Sirianni, Glenn P. A. Yap, and Seán T. Barry, *Surfactant-directed growth of gold metal nanoplates by chemical vapor deposition*, *Chem. Mater.*, 2015, 27, 6116-6124

This article is wholly reproduced and edited for formatting and clarity of presentation. Matthew B. E. Griffiths performed work related to synthesis and characterization of compounds, chemical vapour deposition experiments, and wrote the manuscript in collaboration with Sara E. Koponen and Seán T. Barry. Sara E. Koponen performed work related to synthesis and characterization of compounds and chemical vapour deposition experiments and was closely involved in the writing of the manuscript. David J. Mandia performed XPS analysis of the deposited films and was aided by Jeffrey J. Sims who was supervised by Javier B. Giorgi. Jennifer F. McLeod aided in chemical vapour deposition experiments. Jason P. Coyle synthesized and provided crystallographic data for the compounds included in the manuscript. Crystallography was

performed by Eric R. Sirianni and Glenn P. A. Yap. Seán T. Barry supervised MBEG, SEK, DJM, JFM and JPC.

## **Chapter 4**

**Griffiths, M.B.E.**, Pallister, P.J., Mandia, D.J., and Barry, S.T.\*, *Atomic Layer Deposition of Gold Metal, Chem. Mater.*, **2016**, 28, 44-46

This article is wholly reproduced and edited for formatting and clarity of presentation. Matthew B. E. Griffiths performed synthesis, thermolysis and characterization of  $(\text{PMe}_3)\text{AuMe}_3$ , developed the atomic layer deposition process, and performed SEM imaging and thickness measurements. Peter J. Pallister performed atomic layer deposition experiments, aided in thickness measurements, and collected TEM images. David J. Mandia performed XPS measurements on the deposited films. Seán T. Barry wrote the manuscript in collaboration with Matthew B. E. Griffiths and supervised MBEG, PJP, and DJM.

Michiel Van Daele, **Matthew B. E. Griffiths**, Ali Raza, Matthias Minjauw, Eduardo Solano, Ji-Yu Feng, Ranjith K. Ramachandran, Stéphane Clemmen, Roel Baets, Seán T. Barry, Christophe Detavernier, and Jolien Dendooven\*, *Plasma-Enhanced Atomic Layer Deposition of Nanostructured Gold Near Room Temperature, ACS Appl. Mater. Interfaces*, **2019**, 11, 37229-38

This unpublished article is partially reproduced and edited for formatting and clarity of presentation. Michiel Van Daele performed ALD studies, characterized the thin films, and wrote the manuscript. Matthew B. E. Griffiths performed synthesis, thermolysis and characterization of the gold precursors, and helped interpret results obtained by MVD.

Michiel Van Daele, **Matthew B. E. Griffiths**, Matthias Minjauw, Seán T. Barry, Christophe Detavernier, and Jolien Dendooven\*, *Reaction mechanism of the  $\text{Me}_3\text{AuPMe}_3\text{-H}_2$  plasma-enhanced ALD process, Phys. Chem. Chem. Phys.*, **2020**, 22, 11903

This article is partially reproduced and edited for formatting and clarity of presentation. Michiel Van Daele performed ALD studies, characterized the thin films, and wrote the manuscript. Matthew B. E. Griffiths performed synthesis, thermolysis and characterization of the gold precursors, and helped interpret results obtained by MVD.

## **Chapter 5**

**Matthew B. E. Griffiths\***, Zachary S. Dubrawski, Goran Bačić, Achini Japahuge, Prof. Jason D. Masuda, Prof. Tao Zeng, and Prof. Seán T. Barry, *Controlling thermal stability*

*and volatility of organogold(I) compounds for vapor deposition with complementary ligand design, European Journal of Inorganic Chemistry, 2019, 46, 4927-38*

This article is wholly reproduced and edited for formatting and clarity of presentation. Matthew B. E. Griffiths performed synthesis, thermolysis and characterization of all compounds, developed the figure of merit equation, and wrote the manuscript in collaboration with Seán T. Barry. Zachary S. Dubrawski performed synthesis, thermolysis and characterization of all compounds. Goran Bačić performed some thermolysis experiments and helped develop the figure of merit equation. Achini Japahuge performed DFT experiments and was supervised by Prof. Tao Zeng. Prof. Jason D. Masuda performed crystallography experiments. Seán T. Barry supervised MBEG, ZSD, and GB.

## **Chapter 6**

**Matthew B. E. Griffiths\*** and Seán T. Barry, *In-situ monitoring of the chemisorption behavior of gold vapour deposition precursors and preliminary assessment of a potential kinetically-limited ALD precursor, Manuscript in preparation*

Matthew B. E. Griffiths developed the grounding hypothesis, performed synthesis, thermolysis and characterization of compounds, reconfigured the ALD tool, performed surface chemisorption measurements, performed TGA/DSC experiments, ALD experiments, microscopy, and wrote the manuscript in collaboration with Seán T. Barry.

## **Chapter 7**

**Matthew B. E. Griffiths\***, Aya Kadri, Atilla C. Varga, and Seán T. Barry, *N-Heterocyclic carbenes as self-limiting ligands for ALD, Manuscript in preparation*

Matthew B. E. Griffiths developed the grounding hypothesis, performed synthesis, thermolysis and characterization of compounds, performed surface chemisorption measurements, performed ALD experiments, microscopy and thickness measurements, and wrote the manuscript in collaboration with Aya Kadri and Seán T. Barry. Aya Kadri performed synthesis, thermolysis and characterization of compounds, and aided in surface chemisorption and ALD experiments. Atilla C. Varga aided in synthesis and thermolysis experiments, and in surface chemisorption experiments. Seán T. Barry supervised the authors.

# Acknowledgements

This thesis represents years of work not only by myself but also by many others. To all of my co-authors and collaborators in the Barry Lab and elsewhere, I learned a lot from you, and I hope that you enjoyed working together on these projects as much as I did!

In particular, to the people who first trained me when I began: Sean Barry, Peter Gordon, Jason Coyle, Peter Pallister, Agnieszka Kurek, David Mandia, and Monica Gill; thank you for being patient and excellent role models and for showing me how to work in a lab. Especially Dave, who taught me that hard work always pays off. Goran and Sydney, the three of us have been working together for our entire degrees, and I wouldn't have it any other way. You've made this so enjoyable and fun, and there's no way I'd have the sense of fulfillment that I feel now without you two. Good luck to both of you, and let's work together again some day! Mike Land, I'm counting on you to wrangle all the new chemists coming through the lab. I know you can do it! But if you need a hand, let's chat over fish n' chips. To David Zanders, I would pay a lot of money for a fraction of your work ethic and positivity. You motivated me to become a better scientist, taught me new synthetic techniques, and became a great friend. Prost! To the excellent undergraduate students that I've had the pleasure of mentoring: Zack Dubrawski, Joseph Zurakowski, Aya Kadri, and Atilla Varga; thank you for being so smart, kind, and eager to learn. It's not always easy to teach someone to be a scientist, but with you it wasn't any trouble at all. Good luck in your careers. If I'm ever looking for a bright mind, I know who to ask first.

I owe many thanks to all the staff and faculty of the chemistry department, but in particular Chantelle Gravelle, Xun Sun, Jim Logan, Elena Munteanu, Peter Mosher, Susaritha Chandrabose, Tanya Rudd, and Keith Bourque. If I have a problem, you can solve it, or you've taught me how to solve it on my own. I'm deeply grateful for your collective kindness and support. Thank you!

My family has always been very close, and they've often asked me how my research is going. It's hard to get into the details, but I've always appreciated your thoughtfulness and care. This thesis is dedicated to you all. To Emily and Andrew, we're closer than most siblings, but I think of you more as close friends. Our group is one of the most uplifting parts of my life, and has helped me get through this degree with great happiness.

Finally to McKenzie, without your loving support I couldn't have accomplished all that I have. You always know how to ease my pain, your own passion motivates me to be better, and you're always there for me. I love you, I'm so lucky to have found you!

Thank you

## Table of Contents

<b>Chapter 1 Introduction .....</b>	<b>1</b>
1.1    Motivation for gold thin films and nanoparticles .....	1
1.2    Chemical vapour deposition .....	2
1.3    Atomic Layer deposition .....	7
1.4    Precursor Design .....	14
1.4.1    High vapour pressure .....	14
1.4.2    High stability towards self-decomposition .....	17
1.4.3    Cost and environmental impact of synthesis .....	20
1.5    Thermolysis of the new precursor .....	22
1.5.1    Thermogravimetric analysis (TGA).....	22
1.5.2    Differential scanning calorimetry (DSC).....	24
<b>Chapter 2 Literature review and figure of merit analysis of gold CVD and ALD precursors .....</b>	<b>26</b>
2.1    General information .....	26
2.2    Methodology.....	27
2.3    Precursor Figure of Merit.....	27
2.4    Figure of Merit Methodology .....	30
2.5 $\beta$ -diketonate, $\beta$ -ketoiminate, and double-ylide complexes of dimethylgold(III) .....	30
2.6    Dialkyldithiophosphinate, alkylphosphorodithiolate, dithiocarbamate, salicylaldiminate, and quinolinate complexes of dimethylgold(III) .....	34
2.7    Carboxylate and siloxide complexes of dimethylgold(III), trimethylgold(III) trialkylphosphines, and fluorinated carboxylate complexes of gold(I) .....	36
2.8    Guanidinate, amidinate, amide, and N-heterocyclic carbene complexes of gold(I) .....	39
2.9    Phosphine complexes of chlorogold(I) and alkylgold(I).....	41
2.10    Gold(I) complexes containing alkynyl, trifluoromethyl, and isonitrile ligands .....	45
2.11    Figure of merit minefield diagram .....	47
2.12    Supporting Information .....	49
<b>Chapter 3 Surfactant-directed growth of gold metal nanoplates by chemical vapor deposition .....</b>	<b>56</b>
3.1    Abstract .....	57
3.2    Introduction .....	58

<b>3.3 Results and Discussion.....</b>	<b>60</b>
<b>3.4 Conclusions.....</b>	<b>71</b>
<b>3.5 Experimental Details .....</b>	<b>72</b>
<b>3.6 Supporting Information .....</b>	<b>76</b>
<b>Chapter 4 Atomic layer deposition of gold metal.....</b>	<b>81</b>
<b>4.1 PE-ALD of gold metal using trimethylphosphinotrimethylgold(III) in combination with oxygen plasma and water.....</b>	<b>83</b>
4.1.1 Abstract.....	83
4.1.2 Introduction.....	84
4.1.3 Results and Discussion .....	85
4.1.4 Additional Results.....	91
<b>4.2 PE-ALD of gold metal using trimethylphosphinotrimethylgold(III) and hydrogen plasma.....</b>	<b>94</b>
4.2.1 Introduction.....	94
4.2.2 Results and Discussion .....	97
4.2.3 Comparison of PE-ALD Processes using $(PMe_3)_3AuMe_3$ .....	118
<b>4.3 Conclusions.....</b>	<b>121</b>
<b>4.4 Experimental Details .....</b>	<b>123</b>
<b>4.5 Supporting Information .....</b>	<b>126</b>
<b>Chapter 5 Controlling thermal stability and volatility of organogold(I) compounds for vapor deposition with complementary ligand design .....</b>	<b>138</b>
<b>5.1 Abstract .....</b>	<b>139</b>
<b>5.2 Introduction .....</b>	<b>140</b>
<b>5.3 Results and Discussion .....</b>	<b>144</b>
5.3.1 Synthesis and Characterization of Au(I) compounds .....	144
5.3.2 Crystallography.....	146
5.3.3 Thermolysis .....	154
5.3.3 Density Functional Theory .....	160
<b>5.4 Conclusions.....</b>	<b>163</b>
<b>5.5 Experimental Details .....</b>	<b>164</b>
<b>5.6 Supporting Information .....</b>	<b>175</b>
<b>Chapter 6 <i>In-situ</i> monitoring of the chemisorption behavior of gold vapour deposition precursors and preliminary assessment of a potential kinetically-limited ALD precursor.....</b>	<b>187</b>

<b>6.1 Abstract .....</b>	188
<b>6.2 Introduction .....</b>	189
<b>6.3 Results and Discussion .....</b>	190
6.3.1 Apparatus design and benchmarking of a truly self-limiting precursor .....	190
6.3.2 Surface chemistry of (PMe <sub>3</sub> )AuMe <sub>3</sub> ( <b>1</b> ) with Al <sub>2</sub> O <sub>3</sub> .....	193
6.3.3 CVD of an NHC-Au-CH <sub>2</sub> (SiMe <sub>3</sub> ) precursor on Al <sub>2</sub> O <sub>3</sub> .....	195
6.3.4 Surface chemistry of (PMe <sub>3</sub> )AuCH <sub>2</sub> (SiMe <sub>3</sub> ) ( <b>3</b> ) on Al <sub>2</sub> O <sub>3</sub> .....	197
6.3.5 Surface chemistry of (PMe <sub>3</sub> )AuCH <sub>2</sub> (SiMe <sub>3</sub> ) ( <b>3</b> ) on Au .....	201
6.3.6 Design and preliminary testing of a kinetically limited ALD precursor .....	203
<b>6.4 Conclusions.....</b>	211
<b>6.5 Experimental Details .....</b>	211
<b>6.6 Supporting Information .....</b>	216
<b>Chapter 7 N-Heterocyclic carbenes as self-limiting ligands for ALD .....</b>	<b>220</b>
<b>7.1 Abstract .....</b>	221
<b>7.2 Introduction .....</b>	222
<b>7.3 Results and Discussion .....</b>	224
7.3.1 Synthesis and Thermolysis .....	224
7.3.2 <i>In-situ</i> self-limiting chemisorption behavior of <b>1a</b> and <b>1b</b> .....	234
7.3.4 Deposition behavior of <b>1a</b> and <b>1b</b> using oxygen plasma .....	238
<b>7.4 Future work.....</b>	242
<b>7.5 Conclusions.....</b>	242
<b>7.6 Experimental Details .....</b>	243
<b>7.7 Supporting Information .....</b>	254
<b>Chapter 8 Conclusions .....</b>	<b>265</b>
<b>Chapter 9 References .....</b>	<b>268</b>

# List of Figures

<b>Figure 1.1</b> Schematic of the multiple different elementary steps that occur during CVD. Adapted from Jensen and Kern. <sup>32</sup> .....	4
<b>Figure 1.2</b> Graphical depiction of CVD growth rate (log scale) plotted as a function of inverse temperature .....	5
<b>Figure 1.3</b> Cross-sectional transmission electron microscopy (TEM) image of a void-free Co metal film deposited by CVD .....	6
<b>Figure 1.4</b> Cross-sectional scanning electron microscope (SEM) image of trenches with an aspect ratio of 3 being coated with HfO <sub>2</sub> at different lengths of deposition.....	7
<b>Figure 1.5</b> Diagram showing the different steps of the ALD process.....	9
<b>Figure 1.6</b> A prototypical ALD saturation curve (A) where the GPC of the process saturates at a value of ~ 0.28 Å after a dose of ~15 nmol cm <sup>-2</sup> .....	10
<b>Figure 1.7</b> Cross-sectional scanning electron microscope (SEM) image of a highly conformal 30 nm thick Sc <sub>2</sub> O <sub>3</sub> film deposited by ALD .....	11
<b>Figure 1.8</b> Effect of ligand backbone fluorination on volatility in a series of dimethylgold(III) acetylacetone compounds used for gold CVD.....	16
<b>Figure 1.9</b> β-hydride elimination of a metal alkyl.....	19
<b>Figure 1.10</b> Two metal complexes that bear β-hydrogens (shown explicitly) that cannot undergo the β-hydride elimination reaction. ....	20
<b>Figure 1.11</b> TGA temperature ramp analysis (ramp rate 10 °C min <sup>-1</sup> ) of (PMe <sub>3</sub> )AuCH <sub>2</sub> (SiMe <sub>3</sub> ). <sup>23</sup>	
<b>Figure 1.12</b> DSC ramp experiment (10 °C min <sup>-1</sup> ) of (PMe <sub>3</sub> )AuCH <sub>2</sub> (SiMe <sub>3</sub> ). <sup>25</sup>	
<b>Figure 2.1</b> Au(III) compounds previously used in CVD and ALD. Compounds <b>1</b> , <sup>75,78</sup> <b>2</b> , <sup>78</sup> <b>3</b> , <sup>75,78</sup> and <b>4</b> <sup>74,79</sup> bear a β-diketonate ligand, <b>5</b> , <sup>75,80</sup> <b>6</b> , <sup>80</sup> <b>7</b> , <sup>81</sup> <b>8</b> , <sup>81</sup> and <b>9</b> <sup>75,81</sup> bear a similar β-ketoiminate ligand, <b>10</b> <sup>82,83</sup> and <b>11</b> <sup>83,84</sup> feature rare 1,3-chelating anionic phosphorus-based double ylide ligands .....	32
<b>Figure 2.2</b> Au(III) compounds previously used in CVD and ALD. Compounds <b>12</b> , <sup>86,87</sup> <b>13</b> , <sup>87,88</sup> <b>14</b> , <sup>87,88</sup> and <b>15</b> <sup>74,87,89</sup> bear dithiolate based 1,1-chelating ligands ( <b>12</b> = dialkyldithiophosphinate, <b>13,14</b> = alkylphosphorodithiolate, <b>15</b> = dithiocarbamate. Compound <b>15</b> has been used for Au ALD using O <sub>3</sub> as a co-reagent. Compound <b>16</b> <sup>90</sup> bears a salicylaldiminate ligand (a Schiff base of salicylic acid), <b>17</b> <sup>91</sup> and <b>18</b> <sup>91</sup> bear a hydroxyquinolinate and a thioquinolinate ligand respectively .....	35
<b>Figure 2.3</b> Au(III) and Au(I) compounds previously used in CVD and ALD. Compounds <b>19</b> <sup>79,94,95</sup> and <b>20</b> <sup>94,95</sup> are dimeric carboxylate complexes, <b>21</b> <sup>96,97</sup> is a dimeric siloxide complex, <b>22</b> <sup>98–102</sup> is a trimethylgold(III) complexe bearing a trimethylphosphine coordinative ligand. Compounds <b>23</b> and <b>24</b> bear a fluoroalkyl carboxylate ligand .....	37
<b>Figure 2.4</b> Au(I) compounds previously used in CVD. Compound <b>25</b> <sup>103–105</sup> is a dimeric gold(I) guanidinate, <b>26</b> <sup>106,107</sup> is an iminopyrrolidinate complex, and <b>27</b> <sup>108</sup> is a bicyclic amidinate, <b>28</b> , <sup>109,110</sup> <b>29</b> , <sup>111</sup> and <b>30</b> <sup>110</sup> are trialkylphosphine and N-heterocyclic carbene complexes of gold(I) bis(trimethylsilyl)amide .....	40
<b>Figure 2.5</b> Au(I) compounds previously used in CVD. Compounds <b>31</b> <sup>111,116</sup> and <b>32</b> <sup>116,117</sup> are trialkylphosphine and trifluorophosphine complexes of gold chloride respectively. Compounds <b>33</b> , <sup>118</sup> <b>34</b> , <sup>118</sup> and <b>35</b> <sup>119,120</sup> are complexes of methylgold(I) bearing alkylphosphonite ( <b>33</b> , <b>34</b> ) and trialkylphosphite ligands ( <b>35</b> ). Compounds <b>36</b> , <sup>120–123</sup> <b>37</b> , <sup>120,124</sup> <b>38</b> , <sup>120</sup> and <b>39</b> , <sup>121,125,126</sup> are trialkyl- and dialkylarylpophosphine alkylgold(I) complexes .....	43
<b>Figure 2.6</b> Au(I) compounds previously used in CVD. Compounds <b>40</b> , <sup>127</sup> <b>41</b> , <sup>127,128</sup> and <b>42</b> <sup>129</sup> are trimethylphosphine alkynylgold(I) complexes and trifluoromethylgold(I) complexes, respectively.	

Compounds <b>43</b> , <sup>127</sup> <b>44</b> , <sup>127</sup> <b>45</b> , <sup>127</sup> and <b>46</b> <sup>129</sup> are isocyanate complexes of alkyl, alkynyl, and trifluoromethyl gold(I) .....	46
<b>Figure 2.7</b> Figure of merit minefield diagram for the 46 gold compounds that have been reported to have been used in CVD and ALD under the restrictions given at the beginning of this section .....	48
<b>Figure S-2.8</b> TGA ramp experiment of compound <b>8</b> . Sample mass = 7.413 mg, heating rate = 10 °C min <sup>-1</sup> . A clear inflection point is observed at 151 °C, but the compound still evaporates completely.....	52
<b>Figure S-2.9</b> DSC ramp experiment of compound <b>8</b> . Sample mass = 0.085 mg, heating rate = 10 °C min <sup>-1</sup> . A melting point is observed at 58.6 °C and an exothermic event begins at 168 °C. ....	53
<b>Figure S-2.10</b> TGA ramp experiment of compound <b>42</b> . Sample mass = 9.136 mg, heating rate = 10 °C min <sup>-1</sup> . The residual mass of the analysis was 31.19 %. ....	53
<b>Figure S-2.11</b> DSC ramp experiment of compound <b>42</b> . Sample mass = 0.122 mg, heating rate = 10 °C min <sup>-1</sup> . ....	54
<b>Figure 3.1</b> Molecular structure of <b>1</b> as determined by single crystal X-ray diffraction. Protons are omitted for clarity. Ellipsoids are drawn at 50% probability. ....	61
<b>Figure 3.2</b> TGA ramp experiments of <b>1</b> (green) and <b>2</b> (black) are shown as solid lines. ....	62
<b>Figure 3.3</b> Wires with nanoscale cross sections grown from <b>1</b> (A and B) and <b>2</b> (C and D). ....	63
<b>Figure 3.4</b> Gold plates deposited by <b>1</b> (A-C) and <b>2</b> (D) ....	65
<b>Figure 3.5</b> Top frame shows a TEM image of an irregularly shaped plate grown at 395 °C using <b>1</b> .....	66
<b>Figure 3.6</b> A representation of the proposed mechanism for irregular polygonal plate growth. ....	67
<b>Figure 3.7</b> Time-dependent depositions using <b>1</b> at 430 °C at 0.5, 1, and 2 h points. ....	70
<b>Figure S-3.8</b> Single crystal X-ray diffraction structure of <b>1-Cl</b> .....	76
<b>Figure S-3.9</b> Vapour pressure curves for compounds <b>1</b> and <b>2</b> .....	76
<b>Figure S-3.10</b> SEM images of gold metal deposited from <b>1</b> by CVD shown in order of increasing (A-F) temperature. ....	77
<b>Figure S-3.11</b> SEM images of gold metal deposited from <b>2</b> by CVD shown in order of increasing (A-D) temperature. ....	78
<b>Figure S-3.12</b> XPS survey spectra of the as-deposited gold films on various substrates from either <b>1</b> or <b>2</b> .....	79
<b>Figure 4.1</b> XPS spectra of the phosphorus 2p and gold 4f regions for a film deposited without a water pulse (top) and with a water pulse (bottom). ....	86
<b>Figure 4.2</b> Gold metal deposition from <b>1</b> . Panel a shows the saturation curve as the exposure of <b>1</b> is altered. Panel b shows a photo of the as-deposited film (using a 4 s pulse) with the chemical symbol for “Au” reflected from the surface of a 100 mm wafer.....	89
<b>Figure 4.3</b> TEM of gold metal nanoparticles deposited on a TEM grid after five ALD cycles using <b>1</b> with O <sub>2</sub> * and water as co-reactants. The histogram shows the distribution of particle sizes. ....	90
<b>Figure 4.4</b> (Top) RAIRS difference spectrum after the <b>1</b> dose, (Middle) after the O <sub>2</sub> * pulse, (Bottom) after the H <sub>2</sub> O pulse .....	92
<b>Figure 4.5</b> Equivalent growth per cycle ( <sup>eq</sup> GPC) as a function of injection time of <b>1</b> , and exposure time of H <sub>2</sub> * .....	98
<b>Figure 4.6</b> <sup>eq</sup> GPC as a function of the substrate temperature for injection time lengths of 10 and 20 s for <b>1</b> with a dwell time of 5 s for both. An exposure time of 15 s was used for H <sub>2</sub> *. Depositions were performed on a gold seed layer. A total of 100 ALD cycles were performed	

during each deposition to determine the <sup>eq</sup> GPC value. The error bars for the 10 s Au injection time periods were omitted for clarity. Decomposition of the precursor occurs above 120 °C. ....99	
<b>Figure 4.7</b> a) EDX spectrum of a deposition of the <b>1 + H<sub>2</sub>*</b> process on tissue paper.....100	
<b>Figure 4.8</b> (a) Equivalent thickness of gold as a function of the number of ALD cycles performed on a silicon substrate (native oxide) for a substrate temperature of 50 and 120 °C .....101	
<b>Figure 4.9</b> XPS spectra for a PE-ALD-grown Au film deposited at 120 °C with an equivalent thickness of 21.7 nm .....103	
<b>Figure 4.10</b> Difference spectra for the ( <b>1 + H<sub>2</sub>*</b> ) and ( <b>d<sub>9</sub>-1 + H<sub>2</sub>*</b> ) ALD processes. Thick sputtered gold layers (60nm) were used as substrates and depositions were performed at a substrate temperature of 90 °C. .....105	
<b>Figure 4.11</b> P2p, C1s, Au4f peaks measured by <i>in-vacuo</i> XPS on a gold seed layer after performing the ( <b>1 + H<sub>2</sub>*</b> ) ALD process ending with an H <sub>2</sub> * plasma exposure .....107	
<b>Figure 4.12</b> Mass spectrometry measurements for mass to charge ratios 15 (CH <sub>3</sub> ) and 16 (CH <sub>3</sub> ) during a <b>1 + H<sub>2</sub>*</b> process .....108	
<b>Figure 4.13</b> Deposition using only compound <b>1</b> (black dots) as a function of substrate temperature and the reported growth rate for the gold PEALD process using 1 precursor bubbler (black squares) and 2 precursor bubblers simultaneously (red diamonds) .....111	
<b>Figure 4.14</b> P2p, C1s, Au4f peaks measured by XPS on a gold seed layer after performing a gold ALD process ending with a precursor exposure.....112	
<b>Figure 4.15</b> RAIRS data for an exposure of <b>1</b> on a thick sputtered gold layer at a substrate temperature of 90 °C and 120 °C .....114	
<b>Figure 4.16</b> Reaction scheme of the <b>1 + H<sub>2</sub>*</b> PEALD process in the three different temperature regimes (TMP = PMe <sub>3</sub> ).....117	
<b>Figure 4.17</b> XRD patterns of four ALD deposited gold films on silicon (native oxide), all depositions were performed at a substrate temperature of 120 °C .....119	
<b>Figure 4.18</b> XPS spectra of four gold films on silicon (native oxide) substrates for the air-exposed samples (top panels) and after removal of the top surface by argon sputtering (bottom panels). .....121	
<b>Figure S-4.19</b> The thermogravimetric analysis (TGA) traces for <b>1</b> . a) TGA temperature ramp experiment, ramp rate of 10 °C min <sup>-1</sup> , mass loading = 8.136 mg; b) Isothermal TGA experiment, isothermal temperature = 65 °C, mass loading = 10.051 mg.....131	
<b>Figure S-4.20</b> The evaporation rate for <b>1</b> . The inset is the fitted linear regression and coefficient of determination for the fit. .....132	
<b>Figure S-4.21</b> Scanning electron microscopy images of gold metal films deposited by <b>1</b> . Each of these independent depositions were comprised of 1000 atomic layer deposition cycles using 4s pulses of <b>1</b> , 14 s pulses of O <sub>2</sub> *, and 0.1 s pulses of water with 10 s nitrogen gases purges between each step. .....132	
<b>Figure S-4.22</b> An XPS survey spectrum of a gold film deposited on a Si(100) substrate using 4s pulses of <b>1</b> , 14 s pulses of O <sub>2</sub> *, and 0.1 s pulses of water with 10 s nitrogen gases purges between each step. .....133	
<b>Figure S-4.23</b> A graph of film thickness as a function of cycle number for the <b>1 + O<sub>2</sub>* + H<sub>2</sub>O</b> ALD process. .....133	
<b>Figure S-4.24</b> XRD patterns for deposited gold films with an equivalent thickness between 1.6 and 21.7 nm.....134	
<b>Figure S-4.25</b> <sup>1</sup> H-NMR spectrum of <b>d<sub>9</sub>-1</b> in CDCl <sub>3</sub> . “D” indicates the doublet originating from the PMe <sub>3</sub> group of <b>d<sub>9</sub>-1</b> , * indicates a minor impurity of (PMe <sub>3</sub> )AuCD <sub>3</sub> . .....135	

<b>Figure S-4.26</b> $^{13}\text{C}$ -NMR spectrum of <b>d<sub>9</sub>-1</b> in $\text{CDCl}_3$ . “D” indicates the doublet originating from the $\text{PMe}_3$ group of <b>d<sub>9</sub>-1</b> , * indicates a minor impurity of $(\text{PMe}_3)\text{AuCD}_3$ .....	136
<b>Figure 5.1</b> Solid-state structures of <b>1c</b> , <b>1d</b> , <b>2b</b> , <b>2d</b> , <b>3a</b> , <b>3b</b> , <b>3c</b> , and <b>3d</b> . In the cases of <b>1c</b> and <b>3c</b> only the S enantiomers are shown. Ellipsoids are drawn at 50 % probability in all diagrams.....	147
<b>Figure 5.2</b> Extended structure of <b>3a</b> showing the aurophilic polymer chain. Thermal ellipsoids are shown at 50 % probability.....	150
<b>Figure 5.3</b> $\text{C}_6\text{F}_5 - \text{C}_6\text{F}_5$ intermolecular interactions in <b>3b</b> . The diagram displays pairs that occur along the crystallographic $b \times (a+c)$ plane.....	151
<b>Figure 5.4</b> $\text{C}_6\text{F}_5 - \text{C}_6\text{F}_5$ intermolecular interactions in <b>3c</b> .....	152
<b>Figure 5.5</b> $\text{C}_6\text{F}_5 - \text{C}_6\text{F}_5$ intermolecular interactions in <b>3d</b> . Thermal ellipsoids have been drawn at the 50% probability level .....	153
<b>Figure 5.6</b> TGA of <b>1a-d</b> at a ramp rate of 10 °C/min. The inset vertical ranges show the % mass of Au in each compound (top line) and the final residual mass of the respective analysis (bottom line).....	156
<b>Figure 5.7</b> TGA ramp experiments of <b>2a-d</b> at a ramp rate of 10 °C/min. The inset vertical ranges show the % mass of Au in each compound (top line) and the final residual mass of the respective analysis (bottom line).....	157
<b>Figure 5.8</b> TGA ramp experiments of <b>3a-d</b> at a ramp rate of 10 °C/min. The inset vertical ranges show the % mass of Au in each compound (top line) and the final residual mass of the respective analysis (bottom line).....	158
<b>Figure 5.9</b> Figure of merit “minefield” plot. Green circles indicate a positive figure of merit while red circles indicate a negative figure of merit. The $\sigma$ value of each compound is shown as the radius of each circle in arbitrary units.....	160
<b>Figure 5.10</b> Correlation between <i>ab initio</i> -calculated Au-L bond dissociation energies and the observed self-decomposition temperatures for <b>2a,d</b> and <b>3a,d</b> .....	162
<b>Figure S-5.11</b> Vapour pressure curve of <b>1a</b> , $T_1 \text{ Torr} = 68$ °C.....	175
<b>Figure S-5.12</b> Vapour pressure curve of <b>1d</b> , $T_1 \text{ Torr} = 157$ °C.....	175
<b>Figure S-5.13</b> Vapour pressure curve of <b>2a</b> , $T_1 \text{ Torr} = 87$ °C.....	176
<b>Figure S-5.14</b> Vapour pressure curve of <b>2c</b> , $T_1 \text{ Torr} = 134$ °C.....	176
<b>Figure S-5.15</b> Vapour pressure curve of <b>2d</b> , $T_1 \text{ Torr} = 150$ °C.....	177
<b>Figure S-5.16</b> Vapour pressure curve of <b>3a</b> , $T_1 \text{ Torr} = 152$ °C.....	177
<b>Figure S-5.17</b> Vapour pressure curve of <b>3c</b> , $T_1 \text{ Torr} = 148$ °C.....	178
<b>Figure S-5.18</b> Vapour pressure curve of <b>3d</b> , $T_1 \text{ Torr} = 200$ °C.....	178
<b>Figure S-5.19</b> Differential scanning calorimetry (exotherms up) of <b>1a</b> , $T_m = 62$ °C, $T_{dec} = 130$ °C .....	179
<b>Figure S-5.20</b> Differential scanning calorimetry (exotherms up) of <b>1b</b> , $T_{dec} = 107$ °C.....	180
<b>Figure S-5.21</b> Differential scanning calorimetry (exotherms up) of <b>1c</b> , $T_m$ (dec.) = 129 °C, $T_{dec} = 129$ °C.....	180
<b>Figure S-5.22</b> Differential scanning calorimetry (exotherms up) of <b>1d</b> , $T_m = 111$ °C, $T_{dec} = 189$ °C .....	181
<b>Figure S-5.23</b> Differential scanning calorimetry (exotherms up) of <b>2a</b> , $T_{dec} = 146$ °C .....	181
<b>Figure S-5.24</b> Differential scanning calorimetry (exotherms up) of <b>2b</b> , $T_m = 134$ °C, $T_{dec} = 152$ °C .....	182
<b>Figure S-5.25</b> Differential scanning calorimetry (exotherms up) of <b>2c</b> , $T_m = 66$ °C, $T_{dec} = 118$ °C .....	182

<b>Figure S-5.26</b> Differential scanning calorimetry (exotherms up) of <b>2d</b> , $T_m = 105\text{ }^\circ\text{C}$ , $T_{dec} = 184\text{ }^\circ\text{C}$ .....	183
<b>Figure S-5.27</b> Differential scanning calorimetry (exotherms up) of <b>3a</b> , $T_m = 151\text{ }^\circ\text{C}$ , $T_{dec} = 185\text{ }^\circ\text{C}$ .....	183
<b>Figure S-5.28</b> Differential scanning calorimetry (exotherms up) of <b>3b</b> , $T_m = 157\text{ }^\circ\text{C}$ , $T_{dec} = 220\text{ }^\circ\text{C}$ .....	184
<b>Figure S-5.29</b> Differential scanning calorimetry (exotherms up) of <b>3c</b> , $T_m = 150\text{ }^\circ\text{C}$ , $T_{dec} = 253\text{ }^\circ\text{C}$ .....	185
<b>Figure S-5.30</b> Differential scanning calorimetry (exotherms up) of <b>3d</b> , $T_m = 177\text{ }^\circ\text{C}$ , $T_{dec} = 300\text{ }^\circ\text{C}$ .....	185
<b>Figure 6.1</b> Home-made ALD tool used in this study.....	191
<b>Figure 6.2</b> QCM data obtained from performing 100 cycles of [0.1 s TMA   15 s N <sub>2</sub> purge   0.1 s H <sub>2</sub> O   15 s N <sub>2</sub> purge] at 150 °C.....	192
<b>Figure 6.3</b> a) 100 cycles of [0.1 s TMA   15 s N <sub>2</sub> purge] on an Al <sub>2</sub> O <sub>3</sub> coated QCM crystal at 150 °C .....	193
<b>Figure 6.4</b> a) Full dataset of 100 cycles of [1 s (1)   15 s N <sub>2</sub> purge] at 120 °C deposited on an Al <sub>2</sub> O <sub>3</sub> -coated QCM crystal; b) enhanced view of the first 5 doses of 1; c) enhanced view of 6 doses near the end of the experiment .....	195
<b>Figure 6.5</b> a) QCM data from 60 cycles of [1 s (2)   15 s N <sub>2</sub> purge] at 140 °C QCM temperature. ....	196
<b>Figure 6.6</b> a) Overlay of QCM data obtained from 100 cycle experiments of <b>3</b> alone (blank), <b>3</b> + H <sub>2</sub> O (red), and <b>3</b> + FA (blue) .....	198
<b>Figure 6.7</b> Saturation curve experiments for the <b>3</b> + FA process. 500 cycles were performed for each experiment.. .....	199
<b>Figure 6.8</b> QCM micrograph of the double experiment where 200 cycles of [3s <b>3</b>   15 s N <sub>2</sub> purge   0.2 s FA   15 s N <sub>2</sub> purge] were performed on a gold-coated QCM crystal.....	202
<b>Figure 6.9</b> TGA ramp experiments of <b>3a-d</b> . Ramp rate = 10 °C min <sup>-1</sup> , 10 ± 2 mg mass loading, Pt sample pans were used in all experiments.....	205
<b>Figure 6.10</b> DSC ramp experiments of <b>3a-d</b> . Temperature ramp rate = 10 °C min <sup>-1</sup> , sample loading = 0.4 ± 0.1 mg, aluminum hermetic sample pans were used for all analyses.....	206
<b>Figure 6.11</b> A 10-min exposure experiment of <b>3a</b> at 97 °C .....	207
<b>Figure 6.12</b> Growth rate of the mass-transport-limited regime of the 10-min exposure experiments of <b>3a</b> .....	208
<b>Figure 6.13</b> QCM micrograph data from Figure 5.11 (a) (10 min dose of <b>3a</b> , surface temperature = 97 °C) overlaid with its derivative curve (blue). The peak growth rate was 59 ng cm <sup>-2</sup> s <sup>-1</sup> .....	209
<b>Figure 6.14</b> Peak growth rate of <b>3a</b> (black) and <b>3c</b> (red) plotted as a function of substrate temperature. The source temperatures of <b>3a</b> and <b>3c</b> were 70 °C and 110 °C respectively.....	210
<b>Figure S-6.15</b> Comparison of the total mass gain from 100 cycles of [1 s (1)   15 s N <sub>2</sub> purge] (blank) with 100 cycles of [1 s (1)   15 s N <sub>2</sub> purge   (Co-reagent dose)   15 s N <sub>2</sub> purge].....	216
<b>Figure S-6.16</b> Comparison of the total mass gain from 100 cycles of [1 s (1)   15 s N <sub>2</sub> purge] (blank) with 100 cycles of [1 s (1)   15 s N <sub>2</sub> purge   (Co-reagent dose)   15 s N <sub>2</sub> purge].....	217
<b>Figure S-6.17</b> Langmuir vapour pressure curves for <b>3c</b> and <b>3d</b> . Their respective lines of best fit are $\ln P$ (Torr) = -6576( $T^{-1}$ , °C <sup>-1</sup> ) + 22.51 ( $R^2 = 0.9990$ ) and $\ln P$ (Torr) = -7733( $T^{-1}$ , °C <sup>-1</sup> ) + 23.72 ( $R^2 = 0.9990$ ).....	218
<b>Figure 7.1</b> TGA ramp experiments of <b>1a</b> , <b>1b</b> , and <b>1c</b> (ramp rate = 10 °C min <sup>-1</sup> ).....	228
<b>Figure 7.2</b> TGA ramp experiments of <b>2a</b> , and <b>2b</b> (ramp rate = 10 °C min <sup>-1</sup> ).....	230

<b>Figure 7.3</b> TGA ramp experiments of <b>3a</b> , <b>3b</b> , <b>4a</b> , <b>4b</b> , and <b>4c</b> (ramp rate = 10 °C min <sup>-1</sup> ).....	231
<b>Figure 7.4</b> TGA ramp experiments of <b>5a</b> , and <b>5b</b> (ramp rate = 10 °C min <sup>-1</sup> ).....	233
<b>Figure 7.5</b> Dual QCM / QMS <i>in situ</i> monitoring of <b>1a</b> . The pulse sequence was [6s <b>1a</b>   3 min N <sub>2</sub> purge] x 5 then [10 min <b>1a</b>   5 min purge] x 3 and is depicted graphically above the top frame.	
.....	236
<b>Figure 7.6</b> QCM micrograph of a single hour-long dose of compound <b>1b</b> at 150 °C. ....	237
<b>Figure 7.7</b> AFM images of the 500-cycle film (~30.1 nm thickness) (a) and the 1000-cycle film (~54.9 nm thickness) (b) deposited on glass. The RMS roughness values of the 500-cycle and 1000-cycle films were 4.6 nm and 3.3 nm respectively. ....	239
<b>Figure 7.8</b> XPS spectra the as-deposited (a) and Ar <sup>+</sup> sputtered (b) gold film (54.9 nm thickness) deposited from 1000 cycles of <b>1a</b> and O <sub>2</sub> <sup>*</sup> on a silicon substrate which was terminated in it's native oxide. The asterisks (*) in panel a denote the O 1s (530.7 eV) and C 1s (283.7 eV) peak envelopes. ....	240
<b>Figure S-7.9</b> DSC of compound <b>1a</b> . Ramp rate = 10 °C min <sup>-1</sup> . T <sub>m</sub> = 62 °C, T <sub>D</sub> = 145.4 °C .....	254
<b>Figure S-7.10</b> DSC of compound <b>1b</b> . Ramp rate = 10 °C min <sup>-1</sup> . T <sub>m</sub> = 78 °C, T <sub>D</sub> = 202.5 °C ....	254
<b>Figure S-7.11</b> DSC of compound <b>1c</b> . Ramp rate = 10 °C min <sup>-1</sup> . T <sub>m</sub> = 61 °C, T <sub>D</sub> = 214.4 °C ....	255
<b>Figure S-7.12</b> DSC of compound <b>2a</b> . Ramp rate = 10 °C min <sup>-1</sup> . T <sub>m</sub> = 121 °C, T <sub>D</sub> = 179.7 °C ..	255
<b>Figure S-7.13</b> DSC of compound <b>2b</b> . Ramp rate = 10 °C min <sup>-1</sup> . T <sub>m</sub> = 80 °C, T <sub>D</sub> = 167.0 °C ....	256
<b>Figure S-7.14</b> DSC of compound <b>3a</b> . Ramp rate = 10 °C min <sup>-1</sup> . T <sub>m</sub> = 140 °C, T <sub>D</sub> = 164.5 °C ..	256
<b>Figure S-7.15</b> DSC of compound <b>3b</b> . Ramp rate = 10 °C min <sup>-1</sup> . T <sub>m</sub> = 63 °C, T <sub>D</sub> = 154.9 °C....	257
<b>Figure S-7.16</b> DSC of compound <b>4a</b> . Ramp rate = 10 °C min <sup>-1</sup> . T <sub>m</sub> = 142 °C, T <sub>D</sub> = 167.6 °C ...	257
<b>Figure S-7.17</b> DSC of compound <b>4b</b> . Ramp rate = 10 °C min <sup>-1</sup> . T <sub>m</sub> = 75 °C, T <sub>D</sub> = 150.9 °C ....	258
<b>Figure S-7.18</b> DSC of compound <b>4c</b> . Ramp rate = 10 °C min <sup>-1</sup> . T <sub>D</sub> = 207.0 °C .....	258
<b>Figure S-7.19</b> DSC of compound <b>4c</b> . Ramp rate = 10 °C min <sup>-1</sup> . T <sub>m</sub> = 137 °C, T <sub>D</sub> = 189.0 °C ..	259
<b>Figure S-7.20</b> DSC of compound <b>4c</b> . Ramp rate = 10 °C min <sup>-1</sup> . T <sub>m</sub> = 86 °C, T <sub>D</sub> = 189.0 °C ....	259
<b>Figure S-7.21</b> Picosun R200 PE-ALD apparatus substrate holder carrying (left to right) silicon, glass and Pt-coated Si substrates immediately after the 1000-cycle experiment using <b>1a</b> + O <sub>2</sub> *. Both the substrates and the holder were completely covered in a bright golden film. ....	260
<b>Figure S-7.22</b> High-resolution XPS spectrum of the C 1s peak envelope on the as-deposited film produced by 1000 cycles of <b>1a</b> + O <sub>2</sub> * (full spectrum shown in Figure 6.8a).....	261
<b>Figure S-7.23</b> High-resolution XPS spectrum of the N 1s peak envelope on the as-deposited film produced by 1000 cycles of <b>1a</b> + O <sub>2</sub> * (full spectrum shown in Figure 6.8a).....	262
<b>Figure S-7.24</b> Substrates coated using the 1000-cycle experiment of <b>1b</b> + O <sub>2</sub> * (clockwise from top left) silicon, aluminum, Pt-coated Si, and glass microscope slide. ....	263
<b>Figure S-7.25</b> EDX spectrum of the the as-deposited film produced by 1000 cycles of <b>1b</b> + O <sub>2</sub> * on an aluminum substrate.....	264

## List of Tables

<b>Table 4.1</b> Compositional analysis by XPS of the film formed without water and the film formed with water.....	87
<b>Table 4.2</b> Elemental concentrations of Au, C, O, and P of an Au film grown at 120 °C as determined by XPS. The equivalent thickness of the Au film was 21.7 nm (800 ALD cycles)..	103
<b>Table 4.3</b> Position and assigned vibration modes of the observed features in the FTIR difference spectra displayed in Figure 4.10. The assignment of these peaks is based on reference IR spectra for <b>1</b> and <b>d<sub>9</sub>-1</b> and for the PMe <sub>3</sub> ligand. <sup>212-214</sup> ( $\nu$ stretching, $\delta$ deformation, $\rho$ rocking, as = asymmetric, s = symmetric) .....	106
<b>Table 4.4</b> Atomic concentrations of Au, C, P, and the C/P ratio determined by <i>in-vacuo</i> XPS after exposure of <b>1</b> on a gold seed layer at different temperatures. The samples were transferred from the ALD chamber to the XPS analysis chamber without breaking vacuum. a) Samples transferred immediately after the final precursor exposure. b) Samples transferred 18 hours after the final precursor exposure.....	113
<b>Table 5.1</b> Selected bond distances and angles for the analyzed compounds .....	148
<b>Table 5.2</b> Important metrics obtained from TGA and DSC experiments .....	155
<b>Table 5.3</b> Calculated energies and measured decomposition temperatures of the three ligand dissociation cases for model compounds and synthesized compounds. .....	161
<b>Table 7.1</b> Thermal characteristics of the synthesized precursors. ....	232

# List of Acronyms

<b>4-PP</b>	Four-point probe
<b>AFM</b>	Atomic force microscopy
<b>ALD</b>	Atomic layer deposition
<b>ALE</b>	Atomic layer etching
<b>AZO</b>	Aluminum-doped zinc oxide
<b>BDE</b>	Bond dissociation energy
<b>CCRI</b>	Center for Catalysis Research and Innovation at the University of Ottawa
<b>CVD</b>	Chemical vapour deposition
<b>DCM</b>	Dichloromethane
<b>DFT</b>	Density functional theory
<b>DLR</b>	Diffusion-limited regime
<b>DMSO</b>	Dimethyl sulfoxide
<b>DSC</b>	Differential scanning calorimetry
<b>EBID</b>	Electron-beam-induced deposition
<b>EDX</b>	Energy-dispersive X-ray spectroscopy
<b>FA</b>	Formic acid
<b>FCC</b>	Face-centered-cubic (referring to unit cell of metallic Au)
<b>FESEM</b>	Field-emission scanning electron microscope
<b>FTIR</b>	Fourier-transform infrared (referring to spectroscopy)
<b>GMRFilm</b>	General Motors Research film thickness calculation program
<b>GPC</b>	Growth per cycle
<b>H<sub>2</sub>*</b>	Hydrogen plasma
<b>H-HMDS</b>	Hexamethyldisilazane
<b>HMDS</b>	Hexamethyldisilazide
<b>HR-MS</b>	High-resolution mass spectrometry
<b>IR</b>	Infrared (referring to spectroscopy)

<b>LSPR</b>	Localized surface plasmon resonance
<b>MCT</b>	Mercury cadmium telluride
<b>MTL</b>	Mass-transport-limited (referring to the growth regime of CVD)
<b>MW</b>	Molecular weight
<b>N<sub>2</sub>*</b>	Nitrogen plasma
<b>NHC</b>	N-heterocyclic carbene
<b>NMR</b>	Nuclear magnetic resonance
<b>O<sub>2</sub>*</b>	Oxygen plasma
<b>PE-ALD</b>	Plasma-enhanced atomic layer deposition
<b>PVD</b>	Physical vapour deposition
<b>QCM</b>	Quartz crystal microbalance
<b>QMS</b>	Quadrupole mass spectrometry
<b>RAIRS</b>	Reflection absorption infrared spectroscopy
<b>RBS</b>	Rutherford backscattering spectroscopy
<b>RF</b>	Radio frequency
<b>sc-XRD</b>	Single-crystal X-ray diffraction
<b>SEM</b>	Scanning electron microscopy
<b>SERS</b>	Surface-enhanced Raman spectroscopy
<b>T<sub>D</sub></b>	Decomposition temperature
<b>T<sub>Dec</sub></b>	Decomposition temperature
<b>TEM</b>	Transmission electron microscopy
<b>TGA</b>	Thermogravimetric analysis
<b>THF</b>	Tetrahydrofuran
<b>T<sub>m</sub></b>	Melting temperature
<b>TMA</b>	Trimethylaluminum
<b>TMS</b>	Tetramethylsilane
<b>TMS-ylide</b>	Trimethylphosphonium(trimethylsilyl)methylide
<b>TOF-ERDA</b>	Time-of-flight elastic recoil detection analysis

<b>TOF-SIMS</b>	Time-of-flight secondary-ion mass spectrometry
<b>TPD</b>	Temperature programmed desorption
<b>T<sub>v</sub></b>	1 Torr temperature
<b>UV</b>	Ultraviolet (referring to spectroscopy)
<b>VLS</b>	Vapor-liquid-solid (referring to a mechanism of nanowire growth)
<b>XPS</b>	X-ray photoelectron spectroscopy
<b>XRD</b>	X-ray diffraction
<b>XRF</b>	X-ray fluorescence (referring to spectroscopy)
<b>XRR</b>	X-ray reflectivity
<b>ylide</b>	Trimethylphosphoniummethylide



# Chapter 1 Introduction

## 1.1 Motivation for gold thin films and nanoparticles

Gold is a rare but incredibly useful element due to its chemical inertness and its high electrical conductivity. Since it is so inert, devices that contain gold metal as a critical component last much longer than those with another conductor such as copper or aluminum.

But gold can serve other purposes than being used as a conductive material. Since as early as the 4<sup>th</sup> century CE, metallic nanoparticles have been used to give colour to objects.<sup>1</sup> We now know that these effects are due to the plasmonic absorption of light by the electrons within the metal nanoparticle.<sup>2,3</sup> The metal's electrons are free to move with a very low energy barrier. The electric field of the incoming photon can interact with the electrons in the metal and transfer energy to those metal electrons. This can occur in all metals, no matter the dimension, and we refer to the resulting oscillating plasma in the metal as consisting of plasmons, just as light consists of photons.

The wavelength of light required to excite a plasmon in a metal depends on the size of the metal particle, as well as its electrical conductivity. For a nanoparticle of gold of dimensions between 10 and 100 nm, a plasmon can be excited by light of a wavelength between ~475 to ~800 nm, the blue green to red range of the visible spectrum. Since these nanoparticles are so small, the plasmon extends over the entire particle and is referred to as a localized surface plasmon, and the phenomenon as a localized surface plasmon resonance (LSPR). Isolated particles can possess LSPR, where extended 2-D metals whose thickness is in the range of ~10 to ~100 nm can possess surface plasmon resonance, where the plasmon is delocalized over the 2-D nanomaterial.

Thin films of gold nanoparticles have been used in a multitude of applications, including plasmonic sensing,<sup>4–13</sup> photovoltaic devices,<sup>14–19</sup> catalysis,<sup>20–25</sup> and electrochemical CO<sub>2</sub> reduction,<sup>26–30</sup> and will continue to be a desired material for years to come. For these applications, having a high surface area or a complex surface morphology is often beneficial to the optimal device performance. Furthermore, having fine control over the

nanoparticle's size, size distribution, overall thickness of a film of nanoparticles, and being able to select where on the surface the nanoparticles are deposited are desirable factors when constructing a device. Traditional methods that have been used (e.g., physical vapour deposition, colloidal synthesis, solution-phase deposition) offer some of these benefits, but lack a combination of the ability to fine-tune film thickness control, nanoparticle size, and "conformality" of a coating on a complex substrate. A methodology that accomplishes all these tasks would enable the creation of new plasmonic devices and a new generation of technologies.

## 1.2 Chemical vapour deposition

Nearly all microelectronics are fabricated in part using chemical vapour deposition (CVD).<sup>31</sup> CVD is different from other thin film deposition techniques because the growing film is produced by a chemical reaction at the gas-solid interface, as well as chemical reactions in the gas phase prior to deposition. These depositions are generally done under reduced pressure to ensure that the precursor chemical has a high partial pressure in the system, and to allow better mass-transport of the precursors and byproducts through the system.

These aspects of CVD make it a superior thin film deposition technique compared to many others. For instance, the gaseous reactive species are able to coat complex substrates much more conformally than physical deposition techniques because they behave as a gas inside the deposition chamber and can thus react at surfaces that are out of line-of-sight of the precursor source. Also, the metal-containing compounds used in CVD (called precursors) are much more volatile than the bulk metal that they contain, and so it takes less energy to deliver a metal such as tungsten or gold to the reaction surface as a chemical compound compared to delivery in a physical deposition method. Furthermore, since the vapour can diffuse throughout the entire space of the reactor, CVD is a highly scalable and bottom-up deposition technique for nanomaterials.

The overall CVD process is complex, and many different physical and chemical phenomena occur during deposition. A schematic depicting these phenomena is shown

in Figure 1.1 below. The precursor(s) enter the reaction chamber over top of the substrate (1) and are often carried in an inert gas flow to improve precursor flow in the apparatus. Sometimes the initial precursor undergoes a gas-phase reaction (2) before reacting with the surface. This could be initiated by the increased temperature in the reaction chamber or by the precursor reacting with a gaseous co-reactant. The precursor is then transported to the surface mainly by the turbulent flow of the carrier gas (3), but also by diffusion which becomes more relevant when considering a very low pressure system and/or high surface area substrate where the precursors must diffuse into small pores. When the precursor encounters the surface, it first undergoes physisorption to the surface through intermolecular forces such as dispersion interactions, dipole-dipole interactions, or other non-covalent bonding interactions (4). Then the physisorbed precursor can undergo surface diffusion and migrate to different locations on the surface (5). It can also desorb from the surface and re-enter the gas phase (6), after which the precursor may either re-adsorb to the surface at step 4 or be transported out of the system by the carrier gas. If the physisorbed precursor does not desorb from the surface, it can undergo chemisorption to the surface, and form a chemical bond to the surface. Chemisorption, like other chemical reactions, occurs preferentially at the sites of highest chemical potential on the surface.

At this point, the chemisorbed precursor either undergoes thermal decomposition on the surface to produce the desired material, or it reacts with a co-reagent to form the desired material. If this chemical event is one of the first to occur during the process, then film growth is said to be in the nucleation stage (7). As more material gets deposited, then the overall film begins to grow with one of two distinct morphologies. If the surface energies of the substrate and thin film do not match, then the film's surface energy is most easily minimized by coalescence which results in a minimization of its contact area with the substrate and results in island growth (7) and generally poor adhesion.

If the surface energies of the substrate and thin film are similar, then the depositing material might grow as a continuous 2-D film that is bound to the substrate through strong adhesion. Since the growth rate of the film is dependant on the rate of chemisorption to the substrate, films deposited by CVD preferentially grow on certain substrates in the

presence of others, and thus the technique offers a bottom-up chemical selectivity that physical thin film deposition techniques do not.

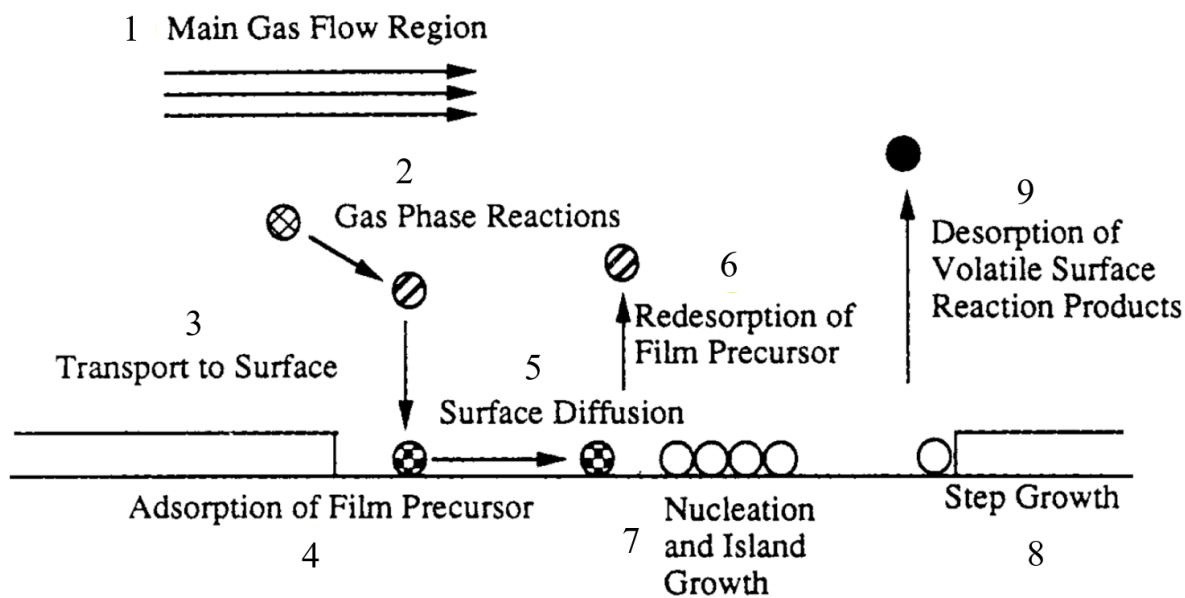


**Figure 1.1** Schematic of the multiple different elementary steps that occur during CVD. Adapted from Jensen and Kern.<sup>32</sup>

Regardless of the mode of growth, physisorbed precursors preferentially undergo chemisorption and further reaction at the surface sites with the highest surface energy. Thus, in an island growth scenario deposition occurs preferentially on vertex atoms of a nanocrystal, then at the edges, then finally on a face, which ultimately results in the deposition of spherical nanoparticles in the absence of a surfactant. In a 2-D film growth scenario, growth occurs preferentially at the step edge (vertex) between the top layer and the 1<sup>st</sup> sublayer which results in continuous film growth (8). After the chemical reaction has taken place, it is ideal that by-products of the reaction be volatile chemical species so that they can desorb from the surface and be exhausted from the system (9). If the by-products are not volatile, they might become incorporated into the film which can ruin its material properties.

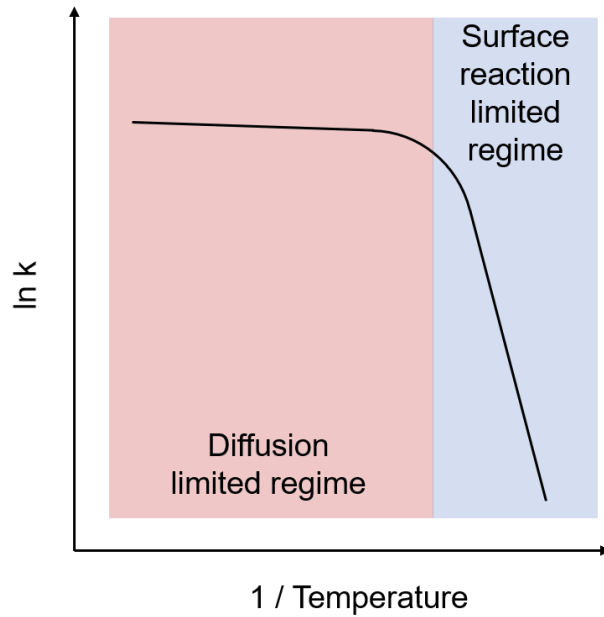


**Figure 1.2** Graphical depiction of CVD growth rate (log scale) plotted as a function of inverse temperature showing the diffusion limited regime (DLR, high T) and surface reaction limited (SRL, low T) regimes.

For CVD to be scalable, significant control over the film growth rate is required. Since CVD is driven by chemical reactions, its reaction rate can be described by the Arrhenius equation when there is an abundance of precursor in the system. At low temperatures, the rate of reaction is slow compared to the rate of precursor delivery to the system, and the process is described as surface reaction rate-limited (Figure 1.2). In this regime, film growth is exponentially dependant on the temperature of the substrate where the reaction is taking place. If we assume that the exposure of precursor to the surface is always constant, then as the temperature of the system increases, there will come a point where the surface reaction becomes faster than the exposure of the precursor. Here, the system enters the diffusion-limited regime. In this regime, the rate limiting step of the overall process is the precursor flux to the surface, and thus a rate dependence on temperature no longer exists (to an ideal approximation). Since depositing a thin film of uniform thickness is generally a requirement for CVD experiments, operating in the surface reaction rate-limited regime is essential because in this growth regime the rate of surface reaction at every point on the substrate is much lower than the precursor flux to the surface, which results in a slower but more uniform thin film deposition.

CVD has been used to grow many different materials for a vast array of applications. In the microelectronics industry, liner materials for metal interconnects and the metal interconnects themselves are just two parts of the overall device that are fabricated with CVD.<sup>33–38</sup> In modern architectures, this means lining or infilling a deep trench or via so that an electrical connection can be made from the top of the device to all logic layers buried within the device. As previously discussed, CVD is superior to physical vapour deposition techniques because it is not hindered by line of sight issues and can thus deposit films on these complex structures with quite high conformality (Figure 1.3).

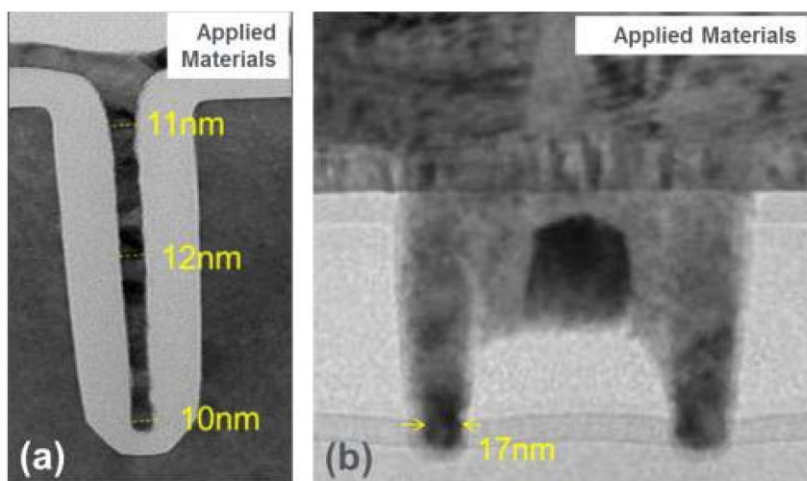


**Figure 1.3** Cross-sectional transmission electron microscopy (TEM) image of a void-free Co metal film deposited by CVD into (a) 10 nm diameter trench and (b) 17 nm critical diameter dual damascene ULk structure.<sup>39</sup> © 2017 IEEE

But these depositions do not always work perfectly, and often suffer from “pinch-off” and void formation phenomena simply due to the fact that there is a higher concentration of precursor at the top of the structure than at the bottom.<sup>40</sup> Even low-aspect-ratio structures can suffer from void formation when being coated by CVD (Figure 1.4). The case shown here is not too severe: almost half of the trench was completely infilled, but as the aspect ratio of a feature increases the problem becomes more and more severe.

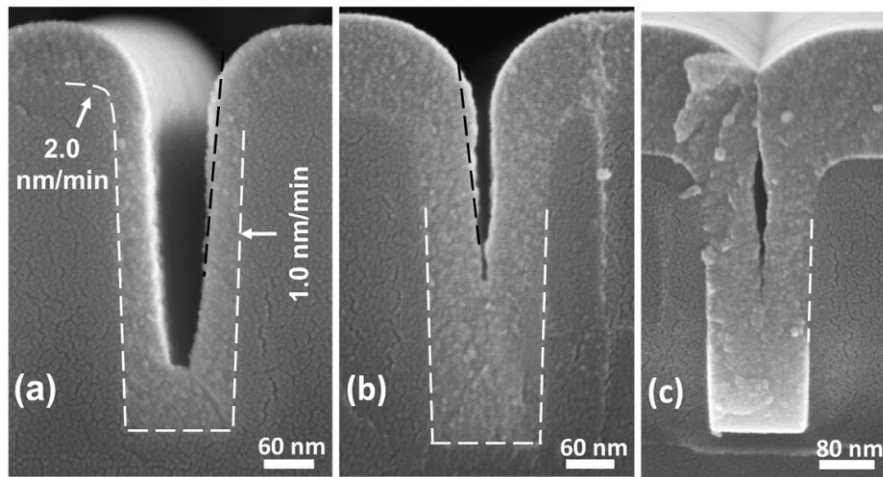


**Figure 1.4** Cross-sectional scanning electron microscope (SEM) image of trenches with an aspect ratio of 3 being coated with HfO<sub>2</sub> at different lengths of deposition. Reproduced from Journal of Vacuum Science & Technology A 37, 021509 (2019); <https://doi.org/10.1116/1.5068684> with permission of the American Vacuum Society

Even when just a very thin liner film is to be deposited on these structures, the deposited film can end up being thicker at the top of the via than at the bottom due to the precursor concentration gradient. Although there are some new methodologies in CVD that have overcome this conformality issue for certain processes, for next generation microelectronics where the size constraints are shrinking rapidly, a better vapour deposition method that can deposit films with perfect conformality has been sought.

### 1.3 Atomic Layer deposition

A diagram of a prototypical ALD process is shown in Figure 1.5. The defining phenomenon of ALD is that when a precursor is dosed into the system, it reacts with the surface in a self-limiting fashion. When a surface is exposed to an excess of precursor A, the reaction between precursor A and the surface goes to completion, and after that point no further reaction or uptake of precursor occurs. This is called self-limiting chemisorption or surface saturation by precursor A (Figure 1.5-1). Once the surface has become saturated, the excess precursor A is removed by the system by flushing the system with a large amount of inert gas in a “purge” step (Figure 1.5-2). The purge step is essential

because any interaction between precursor A and precursor B (which will be introduced in the next step) may lead to gas-phase reactions or uncontrolled surface reactions which are not intended in this process. Once the purge step is complete, a co-reagent (precursor B) is dosed into the system where it reacts with the surface, again in a self-limiting fashion. The purpose of the co-reagent is to reactivate the surface such that precursor A can once again chemisorb, as well as to complete the formation of a layer of target film. Sometimes this is done by the co-reagent leaving an extra functional group on the surface, but it can also be achieved by the co-reagent removing a protective ligand from the surface (Figure 1.5-3). Once the co-reagent surface reaction has gone to completion, excess gas-phase co-reagent is removed from the system by another purge step (Figure 1.5-4). These four steps constitute one ALD cycle, where ideally a single monolayer of the material of interest has been deposited. For a binary material, generally the co-reagent (precursor B) provides the second element to the material, so that ALD using a combination of precursor A and precursor B makes a material of the chemical formula  $A_xB_y$ .

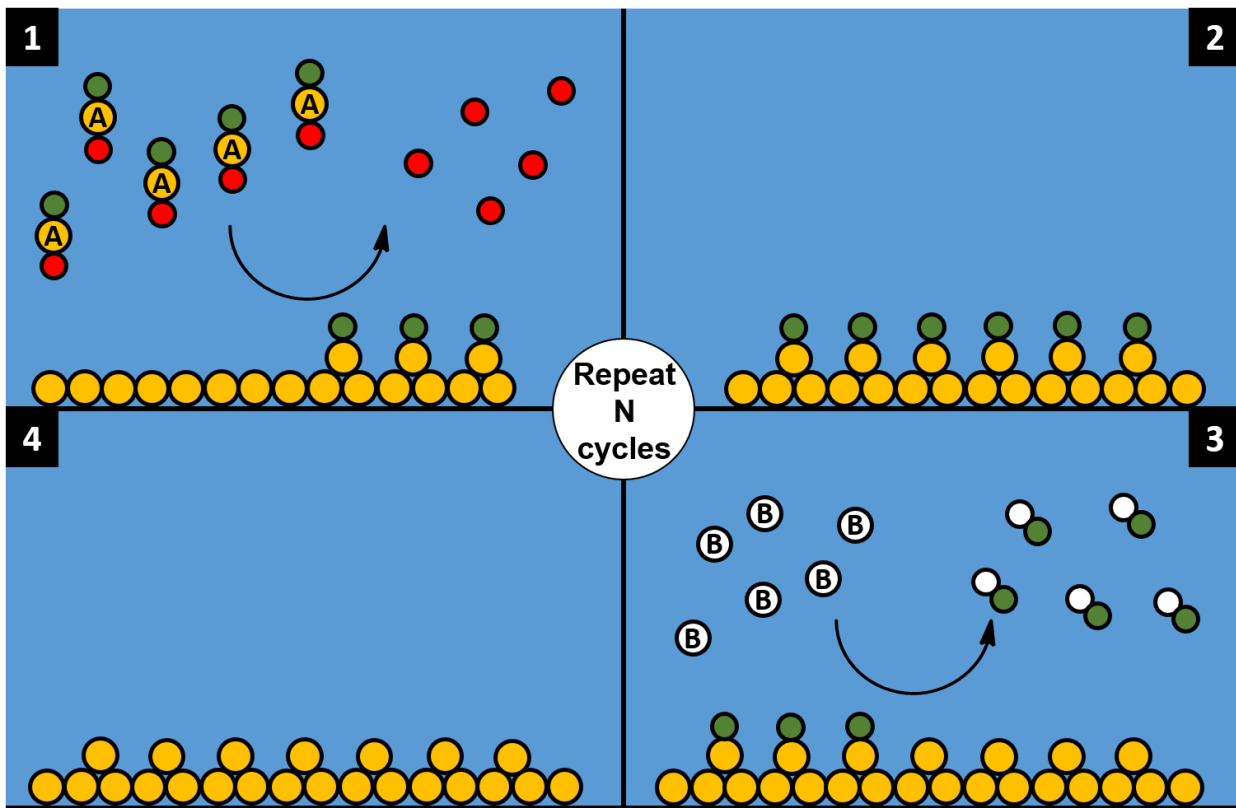


**Figure 1.5** Diagram showing the different steps of the ALD process. 1) Precursor A is dosed into the system and reacts with the surface in a self-limiting fashion. 2) Excess precursor A and byproducts of the first reaction are purged from the system. 3) Precursor B is introduced to the system and reacts with the monolayer that was formed in step 1 in a self-limiting fashion, which reactivates the surface towards chemisorption of precursor A. 4) Excess precursor B and byproducts of its reaction are purged from the system. Steps 1-4 constitute one ALD cycle, which can be performed any number of times to grow a film of the desired thickness.

When depositing thin films of elemental materials (such as metals), the co-reagent is often used to remove protective ligands from the surface and reactivate the surface towards growth. This does not mean that a fragment from precursor B cannot remain on the surface, but in that case the fragment must be somehow removed by reaction with precursor A. For example, when depositing Co metal using  $\text{CoCp}_2$  and  $\text{NH}_3^*$  (ammonia plasma), Vos *et al* found that  $\text{NH}_x$  fragments remained on the surface and participated in the subsequent reaction with  $\text{CoCp}_2$ .<sup>41</sup> Van Daele *et al* found that when depositing Pt metal using  $(\text{Cp}^{\text{Me}})\text{PtMe}_3$  and  $\text{O}_2$  or  $\text{O}_2^*$ , these co-reagents partially oxidize the surface to form Pt-OH functional groups.<sup>42</sup> These Pt-OH functional groups then participate in a

combustion reaction with the ligands of the subsequent  $(Cp^{Me})PtMe_3$  and therefore aid in the chemisorption process. As another example,  $H_2$  or  $H_2^*$  are common co-reagent choices when depositing metals by ALD, and one could envision that catalytically active hydrogenation metals would become terminated in M-H functional groups and serve as the reactive surface species for the subsequent precursor exposure.

There is only one characteristic test that defines a process as an ALD process, which is that the film growth per cycle (GPC) is independent of the dosage of all precursors. By plotting a graph of GPC vs. precursor dose at constant temperature, an ALD process will have a GPC that remains constant at long precursor dose times, but a CVD process will always show an increase in GPC with respect to precursor dose (Figure 1.6).<sup>43</sup> This self-limiting test must be satisfied for all precursors, and most importantly when testing a precursor for saturation the other precursor(s) must be used with saturated doses.

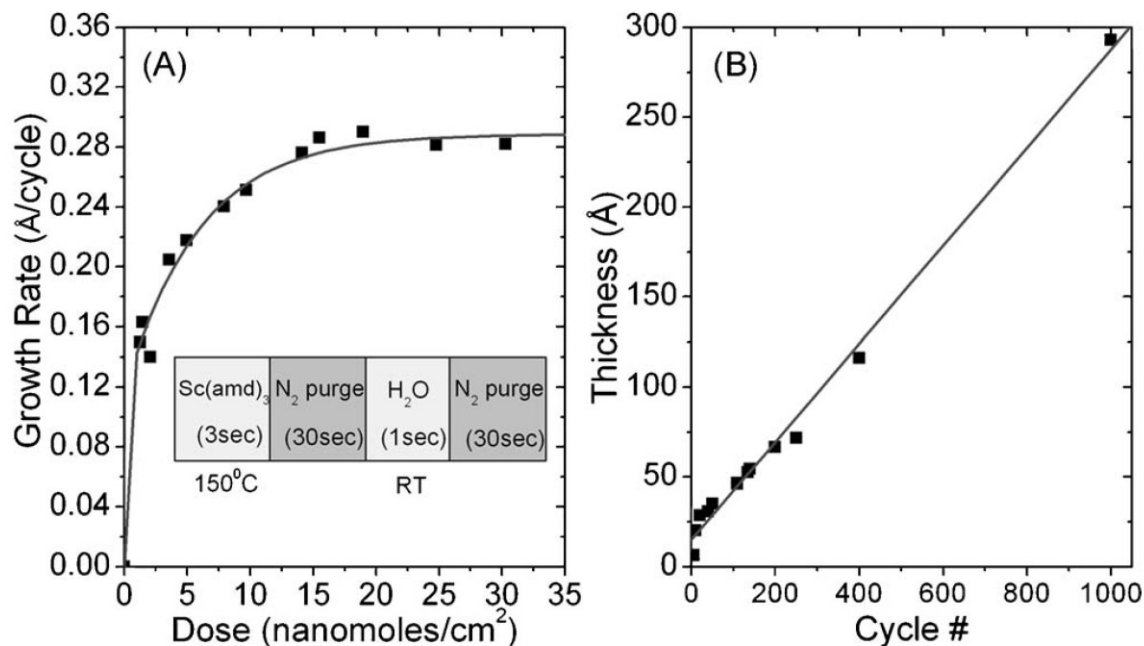


**Figure 1.6** A prototypical ALD saturation curve (A) where the GPC of the process saturates at a value of  $\sim 0.28 \text{ \AA}$  after a dose of  $\sim 15 \text{ nmol cm}^{-2}$ . This process deposits  $Sc_2O_3$  by using an amidinate complex of scandium ( $Sc(\text{amd})_3$ ) as precursor A and  $H_2O$  as precursor B. This process displays a linear film thickness increase with respect to cycle number (B), but the intercept of this trend crosses 0 cycles at a non-0 thickness value, implying that the growth rate of  $Sc_2O_3$  on the

substrate (HF-dipped silicon) is faster than the growth of  $\text{Sc}_2\text{O}_3$  on  $\text{Sc}_2\text{O}_3$ . Reproduced with permission from *Electrochemical and Solid-State Letters*, 9 (6) F45-F48 (2006).

When an ALD process is properly optimized, extremely high conformality can be achieved. Furthermore, the cyclical nature of ALD allows a cycle-by-cycle tuning of the stoichiometry of a film. For example, Figure 1.7 shows a 60:1 aspect ratio via that was coated by the  $\text{Sc}_2\text{O}_3$  process shown in Figure 1.6. This type of conformality is very difficult to achieve with CVD methods, but can be accomplished by ALD with a small amount of process optimization, and is essential to the development of cutting-edge technologies.

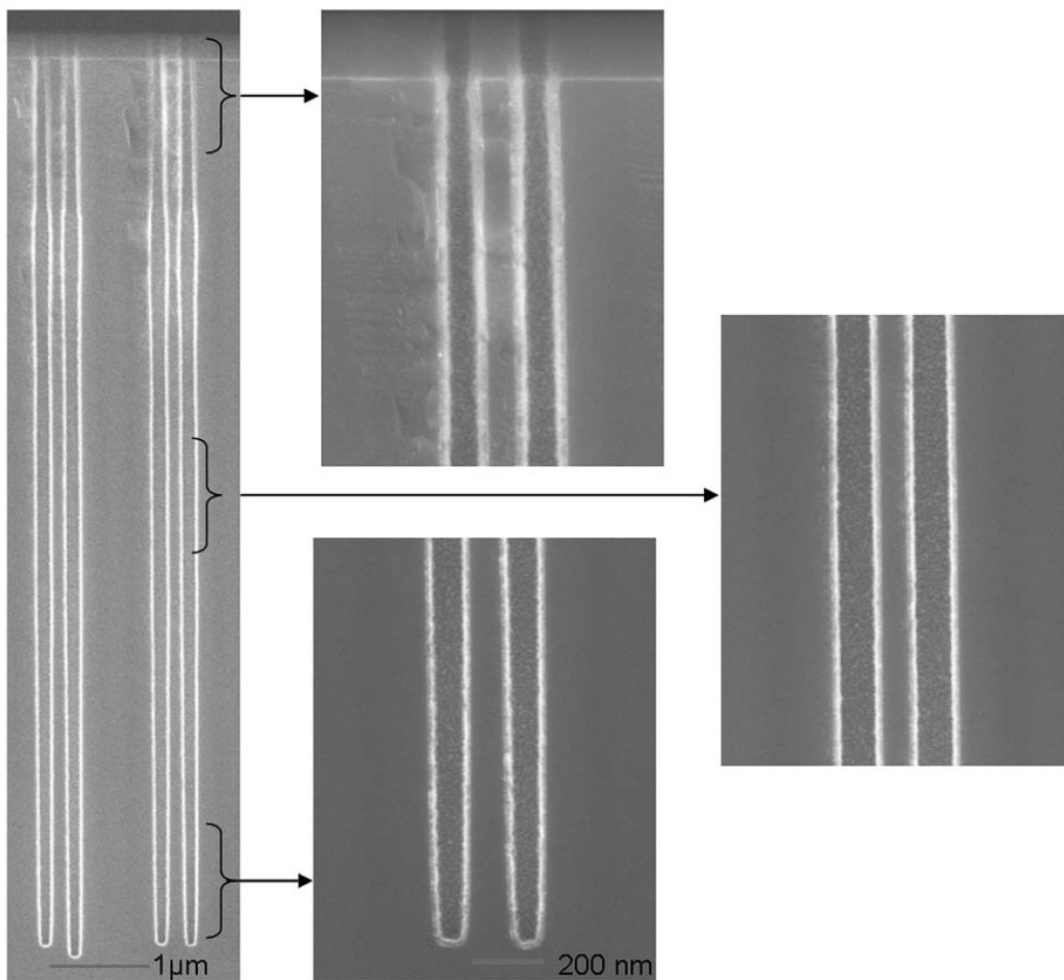


**Figure 1.7** Cross-sectional scanning electron microscope (SEM) image of a highly conformal 30 nm thick  $\text{Sc}_2\text{O}_3$  film deposited by ALD. Reproduced with permission from *Electrochemical and Solid-State Letters*, 9 (6) F45-F48 (2006).

Another phenomenon that is commonly used to assert that a process is in fact an ALD process is the so-called “ALD window”. This is when the saturated GPC remains constant over a range of substrate temperatures. While it is true that many ALD processes do have an ALD window, it is not a requirement. It is possible that the saturated surface coverage of either self-limiting precursor could change with a change in temperature due to several confounding factors such as surface restructuring exposing a higher or lower concentration of reactive surface sites. Other hypothetical cases such as more complex thermally activated precursor-substrate chemistry might also lead to a changing GPC with respect to temperature, but as long as at a given temperature all precursors display self-limiting chemisorption, the process is an ALD process at that temperature.

The main aspects of ALD that make it superior to CVD are conformality and film thickness control. Since ALD necessitates the use of self-limiting precursors, the dose of either precursor can be extended for as long as necessary to completely saturate a surface. This means that for very high surface area substrates or for very high aspect ratio features like the vias mentioned above, if a long enough dose of both precursors is given, then the substrate will be coated in a perfectly conformal thin film of uniform thickness. ALD offers the best film conformality among known thin film deposition techniques. In terms of having a fine-tuned control over a film’s thickness, ALD is also an exceptional deposition technique because each precursor dose can be very easily separated in time, and the film growth is dependant on the chemistry rather than the dose time of the precursors. For example, the most well-cited ALD process is trimethylaluminum (TMA) and H<sub>2</sub>O to form Al<sub>2</sub>O<sub>3</sub> with a GPC of ~ 1.2 Å cycle<sup>-1</sup>,<sup>43</sup> meaning one can theoretically choose the thickness of the deposited film to be any increment of ~ 1.2 Å. This degree of thickness control exists for all ALD processes, which makes the technique very desirable for situations that require very thin, conformal films.

Given these aspects of ALD, many applications would benefit from its use. However, not all materials have existing ALD processes already defined. In the case of developing a new ALD process, a common strategy can be to take a known CVD process and try to adapt it into an ALD process. CVD processes are tested to find the “lower temperature limits” of continuous deposition (i.e., CVD), but processes below that lower temperature

limit are disregarded since no CVD growth occurs. This is precisely the regime where ALD growth should be expected, and one might simply be able to introduce a cyclic pulse sequence of precursors and purge steps to discover a new ALD process. There have been several review articles on ALD as well as an excellent blog post about how to develop and characterize a new ALD process.<sup>44–49</sup>

The first step when developing a new ALD process is to choose suitable precursors and co-reactants that together will produce the desired film. For some thin films such as Al<sub>2</sub>O<sub>3</sub> or ZnO there are clear favourites that are consistently well-performing (trimethylaluminum or diethylzinc as precursor A, and water as the co-reagent). While these processes work very well, sometimes changing the precursor can change the properties of the deposited film. For example, when trimethylaluminum, diethylzinc, and water are used together in a ternary process to deposit aluminum-doped zinc oxide (AZO), the films have a low Al dopant efficiency of 10 %. When the aluminum precursor is changed to dimethylaluminum isopropoxide, the doping efficiency of the films can be increased up to 60%, where in both cases the Al fraction in the AZO film is 4 %.<sup>50</sup> This dramatic effect is an example of why it is important to both continue trying to develop ALD processes with existing CVD precursors, but also to design and create novel precursors to improve upon existing processes.

The search for new precursors is especially necessary when there is no reported ALD processes for the material you wish to deposit. Additionally, some ALD processes use dangerous reagents that cannot be handled in some research tools and require expensive infrastructure to handle safely. For example, WF<sub>6</sub> is used in combination with SiH<sub>4</sub> or Si<sub>2</sub>H<sub>6</sub> to make metallic tungsten by ALD<sup>51</sup> but WF<sub>6</sub> is a gas that forms highly poisonous HF<sub>(g)</sub> upon exposure to atmosphere, and both SiH<sub>4</sub> and Si<sub>2</sub>H<sub>6</sub> are toxic and flammable gases which spontaneously ignite upon exposure to air and can result in an explosion. As well, precursors might require higher delivery temperatures and lower system pressures than can be accommodated, like with PbS or PbO which use the precursor (Pb(tmhd)<sub>2</sub>).<sup>52,53</sup> Some precursors form such stable monolayers that they do not undergo subsequent reaction with normal co-reagents, and so a plasma co-reagent is required. This could necessitate a substantial upgrade or purchase of a new deposition tool.

Furthermore, existing ALD processes for a desired material may exist, but may be sub-optimal. Perhaps the film in question suffers from poor performance due to a high impurity content, or the GPC is very low which could make the process prohibitively expensive. Due to the reliance of ALD on highly specific surface chemistry, these problems can often be solved by a synthetic chemist who's task is to design and test new precursors and co-reagents in order to overcome the pitfalls of previous processes or to invent brand new ALD chemistry.

## 1.4 Precursor Design

### 1.4.1 High vapour pressure

For ALD precursors, the more volatile the compound is, the better it is, if it does not decompose. High vapour pressure makes the precursor dose more reproducible and produces a more efficient process, while it also allows the precursor to diffuse into and through complex substrates more rapidly. The vapour pressure of a substance is governed mostly by the thermodynamics of the evaporation process, and to a lesser degree the molecular weight of the compound.

During a phase transition, if the system is at equilibrium (ex. the rate of evaporation and the rate of condensation are the same) then  $\Delta G = 0$  (Equations 1 and 2).

$$\Delta G_{vol} = \Delta H_{vol} - T\Delta S_{vol} = 0 \quad (\text{Equation 1})$$

$$\Delta H_{vol} = T\Delta S_{vol} \quad (\text{Equation 2})$$

However, if the system is not at equilibrium (like when a precursor leaves the delivery system and flows to an ALD reactor), then for sublimation and evaporation (collectively volatilization)  $\Delta G \leq 0$ . Volatilization is an endothermic phase transition, meaning that the enthalpy of these processes is always positive ( $\Delta H_{vol} > 0$ ). This means that the entropy of volatilization ( $\Delta S_{vol}$ ) must also be positive to maintain the possibility of  $\Delta G \leq 0$ : a gas always has a higher number of microstates (more degrees of freedom / more disorder)

than a condensed phase. Thus, for the evaporation process to go forward and produce a gas, we find:

$$\Delta H_{vol} - T\Delta S_{vol} \leq 0 \quad (\text{Equation 3})$$

$$\Delta H_{vol} \leq T\Delta S_{vol} \quad (\text{Equation 4})$$

The key point from this equation is that one can maximize the volatility of a precursor by minimizing  $\Delta H_{vol}$ .

Volatileization is endothermic, meaning energy is required from the surroundings to break interactions between condensed molecules and liberate them into the gas phase. The less energy required, the smaller  $\Delta H_{vol}$  will become (while still being positive), which makes the temperature required to effect volatileization smaller, which makes the substance more volatile. Thus, if a precursor is designed such that intermolecular interactions (electrostatic, hydrogen bonding, dipole-dipole, ion-dipole, van der Waals interactions, etc.) are minimized both in number and in strength, then that substance will be more volatile.

As a general rule, precursors should be designed such that their ligands do not engage in strong intermolecular interactions. Further, the overall size of the molecule should be kept as small as possible to prevent as much dispersion correlation as possible. Dispersion interactions occur between all atoms and molecules and can be quite strong since they occur over the entire molecule, not just between certain atoms. These unavoidable attractive forces are related to the polarizability of the electrons around each atom of a molecule. Aliphatic (a structure comprised of saturated  $C_xH_y$  linkages) ligand scaffolds are generally preferred for precursor ligands because they are unreactive, non-polar, and have no acidic hydrogen atoms. Making the backbone as small as possible limits the number, and therefore the sum of all dispersion interactions. Some dispersion ligands, such as fluorine-terminated alkyl ligands, are very low energy because the fluorine atoms are very small and have very low polarizability. Ligands such as hfac are famous for enhancing volatility of a precursor but can also leave F impurities in the film depending on the material being deposited.<sup>54,55</sup> Hfac is acidic enough that it can even etch metal ions out of the film and has found use in atomic layer etching (ALE)

processing.<sup>56,57</sup> In the case of gold CVD precursors this etching doesn't occur, and Me<sub>2</sub>Au(hfac) is a high-volatility precursor (Figure 1.8) that deposits high-purity gold films when used in combination with hydrogen gas or laser irradiation as co-reagents.<sup>58</sup>

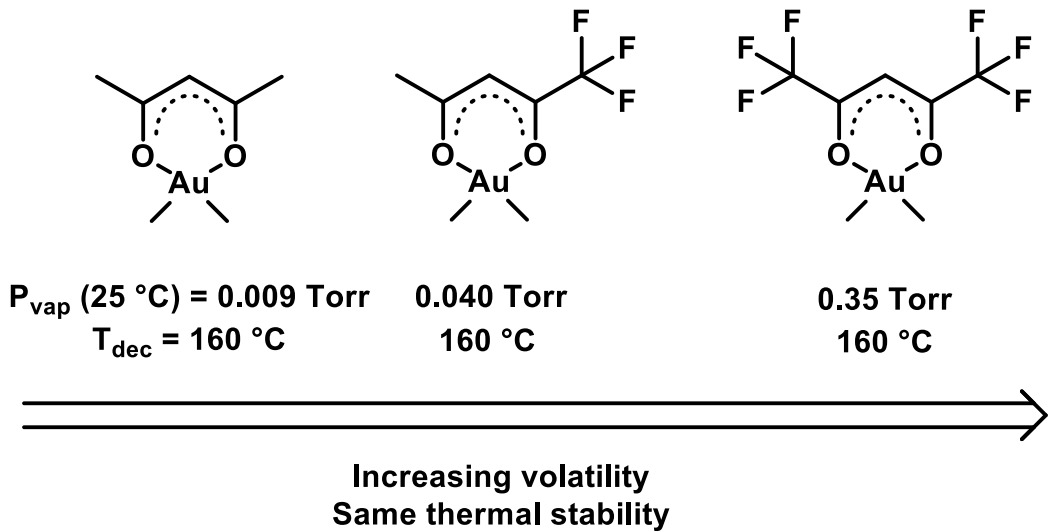


**Figure 1.8** Effect of ligand backbone fluorination on volatility in a series of dimethylgold(III) acetylacetonate compounds used for gold CVD.

While many chemists exploit the use of aryl rings for their stabilizing properties towards metal complexes, aryl rings are rarely used in vapour deposition precursors. Aryl rings engage in  $\pi$ - $\pi$  stacking interactions as well as many more dispersion interactions due to their large size, and they add at least 77.10 g mol<sup>-1</sup> to the system which also has a negative effect on volatility and so they are generally avoided.

Somewhat counterintuitively to this discussion, some metal halides are also highly volatile (ex. UF<sub>6</sub>, TiCl<sub>4</sub>, VF<sub>4</sub>, NbCl<sub>5</sub>), but these are all coordinatively saturated.<sup>59,60</sup> These metal centers have no available coordination that might cause oligomerization to occur. Furthermore, these complexes are highly symmetrical, and the halide ligands that form the outer sphere are highly electron-rich and non-polarizable, so intermolecular interactions in these systems are very weak. By contrast, compounds such as FeCl<sub>2</sub> or CoCl<sub>2</sub> are coordinatively unsaturated, and are non-volatile due to formation of halide-bridged extended crystal lattices. This strategy of coordinative saturation of the metal

center also applies to M-X species where X is considerably more electronegative than M such as RuO<sub>4</sub> and OsO<sub>4</sub>. Coordinative saturation is a general strategy for all precursor design to prevent oligomerization in the condensed phase.

Since the topic of this thesis is gold chemistry, there is one more obscure interatomic interaction that must be discussed: aurophilicity.<sup>61</sup> Aurophilicity has been observed mostly in gold(I) compounds and to a lesser degree in other heavy closed-shell metal compounds like those of Hg(II) and Ag(I), but has never been observed in an Au(III) compound. The strength of this interaction varies largely depending on the system but has been found to be similar to hydrogen bonding and is thus a significant interaction. It is strong enough that supramolecular assemblies can be rationally designed based on this interaction, and has also been used to design luminescent Au(I) compounds.<sup>62</sup>

A recent paper focused on using a computational method to deconvolute the strengths of all of the intermolecular interactions in two (NHC)AuCl compounds (NHC = N-heterocyclic carbene).<sup>63</sup> In regards to overall intermolecular interaction, the strength of the aurophilic interaction can make up a significant portion of the intermolecular forces, but the amount varies wildly depending on the particular case.

#### 1.4.2 High stability towards self-decomposition

Bonds made between the metal and ligand, or bonds within the ligand itself must be sufficiently strong to survive any heating required to volatilize the precursor. In an industrial setting, it is possible that the precursor would be kept at its delivery temperature for months on end. Since the continued delivery of the same purity of precursor is paramount, self-decomposition must be mitigated. There are many ways to increase the thermal stability of a compound, but since the chemistry of the elements differs so greatly it is difficult to define a ligand that works universally. It is most advantageous to learn the chemistry of the element in question (which oxidation states are stable, is the payload element hard or soft, what types of ligands have been used with this element in literature, what is its common coordination number, etc.). When possible, a knowledge of the decomposition mechanism of the compound of interest is of utmost importance as it

allows the possibility of making a very small change that results in a significant improvement in thermal stability. Our group has designed ligands and precursors using this strategy to great success.<sup>64</sup> There are however some general design strategies that apply across much of the periodic table to improve the thermal stability of the precursor.

The chelate effect is an entropic stabilizing effect where a bidentate or multidentate ligand forms a more thermodynamically stable complex compared to an equivalent number of individual ligands. Using chelating ligands generally produces a more stable complex, and this can be a relatively straightforward improvement to design. If a certain precursor is lacking in thermal stability, a ligand that is a variant of the ones already being used but linked together with covalent bonds may add stability to the compound.

This goes hand in hand with a second strategy which is to coordinatively saturate the payload atom. As previously discussed, this has the effect of hindering intermolecular interactions, but it also prevents intramolecular decomposition pathways such as alkyl migration, hydrogen abstraction reactions, ligand insertion reactions, and others. Compared to the chelate effect, this strategy of preventing decomposition is a *kinetic* stabilization rather than a *thermodynamic* stabilization, and there are other ligand design strategies that kinetically hinder decomposition as well.

Until the 1950's it was thought that metal alkyl complexes were thermodynamically unstable due to a weak M-C bond. While it is true that metal alkyls are generally highly reactive species, the reason for their perceived instability was the inability to isolate the complexes at all. Only a few examples (beginning with gold and platinum) were known until some significant advances to the field came to light.<sup>65</sup> It was eventually discovered that metal methyl complexes were the easiest to isolate and were much more stable than their ethyl and higher alkyl counterparts. This is because metal alkyl complexes can undergo  $\beta$ -hydride elimination (Figure 1.9), a thermodynamically favourable reaction. In aliphatic alkyls, the ligand can reorient itself just enough to form the 4-membered metallacycle transition state which can then easily become the metal hydride and alkene products. In many cases, the metal hydride undergoes further decomposition to eliminate hydrogen gas and the elemental metal.

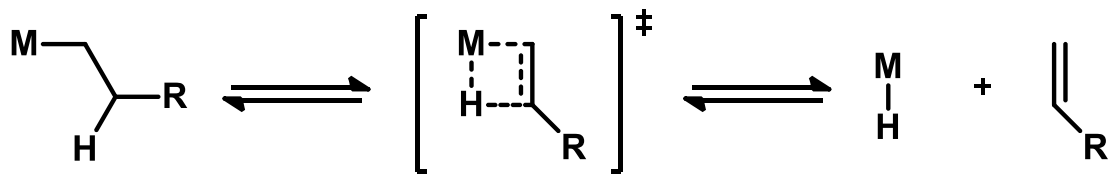


**Figure 1.9**  $\beta$ -hydride elimination of a metal alkyl

Methyl ligands contain only  $\alpha$ -hydrogens, and this hydrogen atom cannot adopt the appropriate orientation for the reaction to occur. Similarly, replacing the beta hydrogen atoms with  $\text{CH}_3$  groups (i.e. a neopentyl ligand) or a phenyl group (i.e. a benzyl ligand) increases the stability of these compounds dramatically compared to those that bear  $\beta$ -hydrogens.<sup>66,67</sup> It was also discovered that if the reaction produces an anti-Bredt alkene like a 1-norbornene or adamantene,<sup>68</sup> then the equilibrium lies at the metal alkyl and not the products because they are too strained to be formed.<sup>69</sup> It was also found that replacing the beta carbon with an atom that cannot form a double bond with carbon greatly stabilizes the complex as it prevents the elimination product from forming. Alkyl ligands that have a  $\beta$ -silicon atom have been used to great effect in the field of organometallic chemistry: these ligands are isoelectronic and isostructural to neopentyl carbon-containing derivatives. As such, metal alkyl complexes that contain P, S, B, and other elements in the  $\beta$  position also possess this attribute of high thermal stability.

There are a few caveats to this notion of preventing  $\beta$ -hydride elimination that should be addressed. The first is that  $\beta$ -hydride elimination can only occur at an anionic ligand, and so ligands such as  $\text{PMe}_3$  which are coordinatively bound to metals as Lewis base – Lewis acid adducts do not undergo this reaction. The second is that the  $\beta$ -hydrogen atom must be able to adopt the correct orientation with the metal for the reaction to go forward. Ligands like diazabutadienyls or amidinates where the N-bound alkyl ligands have no  $\beta$ -hydrogen atoms still contain  $\beta$ -hydrogen atoms in the backbone. However these are held firmly away from the metal center and therefore also cannot undergo this reaction (Figure 1.10).

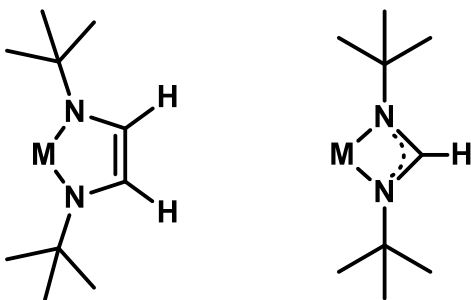


**Figure 1.10** Two metal complexes that bear  $\beta$ -hydrogens (shown explicitly) that cannot undergo the  $\beta$ -hydride elimination reaction. On the left is a diazabutadienyl complex and on the right is an amidinate complex. In both cases the hydrogen atoms shown cannot form the proper molecular orbital overlap with the metal center because of the rigid framework of the ligand.

The third caveat to preventing  $\beta$ -hydrogen elimination is that the reaction can only occur if there is an available coordination site on the metal. Thus, in some cases the reaction can be kinetically hindered by coordinatively saturating the metal center.

### 1.4.3 Cost and environmental impact of synthesis

One often overlooked factor in precursor design is the cost of the synthesis of the precursor. ALD uses a large excess of precursor in order to ensure a completely conformal film is grown. Outside of the ability to recycle unused precursor or utilize a highly precursor efficient process which are both issues of ALD apparatus design, the precursor must be as cheap to synthesize as possible because a rather large amount is needed even for research and development purposes, let alone an industrial purposes. For example, in Chapter 3 of this thesis I detail a set of plasma-enhanced ALD (PE-ALD) studies using  $(\text{PMe}_3)\text{AuMe}_3$  as the precursor. Even to undertake these fundamental studies, I estimate that we synthesized and used roughly 50 g of the precursor.

Thankfully, we were able to synthesize this material from metallic gold which we could often purchase at market value, and the synthesis could be accomplished in high yields after substantial optimization of the reactions. However to purchase 50 g of  $(\text{PMe}_3)\text{AuMe}_3$  from our laboratory would cost 25,000 CA\$ which is not an easy cost to cover for academic research. Other gold CVD and ALD precursors (see discussion of compound

15, Figure 1.14, section 1.6 of this chapter) can only be synthesized in low yields between 40 % and 10 % depending on what compound is used to begin the synthesis. This results not only in a much higher price to purchase an equivalent amount of precursor, but also a more severe environmental impact due to the need to recycle gold-containing by-products of the reaction. One must also ultimately dispose of more reagents and solvents, further harming the environment.

The impact that we as chemists have on the environment should never be underestimated. In developing new technologies during a time of environmental crisis, we have a responsibility to ensure that we minimize our negative impact as much as possible. In an academic setting, the environmental impact of our studies is often neglected or downplayed since the sheer volume of chemistry is tiny compared to the scale on which some industrial processes are performed. Multiple green chemistry textbooks and even an entire high-impact journal (Green Chemistry, RSC) are dedicated specifically to this topic and it should be on the mind of every chemist. Finally, it is important for chemists to be engaged in science awareness and in educational efforts wherever possible so that current and future generations of scientists also learn to address the environmental issues as a community.

## 1.5 Thermolysis of the new precursor

Once the new precursor has been synthesized, it is essential to quantify the thermal properties of the compound. For this thermogravimetric analysis (TGA) and differential scanning calorimetry (DSC) are useful methods because they allow for a quantitative determination of the precursor's volatility and thermal stability.

### 1.5.1 Thermogravimetric analysis (TGA)

TGA is a relatively simply method where a sample's weight is measured while also modulating the temperature of the sample as a function of time. The two simplest TGA experiments are called temperature ramp experiments (where the sample's temperature is changed at a constant rate) and isothermal experiments (where the sample's temperature is held constant for a defined period). When analyzing a volatile substance like an ALD precursor both methods are useful, but the temperature ramp experiment is much more widely used in the field.

A TGA ramp experiment of a well-behaved vapour deposition precursor is shown in Figure 1.11. In this experiment a constant temperature ramp rate of  $10\text{ }^{\circ}\text{C min}^{-1}$  was used, and what is observed is a smooth exponential mass loss with increased temperature as predicted by the Arrhenius equation. If this exponential curve deviates from its original trend (i.e. and inflection point is observed) then this indicates that the compound has undergone a chemical change. This compound begins to evaporate near  $80\text{ }^{\circ}\text{C}$  indicating that it is volatile, and it leaves a residual mass that is close to 0 % indicating that it did not decompose to non-volatile materials during this experiment. Sometimes a compound will have a non-zero residual mass but still show a smooth, exponential evaporation curve, and this is because the compound decomposes into completely volatile and/or completely non-volatile products, neither of which affect the mass loss rate of the sample pan.

It should be mentioned that while it is a sign of thermal robustness that a precursor reaches 0 % residual mass in a TGA experiment, a 0 % residual mass is not essential in order for the precursor to be useful. If the ALD system is kept at temperatures where

decomposition is negligible, and substantial volatility is maintained, then the ALD process will still be viable. If the intended delivery temperature of the precursor is known, then an isothermal TGA experiment can be used to determine if the precursor will completely evaporate under those conditions. If the precursor is stable at the isothermal temperature, then the analysis should show a nearly linear decrease in mass with respect to time until a mass of 0 is reached.

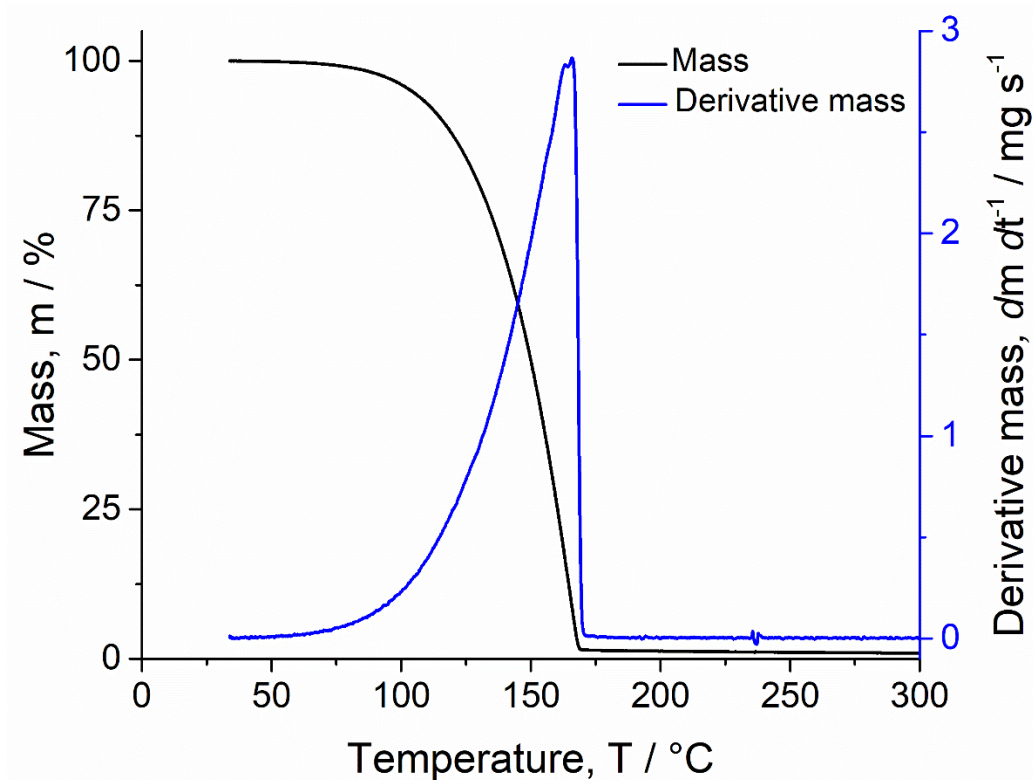


**Figure 1.11** TGA temperature ramp analysis (ramp rate  $10\text{ }^{\circ}\text{C min}^{-1}$ ) of  $(\text{PMe}_3)\text{AuCH}_2(\text{SiMe}_3)$  showing the % mass of the sample (black) and the time derivative of the mass data (blue).

The derivative data of this analysis can be used to determine a compound's vapour pressure using a method previously described by Kunte *et al* (Equation 5) which is based on the Langmuir vapour pressure equation.<sup>70</sup>

$$P = \frac{\partial m}{\partial t} \sqrt{\frac{T}{MW}} \frac{\sqrt{2\pi R}}{\alpha_1} \quad (\text{Equation 5})$$

In this equation, P is the vapour pressure of the analyte,  $\frac{\partial m}{\partial t}$  is the mass loss rate of the analyte per unit time, T is the analyte temperature, MW is the molecular weight of the analyte,  $\frac{\sqrt{2\pi R}}{\alpha_1}$  is a calibration constant that includes the gas constant (R) which is dependant on both the apparatus and the method (variables such as the type and flow rate of gas in the system, the material used as the sample crucible, and the heating rate of the system all impact the value of this constant). This constant must be determined first using a material where the vapour pressure is known over the entirety of the temperature range that will be used for the analyte. A common calibrant is benzoic acid for which Antoine constants exist for a variety of temperatures. Once the calibration constant has been determined for a set of system parameters (i.e. gas flow rate, sample pan volume, type of sample pan) then it can be used in Equation 5 to determine the vapour pressure of a new analyte. Since the derivative data that are obtained are independent of sample size and heating rate, this analysis is theoretically indifferent to variations in analyte loading and TGA ramp rate.

Using this technique, the Clausius-Clapeyron data for a precursor of interest can be obtained, and a comparison of its volatility to other precursors is possible. A typical benchmark for ALD precursors is a so-called 1 Torr temperature (the temperature at which the precursor attains a vapour pressure of 1 Torr) because many ALD tools operate at pressures close to 1 Torr.

### 1.5.2 Differential scanning calorimetry (DSC)

A more definitive method to analyze the thermal stability of a precursor is differential scanning calorimetry (DSC) (Figure 1.12). We make us of DSC to determine the onset of auto-decomposition of a potential precursor. This technique is complementary to TGA because it gives information about thermodynamic events that occur upon heating the precursor in a closed system. In most cases, decomposition of an ALD precursor is exothermic, and physical changes that occur upon increasing temperature (melting or

boiling) are endothermic. The onset of decomposition of the analyte is defined as the intersection point of the tangents between the baseline and the steepest tangent of the exothermic peak.<sup>71</sup> Since the precursors should remain intact until reaction occurs at the substrate, this is a more useful data point than the peak of the exothermic event to determine the onset of decomposition. By combining the delivery temperature from TGA with the onset of decomposition from DSC we can define a temperature range over which the precursor can be useful for an ALD process.

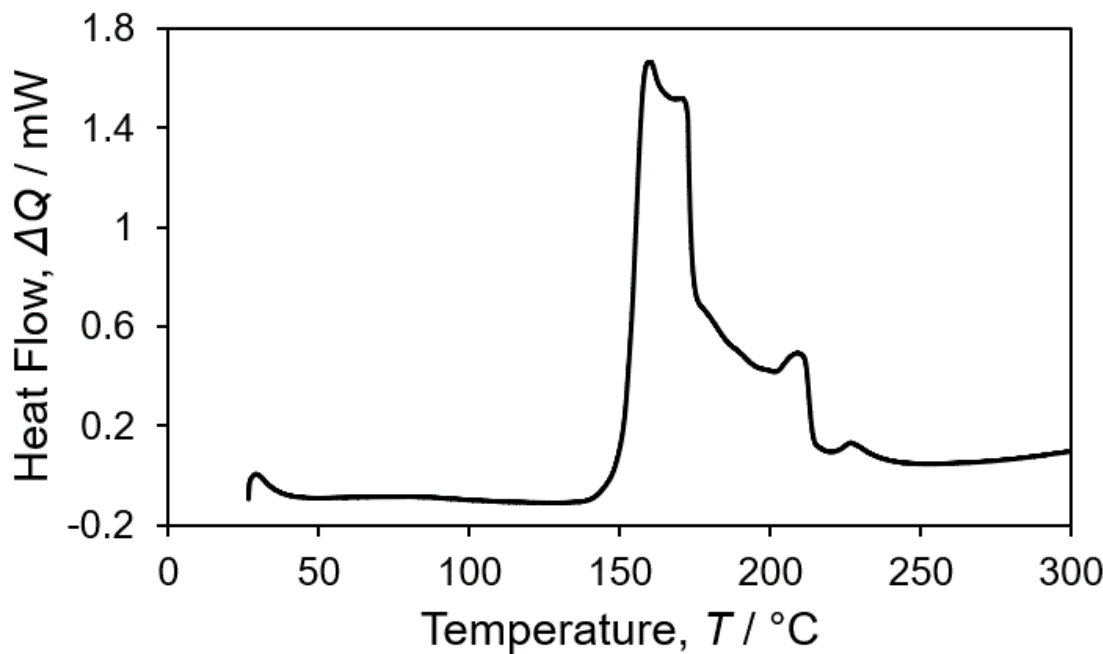


**Figure 1.12** DSC ramp experiment ( $10 \text{ }^\circ\text{C min}^{-1}$ ) of  $(\text{PMe}_3)\text{AuCH}_2(\text{SiMe}_3)$ . The onset of exothermic heat flow was found to be  $146 \text{ }^\circ\text{C}$  which indicates the onset of precursor self-decomposition. Exothermic heat flow is shown as a positive heat flow.

# **Chapter 2 Literature review and figure of merit analysis of gold CVD and ALD precursors**

## **2.1 General information**

Recently a review was published on the topic of gold compounds that had either been used or could potentially be used for CVD or ALD.<sup>72</sup> While this review documented the known precursors as well as some closely related prospects, it didn't emphasize the physical attributes of the precursors themselves. Melting point, volatility data, and decomposition point are three thermal characteristics that can be controlled by precursor design and are very important when developing a new ALD precursor and process. A compendium of this data could serve as a guide for how well certain ligand systems and oxidation states behave in the context of precursor design. Below these data have been compiled for every gold compound reported for use in CVD and ALD. Only plasma-enhanced or thermal variants of CVD and ALD were considered, so variants like laser-enhanced CVD and electron beam-induced deposition (EBID) or aerosol-assisted CVD were not included. There are many CVD and potential ALD precursors that have been used for other variations of CVD (for example  $(PEt_3)_2AuMe_3$ ), or have been synthesized but not tested at all for vapour deposition, and the interested reader should consult the above mentioned review of Basova, Hassan, and Morozova for this information.

Although many of the publications report multiple compounds, only the ones that were actually reported or mentioned to have been used for deposition are included. Some of the references herein do not include CVD or ALD experiments, but were the source of either the melting point, the vapour pressure data, or the decomposition point of the precursors. While many of the compounds have multiple citations associated with them, these lists are by no means exhaustive, and represent precursors reported up to August 2020. **All compound-specific references can be found in the appropriate figure captions.**

## 2.2 Methodology

When volatility data was directly available from Knudsen effusion or another method, that data was used (with the exception for compounds **19** and **20**, see below). If volatility data was not available, but TGA data was available, I extracted the TGA data from the publication using Chemcraft<sup>73</sup> along with any available sample mass data, and the vapour pressure was then calculated using the method of Kunte *et al*<sup>70</sup> in order to determine the 1 Torr temperature. When a range of masses was given for TGA analysis, the highest possible mass was used for the analysis. Unfortunately,  $\alpha_1$  could not be determined for every literature apparatus, so the  $\alpha$  value determined for our apparatus was used throughout.

To assess just how accurate this methodology was, I calculated the 1 Torr temperature of compound **15** from the Knudsen effusion data as well as from the TGA ramp data reported in the same paper.<sup>74</sup> I found values of  $116.6 \pm 3.8$  °C and  $128.5 \pm 5.0$  °C respectively for the two techniques. This discrepancy is likely due to the assumption that  $\alpha$  was the same as for our apparatus. I also calculated the 1 Torr temperature of compound **8** from the reported Clausius-Clapeyron relationship<sup>75</sup> and from our own TGA data (see supporting information) and found values of  $91.2 \pm 4.2$  °C and  $92.6 \pm 0.2$  °C respectively, which are identical within the uncertainty of the calculations. In all cases where vapour pressure data was available from Clausius-Clapeyron data or Knudsen effusion experiments, these data were used to calculate the values reported below. For the exceptions **19** and **20** the Knudsen effusion experiments cited were performed at low temperatures (below 50 °C). This resulted in both compounds having an identical 1 Torr temperature (calculated to be  $98.7 \pm 1.0$  °C and  $99.4 \pm 3.2$  °C respectively) which is clearly erroneous considering their substantially different TGA data.

## 2.3 Precursor Figure of Merit

I applied our published figure of merit calculation to as many compounds as possible. The precursor figure of merit ( $\sigma$ ) was devised as a simple metric by which precursors could

be compared. Instead of comparing all compounds by their TGA and DSC graphical data (the most common literature approach), we decided to combine the data of both analyses into one equation (Equation 1).

$$\sigma = (T_D - T_V) \times \left(1 - \frac{\%m_{res}}{196.97/MW \times 100\%}\right) \quad \text{Equation 1}$$

First, we define the useful thermal window of the compound, where the lowest useful temperature as the “1 Torr temperature” ( $T_V$ ) (where the precursor can be adequately delivered, i.e., at 1 Torr of pressure) and the highest useful temperature as the onset of decomposition of the precursor ( $T_D$ ). The thermal window of the precursor is thus ( $T_D - T_V$ ). Note that this figure of merit is designed with ALD in mind (hence the upper limit being the onset of precursor decomposition) but could be adapted for CVD as well by incorporating an activation energy for the deposition process. In that instance, compounds that are most volatile, have the lowest decomposition temperature, and have the lowest activation energy could be given a high  $\sigma$ . For ALD precursors, the larger this thermal window, the more useful the precursor is for ALD: there is a lower sensitivity towards a CVD component with a given system temperature. The most useful precursors have a large thermal window but also a low  $T_V$ , however a high 1 Torr temperature while maintaining a large thermal range is still adequate if the delivery temperature can be reached on an ALD tool. This first part of the equation combines the thermodynamic parameters of volatility and thermal reactivity.

The second part of the equation was included to account for the kinetic aspect of thermal decomposition. We have found in many cases that a compound may have a very large thermal range but would also leave a high residual mass in a TGA analysis, and likewise demonstrate poor thermal stability in a precursor bubbler during a deposition process. Other compounds appear to persist in TGA analyses far above their decomposition points, which we interpret as significantly different rates of decomposition between precursors. It is also important to note here that if metal catalyzes the decomposition of a precursor, that it should be somehow included in the figure of merit calculation. Thus, the second term is a weighting between 0 and 1, and a compound that decomposes and leaves all of its gold in the sample pan as metal will be given a merit of 0. A compound

that evaporates completely and leaves no residual mass will be given a figure of merit equal to its thermal range which is its maximum possible value.

Since its publication (see Chapter 5), we have discussed this equation many times with other scientists and considering these discussions I wish to explain a few quirks of the method here. If the measured  $T_D$  of the precursor is below its  $T_V$ , then the compound will receive a negative figure of merit. It is possible to determine a compound's  $T_V$  using both the TGA method and other techniques such as Knudsen effusion, as long as these data are collected below the onset of thermal decomposition of the precursor. The  $T_V$  can then be extrapolated from this. This does not necessarily mean that the precursor is useless: if a deposition tool operates at a pressure far below 1 Torr then such a precursor might perform well. However other higher-merit precursors would likely still be easier to use.

Another issue is that the precursor might leave a residual mass that is higher than the "maximum" residual mass (in Equation 1 and specifically for Au precursors, the maximum residual mass is the atomic mass of Au,  $196.97 \text{ g mol}^{-1}$ ), resulting in the second term returning a negative value and giving either a false positive or a false negative figure of merit. For gold (for which this equation was developed) it is rare for a compound to leave a residue that contains substantial amounts of elements other than Au, and in our lab we have yet to observe a gold compound that has left a residual mass higher than the initial % mass of Au in the compound. This issue should be considered for other types of precursors. For example, a published a figure of merit assessment of a family of Mo compounds found that one compound left a residue that contained both  $\text{MoCl}_x$  and  $\text{MoN}_x$  type species.<sup>76</sup> In cases like this the maximum residual mass could be chosen based on prior data about how the precursors might decompose or the weighting factor might be set to  $\left(1 - \frac{\%m_{res}}{100\%}\right)$ . This being said, if an Au compound leaves a residue that contains something other than just Au, it is inherently less useful for Au deposition than a compound that decomposes to only Au and should be discounted for this reason. This was the case for two Au(III) literature compounds below: **17** and **18** left residual masses of 64.9 % and 53.0 % respectively in their reported TGA data (with helium as the carrier gas) which are both higher than the % mass of Au in the original compound.

## 2.4 Figure of Merit Methodology

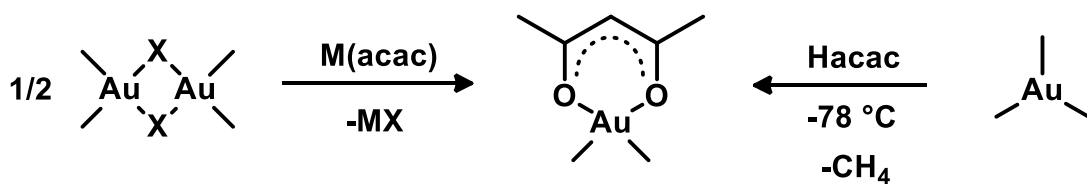
For the figure of merit calculations of the gold CVD and ALD precursors below, a series of limitations were set so that reasonable estimates of  $\sigma$  could be made if literature data were unavailable. Where a residual mass from TGA data was available, the value was extracted using Chemcraft. It was assumed that where a residual mass was observed in these TGA analyses, that it contained only Au<sub>(s)</sub>. Unfortunately, small mass loadings and slow temperature ramp rates artificially increase the calculated  $\sigma$  value since they can result in a lower residual mass. If multiple TGA data were available in literature, a 10 mg mass loading and 10 °C min<sup>-1</sup> were considered the optimal data to use as a comparison. For compounds where no TGA data was reported, the residual mass was assumed to be 0. For compounds where  $T_V$  or decomposition data was missing, the figure of merit was not calculated. Some of these compounds (for example compound **7**) are likely to have very good  $\sigma$  values, and if a reader of this thesis has access to any supplementary data for the compounds below, I would welcome a collaborative effort to complete the data set for these precursors.

## 2.5 $\beta$ -diketonate, $\beta$ -ketoiminate, and double-ylide complexes of dimethylgold(III)

Many of the best gold precursors are Au(III)-derived, and the only two ALD precursors also feature gold in the +3 oxidation state. A very common family of Au(III) precursors is the dimethylgold(III)  $\beta$ -diketonates which are choice precursors for gold CVD processes, with **1** and **2** (Figure 2.1) being sold commercially on demand, and **3** being less common, but still available. Compound **4** has a higher reported decomposition temperature, but the reported TGAs of both **1** and **4** suggests extensive decomposition beginning near 100 and 120 °C respectively. Studies have shown that the first thermal decomposition reaction of **1** is reductive elimination of ethane<sup>77</sup> and it is reasonable to assume that this is also the case for **1-9**, although the nature of the chelating ligand clearly has an effect on the decomposition temperatures of these precursors.

Overall, the dimethylgold(III)  $\beta$ -ketoimimates **5-9** are more thermally stable overall in comparison to **1-4**. Here the effect of fluorination is evident both from the increasing volatility from **1** to **3**, and from **5** to **8** to **9**. Interestingly, fluorination also increases the thermal stability of many of these compounds compared to their aliphatic counterparts. The figure of merit for these compounds increases with increasing fluorination of the chelating ligand. It is notable that **9** has the highest figure of merit of all gold compounds known to date.

**Scheme 2.1** Synthetic routes to dimethylgold(III)  $\beta$ -diketonates and dimethylgold(III)  $\beta$ -ketoimimates. “acac” is an acronym for acetylacetone, but in this scheme represents all of the chelating ligands from compounds **1-9**.



<b>1</b>	<b>2</b>	<b>3</b>	<b>4</b>	
82-84	40	5	68-70	
1.0, $(82.6 \pm 0.72)^a$	1.0, $(50.6 \pm 2.1)^b$	1.0, $(31.0 \pm 0.5)^a$	1.0, $(74.4 \pm 0.1)^b$	
160	160	160	200	
40	109	128	33	
<b>5</b>	<b>6</b>	<b>7</b>	<b>8</b>	<b>9</b>
64	51	98.6	58.6	< 25
1.0, $(103.7 \pm 0.8)^a$	0.150, $(107)^e$	0.035, $(130)^e$	1.0, $(91.2 \pm 4.5)^{c,f}$	1.0, $(36.6 \pm 0.4)^a$
180	193	240	290, 160*	250 <sup>f</sup>
65	n/a	n/a	199	212
<b>Compound</b>				
m.p. (°C)		<b>10</b>	<b>11</b>	
Vapour pressure data: Torr, (°C)		106	155	
Onset of thermal decomposition (°C)		0.001, $(115)^e$	1.0, $(100)^e$	
Figure of merit		325	268	
		n/a	168	

**Figure 2.1** Au(III) compounds previously used in CVD and ALD. Compounds **1**,<sup>75,78</sup> **2**,<sup>78</sup> **3**,<sup>75,78</sup> and **4**<sup>74,79</sup> bear a  $\beta$ -diketonate ligand, **5**,<sup>75,80</sup> **6**,<sup>80</sup> **7**,<sup>81</sup> **8**,<sup>81</sup> and **9**<sup>75,81</sup> bear a similar  $\beta$ -ketoiminate ligand, **10**<sup>82,83</sup> and **11**<sup>83,84</sup> feature rare 1,3-chelating anionic phosphorus-based double ylide ligands. <sup>a</sup> Calculated from Clausius-Clapeyron data, method unknown. <sup>b</sup> Calculated from Knudsen effusion data. <sup>c</sup> Calculated from TGA data collected in the Barry lab using the method of Kunte et al.<sup>70</sup> <sup>d</sup> Calculated from TGA data that was extracted from literature using Chemcraft<sup>73</sup> and then the method of Kunte et al. <sup>e</sup> Sublimation and/or evaporation conditions from synthetic details or CVD delivery. <sup>f</sup> Included as supplementary information for this chapter. <sup>g</sup> CVD begins at or below this

temperature.<sup>h</sup> Literature exists but was unobtainable.<sup>i</sup> System pressure not stated. \* Onset of exothermic event observed by DSC, but TGA leaves 0 residual mass. Further experiments required to identify nature of exothermic event.

The main drawback of compounds **1-9** is that they are difficult to synthesize in high overall yield owing to the reagent  $\text{Me}_2\text{AuX}$  itself being difficult to synthesize (yields range from 5-40 % depending on the halide and author) (Scheme 2.1). This makes these compounds too expensive for many applications. Another less common method that was reported for synthesizing **1** and **2** worked quite well in our hands when we adopted it for the synthesis of **8** (See Figures S-2.8 and S-2.9 for TGA and DSC data respectively).<sup>85</sup> In this method,  $\text{AuMe}_3$  is first synthesized *in-situ* at -78 °C and then the free protonated ligand is added, resulting in liberation of  $\text{CH}_4$  and formation of the product. While our unoptimized yield (25 %) was similar to the  $\text{Me}_2\text{AuX}$  method, this procedure could be performed in one pot without isolating and purifying an Au-containing intermediate.

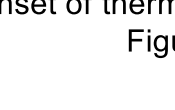
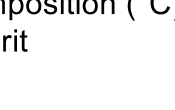
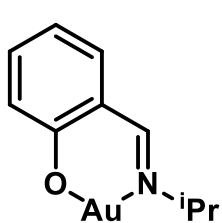
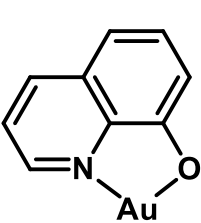
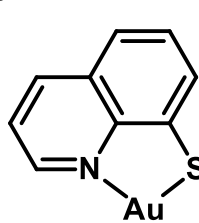
Compounds **10** and **11** have a similar geometry to the previous precursors, but in this case the Au(III) center is bound only to carbon in a totally organometallic, neutral Au(III) compound. Each of these compounds has only been reported twice, originally by Schmidbaur and for CVD by Mitsubishi Corp. in a patent. The compounds were reported by Schmidbaur to sublime at 0.001 Torr, (115 °C) and 1.0 Torr, (100 °C) as part of the purification step during synthesis. Assuming the apparatus for both sublimations was the same, these are a massively different vapour pressures between the two compounds, and it is suspected that the pressure for one of the two compounds might have been misreported. Unfortunately, these conditions are copied verbatim in the patent, which offers no further clarity on the matter. Taking the sublimation conditions of compound **11** as its 1 Torr temperature gives an excellent figure of merit (which is the third best of the entire review, behind only to the fluorinated β-ketoimmines **8** and **9**). These precursors are very interesting and promising, and they deserve a serious assessment as ALD precursors, hopefully accompanied by an improved synthetic route. The only reported routes to these species use  $\text{Me}_2\text{AuX}$  as the gold reagent and therefore the overall yield of these complexes also suffers as described above. Furthermore, the free ligands themselves are difficult to synthesize. This is probably why these compounds have not

been described in more detail, which is a shame considering their seemingly excellent thermal properties.

## 2.6 Dialkyldithiophosphinate, alkylphosphorodithiolate, dithiocarbamate, salicylaldiminate, and quinolinate complexes of dimethylgold(III)

Compounds **12-14** (Figure 2.2) share a structurally similar S-P-S chelating anionic ligand and share a similarly low decomposition point and figure of merit. The substitution of  $\text{iBu}$  to the smaller alkoxide substituents does improve volatility, but also decreases the thermal stability of the compound. In each of these cases however, the substance is a liquid, a desirable property for a precursor. Compound **15** bears a dithiocarbamate ligand and is much more thermally stable than the S-P-S species, giving it a higher figure of merit. While it is not a liquid at room temperature, it does melt well before its  $T_V$ , which is a valuable characteristic since this allows cheaper shipping and handling as a solid while allowing CVD/ALD delivery as a liquid. Notably, compound **15** was used by Mäkelä *et al.* for ALD of highly conductive gold metal films using  $\text{O}_3$  as a co-reagent and was the second reported process for gold ALD. Compound **15** is now commercially available from Strem Chemicals.

Compounds **16-18** do not perform well compared to the rest of the precursors that have been discussed. The phenyl and quinoline backbones make these compounds quite non-volatile, especially in the case of **17** and **18**. While TGA data is reported for these two compounds, the residual mass is substantially higher than the % mass of Au in the original compound. This indicates that both compounds decompose to a residue which contains more than just Au. This makes them inherently worse precursors than the rest and makes their figure of merit meaningless as discussed above. Nevertheless, nanoparticulate gold films could be deposited using **17** and **18** at substrate temperatures between 210 °C and 250 °C but the purity of these films was not reported.

Compound			
	m.p. (°C)	Vapour pressure data: Torr, (°C)	Onset of thermal decomposition (°C)
		Figure of merit	
	<b>12</b>	1.0, $(118.8 \pm 4.0)^d$	104
	18		225
	170		
	12		
	<b>13</b>	1.0, $(89.0 \pm 2.0)^d$	16
	< 25		
	<b>14</b>	1.0, $(106.9 \pm 2.7)^d$	20
	< 25		
	<b>15</b>	1.0, $(116.6 \pm 3.8)^b$	48
	<b>16</b>	1.0, $(124.9 \pm 4.3)^b$	78-79
	110 ± 5		
	-15		
	<b>17</b>	1.0, $(161.1 \pm 4.2)^b$	131
	220		
	n/a <sup>j</sup>		
	<b>18</b>	1.0, $(200.5 \pm 4.2)^b$	133-135
	150		
	n/a <sup>j</sup>		

**Figure 2.2** Au(III) compounds previously used in CVD and ALD. Compounds **12**,<sup>86,87</sup> **13**,<sup>87,88</sup> **14**,<sup>87,88</sup> and **15**<sup>74,87,89</sup> bear dithiolate based 1,1-chelating ligands (**12** = dialkyldithiophosphinate, **13,14** = alkylphosphorodithiolate, **15** = dithiocarbamate. Compound **15** has been used for Au ALD using O<sub>3</sub> as a co-reagent. Compound **16**<sup>90</sup> bears a salicylaldiminate ligand (a Schiff base of salicylic acid), **17**<sup>91</sup> and **18**<sup>91</sup> bear a hydroxyquinolate and a thioquinolate ligand respectively.

<sup>a</sup> Calculated from Clausius-Clapeyron data, method unknown. <sup>b</sup> Calculated from Knudsen effusion data. <sup>c</sup> Calculated from TGA data collected in the Barry lab using the method of Kunte et al.<sup>70</sup> d

Calculated from TGA data that was extracted from literature using Chemcraft<sup>73</sup> and then the

method of Kunte et al.<sup>5</sup> Sublimation and/or evaporation conditions from synthetic details or CVD

delivery. <sup>f</sup> Included as supplementary information for this chapter. <sup>g</sup> CVD begins at or below this

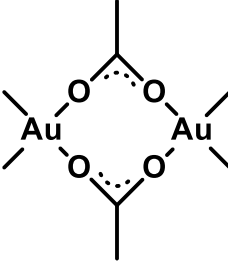
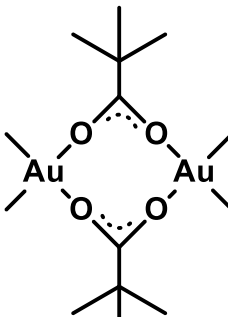
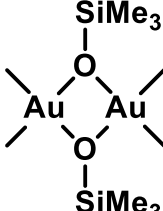
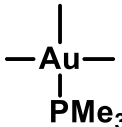
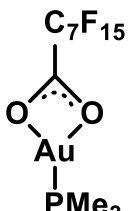
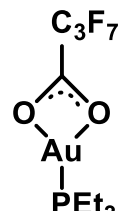
temperature.<sup>h</sup> Literature exists but was unobtainable.<sup>i</sup> System pressure not stated.<sup>j</sup> Figure of merit not calculated because residual mass contained more than just Au.

The same synthetic drawbacks for previous dimethylgold(III) precursors is also prevalent for this set of compounds; the starting material is  $\text{Me}_2\text{AuX}$ , which makes the overall yield quite low. However, there is a single example from 1964 where compound **15** was synthesized by a different method.<sup>92</sup> By first generating the macrocyclic  $[\text{Au}(\text{dithiocarbamate})]_2$  dimer (from  $\text{ClAu}(\text{SC}_4\text{H}_8)$  and  $\text{K}(\text{dithiocarbamate})$ )<sup>93</sup> and then oxidizing with  $\text{Br}_2$  to form  $\text{Br}_2\text{Au}(\text{dithiocarbamate})$ , compound **15** could finally be synthesized by salt metathesis using  $\text{CdMe}_2$ . While there was no mention of using methyl Grignard or methyllithium for the alkylation, Grignards were used to make other compounds in the paper. Unfortunately, the reported melting point was 90 °C with decomposition, in stark contrast to modern melting points between 40 – 50 °C and decomposition well above 200 °C. The only other analytical data were a single IR peak for the C-N stretching frequency and successful elemental analysis, so this strategy should be reviewed as a viable method to synthesize both **15** and other high-merit dimethylgold(III) compounds.

## 2.7 Carboxylate and siloxide complexes of dimethylgold(III), trimethylgold(III) trialkylphosphines, and fluorinated carboxylate complexes of gold(I)

Compounds **19** and **20** (Figure 1.15) have been used several times for CVD of gold metal, while the CVD of gold using **21** was only briefly mentioned in a patent by Mitsubishi Corp. All three are reported to be volatile, and the TGA experiments of **19** and **20** show quite a low residual mass despite their low onsets of decomposition making them attractive CVD precursors (no TGA data exists for **21**). However, given their negative figures of merit a very low pressure system would be required to attempt to develop an ALD process with **19** and **20**. Compound **21** is reported to be substantially more stable and should be assessed as an ALD precursor. The “ $\text{Me}_2\text{AuX}$  synthetic problem” is likely a factor that has prevented widespread use of these precursors. Based on the distillation conditions and

onset of thermal decomposition, **21** could be expected to perform well by TGA and might be comparable to compound **22** in terms of precursor merit.

Compound	m.p. (°C)	
	Vapour Pressure Data: Torr, (°C)	
	Onset of thermal decomposition(°C)	
		
<b>19</b>		
95-96		
1.0, (88.5 ± 3.8) <sup>d</sup>		
70		
-16		
		
<b>20</b>		
75-76		
1.0, (116.5 ± 4.6) <sup>d</sup>		
60		
-34		
		
<b>21</b>		
39-40		
0.010, (40)		
130		
n/a		
		
<b>22</b>		
22-23		
1.0, (85.0 ± 0.1) <sup>c</sup>		
130		
44		
		
<b>23</b>		
n/a <sup>h</sup>		
n/a <sup>h</sup>		
140-160		
n/a		
		
<b>24</b>		
n/a <sup>h</sup>		
n/a <sup>h</sup>		
140-160		
n/a		

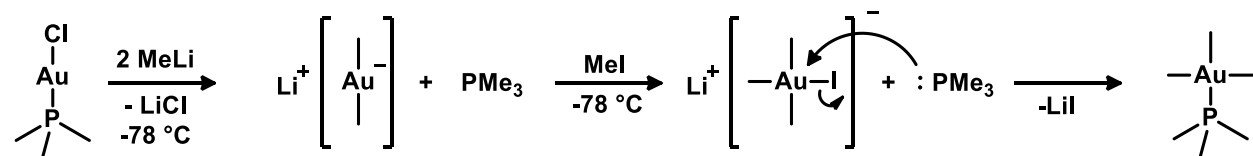
**Figure 2.3** Au(III) and Au(I) compounds previously used in CVD and ALD. Compounds **19**<sup>79,94,95</sup> and **20**<sup>94,95</sup> are dimeric carboxylate complexes, **21**<sup>96,97</sup> is a dimeric siloxide complex, **22**<sup>98-102</sup> is a trimethylgold(III) complexe bearing a trimethylphosphine coordinative ligand. Compounds **23** and **24** bear a fluoroalkyl carboxylate ligand. Compound **22** has been used for Au ALD using O<sub>2</sub>

plasma + H<sub>2</sub>O,<sup>99</sup> H<sub>2</sub> plasma,<sup>100,102</sup> and O<sub>3</sub>.<sup>101</sup> <sup>a</sup> Calculated from Clausius-Clapeyron data, method unknown. <sup>b</sup> Calculated from Knudsen effusion data. <sup>c</sup> Calculated from TGA data collected in the Barry lab using the method of Kunte et al.<sup>70</sup> <sup>d</sup> Calculated from TGA data that was extracted from literature using Chemcraft<sup>73</sup> and then the method of Kunte et al. <sup>e</sup> Sublimation and/or evaporation conditions from synthetic details or CVD delivery. <sup>f</sup> Included as supplementary information for this chapter. <sup>g</sup> CVD begins at or below this temperature. <sup>h</sup> Literature exists but was unobtainable. <sup>i</sup> System pressure not stated.

Compound **22** is the only trimethylgold(III) compound in this review, and has been used for both CVD and ALD. It is the compound that we used to develop the first ALD process for gold metal using O<sub>2</sub><sup>\*</sup> (O<sub>2</sub> plasma) and H<sub>2</sub>O as co-reagents in a three-step process. Since then, two other ALD processes to deposit gold metal using H<sub>2</sub><sup>\*</sup> and O<sub>3</sub>, respectively, have been established. A detailed mechanistic study of the **22** + H<sub>2</sub><sup>\*</sup> process has been published and is included as part of Chapter 3 in this thesis.

While **22** can be synthesized from Me<sub>2</sub>AuX as well as from (PMe<sub>3</sub>)AuX<sub>3</sub> species, we established a much higher-yielding route (Scheme 1.2). Starting from (PMe<sub>3</sub>)AuCl, the addition of two equivalents of methylolithium at low temperature generates lithium dimethylaurate(I) (stable below 0 °C in diethyl ether), a yellow solid at -78 °C. When treated with iodomethane, this species undergoes oxidative addition to form lithium iodotrimethylaurate(III) which then undergoes ligand substitution by the PMe<sub>3</sub> still present in the solution to form the desired product. This procedure produces **22** in high yields near 90 % on up to 30 g scale.

**Scheme 2.2** Synthetic route to compound **22**.



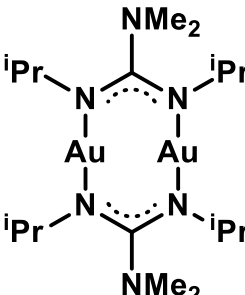
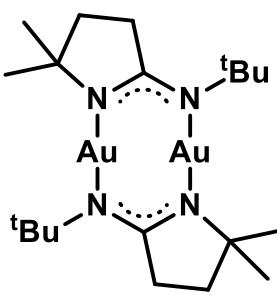
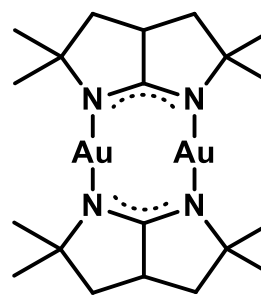
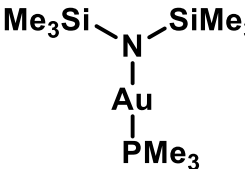
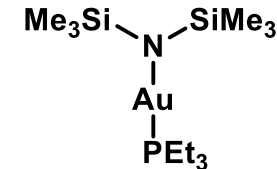
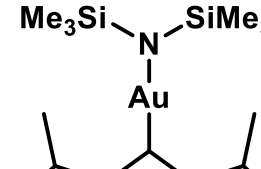
Compounds **23** and **24** have reported CVD processes including microscopy images of the deposited films, but neither the vapour pressure of the compounds nor the operating pressure of the CVD apparatus were described, so these data could not be included here. It would be interesting to synthesize a dimethylgold(III) analogue of **19** using these

fluorinated carboxylates instead of acetate since that might result in an improved vapour pressure.

## 2.8 Guanidinate, amidinate, amide, and N-heterocyclic carbene complexes of gold(I)

Compound **25** (Figure 1.16) was first synthesized and used for CVD in our lab, but it suffers from a low  $T_D$ . While it is possible to isolate some of the compound by sublimation under high vacuum at  $\sim 80$  °C, the recovered yield is low and most of the compound decomposes before subliming. It was possible to use it for CVD if the substrates were placed very close to the delivery zone. The Cu(I) analogue of **25** was the subject of multiple thermal decomposition studies which identified  $\beta$ -hydrogen abstraction and carbodiimide de-insertion as the two main decomposition pathways of the precursor. The ligand of compound **26** was originally developed to mitigate these decomposition pathways for Cu(I), and the ligand worked quite well for this Au(I) compound as well, resulting in a dramatic increase in its thermal stability. However, **26** suffers from low volatility, which contributes to its low figure of merit. A similar effect is observed again in **27** which employs the same ligand design as **26**. An increase in thermal stability is observed, as well in a further reduction in volatility, ultimately leading to a worse figure of merit.

These compounds can be synthesized in reasonably high yields from (THT)AuCl (THT = tetrahydrothiophene) or (Me<sub>2</sub>S)AuCl with the lithiated ligands, and do not suffer from low-yield gold-containing intermediates. However, the ligand syntheses for **26** and **27** are somewhat time-consuming and do not produce the greatest precursors for Au, although the Cu(I) analogue of **26** has superb thermal properties.<sup>64</sup>

Compound	m.p. (°C)	
Vapour Pressure Data: Torr, (°C)		
Onset of thermal decomposition(°C)		
	<b>25</b>	
83	>280	n/a
0.03, (83) <sup>e</sup>	1.0, (238) <sup>c</sup>	1.0, (322.4 ± 6.7) <sup>d</sup>
83	280	310
n/a	11	-6
	<b>26</b>	
	<b>27</b>	
	<b>28</b>	
36-37	< 25	72
1.0, (80.2 ± 0.4) <sup>c</sup>	1.0, (120.3 ± 3.1) <sup>d</sup>	1.0, (114.8 ± 1.0) <sup>c</sup>
170	210	190
78	32	24
	<b>29</b>	
	<b>30</b>	

**Figure 2.4** Au(I) compounds previously used in CVD. Compound **25**<sup>103–105</sup> is a dimeric gold(I) guanidinate, **26**<sup>106,107</sup> is an iminopyrrolidinate complex, and **27**<sup>108</sup> is a bicyclic amidinate, **28**,<sup>109,110</sup> **29**,<sup>111</sup> and **30**<sup>110</sup> are trialkylphosphine and N-heterocyclic carbene complexes of gold(I) bis(trimethylsilyl)amide. <sup>a</sup> Calculated from Clausius-Clapeyron data, method unknown. <sup>b</sup> Calculated from Knudsen effusion data. <sup>c</sup> Calculated from TGA data collected in the Barry lab using the method of Kunte et al.<sup>70</sup> <sup>d</sup> Calculated from TGA data that was extracted from literature using Chemcraft<sup>73</sup> and then the method of Kunte et al. <sup>e</sup> Sublimation and/or evaporation conditions

from synthetic details or CVD delivery.<sup>f</sup> Included as supplementary information for this chapter.<sup>g</sup> CVD begins at or below this temperature.<sup>h</sup> Literature exists but was unobtainable.<sup>i</sup> System pressure not stated.

Compound **28** was originally reported by Schmidbaur as a distillable low-melting solid. We used **28** and **30** in a CVD study that produced large 2-D gold plates (Chapter 2), and we have tested compound **28** for ALD, but found that we could not produce metal films using H<sub>2</sub> (5%) or H<sub>2</sub>O. Compound **29** was tested for ALD by Mäkelä as an ALD precursor but was determined to undergo slow CVD once a gold surface had been established on the oxide substrate. This reactivity is reminiscent of the autocatalytic CVD reported for (PR<sub>3</sub>)AuR' species such as **36** and **37** *vide infra* as well as observations made about (PMe<sub>3</sub>)AuCH<sub>2</sub>(SiMe<sub>3</sub>) which are discussed in Chapter 5 of this thesis. Compound **30** is the only reported NHC-containing precursor to be used in CVD or ALD of gold, but as early as 2011 it was discovered that some NHCs bind very strongly to metallic gold surfaces.<sup>112</sup> In 2014 this phenomenon was popularized by Crudden *et al.* and has spurred a widespread study of the chemistry of NHCs on gold and other surfaces.<sup>113</sup> Given the strength of the NHC-Au<sub>(s)</sub> bond, this ligand is quite appropriate for use in an ALD precursor as could play the role of the self-limiting ligand.

Chapter 2 describes a study where we can observe a stark difference in morphology of gold nanostructures when using **28** or **30** which is due to the relatively faster rate of desorption of PMe<sub>3</sub> from Au<sub>(s)</sub> compared to the slower rate of desorption of an NHC from Au<sub>(s)</sub>. Chapter 6 describes a study where we purposefully synthesize NHC-containing gold precursors for the purpose of inventing a new gold ALD process. Compounds **28-30** are most easily synthesized by reaction of (PR<sub>3</sub>)AuCl or (NHC)AuCl with Li(N(SiMe<sub>3</sub>)) and can all be purified by vacuum distillation (**28**, **29**) or vacuum sublimation (**30**).

## 2.9 Phosphine complexes of chlorogold(I) and alkylgold(I)

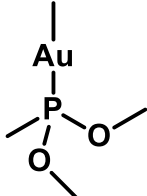
Compounds **31** and **32** (Figure 1.17) are the only Au(I) halides that have been used for thermal CVD. Neither of them are volatile according to the scant literature description that

exists, but this reactivity can be predicted for **31** based on the dipolar nature of the compound (electronegativity of Au = 2.5, Cl = 3.5) causing a substantial amount of intermolecular interaction that suppresses volatility. Compound **32** is expected to be more volatile due to the fluorine atoms reducing intermolecular interactions and somewhat reducing the magnitude of the dipole moment of the molecule. However, while it might increase the volatility slightly, PF<sub>3</sub> is a poor Lewis base and its dissociation from AuCl is likely the cause of the low decomposition point of the precursor. Compound **31** is synthesized either from HAuCl<sub>4</sub> and an excess of PEt<sub>3</sub> in the presence of H<sub>2</sub>O or from a ligand displacement reaction between (THT)AuCl and PEt<sub>3</sub>. Compound **32** is synthesized by reacting Au<sub>2</sub>Cl<sub>6</sub> (AuCl<sub>3</sub>) with an excess of PF<sub>3</sub> in a steel pressure vessel which forms the product and PF<sub>3</sub>Cl<sub>2</sub>.

While these two compounds aren't particularly attractive compared to others in this review (especially considering the danger of the synthesis of **32**), they bear the closest resemblance to very early ALD processes where volatile metal halides were combined with reducing agents to deposit metallic films, with H<sub>2</sub>O to deposit metal oxide films, and with NH<sub>3</sub> to deposit metal nitride films.<sup>114</sup> TGA data for **31** have been reported and it is not volatile enough for routine use in CVD or ALD. However there are examples of thermally stable gold(I) halides that could be explored as ALD precursors, namely small (L)AuBr or (L)AuI where L is an isonitrile or a phosphine, reported to be fairly volatile in vacuo. There also exists TGA data for an (NHC)AuCl complex that leaves no residual mass by TGA.<sup>115</sup> We independently synthesized, characterized, and tested this compound by TGA in our glovebox and confirmed the same result: the compound is thermally stable, but not very volatile. To our knowledge this is the only example of a gold halide of any kind that leaves zero residual mass by TGA.

Compounds **33** and **34** were used in a CVD study to deposit gold metal and could be delivered in that system at room temperature. Unfortunately no TGA or DSC were published for these species, but they appear to have similar properties to **36**. It was also found that they undergo CVD by a similar mechanism to **36**, **37**, and **39** which is bimolecular reductive elimination of the alkyl ligand (Scheme 1.3). CVD details for compound **35** are scarce, and while a deposition was performed at a substrate

temperature of 170 °C, it's likely that this species begins to decompose at temperatures similar to **33** and **34**.

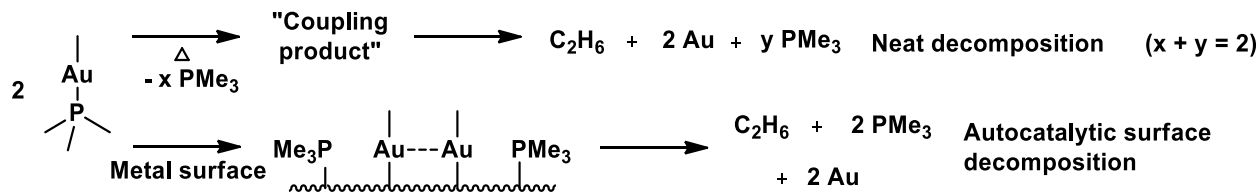
Compound	$\text{Cl} \begin{array}{c}   \\ \text{Au} \\   \\ \text{PEt}_3 \end{array}$	$\text{Cl} \begin{array}{c}   \\ \text{Au} \\   \\ \text{PF}_3 \end{array}$
m.p. (°C)		
Vapour Pressure Data: Torr, (°C)	<b>31</b>	<b>32</b>
Onset of thermal decomposition(°C)	78	n/a
	1.0, $(303.7 \pm 14.9)^d$	0.0001, (25) <sup>e</sup>
	n/a	37-40
	n/a	n/a
		
<b>33</b>	<b>34</b>	<b>35</b>
< 25	< 25	0-2
0.75, (25) <sup>e</sup>	0.75, (25) <sup>e</sup>	0.05, (75) <sup>e</sup>
70 <sup>g</sup>	102 <sup>g</sup>	170 <sup>g</sup>
n/a	n/a	n/a
<b>36</b>	<b>37</b>	<b>38</b>
62	58-60	n/a
1.0, $(67.5 \pm 0.1)^c$	(30) <sup>e,i</sup>	n/a
130	58-60	170 <sup>g</sup>
31	n/a	n/a
<b>39</b>		
< 25		
		0.0001, (22) <sup>e</sup>
		125 <sup>g</sup>
		n/a

**Figure 2.5** Au(I) compounds previously used in CVD. Compounds **31**<sup>111,116</sup> and **32**<sup>116,117</sup> are trialkylphosphine and trifluorophosphine complexes of gold chloride respectively. Compounds **33**,<sup>118</sup> **34**,<sup>118</sup> and **35**<sup>119,120</sup> are complexes of methylgold(I) bearing alkylphosphonite (**33**, **34**) and trialkylphosphite ligands (**35**). Compounds **36**,<sup>120-123</sup> **37**,<sup>120,124</sup> **38**,<sup>120</sup> and **39**,<sup>121,125,126</sup> are trialkyl-

and dialkylarylphosphine alkylgold(I) complexes.<sup>a</sup> Calculated from Clausius-Clapeyron data, method unknown.<sup>b</sup> Calculated from Knudsen effusion data.<sup>c</sup> Calculated from TGA data collected in the Barry lab using the method of Kunte et al.<sup>70</sup><sup>d</sup> Calculated from TGA data that was extracted from literature using Chemcraft<sup>73</sup> and then the method of Kunte et al.<sup>e</sup> Sublimation and/or evaporation conditions from synthetic details or CVD delivery.<sup>f</sup> Included as supplementary information for this chapter.<sup>g</sup> CVD begins at or below this temperature.<sup>h</sup> Literature exists but was unobtainable.<sup>i</sup> System pressure not stated.

Compounds **36-39** are grouped because they are all alkylgold(I) trialkylphosphine complexes. A substantial amount of literature on both the solution phase chemistry as well as the CVD of these types of compounds exists. Notably, compounds **36** and **39** undergo CVD on metallic surfaces at temperatures as low as room temperature. The rate-limiting step of this reaction is dissociation of the PMe<sub>3</sub>-Au bond at the metallic surface, and the subsequent bimolecular reductive elimination occurs rapidly to produce Au<sup>0</sup>. This surface decomposition mechanism does not occur on oxide surfaces but is autocatalytic on metals. This effect where growth was not observed on oxide surfaces in the absence of a co-reagent, but CVD growth is observed in the presence of a co-reagent was also observed in the testing of **29** for an ALD process.

**Scheme 2.3** Decomposition pathways for (PMe<sub>3</sub>)AuMe as a neat liquid and in the presence of an active metal surface.



CVD using compound **37** was only thoroughly described once, where deposition was performed at 400 °C and above. It is likely that both this compound as well as **38** also undergo CVD by a similar mechanism to **33**, **34**, **36** and **39**. Since these species undergo autocatalytic CVD it is impossible to use them as ALD precursors: the rate limiting step is chemisorption to the surface, not the bimolecular reductive elimination. Chapter 5 describes a study where part of the effort was to attempt to design a precursor to circumvent this issue and make the bimolecular reductive elimination step the rate-limiting

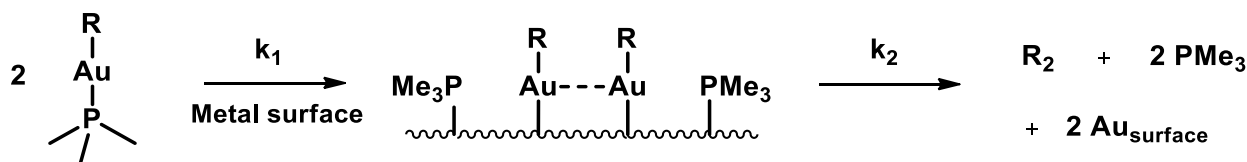
step using sterically bulky alkyl ligands. Compounds **33-39** are synthesized in a similar manner as **28-30** where the appropriate (L)AuCl compound is treated with an alkylolithium or Grignard reagent.

## 2.10 Gold(I) complexes containing alkynyl, trifluoromethyl, and isonitrile ligands

Compounds **40**, **41**, **43**, **44**, and **45** (Figure 1.18) were all reported to have been used for CVD by Puddephatt *et al.*, but no TGA or DSC data has been reported. Although it has not been used frequently at all in CVD, the methyl isocyanide coordinative ligand appears to produce alkyl- and alkynylgold(I) complexes of similar thermal stability to the phosphines and should be studied further to determine which of these species are also more volatile.

The trifluoromethylgold(I) species **42** and **46** were reported as CVD precursors in the same publication. The main topic of the publication was CVD using **46**, however reference 12 therein also mentions that CVD experiments using **42** were conducted. While compound **46** could produce pure gold films at substrate temperatures of 260 °C, compound **42** required substrate temperatures higher than 340 °C to produce gold films that still contained significant amounts of carbon, but with low fluorine content. The rate of CVD of **46** was greatly reduced when methylisocyanide was introduced into the reactor alongside it which was also observed in the case of **33**, **34**, and **36**. This implies that these species as well as **40-45** undergo CVD by a similar mechanism, where the rate limiting step is dissociation of the coordinative ligand (Scheme 1.4).

**Scheme 2.4** Autocatalytic decomposition of  $(\text{PMe}_3)\text{AuR}$  on metallic surfaces. For R = Me,  $k_1 < k_2$  which results in CVD.



Compound	m.p. (°C)	
Vapour Pressure Data: Torr, (°C)		
Onset of thermal decomposition(°C)		

	<b>40</b>		<b>41</b>		<b>42</b>
100		194-196		1.0, (162.1 ± 0.4) <sup>c,f</sup>	115
n/a		0.005, (40-70) <sup>e</sup>			175
100		194-196			6
n/a		n/a			
	<b>43</b>		<b>44</b>		<b>45</b>
95		140		180	109-110
0.005, (30) <sup>e</sup>		n/a		n/a	0.01, (60-70) <sup>e</sup>
95		140		180	260 <sup>g</sup>
n/a		n/a		n/a	n/a
			<b>46</b>		

**Figure 2.6** Au(I) compounds previously used in CVD. Compounds **40**,<sup>127</sup> **41**,<sup>127,128</sup> and **42**<sup>129</sup> are trimethylphosphine alkynylgold(I) complexes and trifluoromethylgold(I) complexes, respectively. Compounds **43**,<sup>127</sup> **44**,<sup>127</sup> **45**,<sup>127</sup> and **46**<sup>129</sup> are isocyanate complexes of alkyl, alkynyl, and trifluoromethyl gold(I). <sup>a</sup> Calculated from Clausius-Clapeyron data, method unknown. <sup>b</sup> Calculated from Knudsen effusion data. <sup>c</sup> Calculated from TGA data collected in the Barry lab using the method of Kunte et al.<sup>70</sup> <sup>d</sup> Calculated from TGA data that was extracted from literature using Chemcraft<sup>73</sup> and then the method of Kunte et al. <sup>e</sup> Sublimation and/or evaporation conditions from

synthetic details or CVD delivery.<sup>f</sup> Included as supplementary information for this chapter.<sup>g</sup> CVD begins at or below this temperature.<sup>h</sup> Literature exists but was unobtainable.<sup>i</sup> System pressure not stated.

We synthesized **42** as part of a different research project (see Figures S-1.22 and S-1.23 for TGA and DSC data respectively),<sup>130</sup> which is how its  $T_V$  and  $T_D$  were determined. To our surprise, the introduction of the  $\text{CF}_3$  group resulted in a much less volatile precursor than when a methyl group was used (as in compound **36**). We have previously observed this reduction in volatility (but simultaneous increase in thermal stability) in Au(I) compounds when introducing a fluorinated alkyl ligand.<sup>123</sup> The reduced volatility is due to an increased number of CH-F intermolecular contacts as well as the larger dipole moment of the molecule. These intermolecular interactions appear to outweigh the expected volatility increase from fluorine atoms reducing the strength of intermolecular dispersion interactions. In the reported crystal structure of **42**, there is also a significant aurophilic interaction ( $\text{Au-Au} = 3.1021(9) \text{ \AA}$ ) which likely contributes to its low volatility.<sup>131</sup>

Simply fluorinating one part of a molecule is not sufficient to produce a volatility increase. One interesting observation is that an increase in volatility from ligand fluorination as in the series **1-3** or **5-9** has thus far only been observed in dimethylgold(III) acac-type compounds. For example, even though  $(\text{PMe}_3)\text{Au}(\text{CF}_3)_3$  is substantially more stable (b.p. =  $214^\circ\text{C}$ , 760 Torr)<sup>132</sup> than  $(\text{PMe}_3)\text{AuMe}_3$  (decomp =  $130^\circ\text{C}$ ), it is still less volatile. Simply adding fluorine to a precursor doesn't always increase its volatility, and we still don't fully understand how to use it to its highest potential.

## 2.11 Figure of merit minefield diagram

To summarize the figure of merit data, we developed a “minefield diagram” shown below in Figure 1.19. Here, the center of each circle indicates the compound’s  $T_V$ , the temperature at which it might be easily delivered for ALD. Lower  $T_V$  are always better from both a cost and ease of use standpoints, but a high  $T_V$  doesn’t immediately doom a precursor: some systems are able to reach these delivery temperatures. The area of each

circle is proportional to that precursor's figure of merit. Green circles represent a positive figure of merit and red circles represent a negative figure of merit.

Although many data points are missing due to a lack of literature data, it is still immediately clear that the best candidate precursors for ALD are in the bottom left-hand corner corresponding essentially to **1-11** from Figure 1.13. Compounds **15** and **22**, currently the only two known gold ALD precursors also stand out, as does **28**. Since we have observed that compound **28** does not undergo ALD, and **29** was observed to undergo slow CVD on gold surfaces, these precursors are good for vapour deposition, but not suitable for ALD. This supports the observation that the best literature candidates for gold ALD precursors are exclusively Au(III) compounds, most of which have the structure of dimethylgold(III)(L) where L is a monoanionic chelating ligand.

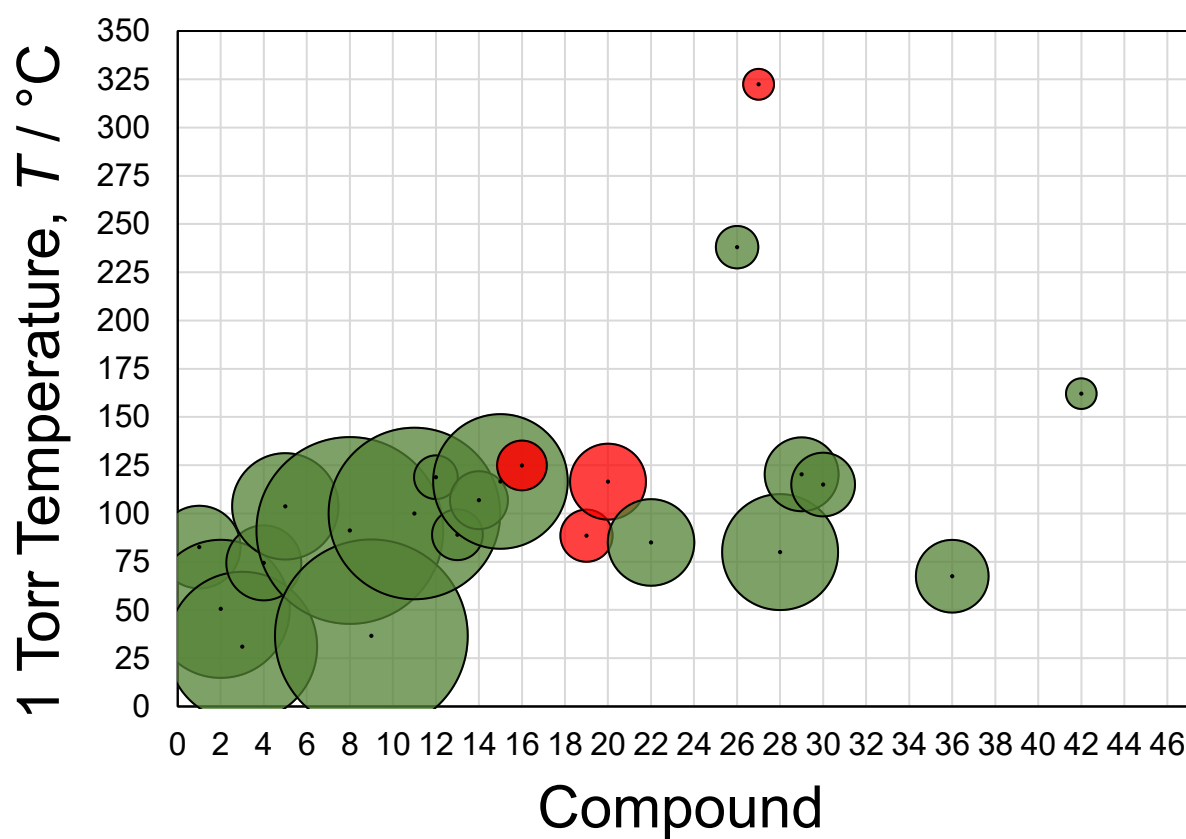


**Figure 2.7** Figure of merit minefield diagram for the 46 gold compounds that have been reported to have been used in CVD and ALD under the restrictions given at the beginning of this section.

The figure of merit is represented by the relative area of each circle. Green circles indicate a positive figure of merit, and red circles indicate a negative figure of merit.

This doesn't mean that a gold ALD precursor derived from gold(I) cannot be achieved, but that class of compounds doesn't possess the good thermal properties that Au(III) systems have. Thus an exploration of Au(I) precursors is a main topic of my research, and chapters 4, 5, and 6 describe a number of investigations and specific strategies that were targeted towards the discovery of Au(I) based precursors for gold ALD.

## 2.12 Supporting Information

All manipulations were performed under an inert atmosphere of dry nitrogen gas using an MBraun Labmaster 130 glovebox or standard Schlenk techniques unless otherwise stated. Both gold compounds were treated as light sensitive, air-stable materials and were stored at 5 °C in a refrigerator. NMR spectra were collected at room temperature on a Bruker 300 MHz or a Jeol 400 MHz spectrometer and were referenced to an internal standard of tetramethylsilane (TMS) in the case of CDCl<sub>3</sub> or the residual protio solvent signal in the case of C<sub>6</sub>D<sub>6</sub> (7.16 ppm relative to TMS). C<sub>6</sub>D<sub>6</sub> was purchased from Aldrich and was degassed using freeze-pump-thaw cycles and subsequently stored over activated 4 Å molecular sieves under inert gas. Gold trichloride was produced by slowly heating HAuCl<sub>4</sub> × H<sub>2</sub>O under vacuum. The conversion was deemed complete once no trace of orange or yellow colour was observed, the solid was dark red, and the vacuum apparatus had once again reached base pressure. (PMe<sub>3</sub>)AuCl was prepared according to literature procedures. Anhydrous acetonitrile, methyl lithium (1.6 M in diethyl ether), trimethyl(trifluoromethyl) silane (CF<sub>3</sub>SiMe<sub>3</sub>) solution (2M), and AgF were purchased from Merck and used as received. 1,1,1-trifluoro-5,5-dimethyl-2,4-hexanedione was purchased from Alfa Aesar and used as received. 1,1,1-trifluoro-4-imino-5,5-dimethyl-2-hexen-2-ol was synthesized using the literature procedure.<sup>133</sup> Diethyl ether, hexanes were purchased from VWR chemicals and purified using an MBraun solvent purification system prior to use. Saturated ammonium hydroxide (NH<sub>4</sub>)OH was purchased from VWR and used as received. HAuCl<sub>4</sub> • xH<sub>2</sub>O was produced using a scaled-up version of a literature

procedure<sup>134</sup> using up to 32.2 g (1 Troy ounce) of fine gold which can be purchased at market price.

### *Synthesis of compound 8*

Based on a modified procedure,<sup>85</sup> 0.550 g (1.8 mmol) of AuCl<sub>3</sub> was placed in a Schlenk flask in a glovebox. To this flask was added 10 mL of diethyl ether which cause the formation of a pale yellow solution and a brown solid. This mixture was brought to a Schlenk line and cooled in a dry ice / isopropanol bath. MeLi (3.4 mL, 1.6 M) was added dropwise to the cooled mixture causing the immediate formation of a dark brown/purple solution. This mixture was left to stir in the cold bath for 1 hr. Then, a solution of 0.350 g (2.9 mmol) in 2 mL of diethyl ether was added to this solution and stirring was continued for an additional 1.5 hours in the cold bath. Then the reaction was allowed to warm to room temperature at which point 10 mL of H<sub>2</sub>O were added dropwise. The dark solids in the flask appeared to be mostly H<sub>2</sub>O-soluble. The mixture was decanted into a separatory funnel, the aqueous layer was decanted, and the remaining ethereal layer was washed with 2 x 20 mL of fresh H<sub>2</sub>O. The ethereal layer was dried over MgSO<sub>4</sub>, filtered, and evaporated to dryness using a rotary evaporator. Final drying on a high vacuum resulted in the crystallization of two distinct shaped of crystals with a fine crystalline solid at the bottom of the flask, and needle like crystals higher up on the walls of the flask. <sup>1</sup>H-NMR analysis of these materials showed a mixture of the free ligand and peaks corresponding to the expected product. Sublimation was not sufficient to purify the two solids from one another and resulted in an enrichment in the product (lower volatility) of only 30%.

The mixture was purified by flash chromatography on silica gel suing a 10 cm length x 1.25 cm width column (wet-packed using a mixture of 1:10 diethyl ether : hexanes). The solvent used for loading the mixture used as eluent was 1:5 diethyl ether : hexanes. The bands could be visualized on the column using UV light. Fractions were collected in 3 mL portions. The desired product was more mobile and was recovered in the first 16 fractions. Yield = 0.178 g, (24 %). Fractions 17 – 21 contained no material. Fractions 22-27 contained the free ligand.

### *Synthesis of compound 42*

Based on a modified literature procedure,<sup>135</sup> 1.680 g (5.4 mmol) of (PMe<sub>3</sub>)AuCl was added to a purged Schlenk flask and dissolved in 40 mL of anhydrous acetonitrile. To this solution were added 0.847 g (6.7 mmol) of AgF, followed by a solution of CF<sub>3</sub>(SiMe<sub>3</sub>) in tetrahydrofuran (11.30 mL, 2 M, 22.6 mmol) which resulted in the immediate formation of a grey suspension. The flask was wrapped in aluminum foil to protect the reaction from light and was left to stir overnight. The next day the suspension was filtered through a plug of celite on a glass frit to give a light yellow filtrate. The solvent was removed using a rotary evaporator leaving an off-white solid. As reported, this solid was found to be a mixture of the desired product and the double-salt [Au(PMe<sub>3</sub>)<sub>2</sub>][Au(CF<sub>3</sub>)<sub>2</sub>] by <sup>1</sup>H-NMR. Instead of using column chromatography we found that vacuum sublimation (100 – 150 °C, 5 mTorr) was a much more effective method of purification, giving a higher yield of the final product as a white solid on a water-cooled cold finger. Yield = 1.451 g (73 %).

**<sup>1</sup>H-NMR** (300 MHz, CDCl<sub>3</sub>):  $\delta$  1.51 (d,  ${}^2J_{H-P}$  = 10.0 Hz, 9H, P-CH<sub>3</sub>)

**<sup>13</sup>C-NMR** (100 MHz, CDCl<sub>3</sub>):  $\delta$  15.19 (d,  ${}^1J_{C-P}$  = 35.2 Hz, P-(CH<sub>3</sub>)<sub>3</sub>), 167.2 (m,  ${}^1J_{C-F}$  = 35.1 Hz, Au-CF<sub>3</sub>)

**<sup>19</sup>F-NMR** (282.4 MHz, CDCl<sub>3</sub>):  $\delta$  -29.6 (376 MHz,  $J_{F-P}$  = 48.9 Hz, CF<sub>3</sub>)

**<sup>31</sup>P-NMR** (121.5 MHz, CDCl<sub>3</sub>): -0.30 (q,  ${}^3J_{P-F}$  = 49.0 Hz, P(CH<sub>3</sub>)<sub>3</sub>)

*TGA and DSC of compounds **8** and **42**.*

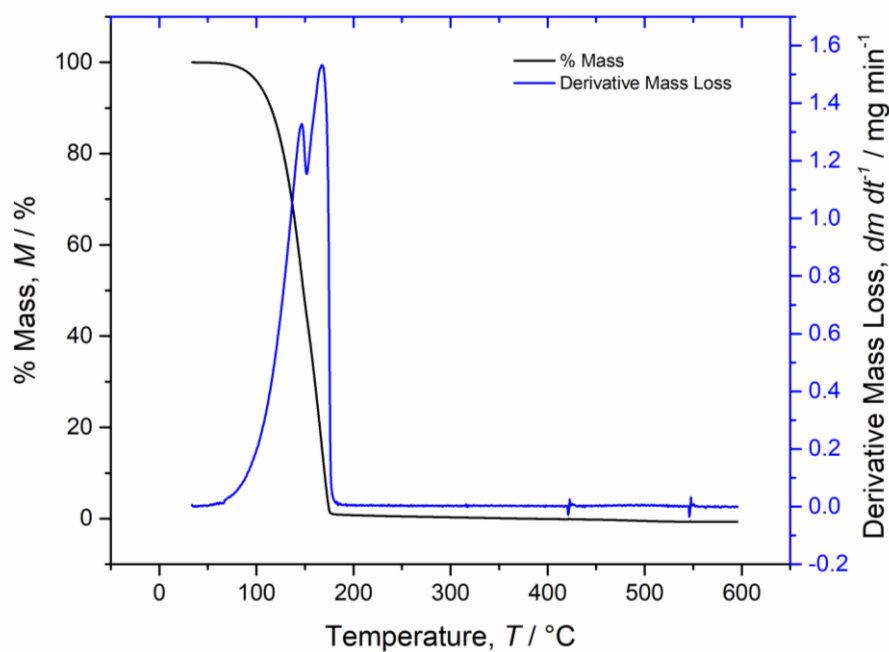


**Figure S-2.8** TGA ramp experiment of compound **8**. Sample mass = 7.413 mg, heating rate = 10  $^\circ\text{C min}^{-1}$ . A clear inflection point is observed at 151  $^\circ\text{C}$ , but the compound still evaporates completely.

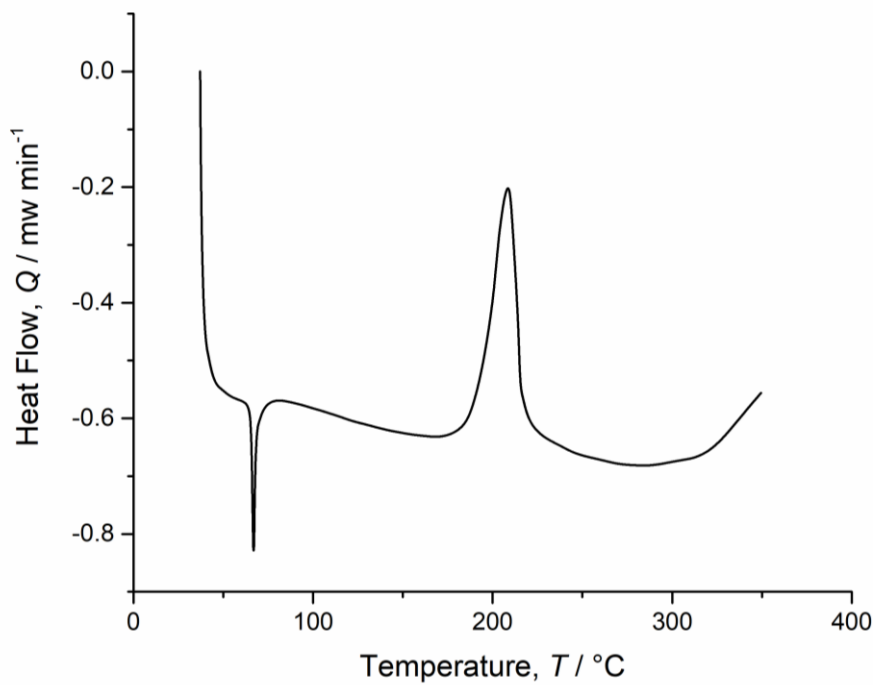


**Figure S-2.9** DSC ramp experiment of compound **8**. Sample mass = 0.085 mg, heating rate = 10  $^\circ\text{C min}^{-1}$ . A melting point is observed at 58.6  $^\circ\text{C}$  and an exothermic event begins at 168  $^\circ\text{C}$ .

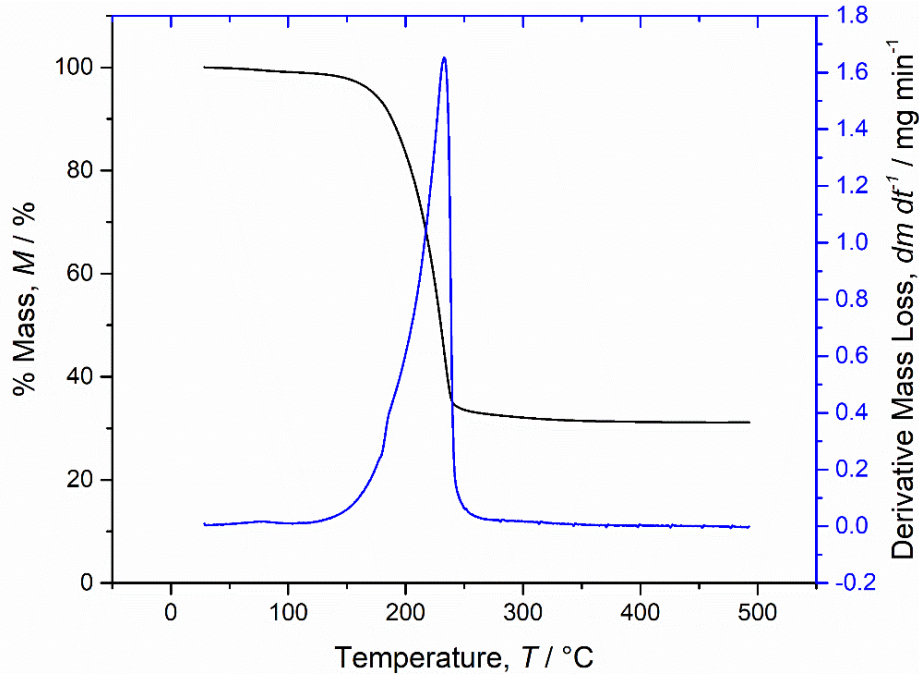


**Figure S-2.10** TGA ramp experiment of compound **42**. Sample mass = 9.136 mg, heating rate = 10  $^\circ\text{C min}^{-1}$ . The residual mass of the analysis was 31.19 %.

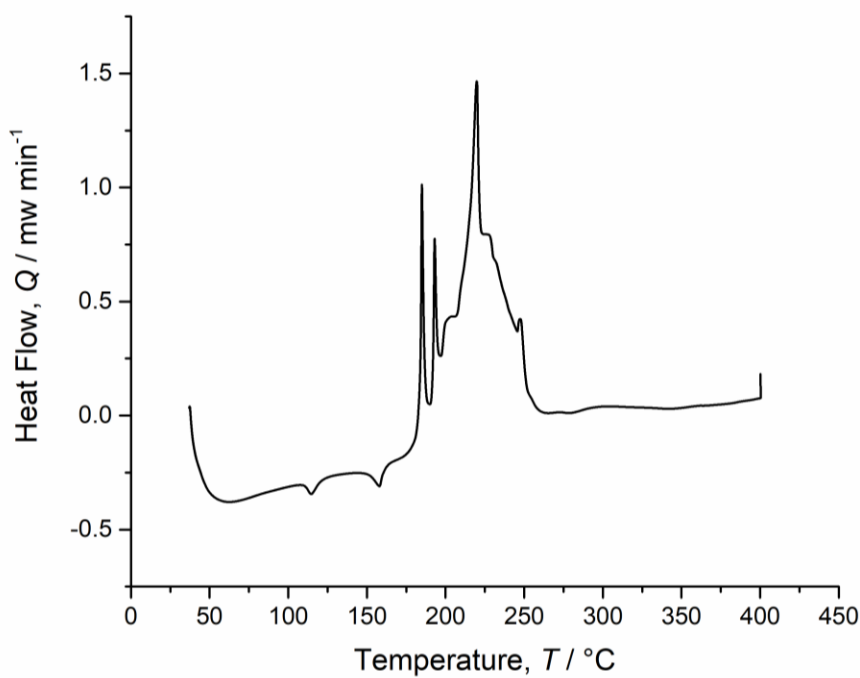


**Figure S-2.11** DSC ramp experiment of compound **42**. Sample mass = 0.122 mg, heating rate =  $10 \text{ } ^\circ\text{C min}^{-1}$ . Two endothermic events were observed at  $115 \text{ } ^\circ\text{C}$  and  $159 \text{ } ^\circ\text{C}$ , the first of which we believe to be a phase transition as no melting is observed in a melting point apparatus until  $\sim 155 \text{ } ^\circ\text{C}$ . The onset of the first exothermic event was determined to be  $175 \text{ } ^\circ\text{C}$ .



# Chapter 3 Surfactant-directed growth of gold metal nanoplates by chemical vapor deposition

Adapted with permission from *Chem. Mater.*, **2015**, 27, 6116-6124, DOI: [10.1021/acs.chemmater.5b02712](https://doi.org/10.1021/acs.chemmater.5b02712). Copyright 2015 American Chemical Society.

Matthew B. E. Griffiths,<sup>\*,†</sup> Sara E. Koponen,<sup>†</sup> David J. Mandia,<sup>†</sup> Jennifer F. McLeod,<sup>†</sup> Jason P. Coyle,<sup>†</sup> Jeffrey J. Sims,<sup>‡</sup> Javier B. Giorgi,<sup>‡</sup> Eric R. Sirianni,<sup>§</sup> Glenn P. A. Yap,<sup>§</sup> and Seán T. Barry<sup>†</sup>, *Chem. Mater.*, **2015**, 27, 6116-6124

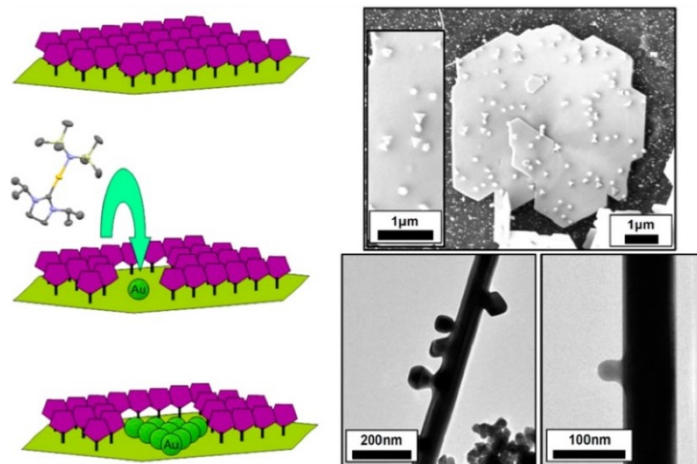
<sup>†</sup> Department of Chemistry, Carleton University, 1125 Colonel By Drive, Ottawa, Ontario K1S 5B6, Canada

<sup>‡</sup> Department of Chemistry and Biomolecular Science, University of Ottawa, 10 Marie Curie Private, Ottawa, Ontario K1N 6N5, Canada

<sup>§</sup> Department of Chemistry and Biochemistry, University of Delaware, Newark, Delaware 19716, United States

### 3.1 Abstract

Surface-supported, low dimensional gold nanostructures are of interest for plasmonic applications. Low dimensional nanostructures are readily accessible by solution-phase growth, where shape control through the addition of growth-directing surfactants is well established. Yet, shape control in chemical vapor deposition (CVD) has not been well explored, and metallic gold films are typically limited to nanoparticulate or thin film morphologies. This article describes the self-seeded growth of high aspect ratio gold plates and wires by CVD. A directed growth mechanism is proposed, where growth is directed by the coordinating N-heterocyclic carbene (NHC) and phosphine ligands originating from the thermal decomposition of the two gas-phase precursors,  $[\text{Au}(\text{HMDS})(\text{NHC})]$  (HMDS = hexamethyldisilazide, NHC = *N,N'*-1,3-diisopropylimidazolidin-2-ylidene) and  $[\text{Au}(\text{HMDS})(\text{PMe}_3)]$ . These ligands acted as transient surfactants for plate growth between 370 and 460 °C and at high precursor flux. Energy dispersive X-ray spectroscopy (EDX) and X-ray photoelectron spectroscopy (XPS) evidence indicates that hydroxyl terminated substrate surfaces are passivated with trimethylsilyl (TMS) moieties originating from the HMDS ligand in both precursors, which promoted island type growth and directed precursor decomposition to occur on gold surfaces. Secondary nucleation is observed on all gold structures and is a crucial component to gas-phase surfactant-mediated CVD growth. This work identifies the potential to use precursor-bound coordinative ligands or gas-phase surfactants to direct growth of metal nanocrystals by CVD.



## 3.2 Introduction

Gold is a useful material for nanoscale applications. The properties of gold nanoparticles have been well explored and have found use in diverse fields like biomedical applications,<sup>136,137</sup> gas sensing,<sup>138–141</sup> and catalysis.<sup>142–144</sup> Surface plasmon resonance in gold nanoparticles results in a strong interaction with visible light, allowing use in photovoltaics<sup>145–147</sup> and many other areas of research.<sup>148</sup> Looking forward, innovative methods for the synthesis and integration of gold nanostructures into complex architectures will be a valuable area of research.

Solution-phase synthesis of gold nanoparticles is well explored and is exploitable for nanoarchitecture design by virtue of facet-specific surfactants and careful control of reaction conditions. Inhibition of the growth of certain facets permits the engineering of nanoparticles with specific shapes; nanorods, nanowires, cubooctahedra, nanoplates, and many other nanostructures of metallic gold are accessible from solution phase synthesis in this fashion.<sup>149,150</sup> Anisotropic particles are of particular interest due to differential quantum confinement in various dimensions that occurs upon miniaturization of the particles.<sup>151–153</sup> In particular, plates with nanoscale thicknesses can cover a large area using very little gold metal and have been used as surface-enhanced Raman scattering substrates.<sup>154,155</sup>

Chemical vapor deposition (CVD) is a widely used process to deposit thin films of many different materials.<sup>156</sup> Applications in microelectronics have directed research and development of CVD processes toward uniform, conformal, and continuous films when considering metal deposition. However, it is possible to direct the growing film toward more exotic morphologies, for example by the addition of catalysts to the substrate to template nanowire<sup>157–159</sup> or nanotube growth.<sup>160,161</sup> Vapor–liquid–solid (VLS)-type growth with gold as the eutectic partner has also been employed to grow nanowires, rods, and more complex structures.<sup>162–164</sup> While these methods have been heavily researched, the ability to synthesize specific shapes of gold metal nanocrystals by CVD has only been reported a few times. Methods used mainly involve pyrolysis of chloroauric acid<sup>165,166</sup> or surface templating.<sup>167,168</sup>

In CVD, the deposition substrate plays an important role in determining the initial structure of deposited features. Using gas-phase chemical precursors, both surface nucleation of the precursor and surface-mediated decomposition will initiate growth.<sup>156</sup> Upon chemisorption, it is typically desirous for coordinative ligands which were bound to the gaseous metal compound to dissociate and become volatile, nonreactive byproducts of the CVD process.<sup>169</sup> However, to control the shape of crystallites that have nucleated at the surface, the precursor's ligands could be selected to be strongly interacting with the growing surface, behaving similarly to surfactants in a typical solution-phase system. In CVD precursor ligand systems, highly Lewis basic coordinating ligands are used to stabilize metal centers, making the compounds more thermally stable and thus useful in vapor deposition techniques. Coordinative ligands such as N-heterocyclic carbenes (NHCs)<sup>170–172</sup> and trialkylphosphines<sup>173–175</sup> are chemically similar to surfactants and capping agents which are used in wet synthesis of metal nanocrystals and so may play similar roles in a CVD process.

Both NHCs and trialkylphosphines form strong coordination bonds to gold. The phosphines PMe<sub>3</sub> and PEt<sub>3</sub> have been used extensively in the development of gold chemistry due to their ability to stabilize reactive alkyl-gold species to thermal decomposition,<sup>176</sup> as well as in CVD processes.<sup>98,177</sup> The development of NHC chemistry for group 11 metal heterogeneous catalysis demonstrates the stabilizing influence of NHCs to gold(I) centers.<sup>178</sup>

The surface chemistry of NHCs and trialkylphosphines is well studied on gold. Phosphines have been used to cap small gold nanoparticles just after formation by coordinating strongly with exposed surfaces and preventing further nucleation and growth. NHCs were recently shown to form tight self-assembled monolayers (SAMs) on gold surfaces, which were highly thermally stable and resilient to oxidation and substitution by alkyl-thiols.<sup>179</sup> By designing a gold precursor bearing phosphine or NHC ligands, these precursors have the potential to play the further role of directing growth during CVD by slowing growth on certain gold facets after dissociation during the CVD process. Herein we describe the single-source CVD of gold using hexamethyldisilylazido

Au(I) compounds with two different coordinating ligands: *N,N'*-1,3-diisopropylimidazolidin-2-ylidene (**1**) and trimethylphosphine (**2**).

### 3.3 Results and Discussion

Two gold compounds,  $[\text{AuN}(\text{SiMe}_3)_2\text{NHC}]$  (**1**) ( $\text{NHC} = N,N'$ -1,3-diisopropylimidazolidin-2-ylidene) and  $[\text{AuN}(\text{SiMe}_3)_2(\text{PMe}_3)]^{180}$  (**2**), were synthesized by salt metathesis from their corresponding metal chloride species with lithiated hexamethyldisilazide in yields of 55% and 90%, respectively. Compound **1** was purified by sublimation (100 °C, 120 mTorr) and obtained as a pale yellow solid which could be handled briefly in ambient conditions but was moisture sensitive. Characterization of **1** by  $^1\text{H}$  and  $^{13}\text{C}$  NMR was straightforward and gave the expected spectra (see experimental). Compound **2** was an air sensitive, highly soluble off-white solid which melted at 32 °C. Characterization by  $^1\text{H}$ ,  $^{13}\text{C}$ , and  $^{31}\text{P}$  NMR was also as expected. Compound **1** was monomeric, as observed by single-crystal x-ray diffraction (sc-XRD). Compound **2** was suspected to be monomeric in the gas phase, as observed by high-resolution mass spectrometry (HR-MS). Unfortunately, its low melting point prevented the collection of its solid-state structure.

Crystals of **1** were grown from toluene under an inert atmosphere. The molecular structure showed a linear coordination geometry at the metal center (Figure 3.1). The Si–N–Si bond angle (134.75 (15)°) was larger than that observed in the analogous copper compound<sup>181</sup> (128.2 (3)°) and also larger than that of  $\{[\text{AuHMDS}]_4\}^{182}$  (120.9 (3)°). The larger angle indicates less steric crowding about the metal center in **1** compared to the tetramer  $[\text{AuHMDS}]_4$ . Au–N and Au–C bond lengths are comparable to other gold(I) NHC compounds.

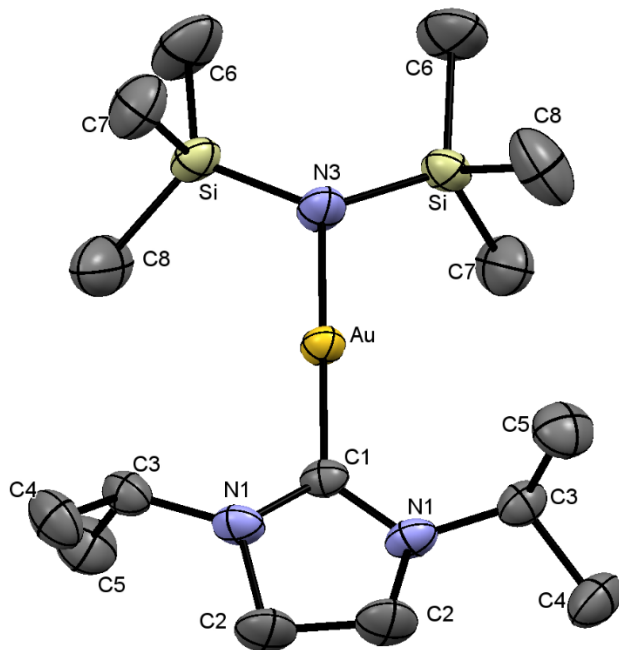


**Figure 3.1** Molecular structure of **1** as determined by single crystal X-ray diffraction. Protons are omitted for clarity. Ellipsoids are drawn at 50% probability.

Compounds **1** and **2** were subjected to air-free thermogravimetric analysis (TGA) to evaluate their thermal stability and volatility. Temperature ramp experiments (10 °C/min) (Figure 3.2, solid lines) show that **1** and **2** begin to volatilize at 110 and 80 °C, respectively. Inflections at 190 °C (**1**) and 170 °C (**2**) hint at thermal decomposition and correlate well with exothermic events observed by differential scanning calorimetry.

Residual masses of 26% for **1** and 6% for **2** were found, and these contained gold according to analysis by energy-dispersive X-ray spectroscopy. Since the mass percentage of gold in each precursor is higher than the residual masses observed (38% Au in **1**, residual mass **1** = 28%, 45% Au in **2**, residual mass **2** = 7%), these compounds decomposed during volatilization in the TGA apparatus. Since they can be sublimed under vacuum, they are still promising for simple CVD experiments. Since we are interested in these compounds as volatile precursors, we determined the temperature that produced sufficient volatility (1 Torr) using a stepped isothermal TGA.<sup>183,184</sup> This method utilizes the known vapor pressure of Cu(tmhd)<sub>2</sub> and comparison of its volatility to

that of **1** or **2**.<sup>185</sup> 1 Torr temperatures were estimated to be 115 and 80 °C for **1** and **2**, respectively (Figure S-3.9, Supporting Information).

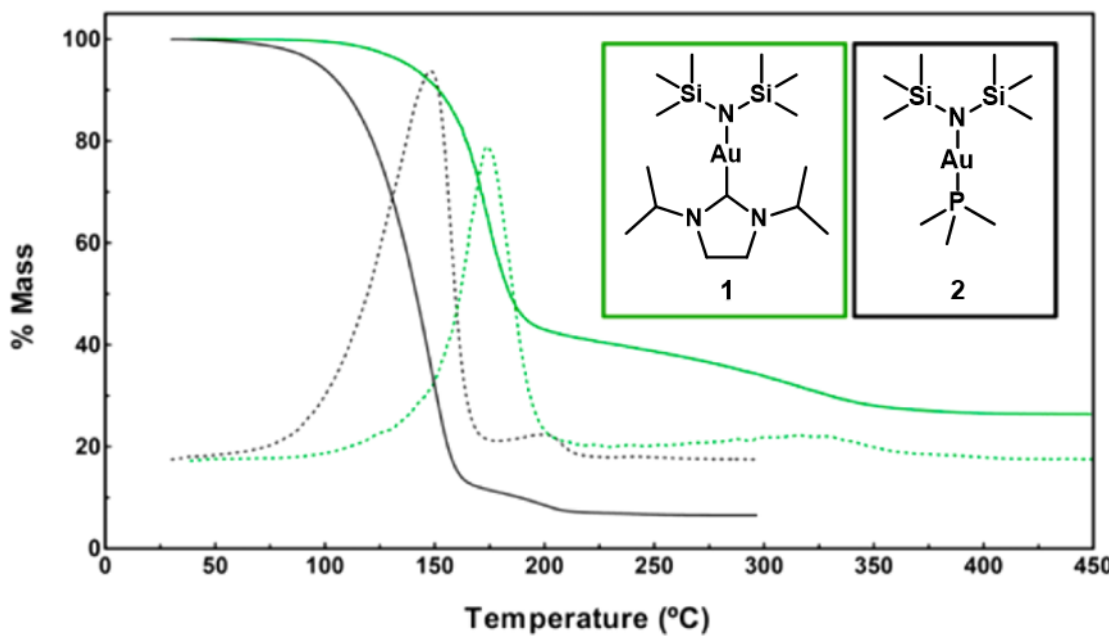


**Figure 3.2** TGA ramp experiments of **1** (green) and **2** (black) are shown as solid lines. Derivative curves are shown by dashed lines of respective color. Experiments were done in an N<sub>2</sub>-atmosphere glovebox at atmospheric pressure.

Single-source, hot-walled CVD experiments were performed using **1** and **2** over a substrate temperature range of 150–500 °C using Si [100] substrates on a home-built apparatus.<sup>186</sup> Both precursors produced nanoparticulate films (these included decahedrons, triangles, and octahedrons as well as amorphous particles) starting at 300 °C. Pentagonal wires with nanoscale cross sections were observed sparsely in all depositions, and there was no apparent trend to their growth (Figure 3.3). The onset of plate growth occurred at 370 °C using **1**, while **2** underwent a more abrupt transition to plate growth at 400 °C (see Figures S-3.10, S-3.11, Supporting Information for an overview of morphology change with increased temperature). This thermally activated transition occurred once the coordinative ligands gained a sufficient surface desorption rate to act as transient surfactants (*vide infra*). Above 460 °C, the rate of desorption of the surface-bound ligands became too high, and the ligands ceased to effectively direct growth. At this point, there was a reversion to a nanoparticle-only morphology for both

precursors. The intermediate temperature range (370 °C–460 °C for **1**, 400 °C–460 °C for **2**) promoted the growth of a wide variety of gold microstructures, as detailed below.

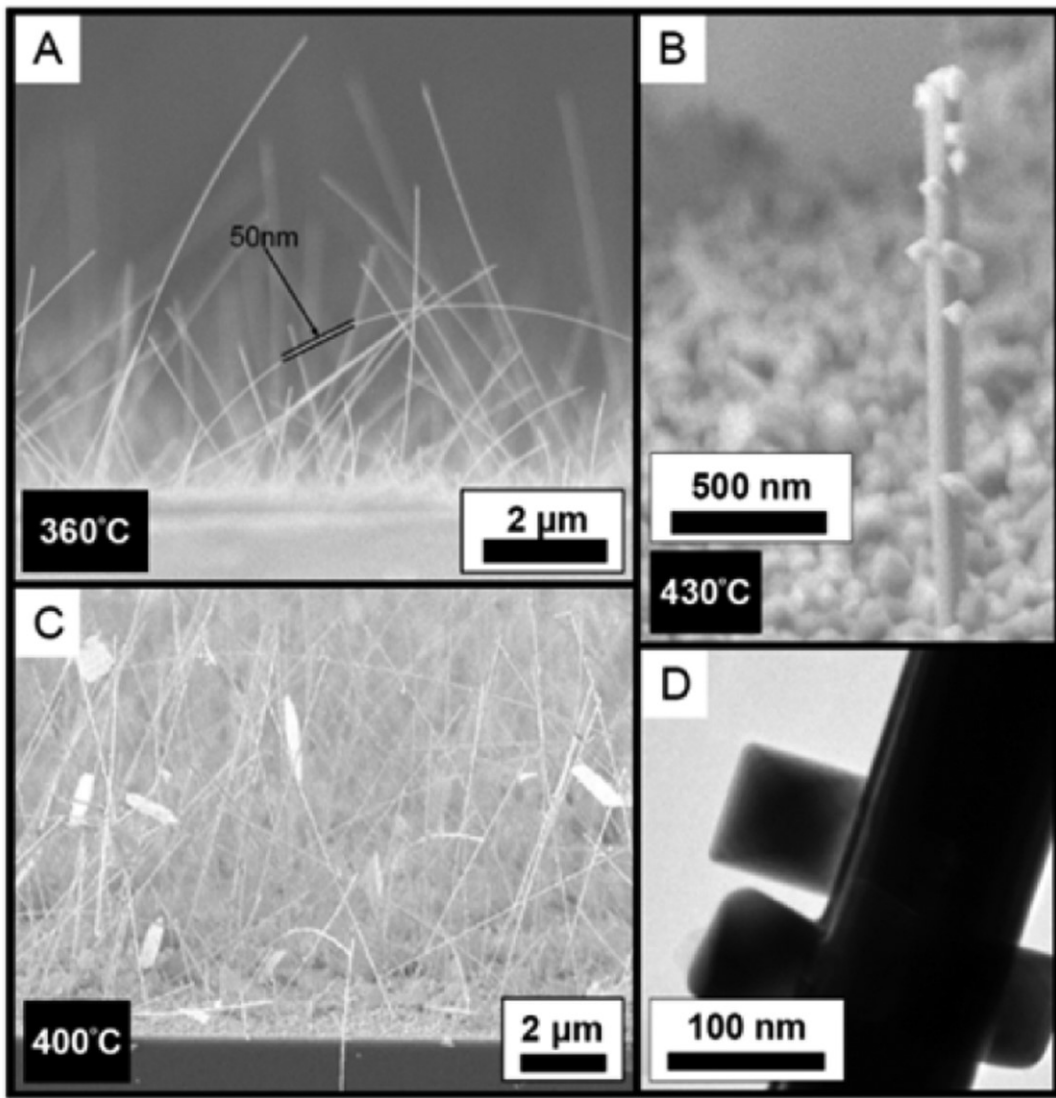


**Figure 3.3** Wires with nanoscale cross sections grown from **1** (A and B) and **2** (C and D). Wires had diameters between 40–140 nm and were always observed growing alongside nanoparticles. Often, as in (C) the wires grew simultaneously with plates creating a dense web-like structure. Secondary nucleation (i.e., budding) occurred on wires (B and D) as well-defined nanoparticles.

From colloidal synthesis, it has been shown that growth anisotropy depends on the symmetry of the seed crystal; hexagonal or triangular plates grow from seeds with planar defects such as stacking faults, while pentagonal prismatic wires grow from decahedral seeds.<sup>187</sup> Lofton and Sigmund have proposed that the pentatwinned seed crystal, which

is a precursor to decahedral particles, must undergo an additional (sixth) twinning event to seed wire growth. Extrapolated to vapor phase growth, this would explain the simultaneous observation of both decahedral particles and pentagonal wires during deposition. Seed crystal geometry is primarily dependent on the rate of reduction in solution,<sup>150</sup> thus it can be expected that in the CVD experiment, the seed shape distribution is dependent on the substrate temperature.

Plate growth (like nanowire growth) is uncommon in CVD of gold, although it was observed with both **1** and **2**. The plates shown in Figure 3.4 are similar to those grown by solution-phase methods, in that they grow as triangles and hexagons with varying edge lengths and larger polygons thereof. Once a plate seed crystal has nucleated, growth anisotropy can be controlled through selective passivation of the flat [111] surface by surfactants.<sup>188</sup> The key difference in our system is that no surfactants were explicitly added to inhibit growth on the terraces of the plates, but rather this growth was likely directed by the coordinating ligands from the precursor compound.

It appears that both the NHC (in **1**) and phosphine (in **2**) are non-innocent to the CVD process. It is difficult to rationalize the anisotropic gold microstructures observed by a simple CVD mechanism since this should lead to island-growth film morphologies. We propose therefore that the coordinative ligands participate as transient surfactants before desorbing from the gold surface. Importantly, the secondary nucleation events (Figures 3.3 and 3.4) are known to be caused by a surfactant-assisted CVD mechanism.<sup>189</sup>

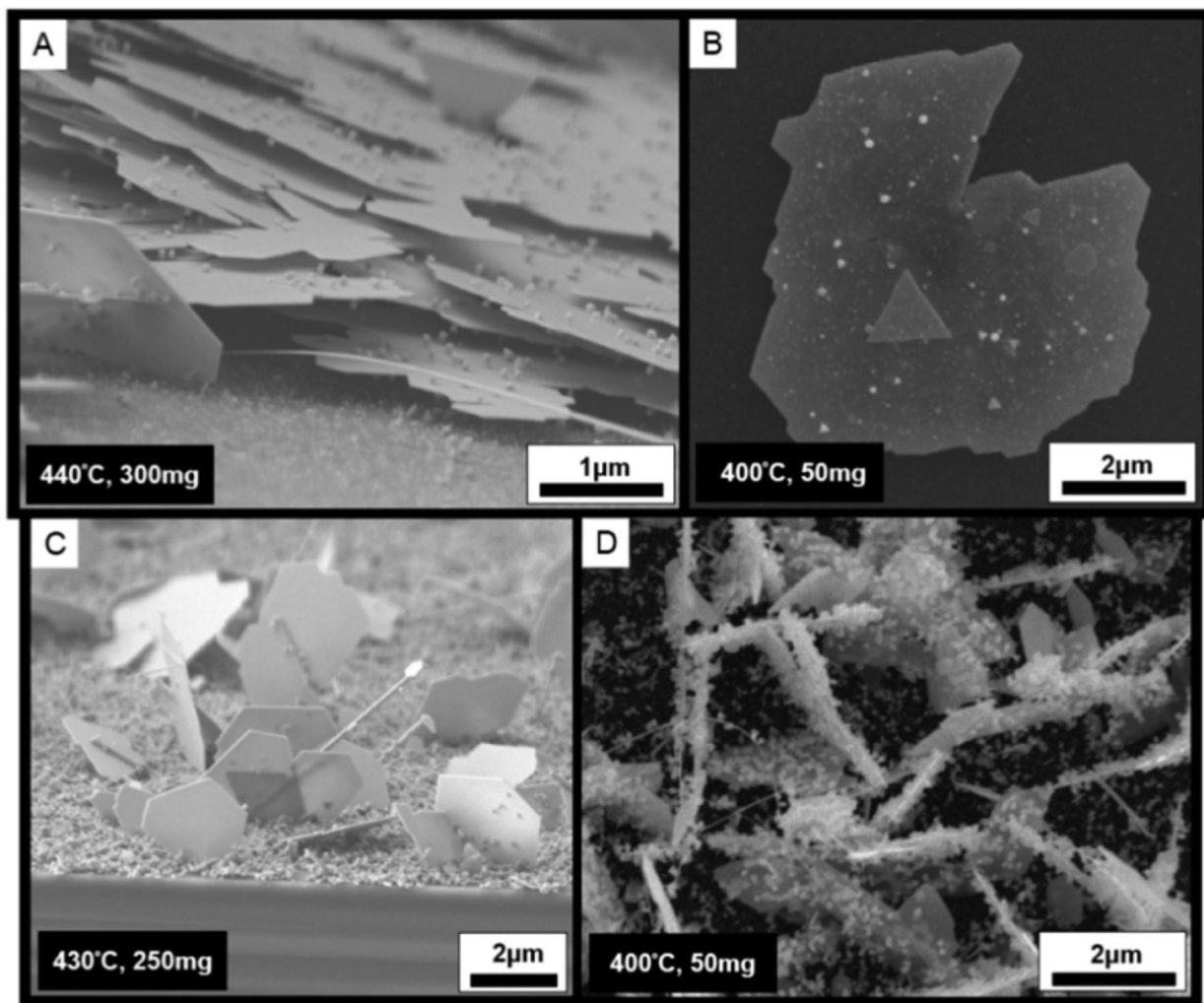


**Figure 3.4** Gold plates deposited by **1** (A-C) and **2** (D). Plate-piling is clearly observed by side-on scanning electron microscopy (SEM) (A), where nucleation onto a growing gold surface was highly favored over a passivated surface. Using lower precursor flux conditions, plates grew with multiple orders of secondary plate nucleation on their faces (B). Perfect hexagons were rarely observed in plate growth, but in this case grew when surface nucleation was also prominent (C). A greater degree of secondary nucleation is observed on plates in the case of deposition from **2** (D).

Plates grew more often as irregular polygons than as hexagons or triangles (Figures 3.4 and 3.5). Edge-on plate sintering has been described in colloidal systems;<sup>188</sup> however, it is unlikely that “oriented attachment” was the mechanism here, since these plates cannot migrate on the substrate surface. Polycrystallinity would be expected at an acute junction if the growth mechanism involved sintering. No visible defects were observed connecting

individual platelets, suggesting epitaxial growth occurred laterally from a mother plate (Figure 3.5).

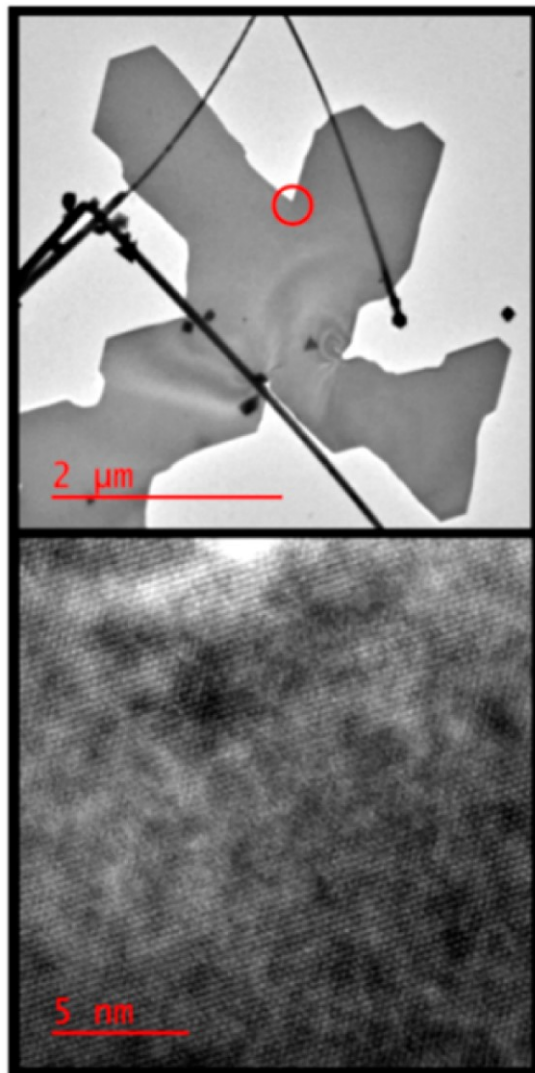


**Figure 3.5** Top frame shows a TEM image of an irregularly shaped plate grown at 395 °C using 1. The bottom frame shows a high-resolution TEM image of the region within the red circle showing a continuous lattice. A joint would be expected by edge-on plate sintering (red circle). The interference patterns on the gold plate (top) were caused by crystal strain.<sup>165</sup>

The epitaxial nucleation of atomic gold layers on plate faces provides a mechanism by which large, irregular polygonal plates could grow. During layer-by-layer growth, the nucleation of a new layer may result in the formation of a stacking fault. Stacking fault formation is reasonably likely, and gold and silver are known to have low stacking fault

energies compared to other metals which promotes plate growth observed here.<sup>53</sup> The new layer could then grow laterally, with the stacking fault propagating to the plate edge (Figure 3.6). The added stacking fault would then accelerate plate growth in the lateral direction by increasing the surface energy of the plate edge. Thus, lateral growth occurs preferentially at the location where the newly nucleated layer first reaches the plate edge, resulting in irregularly shaped plates.

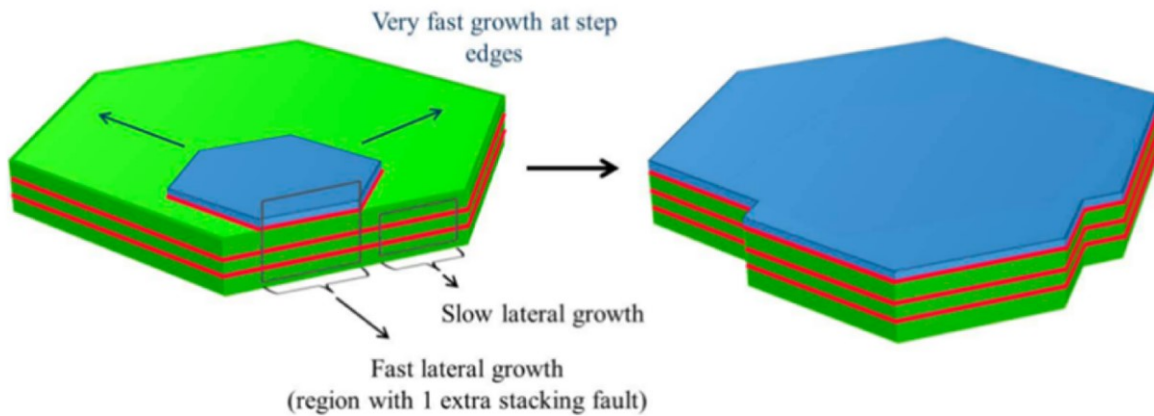
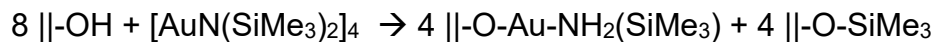


**Figure 3.6** A representation of the proposed mechanism for irregular polygonal plate growth. A new layer (blue) nucleates forming a stacking fault (highlighted in red) with the original plate (green). Where the new layer meets the perimeter of the underlying plate, lateral plate growth is accelerated due to the presence of an additional stacking fault (left). The new layer quickly covers the entire original plate, resulting in a smooth surface and uniform plate thickness (right). Plate edges are depicted as [100] facets (vertical) for simplicity but are likely composed of angled [111] facets.

This mechanism, which describes the growth of irregularly shaped plates from a single seed, is preferred over one involving plate-on-plate secondary nucleation followed by sintering, based on transmission electron microscopy (TEM) evidence. At every location investigated on these plates, we observed a continuous lattice, indicating that plate growth proceeds epitaxially from an original seed. Furthermore, no thickness variations were observed across any given plate.

Interestingly, in many of the depositions, bare substrate was observed, interspersed with nanocrystals, which contrasts typical gold CVD results.<sup>184</sup> Hexamethyldisilazane (H-HMDS) is known to react with surface Si-OH groups to form nonreactive, nonpolar surface

||-O-Si(Me)<sub>3</sub> groups (where || refers to the Si substrate) which passivate available surface hydroxyl sites at high temperatures.<sup>190</sup> In solution, [AuN(SiMe<sub>3</sub>)<sub>2</sub>]<sub>4</sub> reacts with high surface-area silica<sup>191</sup> to form surface bound gold(I) and trimethylsilylated surface hydroxyl groups:



Since the O-Si(Me)<sub>3</sub> surface species cannot react with incoming precursor, the HMDS ligands of **1** and **2** may be causing partial Si surface passivation. To explore this possibility, CVD was performed using both **1** and **2** on (Si free) Al substrates that had been coated with 10 nm of Al<sub>2</sub>O<sub>3</sub> by atomic layer deposition (to provide a homogeneous oxide surface). In these depositions, silicon impurities in the deposited gold film were observed by energy-dispersive X-ray (EDX) analysis in the case of both precursors. Further analysis by XPS (Figure S-3.12, Supporting Information) provided quantitative Si impurity levels of 8.7% Si and 5.1% Si in the films deposited by **1** and **2**, respectively. No nitrogen signals were observed for either precursor, suggesting that the HMDS was shedding its trimethylsilyl moiety as surface groups. Binding energies of the Si 2s signal (normally situated at 149 eV) were shifted to higher energy from the bulk Si 2s signal in the case of both precursors, implying that any Si in the films remained oxidized relative to bulk silicon (Figure S-3.12, Supporting Information). It is reasonable that the silicon inclusion was occurring in an analogous way to the surface chemistry observed with [AuN(SiMe<sub>3</sub>)<sub>2</sub>]<sub>4</sub> in solution.

Originally, the HMDS ligand was chosen for its ability to improve the volatility of the resulting metal compound. Its use also resulted in directing precursor nucleation onto growing gold surfaces rather than at the silicon substrate surface. Interestingly, even when a high precursor mass (300 mg) was used, the size and coverage of gold nanoparticles at the substrate did not increase, and instead plate-piling occurred (Figure 3.4 A), consistent with surface passivation. We suspect that this behavior cannot be entirely attributed to poor wetting between the film and substrate materials. More precursor provided more HMDS ligand which caused a stronger passivation of the surface, which in turn directed nucleation toward the gold surfaces.

Nanobuds (or secondary nucleation events) were observed in many depositions with both precursors and at a variety of temperatures (see Figure 3.3 (B,D) and Figure 3.4 (D) for examples). These sub-100 nm particles appeared to grow on the surface of all gold features, presumably due to the rate of surfactant desorption overcoming adsorption, as has been previously described in copper nanowire CVD.<sup>189,192</sup> This caused exposure of surface gold atoms, where nucleation could occur. Particular to this deposition system, the precursor flux decreased over time as precursor was depleted from the source. Thus, at longer deposition times, more free sites for nanobudding became available. Indeed, lowering the precursor volatilization temperature by 20 °C to produce a sustained, low precursor flux caused multiple orders of secondary nucleation to occur (Figure 3.4 B). Progressively smaller plates and particles resulting from progressively delayed nucleation events were observed growing on top of existing (and continually growing) plates.

To determine a time-dependent growth profile of **1**, depositions at 430 °C were quenched under a stream of room temperature N<sub>2</sub> after 0.5, 1, and 2 h, where 50 mg of precursor was used in each deposition. Plate deposition was sparse after 0.5 h relative to longer deposition times (Figure 3.7), and plates were only observed as isolated triangles or hexagons. These evolved into irregularly shaped plates after 1 h, and secondary nucleation (i.e., budding) of plates was observed as well. Secondary nucleation is much less likely to occur than stacking fault formation, judging by the highly irregular shape of the mother plate. Budding was extensive after 2 h, producing a variety of shapes including octahedrons and decahedrons. Plate stacks were also observed, which resulted from the growth of secondary-nucleated seeds such as those seen at 1 h. The nanoparticulate layer remained sparse in the first hour, suggesting that silicon passivation occurred in the initial stages of deposition.

A diminished surfactant surface concentration toward the 2 h mark allowed access to secondary nucleation sites on all gold surfaces, enabling a densification of the nanoparticulate layer through secondary nucleation on existing nanoparticles. A gradual decline in surfactant concentration over the course of the deposition also explains the delayed appearance of irregularly shaped plates since the facial source of nucleation (with stacking fault formation) was being retarded by a surfactant bound to [111] facets.

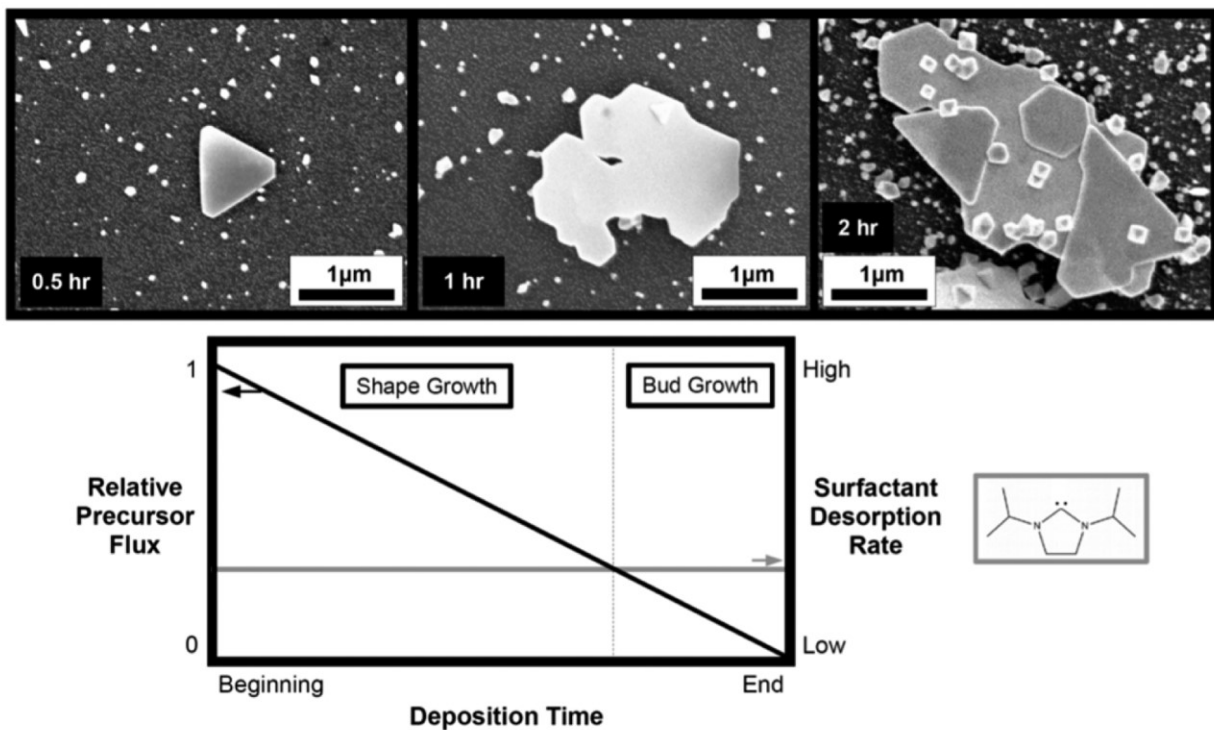


**Figure 3.7** Time-dependent depositions using **1** at 430 °C at 0.5, 1, and 2 h points. A hypothetical plot of both observed growth regimes is shown below. As precursor is depleted from the source, the influx of surfactant also decreases. Plate and wire growth occurs, while there is an excess of surface-bound surfactant. Eventually, the rate of surfactant adsorption to the surface is overtaken by the rate of surfactant desorption and budding occurs.

A hypothetical model (Figure 3.7, bottom) depicts the time-dependent processes governing the surface-concentration of surfactant ligand. The gold surface is assumed to be saturated with surfactant ligand due to the pristine nature of the flakes observed. Thus, the rate of desorption of this surfactant species can be taken as constant at a given temperature, and desorption occurs either by simple dissociation or by decomposition of the ligand to more volatile byproducts. Precursor flux to a growing surface decreases over time as the source is depleted (black line). Where the black and gray lines cross is the theoretical transition point where the surfactant desorption rate overtakes surfactant adsorption rate. Thus, for a less labile surfactant, we expect large features with few buds, and for a more labile surfactant, we expect many buds and small features. This can be seen most predominantly in the greater amount of budding in depositions using **2**.

compared to **1**. Especially at such high temperatures, phosphines are labile when coordinated to gold nanoparticles<sup>175</sup> and thus more easily dissociate than NHCs.

This hypothesis correctly predicts the observed lower and upper bounds of plate growth. When the deposition temperature was low and desorption occurred very slowly relative to precursor flux, no growth of large features or budding occurred, leaving only nanoparticulate growth. When the growth temperature was high, surfactant desorbed too rapidly to effectively hinder nucleation at the surface, and so nanoparticulate growth was again observed (Figure S-3.10, Supporting Information). Thus, in order to push plate deposition to lower temperatures, precursor flux should be decreased, or a ligand that more readily desorbs as a surfactant should be employed. This system is particularly interesting since a single precursor source provided the metal film element and a surfactant ligand in one compound, fixing the ratio of metal atom to surfactant at 1:1. Experiments are ongoing to further probe the usefulness and specificity of feature growth in this system as well as to preferentially cap gold facets in vapor deposition processes.

## 3.4 Conclusions

The synthesis, thermolysis, and deposition behavior of both an NHC- and a phosphine-stabilized gold(I) amide CVD precursors were studied. The coordinating ligand in both precursors played a role in directing metal growth to produce high aspect ratio Au plates and wires. Large plates with nanoscale thicknesses grow only between 370 and 460 °C, with only nanoparticle growth occurring outside of this intermediate temperature range, although nanoparticles are observed in every deposition. The desorption rate of the NHC and phosphine ligands from gold surfaces is thought to be slow enough in the intermediate temperature range to hinder CVD growth at different crystal facets. Furthermore, below 460 °C, the surfactant effectively slows secondary nucleation on gold surfaces, promoting the growth of large nanocrystals from single seeds. The strongest evidence for this is the observation that secondary nucleation occurs most prominently under conditions of low precursor flux, both when this parameter was controlled explicitly and near the end of each deposition. Surface passivation of hydroxyl-terminated

substrate surfaces by the silyl group of precursor-bound HMDS ligand was observed by EDX and XPS and is also thought to play a role in promoting the growth of large nanocrystals. Nanobuds, which appeared on all features at longer growth times, were attributed to a decline in surface concentration of surfactant.

## 3.5 Experimental Details

### General Considerations

All synthetic manipulations were performed with rigorous exclusion of air and moisture, employing either a nitrogen atmosphere Mbraun Labmaster 130 Drybox or standard Schlenk techniques. NMR spectra were recorded on either a 300 MHz Bruker Avance spectrometer or a 400 MHz Bruker AMX spectrometer. NMR analyses were done in C<sub>6</sub>D<sub>6</sub> and referenced against the residual solvent peak. *N,N'*-1,3-Diisopropyl-imidazolidinium chloride,<sup>193</sup> THTAuCl,<sup>194</sup> and (Et<sub>2</sub>O)LiHMDS<sup>195</sup> were synthesized according to literature preparations. Anhydrous tetrahydrofuran, dichloromethane, pentane, and trimethylphosphine (as a 1.0 M solution in toluene) were purchased from Sigma-Aldrich and used as received. Toluene, hexanes, and diethyl ether were purified using an Mbraun Solvent Purification System. TGA experiments were performed on a TA Instruments Q50 apparatus housed in an Mbraun Labmaster 130 Drybox filled with a nitrogen atmosphere. Data obtained was analyzed using TA Universal Analysis software and exported for further manipulation.

### Synthetic details

*N,N'*-1,3-diisopropyl-imidazol-2-ylidene gold(I) chloride (**1-Cl**). *N,N'*-1,3-diisopropyl-imidazolidinium chloride (1.753 g, 9.1 mmol) was suspended in 100 mL of tetrahydrofuran in a 250 mL Schlenk flask and stirred vigorously to break up solid pieces. In a separate flask, (Et<sub>2</sub>O)LiHMDS (2.301 g, 9.5 mmol) was dissolved in 80 mL of diethyl ether. Both flasks were capped with septa, and with the imidazolidinium suspension cooled to 0 °C, the (Et<sub>2</sub>O)LiHMDS solution was added via cannula transfer. The mixture was stirred for 1 h, warming to room temperature, after which the suspension had cleared to a yellow solution. This solution of free *N,N'*-1,3-diisopropylimidazol-2-ylidene was cooled to -78

°C to which (THT)AuCl (2.946 g, 9.1 mmol) was added under a stream of nitrogen in 5 portions over 30 min. This mixture was stirred under protection from light, warming to room temperature, for 4 h, after which time the solvent was removed by trap-to-trap distillation at 0 °C, leaving a dark purple/black solid which was dried under high vacuum for an additional hour. The flask was brought into a drybox, and the solid was extracted with 3 × 20 mL of dichloromethane and filtered through a glass frit to afford a brown filtrate. The filtrate was dried, and the solid was rinsed once with 10 mL of pentane and dried again, affording a brown-purple solid which was used without further purification. Crystals suitable for single crystal X-ray diffraction were grown from toluene. Crude yield: (2.661 g, 85%).  $^1\text{H}$  NMR (300 MHz,  $\text{CDCl}_3$ ):  $\delta$  4.76 (sept, 2H,  $\text{CH}(\text{CH}_3)_2$ ),  $\delta$  3.54 (s, 4H,  $\text{CH}_2\text{CH}_2$ ),  $\delta$  1.23 (d, 12H,  $\text{CH}(\text{CH}_3)_2$ ).  $^{13}\text{C}$  NMR (75.5 MHz,  $\text{CDCl}_3$ ):  $\delta$  190.41,  $\delta$  81.82,  $\delta$  42.23,  $\delta$  20.52.

1,3-Diisopropyl-imidazol-2-ylidene Gold(I) Hexamethyldisilazide (**1**). **1-Cl** (2.661 g, 6.9 mmol) was suspended in 150 mL of toluene in a Schlenk flask and cooled to -35 °C. Meanwhile, (Et<sub>2</sub>O)LiHMDS (1.666 g, 8.1 mmol) was dissolved in 50 mL of toluene and also chilled to -35 °C. The (Et<sub>2</sub>O)LiHMDS is then added dropwise to the stirring suspension of **1-Cl** over 30 min, and the resulting solution was stirred overnight (18 h). Filtration of this suspension through a 0.5 cm Celite pad and washing with 50 mL of toluene afforded a yellow solution which upon drying gave a tan colored solid. This solid was purified by sublimation (100 mTorr, 90 °C) onto a -78 °C coldfinger which gave the title compound as a pale yellow solid (2.217 g, 63%).  $^1\text{H}$  NMR (300 MHz,  $\text{C}_6\text{D}_6$ ):  $\delta$  4.81 (sept, 2H,  $\text{CH}(\text{CH}_3)_2$ ),  $\delta$  2.38 (s, 4H,  $\text{CH}_2\text{CH}_2$ ),  $\delta$  0.77 (d, 12H,  $\text{CH}(\text{CH}_3)_2$ ),  $\delta$  0.77 (s, 18H,  $\text{Si}(\text{CH}_3)_3$ ).  $^{13}\text{C}$  NMR (75.5 MHz,  $\text{C}_6\text{D}_6$ ):  $\delta$  197.68,  $\delta$  50.70,  $\delta$  41.55,  $\delta$  20.04,  $\delta$  6.90.

Trimethylphosphine Gold(I) Chloride (**2-Cl**). Tetrahydrothiophene gold(I) chloride (1.580 g, 4.93 mmol) was added to a 150 mL Schlenk flask and dissolved in dichloromethane. Trimethylphosphine (5.00 mL, 1 M in toluene, 5.00 mmol) was added to the solution dropwise and stirred for 1 h. Removal of the solvent by trap-to-trap distillation gave a white solid which was used without further purification (1.469 g, 98%).  $^1\text{H}$  NMR (300 MHz,  $\text{C}_6\text{D}_6$ ):  $\delta$  0.49 (d, 9H,  $\text{P}(\text{CH}_3)_3$ ).  $^{31}\text{P}\{\text{H}\}$  NMR (162 MHz,  $\text{C}_6\text{D}_6$ ):  $\delta$  -10.34 (s,  $\text{P}(\text{CH}_3)_3$ ).

Trimethylphosphine Gold(I) Hexamethyldisilazide (**2**). **2-Cl** (0.5107 g, 16.6 mmol) was added to a 250 mL Schlenk flask, suspended in 50 mL of toluene, and chilled to  $-35\text{ }^{\circ}\text{C}$ . (Et<sub>2</sub>O)LiHMDS (0.423 g, 17.5 mmol) was dissolved in 15 mL of toluene and chilled to  $-35\text{ }^{\circ}\text{C}$ . Once cold, the (Et<sub>2</sub>O)LiHMDS solution was added dropwise over 10 min to the suspension of trimethylphosphine gold(I) chloride while stirring. The suspension gradually turned from gray to translucent over the course of the addition. The reaction was stirred for 1 h and then filtered through a medium frit, washing with 3  $\times$  5 mL of toluene. The toluene was evaporated under high vacuum to afford a highly air sensitive, off white solid (0.6432 g, 90%). Mp = 36–37  $^{\circ}\text{C}$ . <sup>1</sup>H NMR (300 MHz, C<sub>6</sub>D<sub>6</sub>):  $\delta$  0.57 (s, 18H, N(Si(CH<sub>3</sub>)<sub>3</sub>)), 0.52 (d, 9H, P(CH<sub>3</sub>)<sub>3</sub>). <sup>13</sup>C NMR (75.5 MHz, C<sub>6</sub>D<sub>6</sub>):  $\delta$  15.5 (d, P(CH<sub>3</sub>)<sub>3</sub>), 7.21 (s, Si(CH<sub>3</sub>)<sub>3</sub>). <sup>31</sup>P NMR (162 MHz, C<sub>6</sub>D<sub>6</sub>):  $\delta$  –12.79 (s, P(CH<sub>3</sub>)<sub>3</sub>). HRMS (EI, m/z) (rel. intensity, %): 433.1085 (9.2, M<sup>+</sup>). Mass spectrum (EI, m/z) (rel. intensity, %): 433.1 (9.2, M<sup>+</sup>), 418.1 (100, [(P(CH<sub>3</sub>)<sub>3</sub>Au(N(Si<sub>2</sub>(CH<sub>3</sub>)<sub>5</sub>))]<sup>+</sup>), 331.0 (2.8, [Au(N(Si(CH<sub>3</sub>)<sub>3</sub>)<sub>2</sub>])<sup>+</sup>), 273.0 (12.6, [Au(P(CH<sub>3</sub>)<sub>3</sub>)]<sup>+</sup>), 130.1 (32.8, [N(Si(CH<sub>3</sub>)<sub>4</sub>)]<sup>+</sup>), 100.0 (3.8, [N(Si<sub>2</sub>(CH<sub>3</sub>)<sub>2</sub>)]<sup>+</sup>).

### Chemical Vapor Deposition

Experiments were performed on a home-built, low-pressure, hot-walled CVD apparatus.<sup>186</sup> Precursor masses of 50 to 310 mg were delivered from an open-ended vial placed on its side. In the case of **2**, a valve was placed between the precursor vial and the furnace which allowed the precursor vial to be loaded in a glovebox and remain air-free during system assembly. Substrates were placed end-to-end on a metal substrate holder and were preheated under vacuum at the furnace set point for 1 h prior to deposition. Depositions were initiated by heating the precursor source and terminated by flooding the system with room temperature N<sub>2</sub> gas (99.998%). Regular source temperatures were 85  $^{\circ}\text{C}$  (**1**) and 60  $^{\circ}\text{C}$  (**2**). Depositions were performed under dynamic vacuum, and precursor delivery occurred by diffusion from the source without a carrier gas. Temperatures were monitored using K-type thermocouples at the precursor zone and substrate zone. A pressure gauge, located downstream of the furnace, was used to monitor the chamber pressure and ensure that deposition times (1.5 to 3 h) were sufficiently long for the precursor source to be depleted. The base pressure of the CVD

reactor is 10 mTorr, and during deposition pressures up to 140 mTorr are observed with 1. No pressure change is observed when using **2**.

## **Substrate Preparation**

Si (100) wafers were cut into 0.5–1 cm width coupons and cleaned by sonicating in isopropyl alcohol and then in piranha solution (3:1 H<sub>2</sub>SO<sub>4</sub> : 30% H<sub>2</sub>O<sub>2</sub>), each for 20 min. Distilled water rinses followed each sonication step. Substrates were allowed to dry in an oven at 110 °C in air until use. Al<sub>2</sub>O<sub>3</sub> | Al substrates were prepared by depositing a 50 nm thick alumina coating on aluminum metal substrates by atomic layer deposition using trimethylaluminum (TMA) and water. The pulse program, 500 cycles of [0.1s TMA | 4s N<sub>2</sub> purge | 0.1s H<sub>2</sub>O | 4s N<sub>2</sub> purge], was performed at 300 °C on a Picosun R200 tool.

## **Film Characterization**

Scanning electron microscopy (SEM, JEOL JSM-7500F FESEM) was performed at the uOttawa Centre for Catalysis Research and Innovation (CCRI), and transmission electron microscopy (TEM, FEI Tecnai G2 F20 TEM) was performed at the Carleton University Nano Imaging Facility. XPS spectra were collected in the analysis chamber of a Specs/RHK multitechnique ultrahigh vacuum system using a Phoibos 100 SCD power supply, hemispherical analyzer, and detector. Whenever possible, the sample being analyzed was electrically grounded. An XR-50 X-ray source containing an Al anode (400 W) was used in this study (14.26 keV Al Ka source), and analyses were performed within a base pressure range of  $7 \times 10^{-10}$  to  $1 \times 10^{-9}$  Torr. At acceleration voltages of 1.7–2 keV and filament currents of 15–20 mA, Ar<sup>+</sup> was introduced to the analysis chamber using a manual leak valve until a background pressure of  $1 \times 10^{-5}$  Torr was achieved and held constant for the duration of the Ar<sup>+</sup> -sputter cycle (~2 min/cycle). Survey and high-resolution scans of the as- deposited and sputtered gold films were collected using SpecsLab2 software, postprocessed and deconvoluted using CasaXPS, and plotted using Igor Pro 6.35. Survey and high-resolution spectra were fitted to a Shirley background and fitted using the appropriate Scofield-based factors for photoelectron cross-section.

### 3.6 Supporting Information

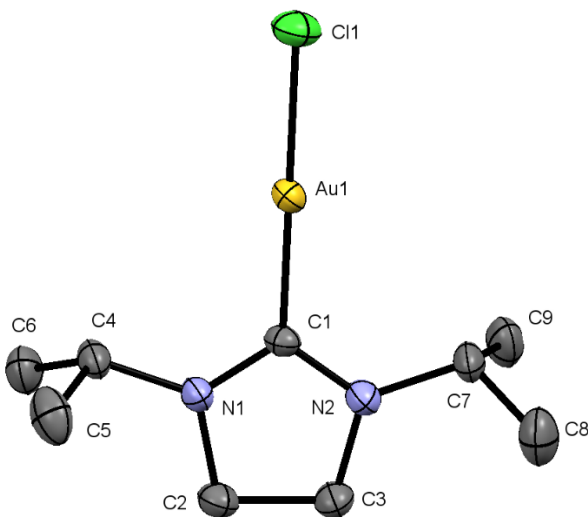


**Figure S-3.8** Single crystal X-ray diffraction structure of **1-Cl**. Heating a light suspension of the compound in toluene and allowing to stand over 1 week produced a single rectangular crystal which was used for structure determination. Ellipsoids shown at 50% probability.

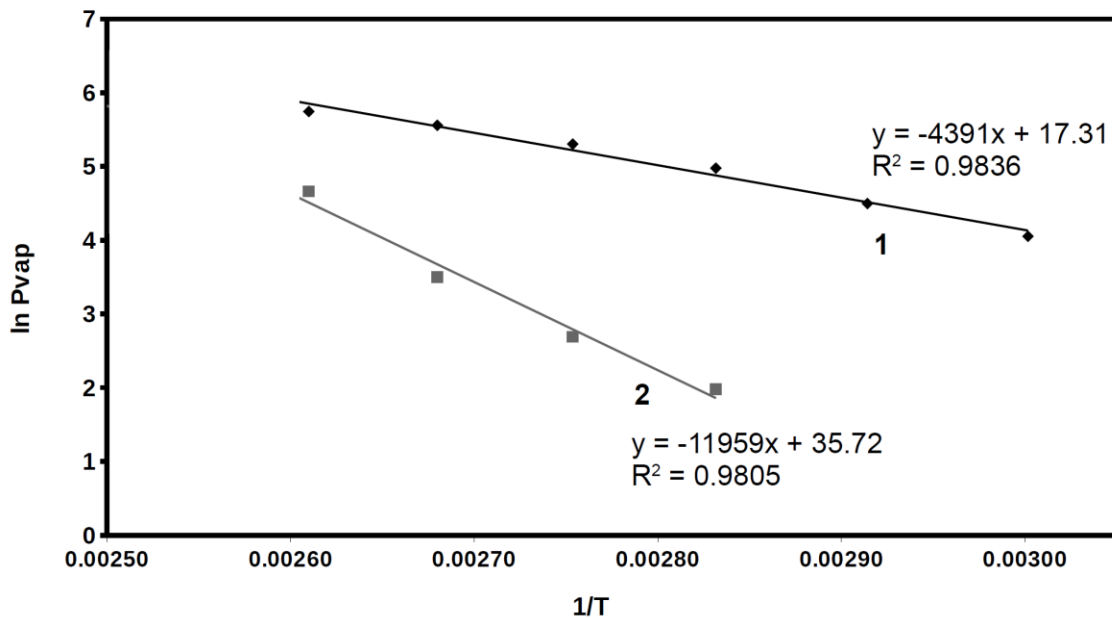


**Figure S-3.9** Vapour pressure curves for compounds **1** and **2**. Stepped isothermal experiments were performed on both precursors, and temperature-dependent mass loss rates were used to determine vapour pressures as per the methods of Kunte et al.<sup>183</sup>

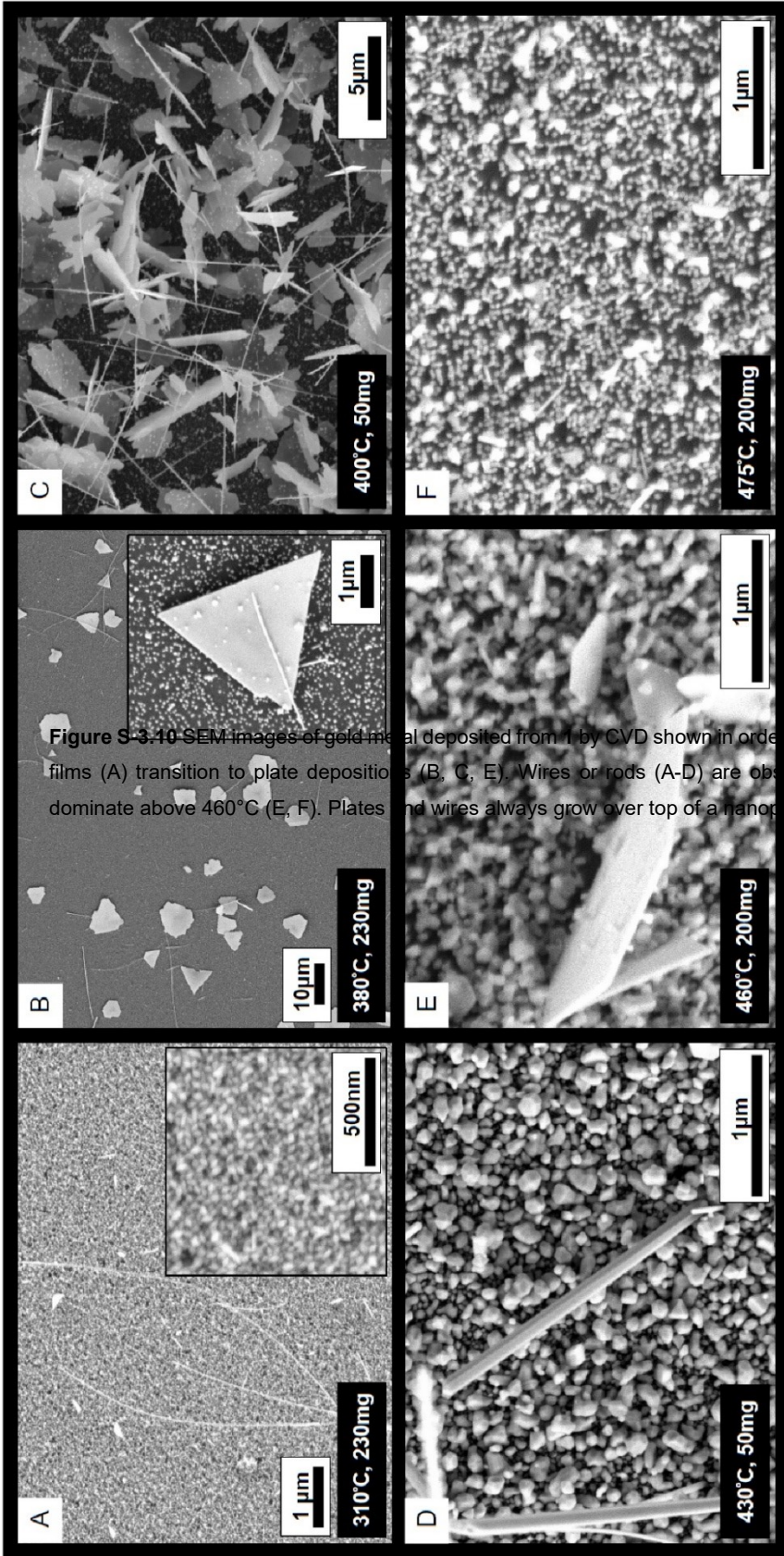


**Figure S-3.10** SEM images of gold metal deposited from I by CVD shown in order of increasing (A-F) temperature. Nanoparticulate films (A) transition to plate depositions (B, C, E). Wires or rods (A-D) are observed at all temperatures. Nanoparticulate films dominate above  $460^{\circ}\text{C}$  (E, F). Plates and wires always grow over top of a nanoparticulate seed layer.

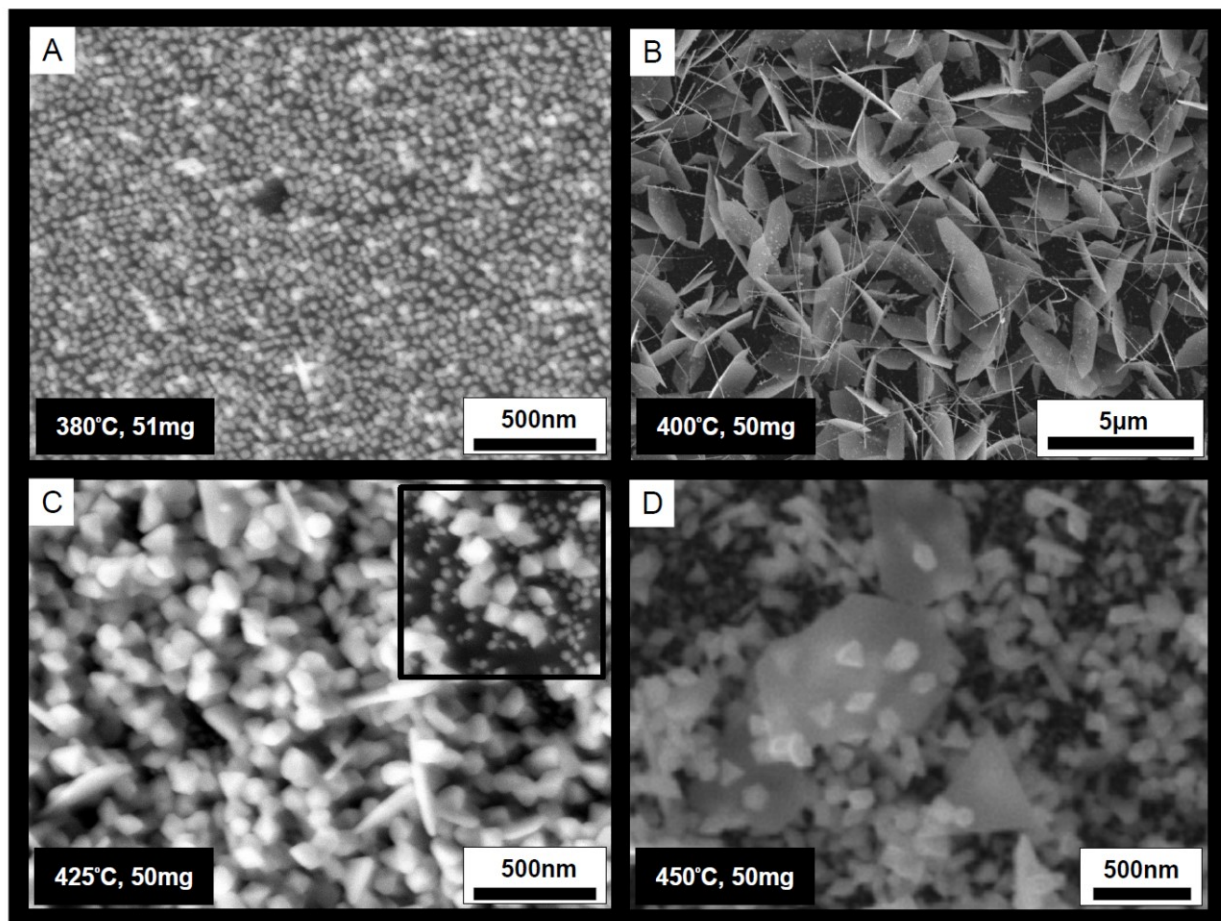


**Figure S-3.11** SEM images of gold metal deposited from **2** by CVD shown in order of increasing (A-D) temperature. Small nanoparticles were observed at 380 °C and below (A). Gold plates and nanowires grew simultaneously in high abundance at 400 °C (B). The transition to large nanoparticle growth is obvious at 425 °C (C), where 100 nm and larger nanoparticles grow over top of a small nanoparticle underlayer (C-inset). Plates and nanoparticles grow simultaneously until 460 °C (D), above which temperature small nanoparticles are observed exclusively.

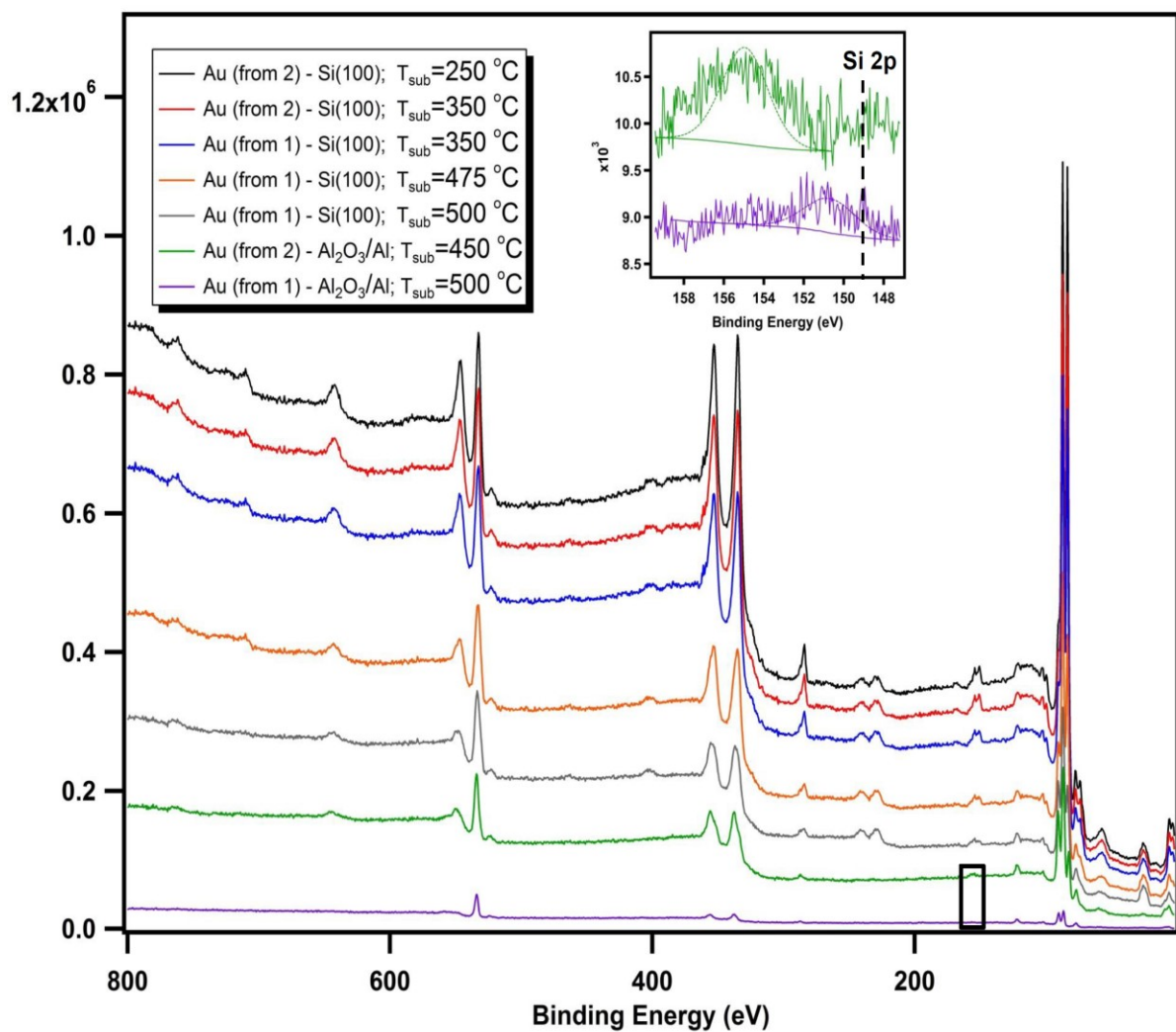


**Figure S-3.12** XPS survey spectra of the as-deposited gold films on various substrates from either **1** or **2**. The inset plot contains the high-resolution scans of the Si 2p peak envelope (the relevant region in the survey scans is enclosed by the black box) corresponding to the as-deposited gold films from **1** and **2** on an  $\text{Al}_2\text{O}_3$ -coated (10 nm by ALD) Al substrates. The plots have been vertically stacked for clarity.



# Chapter 4 Atomic layer deposition of gold metal

*This chapter contains material that has been reproduced in part or in full from the following published articles:*

- (1) Griffiths, M.B.E., Pallister, P.J., Mandia, D.J., and Barry, S.T., Atomic Layer Deposition of Gold Metal, *Chem. Mater.*, **2016**, 28, 44-46.

Department of Chemistry, Carleton University, 1125 Colonel By Drive, Ottawa, Ontario, K1S 5B6, Canada

Adapted with permission from *Chem. Mater.*, **2016**, 28, 44-46, DOI: [10.1021/acs.chemmater.5b04562](https://doi.org/10.1021/acs.chemmater.5b04562). Copyright 2016 American Chemical Society.

- (2) Van Daele, M.V.D.,<sup>[a]</sup> Griffiths, M.B.E.,<sup>[b]</sup> Raza, A.,<sup>[c,d]</sup> Minjauw, M.M.,<sup>[a]</sup> Solano, E.,<sup>[e]</sup> Feng, J.<sup>[a]</sup> Ramachandran, R.K.,<sup>[a]</sup> Clemmen, S.<sup>[c,d,f]</sup> Baets, R.,<sup>[c,d]</sup> Barry, S.T.,<sup>[b]</sup> Detavernier, C.,<sup>[a]</sup> Dendooven, J.,<sup>\*[a]</sup> Plasma-Enhanced Atomic Layer Deposition of Nanostructured Gold Near Room Temperature, *ACS Appl. Mater. Interfaces*, **2019**, 11, 37229-38

[a] Department of Solid State Sciences, CoCooN Group, Ghent University, 9000 Gent, Belgium

[b] Department of Chemistry, Carleton University, K1S 5B6 Ottawa, Canada

[c] Center for Nano- and Biophotonics, Ghent University, 9052 Gent, Belgium

[d] Photonics Research Group, INTEC Department, Ghent University – IMEC, 9052 Gent, Belgium

[e] ALBA Synchrotron Light Source, NCD-SWEET Beamline, 08290 Cerdanyola del Valles, Spain

[f] Laboratoire d'Information Quantique, Université Libre de Bruxelles, 1050 Bruxelles, Belgium

Adapted with permission from *ACS Appl. Mater. Interfaces*, **2019**, 11, 37229-38, DOI: [10.1021/acsami.9b10848](https://doi.org/10.1021/acsami.9b10848). Copyright 2016 American Chemical Society.

- (3) Van Daele, M.V.D.,<sup>[a]</sup> Griffiths, M.B.E.,<sup>[b]</sup> Minjauw, M.M.,<sup>[a]</sup> Barry, S.T.,<sup>[b]</sup> Detavernier, C.,<sup>[a]</sup> Dendooven, J.,<sup>\*[a]</sup> Reaction mechanism of the Me<sub>3</sub>AuPMe<sub>3</sub>-H<sub>2</sub> plasma-enhanced ALD process, *Phys. Chem. Chem. Phys.*, **2020**, 22, 11903

[a] Department of Solid State Sciences, CoCooN Group, Ghent University, 9000 Gent, Belgium

[b] Department of Chemistry, Carleton University, K1S 5B6 Ottawa, Canada

Reproduced with permission from *Phys. Chem. Chem. Phys.*, **2020**, 22, 11903, DOI: [10.1039/c9cp06855d](https://doi.org/10.1039/c9cp06855d) the PCCP Owner Societies

## 4.1 PE-ALD of gold metal using trimethylphosphinotrimethylgold(III) in combination with oxygen plasma and water

### 4.1.1 Abstract

A plasma-enhanced atomic layer deposition (PE-ALD) process for depositing gold metal was developed using the air- and water-stable precursor ( $\text{PMe}_3\text{AuMe}_3$ ) (1),  $\text{O}_2^*$  plasma ( $\text{O}_2^*$ ) and water in a three-step process. When only 1 and  $\text{O}_2^*$  were used, multiple impurities were incorporated into the growing film. We hypothesize that these impurities are a mixture of Au(III) oxide and P(V) oxides. Water served to hydrolyze these impurities, causing them to be converted to Au(0) and  $\text{H}_3\text{PO}_4$ , the latter of which could be removed by the vacuum system to leave the pure gold film as the sole deposition product.



This metal deposition process showed self-limiting behavior of the gold precursor with a growth per cycle (GPC) of  $0.5 \text{ \AA}$ . Using TEM, the nucleation stage of the film was observed to be that of typical metal films grown on oxides by ALD. The nanoparticles observed after 5 ALD cycles had a bimodal size distribution, with the majority having a diameter of  $2.08 \pm 0.66 \text{ nm}$ , and a small population having a larger radius of  $7.64 \pm 0.94 \text{ nm}$ . Reflection absorption infrared spectroscopy (RAIRS) showed that the  $1 + \text{O}_2^* + \text{H}_2\text{O}$  process proceeds through 1 reacting with a partially hydroxylated surface that is only made possible with the strong oxidizing power of  $\text{O}_2^*$ . However, system pressure and

plasma power both have a strong effect on the elemental composition of the deposited film which we contrast between a flow-type reactor and a pump-type reactor.

A PE-ALD process was developed using **1** and H<sub>2</sub>\* in a low-pressure pump type reactor and was found to have a steady state GPC of 0.3 Å. This process was found to deposit gold metal over a large temperature range of 50 – 120 °C and could even deposit gold on tissue paper: a temperature-sensitive substrate. Over this temperature range we observed a difference in growth morphology, and at lower temperatures the growing film becomes electrically conductive at a lower thickness than at higher temperatures. The **1** + H<sub>2</sub>\* process deposits films which have no observable phosphorus, and only a small amount of oxygen and carbon by x-ray photoelectron spectroscopy (XPS).

Using a combination of *in situ* RAIRS and *in vacuo* XPS we determined the identity and kinetic lifetime of surface-bound ligands present after chemisorption of **1**. Through careful experimentation, we discovered that there was a small single-source decomposition component of **1** to the growth of this process which only occurs when the growth surface is gold metal. Below 100 °C desorption of Me radicals from the Au surface is attributed to this small growth using a combination of RAIRS, XPS, quadrupole mass spectrometry (QMS), and literature evidence. PMe<sub>3</sub> desorbs from the surface much more slowly and is the true self-limiting ligand of this system.

Finally we determine a temperature-dependent reaction scheme for the **1** + H<sub>2</sub>\* process based on the relative stability of surface-bound ligands. We also compare the known PE-ALD processes of **1** with one another in terms of film crystallinity, purity, and ALD system conditions.

#### 4.1.2 Introduction

Nanoparticulate gold is a useful material being used in applications like gas-sensing,<sup>5</sup> heterogeneous catalysis,<sup>196</sup> and by virtue of its surface plasmon resonance, photonics.<sup>2</sup> Currently, solution-phase reduction of gold salts in the presence of facet-specific surfactants and capping agents is the method of choice for producing gold nanoparticles.

Solution-phase synthesis can be a drawback if the nanoparticles are needed for an application where the surfactant might interfere. One straightforward method of controlling the nucleation and growth of metallic nanoparticles is atomic layer deposition (ALD). ALD is a layer-by-layer, gas-phase deposition technique that has been used to deposit a wide array of metallic, semiconducting, and insulating films and features.<sup>197</sup> Gold nanoparticles have been deposited by several vapor-based methods including physical vapor deposition (PVD) and chemical vapor deposition (CVD).<sup>198</sup>

Materials that are deposited by ALD are grown from a gas-phase precursor chemical that, by virtue of surface chemical reactions, react on a surface to form the target material. It is surface chemistry, not surfactants, that controls the size and shape of deposited nanofeatures. The versatility of this technique is reflected in the number of available processes that exist to deposit a variety of different materials.<sup>199</sup> A significant amount of research has been undertaken to study the deposition of metal films (including copper),<sup>200</sup> but the other group 11 metals have proved more challenging.<sup>201–203</sup> Reported here for the first time is gold metal deposition by ALD.

### 4.1.3 Results and Discussion

We synthesized trimethylphosphinotrimethylgold(III) (**1**) from a modified literature preparation as the chemical precursor; a compound that has previously been employed in chemical vapor deposition.<sup>98,204</sup> This compound is air and water stable, is a liquid at room temperature, and has a vapor pressure that follows this Langmuir equation:<sup>205</sup>

$$\ln(p) = 0.059T - 1.65$$

where  $p$  is pressure in Pascals, and  $T$  is temperature in Celsius.

Heating **1** to 85 °C was sufficient to deliver the precursor into the deposition furnace. To reduce this compound at the surface to metallic gold, we found that both hydrogen gas and hydrogen plasma were not effective: at temperatures lower than 130 °C, no deposition was observed, and at temperatures over 130 °C, **1** begins to decompose to

gold metal without a reducing co-reagent (i.e., by a chemical vapor deposition mechanism).

Noble metal deposition by ALD can employ molecular oxygen as a co-reagent: the strategy is to oxidize the organic ligand system, leaving the noble metal behind.<sup>206</sup> We found that molecular oxygen did not react with **1** under 130 °C. Other oxygen-containing co-reactants (e.g., H<sub>2</sub>O and O<sub>3</sub>) were similarly unreactive with **1** under thermal conditions. However, using a plasma-assisted process with **1** showed that oxygen plasma produced a film of gold metal by ALD at 120 °C.

Using just oxygen plasma (herein referred to as O<sub>2</sub>\*), the films were discolored and nonmetallic in appearance: typically they were brown or dark purple. These films discolored and delaminated over time in ambient conditions and developed a foul odor. Energy-dispersive X-ray spectroscopy (EDX) and X-ray photoelectron spectroscopy (XPS) (Figure 4.1, Table 4.1) showed that gold metal was certainly present, but so too were oxygen and phosphorus.

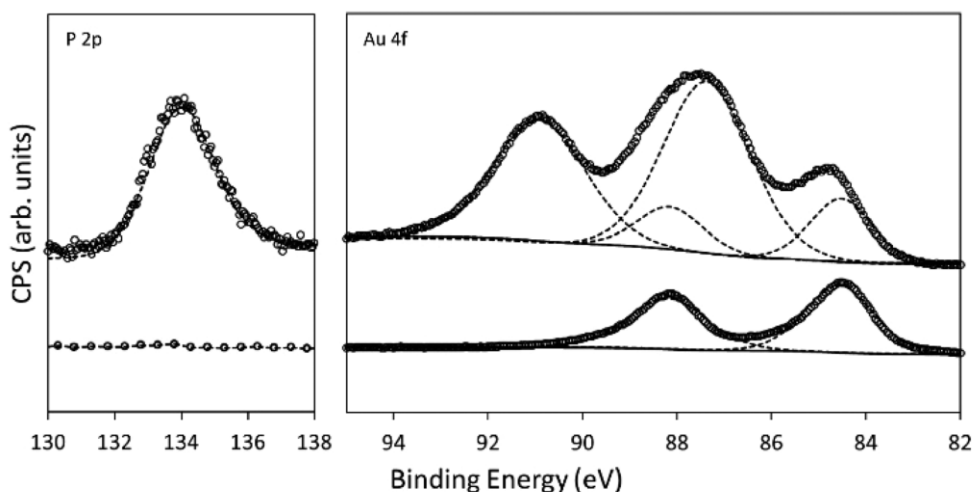


**Figure 4.1** XPS spectra of the phosphorus 2p and gold 4f regions for a film deposited without a water pulse (top) and with a water pulse (bottom).

**Table 4.1** Compositional analysis by XPS of the film formed without water and the film formed with water.

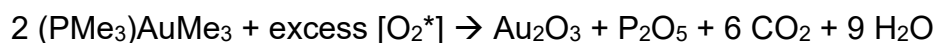
element	without water (at. %)	with water (at. %)
Au	76.16	91.52
C	5.61	6.65
N	1.43	0 <sup>b</sup>
P	6.26	0 <sup>b</sup>
O	10.54	1.83

<sup>a</sup>These data represent the surface measured “as is”, and likely contains carbon and oxygen from adventitious sources. <sup>b</sup>These species were below the limit of detection of the XPS instrument.

In the XPS spectrum, a peak was observed centered at 134.1 eV, which is in the range of the P(V) oxidation state. There was also evidence of Au(0), with peaks at 84.5 and 88.2 eV, and Au(III) at 87.5 and 90.9 eV. This suggests that some of the phosphine ligand from the precursor remained with the gold adatom at the surface and was converted into a gold–phosphine containing film when reacted with O<sub>2</sub>\*.

Although the nature of this film is not presently understood, further characterization has shed some insight. Trimethylphosphine (PMe<sub>3</sub>) is known to react with oxygen to produce trimethylphosphine oxide (Me<sub>3</sub>P=O) and oxygen plasma could likely further oxidize Me<sub>3</sub>P=O to other phosphorus(V) oxides like P<sub>2</sub>O<sub>5</sub>. Because treatment of P<sub>2</sub>O<sub>5</sub> with water yields phosphoric acid, the impure film was sonicated in D<sub>2</sub>O, and D<sub>3</sub>PO<sub>4</sub> was observed as a major product by <sup>31</sup>P{<sup>1</sup>H}-NMR spectroscopy (1.12 ppm rel. to H<sub>3</sub>PO<sub>4</sub>), suggesting the presence of phosphorus(V) oxides in the deposited film. Interestingly, rinsing these films with water was enough to seemingly dissolve them, even though they were well-adhered to the silicon substrate and passed a scotch tape test.

The simplest chemistry that rationalizes these facts is that the oxygen plasma combusts the precursor, forming oxides of both gold and phosphine in the process:



Gold metal is then formed from the gold oxide, which agrees with the presence of both oxidation states in the XPS. This conversion occurs in the bulk at 160 °C,<sup>207</sup> but the higher

chemical potential of a deposited monolayer could allow this conversion to happen at lower temperature:



In an attempt to eliminate the phosphorus impurity in the film, water was chosen as a ternary reactant with the purpose of hydrolyzing the phosphorus impurity to phosphoric acid, which could then be volatilized away. Using an ABC-type pulse sequence of [4 s 1, 10 s N<sub>2</sub> purge | 14 s O<sub>2</sub>\* | 10 s N<sub>2</sub> purge | 0.1 s H<sub>2</sub>O | 10 s N<sub>2</sub> purge] (see Section 4.4, experimental details) produced metallic gold films at 120 °C. XPS analysis of these films showed very clearly that there was only metallic Au(0) (Au4f<sub>7/5</sub> = 84.5 eV and Au4f<sub>5/2</sub> = 88.2 eV) with no phosphorus signals observed (Figure 4.1, Table 4.1). EDX also confirmed the absence of phosphorus in the film. Because gold oxide converts to gold metal faster in the presence of water,<sup>207</sup> this explains the formation of the metallic film. Likewise, the phosphorus oxide is converted into volatile phosphoric acid, and is removed during the purge step:



Using this process, gold thin films were deposited using a range of process parameters with high reproducibility on both silicon and borosilicate substrates. Thickness measurements were calculated from the k-ratios measured by EDX using a program called GMRFilm,<sup>208</sup> and the resulting growth rates demonstrated ALD-characteristic self-limiting growth after 2 s pulse lengths of 1 (Figure 4.2 a). A growth rate of 0.5 Å cycle<sup>-1</sup> was observed which is similar to other ALD processes that deposit metallic films. A graph of growth rate per cycle shows that there is an induction period of ~ 90 cycles (Figure S-4.23). The films themselves were highly reflective metallic gold mirrors (Figure 4.2 b).

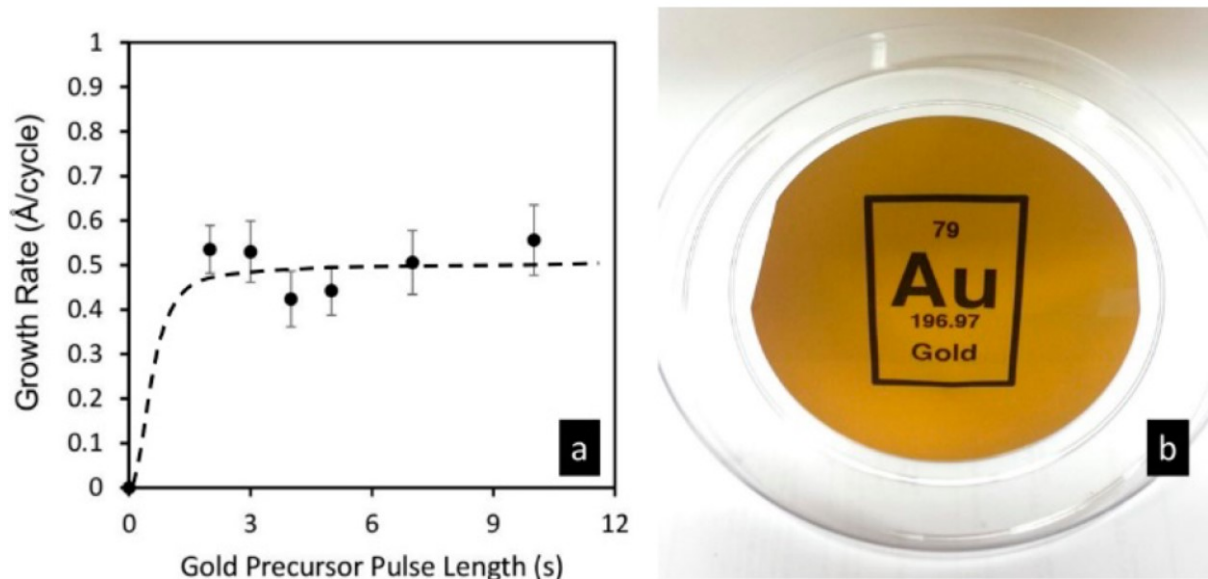


**Figure 4.2** Gold metal deposition from **1**. Panel a shows the saturation curve as the exposure of **1** is altered. Panel b shows a photo of the as-deposited film (using a 4 s pulse) with the chemical symbol for “Au” reflected from the surface of a 100 mm wafer.

Because our desire is to exploit this technique to form metallic nanoparticles, we were very interested in studying the effect of a small number of cycles of the process. Deposition of gold metal on polymer-coated copper transmission electron microscopy (TEM) grids was done with 2 and 5 cycles. With two ALD cycles, EDX showed the presence of gold, but features were difficult to differentiate from the background carbon of the polymer film. With five ALD cycles, obvious gold nanoparticles were observed by transmission electron microscopy (TEM) and EDX (Figure 4.3). The lattice spacing of atoms in the TEM was 0.23 nm, which is indicative of the Au(111) crystal face.<sup>209</sup>

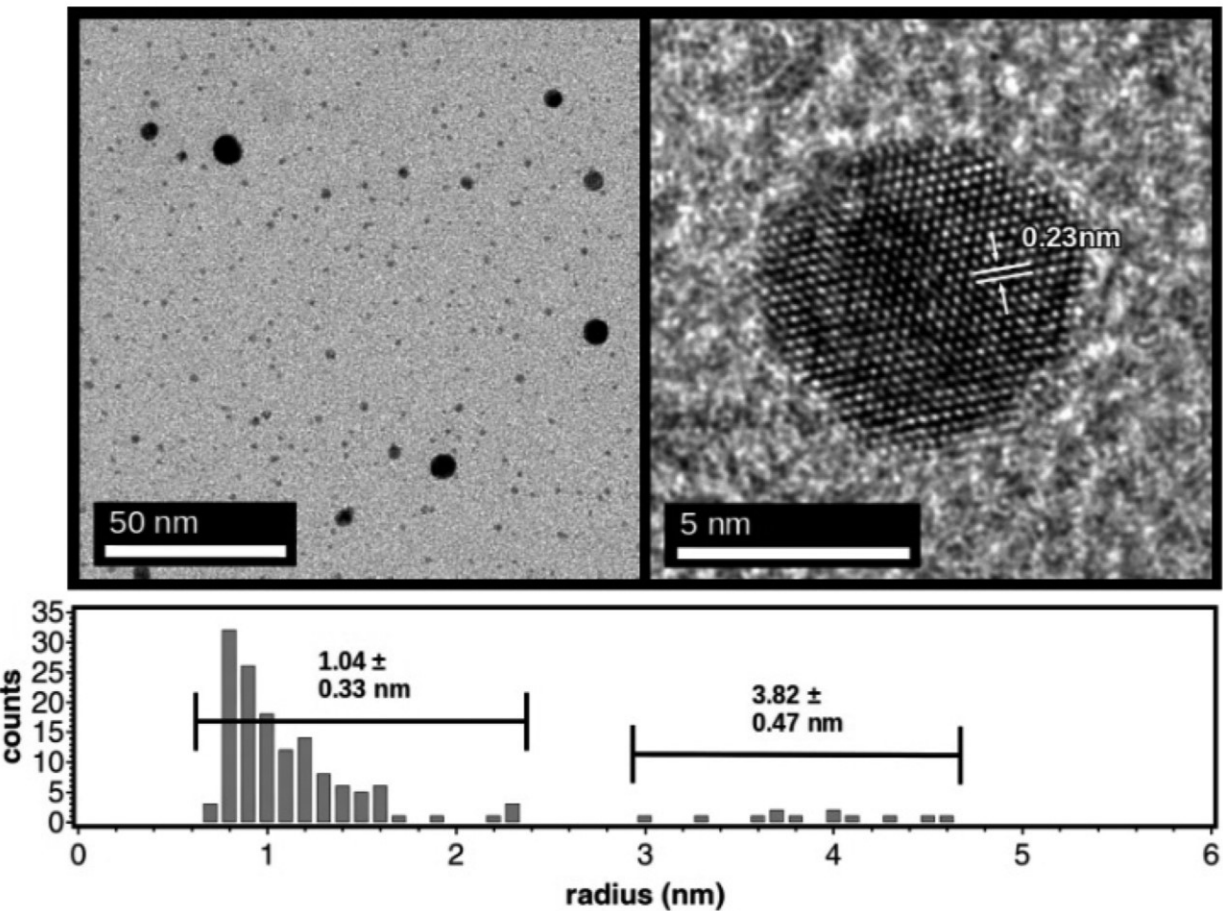


**Figure 4.3** TEM of gold metal nanoparticles deposited on a TEM grid after five ALD cycles using 1 with  $\text{O}_2^*$  and water as co-reactants. The histogram shows the distribution of particle sizes.

The deposited gold metal particles showed some polydispersity, which we attribute to mobility of the reduced gold adatoms formed during the plasma step. At five ALD cycles, the particles had a bimodal size distribution. The large particles were few in number and had an average radius of  $3.8 \pm 0.5 \text{ nm}$  whereas the smaller particles were much more numerous and had an average diameter of  $1.0 \pm 0.3 \text{ nm}$  with the most common radius being 0.8 nm.

This shows that ALD-deposited gold can produce nanoparticles on a substrate without the need for solution-phase chemistry and capping agents (other than the inherent ligand system). The overall growth during ALD cycles as well the movement of adatoms on the surface to various nucleation points suggests a Volmer–Weber type growth. This is

expected due to the energetics of the plasma step and the propensity for precursor nucleation onto metallic gold rather than the carbon mesh of the TEM grid.

#### 4.1.4 Additional Results

Using in-situ Reflection Absorption Infrared Spectroscopy (RAIRS) it is possible to determine which surface groups are present after each precursor or reactant exposure. In collaboration with the CoCooN research group at Ghent University, Belgium, the surface chemistry of the **1** + O<sub>2</sub>\* + H<sub>2</sub>O ALD process was studied through RAIRS measurements on a sputtered gold seed layer (60 nm), at a substrate temperature of 120 °C (see section 4.4 for a description of this experiment and the deposition tool). RAIRS difference spectra are shown in Figure 4.4 for the **1** pulse, the O<sub>2</sub>\* pulse, and the H<sub>2</sub>O pulse.

RAIRS analysis allowed us to elucidate some very interesting surface chemistry which takes place during this process. Firstly, the dose of **1** causes a disappearance of two peaks at 3659 and 3575 cm<sup>-1</sup> which we assign to hydroxylated gold species which are isolated and bridging respectively.<sup>210</sup> These absorptions likely originate from a partially hydroxylated gold surface which is produced during the O<sub>2</sub>\* dose. We believe that it is possible that the interaction of AuO-H with **1** causes the partial oxidation of the phosphine ligands of **1**. It is also possible that this results in a combustion reaction of the Au-Me ligands similar to what is observed in the (<sup>Me</sup>Cp)PtMe<sub>3</sub> + O<sub>2</sub> ALD process.<sup>211</sup> Compound **1** also causes the appearance of C-H stretching absorptions in the 2980-2912 cm<sup>-1</sup> region due to the presence of PMe<sub>3</sub> groups and possibly Au-CH<sub>3</sub> groups. During the dose of **1** we also observed strong bands at 1418, 1298, 1199, and 963 cm<sup>-1</sup>. This correlates well to vibrational absorptions observed for trimethylphosphine (1430 and 1414 cm<sup>-1</sup>, 1298 and 1283 cm<sup>-1</sup>, and 950 cm<sup>-1</sup>) as well as those observed for **1** in the condensed phase (1434 and 1423 cm<sup>-1</sup>, 1293 and 1287 cm<sup>-1</sup>, and 962 cm<sup>-1</sup>).<sup>212-214</sup> However the band observed at 1199 cm<sup>-1</sup> does not originate from PMe<sub>3</sub>-type species. This peak is slightly higher than expected for trimethylphosphine oxide type species<sup>215</sup> (free trimethylphosphine oxide  $\nu(P=O) = 1166\text{ cm}^{-1}$ , coordination to a metal center reduces the

frequency of this absorption), but could be attributed to a further oxidized phosphorus species such as an alkyl phosphinate or an alkyl phosphonate.

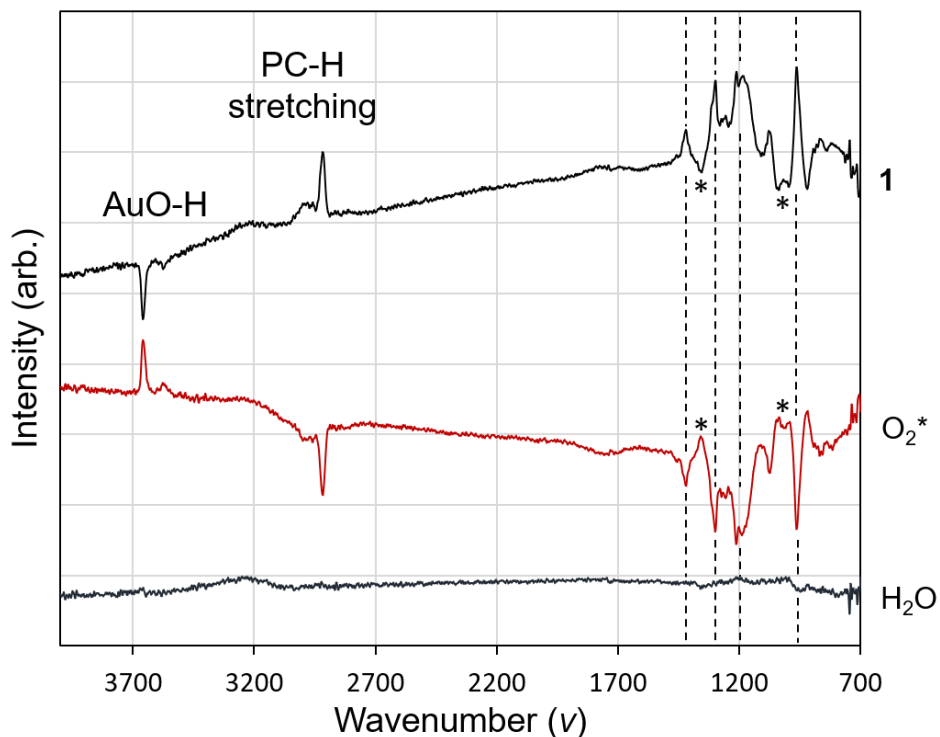


**Figure 4.4** (Top) RAIRS difference spectrum after the **1** dose, (Middle) after the  $O_2^*$  pulse, (Bottom) after the  $H_2O$  pulse. Each spectrum is the average of 10 separate spectra taken at the same timepoint in the pulse sequence in order to increase signal to noise. Peak assignments of the dashed lines from high to low wavenumber: ( $\nu$ , assignment) 1418,  $\delta_{as}(CH_3)-[P]$ ; 1298,  $\delta_s(CH_3)-[P]$ ; 1199,  $\nu(P=O)$ ; 963,  $\rho(PCH_3)$ . Strong peaks produced during the  $O_2^*$  dose are denoted with a \* symbol.

The  $O_2^*$  dose removes the species that absorb at 2980-2912, 1418, 1298, 1199 and 963  $\text{cm}^{-1}$  and causes the appearance of Au-OH species (3659 and 3575  $\text{cm}^{-1}$ ) as well as broad absorptions at 1348, 1109, 1030, 985, and 917  $\text{cm}^{-1}$ . Of these new absorptions, we were able to tentatively assign 1348 and 1030  $\text{cm}^{-1}$ . In one theoretical investigation, researchers calculated the  $\nu(P=O)$  and  $\nu(P-O)$  stretching frequencies of  $P_4O_{10}$  to be 1385 and 1035  $\text{cm}^{-1}$  respectively at the B3LYP/6-311G\* level of theory.<sup>216</sup> Another experimental study found that the range of  $\nu(P=O)$  and  $\nu(P-O)$  stretching frequencies of  $P_4O_{10}$  and lower oxides of the type  $P_4O_n$  ( $n = 6 - 10$ ) appeared in the range of 1408 –

$1362\text{ cm}^{-1}$  and  $1026 - 953\text{ cm}^{-1}$  respectively, where the stretching frequency decreased as  $n$  decreased from 10 to 6.<sup>217</sup> Given these analyses, and given the broadness of the observed peaks, we assign the observed peaks at  $1348$  and  $1030\text{ cm}^{-1}$  to  $\text{P}_4\text{O}_x$  species where  $x = 6 - 10$ . The origin of the other peaks in the  $\text{O}_2^*$  dose spectrum remain elusive.

In these experiments, we were unable to determine if any Au-Me groups were present on the surface after the dose of **1** since the regions where they should be observed as isolated peaks ( $1100 - 750\text{ cm}^{-1}$ ) was obscured by other more strongly absorbing bands. In this system, it appears that the  $\text{H}_2\text{O}$  doesn't affect the surface very much at all, except to add some physisorbed water which appears as a broad low intensity peak at  $\sim 3250\text{ cm}^{-1}$ .

Unfortunately, all films obtained from this process were amorphous and did not show the expected diffraction peaks for  $\text{Au}(0)$  (see section 4.2.4 for XPS and x-ray diffraction (XRD) comparison of all PEALD processes using **1**). *Ex-situ* depth-profile XPS analysis of these films allowed observation of P(V)- and O-containing species within the film which agree with both the RAIRS experiments and previous XPS analysis when water was not used in a flow-type reactor. This deposition tool operates as a pulse-soak-pump reactor with a base pressure of  $2 \times 10^{-6}\text{ mbar}$ , whereas the Picosun R200 tool that we originally developed the process on is a constant-flow type reactor with an operating pressure of 5 mbar. Interestingly, it appeared at this point that the difference in both the deposition tool and plasma power would have a strong influence on the **1** +  $\text{O}_2^*$  +  $\text{H}_2\text{O}$  process.

## **4.2 PE-ALD of gold metal using trimethylphosphinotrimethylgold(III) and hydrogen plasma**

### **4.2.1 Introduction**

Gold as a bulk material has found a widespread use in jewelry, coinage, and decorative pieces because of its unreactive nature. However, nanoparticulate gold has very interesting and useful catalytic properties and has attracted significant interest for heterogeneous catalysis.<sup>20,23,218</sup> The use of nanoparticulate gold for heterogeneous catalysis remains a growing research field.

Suspended gold nanoparticles (or colloidal gold) are often used for their inherent optical properties (e.g., colloidal gold in ruby glass).<sup>1</sup> The optical properties arise because of the localized surface plasmon resonances (LSPR) that develop at the metal surface. The LSPR can create electromagnetic hotspots between metallic structures, and these hotspots can cause enormous enhancement of a Raman signal.<sup>219,220</sup> The most used materials for surface-enhanced Raman spectroscopy (SERS) are silver and gold because of their surface plasmon properties. A drawback of using silver in SERS substrates is that it easily tarnishes while this is not the case for gold. In general, highly ordered nanostructures are required for solid-state SERS substrates. By tuning the properties of the nanostructures on the SERS substrate, it is possible to achieve single molecule detection. A major fallback in present SERS substrates is that fabrication often involves several processing and deposition steps, making the production process expensive, complex, and difficult to implement simply and on a large scale.

Atomic layer deposition (ALD) offers precise control over the amount of material deposited on a substrate because of the alternating exposure of the substrate to the precursor and reactant gases. These gas phase species undergo self-limiting reactions with the substrate, which allows conformal films to be deposited on planar and complex 3D substrates. This makes ALD an extremely useful deposition method for gold

nanoparticles on substrates that are challenging for other deposition methods (e.g., physical vapor deposition or solution-based methods).

Gold metal is extremely challenging to be deposited by ALD: only two gold ALD processes have been reported, although many chemical vapor deposition (CVD) precursors exist to deposit gold.<sup>94,204,221,222</sup> However, finding precursors that are suitable for ALD has proven to be quite difficult because they need to be thermally stable, volatile, have decent surface-limited reactions, and saturation behavior.<sup>223</sup> Another aspect is the need for suitable reducing agents for the precursor. The first gold ALD process was reported by us and is detailed above in section 4.1 of this chapter. This plasma-enhanced ALD (PE-ALD) process consisted of three steps: the surface is first exposed to trimethylphosphinotrimethylgold(III) (**1**), followed by oxygen plasma exposure, and finally, a water vapor exposure. Deposition of metallic gold was reported at a deposition temperature of 120 °C with a growth rate of 0.05 nm per cycle. The deposited films had some impurities, 6.7 at. % carbon, and 1.8 at. % oxygen. The second gold ALD process was reported by Mäkelä, Hatanpää, Mizohata, Räisänen, Ritala, and Leskelä.<sup>224</sup> This process employs  $\text{Me}_2\text{Au}(\text{S}_2\text{CNEt}_2)$  as the gold precursor and ozone as the co-reactant. Deposition between 120 and 180 °C was reported, with self-limiting growth at a substrate temperature of 180 °C. A relatively high growth rate of 0.09 nm per cycle was achieved. These films showed low resistivity (4.6–16  $\mu\Omega \text{ cm}$ ) with some impurities 2.9 at. % oxygen, 0.9 at. % hydrogen, 0.2 at. % carbon, and 0.2 at. % nitrogen.

As far as we know, there are no reports of thermal CVD of **1**, and the mechanism of CVD of **1** has not been studied directly. However, multiple studies have assessed the CVD mechanism of the related Au(I) compound  $(\text{PMe}_3)\text{AuMe}$  and other alkylgold(I) phosphines.<sup>98,118,204,225</sup> These studies have found that the decomposition mechanism of the Au(I) species mirrors the decomposition mechanism that was observed in solution-phase thermal decomposition. In solution, Komiya et al. found that the decomposition of trialkyl(triphenylphosphine)gold complexes proceeds through the reductive elimination of two neighbouring alkyl groups, resulting in the formation of alkyl-alkyl species and the alkyl(triphenylphosphine)gold complex.<sup>226,227</sup> The latter will then undergo further

decomposition as described by Tamaki et al., where alkyl(triphenylphosphine)gold species decomposed into coupled alkyl products, elemental gold, and triphenylphosphine.<sup>228</sup>

Davidson et al. reported laser induced CVD of gold lines using (PMe<sub>3</sub>)AuMe, (PEt<sub>3</sub>)AuMe, and (PEt<sub>3</sub>)AuEt using an argon ion laser at 257 nm, obtaining gold films with resistivity values below a factor of 3 of the bulk value. The elemental composition and inclusion of precursor ligands on the surface was studied using laser ionization microprobe analysis. They observed the presence of chemisorbed PMe<sub>3</sub> species on the gold surface, which remained present on the surface for prolonged periods of time under high vacuum conditions.<sup>229</sup> Indicating that the Au-Me surface species are less stable than the Au-PMe<sub>3</sub> surface species. In addition they found indications of non-dissociative adsorption of (PMe<sub>3</sub>)AuMe on the gold surface. These are interesting implications for the ALD reaction mechanism of **1**.

In this section, we report a gold PE-ALD process using **1** in combination with H<sub>2</sub> plasma as the reactant. Compared to the other two reported gold ALD processes, this process showed self-limiting behavior at temperatures as low as 50 °C. This makes it possible to use the reported process in applications that utilize temperature-sensitive substrates, such as flexible electronics.<sup>230,231</sup> Another advantage over the previously reported gold ALD processes is the use of a reducing co-reactant (H<sub>2</sub>\* ) instead of oxidizing chemistry (O<sub>2</sub>\* or O<sub>3</sub>), hence avoiding potential oxidation of the underlying substrate surface as well as the growing gold film itself. The deposited films have a nanoparticulate structure, which makes them interesting for heterogeneous catalysis and plasmonic applications. We also investigate the ALD reaction mechanism of the **1** + H<sub>2</sub>\* gold ALD process using in-situ characterization techniques. This will be done for the steady growth regime on an Au surface and the temperature dependent decomposition of the precursor will be studied.

## 4.2.2 Results and Discussion

### 4.2.2.1 ALD Process characteristics and growth morphology

In our original study of the **1 + O<sub>2</sub>\*** + H<sub>2</sub>O process, using the Picosun R200 PE-ALD reactor, we found that H<sub>2</sub>\* was ineffective as a co-reagent. However using a lower pressure system increases the potency of a plasma because fewer recombination events. The homemade PE-ALD tool at Ghent university operates with both a lower pressure and is able to utilize a higher concentration of H<sub>2</sub> as a plasma gas. Thus, we were able to develop an ALD process to deposit gold metal with **1 + H<sub>2</sub>\***. The saturation behavior of both **1** and H<sub>2</sub>\* exposure was investigated by determining the equivalent growth per cycle (<sup>eq</sup>GPC), obtained by dividing the equivalent thickness by the number of ALD cycles) on gold seed layers as a function of the respective exposure time (Figure 4.5). We use this term of equivalent growth per cycle because the gold films being deposited are not continuous on the silicon oxide substrates. The nanoparticulate nature of the films makes a film thickness determination difficult since on some parts of the substrate there is no gold, and on much of the rest of the substrate there is (see Figure 4.8). Therefore an equivalent film thickness and an equivalent growth per cycle are values determined from X-ray fluorescence spectroscopy (XRF) where true continuous gold films of known thickness were used to calibrate the analysis.

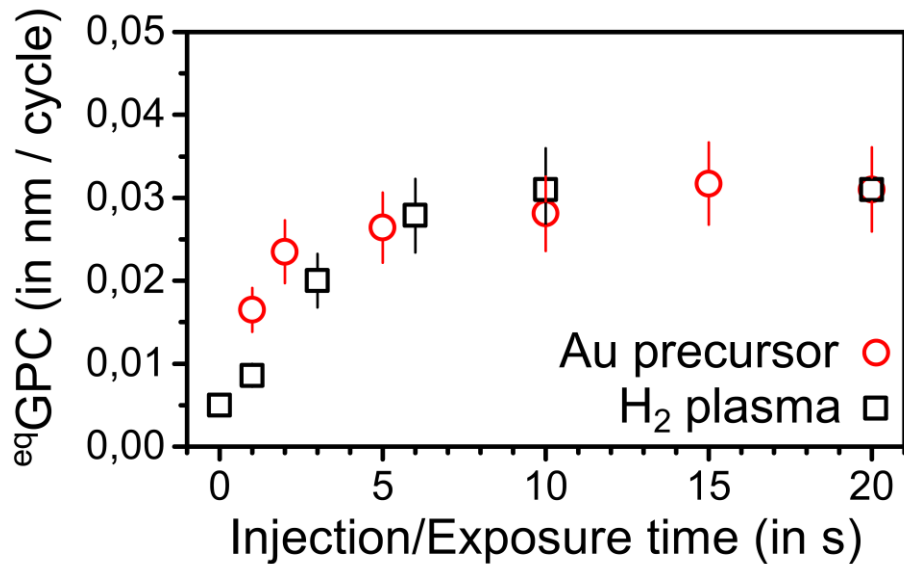


**Figure 4.5** Equivalent growth per cycle ( ${}^{eq}GPC$ ) as a function of injection time of **1**, and exposure time of  $H_2^*$ . Depositions were performed on a gold seed layer (10 nm on silicon substrates) at 100 °C substrate temperature. 100 cycles of **1** +  $H_2^*$  were used in each experiment. The exposure time of  $H_2^*$  was held at 20 s for the saturation experiments of **1**. The injection time of **1** was held at 20 s for the saturation experiments of  $H_2^*$ . The total dose of **1** consisted of the injection time which was varied, followed by a fixed incubation time of 5 s where the system was held in static vacuum to allow **1** to react.

The injection time for the precursor was varied between 1 and 20 s, while the reactant exposure was kept fixed at 20 s. Likewise, the exposure time of the reactant was varied between 1 and 20 s, while the precursor injection time was kept fixed at 20 s. The depositions were performed at a substrate temperature of 100 °C on silicon substrates coated with a thin sputtered gold seed layer (10 nm). Each deposition consisted of 100 cycles of **1** +  $H_2^*$ . The gate valve between the reaction chamber and the turbomolecular pump was closed during the precursor exposure. Self-limiting chemisorption ( ${}^{eq}GPC = 0.030 \pm 0.002$  nm) was achieved after a 10 s injection of **1** and an exposure time of 10 s for  $H_2^*$ . At 100 °C substrate temperature, pulsing only **1** resulted in film growth at an  ${}^{eq}GPC$  of 0.005 nm which implies only a minor CVD component due to thermal decomposition of the monolayer formed after chemisorption of **1**. On a bare silicon substrate, no gold was observed after 100 cycles, meaning that the nature of the

chemisorbed monolayer on Au is different than that formed on Si, and also that the CVD component cannot be attributed to thermal decomposition of the intact precursor.

When the plasma source was switched off, and the same concentration of H<sub>2</sub> was used in a thermal ALD configuration, the same <sup>eq</sup>GPC of 0.005 nm was observed on gold seed layer substrates and no growth was observed on bare Si. This <sup>eq</sup>GPC is therefore attributed to the decomposition from monolayers formed by **1**.

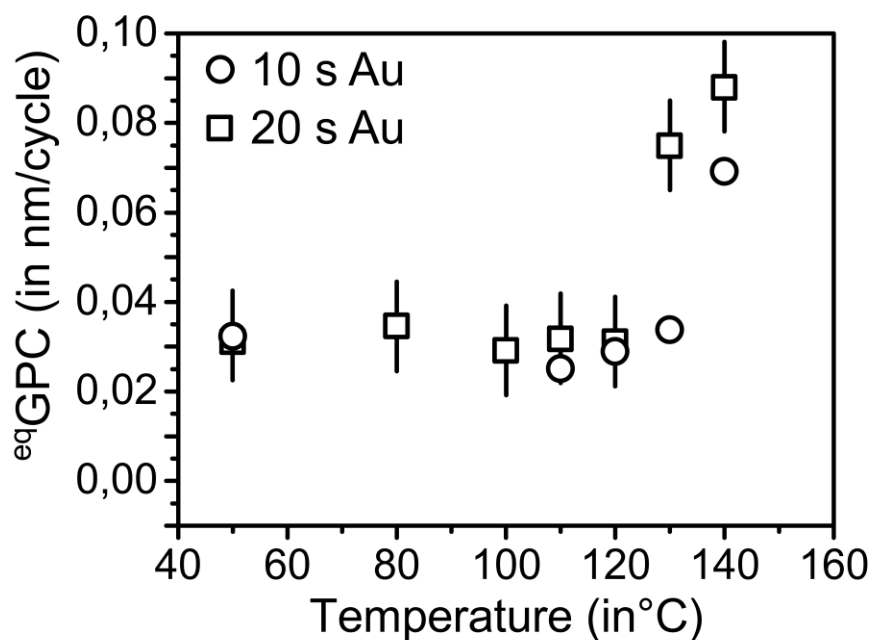


**Figure 4.6** <sup>eq</sup>GPC as a function of the substrate temperature for injection time lengths of 10 and 20 s for **1** with a dwell time of 5 s for both. An exposure time of 15 s was used for H<sub>2</sub>\*. Depositions were performed on a gold seed layer. A total of 100 ALD cycles were performed during each deposition to determine the <sup>eq</sup>GPC value. The error bars for the 10 s Au injection time periods were omitted for clarity. Decomposition of the precursor occurs above 120 °C.

The temperature dependence of the <sup>eq</sup>GPC of this **1** + H<sub>2</sub>\* process is shown in Figure 4.6. To our surprise, the <sup>eq</sup>GPC of 0.03 nm is maintained at temperatures as low as 50 °C, up to 120 °C, and even when doubling the dose of **1**, meaning that this process has the potential to be performed on thermally sensitive materials seemingly without altering the process chemistry. At temperatures of 130 °C and above, the precursor begins to undergo thermal self-decomposition which we had previously observed using the Picosun R200

PE-ALD system as well. Given the low temperature saturation of this process, a deposition was performed on a piece of tissue paper and we observed both a colour change from white to dark golden-brown, as well as the obvious inclusion of Au into the substrate by EDX (Figure 4.7). We could not observe the presence of P in the sample, and therefore we can conclude that this process is potentially applicable to textile deposition, as well as flexible and wearable electronic devices.<sup>230,231</sup>

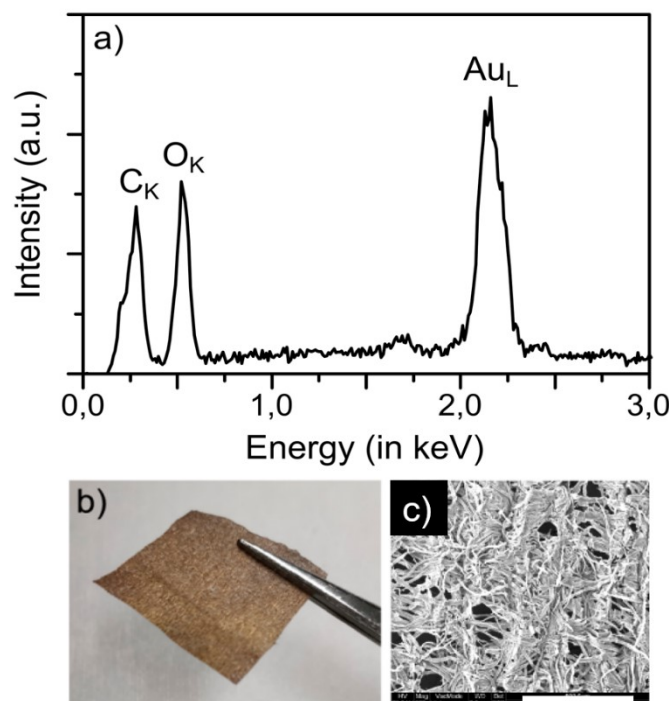


**Figure 4.7** a) EDX spectrum of a deposition of the  $\mathbf{1} + \text{H}_2^*$  process on tissue paper, performed at 50 °C; b) picture of the piece of tissue paper used as the substrate; c) SEM image of sample (scale bar = 500  $\mu\text{m}$ ).

The process was then investigated on  $\text{SiO}_2$  surfaces (from both native  $\text{SiO}_2$  on Si as well as thermally grown  $\text{SiO}_2$ ). As shown in Figure 4.8, the process exhibits linear film thickness with respect to the number of ALD cycles performed, and this dependence is essentially the same for processes performed at 50 °C and 120 °C. However, there is a difference in growth morphology at the two different temperatures. As shown in Figure 4.8b and 4.8c, experiments performed at 120 °C deposited isolated islands of gold on the surface which did not coalesce even at an equivalent thickness of 21.7 nm. None of the substrates deposited at 120 °C showed any evidence of electrical conductivity in the films.

In fact the only film deposited at 120 °C that was observed to have in-film electrical conductivity required 2400 cycles and was an equivalent thickness of 65.6 nm (resistivity =  $5.9 \pm 0.3 \mu\Omega \text{ cm}$ ). At 50 °C isolated islands are also observed initially, but at an equivalent thickness of 12.9 nm which took only 400 ALD cycles, these islands were observed to coalesce. This film did show an appreciable resistivity of  $16.5 \pm 0.8 \mu\Omega \text{ cm}$  (resistivity of bulk gold =  $2.44 \mu\Omega \text{ cm}$ ) which was similar to the film resistivity obtained for a 49 nm thick film deposited by the  $\text{Me}_2\text{Au}(\text{S}_2\text{N}(\text{Et})_2) + \text{O}_3$  process.<sup>224</sup> This demonstrates that temperature is an important consideration when depositing metals on oxide substrates especially if film conductivity is a property of interest.

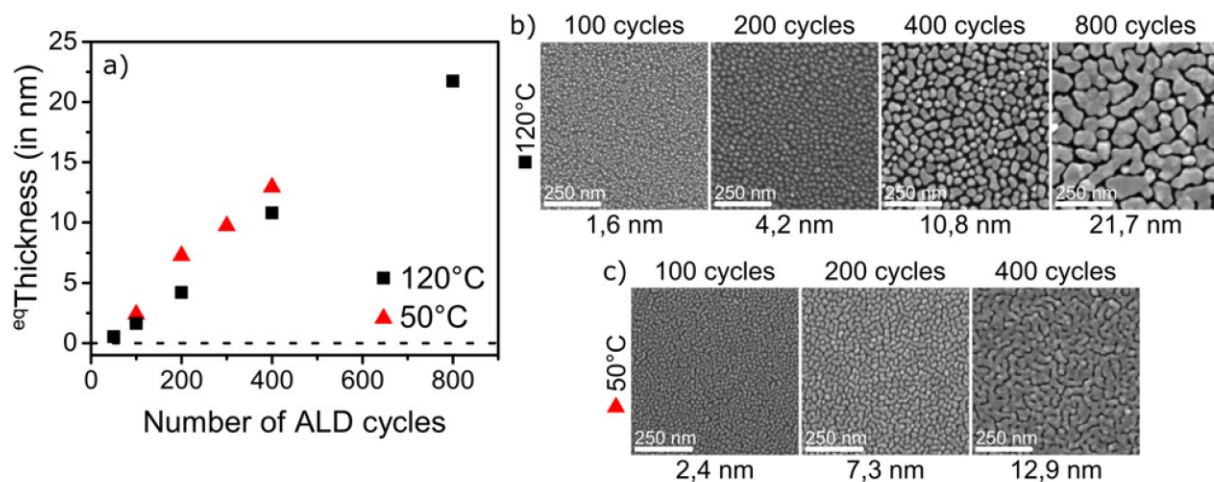


**Figure 4.8** (a) Equivalent thickness of gold as a function of the number of ALD cycles performed on a silicon substrate (native oxide) for a substrate temperature of 50 and 120 °C. Saturating conditions were used for all depositions (i.e., a 15 s exposure time for both **1** and  $\text{H}_2^*$ ). (b) Top SEM micrographs for PE-ALD films deposited at 120 °C. (c) Top SEM micrographs for PE-ALD films deposited at 50 °C.

Films deposited at both 50 °C and 120 °C were polycrystalline as observed by X-ray diffraction (XRD) (Figure S-3.24) and displayed a dominant Au(111) reflection at 38.5 ° and a smaller Au(200) reflection at 44.6 ° which is commonly observed for vapour-deposited gold films.

The elemental composition of the deposited films was then examined using XPS, the results for which are shown in Figure 4.9. The sample was a silicon substrate on which 800 ALD cycles were performed at 120 °C, yielding an equivalent gold thickness of 21.7

nm. This deposition temperature, at the higher limit of the temperature window, was purposefully selected for comparison with the two previously reported gold ALD processes. The deposited film contained Au(0) and no sign of an oxidized state of gold, with the Au 4f<sub>7/2</sub> peak centered at 84.1 eV (bulk gold expected 4f<sub>7/2</sub> peak = 84.0 eV) and a spin-orbit splitting value equal to the expected value of 3.7 eV. This process yielded a surface concentration of P that was below the limit of detection, just as in the case of the  $\text{1} + \text{O}_2^* + \text{H}_2\text{O}$  process. However the as-deposited films from the H<sub>2</sub>\* process performed better in terms of C (3.4 at. %) and O (at. 1.1 at. %) than the O<sub>2</sub>\* process where C (at. 6.7 at. %) and O (1.8 at. %) (Table 2) concentrations were higher. These values are also lower than the observed impurity concentrations for the Me<sub>2</sub>Au(S<sub>2</sub>NEt<sub>2</sub>) + O<sub>3</sub> process.<sup>224</sup>

After removal of possible surface contamination by Ar<sup>+</sup> sputtering, both C and O concentrations were 0.3 at. % which is close to the limit of detection of XPS. In the case of the O 1s peak, it very closely resembles what is expected for SiO<sub>2</sub> and could be due to a small signal originating from photoelectrons that reach the detector through the small gaps in the deposited film (See Figure 4.9, 120 °C, 800 cycles). However, there was no accompanying Si 2p peak which should accompany it. Therefore we were unable to assign the chemical nature of the small O 1s peak. Nevertheless, the overall Au concentration of the deposited film was 99.4 at. % which is the best reported purity out of the four known Au ALD processes to date (Table 4.2).

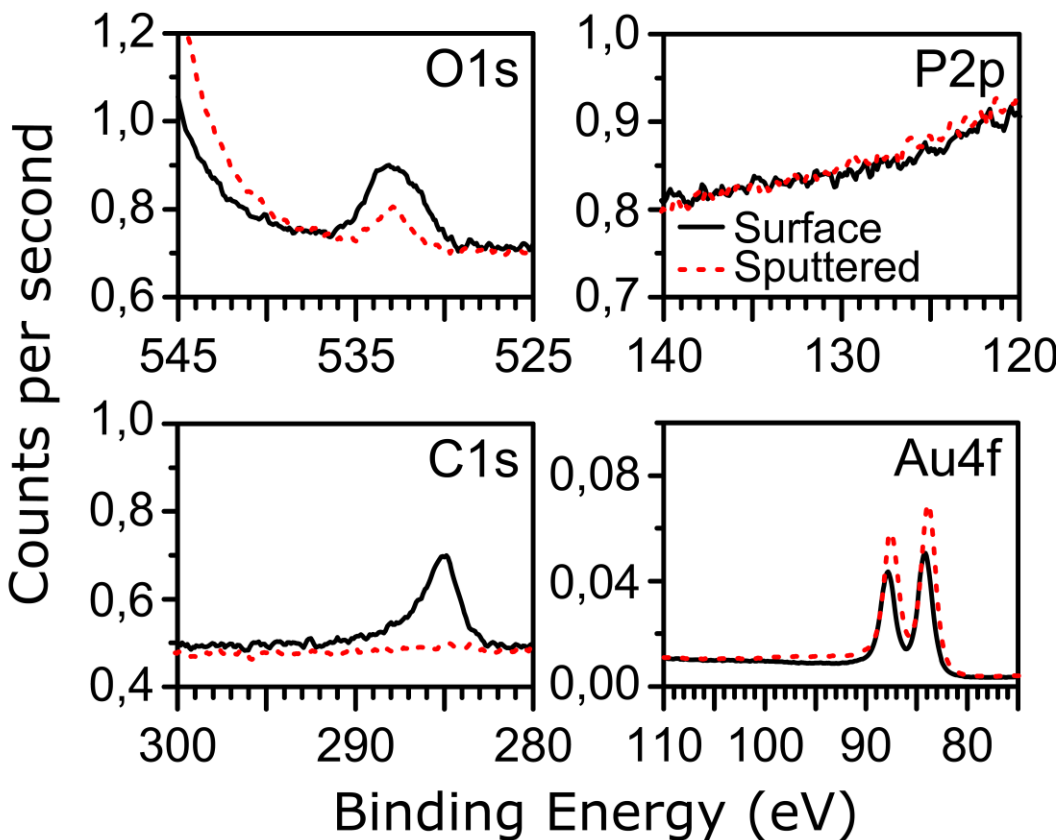


**Figure 4.9** XPS spectra for a PE-ALD-grown Au film deposited at 120 °C with an equivalent thickness of 21.7 nm. The signals are given for the as-deposited film after removing surface contamination by Ar<sup>+</sup> sputtering. The Si 2p peak (99.4 eV) is not visible.

**Table 4.2** Elemental concentrations of Au, C, O, and P of an Au film grown at 120 °C as determined by XPS. The equivalent thickness of the Au film was 21.7 nm (800 ALD cycles).

	Au 4f (at. %)	C 1s (at. %)	O 1s (at. %)	P 2p (at. %)
surface	95.5	3.4	1.1	<0.1
sputtered	99.4	0.3	0.3	<0.1

<sup>a</sup>The atomic concentration is given for the surface of the (air-exposed) as-deposited film on the first row. On the second row the atomic concentration is given after removing the surface contamination from the sample by Ar<sup>+</sup> sputtering in the XPS chamber.

#### 4.2.2.2 Surface Chemistry and Ligand Stability

With this new process in hand, we then moved to examine the surface chemistry in greater detail with the help of a combination of *in-situ* RAIRS and *in-vacuo* XPS. Initially, we again chose to use gold seed layers as the substrate of choice in order to be able to focus on the chemistry of **1** with the growing gold surface.

We performed the **1** + H<sub>2</sub>\* process at 90 °C and analyzed RAIRS difference spectra which were taken as an average of 10 spectra each in order to increase signal to noise (Figure 4.10). We also synthesized a deuterated version of the precursor, (PMe<sub>3</sub>)Au(CD<sub>3</sub>)<sub>3</sub>, **d<sub>9</sub>-1**, in order to deconvolute the surface chemistry of the Me-Au ligands from the PMe<sub>3</sub> ligands. The RAIRS spectra shown in Figure 4.10 of the pulse of **1** (or **d<sub>9</sub>-1**) and of the H<sub>2</sub>\* pulse have been subtracted from one another, so that positive absorptions indicate surface species that have been added by that dose, and negative absorptions indicate surface species that have been removed during that dose.

Exposure of **1** to the sputtered gold surface causes the appearance of absorption peaks which correspond to vibrational modes of the Au-CH<sub>3</sub> and PMe<sub>3</sub> groups. The C-H stretching vibrations of the Au-Me groups were obscured by the PMe<sub>3</sub> C-H stretching vibrations (labelled as 1,2,3 and 4) (see Table 4.3 for a list of all labelled peaks). Use of **d<sub>9</sub>-1** gave conclusive evidence that the Au-Me ligands persist on the growing surface through observation of C-D stretching vibrations labelled as 5 and 6.

The fingerprint region reveals similar absorptions related to the PMe<sub>3</sub> ligand in both cases (labelled as 7, 8, 10, and 11), however peak 9 (1100 cm<sup>-1</sup>) shifts to 778 cm<sup>-1</sup> (labelled as 9'), which is indicative of a lower energy absorption originating from asymmetric deformation of CH<sub>3</sub> and CD<sub>3</sub> groups respectively, bound to Au on the surface. The simplest explanation for the reaction between **1** and the surface is dissociative chemisorption by cleavage of the Au-P bond. One aspect of this analysis which will be discussed later is that it appears that the majority of the species on the surface are PMe<sub>3</sub> ligands simply due to the low intensity of the Au-CH<sub>3</sub> or Au-CD<sub>3</sub> absorptions compared to the PMe<sub>3</sub> absorptions.

Notably, in contrast to what was observed for the  $\mathbf{1} + \text{O}_2^* + \text{H}_2\text{O}$  process, the  $\text{H}_2^*$  from the  $\mathbf{1} + \text{H}_2^*$  process does not chemically alter the surface since we did not observe absorptions that could be related to Au-H vibrations which have been reported to absorb near  $2230 - 2170 \text{ cm}^{-1}$  and  $1642 \text{ cm}^{-1}$ .<sup>232</sup> While it may be possible that transient Au-H species are formed during the  $\text{H}_2^*$  dose and aid in the removal of surface ligands, but Au-H is not known to be stable above  $-148^\circ\text{C}$ .<sup>233,234</sup> What we were able to observe was that the  $\text{H}_2^*$  completely removes all IR-active species from the surface, restoring a seemingly pristine Au surface for the next step of the ALD cycle.

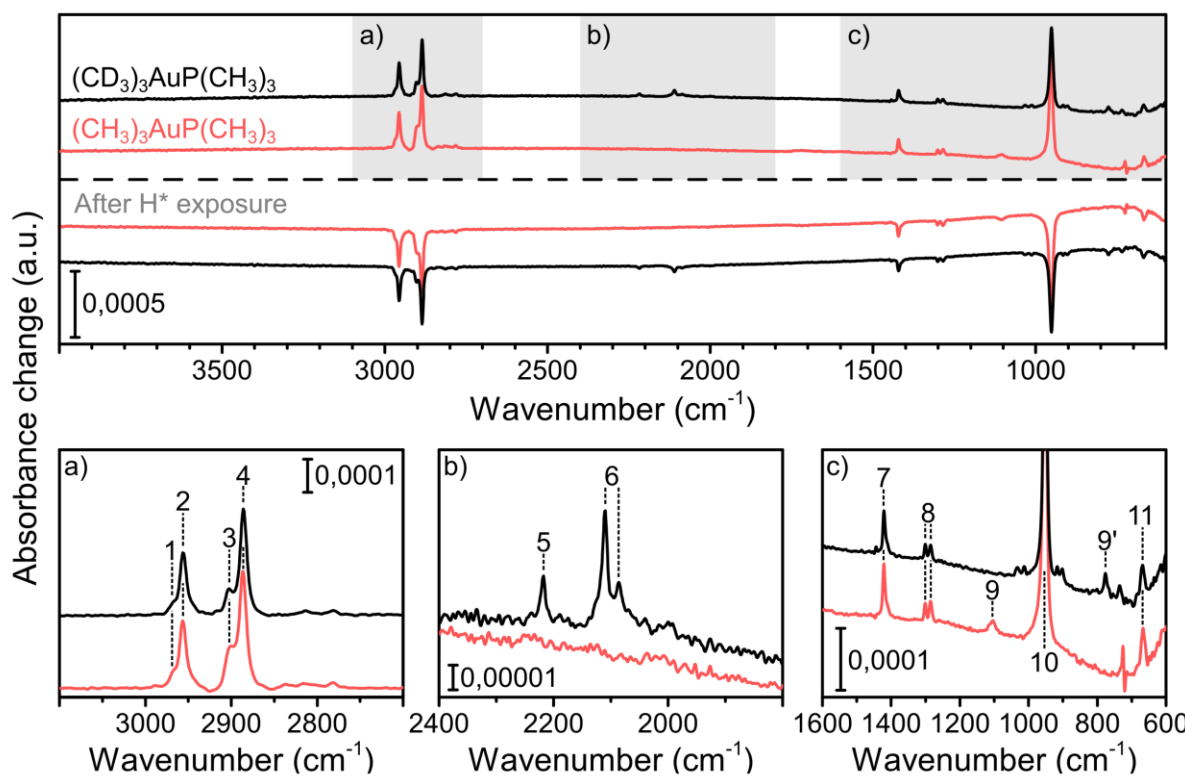


**Figure 4.10** Difference spectra for the  $(\mathbf{1} + \text{H}_2^*)$  and  $(\mathbf{d}_9\text{-}1 + \text{H}_2^*)$  ALD processes. Thick sputtered gold layers (60nm) were used as substrates and depositions were performed at a substrate temperature of  $90^\circ\text{C}$ . The regions marked by a), b), and c) are enhanced views of the CH-stretching, CD-stretching, and fingerprint regions, respectively, after a precursor exposure. Assignments for the marked peaks can be found in Table 4.3.

**Table 4.3** Position and assigned vibration modes of the observed features in the FTIR difference spectra displayed in Figure 4.10. The assignment of these peaks is based on reference IR spectra for **1** and **d<sub>9</sub>-1** and for the PMe<sub>3</sub> ligand.<sup>212–214</sup> ( $\nu$  stretching,  $\delta$  deformation,  $\rho$  rocking, as = asymmetric, s = symmetric)

Peak	Position (cm <sup>-1</sup> )	Vibration mode
1	2968	$\nu_{\text{as}}(\text{CH}_3)\text{-[P]}$
2	2958	$\nu_{\text{as}}(\text{CH}_3)\text{-[P/Au]}$
3	2901	$\nu_{\text{s}}(\text{CH}_3)\text{-[P/Au]}$
4	2887	$\nu_{\text{s}}(\text{CH}_3)\text{-[P/Au]}$
5	2218	$\nu_{\text{as}}(\text{CD}_3)\text{-Au}$
6	2110 and 2086	$\nu_{\text{s}}(\text{CD}_3)\text{-Au}$
7	1422	$\delta_{\text{as}}(\text{CH}_3)\text{-[P]}$
8	1285 and 1301	$\delta_{\text{s}}(\text{CH}_3)\text{-[P]}$
9	1100	$\delta_{\text{as}}(\text{CH}_3)\text{-[Au]}$
9'	778	$\delta_{\text{as}}(\text{CD}_3)\text{-[Au]}$
10	954	$\rho(\text{PCH}_3)$
11	667	$\nu_{\text{s}}(\text{PC}_3)$

To verify that even low concentrations of P and C were not left on the surface, we performed 300 ALD cycles of (**1** + H<sub>2</sub>\* ) onto a thick sputtered gold seed layer at 90 °C and analyzed its elemental composition by *in-vacuo* XPS. This was facilitated through use of an *in-vacuo* load-lock chamber to step down in pressure moving from the ALD chamber to the XPS chamber (transfer time approx. 1 minute). The resulting Au4f, P2p, and C1s peaks are shown in Figure 44.11. It is clear from these spectra that the Au only exists in one oxidation state. This sample was so clean that no C peak was observed at all, and so the Au was assumed to be in the metallic state and the Au4f<sub>7/2</sub> peak was used to calibrate the spectrum (Au4f<sub>7/2</sub> = 84.0 eV). No P was observed either, and so we concluded that the H<sub>2</sub>\* dose effectively removes all surface ligands and regenerates a metallic gold surface.

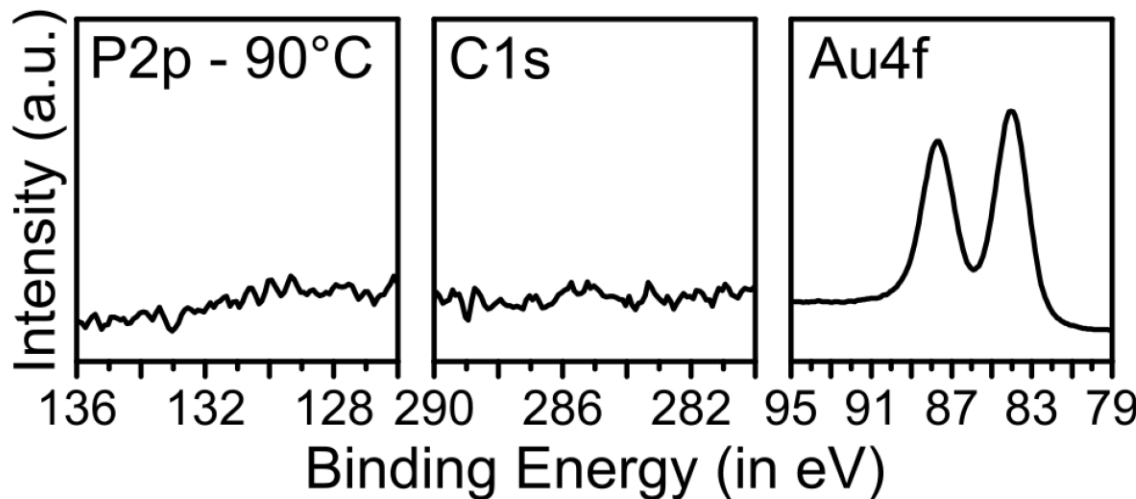


**Figure 4.11** P2p, C1s, Au4f peaks measured by *in-vacuo* XPS on a gold seed layer after performing the  $(\mathbf{1} + \text{H}_2^*)$  ALD process ending with an  $\text{H}_2^*$  plasma exposure. The deposition was performed at a substrate temperature of  $90^\circ\text{C}$ . After ending the ALD process the sample was transferred within 1 minute from the ALD chamber to the XPS analysis chamber without breaking vacuum.

To further study what surface chemistry was occurring during the **1** and  $\text{H}_2^*$  pulses, we employed *in-situ* quadrupole mass spectrometry (QMS) to characterize gas-phase by-products of the respective surface reactions. For this experiment, the pulse sequence used was:

3x [15 s **1** | 15 s pump down]

then

5x [15 s **1** | 15 s pump down | 15 s  $\text{H}_2^*$  | 15 s pump down]

then

3 x [15 s  $\text{H}_2^*$  | 15 s pump down]

This program accomplished: a) pre-saturation of the surface and the reactor walls; b) the reaction can be monitored over the course of 5 ALD cycles; c) the extent of the  $\text{H}_2^*$  effectiveness can be evaluated. The QMS data of this experiment are shown in figure 4.12.

While mass-to-charge ratios ( $m/z$ ) were tracked for  $\text{CH}_3^+$ ,  $\text{CH}_4^+$ ,  $\text{C}_2\text{H}_6^+$ ,  $\text{PH}_x^+$ , and  $\text{PMex}^+$  ( $x = 1 - 3$ ), only signals for  $\text{CH}_3^+$  and  $\text{CH}_4^+$  could be observed after either of the reactant doses. During the  $\text{H}_2^*$  pulses, a larger amount of both  $\text{CH}_3^+$  and  $\text{CH}_4^+$  was produced than during the pulses of **1**, which is indicative of the  $\text{H}_2^*$  removing surface-bound  $\text{CH}_3$  groups as  $\text{CH}_4$ , which is then ionized in the QMS to  $\text{CH}_4^+$  which is detected along with its daughter fragment  $\text{CH}_3^+$ .

The nature of the removal of the  $\text{PMe}_3$  ligands by  $\text{H}_2^*$  is unclear from the QMS data since  $\text{PMe}_3$  would ionize and fragment into  $\text{CH}_3^+$ . We attempted to use optical emission spectroscopy during the  $\text{H}_2^*$  exposure and while preliminary experiments suggested the presence of excites state  $\text{PH}_x$ -type species, other attempts remained inconclusive.

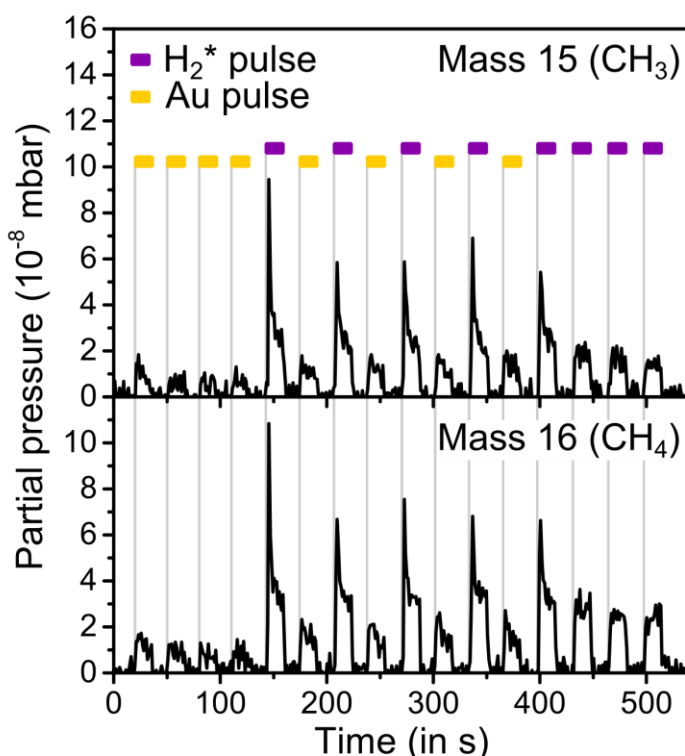


**Figure 4.12** Mass spectrometry measurements for mass to charge ratios 15 ( $\text{CH}_3$ ) and 16 ( $\text{CH}_3$ ) during a **1** +  $\text{H}_2^*$  process. The data shows 3 precursor pulses, followed by 5 ALD cycles and ending with an additional 3  $\text{H}_2^*$  pulses. The deposition was carried out using a substrate temperature of 90 °C.

During the first 5 doses of **1**, there is a small signal observed for both  $\text{CH}_3^+$  and  $\text{CH}_4^+$ , which indicates that the precursor itself fragments into these ions inside the QMS. During the doses of **1** during the 5-cycle process, a slightly larger signal for both ions is observed. This indicates that a reaction between **1** and the fresh Au surface is producing these ions, and we believe that this is linked to the low intensity observed for Au-Me groups by RAIRS. Since literature suggests that Au-H is not stable above -148 °C and we have not found any evidence for Au-H after the  $\text{H}_2^*$ , we were left with the explanation that surface-bound Au-Me groups undergo homolytic cleavage to produce Au(0) and  $\cdot\text{CH}_3$ . These  $\cdot\text{CH}_3$  radicals then go on to pick up H from the walls of the reactor leading up to the QMS.

The detection of methyl and methane indicates that during chemisorption of the precursor a part of the methyl ligands desorb from the surface. This could be due to the removal of methyl species from the gold atom during the expected first step in the reduction of Au(III) to Au(0). Based on decomposition literature of similar liquid gold compounds the first step occurs by alkyl-coupling, causing the removal of two of the methyl groups, forming ethane, and result in the reduction of the gold atom from a +3 to a +1 oxidation state.<sup>226–228</sup> This is also seen when adsorbing alkyl-halide molecules on gold surfaces with the onset of ethane desorption at -33 °C from Au(111) planes and at 27 °C from Au(100) planes.<sup>234,235</sup> However when co-adsorbing iodomethane with trimethylphosphine on a Au(100) surface, the formation of ethane does not occur and instead the methyl species desorb as methyl radicals above a substrate temperature of 100 °C. This indicates that the removal of methyl groups from Au(111) planes occurs below 0 °C, which in our case would mean that the methyl groups that are adsorbed during the precursor exposure will quickly be removed from the gold surface. And, as no ethane is detected in the mass-spectrometer, it is likely that the co-adsorption of trimethylphosphine on Au(111) planes has a similar effect as the co-adsorption on Au(100) planes. Thus we attribute the  $\text{CH}_3^+$  and  $\text{CH}_4^+$  signals observed during the pulse of **1** to originate from  $\cdot\text{CH}_3$  desorption from Au(111) planes, which eventually become saturated with only  $\text{PMe}_3$  by further chemisorption of **1**.

### 4.2.2.3 Temperature-Dependent Monolayer Decomposition

The in-situ FTIR measurements show that a small number of CH<sub>3</sub> and a larger amount of PMe<sub>3</sub> ligands of compound **1** are present on the surface after the precursor exposure and are removed by the H<sub>2</sub>\* plasma exposure. The presence of these ligands on the gold surface prevents further adsorption of precursor molecules on the surface and cause saturation. However we observed that there was a minor decomposition component present for this process (Figure 4.13) that we were now able to attribute primarily to slow dissociation of surface bound methyl ligands. Additional experiments were performed to investigate the extent of this precursor decomposition. This was done by exposing gold seed layers to **1** only (without co-reactant) at temperatures spanning the entire ALD temperature window (50 °C to 120 °C). The obtained growth per cycle for these experiments, together with the previously reported GPC for the ALD process, using 1 precursor bubbler and additional experiments using 2 precursor bubblers simultaneously during the ALD process are shown in Figure 4.13. The decomposition curve shows that there are two regions with a threshold substrate temperature at 100 °C. Below the threshold the decomposition is limited to the previously reported GPC value of 0,005 nm. Above a substrate temperature of 100 °C the decomposition component increases with increasing substrate temperature. At 120 °C the decomposition component becomes larger than the expected GPC of the ALD process with a large spread on the obtained GPC. The latter is most likely due to the position of the sample on the substrate holder indicating that at this point the supply of precursor starts to play a large role. To verify this behavior, additional experiments were performed using two precursor bubblers simultaneously during each precursor exposure, doubling the precursor exposure during the process. At 50 °C and 90 °C the GPC showed no increase with respect to the expected GPC of the ALD process when using a single precursor source. However, at 120 °C the GPC was doubled when doubling the precursor exposure. Indicating that at this temperature the decomposition is unsaturated and governed by the supply of precursor. This indicates that the previously reported upper limit of the ALD temperature window

needs to be lowered from 120 °C to 100 °C. Since no such decomposition is observed on adjacent SiO<sub>2</sub> witness substrates present in these experiments, the slow self-decomposition must be due to ligand instability on a gold surface.

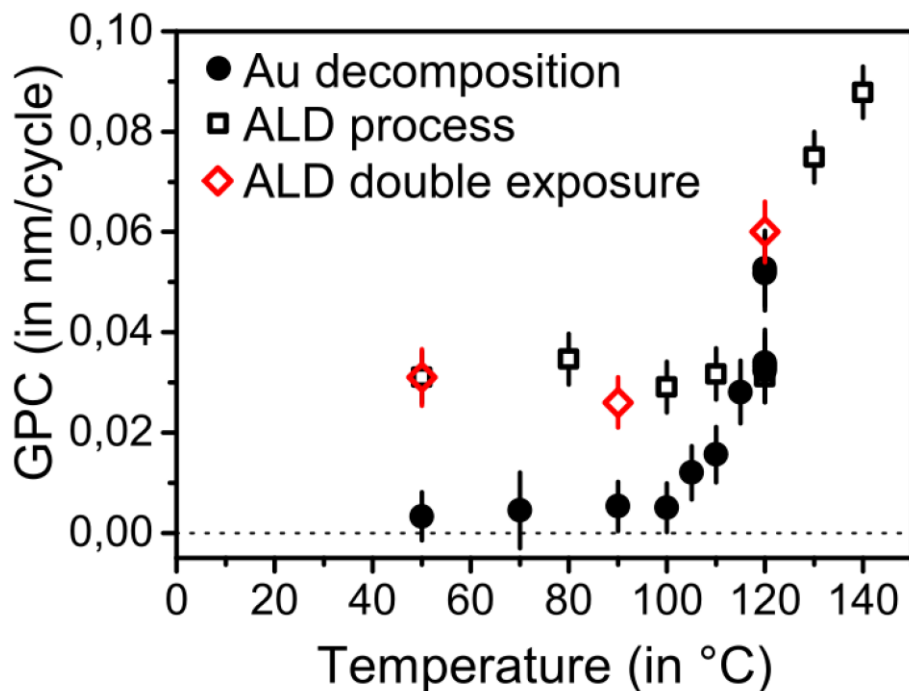


**Figure 4.13** Deposition using only compound **1** (black dots) as a function of substrate temperature and the reported growth rate for the gold PEALD process using 1 precursor bubbler (black squares) and 2 precursor bubblers simultaneously (red diamonds). All experiments were performed on gold seed layers, using 20 second precursor exposures.

To take a closer look at the ratio of CH<sub>3</sub> to PMe<sub>3</sub> ligands on the surface, we turned to *in vacuo* XPS and analyzed films on which 100 cycles of (**1** + H<sub>2</sub>\* ) plus one additional pulse of **1** had been dosed onto a gold seed layer. The obtained Au4f, P2p, and C1s peaks of these experiments are shown in Figure 4.14. These spectra were obtained immediately after the precursor exposure with a transfer time to the XPS chamber of ~ 1 min. The atomic concentrations and carbon to phosphorus ratios (C/P ratio) are shown in Table 4.4 (a) for these immediate-transfer samples along with samples that were forced to wait for 18 hours at deposition temperature (Table 4.4 b) before being analyzed by XPS.

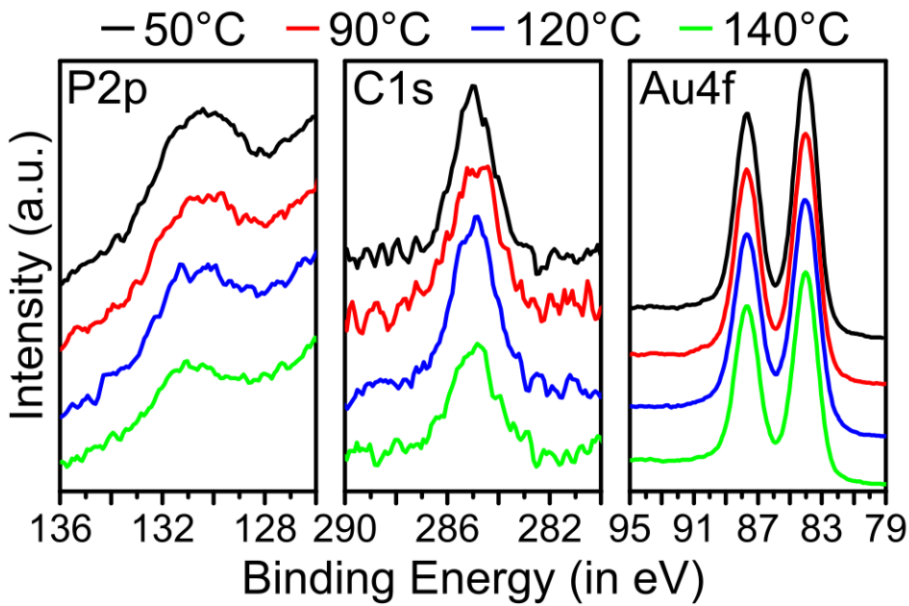


**Figure 4.14** P2p, C1s, Au4f peaks measured by XPS on a gold seed layer after performing a gold ALD process ending with a precursor exposure. Depositions were performed at a substrate temperature of 50 °C, 90 °C, 120 °C, and 140 °C. After ending the ALD process the samples were transferred as quickly as possible from the ALD chamber to the XPS analysis chamber without breaking vacuum.

For the samples that were transferred immediately, the atomic concentrations show that there is an increase in the atomic concentration of the Au4f peak with increasing temperature, which indicates that the amount of C and P on the surface is lower. The C/P ratios fluctuate between 2,2 and 3,5 which is in agreement with the presence of PMe<sub>3</sub> groups on the surface and only a minority component of methyl. A ratio of 6 would indicate that all of the precursor ligands remain on the surface, while lower values indicate the partial removal of the [Au]-CH<sub>3</sub> species from the surface. The amount of phosphorous present on the surface is the largest at 50 °C and at the other temperatures there is roughly a third less phosphorous present. The amount of phosphorous is directly linked to the amount of PMe<sub>3</sub> on the surface and this result suggests that PMe<sub>3</sub> is less stable on the gold surface with increasing substrate temperature, as can be expected from surface science literature, based on temperature programmed desorption (TPD) experiments of dimethylphenylphosphine from Au(111) surfaces.<sup>236</sup> The TPD experiments indicated the onset of desorption of chemisorbed dimethylphosphine at a substrate temperature of 60

°C with the peak of desorption above a substrate temperature of 170 °C. For the samples that were transferred after an 18 hour waiting period (Table 4.4 (b)), no significant change in the P2p atomic concentration is observed, but an increase in the carbon signal is present for all of them. The phosphorous signal indicates that at least a fraction of the PMe<sub>3</sub> ligands remains on the surface. Adventitious carbon contaminating the surface can explain the increase in the carbon signal.

**Table 4.4** Atomic concentrations of Au, C, P, and the C/P ratio determined by *in-vacuo* XPS after exposure of **1** on a gold seed layer at different temperatures. The samples were transferred from the ALD chamber to the XPS analysis chamber without breaking vacuum. a) Samples transferred immediately after the final precursor exposure. b) Samples transferred 18 hours after the final precursor exposure.

	Substrate Temperature (°C)	Au4f (at. %)	C1s (at. %)	P2p (at. %)	C/P ratio
a)	50	86.6	9.9	4.5	2.2
	90	87.7	9.4	3	3.1
	120	89.1	7.6	3.3	2.3
	140	90.8	6.8	2.4	2.8
b	50	84	12.1	3.9	3.1
	90	82.5	14.1	3.4	4.2
	120	85.6	11.7	2.7	4.3
	140	84.4	12.7	2.9	4.4

The *in-vacuo* XPS results indicate that only the PMe<sub>3</sub> ligand remains on the surface, while the *in-situ* IR measurements prove the existence of both PMe<sub>3</sub> and methyl species on the surface. It should be noted that the measurement time of both methods differs significantly. Each IR measurement is completed within 2 minutes after the precursor exposure, while each *in-vacuo* XPS experiment lasted for several hours. To bridge this gap, we performed several RAIRS measurements over the course of an hour after a precursor exposure. This was done at a substrate temperature of 90 °C and 120 °C. The obtained results can be seen in Figure 4.15. The normalized intensity of the main PMe<sub>3</sub> rocking mode (954 cm<sup>-1</sup>) is plotted as a function of time after precursor exposure in Figure 4.15 (a). The intensity decays over time for both temperatures and this decay occurs

faster at 120 °C than at 90 °C, suggesting that these groups are less stable at higher substrate temperatures.

Figure 4.15 (b) shows the 1250-900 cm<sup>-1</sup> region of the first two spectra that were obtained during these experiments at 90 °C and 120 °C. The first notable observation is that the initial spectrum obtained at 90 °C shows the [Au]-Me mode at 1100 cm<sup>-1</sup>, while the spectrum obtained at 120 °C does not, indicating that the [Au]-Me groups are less stable at higher substrate temperatures. The second spectrum obtained at 90 °C shows that the [Au]-Me vibration mode has decreased to the noise level, indicating that the methyl groups quickly desorb from the surface, which is in agreement with the observed in-vacuo XPS results.

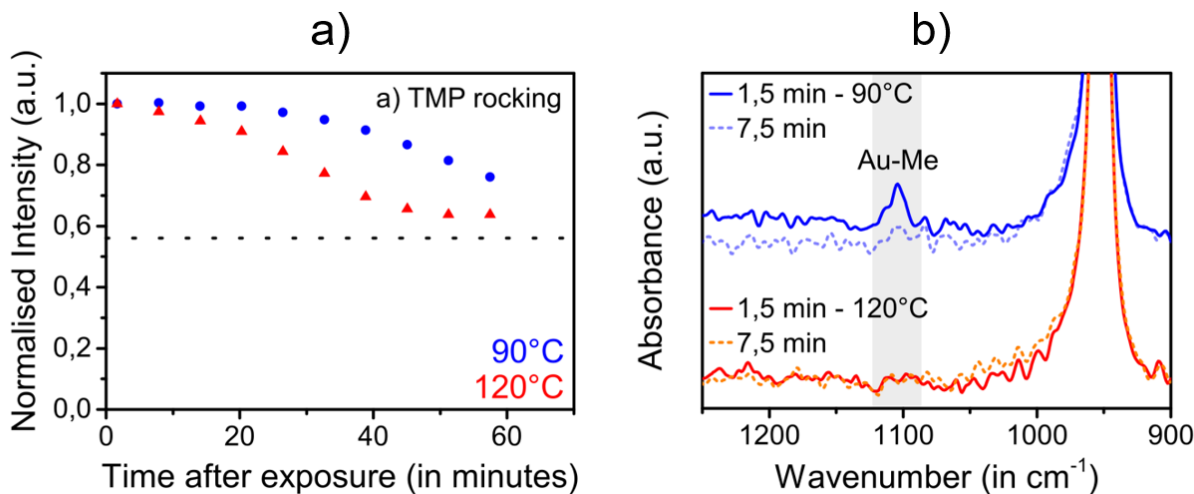


**Figure 4.15** RAIRS data for an exposure of **1** on a thick sputtered gold layer at a substrate temperature of 90 °C and 120 °C. a) Normalized intensity of the main PMe<sub>3</sub> rocking mode at 954 cm<sup>-1</sup> as a function of the elapsed time after a precursor exposure. The dotted line represents the normalized intensity at 120 °C after 2 hours and 30 minutes. b) fingerprint region, covering the δ as (CH<sub>3</sub>)-[Au] deformation mode (grey box, 1100 cm<sup>-1</sup>) and the main PMe<sub>3</sub> rocking mode. The shown spectra are recorded 30 seconds after the precursor exposure and 6 minutes and 30 seconds after the precursor exposure.

With the gathered data on the precursor decomposition and precursor ligand stability, it is possible to propose a temperature-dependent reaction scheme for the **1** + H<sub>2</sub>\* ALD process under steady state growth conditions (Figure 4.16). We first assume that the

starting point is a fresh gold surface without any contamination. The first step in the ALD process will be to expose this surface to the molecules of **1**, which will physisorb on the surface (Figure 4.16 (a)). After physisorption, the precursor molecules can undergo reactions with the surface and chemisorb. Based on how similar gold molecules behave in a liquid the most likely pathway for chemisorption on the gold surface is by breaking the Au-P bond (Figure 4.16 (b)).<sup>226,227</sup> Figure 4.16 (c) shows the desorption of methyl groups from the surface after the initial chemisorption, as evidenced by the QMS data. The C/P ratio obtained from the in-vacuo XPS data shows that the desorption of methyl groups occurs at all substrate temperatures. Based on the results from Paul and Bent this is expected for Au(111) planes at the used substrate temperatures, while on Au(100) planes methyl radical desorption should only occur above a substrate temperature of 100 °C.<sup>234</sup> The in-situ RAIRS experiments (Figure 4.15 (b)) indicate that at 90 °C some (but not all) methyl groups persist at least long enough for the H<sub>2</sub>\* dose, however we cannot observe them at all at 120 °C. Methyl desorption is likely the origin of the small observed single-source deposition (0.005 nm Au cycle<sup>-1</sup>). The increased desorption of Me above 90 °C correlates with literature evidence for Me desorption<sup>234</sup> and with our observed increase in single-source deposition using only **1** between 100 and 120 °C. For this reason we separated the mechanism into the three temperature regimes shown. Below 100 °C, Me desorption occurs slowly at all temperatures. Above 100 °C, Me desorption is activated on Au(100) and occurs more rapidly, causing an increase in single-source deposition of Au.

Jewell et al. reported that annealing one monolayer of adsorbed PMe<sub>3</sub> on a Au(111) surface to 77 °C results in a coverage of 88% of a monolayer.<sup>237</sup> Temperature programmed desorption experiments of dimethylphenylphosphine on Au(111) indicate an onset of desorption around 77 °C, although the maximum of the desorption peak is located above 177 °C.<sup>236</sup> In addition, it is expected that in the class of alkylphosphine molecules swapping the phenyl groups with a methyl group results in a stronger Au-P bond,<sup>238</sup> which would indicate a higher desorption temperature for PMe<sub>3</sub> compared to dimethylphenylphosphine, meaning that the PMe<sub>3</sub> groups remain stable for a longer period of time at substrate temperatures below 100 °C. This is also corroborated by the in-situ RAIRS experiments (Figure 4.15 (a)), showing that while at 90 °C the PMe<sub>3</sub> groups are

being removed from the surface they remain stable for a rather long time period. On the timescale of one ALD cycle for this process ( $\sim 1$  min), Even at 120 °C the PMe<sub>3</sub> desorption is rather slow on the timescale of the ALD experiment, but a large increase in CVD of gold is observed at this temperature. Therefore it must be that chemisorption of **1** onto a PMe<sub>3</sub>-covered Au surface becomes energetically favourable at 120 °C and this begins to break the self-limiting behavior of the system.

After a long period of time (Figure 4.16 (d)), desorption of all methyl groups is expected regardless of temperature, based on the C/P ratio of 3 determined from the XPS experiments. At this point, the surface will be covered by a varying amount of PMe<sub>3</sub> molecules which is dependent on the substrate temperature. The last step in the ALD process (Figure 4.16 (e)) is to expose the surface to H<sub>2</sub>\*<sup>\*</sup>, which removes the remaining PMe<sub>3</sub> species from the surface. The result is a clean gold surface because we found no direct evidence of atomic hydrogen or any other element on the gold surface. The H<sub>2</sub> radicals created by the plasma can remove the methyl groups of the PMe<sub>3</sub> group and during this process create methane. It is unclear how the phosphorous is removed from the surface, however, it is likely that it is removed in the form of phosphine species (PH<sub>x</sub>). After the plasma exposure the ALD cycle can start over by performing a precursor exposure.

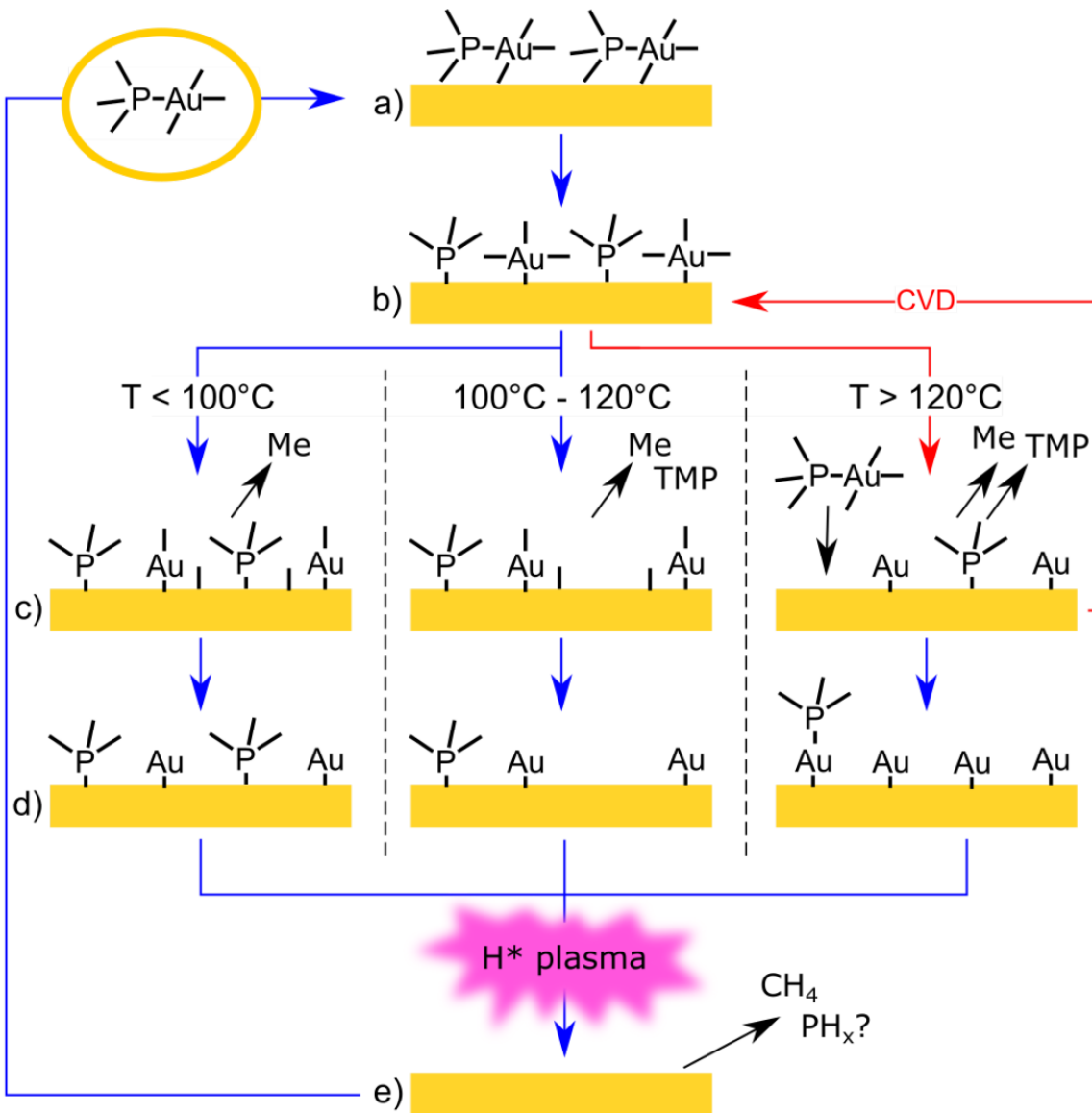


**Figure 4.16** Reaction scheme of the  $1 + \text{H}_2^*$  PEALD process in the three different temperature regimes (TMP =  $\text{PMe}_3$ ). a) Physisorption of the precursor onto a clean gold surface. b) Initial chemisorption to the gold surface. c) Desorption of Me and TMP species. d) Final surface state after removal of gas-phase species during purge step. e) removal of remaining surface species by  $\text{H}_2^*$ .

### 4.2.3 Comparison of PE-ALD Processes using $(PMe_3)_3AuMe_3$

Currently, two **1**-based gold ALD processes have been reported. We have presented results for the **1** +  $O_2^*$  +  $H_2O$  process and the  $H_2^*$  plasma process and at this point we will compare the two processes. It is noteworthy that applying the 3-step process with  $O_2^*$  and  $H_2O$  in the pump-type reactor did not result in the reproducible formation of metallic gold, but rather in the growth of an amorphous gold containing film. This was a very similar amorphous material to what was observed using only **1** and  $O_2^*$  originally on the Picosun R200.

By swapping the  $H_2O$  exposure in the three-step process with an  $H_2^*$  dose (**1** +  $O_2^*$  +  $H_2^*$ ) it was possible to deposit metallic gold films in the pump-type reactor at Ghent University. XRD patterns for the above-mentioned deposition processes are shown in Figure 4.17, together with a reference of a sample grown by the  $O_2^*$  +  $H_2O$  process in the Picosun R200 flow-type reactor at Carleton University. The patterns indicate that the only process that does not yield crystalline gold films is the (**1** +  $O_2^*$  +  $H_2O$ ) process performed in a pump-type reactor. The other films show diffraction peaks for Au(111) and Au(200) planes, proving their crystalline nature.

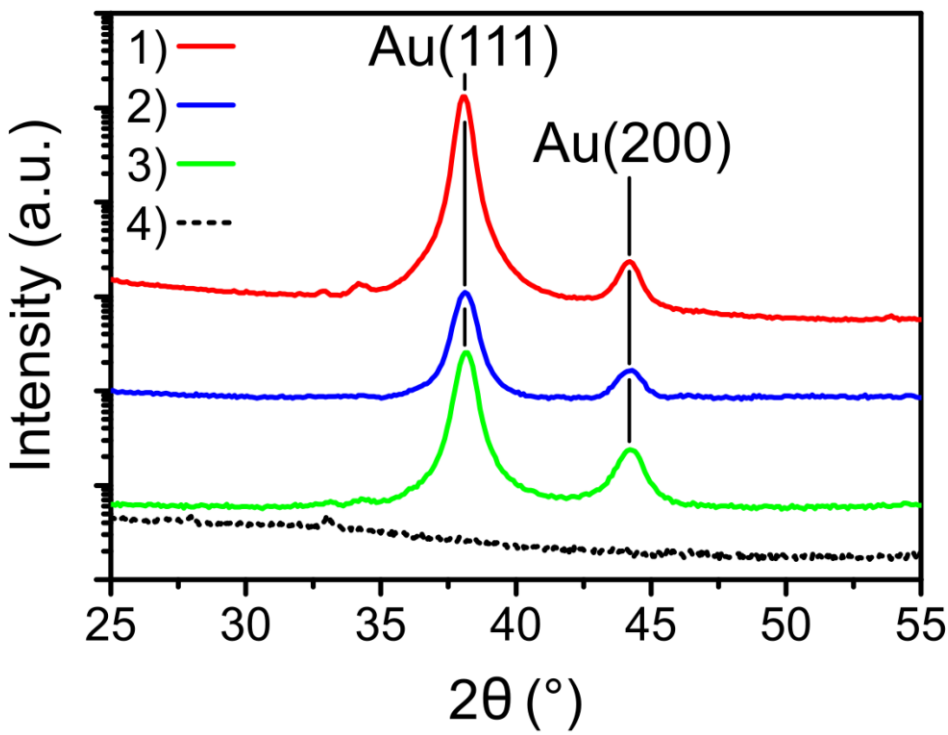


**Figure 4.17** XRD patterns of four ALD deposited gold films on silicon (native oxide), all depositions were performed at a substrate temperature of 120 °C. The Au(111) and Au(200) peaks are respectively marked at 38.3 ° and 44.5 °. 1) The **1 + H<sub>2</sub>\*** ALD process, performed in a pump-type reactor (equivalent to 21 nm of sputtered gold). 2) The **1 + O<sub>2</sub>\* + H<sub>2</sub>\*** process, performed in a pump-type reactor (equivalent to 6 nm of sputtered gold). 3) The **1 + O<sub>2</sub>\* + H<sub>2</sub>O** ALD process, performed in a flow-type reactor (equivalent to 9 nm of sputtered gold). 4) The **1 + O<sub>2</sub>\* + H<sub>2</sub>O** ALD process, performed in a pump-type reactor (equivalent to 10nm of sputtered gold). The diffractograms were offset for clarity of presentation.

We also compared XPS analysis between these samples, and analyzed the O 1s, C 1s, P 2p, and Au 4f peaks on the air-exposed surface as well as after 100 seconds of argon sputtering. These results are displayed in Figure 4.18. For all samples there is adventitious carbon present on the surface, but no carbon is present in the film itself. The Au4f peaks are not in a pure metallic state for the **1 + O<sub>2</sub>\* + H<sub>2</sub>O** ALD process, performed in a pump-type reactor, showing gold in both Au(0) ( $\text{Au } 4f_{7/2} = 84.1 \text{ eV}$ ) and Au(III) ( $\text{Au } 4f_{7/2} = 87.4 \text{ eV}$ ) oxidation states. After sputtering the Au 4f peaks are of a metallic nature, however it is most likely that the Au(III) species are reduced to Au(0) as a consequence

of the sputtering process and as such this cannot be taken as an indication that the underlying gold is in a metallic state, which would otherwise conflict with the observed XRD pattern of this film (Figure 4.17). The gold in the other three samples is in a metallic state as deposited and after sputtering, which agrees with the measured XRD patterns. On all samples we observe an O1s peak, which for the **1 + O<sub>2</sub>\*** + H<sub>2</sub>O flow-type ALD process and for the **1 + H<sub>2</sub>\*** ALD process has a binding energy around 532.9 eV, and most likely originates from the silicon oxide of the substrate. For these two samples, there is also no phosphorous present on the surface or after sputtering, showing that these films consist of pure gold. For the other two samples, we observe a clear signal for phosphorous both on the surface and after sputtering. The P 2p peaks have a binding energy between 133.5 eV and 134.6 eV, consistent with P-O and P=O bonds originating from phosphate groups.<sup>239,240</sup> These peaks are similar to what was observed in the preliminary **1 + O<sub>2</sub>\*** process which did not contain water in a flow-type reactor.

These results show that pure gold films can be deposited in a flow-type reactor using O<sub>2</sub>\* and H<sub>2</sub>O as co-reactants and in a pump-type reactor when using H<sub>2</sub>\*. The use of O<sub>2</sub>\* results in the formation of a gold containing phosphate layer which can be removed by using H<sub>2</sub>O in a flow-type reactor, but not in a pump-type reactor. Hydrating the phosphate layer by using H<sub>2</sub>O is most likely followed by dehydration in a pump-type reactor, instead of allowing removal from the surface. In the pump-type reactor environment, the amorphous gold-containing material deposited from **1 + O<sub>2</sub>\*** + H<sub>2</sub>O contains Au(0), Au(III), P(V) and O. When H<sub>2</sub>\* is used as the ternary reagent instead of H<sub>2</sub>O, the Au(III) can be reduced to Au(0), and these films do show crystalline Au diffractions. However, using H<sub>2</sub>\* is still not adequate to remove the P(V) and O impurities.

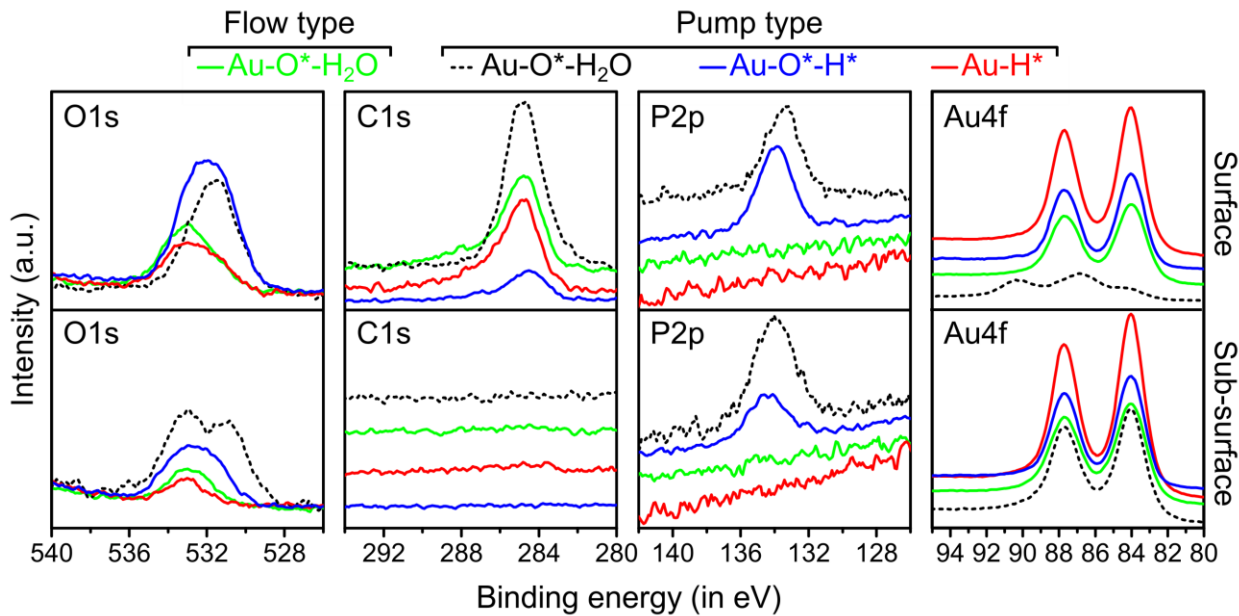


**Figure 4.18** XPS spectra of four gold films on silicon (native oxide) substrates for the air-exposed samples (top panels) and after removal of the top surface by argon sputtering (bottom panels). 1) The **1 + H<sub>2</sub>\*** ALD process, performed in a pump-type reactor (equivalent to 21 nm of sputtered gold). 2) The **1 + O<sub>2</sub>\* + H<sub>2</sub>** process, performed in a pump-type reactor (equivalent to 6 nm of sputtered gold). 3) The **1 + O<sub>2</sub>\* + H<sub>2</sub>O** ALD process, performed in a flow-type reactor (equivalent to 9 nm of sputtered gold). 4) The **1 + O<sub>2</sub>\* + H<sub>2</sub>O** process, performed in a pump-type reactor (equivalent to 10 nm of sputtered gold). The displayed spectra were offset for clarity of presentation.

## 4.3 Conclusions

Compound **1** has excellent precursor characteristics: it is an ambient-stable liquid at room temperature and has high volatility. The **1 + O<sub>2</sub>\* + H<sub>2</sub>O** process is robust, with a steady-state GPC of 0.05 nm, and allows Ångström-level control over the deposition of gold metal nanostructures. This process was the first Au ALD process discovered and is a vast improvement over typical chemical vapor deposition processes in terms of thickness control and conformality of deposition.

Growth of pure metallic gold films at the lowest reported temperature to date has been demonstrated with a PE-ALD process, using **1** as the precursor and H<sub>2</sub>\* as the reactant. The process exhibits self-limiting chemisorption of both the precursor and reactant half cycles on gold seed layers with a steady growth rate of  $0.030 \pm 0.002 \text{ nm cycle}^{-1}$ . A similar steady growth rate is obtained on bare SiO<sub>2</sub> surfaces, after a sufficient number of cycles. Initially, the growth rate is lower because of nucleation, leading to island-like growth and high film roughness, but percolating films are obtained when the films are sufficiently thick. A resistivity value of  $5.9 \pm 0.3 \mu\Omega \text{ cm}$  is obtained for the thickest films, close to the bulk resistivity value of gold ( $2.44 \mu\Omega \text{ cm}$ ). The deposited films are pure gold with <1 at. % carbon and oxygen impurities in the film.

The reaction mechanism and ligand stability of the **1** + H<sub>2</sub>\* plasma process in the steady growth regime has been investigated in a pump-type reactor. During the main reaction mechanism, the PMe<sub>3</sub> and CH<sub>3</sub> ligands of the precursor remain on the gold surface after chemisorption of **1**, causing self-saturating behaviour during the precursor exposure. The ligands are removed by the H<sub>2</sub>\* exposure, resulting in the formation of methane and possibly phosphine groups.

A minor fraction of precursor decomposition occurs due to the desorption of the ligands from the surface, as this effect creates additional adsorption sites for the next precursor exposure in a decomposition experiment. For substrate temperatures above 100 °C the amount of precursor decomposition increases with substrate temperature and at 120 °C the decomposition is unsaturated and becomes larger than the GPC of the ALD process. Indicating that at this temperature the deposition occurs through CVD and there is no self-limiting behavior of the surface during the precursor exposure. At all substrate temperatures the CH<sub>3</sub> groups desorb from the surface over time, occurring faster at higher substrate temperatures. The desorption of the PMe<sub>3</sub> groups from the surface, which increases with temperature, seems to be the main factor that determines the precursor decomposition behavior. This also suggests that the previously reported upper limit for the temperature window needs to be lowered from 120 °C to 100 °C.

Finally, we used O<sub>2</sub>\* plasma and H<sub>2</sub>O as co-reactants in a pump-type ALD system and compared the obtained film to a metallic and chemically pure gold film that was deposited

in a commercial flow-type reactor, using the  $\mathbf{1} + \text{O}_2^* + \text{H}_2\text{O}$  gold ALD process. Instead of a metallic gold film we obtained amorphous gold-containing phosphate films, as verified by XPS and XRD measurements. Exchanging the  $\text{H}_2\text{O}$  exposure step with  $\text{H}_2^*$  resulted in the formation of metallic gold films, showing that a stronger reducing co-reactant is required in pump-type systems. However, the use of a  $\text{H}_2^*$  plasma in the process was not sufficient to completely remove the phosphate layer that is formed during the  $\text{O}_2^*$  plasma step. This indicates that, once formed, it is difficult to remove the phosphate layer in a pump-type ALD system.

## 4.4 Experimental Details

Compound **1** was synthesized as described in the supporting information, and its deuterated analogue,  $(\text{PMe}_3)\text{Au}(\text{CD}_3)_3$  (**d<sub>9</sub>-1**) precursor ( $\geq 95\%$  purity, and  $> 99\%$  deuteration) was synthesized as described by Shaw and Tobias.<sup>212</sup> The purity of the precursors was verified by NMR measurements (see Figure S-4.25 and S-4.26). Thin films deposited in section 4.1.3 were deposited using a Picosun R200 ALD reactor with a Picoplasma remote plasma source system (plasma RF power of 2800 W). Oxygen gas ( $\geq 99.999\%$ ) was mixed with Argon gas ( $\geq 99.999\%$ ) at flow rates of 110 and 185 sccm respectively during plasma ignition. A charged screen between the plasma source and the substrate blocked charged species from participating in surface chemistry. The reactor pressure and temperature were 5 mbar and 120 °C respectively. Silicon (100) with native oxide and soda lime microscope slides were used as substrates and were pretreated with 10 plasma pulses (14 s  $\text{O}_2^*$  | 10 s  $\text{N}_2$ ) before beginning ALD experiments. Milli-Q deionized water was used in the water bubbler and was cooled to 19 °C using a Pelletier cooler. A fresh sample of **1** was loaded into a cleaned glass vial and then inserted into the Picosolid booster crucible before each experiment. The headspace of the bubbler was purged of air and replaced with nitrogen before heating to 85 °C. In a typical experiment, 1000 cycles with a duration of 4 s volatilized approximately 550 mg of **1**, and 1250 10 s cycles used between 1 and 1.2 g of **1**. The typical pulse sequence was 4 s Au | 14 s  $\text{O}_2^*$  | 0.1 s water each separated by a 10 s nitrogen gas ( $\geq 99.999\%$ ) purge. The

purge times were chosen to be reliable, rather than optimal. The flow rates of N<sub>2</sub> carrier gas for the gold precursor and water were (120 sccm) and (100 sccm) respectively. Leftover precursor from each experiment was stored in a separate vial, and the booster vial wiped clean with ethanol. Accumulated spent precursor was repurified by vacuum distillation as described in the synthetic procedure (included as Supporting Information) and used without noticeable loss of film quality.

ALD experiments performed in section 4.2.3 were carried out in a home-built pump-type ALD reactor with a base pressure of  $2 \times 10^{-6}$  mbar.<sup>241</sup> Computer-controlled pneumatic valves and manually adjustable needle valves were used to control the dose of the precursor vapor and reactant gas. The precursor liquids were kept in a glass container which was heated to 50 °C during deposition processes, and the delivery line was heated to 55 °C. Argon was used as the carrier gas during all deposition processes. The flow of the carrier gas was adjusted to reach  $6 \times 10^{-3}$  mbar in the chamber when pulsing. The precursor exposure during the ALD processes were carried out by injecting **1** after closing the gate valve between the turbomolecular pump and the reactor chamber. By varying the injection time, the pressure during the pulse varied between  $6 \times 10^{-3}$  and 5 mbar. After injection, the precursor vapor was kept in the ALD chamber for an additional 5 s before evacuating the chamber. H<sub>2</sub>\* (20% H<sub>2</sub> in argon) was used as the reactant for all deposition processes. Previously, we reported that using H<sub>2</sub> gas or H<sub>2</sub>\* plasma as the reactant in combination with **1** in the Picosun R200 flow-type reactor does not lead to gold deposition. However, on that system a low concentration of H<sub>2</sub>\* (5% H<sub>2</sub> in Ar, with additional Ar carrier gas) in comparison with the 20 % that was used in this work, possibly explaining this different result. H<sub>2</sub> gas was introduced through the plasma column mounted on top of the chamber, and the flow of H<sub>2</sub> gas was limited by a needle valve to obtain a chamber pressure of  $6 \times 10^{-3}$  mbar during all deposition processes. A 13.56 MHz radio frequency generator (Advanced Energy, model CESAR 136) and a matching network were used to generate an inductively coupled plasma in the plasma column. For all the experiments, a plasma power of 200 W was used, and the impedance matching parameters were adjusted to minimize the reflected power. An H<sub>2</sub>\* exposure of 10 s was used before each deposition to clean the substrates. The used substrates were pieces of p-type silicon (100) with native or thermal silicon oxide or 10 nm sputtered gold films on

p-type silicon (100). The samples were mounted directly on a heated copper block. The temperature of the copper block was adjusted with a proportional-integral-derivative (PID) controller. The chamber walls were heated to 100 °C for all experiments, except for the experiments to determine the temperature window, for these experiments, the chamber walls were heated to 50 °C. This was necessary to allow the copper block to be heated at temperatures below 80 °C because it was not possible to use active cooling of the copper block.

Several *ex-situ* measurement techniques were used to determine the physical properties of the deposited Au films. X-ray diffraction (XRD) patterns were acquired to determine the crystallinity of the deposited films. XRD measurements were done on a diffractometer (Bruker D8) equipped with a linear detector (Vantec) and a copper X-ray source (Cu K $\alpha$  radiation). Thickness determination via X-ray reflectivity (XRR) measurements was done on a diffractometer (Bruker D8) equipped with a copper X-ray source (Cu K $\alpha$  radiation) and a scintillator point detector. However, because the gold ALD films were generally too rough for accurate thickness determination with XRR, X-ray fluorescence (XRF) measurements were used to determine an equivalent film thickness based on a calibration curve which was made using sputtered gold films. The obtained standard deviation of the data points from the obtained calibration line was multiplied by 3 and used as an estimated error for each XRF measurement. The XRF measurements were performed using a Mo X-ray source and an XFlash 5010 silicon drift detector placed at an angle of 45° and 52° with the sample surface, respectively. An integration time of 200 s was used to acquire the fluorescence spectra. X-ray photoelectron spectroscopy (XPS) was used to determine the chemical composition and binding energy of the deposited films. The XPS measurements were carried out on a Thermo Scientific Theta Probe XPS instrument. The X-rays were generated using a monochromatic Al source (Al K $\alpha$ ). To etch the surface of the deposited films, an Ar $^+$  ion gun was used at an acceleration voltage of 3 keV and a current of 2  $\mu$ A. An FEI Quanta 200F instrument was used to perform scanning electron microscopy (SEM) using secondary electrons and energy-dispersive X-ray spectroscopy (EDX) on the deposited films. Four-point probe measurements were performed to determine the resistivity of the deposited gold films. Atomic force microscopy

(AFM) measurements were performed on a Bruker Dimension Edge system to determine the surface roughness of the films. AFM was operated in tapping mode in air.

To study the ALD reaction mechanism, in-situ infrared spectroscopy, in-vacuo X-ray photoelectron spectroscopy (XPS), mass spectrometry, and optical emission spectroscopy are used. The infrared measurements are carried out with a Vertex 70V from Bruker and a medium band mercury cadmium telluride (MCT) detector cooled with liquid nitrogen. The infrared measurements can be performed in two different geometries, either in reflection or in transmission. For the Reflection Absorption Infra-Red Spectroscopy mode (RAIRS), a thick gold seed layer of 60nm is used to avoid nucleation effects and to avoid interaction between the IR beam and the underlying silicon substrate.<sup>211</sup> In-vacuo XPS measurements were performed with a Thermo Scientific Theta Probe XPS instrument on an ALD-XPS cluster.<sup>242</sup> Using this cluster it is possible to perform through vacuum transfer of samples from the ALD chamber ( $10^{-7}$  mbar) to the XPS analysis chamber ( $10^{-10}$  mbar) in less than 60 seconds, which is sufficiently fast to avoid carbon contamination on the used samples. In-situ mass spectrometry experiments are carried out using a Hiden HPR-30 mass spectrometer, 70 eV electron impact ionisation and a quadrupole mass filter combined with a Faraday detector. The in-situ optical emission spectra are recorded during the  $H_2^*$  exposure. An Ocean Optics QE Pro spectrometer is used and is coupled to the plasma column with an optical fiber. For each spectrum an integration time of 10ms is used.

## 4.5 Supporting Information

### *Precursor Synthesis*

All manipulations were performed with rigorous exclusion of air using an Mbraun Labmaster 130 glovebox, Schlenk techniques, and N<sub>2</sub> ( $\geq 99.998$ ) gas. NMR analysis was performed using a 300 MHz Bruker Avance spectrometer. HAuCl<sub>4</sub> x H<sub>2</sub>O (49.9 weight % Au) was purchased from Strem Chemicals and used as received. Trimethylphosphine was also purchased from Strem Chemicals as 5 g in an ampoule and was diluted to 1.31

M solution in toluene and then stored in an N<sub>2</sub>-atmosphere glovebox in a teflon screwcap bottle. MeLi (1.6 M in diethyl ether) was purchased from Sigma-Aldrich as 4 x 25 mL bottles packaged under nitrogen in SureSeal septa and used as received. Anhydrous dichloromethane, tetrahydrothiophene, and iodomethane were purchased from Sigma-Aldrich and was used as received. Diethyl ether was purified using an Mbraun Solvent Purification System.

**Tetrahydrothiophenegold(I) chloride:** HAuCl<sub>4</sub> x H<sub>2</sub>O (49.9 weight % Au, 20.45 mmol) was dissolved in 120 mL of 5:1 EtOH : H<sub>2</sub>O in a 400 mL beaker. 4.2 mL (47.64 mmol) of tetrahydrothiophene (THT) was added dropwise causing the precipitation of a flocculent white solid. This was stirred for 1 hr and then filtered, washed sequentially with 3 x 20 mL of ethanol, 3 x 20 mL of diethyl ether, and then dried under high vacuum for 12 hours. The yield was 90 – 98 %, based on multiple trials (typical mass ≈ 6.5 g).

**Trimethylphosphinogold(I) chloride:** In a glove box, dry tetrahydrothiophenegold(I) chloride (6.55 g, 20.4 mmol) was dissolved in a minimum of dichloromethane in a 250 mL Schlenk flask. Dilute PMe<sub>3</sub> (15.5 mL, 1.31 M in toluene, 20.4 mmol) was added dropwise, and the reaction was stirred for 1 hour. In a fume hood, this solution was filtered through a medium frit, washing with dichloromethane to pass all of the product. The resulting solution was left in a fume hood overnight to evaporate, resulting in the formation of a bright white crystalline solid. Yield = 6.20 g, 99 %. <sup>1</sup>H-NMR (300 MHz, CDCl<sub>3</sub>): δ 1.62 (d, (PMe<sub>3</sub>)), <sup>2</sup>J<sub>H-P</sub> = 11.4 Hz.

**Trimethylphosphinotrimethylgold(III):** 5.533 g (18 mmol) of (PMe<sub>3</sub>)AuCl was placed in a 500 mL Schlenk flask along with a stir bar and was then dried under high vacuum for 2 hours. Meanwhile, a 100 mL dropping funnel was flame dried under high vacuum, then cooled to room temperature under vacuum. Both Schlenk flask and dropping funnel were then backfilled with N<sub>2</sub>. The (PMe<sub>3</sub>)AuCl was suspended in 300 mL of dry Et<sub>2</sub>O, and the dropping funnel was then attached under a stream of N<sub>2</sub> from both flask and funnel. The top of the dropping funnel was then fitted with a dry rubber septum, flowing nitrogen from the Schlenk arm of the 500 mL flask. With the apparatus assembled, the suspension was cooled to -78 °C in a dry ice / isopropanol bath.

One bottle of MeLi (25 mL, 40 mmol, 1.6 M in Et<sub>2</sub>O) was transferred to the dropping funnel via cannula using a slight vacuum assist from the Schlenk arm. The Schlenk arm was only slightly cracked to vacuum, and then closed again. This was repeated until all the MeLi has been transferred. Care was taken not to keep the system under active vacuum since this was found to cause MeLi to precipitate in the dropping funnel. An anti-backflow bubbler was used on the nitrogen line to ensure that no air could enter the system during the vacuum-assist. Once transferred, the cannula was removed, and MeLi solution was added very slowly drop-wise at a rate of 1 drop every 6-8 seconds. A very slow addition was key to a high yield since the intermediate formed was very thermally unstable. A total addition time of 50-60 min was ideal. Once all the MeLi was added, the funnel was rinsed with 20 mL of dry Et<sub>2</sub>O, which was then added dropwise to the stirring solution. By this point, the suspension often appeared yellow to green in colour. This suspension was stirred for 2 hours after completion of MeLi addition at -78 °C.

Mel (1.91 mL, 30.6 mmol) was then added very slowly dropwise over 10 min, and the reaction was stirred for a further 2 hours at -78 °C. The colour of the suspension usually returned to white at this point, but yellow or grey was also observed. The reaction was allowed to warm to room temperature over 1 hour and was then cooled in an ice bath. Then, 40 mL of distilled water was added to the funnel, and this was then added dropwise to the stirring suspension at an initial rate of one drop every 10 seconds. Colour change or consistency change of the reaction warranted stopping addition and allowing for the reaction to subside before continuing again. When addition was done too quickly, the flask would turn dark purple. If done correctly, a slight purple to clear ethereal solution formed above an aqueous solution, generally about 30 minutes of drop-wise addition. Gradual darkening of the solution was normal.

The ethereal layer was separated using a separatory funnel without shaking and dried over excess MgSO<sub>4</sub> which served as both a drying agent and a nanoparticle sequestering agent. The solution was filtered and dried on a rotary evaporator yielding a colourless liquid. If this liquid was contaminated by (PMe<sub>3</sub>)AuMe, then an additional purification step was required before proceeding. (PMe<sub>3</sub>)AuMe: <sup>1</sup>H-NMR (300 MHz, CDCl<sub>3</sub>): δ 1.43 (d, 9H, (PMe<sub>3</sub>), <sup>2</sup>J<sub>H-P</sub> = 8.8 Hz), δ 0.33 (d, 3H, (Au(CH<sub>3</sub>)), <sup>3</sup>J<sub>H-P</sub> = 8.4 Hz).

**Purification Step:** If  $(\text{PMe}_3)\text{AuCH}_3$  was present in the product mixture as observed by NMR, the mixture was then dissolved in 3 volume equivalents of neat iodomethane and stirred in a sealed flask for 6 hours. The iodomethane was then evaporated, leaving a mixture of the product,  $(\text{PMe}_3)\text{AuMe}_3$ , and  $(\text{PMe}_3)\text{Aul}$ , the latter of which is non-volatile under our subsequent distillation conditions.

This liquid (or purified / recycled material) was purified by vacuum distillation ( $80\text{ }^\circ\text{C}$ , 100 mTorr) using a cold water condenser and an ice-cooled receiving flask. The product was dislodged from the condenser periodically by gentle heating with a heat gun or Bunsen burner until it liquified and flowed again into the receiving flask. Yield = 5.30 g, (93 %). m.p. =  $22\text{ }^\circ\text{C}$ .

$^1\text{H-NMR}$  (300 MHz,  $\text{CDCl}_3$ ):  $\delta$  1.49 (d, 9H,  $(\text{P}(\text{CH}_3)_3)$ ,  $^2J_{\text{H-P}} = 9.6\text{ Hz}$ ),  $\delta$  0.81 (d, 3H,  $(\text{Au}(\text{CH}_3)_2(\text{CH}_3))$ ,  $^3J_{\text{H-P}}$  (trans) = 9.6 Hz),  $\delta$  0.09 (d, 6H,  $(\text{Au}(\text{CH}_3)_2(\text{CH}_3))$ ,  $^3J_{\text{H-P}}$  (cis) = 7.6 Hz).  $^{13}\text{C}\{\text{H}\}$ -NMR (75 MHz,  $\text{CDCl}_3$ ):  $\delta$  12.02 (d,  $\text{P}(\text{CH}_3)_3$ ,  $^1J_{\text{C-P}} = 28.9\text{ Hz}$ ),  $\delta$  10.87 (d,  $(\text{Au}(\text{CH}_3)_2(\text{CH}_3))$ ,  $^2J_{\text{C-P}}$  (trans) = 133.0 Hz),  $\delta$  6.46 (d,  $(\text{Au}(\text{CH}_3)_2(\text{CH}_3))$ ,  $^2J_{\text{C-P}}$  (cis) = 28.9 Hz).  $^{31}\text{P}\{\text{H}\}$ -NMR (121 MHz,  $\text{CDCl}_3$ ):  $\delta$  -9.75 ( $\text{P}(\text{CH}_3)$ ).

**Thermogravimetric (TG) Characterization Experimental:** In a typical experiment, ~10 mg of 1 was loaded in a platinum pan which was hung on the microbalance arm of a TA Instruments Q500 TGA, which is housed in an inert atmosphere MBraun glovebox. All experiments were purged by nitrogen gas. In the ramp experiment (Supplemental Figure 1a), a ramp rate of  $10\text{ }^\circ\text{C min}^{-1}$  was employed from room temperature to  $500\text{ }^\circ\text{C}$ . For the isothermal experiment (Supplemental Figure S-4.19), the temperature was ramped automatically to a set-point of  $65\text{ }^\circ\text{C}$  and held at this temperature for 175 minutes.

**Vapor Pressure Determination Experimental:** To calculate a Langmuir vapor pressure curve for 1, ~50 mg of 1 was loaded in a platinum pan which was hung on the microbalance arm of a TA Instruments Q500 TGA, which is housed in an inert atmosphere MBraun glovebox. A temperature program was run such that the temperature was increased by  $10\text{ }^\circ\text{C}$  and then held isothermally for 10 minutes. This was repeated from room temperature to  $400\text{ }^\circ\text{C}$ . The slope of the linear weight loss per unit time at each isothermal step was calculated and expressed with respect to the area of the pan. This was graphed on a logarithmic scale against  $1/\text{temperature}$  to extract a relationship for

mass delivery by temperature (Figure S-4.20). A known method 1 was used to calculate the Langmuir expression for vapor pressure.

**Thin Film Characterization Experimental:** Typically, the gold films were deposited using 100 cycles using 4 s pulses of 1, 14 s pulses of O<sub>2</sub>\*<sup>+</sup>, and 0.1 s pulses of water with 10 s nitrogen gases purges between each step. These films were imaged using a Tescan Vega-II XMU Scanning Electron Microscope with 20 keV potential (Figure S-4.21). The films appeared well connected and uniform. Attempts at characterizing the resistivity were unsuccessful due to poor adhesion of the gold metal film on glass and silicon/SiO<sub>2</sub> substrates. XPS spectra were collected in the analysis chamber of a Specs/RHK multi-technique ultrahigh vacuum system using a Phoibos 100 SCD power supply, hemispherical analyzer, and detector. Whenever possible, the sample being analyzed was electrically grounded. An XR-50 X-ray source containing an Al anode (400 W) was used in this study (14.26 keV Al K $\alpha$  source), and analyses were performed within a base pressure range of  $7 \times 10^{-10}$  to  $1 \times 10^{-9}$  Torr. Survey (Figure S-4.22) and high-resolution scans of the as-deposited gold films were collected using SpecsLab2 software, and post-processed and deconvoluted using CasaXPS. High-resolution spectra were fitted to a Shirley background and fitted using the appropriate Scofield- based factors for photoelectron cross-section. The film appears to have a nucleation delay of 96 cycles according to the growth per cycle fit (Figure S-4.23), and this is presently under scrutiny in our lab.

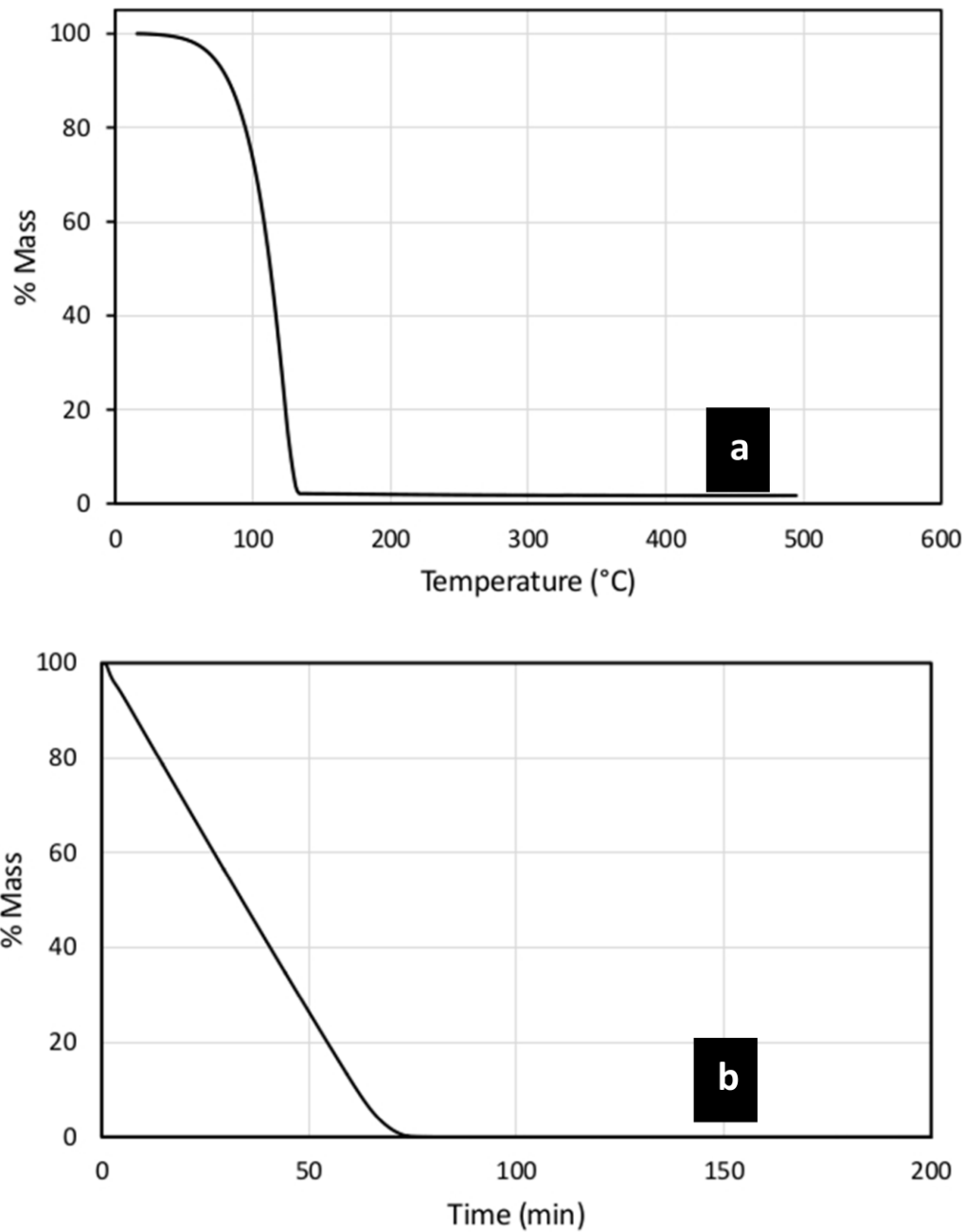


**Figure S-4.19** The thermogravimetric analysis (TGA) traces for **1**. a) TGA temperature ramp experiment, ramp rate of  $10\text{ }^{\circ}\text{C min}^{-1}$ , mass loading = 8.136 mg; b) Isothermal TGA experiment, isothermal temperature =  $65\text{ }^{\circ}\text{C}$ , mass loading = 10.051 mg.

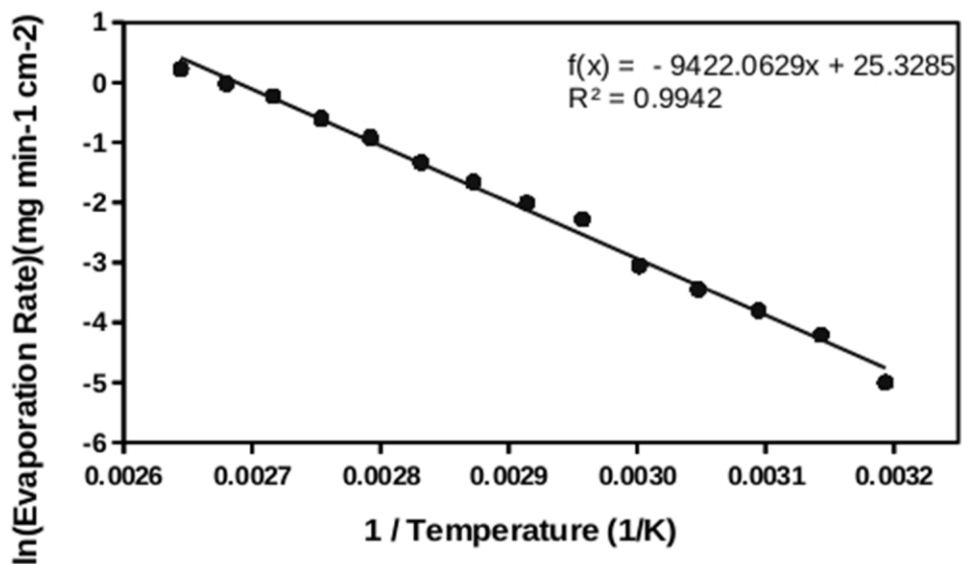


**Figure S-4.20** The evaporation rate for **1**. The inset is the fitted linear regression and coefficient of determination for the fit.

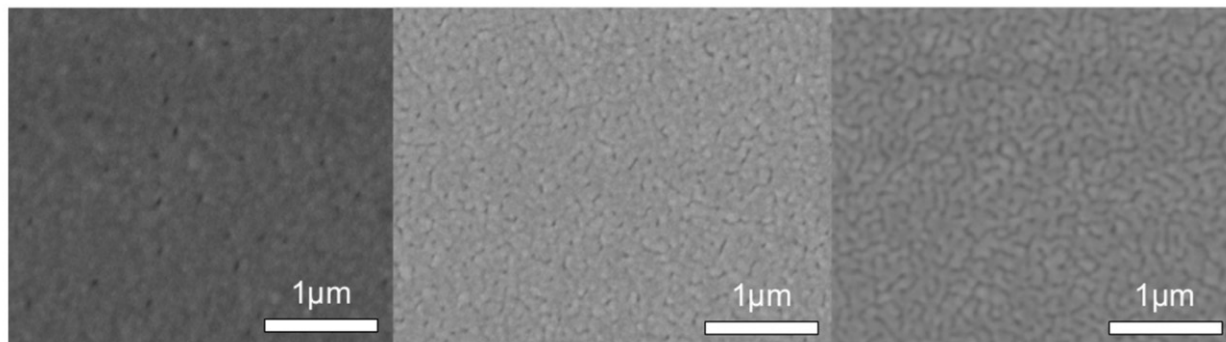


**Figure S-4.21** Scanning electron microscopy images of gold metal films deposited by **1**. Each of these independent depositions were comprised of 1000 atomic layer deposition cycles using 4s pulses of **1**, 14 s pulses of O<sub>2</sub><sup>\*</sup>, and 0.1 s pulses of water with 10 s nitrogen gases purges between each step.

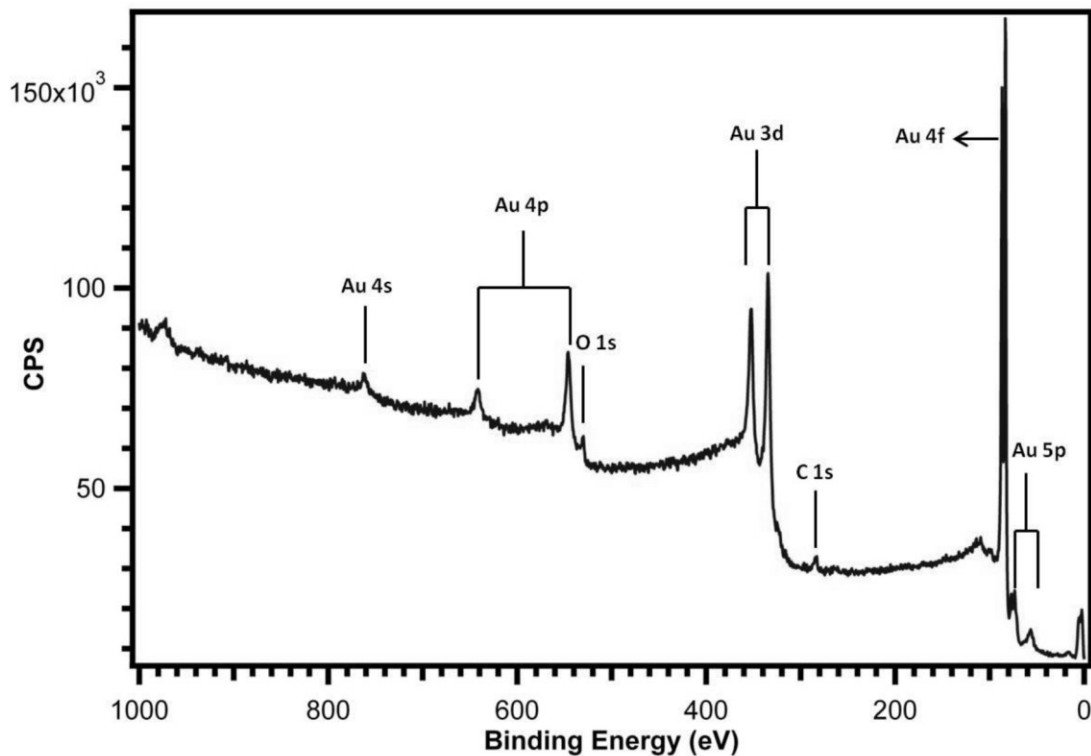


**Figure S-4.22** An XPS survey spectrum of a gold film deposited on a Si(100) substrate using 4 s pulses of **1**, 14 s pulses of  $O_2^*$ , and 0.1 s pulses of water with 10 s nitrogen gases purges between each step.

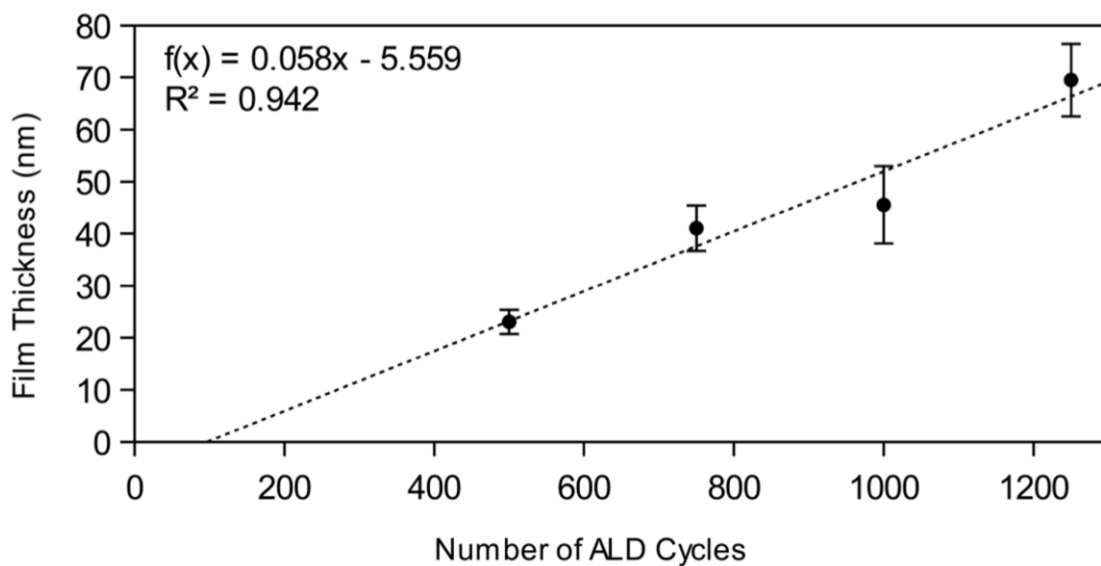


**Figure S-4.23** A graph of film thickness as a function of cycle number for the **1 +  $O_2^*$  + H<sub>2</sub>O** ALD process.

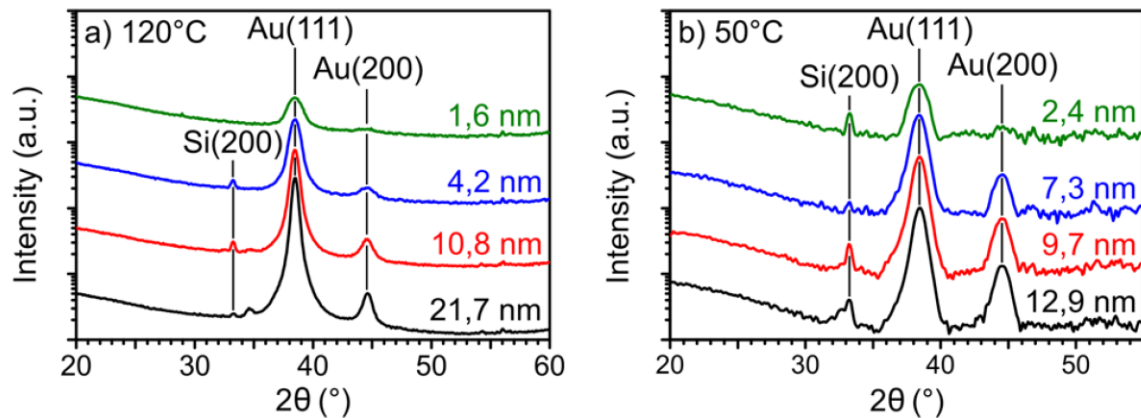


**Figure S-4.24** XRD patterns for deposited gold films with an equivalent thickness between 1.6 and 21.7 nm. For all thicknesses, the Au(111) and Au(200) peaks are visible at  $38.5^{\circ}$  and  $44.6^{\circ}$ , respectively. The patterns were given an offset for clarity. (a) Films deposited at  $120^{\circ}\text{C}$  and (b) films deposited at  $50^{\circ}\text{C}$ .

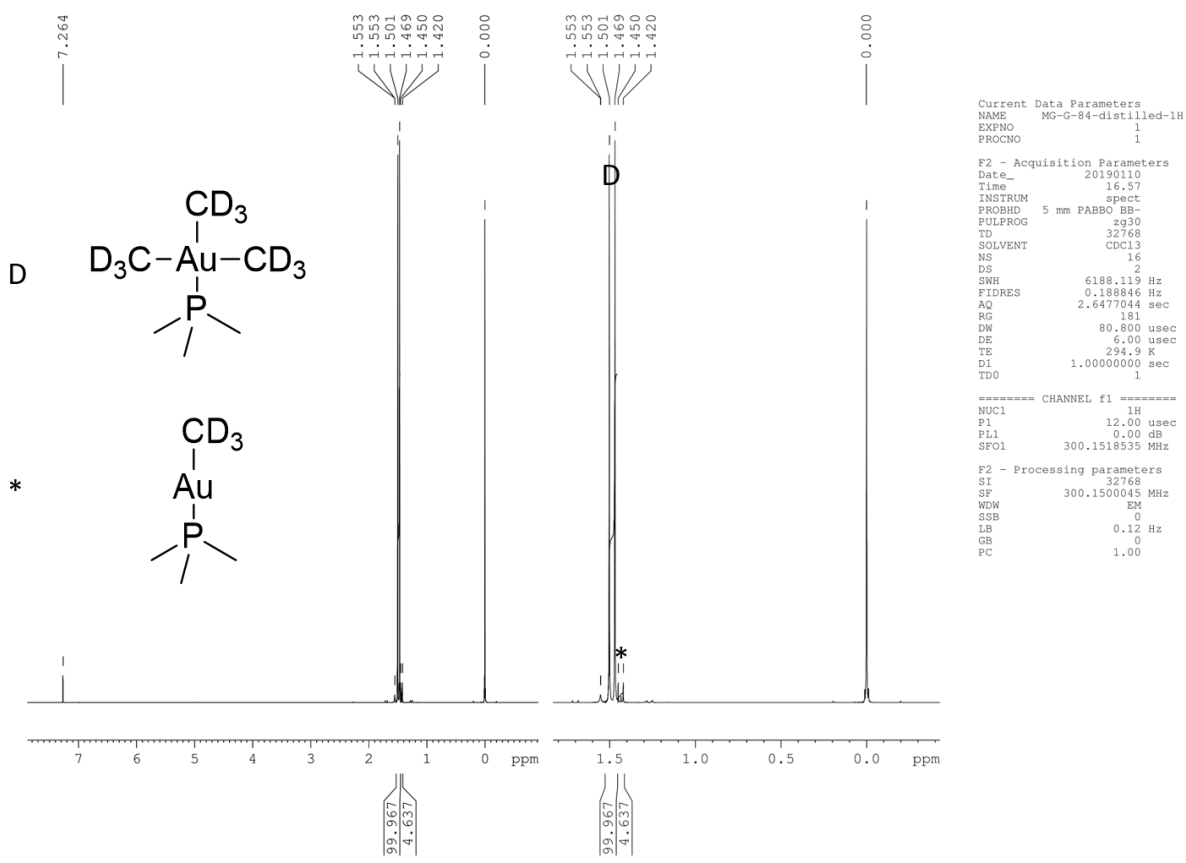


**Figure S-4.25** <sup>1</sup>H-NMR spectrum of **d<sub>9</sub>-1** in CDCl<sub>3</sub>. “D” indicates the doublet originating from the PMe<sub>3</sub> group of **d<sub>9</sub>-1**, \* indicates a minor impurity of (PMe<sub>3</sub>)AuCD<sub>3</sub>.

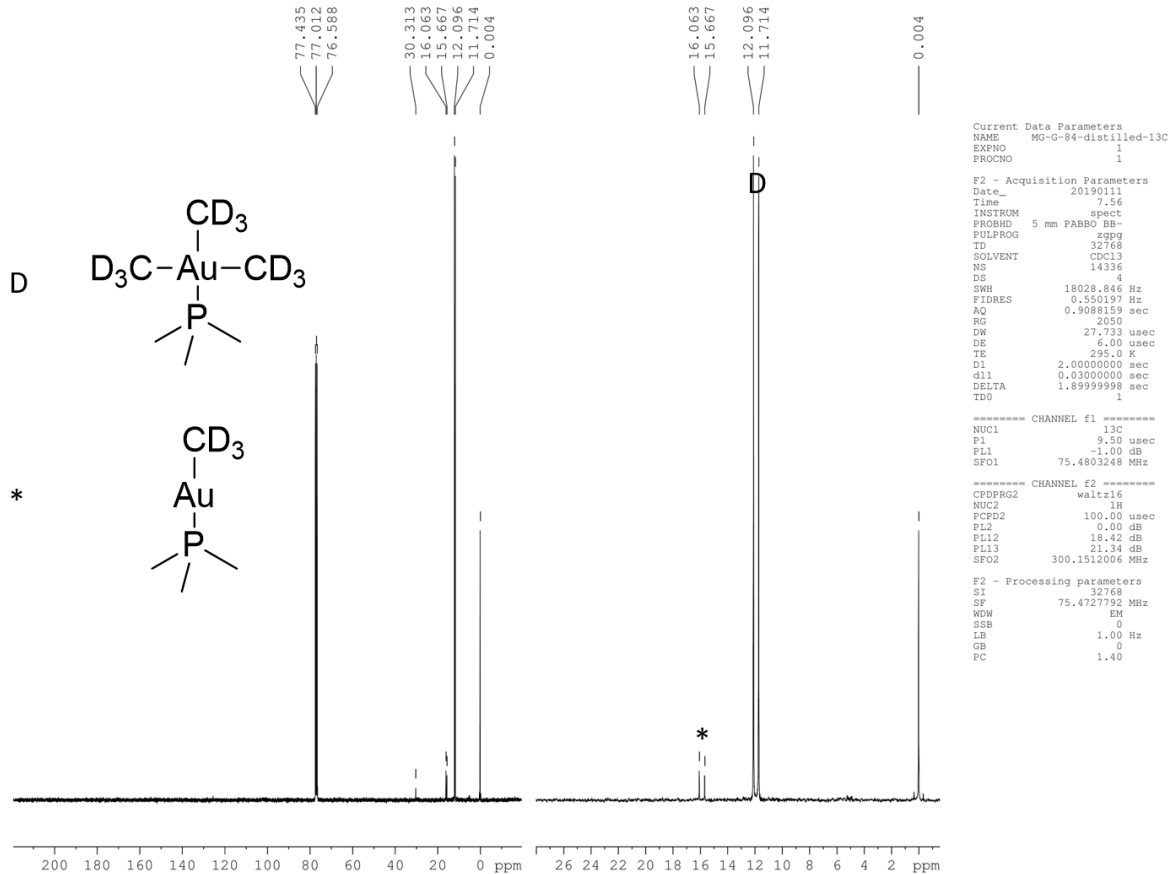


**Figure S-4.26**  $^{13}\text{C}$ -NMR spectrum of **d<sub>9</sub>-1** in  $\text{CDCl}_3$ . “D” indicates the doublet originating from the  $\text{PMe}_3$  group of **d<sub>9</sub>-1**, \* indicates a minor impurity of  $(\text{PMe}_3)\text{AuCD}_3$ .



# **Chapter 5 Controlling thermal stability and volatility of organogold(I) compounds for vapor deposition with complementary ligand design**

Adapted with permission from *European Journal of Inorganic Chemistry*, **2019**, 46, 4927-38, DOI: [10.1002/ejic.201901087](https://doi.org/10.1002/ejic.201901087). Copyright 2019 John Wiley and Sons.

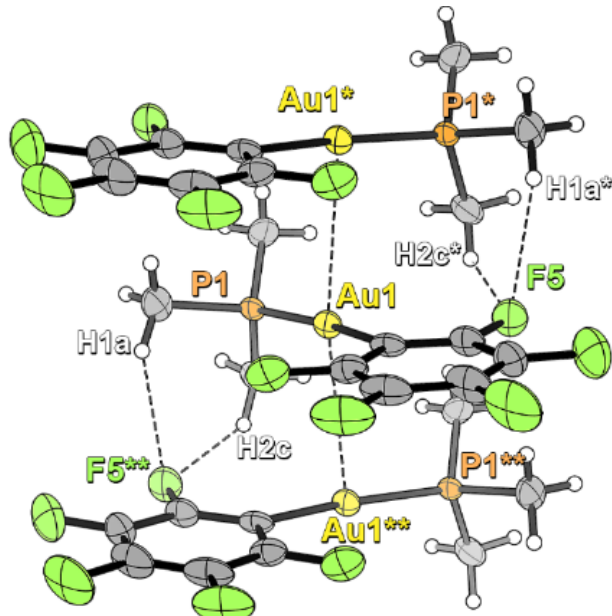
Matthew B. E. Griffiths<sup>\*[a]</sup>, Zachary S. Dubrawski <sup>[a]</sup>, Goran Bačić <sup>[a]</sup>, Achini Japahuge <sup>[a]</sup>, Prof. Jason D. Masuda <sup>[b]</sup>, Prof. Tao Zeng <sup>[a]</sup>, and Prof. Seán T. Barry <sup>[a]</sup>

[a] Department of Chemistry, Carleton University, 1125 Colonel By Drive, Ottawa, Ontario, K1S 5B6, Canada

[b] Department of Chemistry, Saint Mary's University, 923 Robie Street, Halifax, Nova Scotia, B3H 3C3, Canada

## 5.1 Abstract

Atomic layer deposition (ALD) of gold is being studied by multiple research groups, but to date no process using non-energetic co-reactants has been demonstrated. In order to access milder co-reactants, precursors with higher thermal stability are required. We set out to uncover how structure and bonding affect the stability and volatility of a family of twelve organogold(I) compounds using a combination of techniques: X-ray diffraction (XRD), thermogravimetric analysis (TGA), differential scanning calorimetry (DSC), and density functional theory (DFT). Small, unsubstituted phosphonium ylide ligands bind more strongly to Au(I) than their silyl-substituted analogues, but the utility of both these ligands suffers due to their poor volatility and substantial thermal decomposition. Pentafluorophenyl ( $C_6F_5$ ) is introduced as a new, very electronegative ligand for gold vapor deposition precursors, and it was found that the disadvantage to volatility due to  $\pi$ -stacking and other intermolecular interactions in the solid state was overshadowed by dramatic improvements to kinetic and thermodynamic stability. We introduce a new figure of merit to compare and rank the suitability of these and other complexes as precursors for vapor deposition. Finally, DFT calculations on four compounds that have high figures of merit show a linear correlation between the gold-coordinative ligand bond dissociation energies and the observed decomposition temperatures, highlighting and justifying this design strategy.



## 5.2 Introduction

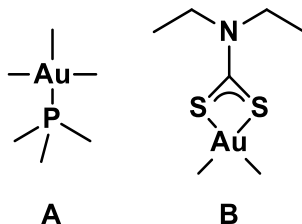
Atomic layer deposition (ALD) is a chemical vapor deposition (CVD) technique that relies on specific surface chemistries to force film growth into a self-limiting layer-by-layer regime.<sup>45</sup> Films deposited by ALD are highly conformal to substrate geometry, and sub-nanometer thickness control can be easily achieved by changing the number of sequential reactant exposures (i.e., cycles). Recently, two different ALD processes to deposit gold metal were reported using organogold(III) precursors: one by our group using oxygen-plasma and water as co-reagents, and the other by Mäkelä and co-workers using ozone.<sup>89,243</sup> While both processes were effective at depositing gold metal with high growth rates at low temperatures, they inherently suffer similar limitations in their scope. Firstly, thermal instability due to recombination of energetic oxygen species prevents high-degree of thickness uniformity of the films down high-aspect ratio trenches, vias, or tortuous geometries.<sup>244,245</sup> Secondly, many substrates are incompatible with oxygen plasma or ozone and are therefore incompatible with these processes.

The strategy most often used for selecting viable compounds to use as new potential ALD precursors is to turn to previous literature; pick the best candidates based on volatility, thermal stability, and reactivity; and try to adapt them for use in an ALD process. While this was fruitful for gold, as shown by both reported processes using previously reported CVD precursors,<sup>87,127,246</sup> this selection process only returns a handful of molecules that are often quite different from one another in their structure and chemistry. ALD precursor design for other materials is quite mature in some cases and has been proven to be a useful tool in accelerating process development for Cu, Ru, Co, Ni, and many other metallic films.<sup>247,248</sup> As such, we felt that a thorough study on the fundamental factors that govern thermal stability and volatility would be useful in the development of new gold ALD precursors.

Many Au(I) CVD precursors decompose below 200°C.<sup>31</sup> By comparison, the current two ALD precursors undergo thermolysis: at 140°C for trimethylgold(III) trimethylphosphine (**A**) and at 220°C for dimethyl(diethyldithiocarbamato- $\kappa^2$ -S,S')gold(III) (**B**) (Scheme 5.1), which manifested in upper process temperatures being limited to 120 °C and 180 °C, respectively. We hypothesize that milder co-reagents than plasma or ozone could be

used if higher deposition temperatures could be accessed, therefore requiring precursors with higher thermal stability.

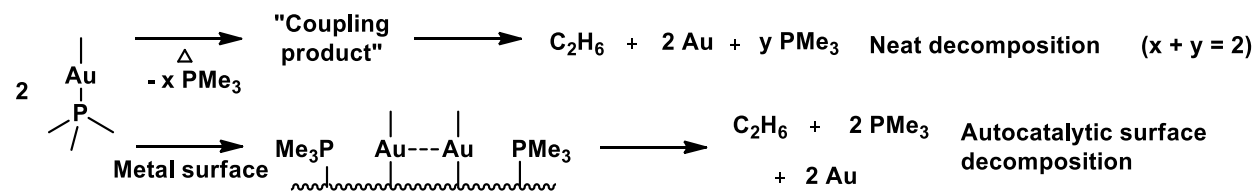
**Scheme 5.1** Two previously reported precursors for gold ALD.



This work reports a study of a family of potential gold(I) vapor deposition precursors based on a framework with interchangeable coordinative and anionic ligands to allow a systematic structure-function understanding not only of the steric and electronic effects of these ligands, but also of their cooperative effects on the volatility and thermal stability of the compound.

Alkylgold(I) phosphine compounds are known to decompose through a bimolecular reductive elimination pathway (Scheme 5.2). Trimethylphosphine methylgold(I) (**1a**) is reported to be stable as a neat liquid until 150°C, at which point dissociation of trimethylphosphine occurs followed by bimolecular reductive elimination of ethane gas.<sup>249</sup> However, on active metal surfaces this decomposition is known to occur as low as room temperature: the Au-PMe<sub>3</sub> bond dissociates on the surface, allowing bimolecular reductive elimination to take place.<sup>121,250</sup>

**Scheme 5.2** Decomposition pathways for (PMe<sub>3</sub>)AuMe as a neat liquid and in the presence of an active metal surface.



Given this, we focused on three complementary synthetic strategies to increase the thermal stability of Au(I) complexes. First, increasing the steric bulk of the anionic ligand should hinder the bimolecular reductive elimination pathway by preventing the association

of adjacent surface-bound Au(I) species. Second, since the rate-limiting step of this reaction is dissociation of the coordinative phosphine ligand, a more electron-withdrawing anionic ligand should make the Au(I) center more acidic, thus strengthening the bond of the coordinative ligand. Lastly, using coordinative ligands of other known thermally stable Au(I) complexes may yield novel and useful ligand combinations. Thus, we envisioned a family of compounds that would allow us to discover which factors conferred the most thermal stability to organogold(I) compounds (Scheme 5.3).

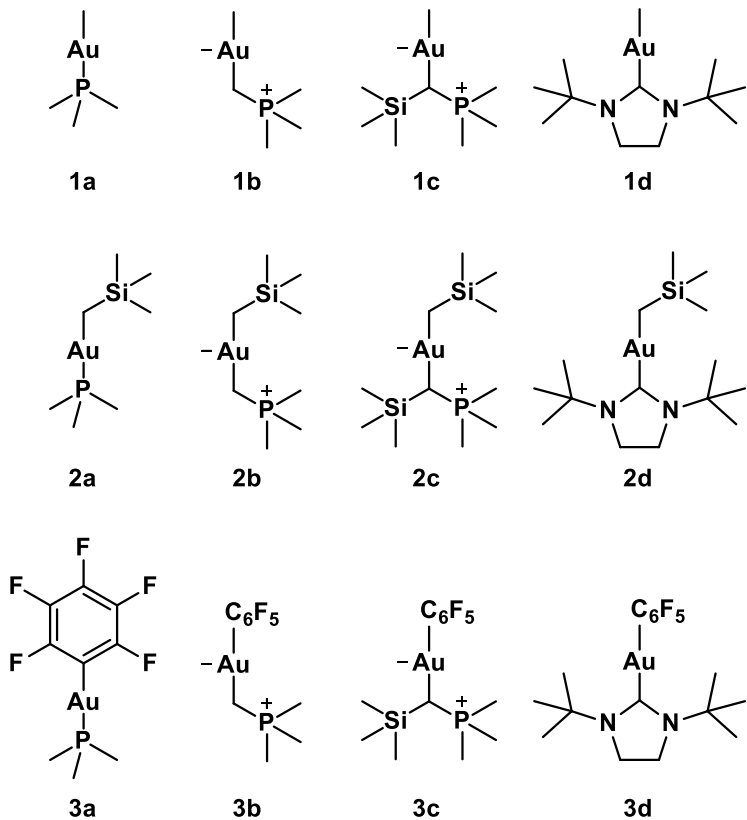
Starting from the known methylgold(I) CVD precursor **1a**, substituting trimethylsilylmethyl ( $\text{CH}_2(\text{SiMe}_3)$ ) and pentafluorophenyl ( $\text{C}_6\text{F}_5$ ) ligands should impart a stepwise increase in the overall thermal stability of the compound.  $\text{CH}_2(\text{SiMe}_3)$  is sterically bulkier than Me and is known to stabilize Au(I) species more so than non-silylated ligands.<sup>66,67</sup> Both factors increase the thermal stability of transition metal complexes bearing this ligand, and have been used previously for manganese ALD precursor design.<sup>251</sup> The  $\text{C}_6\text{F}_5$  is much more  $\sigma$ -electron withdrawing due to perfluorination, which should result coordinative ligands forming a stronger bond to the gold center and increase the activation energy required for decomposition via bimolecular reductive coupling. Some  $\text{C}_6\text{F}_5$  complexes of gold with and without phosphine coordinative ligands have previously been shown to have high thermal stability, but have not been used for CVD or ALD.<sup>252,253</sup>

Phosphines are strongly binding coordinative ligands for organogold(I) compounds. Their chemistry is well known and predictable, the gold(I) compounds are stable to air and moisture, and they are generally quite volatile. We chose trimethylphosphine ( $\text{PMe}_3$ ) as one of four neutral coordinative ligands (**1a**, **2a**, **3a**) due to its low molecular weight, ease of use in synthesis, and good  $\sigma$ -donation capabilities.

Schmidbaur and Franke reported “remarkably stable” organometallic gold(I) complexes bearing trimethylmethylenephosphorane (ylide) and trimethyl(trimethylsilylmethylene) phosphorane (TMS-ylide) phosphonium ylides as neutral coordinative ligands.<sup>254</sup> These phosphonium ylides readily displace  $\text{PMe}_3$  from **1a** and **2a** giving **1b** and **1c**, and **2b** and **2c** which were reported to be more thermally stable than the parent  $\text{PMe}_3$  complexes (decomposing above 150 °C in the case of **1b**). Since phosphonium ylide compounds of Au(I) have to our knowledge not yet been tested for vapor deposition applications, and

their volatilities have not been assessed, we included them and their  $C_6F_5$  analogues in this study.

**Scheme 5.3** Family of Au(I) compounds considered in this study.



*N*-Heterocyclic carbenes (NHCs) have been successfully used in the design of ALD precursors for copper metal, a CVD precursor for gold metal, and an ALD precursor for silver metal.<sup>255–258</sup> The compound *N,N'*-di-*tert*-butylimidazolidin-2-ylidene<sup>259</sup> (NHC) is a monomeric, thermally stable, and sterically bulky saturated NHC with better  $\sigma$ -donor and  $\pi$ - acceptor properties than the more common imidazol-2-ylidene ligand class. This NHC should enhance the thermal stability of organogold(I) compounds due to its strong electron donating ability as well as its ability to sterically protect the Au(I) center.

## 5.3 Results and Discussion

### 5.3.1 Synthesis and Characterization of Au(I) compounds

In literature examples of alkylgold(I) compounds, the desired species is often synthesized by salt metathesis from the corresponding gold(I) halide. However, given the propensity of phosphonium ylide- and NHC-gold(I) halides to form salts of the type  $[\text{Au}(\text{L})_2]^+ [\text{AuX}_2]^-$ <sup>260,261</sup> and to reduce the required number of compounds for this study, we opted for a divergent synthetic strategy where the phosphonium ylide and NHC compounds would be synthesized from their respective parent alkylgold(I) phosphine complexes (Scheme 5.4). Compounds **1a-c**, **2a-c**, and **3a** have been previously reported, and **1d**, **2d**, and **3b-d** are novel.

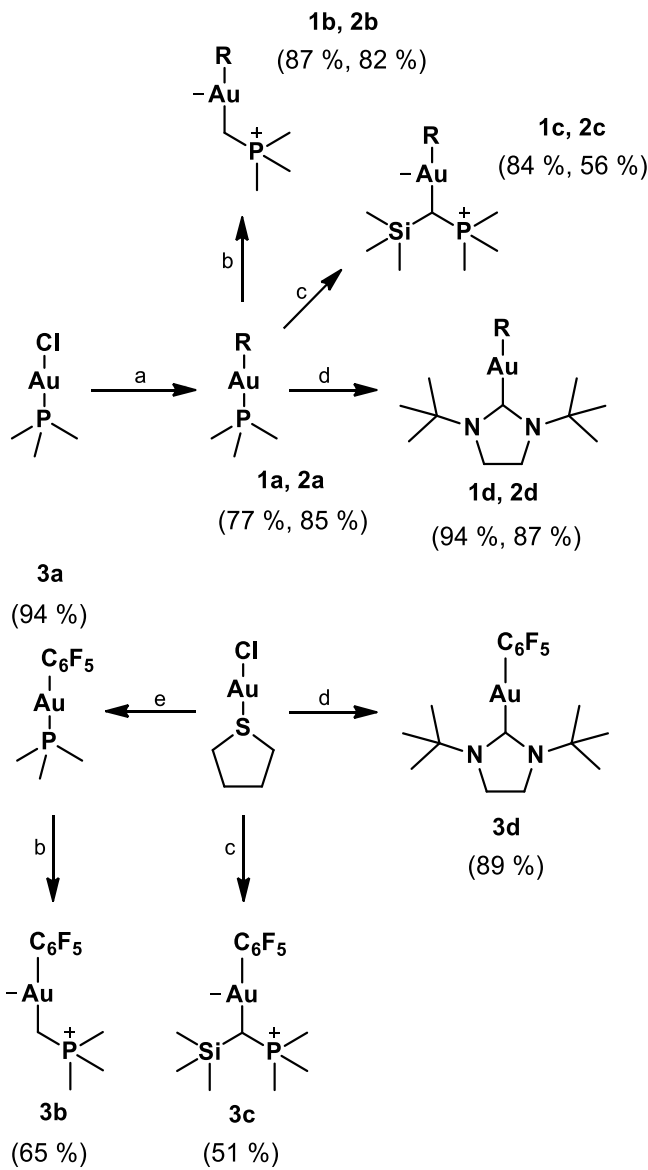
The ligand exchange reaction produced volatile  $\text{PMe}_3$  and no other by-products which allowed for facile workup of these reactions. As detailed in the experimental section, an excess of the desired ligand was often used in order to completely consume the starting gold(I) phosphines which are difficult to remove by recrystallization or sublimation.

Synthesis of **3b** was initially attempted from the known compound  $(\text{THT})\text{AuC}_6\text{F}_5$  since this saved one step in its synthesis (bypassing  $(\text{PMe}_3)\text{AuC}_6\text{F}_5$ ). Unfortunately, this reaction produced a mixture of  $\text{PMe}_3$ --, phosphonium ylide-, and  $\text{C}_6\text{F}_5$ -containing compounds. However, when we attempted the same exchange reaction with **3a** instead of  $(\text{THT})\text{AuC}_6\text{F}_5$ , **3b** and **3c** were produced as the majority products and were isolated by recrystallization. Compound **3d** could be synthesized successfully from both  $(\text{THT})\text{AuC}_6\text{F}_5$  and **3a** by ligand exchange, but we deem the former procedure superior due to a reduction in synthetic steps.

We observed during workup that the ylide-containing complexes **1b** and **1c** decomposed upon attempted sublimation, and so we chose to purify phosphonium ylide species exclusively by recrystallization. All  $\text{PMe}_3$  and NHC complexes were purified by sublimation (or by distillation for **2a**).

All compounds were characterized by  $^1\text{H}$ -,  $^{31}\text{P}$ -,  $^{19}\text{F}$ -, and  $^{13}\text{C}$ -NMR spectroscopy, and were matched to literature reports where appropriate (**1a**,<sup>262</sup> **1b**,<sup>263</sup> **1c**,<sup>264</sup> **2a**,<sup>264</sup> **2b**,<sup>264</sup> **2c**,<sup>265</sup> **3a**<sup>266</sup> are known, compounds **1d**, **2d**, **3b**, **3c**, **3d** are novel). Our analysis of **3a** differed slightly by  $^{31}\text{P}$ -NMR analysis where the literature gives a chemical shift of 3.28 ppm and we instead observed the resonance at -5.00 ppm after purifying the compound by vacuum sublimation. The NHC compounds **1d**, **2d**, and **3d** display characteristic NHC carbon resonances at 221.74, 219.94, and 211.05 ppm in the  $^{13}\text{C}$ -NMR spectra which are similar to the free NHC (218.7 ppm)<sup>267</sup>. The compounds **3b** and **3c** were characterized by their  $^{31}\text{P}$ -NMR resonances which were observed at 26.50 and 23.65 ppm respectively, whose chemical shifts are very similar to **1b** and **1c**, and **2b** and **2c**. The  $\text{CH}(\text{SiMe}_3)\text{PMe}_3$  resonances (**1c**, **2c**, **3c**) were shielded by the increased electron density from the SiMe<sub>3</sub> group compared to the non-substituted ylide compounds. Compounds **3a**, **2b**, **2c**, and **2d** could not be differentiated from ionic salts of the type  $[\text{Au}(\text{L})_2]^+$   $[\text{AuX}_2]^-$  using NMR spectroscopy alone if the sample contains only one species, so the following X-ray crystallographic analyses served to confirm their neutral molecular arrangement.

**Scheme 5.4** Synthesis of all compounds. Reagents: **a**, MeLi (**1a**, 77%),  $(\text{SiMe}_3)\text{CH}_2\text{Li}$  (**2a**, 85%); **b**,  $\text{CH}_2\text{PMe}_3$  (**1b**, 87%), (**2b**, 82%), (**3b**, 65%); **c**,  $\text{CH}(\text{PMe}_3)(\text{SiMe}_3)$  (**1c**, 84%), (**2c**, 56%), (**3c**, 51%); **d**, *N,N'*-di-*tert*-butylimidazolidin-2-ylidene (**1d**, 94%), (**2d**, 87%), (**3d**, 89%), **e**,  $\text{PMe}_3$  (**3a**, 94%). Synthetic yields are given in parentheses alongside the compound names (%).



### 5.3.2 Crystallography

Volatility is arguably the most important property of an ALD precursor as it sets the lower limit of useable process temperatures. It is primarily dictated by intermolecular forces and, to a lesser extent, by the molecular weight of the compound. Since a compound's volatility can be readily determined by TGA, we wanted to understand which intermolecular interactions most affect volatility. Single crystal X-ray crystallography was used to determine the solid-state packing of **1c** and **1d**, **2b** and **2d**, and **3a**, **3b**, **3c**, and **3d** (Figure

5.1). Selected bond lengths, angles, and other data are displayed for comparison in Table 5.1.

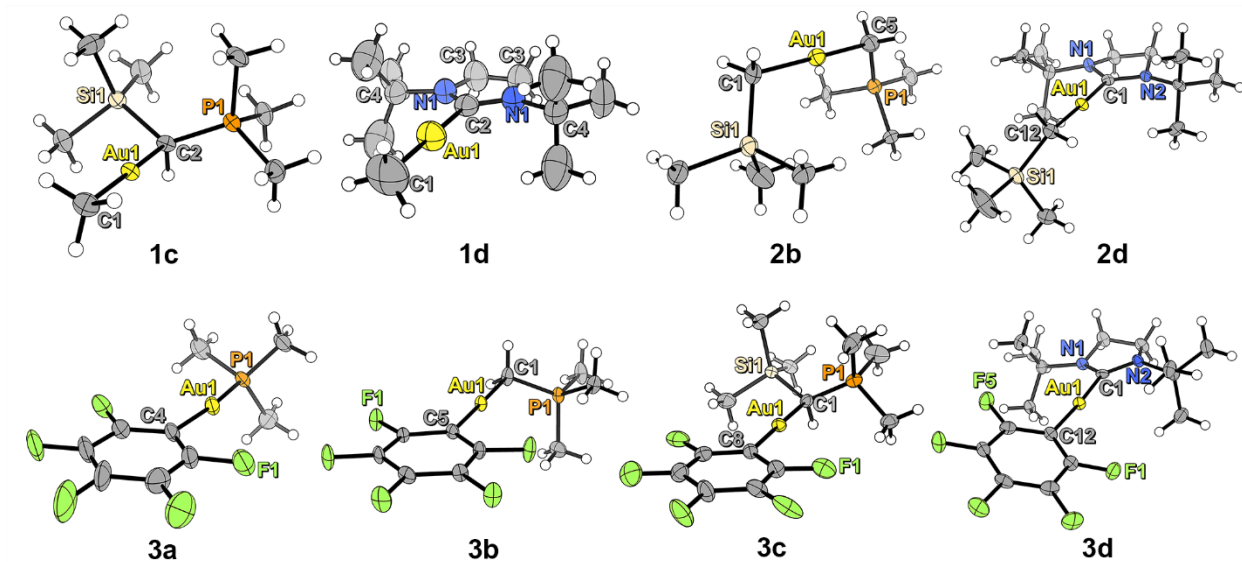


**Figure 5.1** Solid-state structures of **1c**, **1d**, **2b**, **2d**, **3a**, **3b**, **3c**, and **3d**. In the cases of **1c** and **3c** only the S enantiomers are shown. Ellipsoids are drawn at 50 % probability in all diagrams.

Compound **1c**, like its TMS-ylide derivative **3c**, crystallizes as a 1:1 mixture of *R* and *S* enantiomers at the chiral ylidic carbon center coordinated to Au. The P-C<sub>ylide</sub> bond length is shorter than the mean P-Me bond length (1.742(3) Å vs. 1.793(9) Å respectively), and the P-C<sub>ylide</sub>-Si angle (121.6(2)°) is much larger than expected for a tetrahedral geometry. These factors indicate that the bonding of this ligand lies somewhere between its two extreme canonical structures (Scheme 5.5). Steric repulsion between the PMe<sub>3</sub> and SiMe<sub>3</sub> groups of the ylide may influence the large angle and therefore hinder the σ-donating ability of this ligand. Likewise, compound **3c** displays a P-C<sub>ylide</sub> bond length of 1.759(3) Å, an average P-Me bond length of 1.798(11) Å, and a P-C<sub>ylide</sub>-Si bond angle of 121.7(2)°, all of which implies a significant ylene character. More ylene character translated to higher volatility in TMS-ylide compounds (*vide infra*). All bond length comparison in this section was performed in accordance with the statistical rules found in Koojiman.<sup>268</sup>

In the structure of **2b**, the acceptance of electron density from the ylidic carbon by the Au center is much more pronounced as shown by the shorter Au-L bond. The P-C<sub>ylide</sub> bond

length in **2b** is elongated compared to that of trimethylmethylenephosphorane ( $1.77(1)$  Å and  $1.640(6)$  Å respectively)<sup>269</sup> and the P-C<sub>ylide</sub> bond length is not significantly different from the mean P-Me bond length ( $1.77(1)$  Å vs.  $1.80(4)$  Å, respectively). This is similarly observed in **3b** and distinguishes **2b** and **3b** from **1c** and **3c** as being primarily ylidic in nature, which led to a suppression of volatility.

**Scheme 5.5** Resonance structures depicting the extreme canonical resonance structures and ligand geometries of compounds **1,2,3c**.

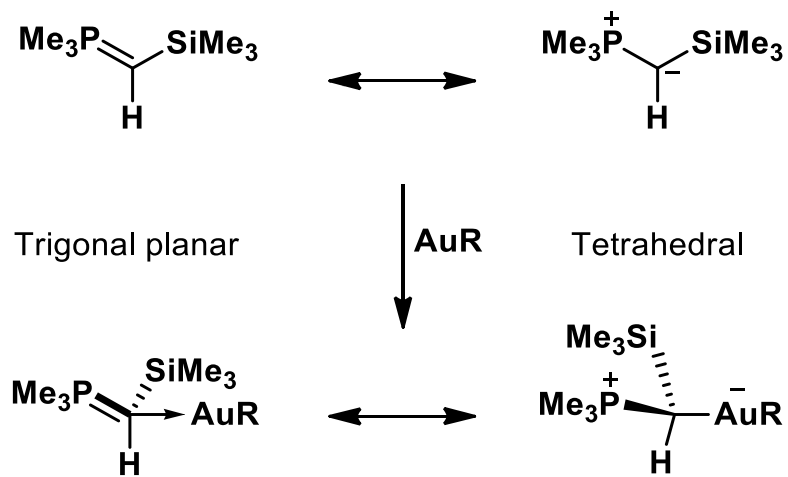


**Table 5.1** Selected bond distances and angles for the analyzed compounds

<i>R</i>	<i>L</i>	<i>Au-R</i> (Å)	<i>Au-L</i> (Å)	<i>P-C<sub>ylide</sub></i> (Å)	Average <i>P-Me</i> (Å)	<i>NCN bond angle</i> (°)	<i>R-Au-L</i> (°)
TMS-							
<b>1c</b>	Me	ylide	2.057(3)	2.136(3)	1.742(3)	1.793(9)	-
<b>1d</b>	Me	NHC	2.069(8)	2.055(6)	-	-	108.5(5) 180
<b>2b</b>	$\text{CH}_2(\text{SiMe}_3)$	Ylide	2.10(1)	2.09(1)	1.77(1)	1.80(4)	-
<b>2d</b>	$\text{CH}_2(\text{SiMe}_3)$	NHC	2.059(7)	2.045(7)	-	-	108.5(6) 178.1(3)
<b>3a</b>	$\text{C}_6\text{F}_5$	$\text{PMe}_3$	2.053(5)	2.280(1)	-	-	-
<b>3b</b>	$\text{C}_6\text{F}_5$	Ylide	2.046(3)	2.081(4)	1.763(3)	1.789(10)	-
TMS-							
<b>3c</b>	$\text{C}_6\text{F}_5$	ylide	2.041(3)	2.104(3)	1.759(3)	1.789(11)	-
							178.4(1)

<b>3d</b>	C <sub>6</sub> F <sub>5</sub>	NHC	2.039(4)	2.031(4)	-	-	109.4(3)	176.7(1)
-----------	-------------------------------	-----	----------	----------	---	---	----------	----------

When comparing R-Au bond lengths, the C<sub>6</sub>F<sub>5</sub> compounds all exhibit shorter bonds than other compounds with the same coordinative ligand: **1d** ≈ **2d** > **3d**, **1c** > **3c**, and **2b** > **3b**. This is primarily due to the covalent radius of the sp<sup>2</sup>-hybridized carbon in the C<sub>6</sub>F<sub>5</sub> ring being slightly smaller than that of the sp<sup>3</sup>-hybridized carbon atoms in the Me and CH<sub>2</sub>(SiMe<sub>3</sub>) ligands. Furthermore, C<sub>6</sub>F<sub>5</sub> complexes **3a**, **3b**, **3c**, and **3d** display shorter Au-L bond lengths than their aliphatic derivatives, which is due to the strong electron-withdrawing ability of the C<sub>6</sub>F<sub>5</sub> ligand. From these results, it appeared that C<sub>6</sub>F<sub>5</sub> was an especially good ligand for improving the thermal stability of Au(I) compounds for two reasons. Firstly, the rate-limiting step for decomposition must proceed through cleavage of a stronger coordinative bond, and secondly because the final reductive elimination step must occur between two strongly bound, electron-deficient carbon atoms.

In the solid state, each molecule of **3a** is associated to its neighbors by polymeric Au-Au aurophilic interactions (Au-Au distance 3.3703(6) Å). This was the only compound structurally characterized in this work that displayed aurophilicity (Figure 5.2). This is an intermediate-to-long range aurophilic interaction,<sup>270</sup> and is likely only observed for **3a** because PMe<sub>3</sub> is the least sterically ligand in this study. By comparison the previously reported PPh<sub>3</sub> analogue does not display aurophilic interactions, but instead undergoes a π-stacking interaction between the C<sub>6</sub>F<sub>5</sub> ligands, possibly due to the steric bulk of the PPh<sub>3</sub> ligand interfering with the Au-Au interaction.<sup>271</sup>

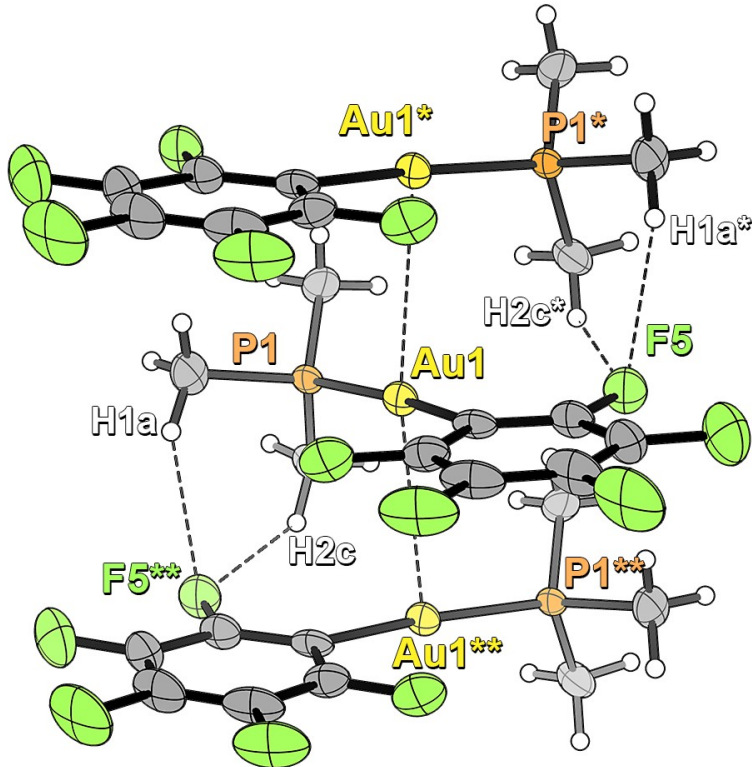


**Figure 5.2** Extended structure of **3a** showing the aurophilic polymer chain. Thermal ellipsoids are shown at 50 % probability. Selected intermolecular interaction distances ( $\text{\AA}$ ): Au(1)-Au(2) 3.3703(6), H(1a) – F(5\*\*) 2.492, H(2c) – F(5\*\*) 2.527.

Some studies have previously linked the volatility of Au(I) compounds to solid-state aurophilic interactions.<sup>272,273</sup> However a recent computational paper by Mata *et al*<sup>63</sup> cautioned that aurophilic interactions aren't necessarily the dominant intermolecular force holding the molecules together, and Au-ligand interactions or inter-ligand interactions dictate solid-state packing arrangements to a greater degree. Thus, we have attempted to describe the number and types of interactions that occur throughout the system which overall affect the compound's volatility.

In Figure 5.2 other in-chain intermolecular interactions are observed between the  $\text{PMe}_3$  ligands. Each phosphine engages in two H – F interactions to an adjacent molecule (H(1a) – F(5\*\*) 2.492  $\text{\AA}$ , H(2c) – F(5\*\*) 2.527  $\text{\AA}$ ). These strong hydrogen bonding interactions translated to a suppression of the volatility of **3a** compared to **1a** and **2a**.

Compound **3b** is involved in a  $\pi$ -stacking interaction with a centroid to centroid distance of 3.497 Å. These  $\pi$ -stacked dimers are involved in secondary interactions with other  $\pi$ -stacked dimers along the crystallographic  $b \times (a+c)$  plane through a set of F-F, C-F, and C-C interactions (Figure 5.3). The extensive intermolecular network formed by **3b** shows that the addition of a  $C_6F_5$  group introduces many more intermolecular interactions when coupled with a small ligand like  $PM\acute{e}_3$  or  $CH_2PM\acute{e}_3$  than with larger ligands like  $CH_2PPh_3$  and resulted in a reduced volatility of this compound. This compound displayed the largest number of intermolecular interactions of the family.

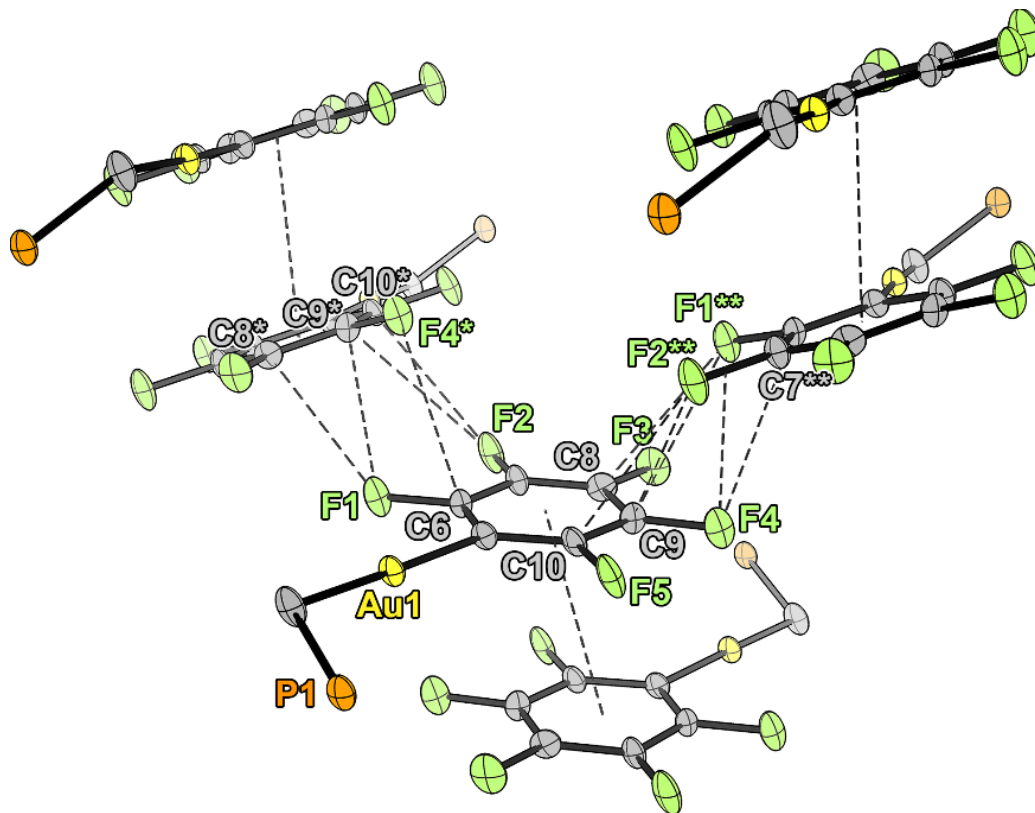


**Figure 5.3**  $C_6F_5 - C_6F_5$  intermolecular interactions in **3b**. The diagram displays pairs that occur along the crystallographic  $b \times (a+c)$  plane. Methyl moieties of the ylide and hydrogen atoms have been omitted for clarity. Thermal ellipsoids are shown at 50 % probability. Selected intermolecular interaction distances (Å): centroid-to-centroid 3.497,  $F(2^{**}) - C(10)$  3.210(3),  $F(2^{**}) - C(9)$  3.166(3),  $C(7^{**}) - F(4)$  3.231(6),  $F(1^{**}) - F(4)$  2.928(2),  $F(1^{**}) - C(9)$  3.127(3),  $F(1^{**}) - C(8)$  3.145(3).

Compound **3c** does not  $\pi$ -stack in the solid state, instead the  $C_6F_5$  ligands interact to form chains via (C-F)-F interactions, although there are considerably fewer than observed in **3b** (Figure 5.4). This demonstrates the ability of sterically bulky coordinative ligands to suppress intermolecular interactions in  $C_6F_5$ -Au complexes.

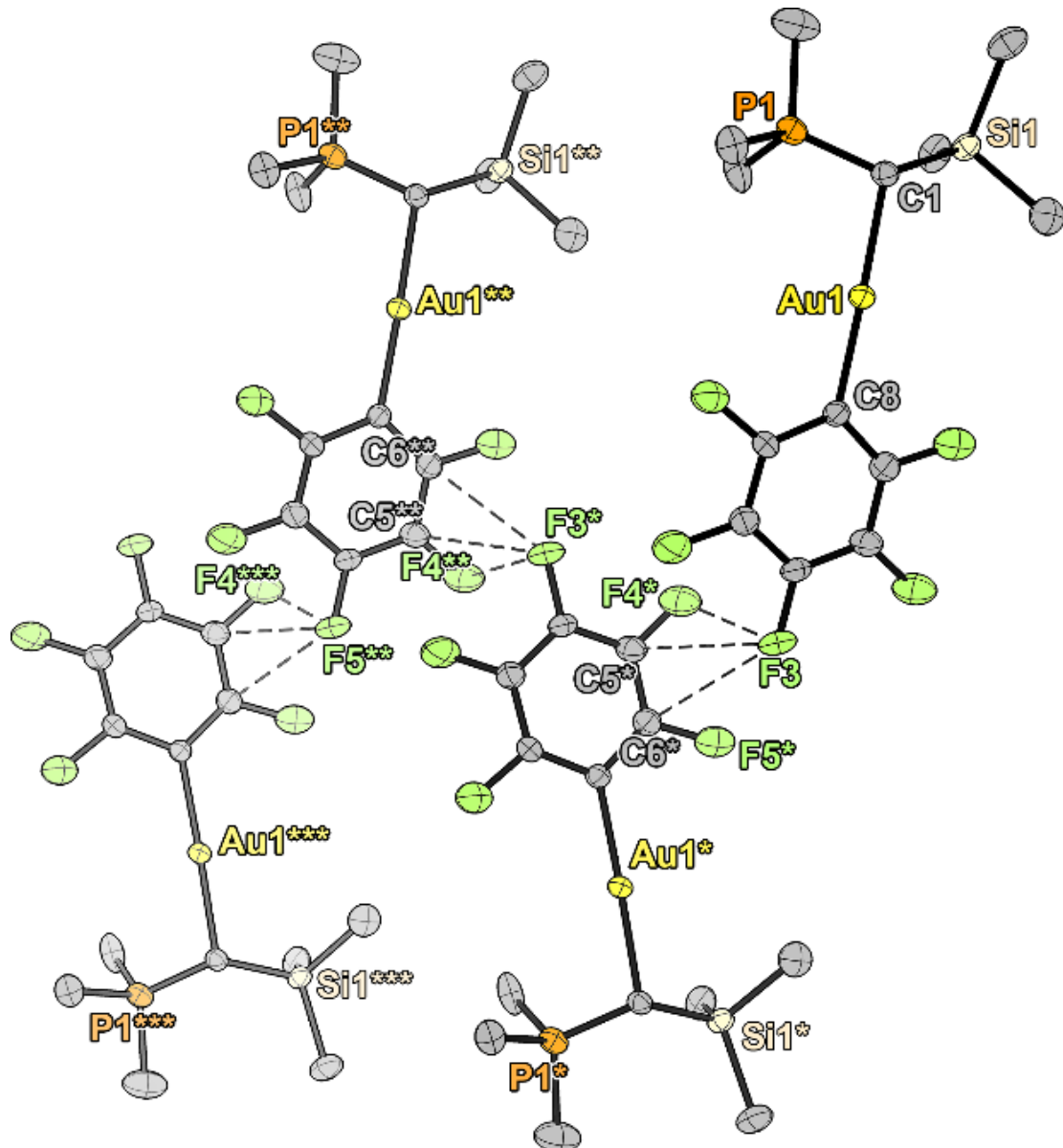


**Figure 5.4**  $C_6F_5 - C_6F_5$  intermolecular interactions in **3c**. Hydrogen atoms have been omitted for clarity and thermal ellipsoids have been drawn at the 50% probability level. The top two molecules are the (S) enantiomer while the bottom two are the (R) enantiomer. Selected intermolecular interaction distances ( $\text{\AA}$ ):  $F(3) - F(4^*)$  2.912(3),  $F(3) - C(2^*)$  3.151(4),  $F(3) - C(3^*)$  3.214(3).

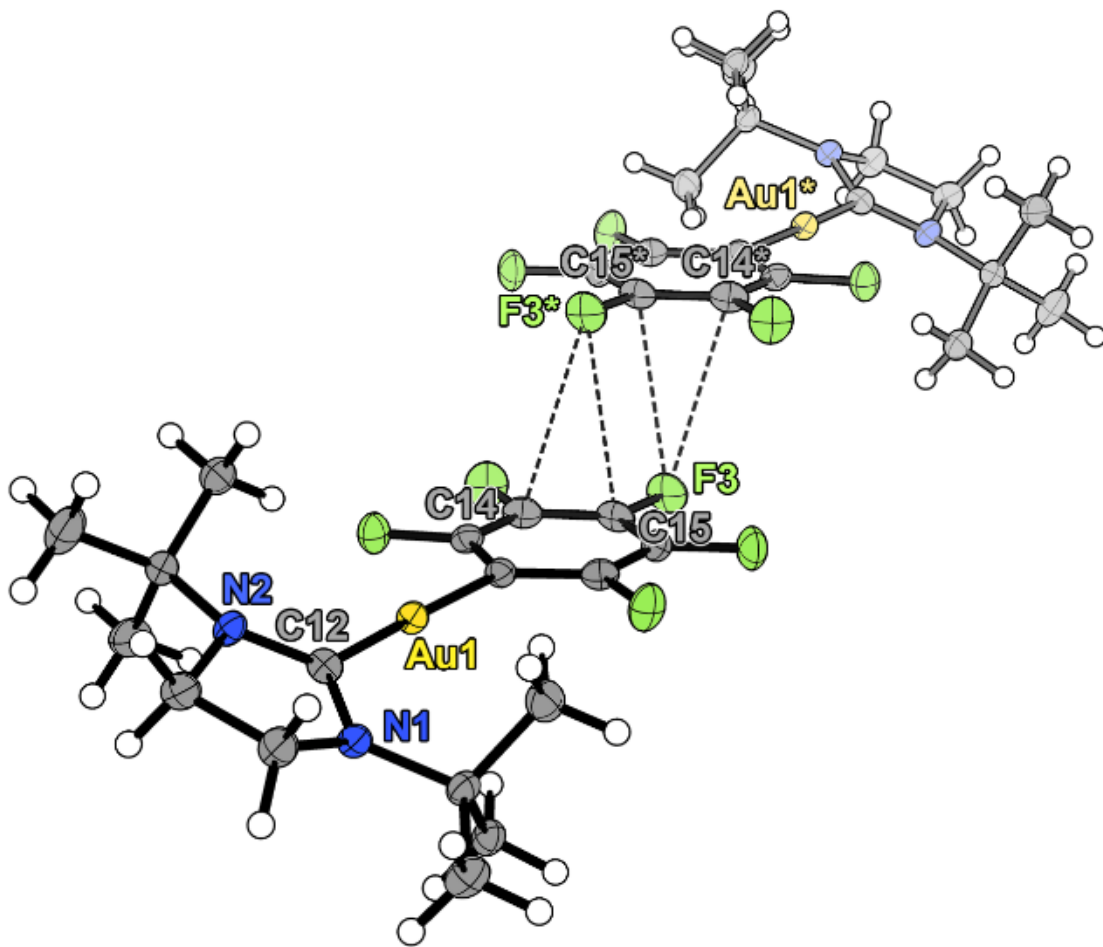


**Figure 5.5**  $\text{C}_6\text{F}_5 - \text{C}_6\text{F}_5$  intermolecular interactions in **3d**. Thermal ellipsoids have been drawn at the 50% probability level. Selected intermolecular interaction distances ( $\text{\AA}$ ): C(14) – F(3\*) 3.095(4), C(15) – F(3\*) 3.043(4).

Compound **3d** displays fewer overall intermolecular contacts than other  $\text{C}_6\text{F}_5$  compounds which we attribute to the large steric bulk of the NHC. The  $\text{C}_6\text{F}_5$  inter-ligand interactions are suppressed compared to **3c**, where here only a single pair of (C-C) – F p- $\pi$  interactions (Figure 5.5) are allowed.

Complexes bearing Me (**1c** and **1d**) or  $\text{CH}_2(\text{SiMe}_3)$  (**2b** and **2d**) ligands display no intermolecular contacts. In contrast,  $\text{C}_6\text{F}_5$  complexes (**3a**, **3b**, **3c**, and **3d**) display far more intermolecular interactions in the solid state, and we surmise that this is the main reason for their decreased volatility (see below).

### 5.3.3 Thermolysis

For a compound to be a potential ALD candidate, high thermal stability and volatility are required. Thermogravimetric analysis (TGA) of a thermally stable and volatile compound shows an exponential mass loss with constantly increasing temperature as described by the Clausius-Clapeyron equation. Thermally stable compounds also leave a very low final residual mass indicative of evaporation without decomposition to non-volatile by-products. The vapor pressure of a compound can be calculated from TGA data using a previously developed method (Figures S-5.11 to S-5.18).<sup>70</sup> The temperature at which a compound achieves a vapor pressure of 1 Torr (i.e., its 1 Torr temperature,  $T_v$ ) may be used as a benchmark for comparison since commercial ALD reactors typically operate close to this pressure. While TGA can also give clues about decomposition of the sample compound, differential scanning calorimetry (DSC) is better at analyzing the onset of decomposition of these compounds. By graphically determining the point at which the decomposition exotherm has reached 5 % of its maximum height, we obtained a decomposition temperature ( $T_D$ ) for the compound in question (Figures S-5.19 to S-5.30). The results of these analyses are tabulated below (Table 5.2).

In the TGA ramp experiments of **1a-d** (Figure 5.6), none of the compounds were thermally stable enough to evaporate completely, however in each case some sample did evaporate intact which we can infer from the percent atomic mass of Au in the compound compared to the final residual mass of the experiment (see inset). All sample pans were left with a visibly golden coating after the experiments.

**Table 5.2** Important metrics obtained from TGA and DSC experiments

	$T_V$ (°C)	$T_D$ (°C)	Useful temperature range (°C) <sup>a</sup>	Residual mass (%)	Fractional Gold remaining (%)	Figure of Merit ( $\sigma$ ) <sup>b</sup>
<b>1a</b>	68	130	62.5	34.3	50.2	31.1
<b>1b</b>	-	107	-	22.9	35.1	-
<b>1c</b>	-	129	-	36.9	70.1	-
<b>1d</b>	157	189	32.5	34.9	69.9	9.8
<b>2a</b>	87	146	59.1	0.8	1.5	58.2
<b>2b</b>	-	152	-	2.5	4.8	-
<b>2c</b>	134	118	-16.8	5.9	13.4	-14.6
<b>2d</b>	150	184	33.1	11.9	28.2	23.8
<b>3a</b>	152	185	33.1	1.1	2.5	32.3
<b>3b</b>	-	220	-	41.3	95.2	-
<b>3c</b>	148	253	104.7	33.3	88.8	11.7
<b>3d</b>	200	300	99.7	1.6	4.4	95.3

<sup>a</sup> Difference between  $T_V$  and  $T_D$ . <sup>b</sup> See Equation 1. Dashes indicate that insufficient mass loss data could be obtained before the measured self-decomposition temperature of that compound.

In the case of **1a** it is interesting that such a high residual mass is observed, given that the self-decomposition point (130 °C) is close to the end of the mass loss curve. This can be explained by the known autocatalytic decomposition of alkylgold(I) phosphines that occurs as low as room temperature on Cr, Cu and Au surfaces.<sup>121</sup> Some decomposition likely occurs on the Pt surface of the pan at temperatures below the onset of self-decomposition results in an increased residual mass. This occurs more readily for the phosphine than for the NHC which implies a strong NHC–Au bond. No inflection is observed in the exponential mass loss curves of **1a** and **1d** suggesting that the decomposition products are gaseous (ethane, PMe<sub>3</sub>, NHC) or non-volatile (metallic gold), and therefore their production does not affect the rate of mass loss of the sample.

In the case of compounds **1b** and **1c**, concurrent evaporation and decomposition were observed by the presence of multiple inflection points in their respective mass loss curves.

Here the products formed by thermolysis are semi-volatile or are themselves thermally unstable. This makes the by-products observable as changes to the mass loss rate, implying low-volatility organic molecules or other gold complexes are the primary decomposition products of **1b** and **1c**.

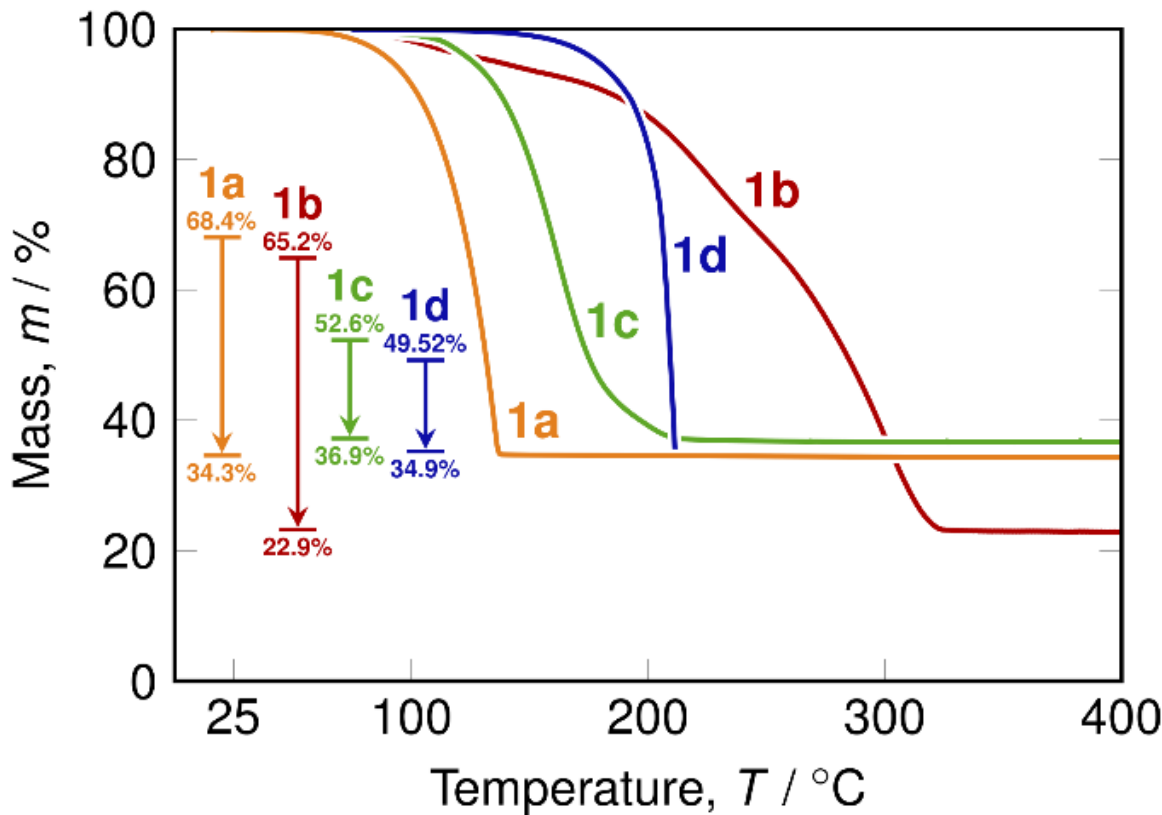


**Figure 5.6** TGA of **1a-d** at a ramp rate of 10 °C/min. The inset vertical ranges show the % mass of Au in each compound (top line) and the final residual mass of the respective analysis (bottom line).

The  $\text{CH}_2(\text{SiMe}_3)\text{gold(I)}$  compounds **2a** and **2d** performed much better in TGA analyses (Figure 5.7) than **1a** and **1d**. Compound **2a** appears to evaporate very cleanly, the only indication of slight decomposition being the small residual mass of 0.8 %. Compound **2d** evaporates with decomposition in a single step to 11.9 %.

Compounds **2b** and **2c** undergo multiple decomposition events like **1b** and **1c**. However, it is obvious that the  $\text{CH}_2(\text{SiMe}_3)$  ligand improves thermal performance by TGA because

the residual masses of **2b** and **2c** are much lower, meaning more of the gold has ultimately evaporated from the system.

The  $C_6F_5$  compounds **3a** and **3d** performed very well by TGA (Figure 5.8), each evaporating in a single step and leaving a very low residual mass (**3a**: 1.1%; **3d**: 1.6%). Volatilization occurs at higher temperatures for these species, and **3d** shows a marked improvement in its thermal stability compared to **1d** and **2d**. Clearly  $C_6F_5$  imparts a strong stabilization to gold(I) and improves the thermal stability of the system, although at the expense of volatility.

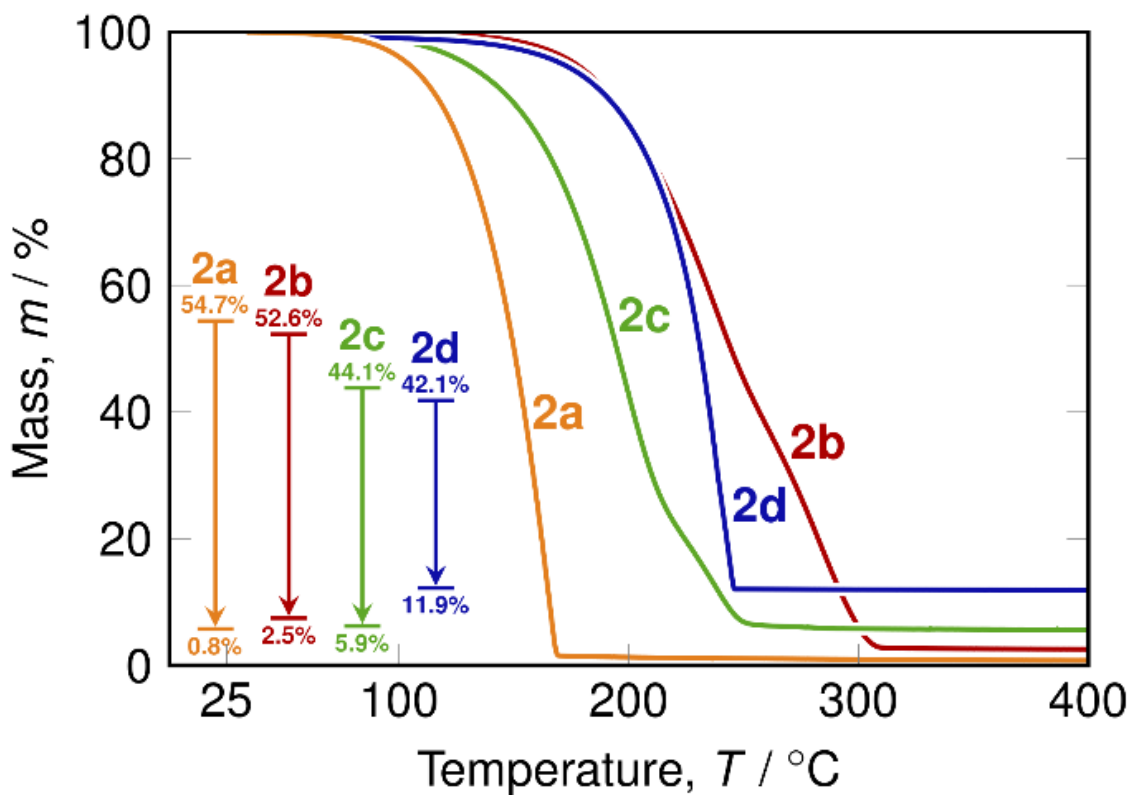


**Figure 5.7** TGA ramp experiments of **2a-d** at a ramp rate of  $10\text{ }^{\circ}\text{C/min}$ . The inset vertical ranges show the % mass of Au in each compound (top line) and the final residual mass of the respective analysis (bottom line).

Compounds **3b** and **3c** performed worse than their Me and  $\text{CH}_2(\text{SiMe}_3)$  counterparts, decomposing extensively and leaving the highest gold residues of the family (>85%). The

introduction of the C<sub>6</sub>F<sub>5</sub> ligand does improve thermal stability when compared with the aliphatic derivatives, but in the case of **3b** and **3c**, the reduction in volatility is too great to result in a useful precursor.

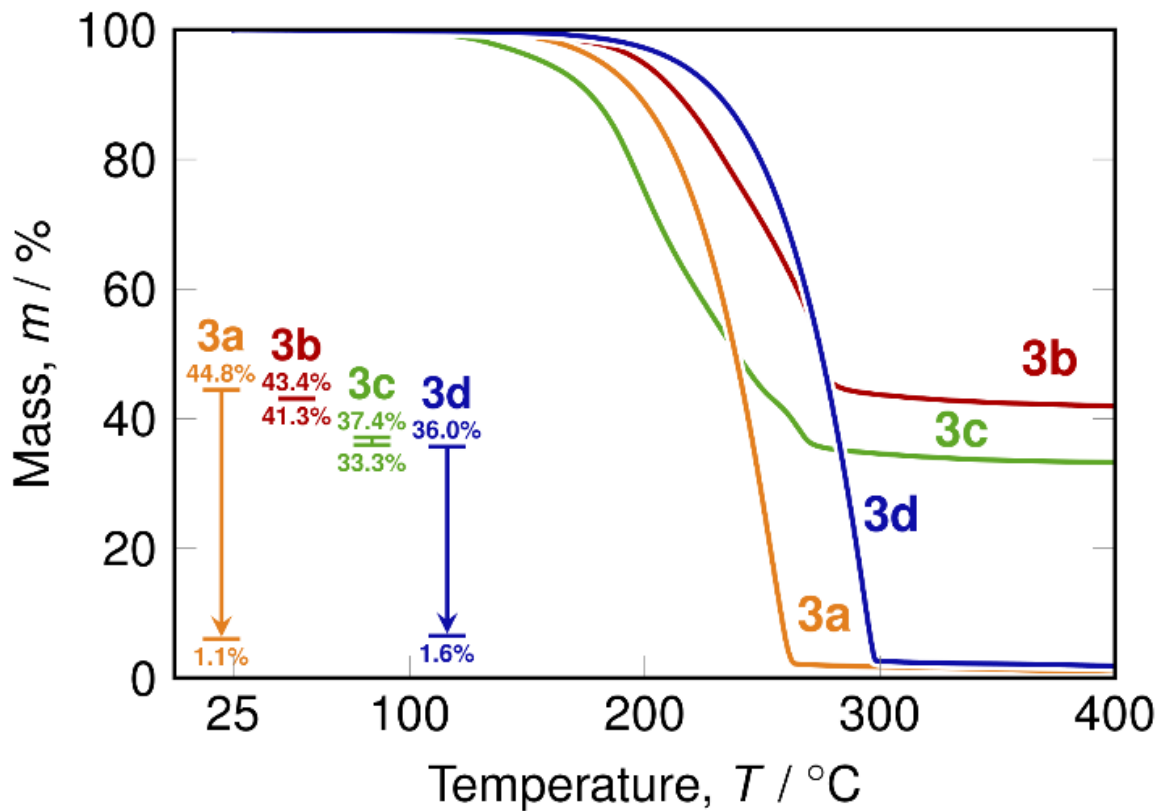


**Figure 5.8** TGA ramp experiments of **3a-d** at a ramp rate of 10 °C/min. The inset vertical ranges show the % mass of Au in each compound (top line) and the final residual mass of the respective analysis (bottom line).

Using the thermal data collected, we defined a figure of merit ( $\sigma$ ) to compare the viability of these compounds for use in vapor deposition processes (Equation 1). This figure of merit is made up of thermodynamic and kinetic terms that together describe the suitability of the vapor deposition precursor. Not only does it include decomposition temperature and vapor pressure, but if two compounds that both undergo the same decomposition mechanism are compared, the one which resists decomposition longer will receive a higher figure of merit. This highlights, for instance, that some of the compounds are more

kinetically stable (e.g. **2a**, **3a**) than others (e.g. **1a**). Particularly, **3a** persists in the TGA experiment far past its onset of self-decomposition measured by DSC (185 °C). Thus, weighting the figure of merit by the residual mass demonstrates the importance of kinetic and thermodynamic stability of a potential precursor compound.

**Equation 1.** Figure of merit equation for vapor deposition precursor usefulness.

$$\sigma = (T_D - T_V) \times \left( 1 - \frac{\%m_{res}}{196.97/MW \times 100\%} \right)$$

The calculated  $\sigma$  values for the family of compounds are included in Table 5.2. Certain compounds (**1b**, **1c**, **2b**, **3b**) were not given a  $\sigma$  value because insufficient mass loss data could be obtained before the TGA experiment reached the self-decomposition temperature (DSC) of the analyte in question. The merits of each compound in this family can be visualized using a “minefield” diagram (Figure 5.9). Since the delivery temperature of a precursor is an unavoidable consideration in process design, each circle is centered at the compound’s respective  $T_V$ .

If delivery temperature is not an important requirement, then clearly compound **3d** is the most promising precursor candidate for vapor deposition. It has a  $T_V$  of 200 °C however, so if only lower delivery temperatures are desired **2a** is likely the preferred candidate. These are two excellent candidates for the development of ALD processes that include gold, and they are currently under investigation in our group.

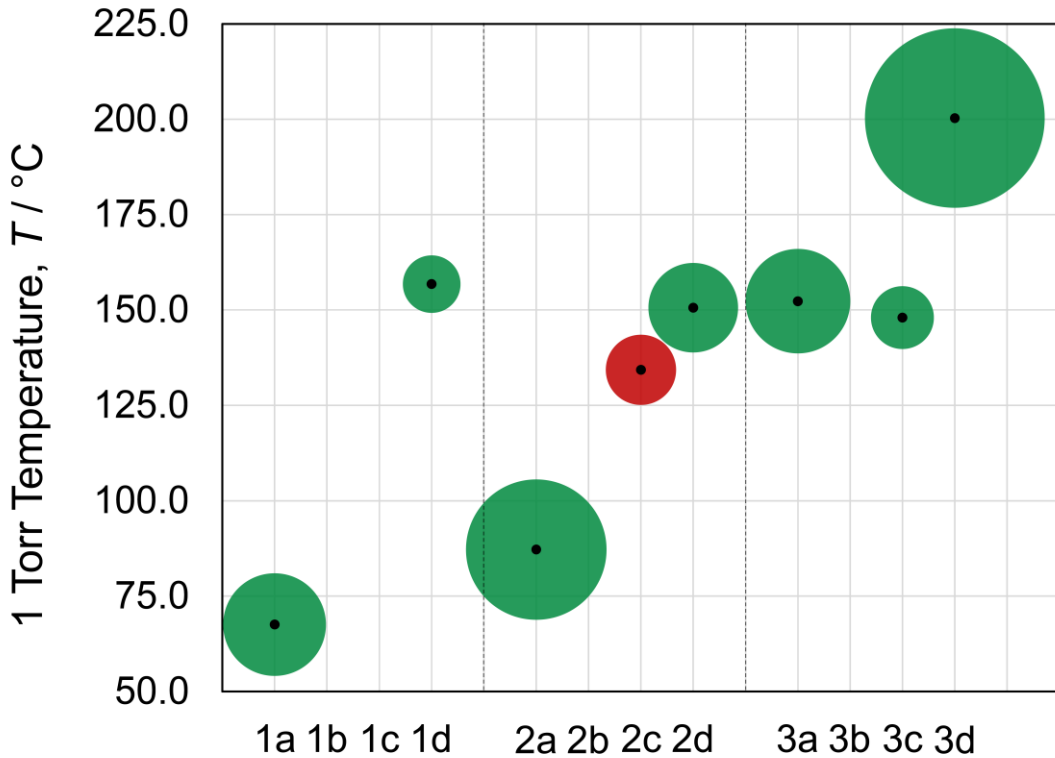


**Figure 5.9** Figure of merit “minefield” plot. Green circles indicate a positive figure of merit while red circles indicate a negative figure of merit. The  $\sigma$  value of each compound is shown as the radius of each circle in arbitrary units.

### 5.3.3 Density Functional Theory

To better understand the reason behind the high figures of merit obtained for phosphine and NHC systems, we undertook a density functional theory (DFT) study of compounds **2a**, **2d**, **3a**, and **3d**. The calculations were first performed using model compounds **2a\***, **2d\***, **3a\***, and **3d\*** where the  $\text{PMe}_3$  and NHC ligands were replaced with proto analogues ( $\text{PH}_3$  and  $\text{N,N}'\text{-dihydroimidazolidin-2-ylidene}$  ( $\text{H}_2\text{-NHC}$ ), to examine the energy required to break the Au-R and Au-L bonds. All calculations were carried out using the  $\omega\text{B97X-D}$  functional<sup>274,275</sup> and the iMCP-SR2 model core potentials and basis sets.<sup>276</sup> Scalar-relativistic model core potentials are known to provide satisfactory description for heavy elements like Au.<sup>277</sup> The dissociation energies of the R<sup>-</sup> and L ligand fragments were determined by calculating the difference in energy between the free ligand in question

and the remaining Au-L or Au-R fragment. Three scenarios were considered: dissociation of the coordinative ligand, forming a neutral R-Au fragment and a neutral L fragment; homolytic cleavage of the R-Au bond resulting in R<sup>•</sup> and •Au-L fragments; and heterolytic cleavage of the R-Au bond resulting in R<sup>-</sup> and <sup>+</sup>Au-L fragments (Table 5.3). Heterolytic cleavage was discounted after considering the results of **3a\*** and **3d\***, because it was consistently the highest energy case and was therefore unlikely to contribute to the first thermolysis events of the molecules. For **2a**, **2d**, **3a**, and **3d**, only dissociation of the neutral L ligand was considered since it is known to be the primary decomposition pathway for alkylgold(I) compounds. It was also the lowest energy case, implying it was the largest contributor to thermal decomposition.

**Table 5.3** Calculated energies and measured decomposition temperatures of the three ligand dissociation cases for model compounds and synthesized compounds.

Compound	Dissociation of coordinative ligand (kJ/mol)	Homolytic cleavage (kJ/mol)	Heterolytic cleavage (kJ/mol)	T <sub>d</sub> (°C) <sup>a</sup>
CH <sub>2</sub> (SiMe <sub>3</sub> )-Au-PH <sub>3</sub> ( <b>2a*</b> )	119	293	-	-
CH <sub>2</sub> (SiMe <sub>3</sub> )-Au-PMe <sub>3</sub> ( <b>2a</b> )	171	-	-	145
CH <sub>2</sub> (SiMe <sub>3</sub> )-Au-H <sub>2</sub> NHC ( <b>2d*</b> )	215	452	-	-
CH <sub>2</sub> (SiMe <sub>3</sub> )-Au- <sup>t</sup> BuNHC ( <b>2d</b> )	221	-	-	184
C <sub>6</sub> F <sub>5</sub> -Au-PH <sub>3</sub> ( <b>3a*</b> )	153	422	727	-
C <sub>6</sub> F <sub>5</sub> -Au-PMe <sub>3</sub> ( <b>3a</b> )	212	-	-	185
C <sub>6</sub> F <sub>5</sub> -Au-H <sub>2</sub> NHC ( <b>3d*</b> )	263	593	665	-
C <sub>6</sub> F <sub>5</sub> -Au- <sup>t</sup> BuNHC ( <b>3d</b> )	277	-	-	300

<sup>a</sup> Onset of self-decomposition as measured by DSC.

The model compounds **2a\***, **2d\***, **3a\***, and **3d\*** mirrored the general trends of thermal stability that were observed experimentally. The energy required for homolytic R-Au bond cleavage increased from CH<sub>2</sub>(SiMe<sub>3</sub>) to C<sub>6</sub>F<sub>5</sub> which reflects the tendency for C<sub>6</sub>F<sub>5</sub> ligands to resist reductive elimination. Exchanging PH<sub>3</sub> for H<sub>2</sub>-NHC resulted in an increase in both Au-L dissociation energy and R-Au homolytic bond cleavage energy, which is due to the relatively higher electron donating ability of the NHC ligand. The Au-L bond dissociation energies increased from CH<sub>2</sub>(SiMe<sub>3</sub>) to C<sub>6</sub>F<sub>5</sub> and from PMe<sub>3</sub> to NHC which is reflective of

the  $\sigma$ -withdrawing capability of the  $C_6F_5$  ligand as well as the increased  $\sigma$ -donor ability of the NHC compared to  $PMes_3$ .

Compounds **2a** and **3a** show significantly higher Au-L bond dissociation energy than **2a\*** and **3a\*** since  $PH_3$  is a much worse  $\sigma$ -donor than  $PMes_3$  due to the electron donating Me groups being directly bound to the ligating atom (P). The change in N-substituents in the NHC compounds has comparatively little effect on the Au-L bond strength since the alkyl group is relatively remote from the ligating C atom. Compounds **2d\*** and **3d\*** were calculated to have Au-L bond dissociation energies that were comparable to **2d** and **3d**.

Thermal stability observed by DSC correlates well to the calculated Au-L bond dissociation energies (Figure 5.10). Since the decomposition of these compounds is known to proceed via the rate-limiting step of Au-L bond dissociation, a linear correlation between the observed decomposition temperature and the calculated Au-L bond dissociation energy is expected and is observed for these compounds. The calculational and experimental thermal results corroborate each other.

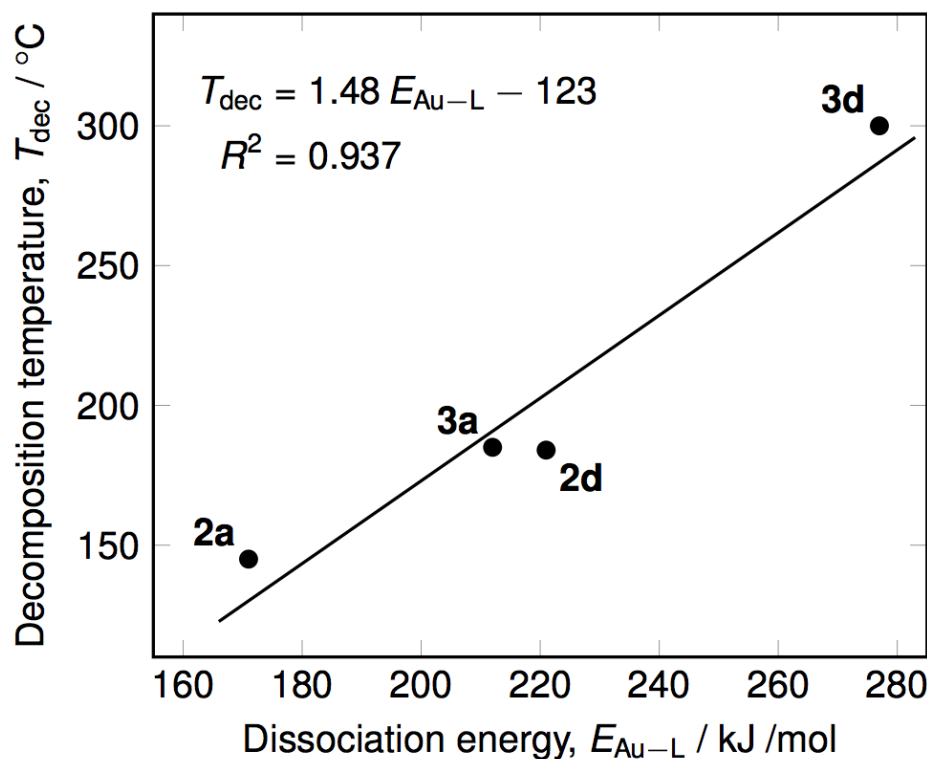


**Figure 5.10** Correlation between *ab initio*-calculated Au-L bond dissociation energies and the observed self-decomposition temperatures for **2a,d** and **3a,d**.

Being able to predict a compound's thermal stability from ligand choice is a useful tool that allows for rational design and theoretical evaluation of different ligand classes before undertaking synthesis and testing. Furthermore, for a single type of ligand, if the nature of alkyl groups has little effect on the overall thermal stability of the compound (such as  $3d^* \approx 3d$ ) then these alkyl groups can be repurposed to introduce volatility or other desirable properties for the potential precursor. The implementation of this strategy is of ongoing interest to us in the further development of vapor deposition precursors for Au and other metals.

## 5.4 Conclusions

A family of 12 gold(I) compounds were synthesized and analyzed for their use as potential precursors for gold metal vapor deposition applications. Single crystal x-ray diffraction was used to structurally characterize 8 of these compounds to assess the effect of the anionic and coordinative ligands on intermolecular interactions. Compounds with Me and  $\text{CH}_2(\text{SiMe}_3)$  ligands displayed fewer intermolecular interactions than those with  $\text{C}_6\text{F}_5$  ligands due to the ability of the latter to undergo  $\pi$ -stacking and p- $\pi$  interactions. These strong intermolecular interactions resulted in a substantial decrease in the volatility of  $\text{C}_6\text{F}_5$ -containing compounds. Ylide compound **3b** displays more intermolecular interactions than TMS-ylide compound **3c**, which translated to an increase in volatility of TMS-ylide containing compounds vs. their ylide counterparts. TGA and DSC were used to assess the volatility and thermal stability of the family of compounds, and it was found that  $\text{CH}_2(\text{SiMe}_3)$  provides higher kinetic stability than Me. NHC and  $\text{C}_6\text{F}_5$  ligands provide substantially higher thermodynamic stability to the gold(I) center, but adversely affected volatility. To deconvolute these effects we derived a figure of merit with which the viability of all gold(I) compounds may be compared for vapor deposition. **3d** has the highest merit, but is only useful at high delivery temperatures, while **2a** is most suitable for lower delivery temperature applications. We are currently studying these two compounds as precursors in ALD process development. Using DFT we found a linear correlation between the calculated Au-L bond strength and the measured onset of self-decomposition as measured by DSC. In future studies, using this computational method for the design of

vapor deposition precursors should inform the process of potential candidates prior to undertaking chemical synthesis.

## 5.5 Experimental Details

### Crystallography

A crystal of the desired compound was mounted from Paratone-N oil on an appropriately sized MiTeGen MicroMount. The data were collected on a Bruker APEX II charge-coupled-device (CCD) diffractometer, with an Oxford 700 Cryocool sample cooling device. The instrument was equipped with graphite-monochromated Mo K $\alpha$  radiation ( $\lambda = 0.71073 \text{ \AA}$ ; 30 mA, 50 mV), with MonoCap X-ray source optics. For data collection, four  $\omega$ -scan frame series were collected with 0.5° wide scans, 5-30 second frames and 366 frames per series at varying  $\varphi$  angles ( $\varphi = 0^\circ, 90^\circ, 180^\circ, 270^\circ$ ). Data collection, unit cell refinement, data processing and multi-scan absorption correction were applied using the APEX2<sup>11</sup> or APEX3<sup>12</sup> software packages. The structures were solved using SHELXT<sup>13</sup> and all non-hydrogen atoms were refined anisotropically with SHELXL<sup>14</sup> using a combination of shelXle<sup>15</sup> and OLEX2<sup>16</sup> graphical user interfaces. Unless otherwise noted, all hydrogen atom positions were idealized and ride on the atom to which they were attached. The final refinement included anisotropic temperature factors on all non-hydrogen atoms. Figures were made using UCSF-Chimera.<sup>17</sup> Crystal structures were deposited in the (reference numbers 1915544, 1915545, 1915546, 1915547, 1915548, 1915549, 1915550, and 1915551)

### Thermogravimetric analysis (TGA) and differential scanning calorimetry (DSC)

TGA was performed on a TA Instruments Q500 instrument which was housed in a nitrogen-filled MBraun glovebox. The purge gas during TGA and DSC experiments was nitrogen gas of (99.999 %, 5.0) and (99.998 %, 4.8) respectively. In a typical TGA experiment  $10.000 \pm 2$  mg of analyte was placed in a platinum pan whose mass was

monitored by the instrument during the analysis. For DSC experiments, due to the volatile nature of the analytes and their decomposition products, mass loadings greater than 1.000 mg often lead to a rupturing of the hermetically sealed aluminum pans. Thus, small mass loadings of  $0.300 \pm 0.200$  mg were used for typical DSC experiment. DSC samples were hermetically sealed in aluminum pans inside the glovebox before analysis. Both TGA and DSC temperature ramp rates were  $10.0\text{ }^{\circ}\text{C} / \text{min}$ . Langmuir vapour pressure equations were derived from TGA data using a previously reported method with Cu(tmhd)<sub>2</sub> as the calibrant.<sup>70,278</sup>

## Synthetic procedures

**CAUTION:** After the preparation of this manuscript we learned that suspensions of pentafluorophenyllithium<sup>279</sup> have been reported to explode violently upon standing even when prepared at  $-78\text{ }^{\circ}\text{C}$  under inert atmosphere. People performing this reaction have been seriously injured by such explosions in other laboratories. We must therefore recommend that the reaction to prepare pentafluorophenyllithium and its subsequent use to synthesize (THT)AuC<sub>6</sub>F<sub>5</sub> be performed behind a blast shield in dilute conditions, or not at all. An alternate route using the safer analogous Grignard reagent should produce the desired product, but we have not attempted that reaction.

## General details

All manipulations were performed under an inert atmosphere of dry nitrogen gas using an MBraun Labmaster 130 glovebox or standard Schlenk techniques unless otherwise stated. All synthesized compounds were treated as light sensitive materials during synthetic procedures, and were stored at  $-35\text{ }^{\circ}\text{C}$  in the freezer of a glovebox. NMR spectra were collected at room temperature on a Bruker 300 MHz or a Jeol 400 MHz spectrometer and were referenced to an internal standard of tetramethylsilane (TMS) in the case of CDCl<sub>3</sub> or residual protio solvent signal in the case of C<sub>6</sub>D<sub>6</sub> (7.16 ppm relative to TMS). C<sub>6</sub>D<sub>6</sub> was purchased from Aldrich and was degassed using freeze-pump-thaw cycles and subsequently stored over activated 4 Å molecular sieves under inert gas. Trimethylmethylenephosphorane (Ylide), trimethyl(trimethylsilylmethylene) phosphorane

(TMS-ylide),<sup>280</sup> (THT)AuCl, (PMe<sub>3</sub>)AuCl,<sup>281</sup> and N,N'-di-tert-butylimidazolidinium chloride<sup>282</sup> were prepared according to literature procedures. Trimethylphosphine (PMe<sub>3</sub>) was prepared by the literature procedure using iodomethane instead of bromomethane.<sup>283</sup> Tetrahydrothiophene pentafluorophenylgold(I), (THT)AuC<sub>6</sub>F<sub>5</sub>, was prepared using chloropentafluorophenylbenzene instead of the bromo- derivative.<sup>279</sup> Methylolithium (1.6 M in diethyl ether), (trimethylsilyl)methylolithium (1.0 M in pentane), n-butyllithium (1.6 M in hexanes), potassium hydride (30 weight % dispersion in mineral oil), sodium tert-butoxide, tetrahydrofuran (anhydrous), pentane (anhydrous), and dichloromethane (anhydrous) were purchased from Aldrich and used as received. Diethyl ether, hexanes, and toluene were purchased from VWR chemicals and purified using an MBraun solvent purification system prior to use. Gold metal (99.99 %) was purchased at market price and was used as received. HAuCl<sub>4</sub> • x H<sub>2</sub>O was obtained from the digestion of gold metal by chlorine gas as previously described, with the modification of using up to 1 Troy ounce of (32.2 g) gold metal in 250 mL of H<sub>2</sub>O.

Elemental analysis was performed by the elemental analysis laboratory at the Université de Montréal.

#### *N,N'-di-tert-butylimidazolidin-2-ylidene*

A modification of a previously reported procedure was used.<sup>267</sup> To a 500 mL Schlenk flask containing 150 mL of tetrahydrofuran was added 10.01 g (45.76 mmol) of dry N,N-di-tert-butylimidazolidinium chloride, 4.366 g (181.9 mmol) of sodium hydride, 0.262 g (2.7 mmol) of sodium *tert*-butoxide, and a teflon-coated stir bar. This white suspension was sealed and stirred overnight, at which time it was filtered through a plug of celite in a medium frit into a 250 mL Schlenk flask which contained a Teflon-coated stir bar. Approximately two-thirds of the THF was removed by evaporation, then the flask was cooled in a -20 °C bath and the residual tetrahydrofuran was stripped under high vacuum leaving an off-white solid in the flask which is the frozen free carbene product. This solid was then purified by static high-vacuum (10 mTorr) distillation using a warm water pot flask (approx. 40 °C) and a -78 °C receiving flask. The clear crystalline solid caught in the receiving flask was allowed to warm to room temperature and liquify under nitrogen, and

was then transferred into a glovebox for storage in a -35 °C freezer. Yield = 7.501 g, 90%. NMR analysis was consistent with the reported literature values.

*Trimethylphosphine methylgold(I), (PMe<sub>3</sub>)AuMe (1a)*

4.151 g (13.46 mmol) of (PMe<sub>3</sub>)AuCl was suspended in 150 mL of diethyl ether and cooled to -78 °C. Then, 8.41 mL (1.6 M in diethyl ether, 13.50 mol) of methylolithium solution was then added dropwise over 5 minutes. The resulting yellow suspension was stirred at -78 °C for 1 hour, and was then allowed to warm to room temperature, at which point the colour of the suspension had returned to white. Then the reaction mixture was cooled to 0 °C and quenched by adding 20 mL of distilled and degassed water dropwise. The resulting biphasic mixture was separated, and the ethereal layer was dried over MgSO<sub>4</sub>. After filtration the solvent was removed using a rotary evaporator leaving a slightly purple crystalline solid. This material was purified by sublimation (50 °C, 10 mTorr) which gave a white crystalline solid and left a purple-brown coloured residue in the pot. Yield 3.007 g (77 %).

T<sub>m</sub> (DSC) = 62 °C

**<sup>1</sup>H-NMR** (300 MHz, C<sub>6</sub>D<sub>6</sub>): δ = 1.22 (d, <sup>3</sup>J<sub>H-P</sub> = 8.7 Hz, 3H, Au-CH<sub>3</sub>), 0.62 (d, <sup>2</sup>J<sub>H-P</sub> = 8.7 Hz, 9H, P-CH<sub>3</sub>).

**<sup>13</sup>C-NMR** (75.5 MHz, C<sub>6</sub>D<sub>6</sub>): δ = 15.56 (d, <sup>1</sup>J<sub>C-P</sub> = 29.1 Hz, P-CH<sub>3</sub>), 8.73 (d, <sup>2</sup>J<sub>C-P</sub> = 102.5 Hz, Au-CH<sub>3</sub>).

**<sup>31</sup>P-NMR** (121.5 MHz, C<sub>6</sub>D<sub>6</sub>): δ = 13.84.

*Methyl(trimethylphosphoniummethylide)gold(I), (Ylide)AuMe (1b)*

Modifying the previously reported procedure,<sup>280</sup> 0.144 g (0.501 mmol) of (PMe<sub>3</sub>)AuMe was dissolved in 10 mL of diethyl ether. To this was added 0.050 mL (ρ = 0.90 g / mL, 0.499 mmol) of neat trimethylphosphoniummethylide (ylide) which immediately produced a white precipitate. This suspension was stirred for one hour, filtered through a medium frit, washed with 3 x 1 mL of cold pentane and dried under high vacuum. Yield = 0.131 g, 87% of a white powder.

$T_m$  (DSC) = N/A. Decomposition begins at 107 °C

**$^1\text{H-NMR}$**  (300 MHz, C<sub>6</sub>D<sub>6</sub>):  $\delta$  = 1.16 (d,  $^4J_{H-P}$  = 1.2 Hz, 3H, Au-CH<sub>3</sub>), 0.61 (d,  $^2J_{H-P}$  = 12.9 Hz, 9H, P-CH<sub>3</sub>), 0.45 (d,  $^2J_{H-P}$  = 12.6 Hz, 2H, P-CH<sub>2</sub>).

**$^{13}\text{C-NMR}$**  (75.5 MHz, C<sub>6</sub>D<sub>6</sub>):  $\delta$  = 18.02 (d,  $^1J_{C-P}$  = 36.8 Hz, P-CH<sub>2</sub>), 15.11 (d,  $^1J_{C-P}$  = 56.2 Hz, P-CH<sub>3</sub>), 2.52 (d,  $^3J_{C-P}$  = 3.0 Hz, Au-CH<sub>3</sub>).

**$^{31}\text{P-NMR}$**  (121.5 MHz, C<sub>6</sub>D<sub>6</sub>):  $\delta$  = 25.83.

*Methyl(trimethylphosphonium(trimethylsilyl)methylide)gold(I), (TMS-ylide)AuMe (**1c**)*

Modifying the previously reported procedure,<sup>264</sup> 0.106 g (0.368 mmol) of (PMe<sub>3</sub>)AuMe was dissolved in 10 mL of diethyl ether. To this was added 0.114 g (0.702 mmol) trimethylphosphonium(trimethylsilyl)methylide (TMS-ylide) and the solution was stirred overnight. The solvent was removed under high vacuum resulting leaving an off-white solid. Yield = 0.117 g (84 %). Crystals of this compound suitable for X-ray crystallography were grown from hot toluene.

$T_m$  (DSC) = 129 °C (dec.)

**$^1\text{H-NMR}$**  (300 MHz, C<sub>6</sub>D<sub>6</sub>):  $\delta$  = 1.16 (d,  $^4J_{H-P}$  = 0.9 Hz, 3H, Au-CH<sub>3</sub>), 0.72 (d,  $^2J_{H-P}$  = 12.6 Hz, 9H, P-CH<sub>3</sub>), 0.25 (s, 9H, Si-CH<sub>3</sub>), -0.17 (d,  $^2J_{H-P}$  = 18.3 Hz, 1H, P-CH<sub>3</sub>).

**$^{13}\text{C-NMR}$**  (75.5 MHz, C<sub>6</sub>D<sub>6</sub>):  $\delta$  = 17.20 (d,  $^1J_{C-P}$  = 54.1 Hz, P-CH<sub>3</sub>), 16.58 (d,  $^1J_{C-P}$  = 33.4 Hz, P-CH<sub>2</sub>), 4.46 (d,  $^3J_{C-P}$  = 4.7 Hz, Si-CH<sub>3</sub>), 0.77 (d,  $^3J_{C-P}$  = 4.0 Hz, Au-CH<sub>3</sub>).

**$^{31}\text{P-NMR}$**  (121.5 MHz, C<sub>6</sub>D<sub>6</sub>):  $\delta$  = 20.00

\*Note: The excess of TMS-ylide was necessary to push the reaction to completion. 1:1 stoichiometry only converted 75 % of **1a** to **1c**.

*N,N'-di-tert-butylimidazolidin-2-ylidene methylgold(I), (NHC)AuMe (**1d**)*

1.554 g (5.40 mmol) of (PMe<sub>3</sub>)AuMe and 1.588 g (8.71 mmol) of N,N'-di-tert-butylimidazolidin-2-ylidene were added to 30 mL of toluene and the solution was stirred overnight. The next day, a very small amount of purple precipitate was present in the otherwise clear solution. The solution was filtered through a medium frit, and the solvent

was removed under high vacuum. Then the material was dried for a further 3 hours at 40 °C under high vacuum to remove excess free NHC. The resulting slightly purple white solid was then purified by sublimation (100 °C, 10 mTorr) giving a white crystalline solid. Yield = 2.002 g (94%). Crystals of this compound suitable for X-ray crystallography were grown from hot toluene.

T<sub>m</sub> (DSC) = 111 °C

**Elemental analysis:** Calcd. for C<sub>12</sub>H<sub>25</sub>N<sub>2</sub>Au: C, 36.51; H, 6.34; N, 7.10. Found: C, 36.60; H, 6.26; N, 6.97.

**<sup>1</sup>H-NMR** (300 MHz, C<sub>6</sub>D<sub>6</sub>): δ = 2.65 (s, 4H, CH<sub>2</sub>-CH<sub>2</sub>), 1.52 (s, 18H, C(CH<sub>3</sub>)<sub>3</sub>), 1.20 (s, 3H, Au-CH<sub>3</sub>).

**<sup>13</sup>C-NMR** (75.5 MHz, C<sub>6</sub>D<sub>6</sub>): δ = 221.74 (s, NCN), 56.15 (s, C(CH<sub>3</sub>)<sub>3</sub>), 46.31 (s, CH<sub>2</sub>-CH<sub>2</sub>), 31.35 (s, C(CH<sub>3</sub>)<sub>3</sub>), -3.26 (s, Au-CH<sub>3</sub>).

\*Note: The excess of free NHC was used in order to push the reaction to completion. At 1:1 stoichiometry, the starting material **1a** persisted in ~25 mol %, and it is difficult to purify **1d** when **1a** is present.

*Trimethylphosphine trimethylsilylmethylgold(I), (PMe<sub>3</sub>)AuNeosSi (**2a**)*

7.80 g (25.3 mmol) of (PMe<sub>3</sub>)AuCl was suspended in 150 mL of diethyl ether and cooled to -78 °C. (Trimethylsilyl)methyl lithium solution (1.0 M, 27.8 mL) was added dropwise over 20 minutes. The mixture was then allowed to warm to room temperature. The resulting white suspension was then cooled to 0 °C and quenched by adding 25 mL of distilled and degassed water dropwise over 10 minutes. The resulting biphasic mixture was separated, the brown-purple coloured water layer was washed with 2 x 20 mL of diethyl ether, and the organic layers were combined and dried over MgSO<sub>4</sub>. After filtration, the solvent was removed using a rotary evaporator and the resulting dark purple liquid was purified by vacuum distillation (90 °C, 10 mTorr) giving a clear liquid. Yield 7.735 g (85 %).

**<sup>1</sup>H-NMR** (300 MHz, C<sub>6</sub>D<sub>6</sub>): δ = 0.84 (d, <sup>3</sup>J<sub>H-P</sub> = 10.5 Hz, 2H, Au-CH<sub>2</sub>), 0.54 (d, <sup>2</sup>J<sub>H-P</sub> = 8.7 Hz, 9H, P-CH<sub>3</sub>), 0.51 (s, 9H, Si-CH<sub>3</sub>).

**<sup>13</sup>C-NMR** (75.5 MHz, C<sub>6</sub>D<sub>6</sub>):  $\delta$  = 15.58 (d,  $^2J_{C-P}$  = 85.7 Hz, Au-CH<sub>2</sub>), 15.39 (d,  $^1J_{C-P}$  = 29.6 Hz, P-CH<sub>3</sub>), 4.78 (d,  $^4J_{C-P}$  = 2.2 Hz, Si-CH<sub>3</sub>).

**<sup>31</sup>P-NMR** (121.5 MHz, C<sub>6</sub>D<sub>6</sub>):  $\delta$  = 12.70

*Trimethylsilylmethyl(trimethylphosphoniummethylide)gold(I), (Ylide)AuNeoSi (2b)*

Modifying the previously reported procedure,<sup>264</sup> 0.481 g (1.33 mmol) of (PMe<sub>3</sub>)AuNeoSi was dissolved in 10 mL of diethyl ether in a glovebox. To this was added 0.233 mL ( $\rho$  = 0.90 g / mL. 2.33 mmol) of neat trimethylphosphoniummethylide (ylide). The resulting solution was stirred overnight and then dried under high vacuum leaving a white solid. Yield 0.411 g (82 %). Crystals of this compound suitable for X-ray crystallography were grown from hot toluene.

T<sub>m</sub> (DSC) = 134 °C

**<sup>1</sup>H-NMR** (300 MHz, C<sub>6</sub>D<sub>6</sub>):  $\delta$  = 0.62 (br, 2H, Au-CH<sub>2</sub>), 0.61 (d,  $^2J_{H-P}$  = 12.9 Hz, 9H, P-CH<sub>3</sub>), 0.57 (s, 9H, Si-CH<sub>3</sub>), 0.42 (d,  $^2J_{H-P}$  = 12.6 Hz, 2H, P-CH<sub>2</sub>).

**<sup>13</sup>C-NMR** (75.5 MHz, C<sub>6</sub>D<sub>6</sub>):  $\delta$  = 17.36 (d,  $^1J_{C-P}$  = 37.3 Hz, P-CH<sub>2</sub>), 15.04 (d,  $^1J_{C-P}$  = 56.2 Hz, P-CH<sub>3</sub>), 8.47 (d,  $^3J_{C-P}$  = 2.6 Hz, Au-CH<sub>2</sub>), 5.01 (s, Si-CH<sub>3</sub>).

**<sup>31</sup>P-NMR** (121.5 MHz, C<sub>6</sub>D<sub>6</sub>):  $\delta$  = 25.51

*Trimethylsilylmethyl(trimethylphosphonium(trimethylsilyl)methylide)gold(I),*

*(TMS-ylide)AuNeoSi (2c)*

Modifying the previously reported procedure,<sup>264</sup> 0.121 g (0.335 mmol) of (PMe<sub>3</sub>)AuNeoSi and 0.062 g (0.382 mmol) of trimethylphosphonium(trimethylsilyl)methylide (TMS-ylide) were dissolved in 4 mL of pentane. The resulting solution was stirred overnight, and then the solvent was removed leaving a white crystalline solid which was purified by recrystallization from a minimum of pentane. Yield 0.084 g (56 %).

T<sub>m</sub> (DSC) = 66 °C

**<sup>1</sup>H-NMR** (300 MHz, C<sub>6</sub>D<sub>6</sub>):  $\delta$  = 0.72 (d,  $^2J_{H-P}$  = 12.6 Hz, 9H, P-CH<sub>3</sub>), 0.65 (br, 2H, Au-CH<sub>2</sub>), 0.54 (s, 9H, NeoSi-CH<sub>3</sub>), 0.23 (s, 9H, TMS-ylide-Si-CH<sub>3</sub>), -0.21 (d,  $^2J_{H-P}$  = 18.3 Hz, 1H, P-CH).

**$^{13}\text{C-NMR}$**  (75.5 MHz,  $\text{C}_6\text{D}_6$ ):  $\delta$  = 16.72 (d,  $^1J_{\text{C-P}} = 42.7$  Hz, P-CH<sub>3</sub>), 15.97 (d,  $^1J_{\text{C-P}} = 27.6$  Hz, P-CH<sub>2</sub>), 6.94 (s, Au-CH<sub>2</sub>), 4.37 (s, NeoSi-CH<sub>3</sub>), 4.03 (d,  $^3J_{\text{C-P}} = 3.6$  Hz, TMS-ylide-Si-CH<sub>3</sub>).

**$^{31}\text{P-NMR}$**  (121.5 MHz,  $\text{C}_6\text{D}_6$ ):  $\delta$  = 19.80

*N,N'-di-tert-butylimidazolidin-2-ylidene trimethylsilylmethylgold(I), (NHC)AuNeoSi (2d)*

1.551 g (4.31 mmol) of (PM<sub>3</sub>)AuNeoSi and 0.794 g (4.36 mmol) of N,N'-di-tert-butylimidazolidin-2-ylidene were added to 30 mL of diethyl ether and the solution was stirred overnight. The next day, the solution was evaporated to dryness leaving a white crystalline material. Then the material was dried for a further 3 hours at 40 °C under high vacuum to remove excess free NHC. The resulting white solid was then purified by sublimation (100 to 120 °C, 10 mTorr) giving a white crystalline solid. Yield = 1.754 g (87 %). Crystals of this compound suitable for X-ray crystallography were grown from hot toluene.

$T_m$  (DSC) = 105 °C

**Elemental analysis:** Calcd for C<sub>15</sub>H<sub>33</sub>N<sub>2</sub>AuSi: C, 38.58; H, 7.07; N, 6.00. Found: C, 37.95; H, 6.97; N, 5.67.

**$^1\text{H-NMR}$**  (300 MHz,  $\text{C}_6\text{D}_6$ ):  $\delta$  = 2.58 (s, 4H, CH<sub>2</sub>-CH<sub>2</sub>), 1.49 (s, 18H, C(CH<sub>3</sub>)<sub>3</sub>), 0.75 (s, 2H, Au-CH<sub>2</sub>), 0.54 (s, 9H, Si-CH<sub>3</sub>).

**$^{13}\text{C-NMR}$**  (75.5 MHz,  $\text{C}_6\text{D}_6$ ):  $\delta$  = 219.94 (NCN), 56.15 (C(CH<sub>3</sub>)<sub>3</sub>), 46.23 (CH<sub>2</sub>-CH<sub>2</sub>), 31.26 (C(CH<sub>3</sub>)<sub>3</sub>), 4.30 (Si-CH<sub>3</sub>), 3.30 (Au-CH<sub>2</sub>).

*Trimethylphosphine pentafluorophenylgold(I), (PM<sub>3</sub>)AuC<sub>6</sub>F<sub>5</sub> (3a)*

0.550 g (1.22 mmol) of (THT)AuC<sub>6</sub>F<sub>5</sub> and 0.142 g (1.82 mmol) of PM<sub>3</sub> were dissolved in 15 mL of diethyl ether and the solution was stirred overnight. The next day the solution was filtered through a medium frit and evaporated to dryness leaving a white solid. This solid was then purified by sublimation (100 to 120 °C, 10 mTorr). Yield = 0.503 g (94 %). Crystals of this compound suitable for x-ray crystallography were grown from hot toluene.

$T_m$  (DSC) = 151 °C

**$^1\text{H-NMR}$**  (300 MHz,  $\text{CDCl}_3$ ):  $\delta$  = 1.51 (d,  $^2J_{H-P}$  = 8.1 Hz, 9H, P- $\text{CH}_3$ ).

**$^{13}\text{C-NMR}$**  (75.5 MHz,  $\text{CDCl}_3$ ):  $\delta$  = 15.64 (d,  $^1J_{C-P}$  = 35.2 Hz, P- $\text{CH}_3$ ).

**$^{31}\text{P-NMR}$**  (121.5 MHz,  $\text{CDCl}_3$ ):  $\delta$  = -5.00.

**$^{19}\text{F-NMR}$**  (282.4 MHz,  $\text{CDCl}_3$ ):  $\delta$  = -118.51 (m, *ortho*-F), -160.63 (t,  $^3J_{F-F}$  = 19.8 Hz, *para*-F), -164.49 (m, *meta*-F).

*Pentafluorophenyl(trimethylphosphoniummethylide)gold(I), (*Ylide*)AuC<sub>6</sub>F<sub>5</sub> (3b)*

0.120 g (0.273 mmol) of  $(\text{PMe}_3)\text{AuC}_6\text{F}_5$  and 0.031 mL ( $\rho$  = 0.90 g / mL. 0.310 mmol) of trimethylphosphoniummethylide (ylide) were added to 5 mL of diethyl ether which caused a white precipitate to form. The mixture was stirred for one hour and then filtered, washes with diethyl ether and dried under high vacuum giving a white crystalline solid. This material was purified by recrystallization from hot toluene, which also produced crystals that were suitable for x-ray crystallography. Yield = 0.080 g (65 %).

$T_m$  (DSC) = 157 °C

**Elemental analysis:** Calcd for C<sub>10</sub>H<sub>11</sub>AuF<sub>5</sub>P: C, 26.42; H, 2.42. Found: C, 26.59; H, 2.50.

**$^1\text{H-NMR}$**  (300 MHz, C<sub>6</sub>D<sub>6</sub>):  $\delta$  = 0.56 (d,  $^2J_{H-P}$  = 9.6 Hz, 2H, P- $\text{CH}_2$ ), 0.42 (d,  $^2J_{H-P}$  = 9.6 Hz, 9H, P- $\text{CH}_3$ ).

**$^{13}\text{C-NMR}$**  (75.5 MHz, C<sub>6</sub>D<sub>6</sub>):  $\delta$  = 14.26 (d,  $^1J_{C-P}$  = 42.7 Hz, P- $\text{CH}_3$ ), 12.52 (d,  $^1J_{C-P}$  = 28.9 Hz, P- $\text{CH}_2$ ).

**$^{31}\text{P-NMR}$**  (121.5 MHz, C<sub>6</sub>D<sub>6</sub>):  $\delta$  = 26.50.

**$^{19}\text{F-NMR}$**  (282.4 MHz, C<sub>6</sub>D<sub>6</sub>):  $\delta$  = -116.23 (m, *ortho*-F), -161.29 (t,  $^3J_{F-F}$  = 15.2 Hz, *para*-F), -162.86 (m, *meta*-F).

\*Note: We observed that reaction of (THT)AuC<sub>6</sub>F<sub>5</sub> with trimethylphosphoniummethylide produced a mixture of phosphonium ylide-containing solids (soluble in DMSO-d<sub>6</sub>) which included the desired product. Therefore we chose to use  $(\text{PMe}_3)\text{AuC}_6\text{F}_5$  instead and found the results to be much more reproducible.

*Pentafluorophenyl(trimethylphosphonium(trimethylsilyl)methylide)gold(I), (TMS-ylide)AuC<sub>6</sub>F<sub>5</sub> (3c)*

0.478 g (2.94 mmol) of trimethylphosphonium(trimethylsilyl)methylide (TMS-ylide) was added to a solution of 1.070 g (2.45 mmol) (THT)AuC<sub>6</sub>F<sub>5</sub> in 10 mL of diethyl ether causing a white precipitate to form immediately. The suspension was allowed to stir overnight and was then stripped of its solvent, re-dissolved in a minimum of toluene, filtered, and left in a -35 °C freezer overnight to recrystallize. Clear platelike crystals were observed in a mother liquor of brown-red solution. These crystals were of suitable quality for crystallography (0.211 g, 33%). A second batch of crystals was grown by concentrating the mother liquor by 2/3, filtering and storing at -35 °C overnight (0.114 g, 18%). Yield = 0.325 g (51 %).

T<sub>m</sub> (DSC) = 150 °C

**Elemental analysis:** Calcd for C<sub>13</sub>H<sub>19</sub>AuF<sub>5</sub>PSi: C, 29.64; H, 3.61. Found: C, 29.37; H, 3.76.

**<sup>1</sup>H-NMR** (300 MHz, C<sub>6</sub>D<sub>6</sub>): δ = 0.62 (d, <sup>2</sup>J<sub>H-P</sub> = 12.6 Hz, 9H, P-CH<sub>3</sub>), 0.17 (s, Si-CH<sub>3</sub>), 0.03 (d, <sup>2</sup>J<sub>H-P</sub> = 18.3 Hz, 1H, P-CH).

**<sup>13</sup>C-NMR** (75.5 MHz, C<sub>6</sub>D<sub>6</sub>): δ = 16.61 (d, <sup>1</sup>J<sub>C-P</sub> = 57.2 Hz, P-CH<sub>3</sub>), 13.20 (d, <sup>1</sup>J<sub>C-P</sub> = 36.4 Hz, P-CH), 4.14 (d, <sup>3</sup>J<sub>C-P</sub> = 4.6 Hz, Si-CH<sub>3</sub>).

**<sup>31</sup>P-NMR** (121.5 MHz, C<sub>6</sub>D<sub>6</sub>): δ = 23.65.

**<sup>19</sup>F-NMR** (282.4 MHz, C<sub>6</sub>D<sub>6</sub>): δ = -118.67 (m, *ortho*-F), -163.36 (t, <sup>3</sup>J<sub>F-F</sub> = 20.3 Hz, *para*-F), -165.07 (m, *meta*-F).

*N,N'-di-tert-butylimidazolidin-2-ylidene pentafluorophenylgold(I), (NHC)AuC<sub>6</sub>F<sub>5</sub> (3d)*

0.278 g (0.615 mmol) of (THT)AuC<sub>6</sub>F<sub>5</sub> and 0.168 g (0.922 mmol) of N,N'-di-tert-butylimidazolidin-2-ylidene were dissolved in 5 mL of diethyl ether and the solution was stirred overnight. The solvent was removed, and the residue was extracted with 3 x 3 mL of toluene, filtered, and dried under high vacuum at 40 °C for at least 3 hours to remove excess free NHC, leaving a slightly purple solid. This material was purified by sublimation

(110 to 130 °C, 10 mTorr) which gave a white crystalline solid on the cold finger and a purple residue in the pot. Crystals suitable for x-ray crystallography were grown from hot toluene. Yield = 0.292 g (89%).

T<sub>m</sub> (DSC) = 177 °C

**Elemental analysis:** Calcd for C<sub>17</sub>H<sub>22</sub>AuF<sub>5</sub>N<sub>2</sub>: C, 37.33; H, 4.026; N, 5.13. Found: C, 37.42; H, 4.15; N, 4.99.

**<sup>1</sup>H-NMR** (300 MHz, C<sub>6</sub>D<sub>6</sub>): δ = 2.55 (s, 4H, CH<sub>2</sub>-CH<sub>2</sub>), 1.42 (s, 18H, C(CH<sub>3</sub>)<sub>3</sub>).

**<sup>13</sup>C-NMR** (75.5 MHz, C<sub>6</sub>D<sub>6</sub>): δ = 211.05 (NCN), 56.44 (C(CH<sub>3</sub>)<sub>3</sub>), 46.21 (CH<sub>2</sub>-CH<sub>2</sub>), 31.25 (C(CH<sub>3</sub>)<sub>3</sub>).

**<sup>19</sup>F-NMR** (282.4 MHz, C<sub>6</sub>D<sub>6</sub>): δ = -117.46 (m, *ortho*-F), -162.16 (t, <sup>3</sup>J<sub>F-F</sub> = 20.1 Hz, *para*-F), -165.12 (m, *meta*-F).

## 5.6 Supporting Information

Vapour pressure curves

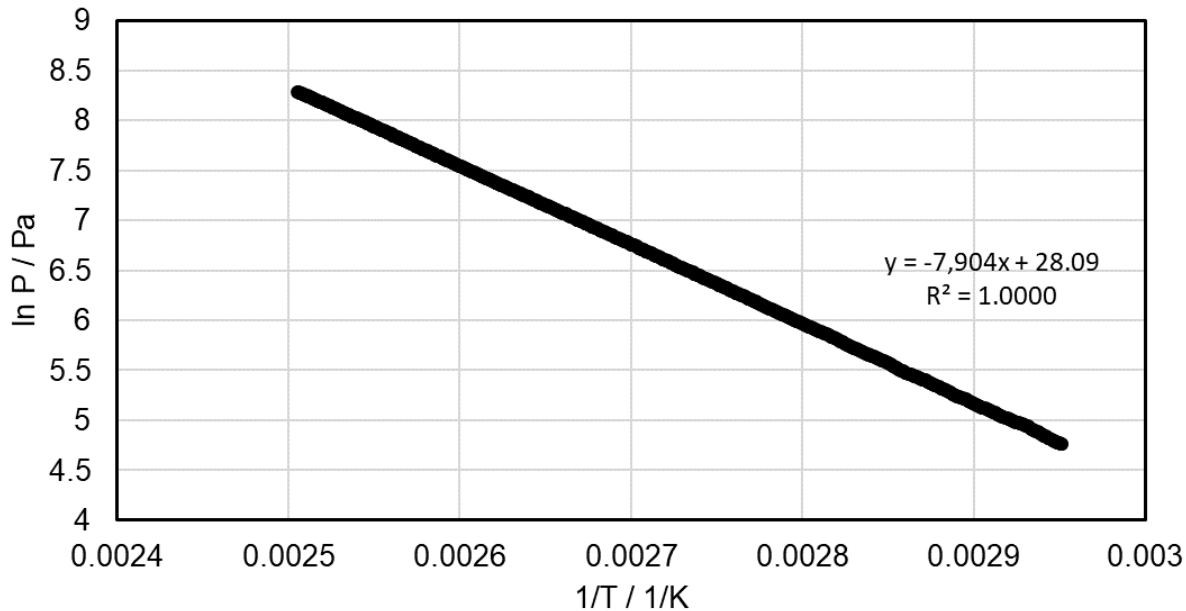


Figure S-5.11 Vapour pressure curve of **1a**,  $T_1$   $\text{Torr} = 68$   $^\circ\text{C}$

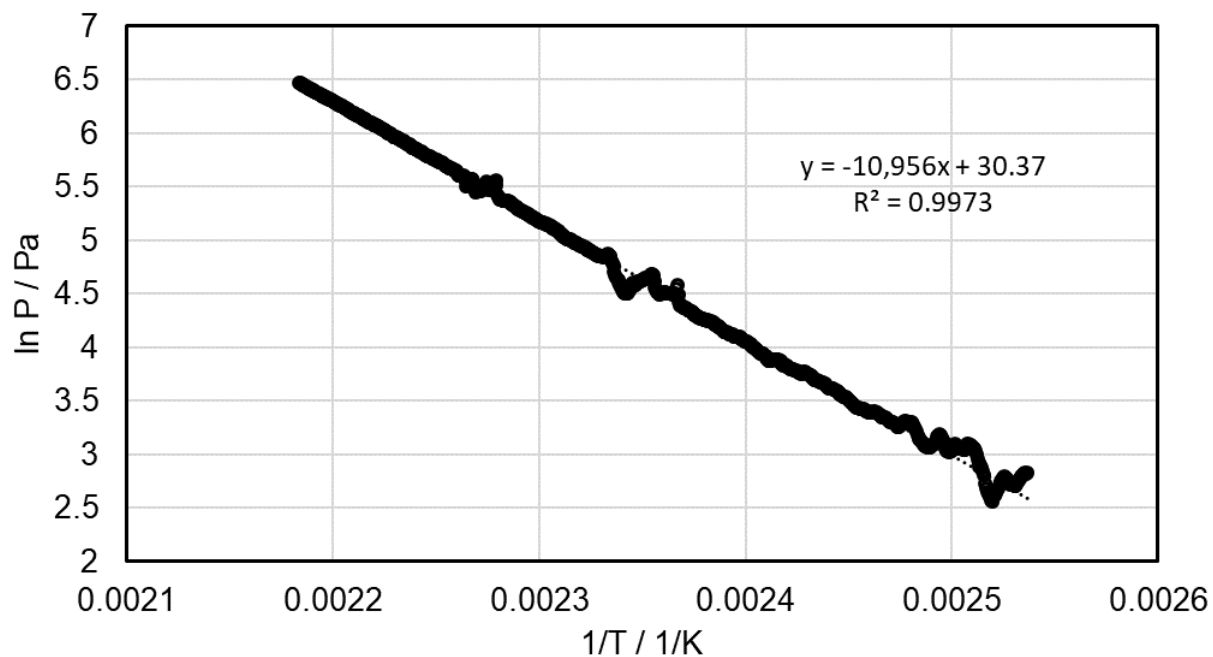


Figure S-5.12 Vapour pressure curve of **1d**,  $T_1$   $\text{Torr} = 157$   $^\circ\text{C}$

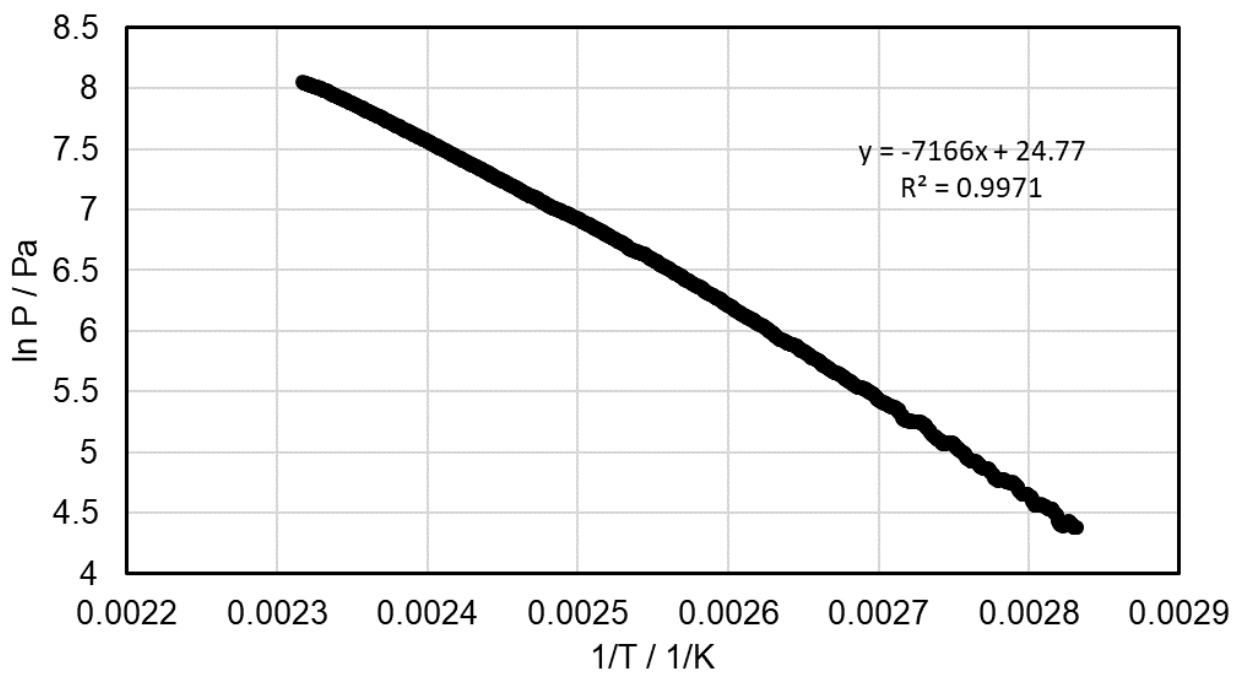


Figure S-5.13 Vapour pressure curve of **2a**,  $T_1$   $\text{Torr} = 87$   $^\circ\text{C}$

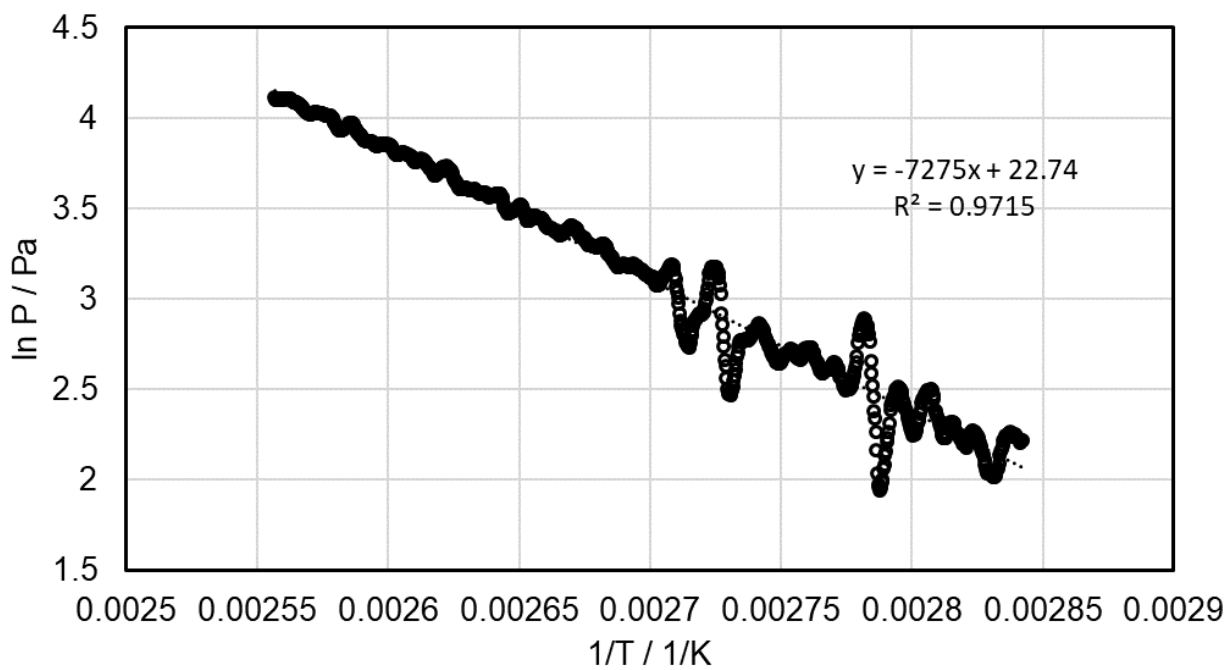


Figure S-5.14 Vapour pressure curve of **2c**,  $T_1$   $\text{Torr} = 134$   $^\circ\text{C}$

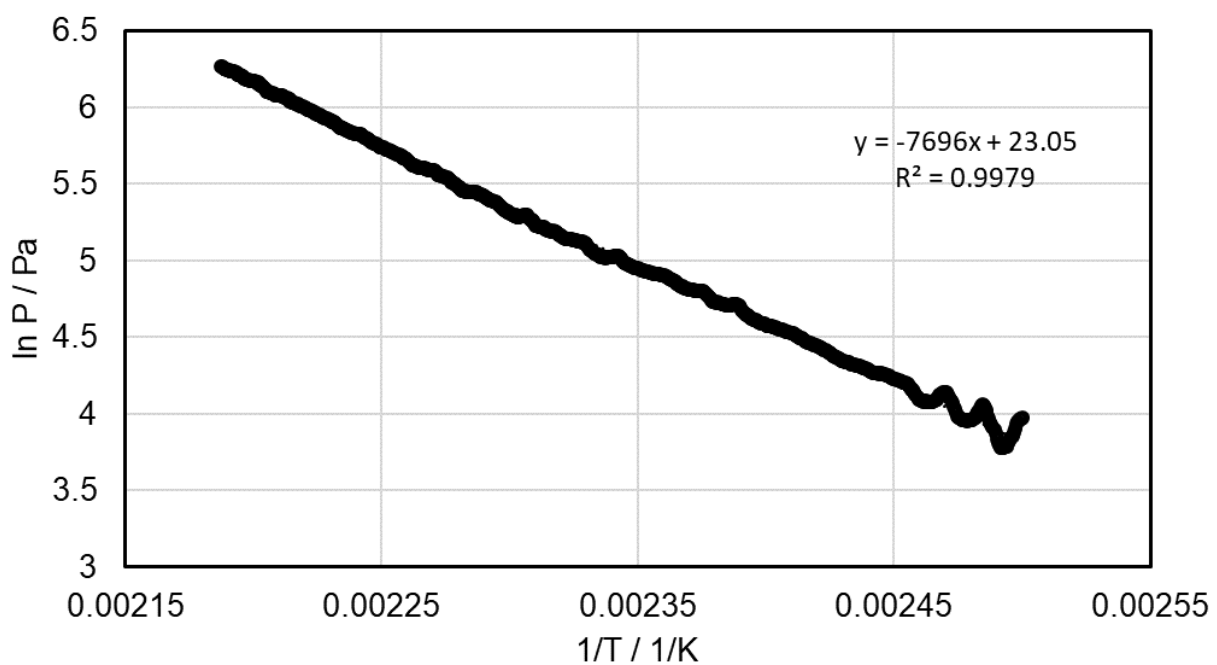


Figure S-5.15 Vapour pressure curve of **2d**,  $T_1$  Torr = 150 °C

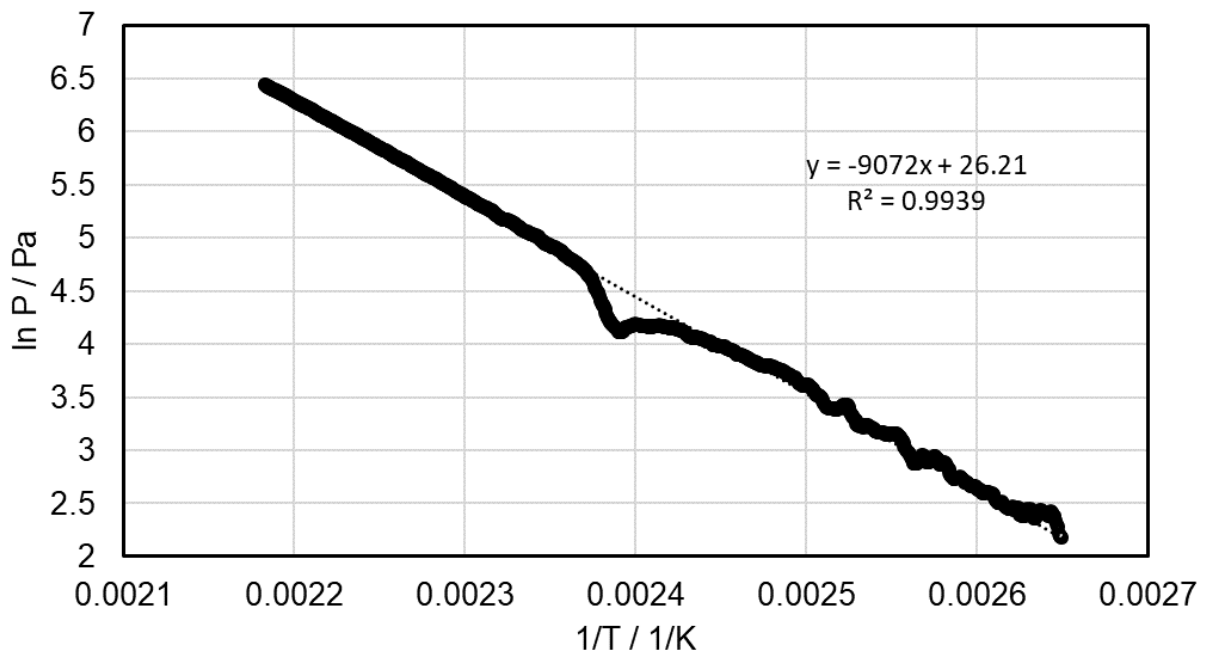
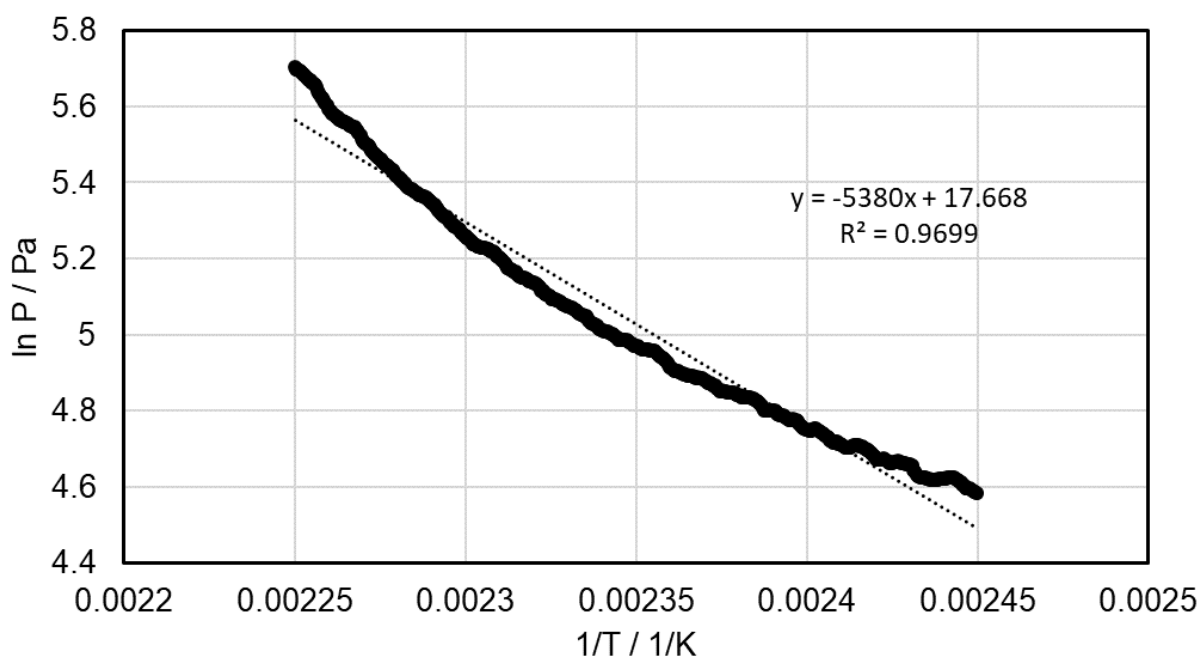
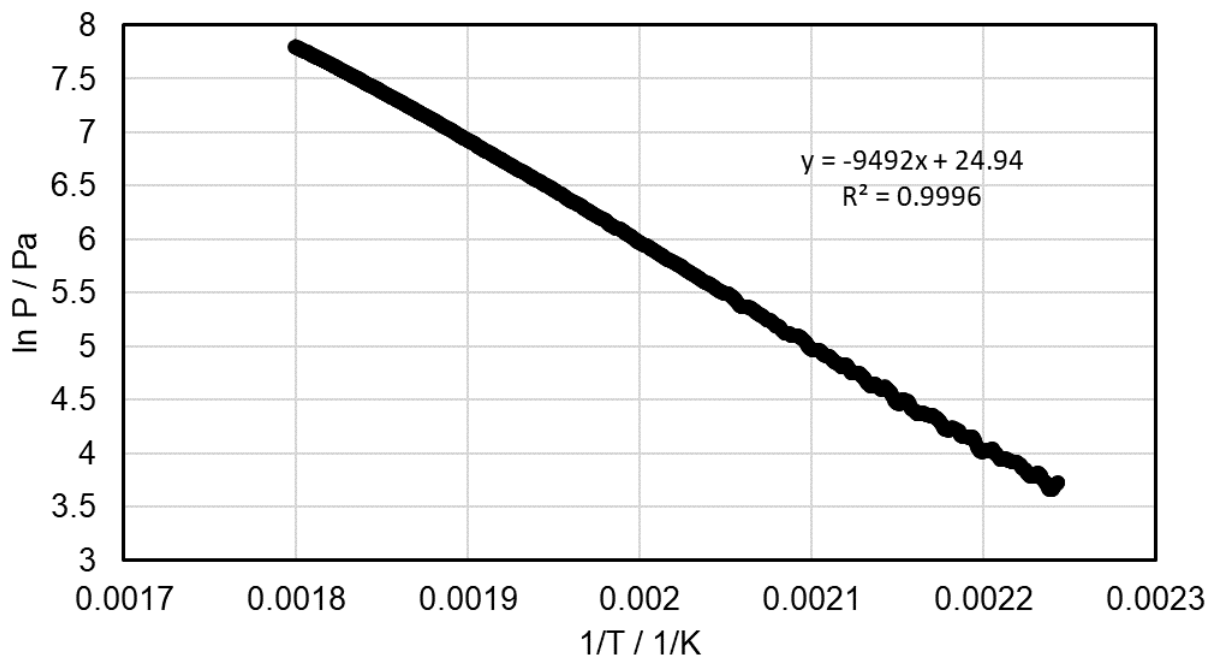


Figure S-5.16 Vapour pressure curve of **3a**,  $T_1$  Torr = 152 °C



**Figure S-5.17** Vapour pressure curve of **3c**,  $T_1 \text{ Torr} = 148 \text{ }^\circ\text{C}$



**Figure S-5.18** Vapour pressure curve of **3d**,  $T_1 \text{ Torr} = 200 \text{ }^\circ\text{C}$

## Differential Scanning Calorimetry

Black traces correspond to heat flow and orange traces correspond to the 1<sup>st</sup> derivative of heat flow. Decomposition points were determined by finding the point at which the heat flow of the system had increased to 5 % of the total height of the decomposition exotherm.

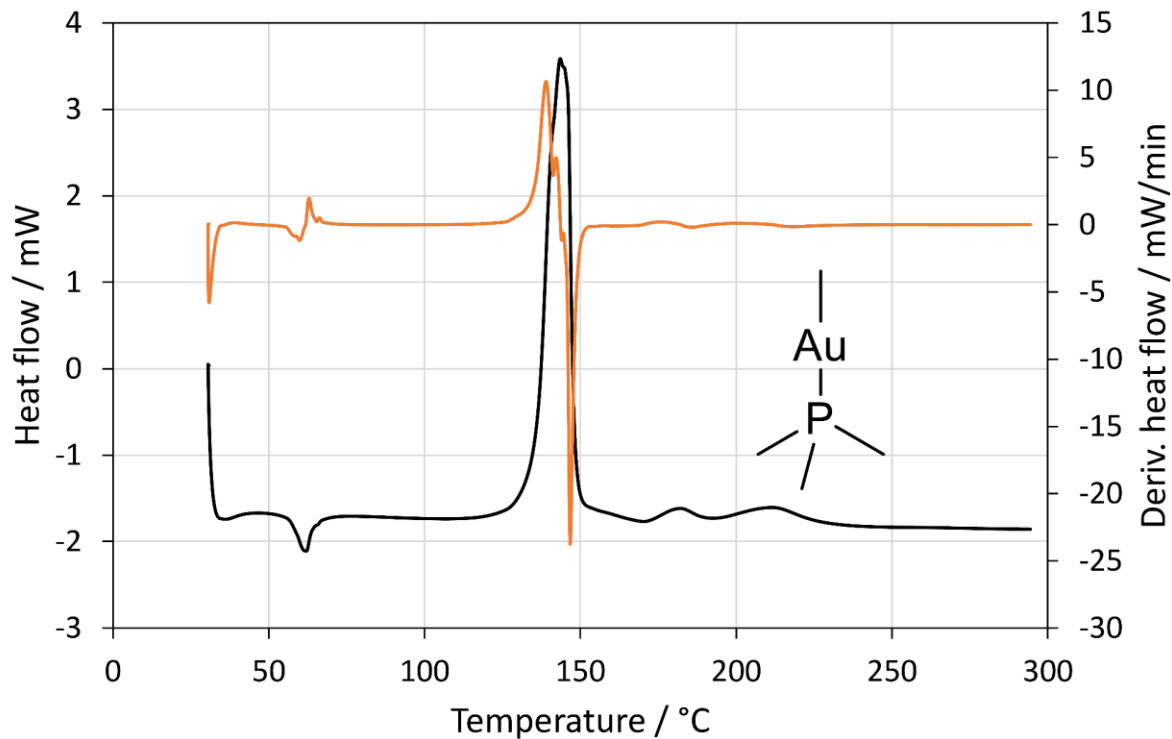


**Figure S-5.19** Differential scanning calorimetry (exotherms up) of **1a**,  $T_m = 62\text{ }^\circ\text{C}$ ,  $T_{dec} = 130\text{ }^\circ\text{C}$

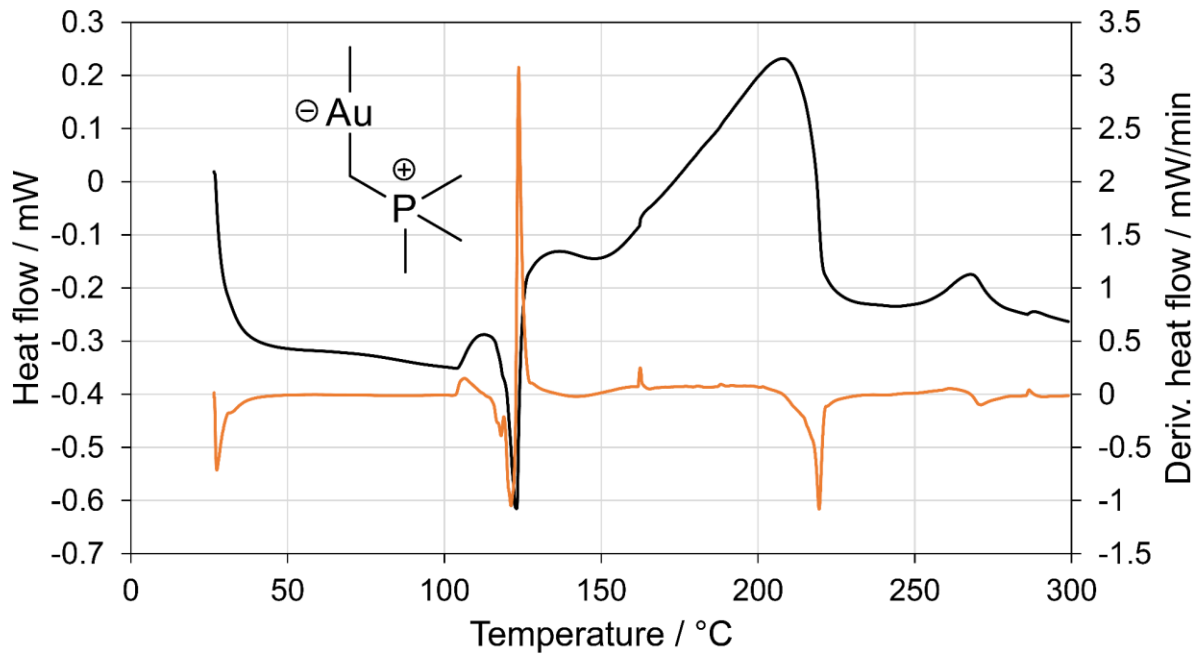


**Figure S-5.20** Differential scanning calorimetry (exotherms up) of **1b**,  $T_{\text{dec}} = 107$  °C

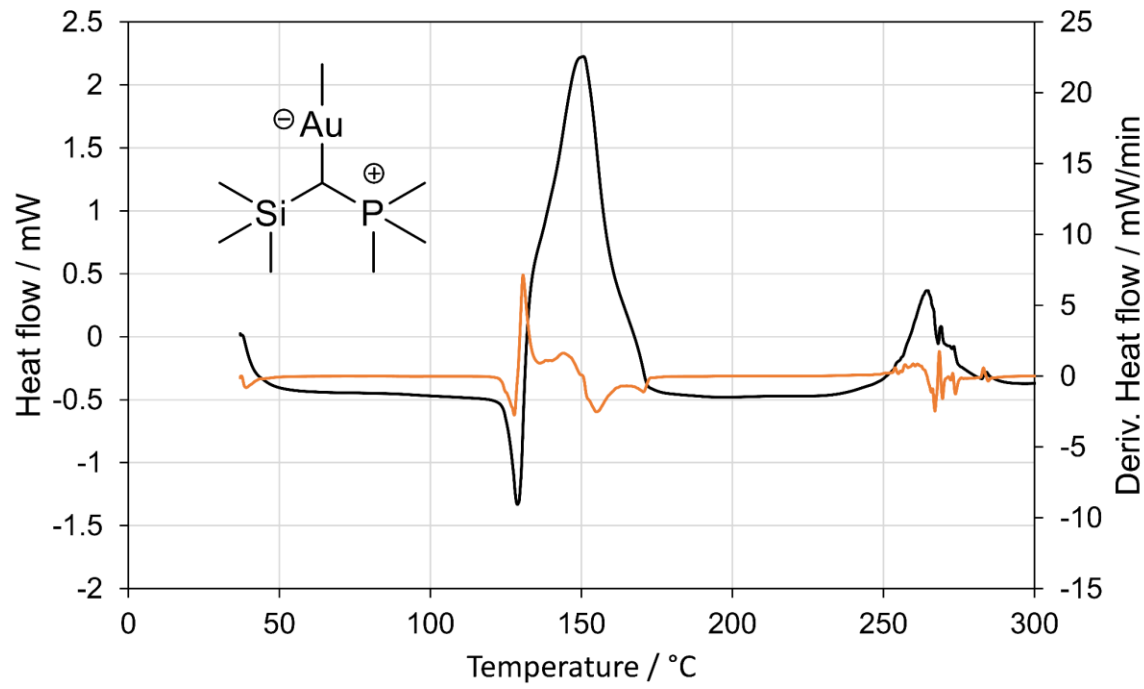


**Figure S-5.21** Differential scanning calorimetry (exotherms up) of **1c**,  $T_m$  (dec.) = 129 °C,  $T_{\text{dec}} = 129$  °C

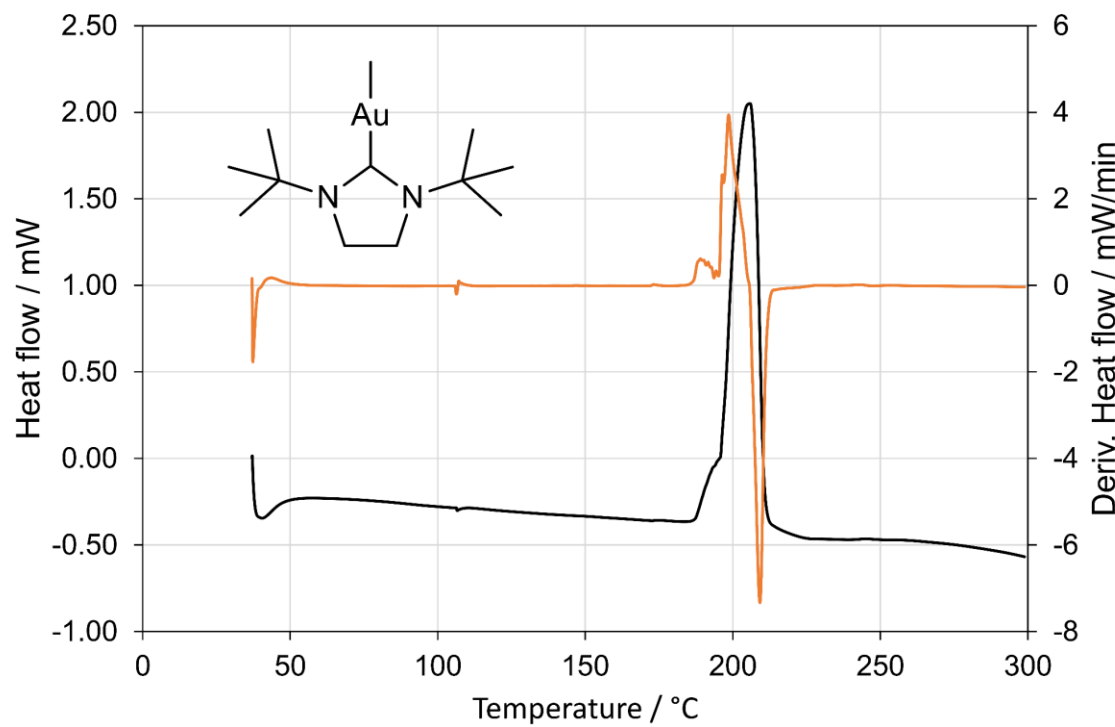


**Figure S-5.22** Differential scanning calorimetry (exotherms up) of **1d**,  $T_m = 111\text{ }^\circ\text{C}$ ,  $T_{dec} = 189\text{ }^\circ\text{C}$

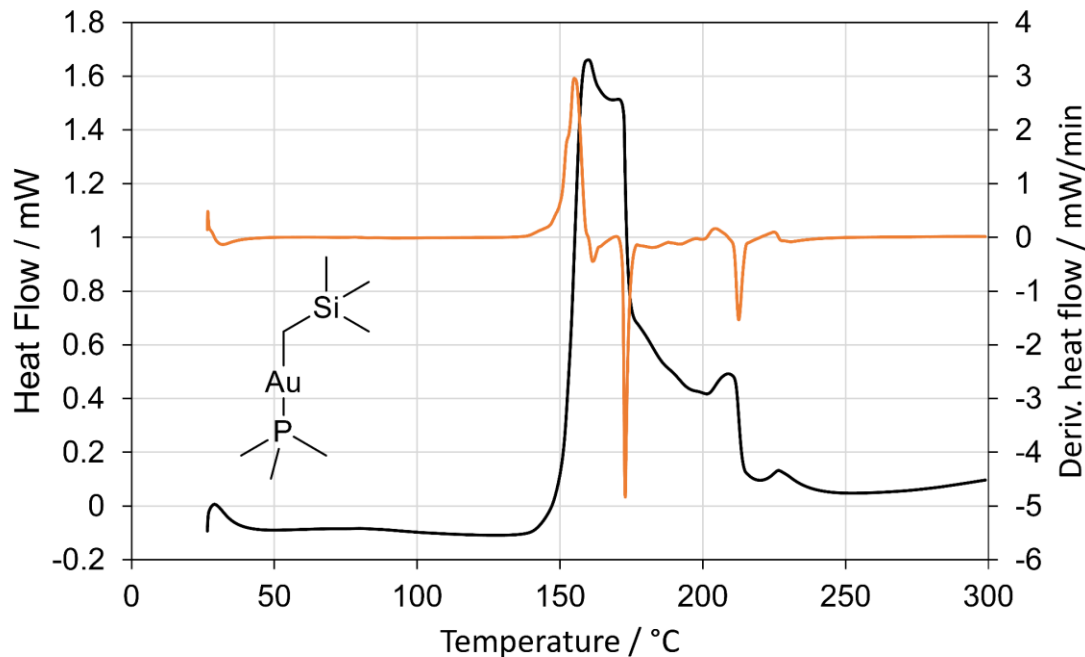


**Figure S-5.23** Differential scanning calorimetry (exotherms up) of **2a**,  $T_{dec} = 146\text{ }^\circ\text{C}$

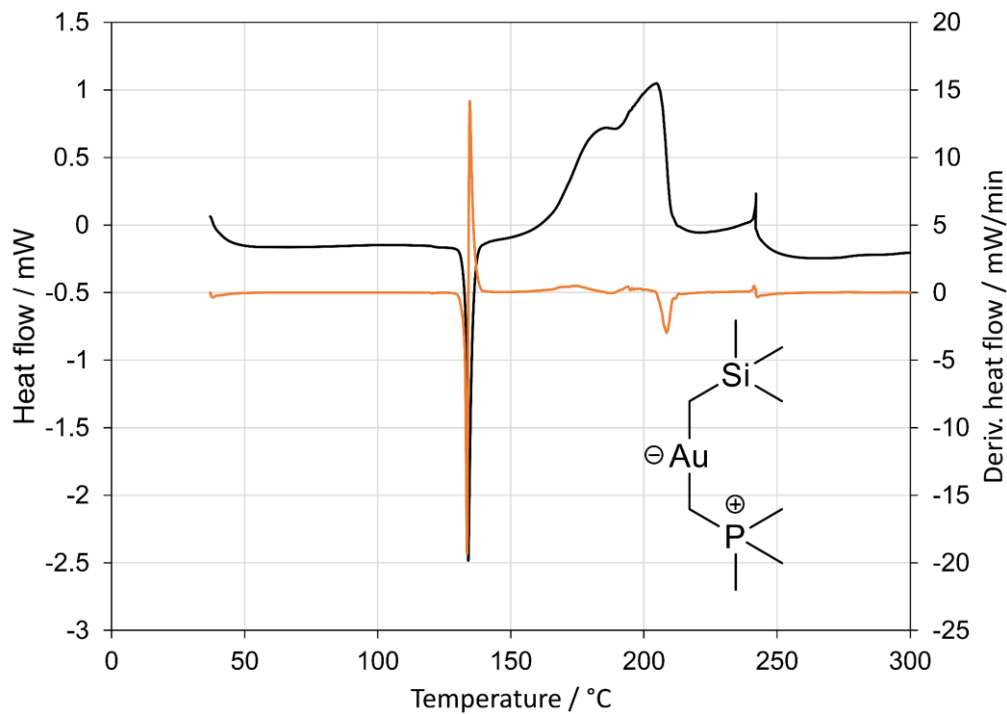


**Figure S-5.24** Differential scanning calorimetry (exotherms up) of **2b**,  $T_m = 134\text{ }^\circ\text{C}$ ,  $T_{dec} = 152\text{ }^\circ\text{C}$

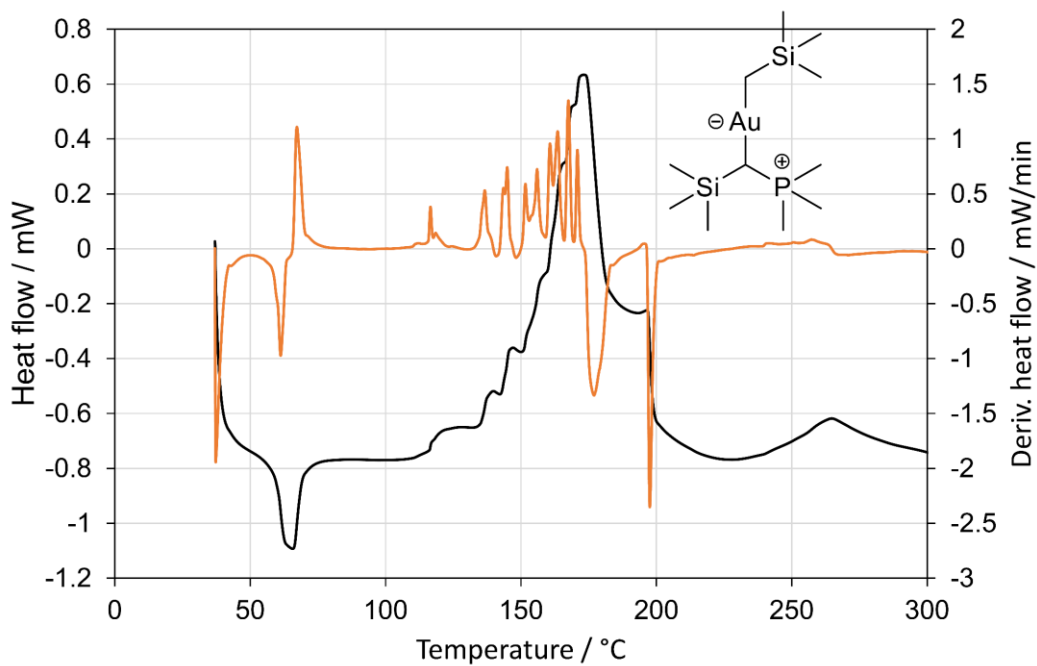


**Figure S-5.25** Differential scanning calorimetry (exotherms up) of **2c**,  $T_m = 66\text{ }^\circ\text{C}$ ,  $T_{dec} = 118\text{ }^\circ\text{C}$

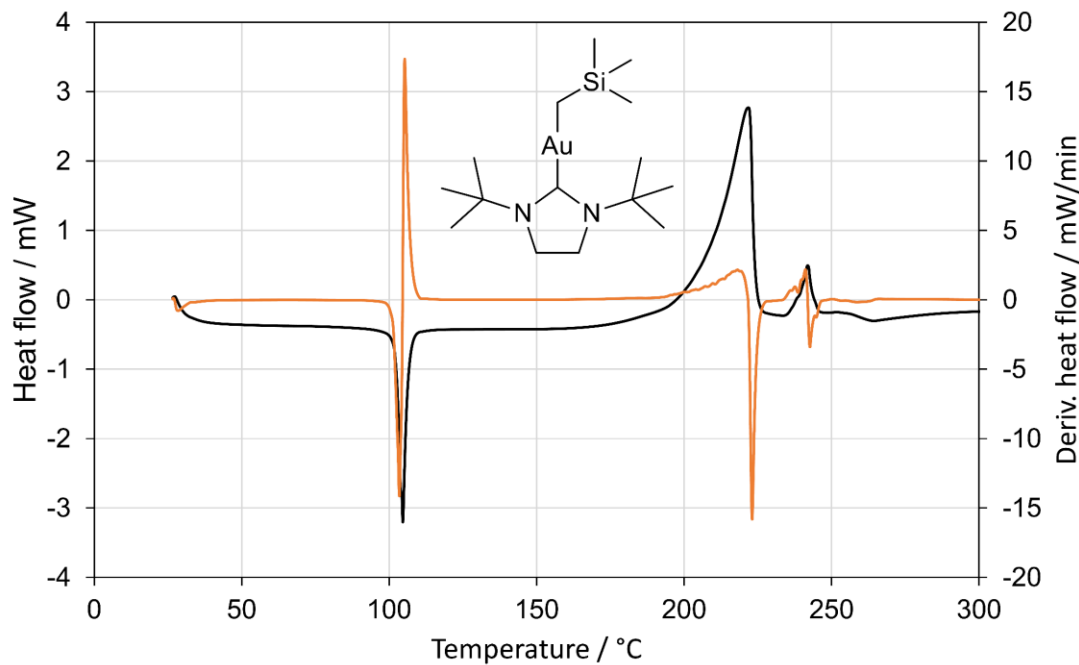


**Figure S-5.26** Differential scanning calorimetry (exotherms up) of **2d**,  $T_m = 105\text{ }^\circ\text{C}$ ,  $T_{dec} = 184\text{ }^\circ\text{C}$

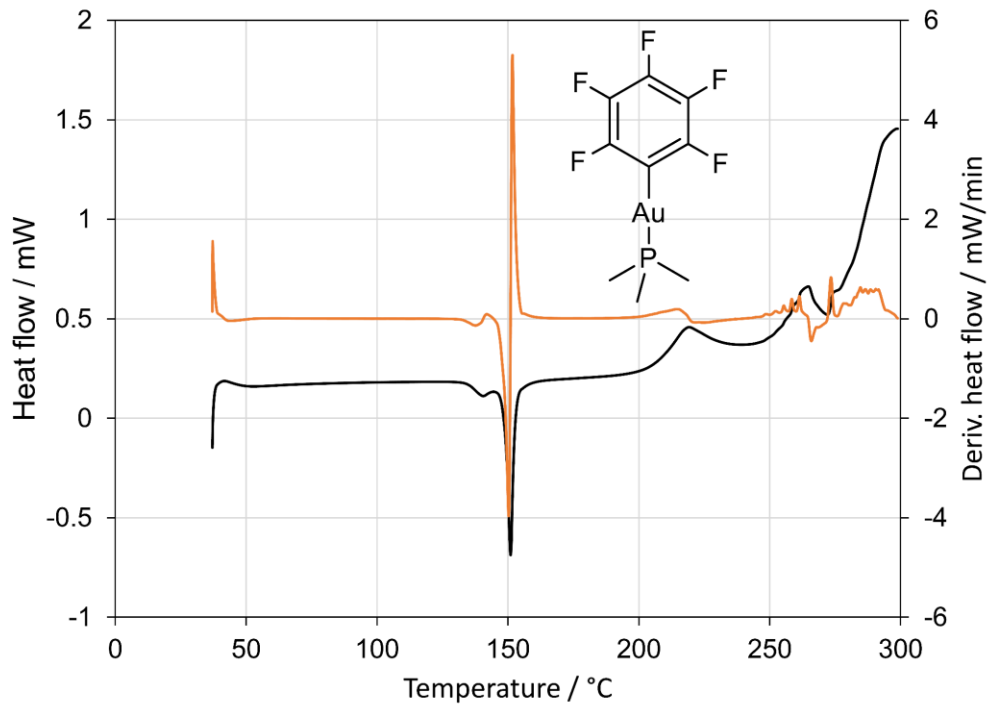


**Figure S-5.27** Differential scanning calorimetry (exotherms up) of **3a**,  $T_m = 151\text{ }^\circ\text{C}$ ,  $T_{dec} = 185\text{ }^\circ\text{C}$

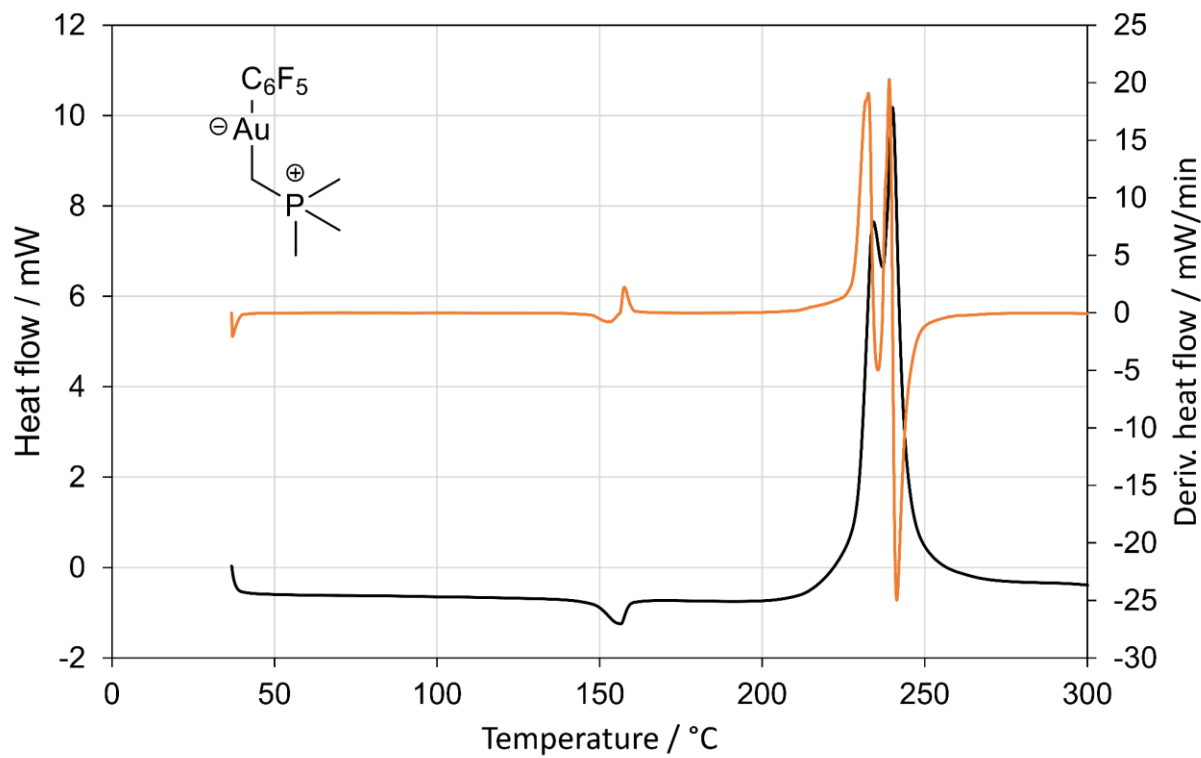


**Figure S-5.28** Differential scanning calorimetry (exotherms up) of **3b**,  $T_m = 157^\circ\text{C}$ ,  $T_{\text{dec}} = 220^\circ\text{C}$

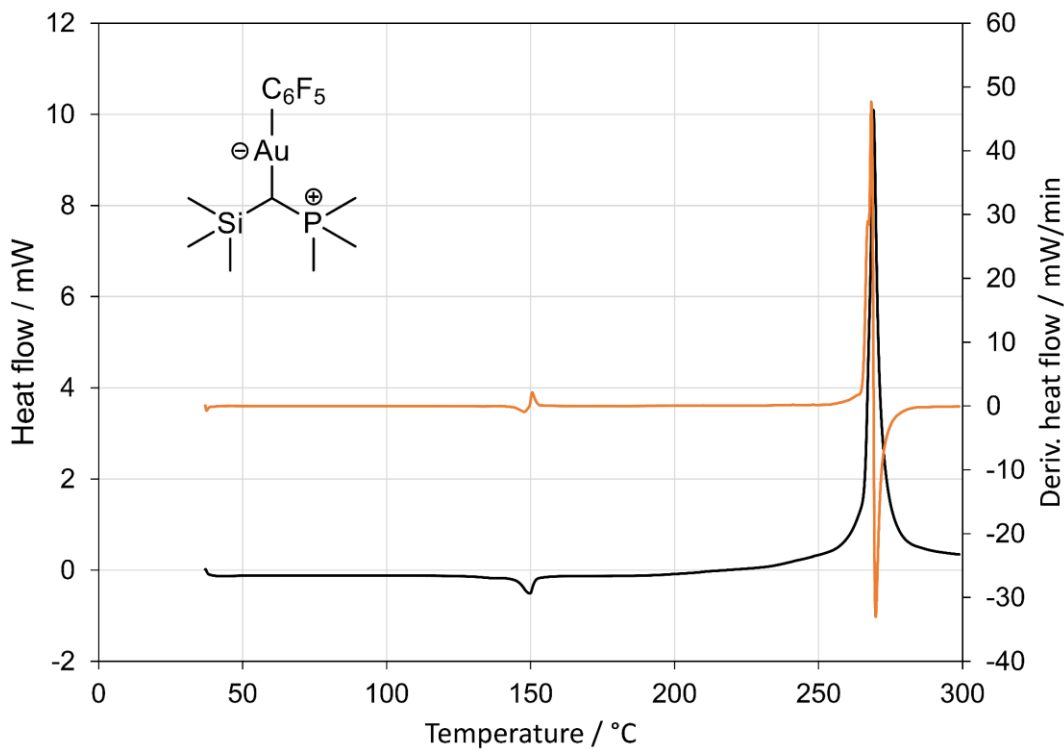


**Figure S-5.29** Differential scanning calorimetry (exotherms up) of **3c**,  $T_m = 150\text{ }^\circ\text{C}$ ,  $T_{dec} = 253\text{ }^\circ\text{C}$

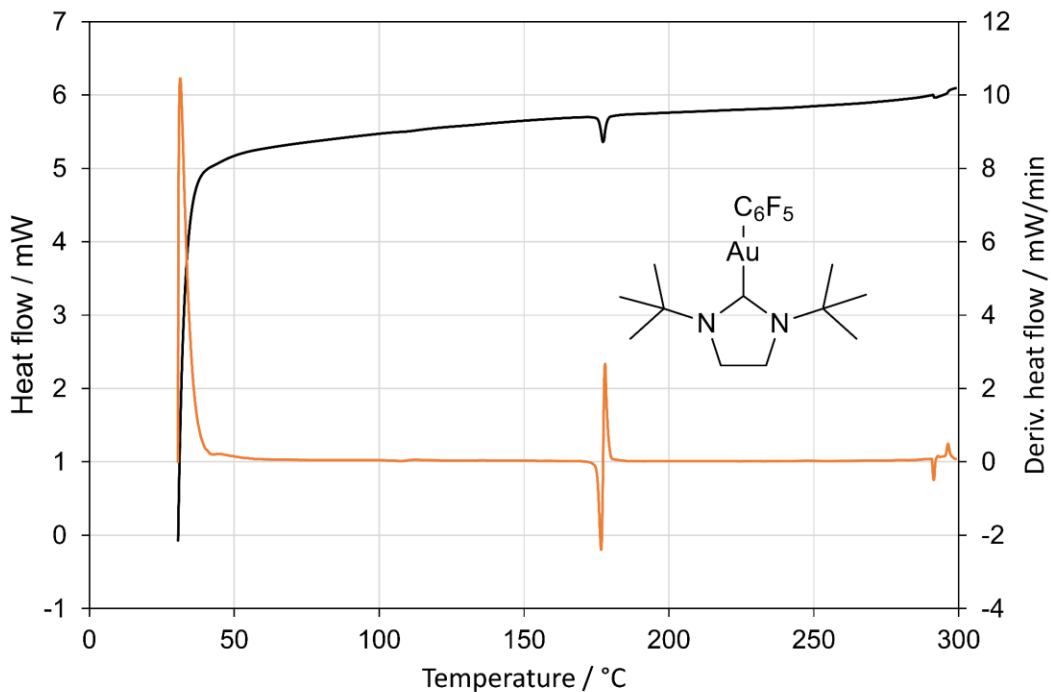


**Figure S-5.30** Differential scanning calorimetry (exotherms up) of **3d**,  $T_m = 177\text{ }^\circ\text{C}$ ,  $T_{dec} = 300\text{ }^\circ\text{C}$



# **Chapter 6 *In-situ* monitoring of the chemisorption behavior of gold vapour deposition precursors and preliminary assessment of a potential kinetically-limited ALD precursor**

*Manuscript in preparation:*

Matthew B. E. Griffiths\* and Seán T. Barry

Department of Chemistry, Carleton University, 1125 Colonel By Drive, Ottawa, Ontario, K1S 5B6, Canada

## 6.1 Abstract

The development of atomic layer deposition (ALD) processes requires a large amount of time and resources in order to complete. To circumvent the expenditure of resources, we implemented a quartz crystal microbalance (QCM) and quadrupole mass spectrometer (QMS) to analyze self-limiting behaviour *in situ*. Using this apparatus, we were able to rapidly screen multiple precursors and co-reagents for ALD-like behaviour. We found that the ALD precursor  $(\text{PMe}_3)\text{AuMe}_3$  (**1**) does not react with many conventional ALD co-reagents. The Au(I) compound  $(\text{NHC})\text{AuCH}_2(\text{SiMe}_3)$  (**2**) undergoes rapid CVD on  $\text{Al}_2\text{O}_3$  and Au surfaces.  $(\text{PMe}_3)\text{AuCH}_2(\text{SiMe}_3)$  (**3**) undergoes very slow CVD on  $\text{Al}_2\text{O}_3$  but rapid CVD on Au surfaces. We then attempted to re-design **3** based on its known CVD mechanism and employed persilylated alkyl ligands in order to increase the activation energy of a surface-mediated bimolecular reductive elimination step. The new persilylated Au(I) compounds **3a-d** possess good precursor figures of merit ( $\sigma$ ). Using a combination of the QCM and QMS, we developed a method to rapidly determine the activation energy of **3a** and **3c**. We show that persilylation induces a substantially higher activation energy for CVD, and that **3c** and **3d** are likely candidates for a kinetically-limited gold ALD process.

## 6.2 Introduction

Atomic layer deposition (ALD) is a thin film deposition technique that can deposit thin films with high degrees of conformality and control of the final film thickness. Its prowess relies on self-limiting chemisorption of the desired precursors, and not all compounds possess this characteristic.<sup>48,284</sup> The chemistry that occurs at a surface (solid-gas or solid-liquid interface) can differ substantially from single-phase solution or liquid chemistry.<sup>285</sup> Unfortunately, it is quite difficult to screen a compound's ability to undergo self-limiting chemisorption on a surface without carrying out a series of repetitive experiments. Such studies are time consuming to perform, and they require the synthesis of multiple grams of chemical compounds that are sometimes very costly, and often not particularly green. Furthermore, sometimes the first compound in a particular study doesn't undergo self-limiting chemisorption, which means performing more synthetic experiments, and performing more ALD studies. Even with the most efficient apparatus, this is a wasteful and time-consuming methodology. Considering the substantial impact that chemical research already has on the environment, we should be attempting to increase the efficiency with which we do research and reduce our environmental impact accordingly.

Previously, we described a precursor figure of merit ( $\sigma$ ) which allows compounds to be ranked based on their potential to be studied as precursors in an ALD process.<sup>123</sup> This figure of merit incorporates information about the volatility and thermal stability of the compound and can be used to identify which compounds are the best first choice for ALD studies out of a series of compounds. However, this figure of merit contains no information about how well the precursor might undergo self-limiting surface chemisorption and thus participate in an ALD process. Sticking to existing ALD methodology, it would be suitable to have an *in-situ* technique that would allow us to determine a precursor's ability to undergo self-limiting chemisorption while under ALD-like conditions. Ideally this methodology would cut down on experiment time, precursor consumption, and provide near-real-time conclusions about a precursor's ability to undergo self-liming chemisorption.

The quartz-crystal microbalance (QCM) has become a standard *in-situ* monitoring tool for both ALD and atomic layer etching (ALE) processes since it provides excellent resolution

when measuring mass fluctuations caused by the sequential precursor exposures during an ALD process.<sup>286–290</sup> With a resolution of < 1 ng cm<sup>-2</sup>, an instantaneous output which can be easily processed in minutes using simple spreadsheet software, and a low cost, the QCM has the potential to accelerate the process of precursor selection. Thus, we set out to develop a methodology to rapidly screen potential candidates for their ability to undergo self-limiting chemisorption using an *in-situ* QCM monitoring approach.

## 6.3 Results and Discussion

### 6.3.1 Apparatus design and benchmarking of a truly self-limiting precursor

For this study we elected to design a home-made ALD reactor that could be cheap and could also be easily modified to suit various *in-situ* monitoring devices simultaneously. Often times commercial equipment is not designed with in-house modifications in mind and this meant that using a tube furnace was the only way forward. This design isn't space-effective, but a straight furnace allows one to easily insert and remove an *in-situ* probe such as a titled-fiber Bragg grating (TFBG) optical sensor or in our case a QCM. The exhaust of the system consists of a 6-way CF flange adaptor which allowed the addition of a QMS along with the other essential features of the reactor such as the sample loading port. This reactor design allowed us to employ new *in-situ* monitoring equipment to analyze the surface chemistry of CVD and ALD processes while sacrificing the ability to deposit on large substrates.

The QCM was equipped with an onboard thermocouple which allowed accurate temperature determination for the mass gain but was not configured with a backside purge (as is common in other ALD studies).<sup>286</sup> Thus we could not rule out backside deposition as being a source of larger-than-normal growth per cycle (GPC) values when characterizing known processes; this does not, however, affect the self-limiting diagnosis of the precursors in question.

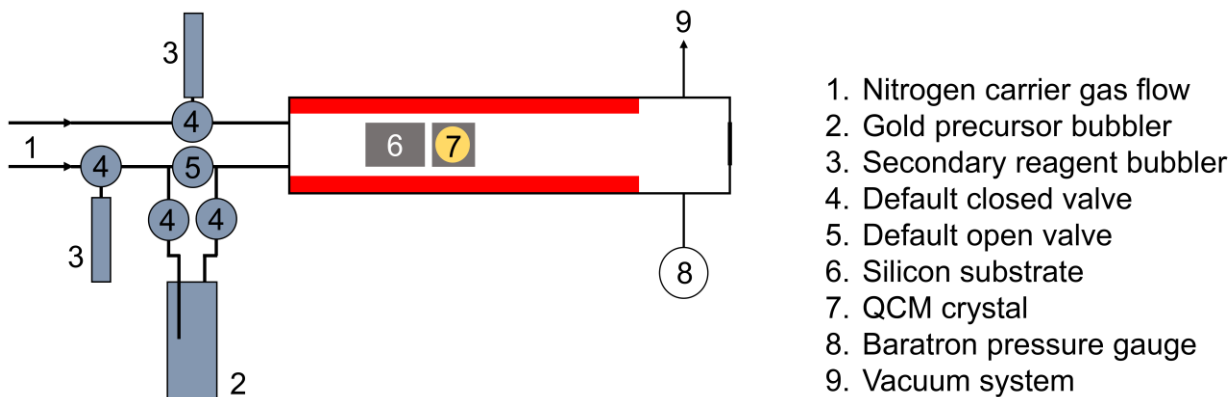


**Figure 6.1** Home-made ALD tool used in this study. The nitrogen carrier gas flows were controlled by two separate mass flow controllers (range 0-200 sccm). The gold precursor bubbler was heated using a computer-controlled temperature relay. Precursor delivery lines downstream of the gold bubbler were heated to between 10 and 20 °C higher than the gold bubbler itself to prevent precursor condensation in the delivery lines. The system pressure at 200 + 200 sccm flow rate was 2.23 Torr.

We elected to first characterize the self-limiting behaviour of the trimethylaluminum (TMA) + water ALD process, by far the most well-studied ALD process to date. At 150 °C, 100 cycles of 0.1 s TMA and 0.1 s H<sub>2</sub>O with 15 s N<sub>2</sub> purges between each pulse showed a nucleation delay on the gold-coated QCM crystal of approximately 15 cycles (Figure 6.2). After this nucleation delay, a linear growth rate was observed. The calculated growth per cycle (GPC) of this process was 1.43 Å, slightly higher than literature<sup>291,292</sup> and is likely due to backside deposition on the QCM.<sup>291</sup> In this GPC calculation, it was assumed that the density of Al<sub>2</sub>O<sub>3</sub> deposited is identical to that observed by Elam *et al.*<sup>293</sup>

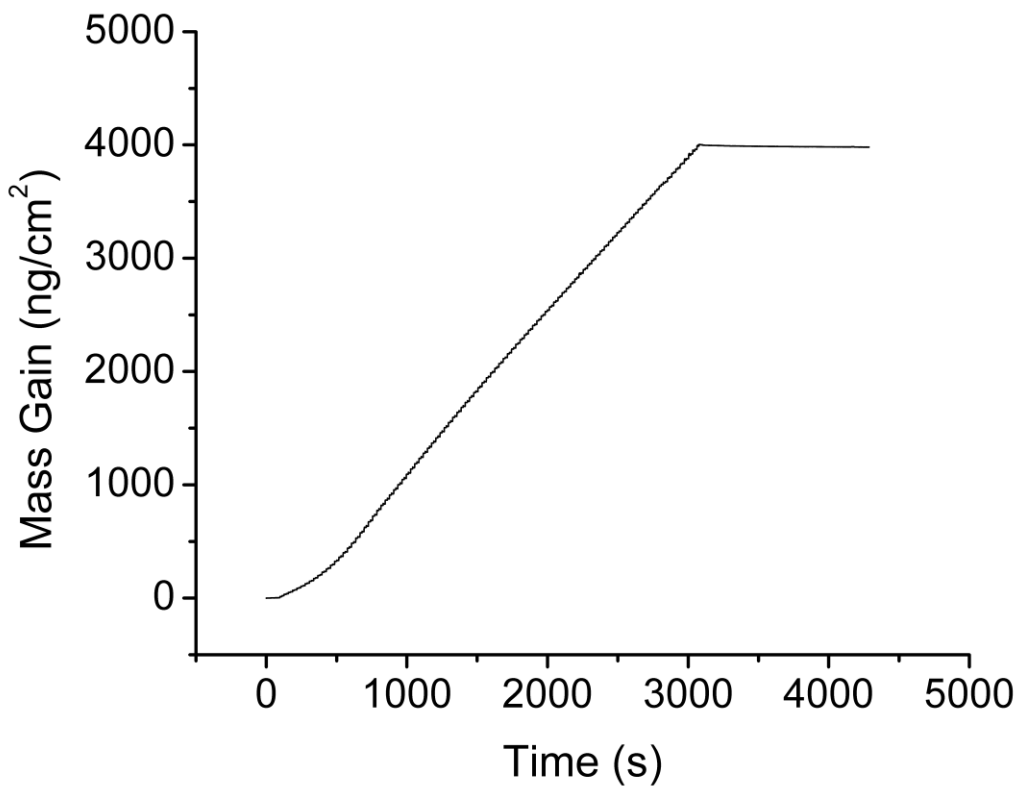


**Figure 6.2** QCM data obtained from performing 100 cycles of [0.1 s TMA | 15 s N<sub>2</sub> purge | 0.1 s H<sub>2</sub>O | 15 s N<sub>2</sub> purge] at 150 °C.

We then analyzed the TMA and H<sub>2</sub>O precursors separately for self-limiting behaviour to act as a benchmark dataset for ideal ALD self-limiting behaviour. In these experiments, the growth surface was the Al<sub>2</sub>O<sub>3</sub> deposited in the previous experiment and the system was not exposed to ambient conditions between experiments to maintain an as-deposited Al<sub>2</sub>O<sub>3</sub> surface. We performed 100 cycles of 0.1 s TMA with 15 s N<sub>2</sub> purges and observed very clearly that the surface became saturated with TMA (Figure 6.3 (a)). Interestingly, it took more than 10 doses of 0.1 s of TMA to reach a saturated value of 68 ng cm<sup>-2</sup>, approximately double the value commonly reported for TMA + H<sub>2</sub>O processes. This was again attributed to deposition on the back side of the QCM crystal. As expected, an experiment consisting of 70 cycles of 0.1 s H<sub>2</sub>O with 15 s N<sub>2</sub> purges also showed self-limiting behaviour on the TMA-exposed surface (Figure 6.3 (b)), but again at least 10 doses of 0.1 s were required to reach saturation on the crystal surface.

We could see that in both cases a rapid initial mass gain was initially observed, indicative of a strong chemisorption event. Subsequent dosing of the precursors results in a diminishing return of mass gain of the QCM. Finally, after  $\sim$  10 doses a plateau is reached where no further mass gain occurs. Overall, these factors indicated that the precursors were undergoing self-limiting chemisorption.

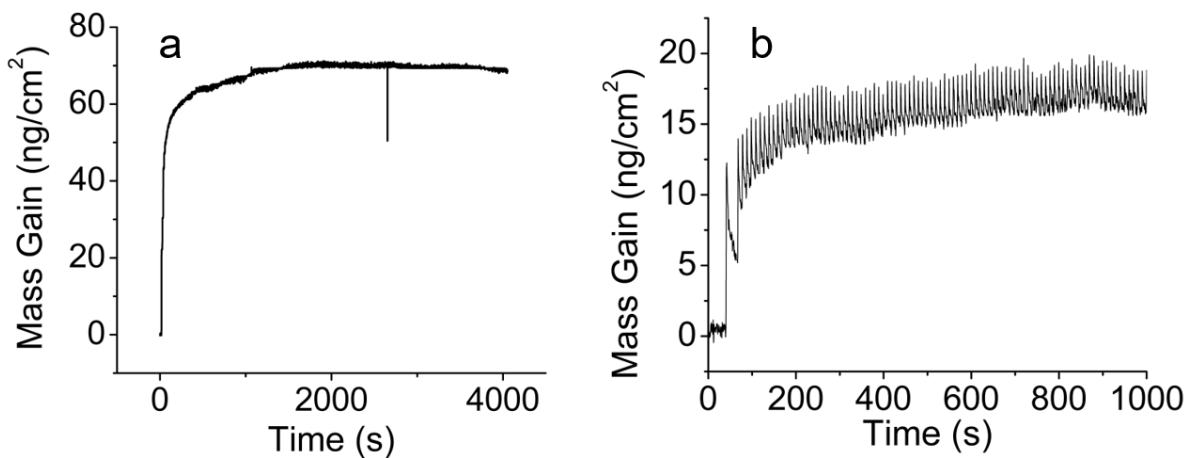


**Figure 6.3** a) 100 cycles of [0.1 s TMA | 15 s N<sub>2</sub> purge] on an Al<sub>2</sub>O<sub>3</sub> coated QCM crystal at 150 °C. In this figure, the pulsing experiment ends at the 1510 s point; b) 70 cycles of [0.1 s H<sub>2</sub>O | 15 s N<sub>2</sub> purge] on an Al<sub>2</sub>O<sub>3</sub> coated QCM crystal at 150 °C which had been previously exposed to 100 pulses of TMA from Figure 6.3 (a).

### 6.3.2 Surface chemistry of (PMe<sub>3</sub>)AuMe<sub>3</sub> (**1**) with Al<sub>2</sub>O<sub>3</sub>

We attempted to detect self-limiting chemisorption in our existing gold ALD precursor, (PMe<sub>3</sub>)AuMe<sub>3</sub> (**1**).<sup>99</sup> We performed 100 cycles of 1 s of **1** with 15 s N<sub>2</sub> purges at 120 °C, which was found to be the upper limit at which this precursor produced ALD-like growth in our Picosun R200 PE-ALD tool. This experiment was performed on an Al<sub>2</sub>O<sub>3</sub> coated QCM crystal. As shown in Figure 6.4 (a), this precursor does not undergo perfect self-limiting chemisorption since there is a slow but steady increase in the mass loading of the QCM with each additional dose of **1**. However, it is clear that a large portion of the growth occurs in the first two pulses as **1** reacts with Al<sub>2</sub>O<sub>3</sub>-OH surface sites (Figure 6.4 (b)). Each dose afterwards produces only a very small mass gain, likely due to a slow self-decomposition

of **1** which would contribute to a chemical vapour deposition (CVD) component of growth in an ALD cycle. We can calculate the parasitic CVD component that **1** brings to a process at 120 °C. The average mass gain in Figure 6.4 (c) was 1.7 ng cm<sup>-2</sup> cycle<sup>-1</sup>, which equates to 0.0088 Å cycle<sup>-1</sup> of CVD growth, which constitutes 1.8 % of the total growth rate of the published ALD process of 0.5 Å cycle<sup>-1</sup>. Such a small CVD component to the overall ALD process would be very difficult to measure with traditional thin film thickness measurement techniques and highlights the ability of this method to diagnose these conditions. In Chapter 4 we discuss the surface chemistry which leads to this slow CVD component, and that a temperature of 100 °C is a more reasonable upper limit of ALD processes that use **1** if avoiding the CVD component is essential.

We screened some popular co-reagents to test their ability to enhance the growth rate of gold metal deposited by **1**. The QCM not only allows the study of self-limiting chemisorption, but it can also demonstrate rapid screening of co-reagents for their potential to enable ALD-like behaviour by removing self-limiting ligands or otherwise reactivating the surface towards growth. Thus, we compared 100 cycle experiments of 1 s pulses of **1** and variable co-reagent pulses, each followed by 15 s N<sub>2</sub> purges to the original 100 cycles described above. An increase in final mass gain of the experiment would indicate that a particular co-reagent had allowed more **1** to be deposited by removing the self-limiting phosphine ligands from the surface. As shown in Figure S-6.15 and Figure S-6.16, none of BH<sub>3</sub>(NHMe<sub>2</sub>), formic acid (FA), 100% N<sub>2</sub>O, 10% O<sub>2</sub>, or various combinations of (FA + BH<sub>3</sub>(NHMe<sub>2</sub>)) enhanced the overall growth of the process.

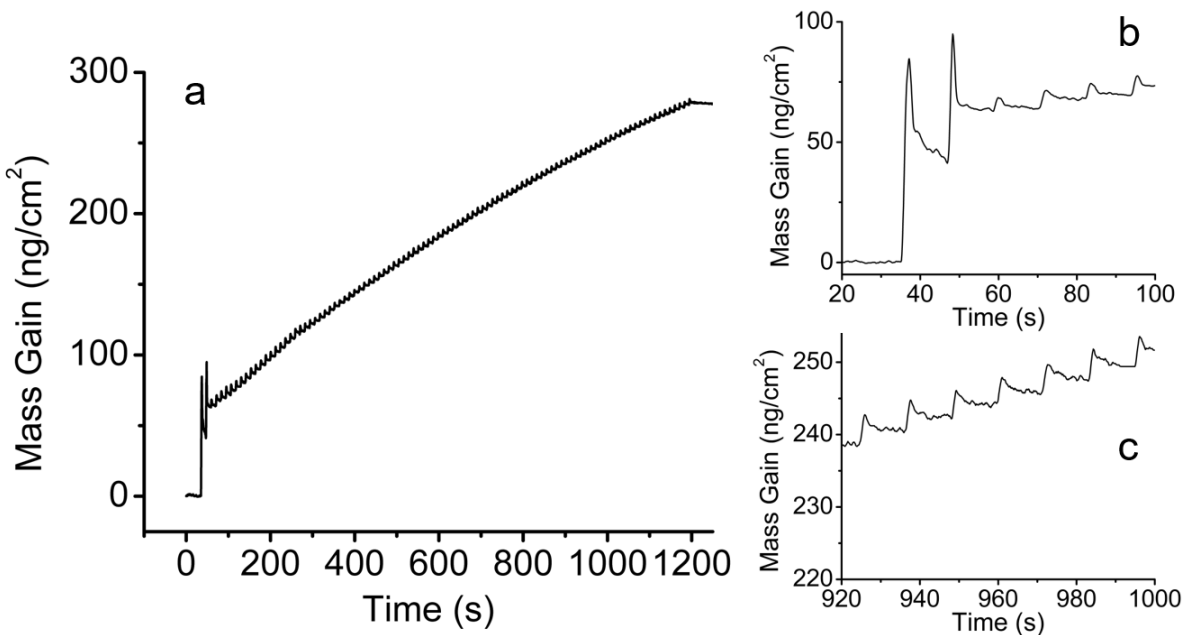


**Figure 6.4** a) Full dataset of 100 cycles of [1 s (**1**) | 15 s N<sub>2</sub> purge] at 120 °C deposited on an Al<sub>2</sub>O<sub>3</sub>-coated QCM crystal; b) enhanced view of the first 5 doses of **1**; c) enhanced view of 6 doses near the end of the experiment.

### 6.3.3 CVD of an NHC-Au-CH<sub>2</sub>(SiMe<sub>3</sub>) precursor on Al<sub>2</sub>O<sub>3</sub>

We then analyzed a different precursor, *N,N'*-di-*tert*-butylimidazolidin-2-ylidene trimethylsilylmethylgold(I) (**2**) which bears an N-heterocyclic carbene (NHC) as the coordinative ligand. NHCs have been shown previously to bind more strongly to gold surfaces than tertiary phosphines,<sup>113</sup> and so we hypothesized that this NHC might act as the self-limiting ligand during chemisorption. Although **2** has a good precursor figure of merit ( $\sigma = 23.8$ ), it has a substantially lower vapour pressure ( $T_{1\text{ Torr}} = 150\text{ }^{\circ}\text{C}$ ) than **1**, and so we elected to heat the bubbler to 140 °C and hold the QCM temperature at 160 °C. To our surprise, this compound deposited a substantial amount of gold even at a substrate temperature below its self-decomposition temperature ( $T_D$  (**2**) = 184 °C).<sup>123</sup> Performing 60 cycles of 1 s precursor pulse with 15 s purges resulted in a mass gain of 68,542 ng cm<sup>-2</sup>, an effective thickness of 35.4 nm of gold and a GPC of 5.9 Å. Clearly this NHC is

not acting as a self-limiting ligand under these conditions, there is no evidence of saturation of the mass gain signal (Figure 6.5). This is likely due to the <sup>t</sup>Bu wingtip groups being too sterically bulky to allow the NHC to bind strongly to the surface. In Chapter 6, we detail the study of a number of NHC-Au-R precursors in a direct attempt to design NHC-Au precursors for ALD.

Using scanning electron microscopy (SEM) (Figure 6.5 (b)) we observed that the gold film exhibited island-type growth, and the precursor clearly undergoes preferential chemisorption with the gold surface rather than the native SiO<sub>2</sub>/Si substrate. This was supported by a nucleation delay of approximately 10 cycles (6139 ng cm<sup>-2</sup>, 3.2 nm effective thickness of Au) which can be observed in by QCM (Figure 6.5 (a)). Using energy-dispersive X-ray spectroscopy (EDX), k-ratio analysis of this film we found an effective thickness of 38 nm (Figure 6.5 (b)). The 2.6 nm discrepancy between the film thicknesses is due to the witness substrate (SiO<sub>2</sub> | Si) being placed closer to the precursor inlet than the QCM crystal.

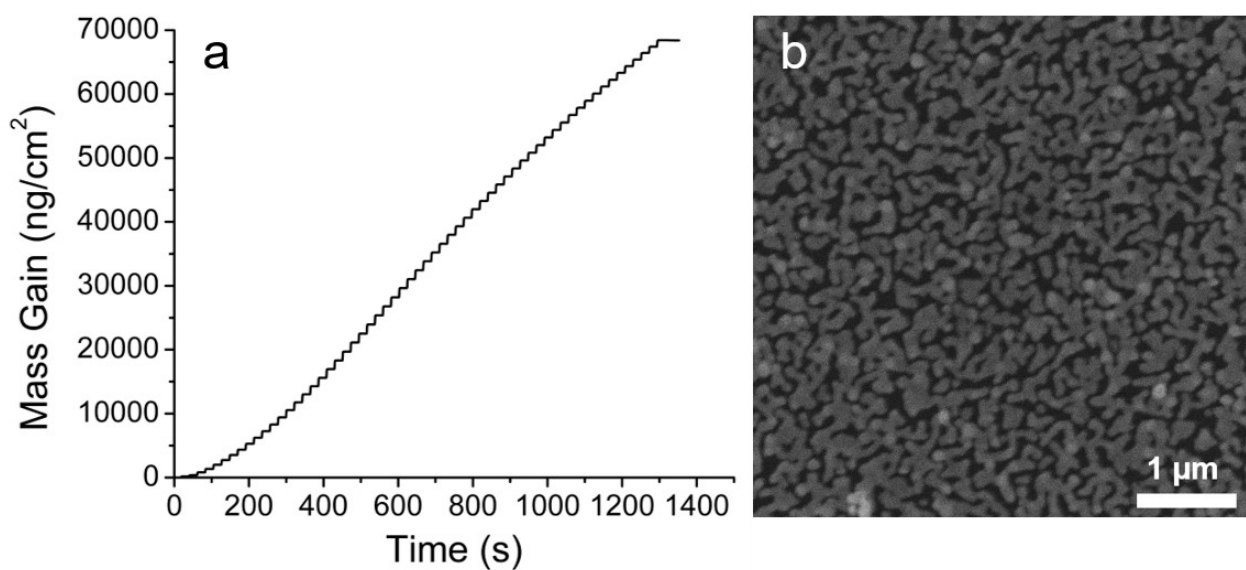


**Figure 6.5** a) QCM data from 60 cycles of [1 s (2) | 15 s N<sub>2</sub> purge] at 140 °C QCM temperature. The QCM was pre-coated with 10 nm of Al<sub>2</sub>O<sub>3</sub> the calculated thickness of the Au film was 35.4 nm; b) SEM image of the deposited gold film on native SiO<sub>2</sub> | Si. The observed film thickness of this Au film by EDX was 38 nm. The SiO<sub>2</sub> | Si film was placed closer to the precursor inlet than the QCM crystal.

### 6.3.4 Surface chemistry of $(\text{PMe}_3)\text{AuCH}_2(\text{SiMe}_3)$ (**3**) on $\text{Al}_2\text{O}_3$

Having analyzed our existing gold precursor (**1**) and a more exotic NHC-Au-NeoSi precursor (**2**), we turned to trimethylphosphine trimethylsilylmethylgold(I) (**3**), which has a high figure of merit ( $\sigma = 58.2$ ), a good volatility ( $T_{1\text{ Torr}} = 87^\circ\text{C}$ ), and a large thermal window before it undergoes thermal auto-decomposition ( $T_D = 146^\circ\text{C}$ ).<sup>123</sup> This compound is analogous to trimethylphosphine methylgold(I) which is known to undergo autocatalyzed decomposition on gold and other metal surfaces at temperatures as low as  $25^\circ\text{C}$ .<sup>225</sup> We hypothesized that (**3**) would behave similarly to its methyl analogue and undergo CVD, but hopefully at a much slower rate due to its larger steric bulk. In this case, the trimethylsilylmethyl ligands as well as  $\text{PMe}_3$  ligands might both act as the self-limiting ligands.

We performed 100 cycles of 1 s pulses of **3** with 30 s  $\text{N}_2$  purges at  $120^\circ\text{C}$ , this time incorporating a longer purge to force the timelength of the experiment to match those of subsequent co-reagent experiments. As shown in Figure 6.6 (a), the **3**-only experiment (blank) produced a mass gain of  $1947 \text{ ng cm}^{-2}$  or  $1.008 \text{ nm}$  equivalent thickness of gold, and a growth rate of  $0.10 \text{ \AA cycle}^{-1}$  which is purely due to a slow auto-decomposition of the precursor. It is clear that under these conditions **3** is not a true ALD precursor, but rather it undergoes slow single-source CVD.

We then considered volatile proton sources  $\text{H}_2\text{O}$  and FA to protonate surface bound trimethylsilylmethyl ligands and/or to remove surface-bound  $\text{PMe}_3$  in some fashion and accelerate the growth process. Using  $\text{H}_2\text{O}$  as a co-reagent in the pulse sequence: 1 s pulses of **3**, 0.1 s  $\text{H}_2\text{O}$  pulses and 15 s  $\text{N}_2$  purges, the final film thickness is only slightly greater than the blank:  $2370 \text{ ng cm}^{-2}$  or  $1.227 \text{ nm}$  equivalent thickness of gold, and a GPC of  $0.12 \text{ \AA}$ . Even though  $\text{H}_2\text{O}$  increases the growth rate of the process by 17 %, the majority of the growth of the film was still occurring from self-decomposition of **3**.

We then used FA as a co-reagent and performed 100 cycles of 1 s pulses of **3**, 0.2 s FA pulses and 15 s  $\text{N}_2$  purges. This time a clear activation of growth was observed, resulting in a final mass gain of  $3519 \text{ ng cm}^{-2}$  ( $1.821 \text{ nm}$  equivalent thickness of gold) and a GPC

of  $0.18 \text{ \AA}$ . The process also appears to undergo a nucleation delay that lasts approximately 50 cycles before increasing dramatically. Figure 6.6 (b) shows an enhanced view of the 61<sup>st</sup> cycle, and interestingly it appears that the FA has no effect on the mass loading of the QCM, although its inclusion in the experiment does almost double the final film thickness. The mass gain per cycle after the nucleation is  $62 \text{ ng} \cdot \text{cm}^{-2}$ , which is a GPC 0.32  $\text{\AA}$ .

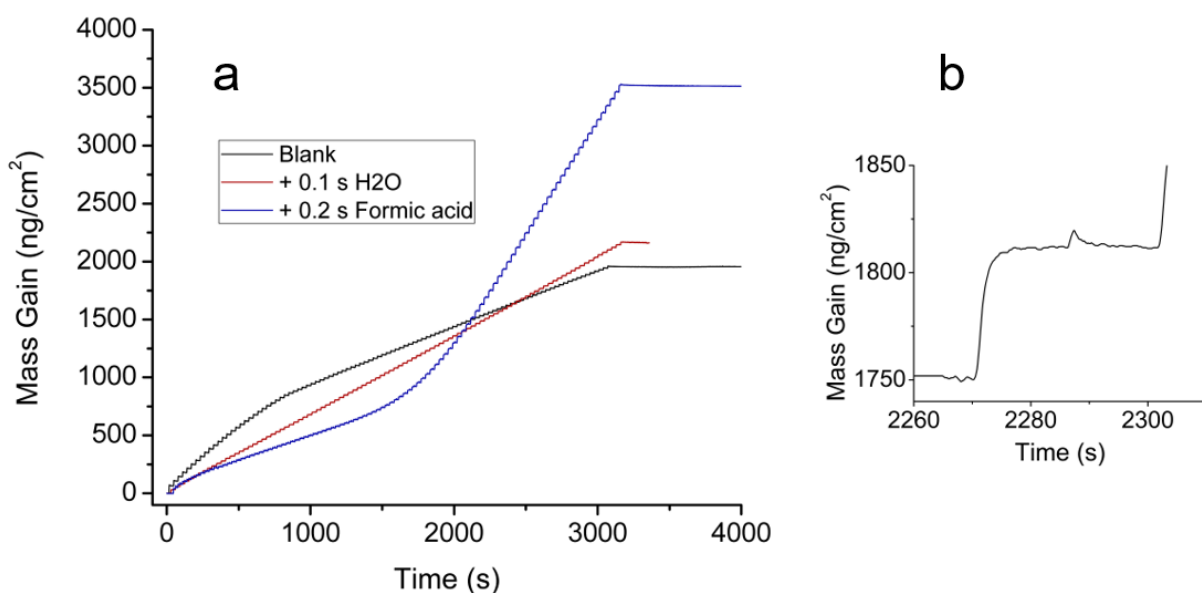


**Figure 6.6** a) Overlay of QCM data obtained from 100 cycle experiments of **3** alone (blank), **3** +  $\text{H}_2\text{O}$  (red), and **3** + FA (blue). b) Enhanced view of the 61<sup>st</sup> cycle of the **3** + FA experiment. All experiments were performed on  $\text{Al}_2\text{O}_3$ -coated QCM crystals at  $120^\circ\text{C}$ .

Given this positive result with **3** and FA, we decided to perform saturation curve experiments at  $120^\circ\text{C}$  by varying the pulse length of **3** (1, 3, and 5 s) and determining the film GPC (Figure 6.7). For a perfectly behaved ALD system, the GPC should be independent of precursor pulse length after a certain saturating pulse is given. We observed that the GPC increased linearly with no real sign of saturation. To ensure that the reagents weren't undergoing CVD due to a long residence time at the surface or inside the reactor we doubled the purge lengths after both **3** and FA and repeated the experiments and found an identical trend of steadily increasing GPC. We decided to repeat the experiments on an industrially relevant Picosun R200 PE-ALD tool to rule out

a possible tool dependency for these experiments. Interestingly after performing only 1, 3, and 5 s pulses of **3** for the saturation curve experiment on the Picosun R200 it appeared that the process had saturated at a GPC of 0.85 Å (Figure 6.7, black circles). We pushed the saturation experiment to a 10 s dose, where a slow CVD growth component finally became apparent. This highlights the difference in the kinetics of the growth in the industrial tool vs. the homemade tool and could be the result of flow design or confounding factors with respect to temperature and pressure control. Saturation curve experiments are not often pushed to such long pulse lengths in ALD literature. Had we performed the experiments on the Picosun R200 tool first, we would have been more inclined to believe that the process was a truly ALD process, albeit within the time frame of the shorter saturation curve. We could only conclude that at 120 °C this was ultimately a slow CVD process.

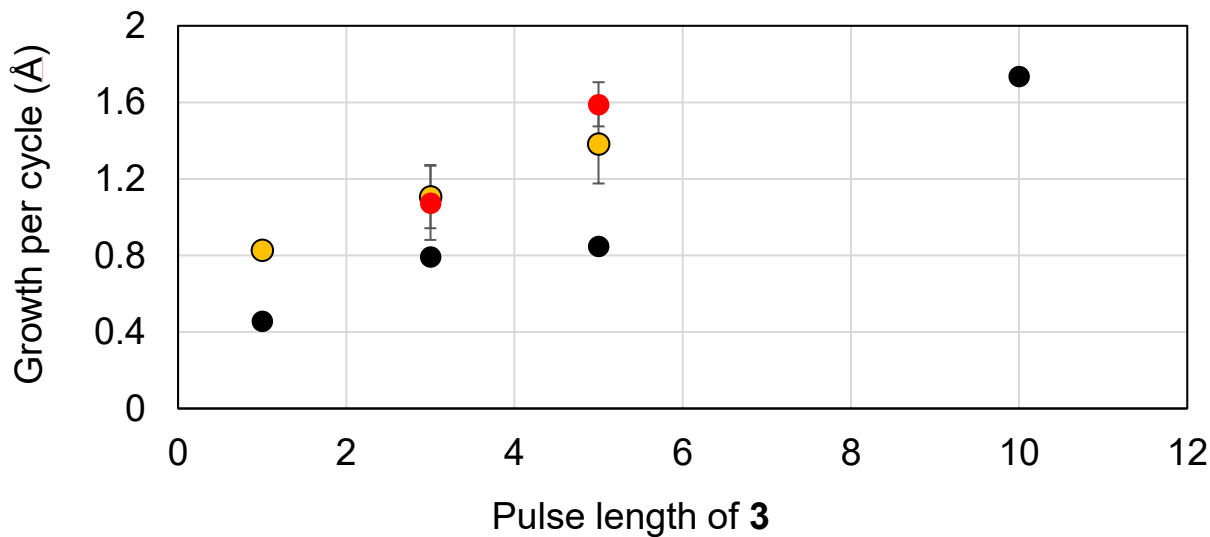
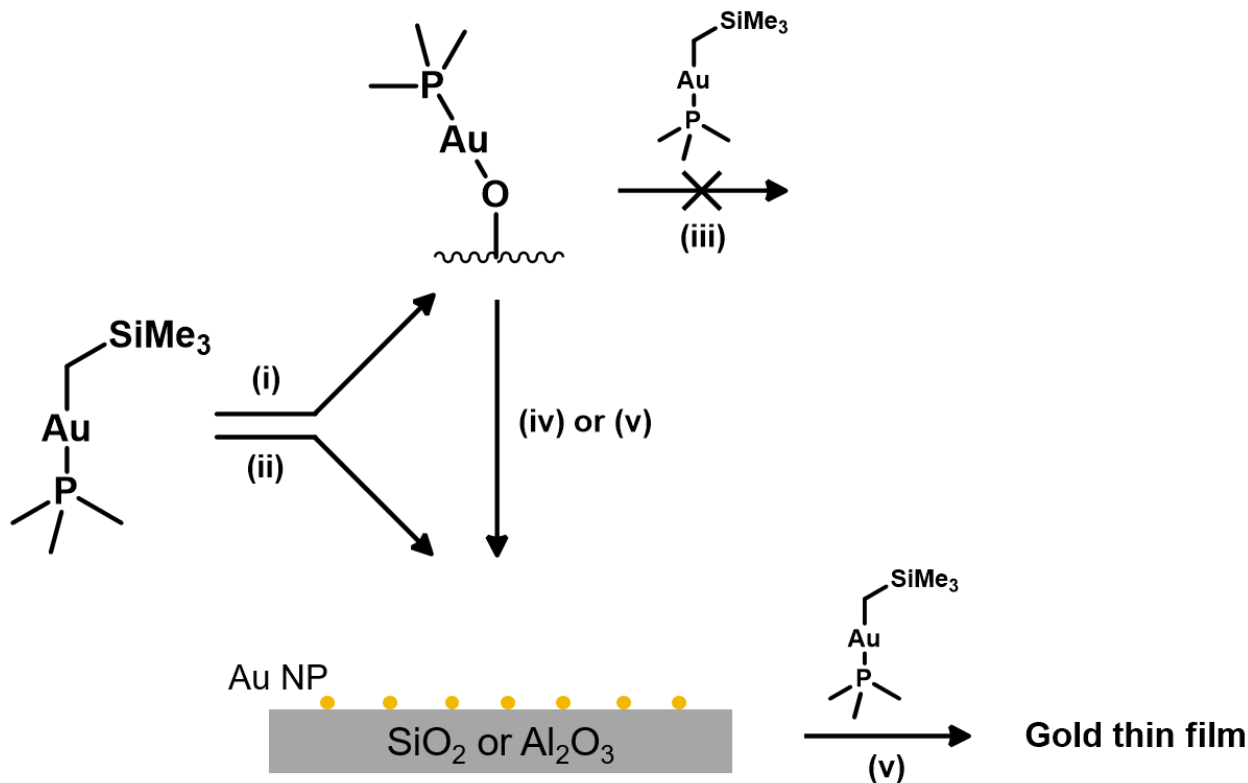


**Figure 6.7** Saturation curve experiments for the **3 + FA** process. 500 cycles were performed for each experiment. Film thicknesses were determined using EDX with the help of GMRFilm. (Yellow circles) [(**3**) | 15 s N<sub>2</sub> purges | 0.2 s FA | 15 s N<sub>2</sub> purge] on the homemade ALD tool, (red circles) [(**3**) | 30 s N<sub>2</sub> purges | 0.2 s FA | 30 s N<sub>2</sub> purge] on the homemade ALD tool, (black circles) [(**3**) | 15 s N<sub>2</sub> purges | 0.2 s FA | 15 s N<sub>2</sub> purge] on the Picosun R200 PE-ALD tool.

This was a conflicting result to what was observed in Figure 6.6 (a). Since we initially observed enhanced growth with FA but could not apparently replicate this behaviour at higher cycle numbers, we began to question how these two phenomena could co-exist.

Considering our prior data, we hypothesized that the only role FA plays in this process is to accelerate the initial nucleation of metallic gold nanoparticles as a seed layer on  $\text{Al}_2\text{O}_3$  (Scheme 6.1). Once FA has helped to decompose the initial monolayer formed by reaction of **3** with the hydroxylated  $\text{Al}_2\text{O}_3$  surface, then the growth rate of the process increases dramatically on the gold seed layer. At this point the growth rate of the process is no longer dependent on the dose of FA which also explains its net 0 mass change after the nucleation delay of the process (Figure 6.6 (b)). We realized that to truly differentiate self-limiting behaviour from CVD-like behaviour, we needed to modify our *in situ* QCM monitoring experiment and grow on gold surfaces instead of  $\text{Al}_2\text{O}_3$  surfaces.

**Scheme 6.1** Proposed reaction pathway summarizing the hypothesized surface chemistry of **3** and FA on both  $\text{Al}_2\text{O}_3$  and Au surfaces. Legend: (i)  $\text{Al}_2\text{O}_3\text{-OH}$  surface, loss of  $\text{SiMe}_4$ ; (ii) Au surface, loss of  $(\text{Me}_3\text{Si})\text{CH}_2\text{CH}_2(\text{SiMe}_3)$  through bimolecular reductive elimination; (iii) no reaction; (iv) slow thermal decomposition without FA; (v) fast decomposition in the presence of FA; (vi) chemical vapour deposition.



### 6.3.5 Surface chemistry of $(\text{PMe}_3)\text{AuCH}_2(\text{SiMe}_3)$ (**3**) on Au

We performed two experiments in series while monitoring by QCM. The first process was 200 cycles of 3s pulses of **3** and 0.2 s pulses of FA with 15 s  $\text{N}_2$  purges in between, and the second process was simply 200 cycles of 3s pulses of **3** with 15 s  $\text{N}_2$  purges. The first process was performed on a fresh gold-coated QCM crystal, and the second experiment was performed directly onto the gold metal growth surface left by the first process. The results of this double experiment are shown in Figure 6.8. We observed that the **3** + FA still produced only a very slightly thicker film than the **3**-only experiment. The calculated effective film thickness for the **3** + FA experiment was 5.9 nm (GPC = 0.30 Å, and the **3**-only experiment was 5.1 nm (GPC = 0.26 Å), which implies that the overall growth rate of **3** + FA is comprised of 87 % CVD of **3**, with the remaining 13 % being some kind of enhanced growth due to the dosing of FA. This was a starkly different result compared to what we observed in the experiments from Figure 6.6 and highlights the importance that the chemistry of initial substrate can have on the experiment. This result is conducive to FA only really participating in surface chemistry during the nucleation phase of **3** on  $\text{Al}_2\text{O}_3$  as shown in Scheme 6.1 above.

There remained a mystery however, which was that a slight enhancement was still observed with the inclusion of FA. We have evidence from our studies of compound **1** (See Chapter 4) that some  $\text{PMe}_3$  remains on the surface when a gold surface is dosed with **1**. Methyl ligands also remain on the surface with lifetimes on the order of seconds.<sup>113</sup> Thus, it is possible that  $\text{NeoSi}^-$  ligands also persist long enough and might act as a short-lived surface protecting ligand. If these ligands could be removed by FA, then this could explain the enhanced growth when FA is included.

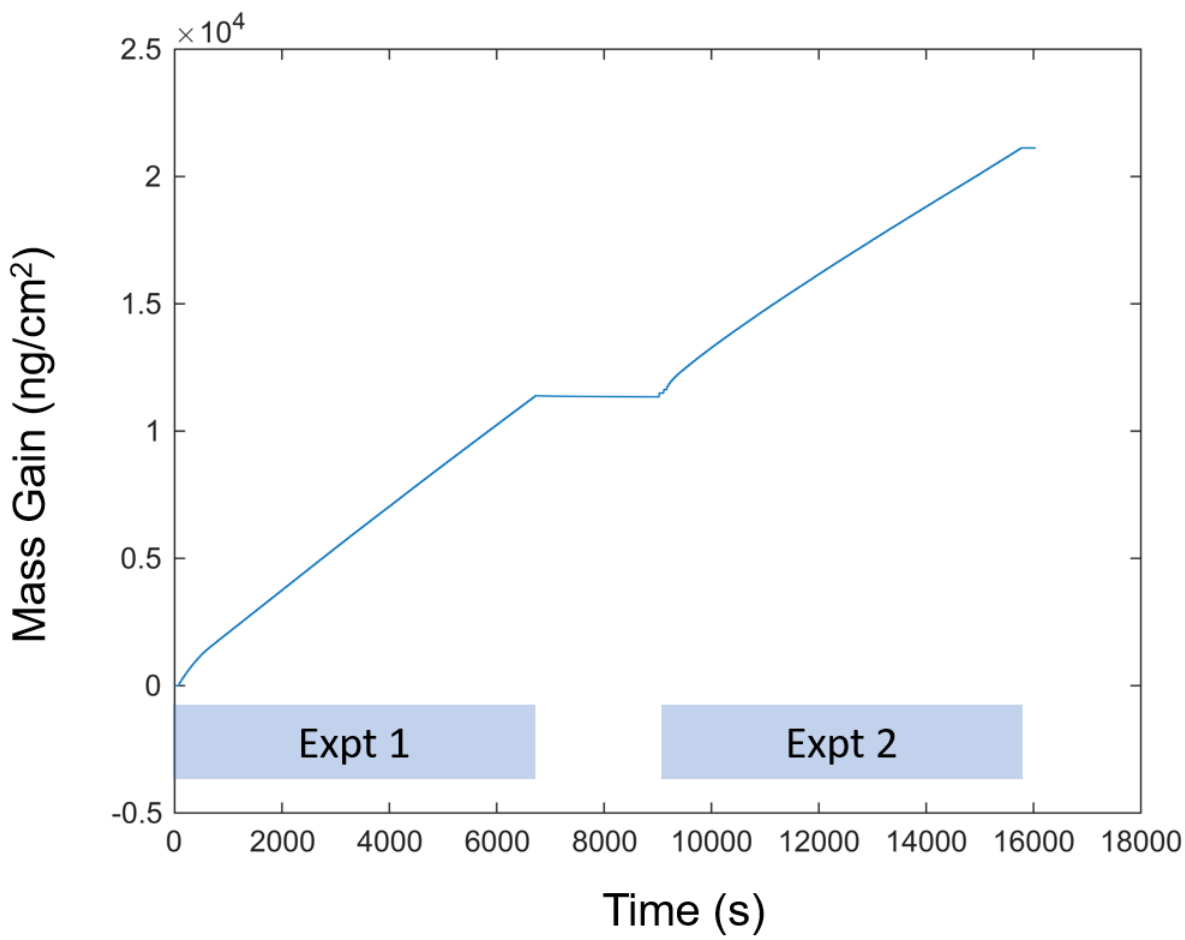


**Figure 6.8** QCM micrograph of the double experiment where 200 cycles of [3s **3** | 15 s N<sub>2</sub> purge | 0.2 s FA | 15 s N<sub>2</sub> purge] were performed on a gold-coated QCM crystal, immediately followed by 200 cycles of [3s **3** | 30.2 s N<sub>2</sub> purge]. The calculated effective film thicknesses of the two experiments were 5.9 nm and 5.1 nm respectively.

Generally, the ALD community has held the notion that a true ALD process must be a thermodynamically limited process where each half-cycle produces a surface that is perpetually stable. However this is likely not the case for most “ALD” processes and we believe that many of the well-described and well-used processes possess a non-0 CVD component to their growth. This phenomenon does not prevent these processes from excelling in device fabrication or cutting-edge research: ALD has now clearly been cemented as a revolutionary thin film deposition technique. This begs the question: if a

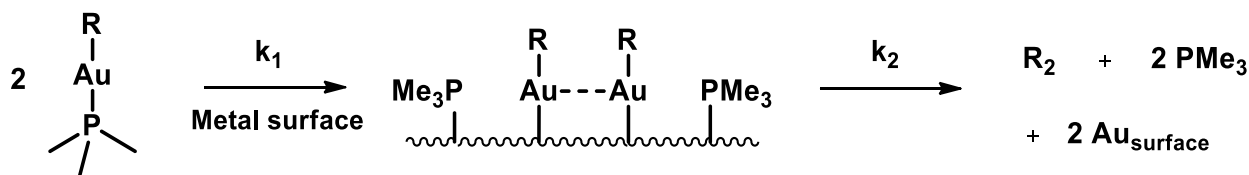
very slow CVD process can be an ALD process, then can any CVD process be an ALD process if given the right conditions and precursor design?

### 6.3.6 Design and preliminary testing of a kinetically limited ALD precursor

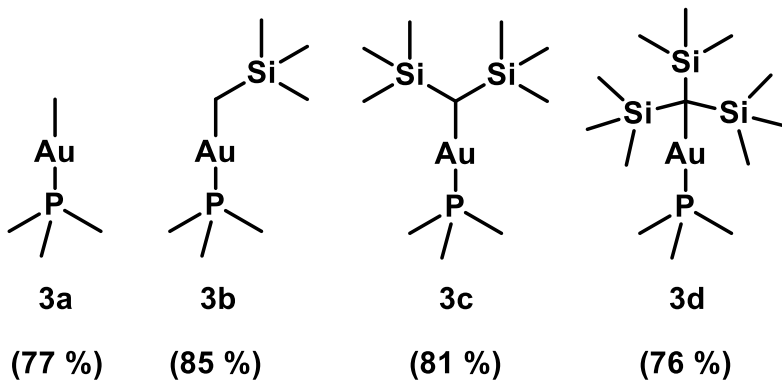
To our knowledge the first description of a kinetically-limited ALD process was in 1992 by Sugahara for a hydrogen radical-enhanced ALD process which deposited elemental germanium.<sup>294</sup> More recently, Henrik Pedersen has revitalized the concept such that all ALD processes can be described as CVD processes where the self-limiting chemisorption of the precursor is much faster than the reaction of the precursor with the formed monolayer.<sup>295</sup> As the rate of reaction of the precursor with the first monolayer approaches 0, and/or as the rate of self-decomposition of the first monolayer approaches 0, then the process approaches true ALD-like behaviour. We found this description intriguing as it bears a strong resemblance to synthetic chemistry where a kinetically favoured product can be selectively formed over a thermodynamically favoured product. Often this is done through use of large steric bulk to prevent the thermodynamically preferred reaction.

We hypothesized that we might be able to exploit kinetically-limited ALD and re-design **3** so that its mode of CVD was impeded by steric bulk. As shown in Scheme 6.2, alkylgold(I) phosphines undergo autocatalytic decomposition on metallic surfaces, including gold.<sup>125</sup> As previously described, the rate-limiting step of decomposition for  $(\text{PMe}_3)\text{AuMe}$  is dissociative chemisorption of the intact precursor onto the metallic surface ( $k_1$ ). Bimolecular reductive elimination ( $k_2$ ) is much faster ( $k_1 < k_2$ ), which means the activation energy of the first reaction is larger than the second ( $E_{a1} > E_{a2}$ ), and thus this process cannot be trapped at the intermediate  $\text{PMe}_3$  and Au-Me covered surface regardless of the temperature of the system. However, if R was very bulky, then the association of two Au-R surface species would require a lot more energy than for the R = Me case. If we assume that the nature of R has little effect on the Au-P bond dissociation energy (BDE), then as R becomes larger, eventually  $E_{a2}$  will become larger than  $E_{a1}$  and the process will shift from a CVD process to a kinetically-limited ALD process.

**Scheme 6.2** Autocatalytic decomposition of  $(\text{PMe}_3)\text{AuR}$  on metallic surfaces. For  $\text{R} = \text{Me}$ ,  $k_1 < k_2$  which results in CVD at all temperatures, or  $E_{a1} > E_{a2}$ . Increasing the steric bulk of R should result in a shift in the magnitude of  $k_2$  and  $E_{a2}$ , which will eventually result in the case  $E_{a2} > E_{a1}$  and a paradigm shift of the process from CVD to kinetically-limited ALD.



**Scheme 6.3** New precursor design series of increasing steric bulk of the alkyl group. The numbering scheme includes (**3** = **3b**) in order to facilitate discussion in the following section. Synthetic yields are given in parentheses below the compounds (%).



Thus we set about synthesizing and characterizing compounds **3c** and **3d** to add to our previously examples, **3a** and **3b** (Scheme 6.3). Compounds **3c,d** are novel and were synthesized as air-stable clear crystalline solids by salt metathesis reactions from the appropriate organometallic ligand reagent and  $(\text{PMe}_3)\text{AuCl}$  in high yield (see experimental section). They were purified by sublimation and performed very well in thermogravimetric analysis (TGA) ramp experiments (Figure 6.9). Compounds **3c** and **3d** left residual masses < 1 % and were calculated to have 1 Torr temperatures ( $T_v$ ) of 100 °C and 138 °C, respectively (Figure S-6.17).<sup>70</sup> The volatility of the series decreases from **3a** > **3b** > **3c** > **3d**.

Using differential scanning calorimetry (DSC) we observed that the thermal stability of the neat compounds increases in the series **3a** < **3b** < **3c** < **3d** (Figure 6.10) due to a shift of

the first exothermic peak to higher and higher temperatures going across the series. The onsets of thermal decomposition ( $T_D$ ) of **3c** and **3d** were found to be 168 °C and 194 °C respectively. Interestingly, this demonstrated that the most volatile compound was also the least stable and vice versa. The precursor figures of merit ( $\sigma^{123}$ ) of **3c** and **3d** were found to be 68 and 54 respectively.

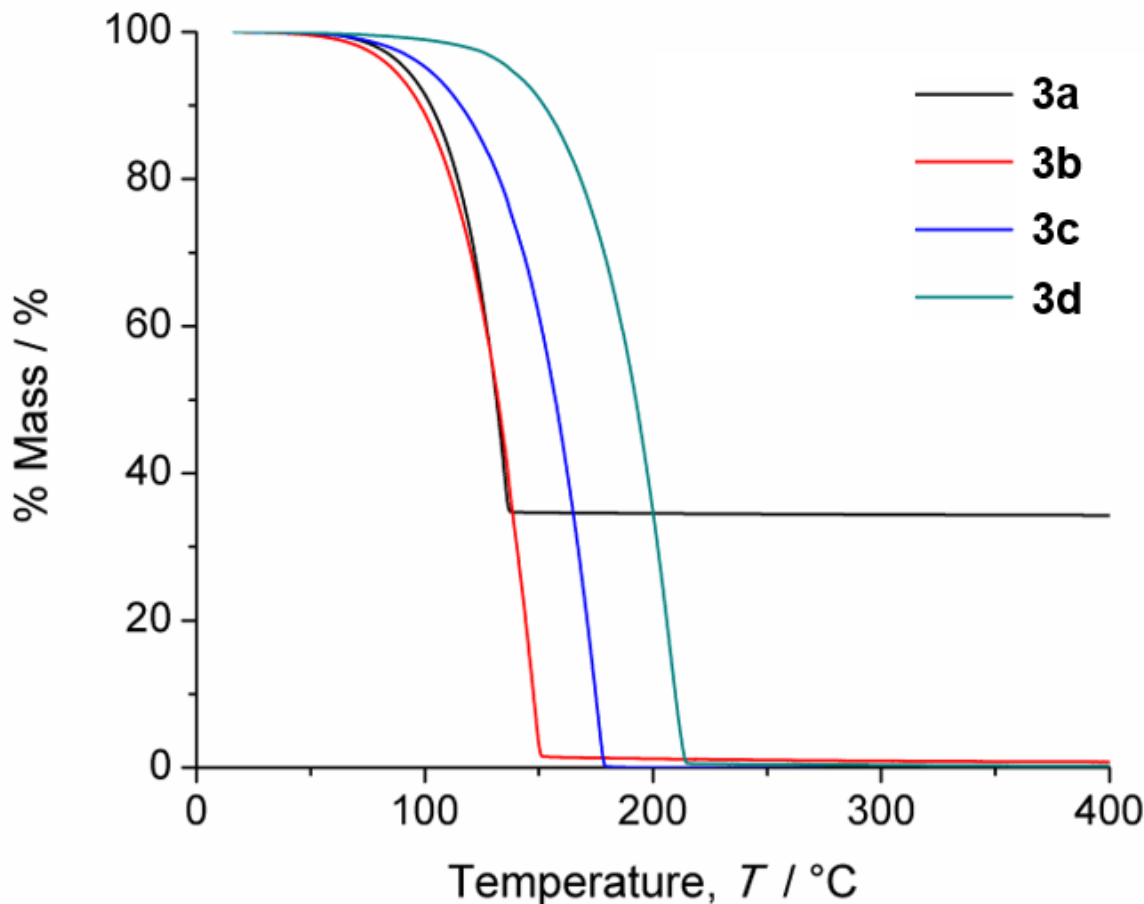


**Figure 6.9** TGA ramp experiments of **3a-d**. Ramp rate = 10 °C min<sup>-1</sup>, 10 ± 2 mg mass loading, Pt sample pans were used in all experiments.

With these new compounds in hand, we set out to devise a QCM experiment that would allow us to determine the activation energy of thermal CVD of each compound, and thus whether we could change the activation energy of the reductive elimination step. We began by studying **3a** because of the large body of CVD literature surrounding this compound.

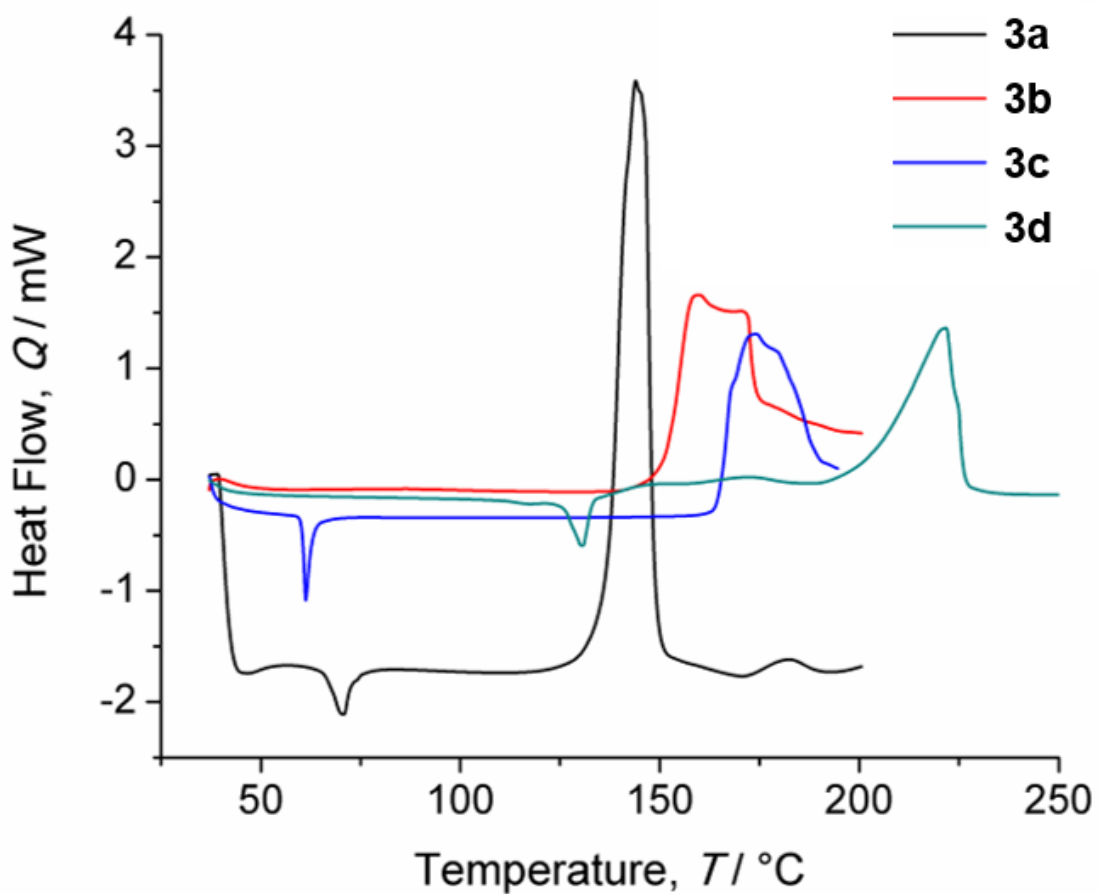


**Figure 6.10** DSC ramp experiments of **3a-d**. Temperature ramp rate =  $10\text{ }^{\circ}\text{C min}^{-1}$ , sample loading =  $0.4 \pm 0.1\text{ mg}$ , aluminum hermetic sample pans were used for all analyses.

CVD is generally broken down into two different growth regimes: a surface-reaction, rate-limited (SRL) regime where an excess of precursor exists and the growth rate is governed by system temperature; and a mass-transport-limited (MTL) regime where the concentration of precursor is sparse and the rate of CVD is governed by precursor flux and is independent of temperature (to a first approximation). The activation energy of CVD can be determined by holding precursor delivery constant, varying the deposition temperature, and recording the change in deposition rate in the SRL regime.

We devised an experiment consisting of a 10-minute exposure of **3a** to the system. This long exposure was used to differentiate SRL and MTL regimes in the process and thus calculate an appropriate growth rate. To help this analysis, we used a quadrupole mass

spectrometer (QMS) onto the exhaust of our deposition tool to analyze the partial pressures of gas-phase byproducts of the CVD process. Using our QCM in combination with the QMS, we performed 10-min exposures of **3a** in triplicate and tracked the growth rate and reaction byproduct concentration.

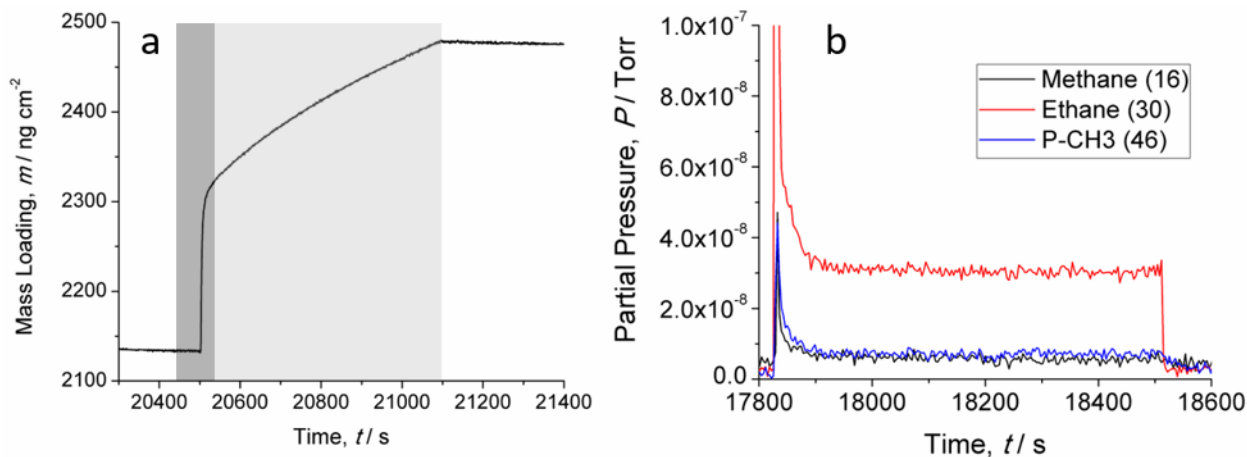


**Figure 6.11** A 10-min exposure experiment of **3a** at 97 °C. a) QCM micrograph of the 10-min exposure experiment where the suspected SRL and MTL regimes are highlighted with dark and light grey shading respectively. b) QMS data tracking  $\text{CH}_4^+$  ( $m/z = 16$ ),  $\text{C}_2\text{H}_6^+$  ( $m/z = 30$ ) and  $\text{PCH}_3^+$  ( $m/z = 46$ ). A large spike in reaction products is observed during the rapid growth regime in Figure 6.11 (a).

We observed what appeared to be two clearly defined growth regimes in the QCM data (Figure 6.11 (a)), one initial rapid growth regime, followed by a slow growth regime where the growth rate remained constant for the remainder of the experiment. The QMS data (Figure 6.11 (b)) mirrored the QCM data, showing a large partial pressure of  $\text{CH}_4^+$ ,  $\text{C}_2\text{H}_6^+$  and  $\text{PCH}_3^+$  at the beginning of the experiment, indicating a strong CVD reactivity that correlated well with the large mass gain in the QCM data.

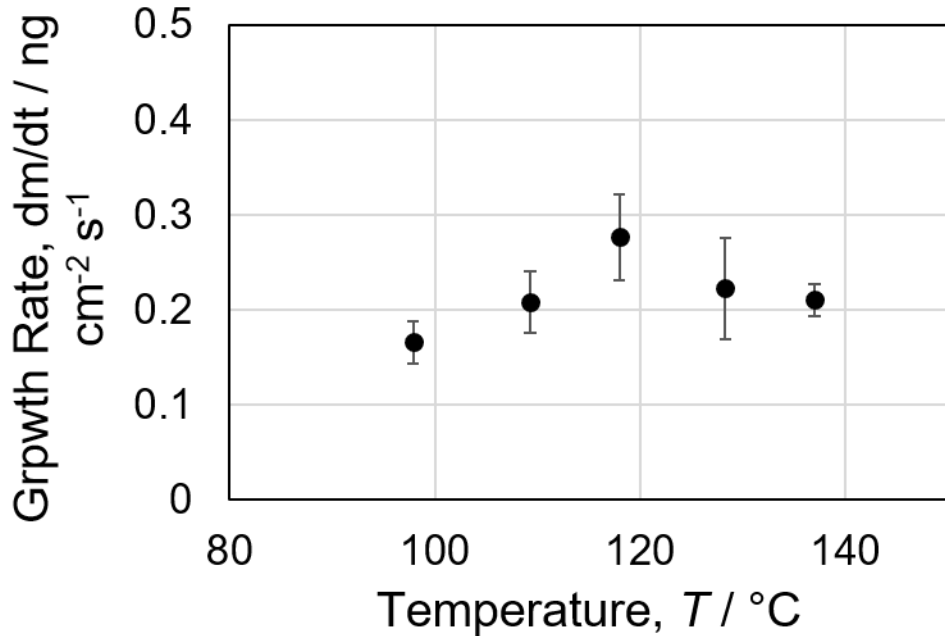


**Figure 6.12** Growth rate of the mass-transport-limited regime of the 10-min exposure experiments of **3a**.

Prior to the experiment, the precursor was held for 10 minutes at the delivery temperature of 70 °C to ensure adequate equilibration of the temperature of the sample. Thus at the beginning of the 10-minute exposure, the dose of precursor was the highest, and the partial pressure of precursor decreased over the course of the dose. This meant that the second slow and constant growth regime in the QCM data was likely an MTL regime. To confirm this, we performed the identical exposure experiment of **3a** at 5 different temperatures. We calculated the growth rate of the MTL region of these experiments and observed no temperature dependence on this growth rate (Figure 6.12), indicating that it was indeed a MTL regime.

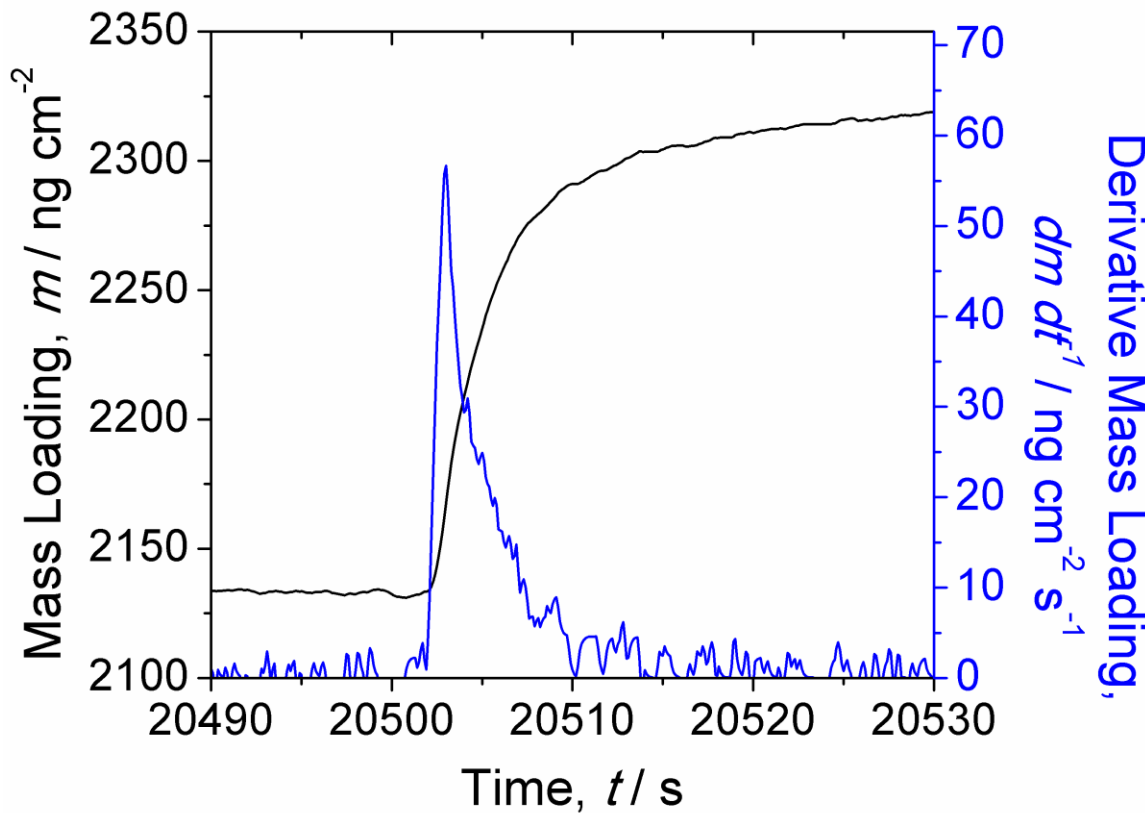


**Figure 6.13** QCM micrograph data from Figure 5.11 (a) (10 min dose of **3a**, surface temperature = 97 °C) overlaid with its derivative curve (blue). The peak growth rate was  $59 \text{ ng cm}^{-2} \text{ s}^{-1}$ .

We then needed a consistent method to analyze the film's growth rate within the SRL regime. We took the first derivative of the mass gain curve (Figure 6.13) and use the position of the maximum, which is the maximum rate of film growth. While this is not the overall growth rate throughout the entire SRL regime, it should function as a suitable surrogate.

We then performed 10-min dose experiments using compound **3c** and found an exponential increase in peak growth rate with respect to temperature, confirming that this was in the SRL regime (Figure 6.14). Notably, compound **3c** begins to deposit a film at a higher temperature than **3a**, which fits our hypothesis that a bulkier alkyl group will result in a higher activation energy for the CVD process.

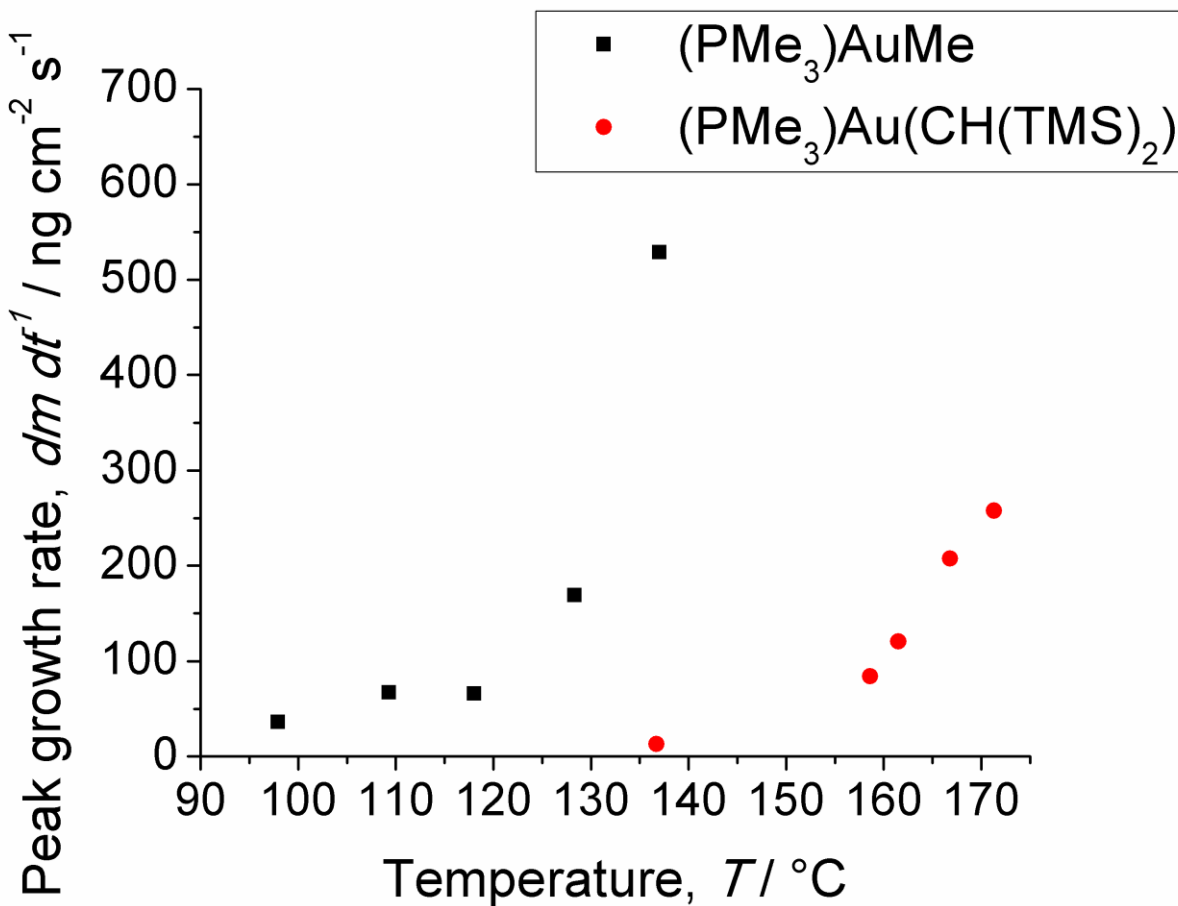


**Figure 6.14** Peak growth rate of **3a** (black) and **3c** (red) plotted as a function of substrate temperature. The source temperatures of **3a** and **3c** were 70 °C and 110 °C respectively.

While we cannot directly assess the activation energy of the two processes, since the rate of reaction is proportional to the rate constant of the reaction, we can qualitatively say that the activation energy for CVD of **3c** is higher than **3a**. In order to determine the true rate constants, a knowledge of the partial pressure of the precursor in the system (unfortunately not constant in our apparatus) at the point of maximum growth rate would be required. Furthermore, a knowledge of the surface coverage of each precursor on a gold surface would be useful in order to rule out the necessity of this term in the kinetic analysis. Previously we found that compound **3b** underwent slow CVD at 120 °C, and based on this activation energy analysis compounds **3c** and **3d** should prove fruitful candidates for kinetically-limited ALD studies.

## 6.4 Conclusions

We developed, qualified, and tested an *in-situ* methodology for testing the self-limiting capabilities of various gold CVD and ALD precursors. We found that **1** showed a very slow CVD component at 120 °C (approximately 2% of its reported ALD growth rate using the O<sub>2</sub>\* + H<sub>2</sub>O process reported by us). Bulky NHC-Au(I) compounds like compound **2** where the NHC bears <sup>t</sup>Bu wingtips are likely not adequate as ALD precursors since we observed a non-saturative growth per pulse of 5.9 Å pulse<sup>-1</sup>. Compound **3** undergoes very slow CVD on Al<sub>2</sub>O<sub>3</sub> surfaces, but the presence of formic acid causes an acceleration of growth which is likely due to formic acid accelerating the formation of Au<sup>0</sup> on Al<sub>2</sub>O<sub>3</sub> surfaces. Once formed, Au<sup>0</sup> catalyzes the CVD of **3** and precludes its use as an ALD precursor for gold. Given its relatively slow rate of CVD compared to **2**, we synthesized a series of (PMe<sub>3</sub>)Au-R compounds based on **3** where R increased in steric bulk. While compound **3a** undergoes rapid CVD in our system we can qualitatively say from *in situ* QCM and QMS analysis that CVD of **3c** has a much higher activation energy. If the increase in activation energy is indeed due to a mechanistic change of the rate-limiting step of the CVD reaction, then **3c** and likely **3d** should serve as kinetically-limited ALD precursors for gold metal.

## 6.5 Experimental Details

### In-situ monitoring CVD experiments

A quartz-crystal microbalance was purchased from Colnatech and used as received. Polished, gold-coated, RC-cut quartz crystals were purchased from Philip Tech and came packaged in clean-room compatible, dust-free carousels in which they were stored until use. Mechanical grade silicon was purchased from University Wafer and was cleaned using the RCA cleaning procedure before use. For experiments that were conducted on Al<sub>2</sub>O<sub>3</sub> surfaces, both the QCM crystal and the silicon wafer were coated with 100 cycles of Al<sub>2</sub>O<sub>3</sub> using the standard ALD process: [0.1 s AlMe<sub>3</sub> | 10 s N<sub>2</sub> purge | 0.1 s H<sub>2</sub>O | 10 s N<sub>2</sub> purge] at 200 °C. The system was then allowed to cool and equilibrate to the desired

temperature overnight under vacuum so as to not contaminate the surface with ambient chemicals and particles. When depositing on gold surfaces, the crystals were used as received and the system was allowed to equilibrate to the desired temperature for at least 3 hours under vacuum. For small increases in temperature such as the experiments performed to collect data for figures 6.12 to 6.14, only a few hours are required for the QCM signal to equilibrate. But if the system was to be heated or cooled over a much larger range like from room temperature to 150 °C then an overnight equilibration was necessary for the QCM signal to stabilize.

Prior to deposition, the delivery lines through which the precursors travel towards the furnace were allowed to pre-heat under vacuum overnight to their desired temperatures. The delivery lines were always heated such that a temperature gradient of at least + 10 °C was established between the gold bubbler (lower temp) and the entrance to the furnace (higher temp) in order to prevent precursor condensation in the delivery lines. On the day of the experiment, precursors were loaded into the gold precursor bubbler in an N<sub>2</sub>-filled glovebox, sealed, and then attached to the apparatus where they were evacuated to the operating pressure of the system. The bubbler was then allowed to heat to the 1 Torr temperature of the precursor in question (in order to ensure comparable molar deliveries and was held at temperature for 30 minutes before beginning the experiment.

## TGA and DSC

TGA was performed on a TA Instruments Q500 instrument which was housed in a nitrogen-filled glovebox. The purge gas during TGA and DSC experiments was nitrogen gas of (99.999 %, 5.0) and (99.998 %, 4.8) respectively. In a typical TGA experiment 10.000 ± 2 mg of analyte was placed in a platinum pan whose mass was monitored by the instrument during the analysis. For DSC experiments, due to the volatile nature of the analytes and their decomposition products, mass loadings greater than 1.000 mg often lead to a rupturing of the hermetically sealed aluminum pans. Thus, small mass loadings of 0.300 ± 0.200 mg were used for typical DSC experiment. DSC samples were

hermetically sealed in aluminum pans inside the glovebox before analysis. Both TGA and DSC temperature ramp rates were 10.0 °C / min. Langmuir vapour pressure data were derived from TGA data using a previously reported method with Cu(tmhd)<sub>2</sub> as the calibrant.<sup>70,278</sup>

## Synthetic Details

All manipulations were performed under an inert atmosphere of dry nitrogen gas using an MBraun Labmaster 130 glovebox or standard Schlenk techniques unless otherwise stated. All synthesized compounds were treated as light sensitive materials during synthetic procedures and were stored at 5 °C in a refrigerator. NMR spectra were collected at room temperature on a Bruker 300 MHz or a Jeol 400 MHz spectrometer and were referenced to an internal standard of tetramethylsilane (TMS) in the case of CDCl<sub>3</sub> or residual protio solvent signal in the case of C<sub>6</sub>D<sub>6</sub> (7.16 ppm relative to TMS). C<sub>6</sub>D<sub>6</sub> was purchased from Aldrich and was degassed using freeze-pump-thaw cycles and subsequently stored over activated 4 Å molecular sieves under inert gas. Compounds **1**,<sup>99</sup> **2**,<sup>123</sup> **3a**,<sup>123</sup> **3b**<sup>123</sup> were prepared using our reported methods. Methylolithium (1.6 M in diethyl ether), tetrahydrofuran (anhydrous), pentane (anhydrous), and dichloromethane (anhydrous) were purchased from Aldrich and used as received. Diethyl ether, hexanes, and toluene were purchased from VWR chemicals and purified using an MBraun solvent purification system prior to use. Synthesis of **3c** via a lithiation of H<sub>2</sub>C(SiMe<sub>3</sub>)<sub>2</sub> was discounted based on the reported difficulty of metalating this species.<sup>296</sup> Instead, we purchased (SiMe<sub>3</sub>)<sub>2</sub>CHCl from Merck which was used as received with the intention of using it to form a Grignard reagent. HC(SiMe<sub>3</sub>)<sub>3</sub> and [Li(THF)<sub>4</sub>][Li(C(SiMe<sub>3</sub>)<sub>3</sub>)<sub>2</sub>] were synthesized and purified according to literature methods.<sup>297,298</sup>

### Synthesis of **3c**:

Magnesium metal (0.552 g, 22.7 mmol) was added to a 100 mL Schlenk flask and flame dried under high vacuum. After cooling to room temperature, a solution of 5.313 g (27.3 mmol, 1.2 eq.) of (SiMe<sub>3</sub>)<sub>2</sub>CHCl in 36 mL of tetrahydrofuran (prepared in a glovebox) was added dropwise under a stream of nitrogen. Then a pre-dried reflux condenser was

attached to the flask and the solution was brought to reflux for 18 hours. The resulting pale yellow solution was then cooled to room temperature and added dropwise to a -78 °C suspension of 7.000 g (22.7 mmol) of (PMe<sub>3</sub>)AuCl in 100 mL of tetrahydrofuran. This caused the white suspension of (PMe<sub>3</sub>)AuCl to clear slightly to a more opaque mixture. Once the addition was complete, the mixture was allowed to warm slowly to room temperature where a substantial amount of white solid was still observed. To push the reaction to completion, the mixture was then brought to reflux for 30 minutes. The mixture was cooled to room temperature, at which point a slight purple discolouration was observed but much of the remaining white solid had disappeared. To this mixture was added 100 mL of hexanes, which caused the precipitation of a white solid. Then, 10 mL of deionized water was added dropwise while stirring to destroy any leftover Grignard reagent. The mixture was decanted into a separatory funnel with as little agitation as possible in order to prevent an emulsion from forming. The organic layer was kept, and the aqueous layer was then washed with shaking with 3 x 100 mL portions of hexanes which were combined with the initial organic phase. The organic phase was dried with MgSO<sub>4</sub>, filtered, and then the solvent was removed on a rotary evaporator leaving an off-white solid. This solid was air-stable and could be purified by vacuum sublimation (75 °C, 40 mTorr) onto a water-cooled cold finger. Yield = 7.972 g (81 %). 0.9389

T<sub>m</sub> (DSC) = 61 °C

**<sup>1</sup>H-NMR** (300 MHz, C<sub>6</sub>D<sub>6</sub>): δ = 0.53 (d, <sup>3</sup>J<sub>H-P</sub> = 9.1 Hz, 9H, P-CH<sub>3</sub>), 0.50 (s, 18H, Si-CH<sub>3</sub>), 0.37 (d, 1H, C-H).

**<sup>13</sup>C-NMR** (75.5 MHz, C<sub>6</sub>D<sub>6</sub>): δ = 21.50 (d, <sup>2</sup>J<sub>C-P</sub> = 70.9 Hz, P-Au-C(H)), 15.28 (d, <sup>1</sup>J<sub>C-P</sub> = 30.6 Hz, P-CH<sub>3</sub>), 6.34 (d, <sup>4</sup>J<sub>C-P</sub> = 1.9 Hz, P-Au-C-Si(CH<sub>3</sub>)<sub>3</sub>))

**<sup>31</sup>P-NMR** (121.5 MHz, C<sub>6</sub>D<sub>6</sub>): δ = 10.69.

### Synthesis of 3d:

In a glovebox was prepared a solution of 1.406 g (1.84 mmol, 0.55 eq.) of [Li(THF)<sub>4</sub>][Li(C(SiMe<sub>3</sub>)<sub>3</sub>)<sub>2</sub>] in tetrahydrofuran. This solution was added dropwise to a -78 °C suspension of 1.03 g (3.34 mmol, 1 eq.) of (PMe<sub>3</sub>)AuCl in 50 mL tetrahydrofuran. Once the addition was complete, the reaction was allowed to warm to room temperature. Once

warm, it was brought to reflux for 20 minutes which caused it to darken somewhat alarmingly. Once it had cooled down to room temperature, hexanes (100 mL) was added, followed by 10 mL of deionized water while stirring. The organic layer was decanted from the aqueous phase, and the aqueous layer was washed vigorously with 3 x 30 mL of hexanes. The combined organic layers were dried over MgSO<sub>4</sub>, filtered, and then the solvent was removed on a rotary evaporator. The resulting light purple solid appeared to be air-stable and was purified by vacuum sublimation (105 °C, 10 mTorr). Yield = 1.29 g (76 %).

T<sub>m</sub> (DSC) = 131 °C

**<sup>1</sup>H-NMR** (300 MHz, C<sub>6</sub>D<sub>6</sub>):  $\delta$  = 0.50 (d, <sup>3</sup>J<sub>H-P</sub> = 8.9 Hz, 9H, Au-CH<sub>3</sub>), 0.48 (s, 18H, SiMe<sub>3</sub>).

**<sup>13</sup>C-NMR** (75.5 MHz, C<sub>6</sub>D<sub>6</sub>):  $\delta$  = 24.11 (d, <sup>2</sup>J<sub>C-P</sub> = 83.2 Hz, P-Au-C(H)), 13.20 (d, <sup>1</sup>J<sub>C-P</sub> = 33.6 Hz, P-CH<sub>3</sub>), 5.01 (d, <sup>4</sup>J<sub>C-P</sub> = 2.3 Hz, P-Au-C-Si(CH<sub>3</sub>)<sub>3</sub>))

**<sup>31</sup>P-NMR** (121.5 MHz, C<sub>6</sub>D<sub>6</sub>):  $\delta$  = 14.65.

## 6.6 Supporting Information

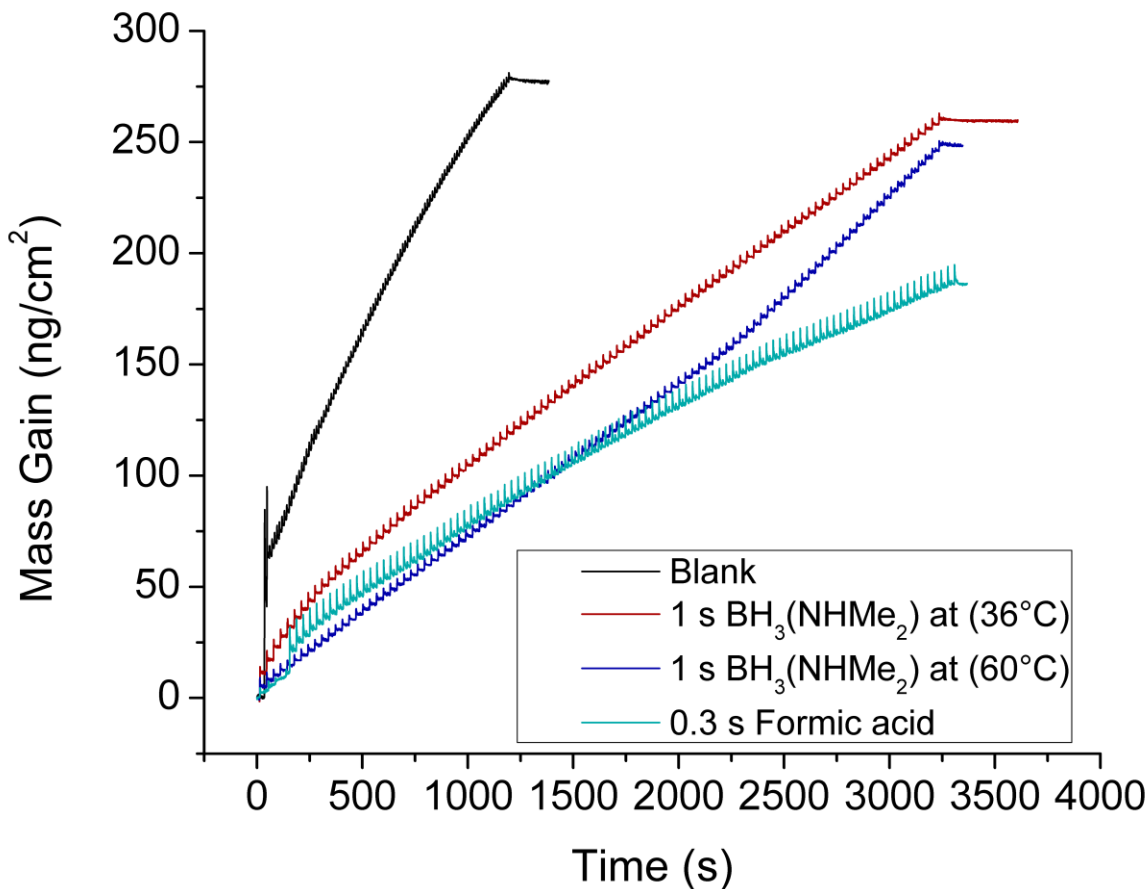


**Figure S-6.15** Comparison of the total mass gain from 100 cycles of [1 s (1) | 15 s  $\text{N}_2$  purge] (blank) with 100 cycles of [1 s (1) | 15 s  $\text{N}_2$  purge | (Co-reagent dose) | 15 s  $\text{N}_2$  purge]. The co-reagent, its pulse time, and its bubbler temperature if applicable are listed in the legend.

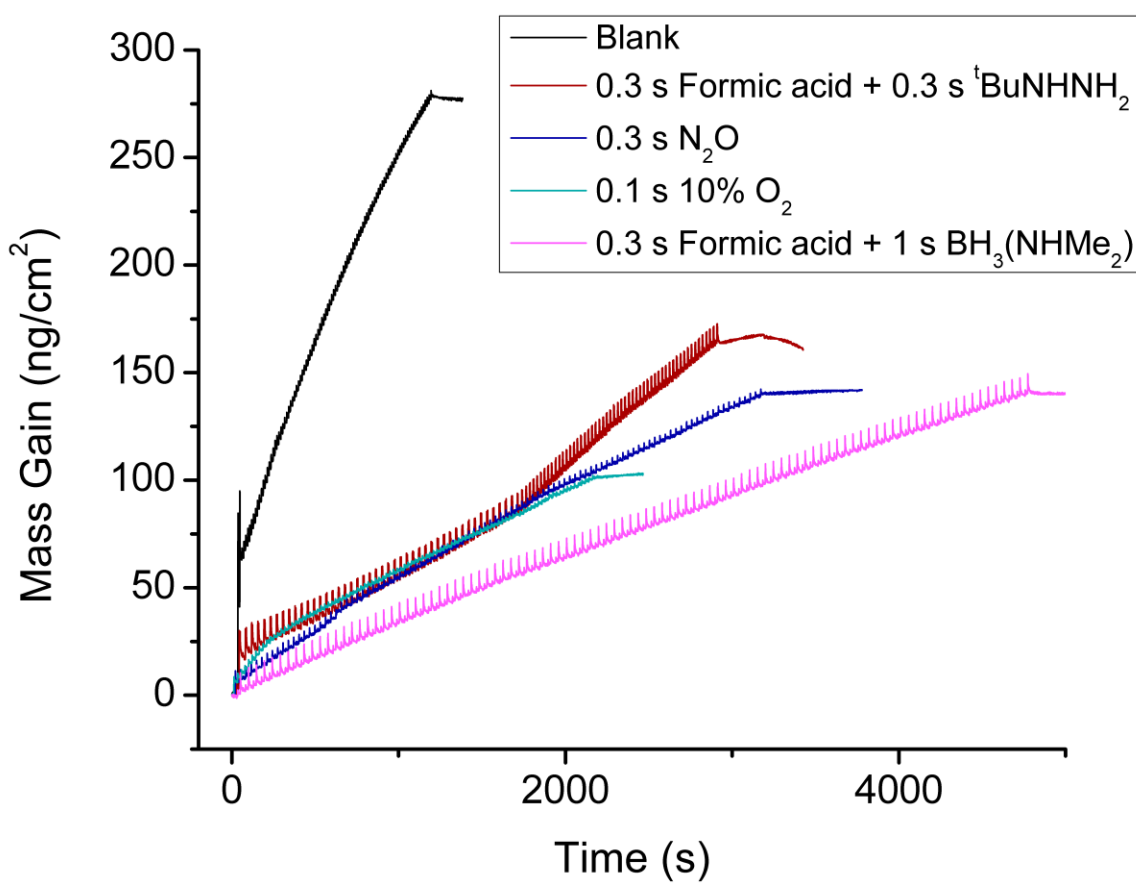


**Figure S-6.16** Comparison of the total mass gain from 100 cycles of [1 s (1) | 15 s N<sub>2</sub> purge] (blank) with 100 cycles of [1 s (1) | 15 s N<sub>2</sub> purge | (Co-reagent dose) | 15 s N<sub>2</sub> purge]. The co-reagent and its pulse time are listed in the legend. The BH<sub>3</sub>(NHMe<sub>2</sub>) was held at 36 °C.

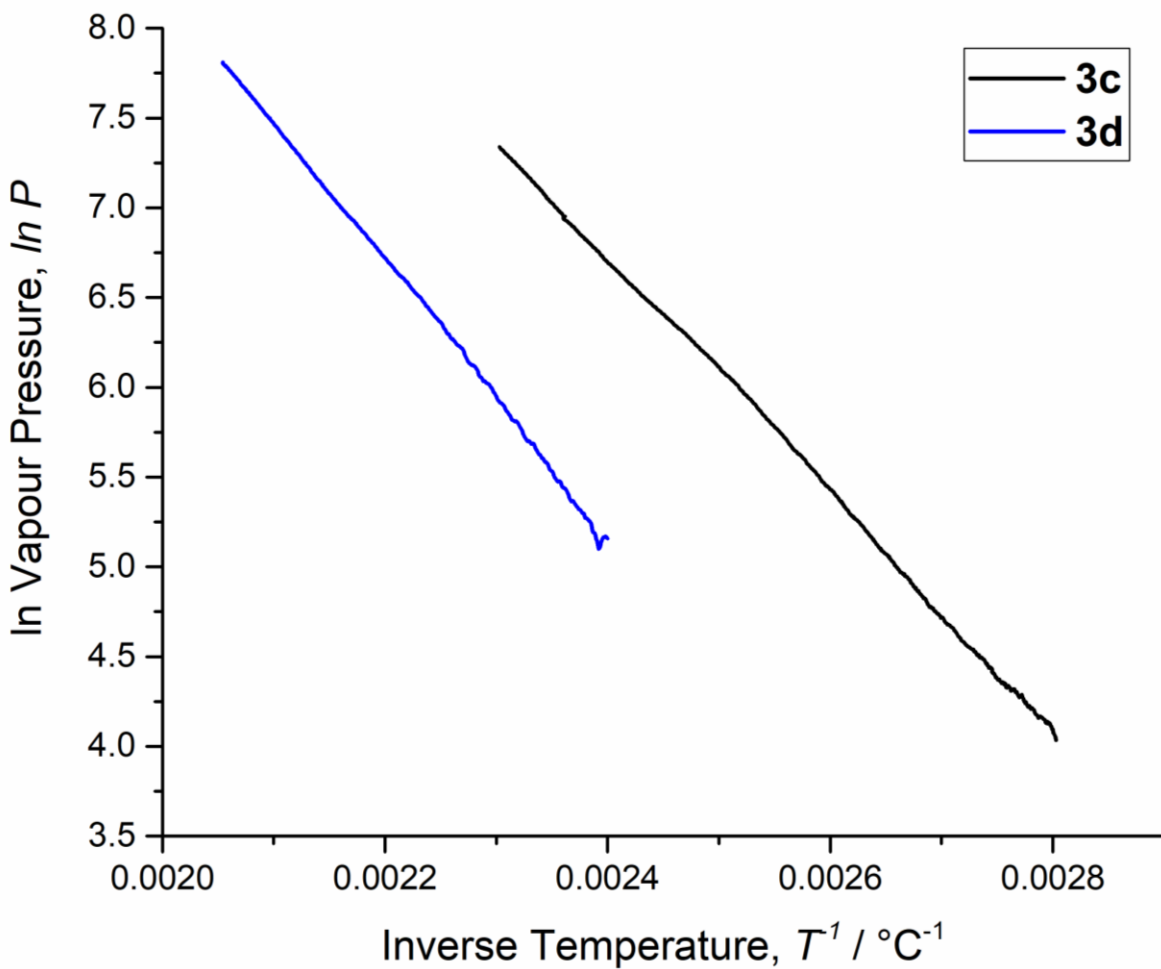


**Figure S-6.17** Langmuir vapour pressure curves for **3c** and **3d**. Their respective lines of best fit are  $\ln P$  (Torr) =  $-6576(T^{-1}, ^\circ\text{C}^{-1}) + 22.51$  ( $R^2 = 0.9990$ ) and  $\ln P$  (Torr) =  $-7733(T^{-1}, ^\circ\text{C}^{-1}) + 23.72$  ( $R^2 = 0.9990$ ).



# **Chapter 7 N-Heterocyclic carbenes as self-limiting ligands for ALD**

*Manuscript in preparation:*

Matthew B. E. Griffiths, Aya Kadri, Atilla C. Varga, and Seán T. Barry

Department of Chemistry, Carleton University, 1125 Colonel By Drive, Ottawa, Ontario,  
K1S 5B6, Canada

## 7.1 Abstract

Lead by our hypothesis that NHC's could be used as effective self-limiting ligands for gold atomic layer deposition (ALD), we designed a family of organometallic Au(I) precursors of the type NHC-Au-R, where we iteratively varied the anionic (R) alkyl ligand (R = Me, CH<sub>2</sub>(SiMe<sub>3</sub>), CH(SiMe<sub>3</sub>)<sub>2</sub>, CF<sub>3</sub>) as well as the NHC coordinative ligand, where both wingtip and backbone substitutions were altered. While the CF<sub>3</sub> complex was more thermally stable than its aliphatic counterparts, it also suffered from a poor volatility. We determined that the CH(SiMe<sub>3</sub>)<sub>2</sub> ligand was unsuitable as an anionic ligand because it decomposes rapidly during thermogravimetric analysis (TGA) experiments. TGA demonstrated, in the case of the small NHC *N,N'*-dimethylimidazole-2-ylidene, that it would thermally persist on a metallic gold surface only desorbing in the temperature range of 370 – 400 °C. We determined the precursor figures of merit for this family of compounds, and found that the NHC *N,N'*-diisopropyl-4,5-dimethylimidazole-2-ylidene produced the best-performing precursors from the standpoint of thermolysis. Using a combination of *in-situ* QCM and QMS, we found that two compounds in this family undergo self-limiting chemisorption on a gold surface at 150 °C accompanied by a very minor CVD component. We then undertook a preliminary set of experiments where we studied their deposition characteristics using plasma co-reagents in a plasma-enhanced atomic layer deposition (PE-ALD) apparatus, and analyzed the deposited films using atomic force microscopy (AFM), four-point probe resistivity (4-PP), and x-ray photoelectron spectroscopy (XPS).

## 7.2 Introduction

Atomic layer deposition (ALD) is deposition technique capable of depositing thin films of a multitude of materials with high precision due to self-limiting chemisorption of the various reagents being employed.<sup>48,284</sup> It is common for homoleptic metal halides, alkyls, alkoxides, amides, and other compounds to exhibit self-limiting chemisorption due to the persistence of one or more of the anionic ligands at the surface.

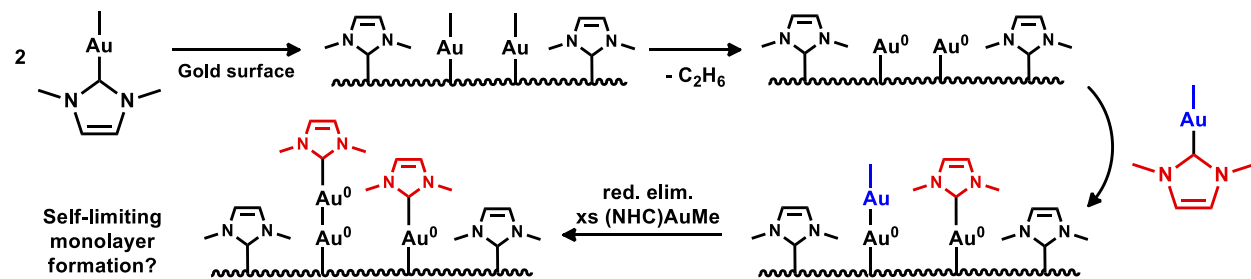
We have recently found that the self-limiting growth of our gold ALD precursor, trimethylphosphine trimethylgold(III), is actually due to the trimethylphosphine ligand and not to the methyl ligands.<sup>299</sup> A recent surge in research of the surface chemistry of N-heterocyclic carbenes (NHCs) has shown that these ligands are far more strongly bound to metallic surfaces than tertiary phosphines or dialkylthiols, and that they possess very interesting and useful properties as “surface ligands”.<sup>113,300–303</sup> Given our interest in ALD of gold metal, the natural extension of these findings would be to purposefully use an NHC as the self-limiting ligand for an ALD-deposited gold metal film.

Alkylgold(I) phosphines, a popular class of chemical vapour deposition (CVD) precursors, readily undergo an autocatalytic decomposition reaction on gold and other metal surfaces.<sup>118,125</sup> To date, no studies exist that interrogate the surface chemistry of an analogous class of gold compounds: alkylgold(I) NHCs. However, given the known strength of the  $\text{Au}^*-\text{NHC}$  bond (where “\*” denotes a surface), the NHC will remain bound to the surface whereas trimethylphosphine begins to desorb above 100 °C. Based on the known alkylgold(I) phosphine CVD mechanism, we hypothesized a surface chemisorption reaction to guide our experimental design (Scheme 7.1).

This idealized reaction scheme is based on alkylgold(I) phosphines, where the initial chemisorption reaction is expected to cleave the Au-NHC bond, forming surface bound NHC and surface bound Au-Me species. As with the alkylgold(I) phosphines, Au-Me surface groups readily eliminate  $\text{C}_2\text{H}_6$  through bimolecular reductive elimination, which occurs rapidly, leaving surface bound NHC and empty  $\text{Au}^0$  surface sites. If the precursor is in sufficient concentration above the surface during this step, then these newly formed  $\text{Au}^0$  sites can be the site of a new chemisorption event. This not only leaves the surface

terminated in NHCs but allows multiple orders of chemisorption per beginning surface site and should theoretically allow a higher growth per cycle of gold compared to a single-chemisorption type system.

**Scheme 7.1** Hypothesized chemisorption reaction of a small alkylgold(I) NHC complex on a gold surface.



Not all NHCs behave equally on gold surfaces, and it has been shown that the size of the wingtip groups of NHCs can have a dramatic effect on their surface chemistry. Particularly, on Cu it was shown that when NHCs with Me or Et wingtips were used, they could not be completely removed from the surface in a temperature-programmed desorption (TPD) experiment.<sup>304</sup> In contrast, the larger <sup>t</sup>Pr wingtip carbene could be completely removed from the surface. This hints at a possible contamination in a growing film if small-wingtip NHCs are used in the ALD precursor design. We have previously observed the ability of <sup>t</sup>Pr wingtip NHCs to modify the growth morphology of gold nanoparticles (Chapter 3).<sup>110</sup> We have also observed that <sup>t</sup>Bu wingtip NHCs do not behave as self-limiting ligands in experiments detailed in Chapter 6 of this thesis.<sup>123</sup> Given the ever-growing amount of evidence that NHCs can play the role of the self-limiting ligand for Au ALD, we decided to begin a precursor design study to determine which of a family of precursors might be the best candidate for deposition testing. We herein describe a combined precursor design, *in-situ* self-limiting chemisorption detection, and preliminary ALD study of these new compounds.

## 7.3 Results and Discussion

### 7.3.1 Synthesis and Thermolysis

Compounds in the families **1-3** (Scheme 7.2) are readily synthesized in a one-pot procedure from the corresponding alkylgold(I) phosphine in good yield (Scheme 7.3) and can be purified by vacuum sublimation between 110 and 140 °C (5 mTorr). We found that all syntheses prepared by this method required an excess of NHC and NaH to push the reaction to completion. For compounds **4a-c** we found that very low conversions (below 25 %) were achieved under similar conditions with NaH as a base, and we were able to remedy the situation using a 25 % excess of both the NHC salt and LiN(SiMe<sub>3</sub>)<sub>2</sub> as a base instead. When we used a free NHC for **5a** and **5b**, only a slight excess was necessary to achieve good conversion. The most efficient workup we developed, which was applicable for all reactions, involved a liquid-liquid extraction (H<sub>2</sub>O / DCM) which removes unreacted free NHC from the mixture by hydrolyzing it, thus leaving only starting material (if present), and the product which are both highly soluble in organic solvents (see experimental section). Although their persistence in the workup of the crude mixture was uncommon due to the large excess of NaH, unreacted NHC salts that were organic soluble (specifically the tetrafluoroborates) sometimes persisted through the synthesis and were observed in the crude mixture after workup. Since they were not volatile, they could be removed by subliming the gold compounds out of the crude mixture which was the final purification step of nearly all compounds.

When conducting this study, we opted for a general synthesis that would facilitate making the whole family of compounds. While the yields reported here aren't optimal from a green chemistry standpoint, future efforts with these compounds for large-scale ALD studies will involve improved and more careful synthetic methods. Likely this will entail two-pot procedures where the NHC is first carefully generated and isolated from reaction byproducts and excess strong base before addition to the starting gold compound.

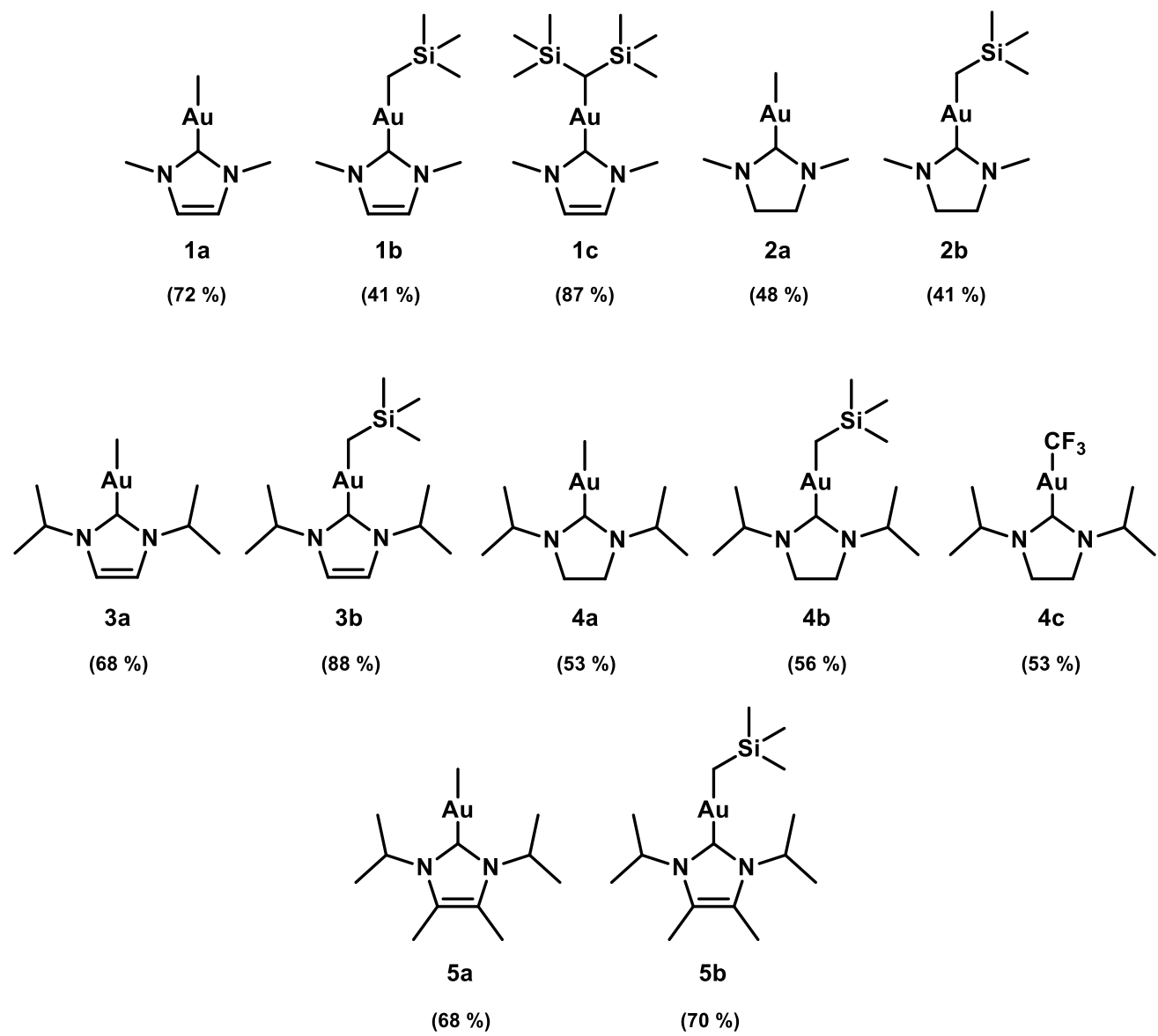
All compounds shown in Scheme 7.3 are novel, and their structure was determined using a combination of NMR techniques. To rule out the presence of cationic gold species of the type  $[(\text{NHC})_2\text{Au}]^+[\text{AuX}_2]^-$  we used <sup>1</sup>H- and <sup>13</sup>C-NMR techniques to ensure that we

observed the expected number and multiplicity of peaks. Then, the connectivity of the compounds was confirmed with HMBC which successfully correlated the carbenic carbon to the H atoms of the NHC ligand ( $^3J_{C-H}$ ) and to the H atoms of the alkyl ligand ( $^3J_{C-H}$ ). This confirmed that no double-salt type species were present, and that the expected neutral Au(I) compounds were indeed being formed.

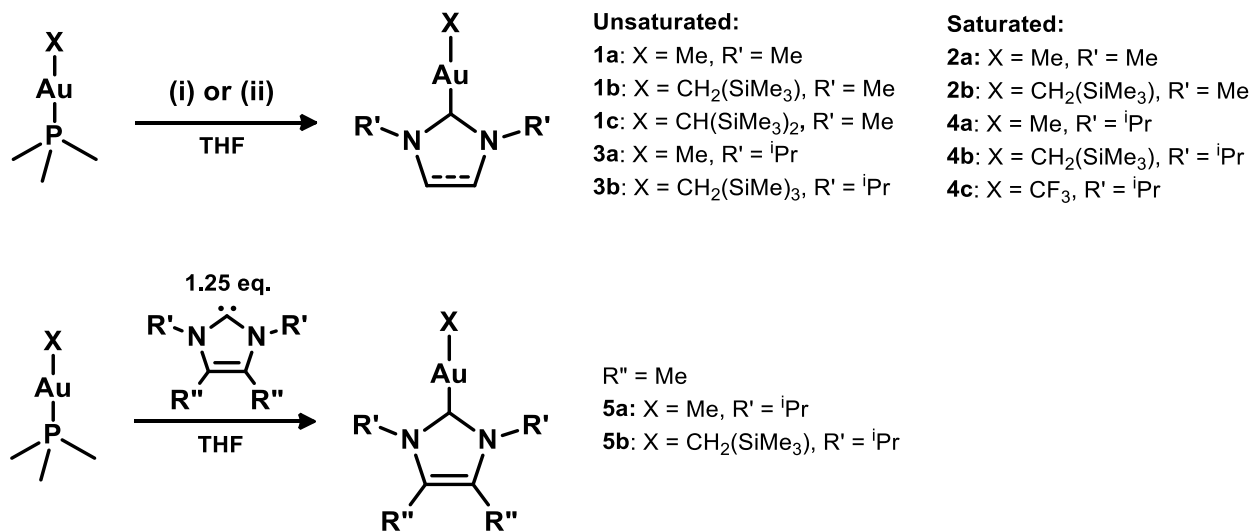
Compounds bearing unsaturated and saturated NHC ligands also showed the expected  $^{13}C$ -NMR shifts of the carbenic carbon with the aromatic NHC chemical shifts ranging between 194-197 ppm and the saturated NHC chemical shifts ranging from 215-217 ppm.

Using thermogravimetric analysis (TGA) (Figures 7.1 to 7.4) and differential scanning calorimetry (DSC) (Figures S-7.9 to S-7.20), several useful thermal characteristics of the precursors can be determined.<sup>123</sup> The temperature at which the analyte reaches a vapor pressure of 1 Torr ( $T_V$ ) can be used to benchmark a compound's volatility. The residual mass of the ramp experiment can be used to determine the mole fraction of gold remaining ( $\%_{Au}$ ) which can give information about the kinetics of a compound's thermal stability. The onset of thermal decomposition ( $T_D$ ) can be determined using DSC and allows a thermodynamic (constant volume) determination of the onset of thermal decomposition. TGA ramp experiments (10 °C /min) (Figure 7.1) and DSC ramp experiments (10 °C / min) revealed that the volatility and thermal stability of the compounds increases in the order **1a < 1b < 1c** (Table 7.1).

**Scheme 7.2** New NHC-Au-R compounds synthesized for this study



**Scheme 7.3.** Synthetic method for the NHC-Au-R precursors. Conditions: (i) 1.3 – 3 eq. [NHC]X + 2.4 – 4.2 eq. NaH + 5 mol % NaO<sup>t</sup>Bu relative to NaH ; (ii) For **4a-c** only, 1.25 eq. [NHC]X + 1.25 eq. LiN(SiMe<sub>3</sub>)<sub>2</sub>. Synthetic yields are given under the compounds in parentheses (%).



Interestingly, the kinetic stability of **1c** does not mirror the trend of increasing decomposition temperatures, and **1c** ( $\%_{Au} = 65.2$ ) is much less kinetically stable than **1a** ( $\%_{Au} = 10.5$ ) or **1b** ( $\%_{Au} = 7.7$ ). Compound **1c** clearly undergoes a two-step thermolysis, and upon closer inspection it is evident that in fact **1a** and **1b** also thermolyze in two steps. Initially, evaporation and decomposition occurred simultaneously, but the rate of decomposition of **1c** appears to be much higher than the other two compounds. A second mass loss event was observed at 370 °C for **1c** and 395 °C for **1a** and **1b**.

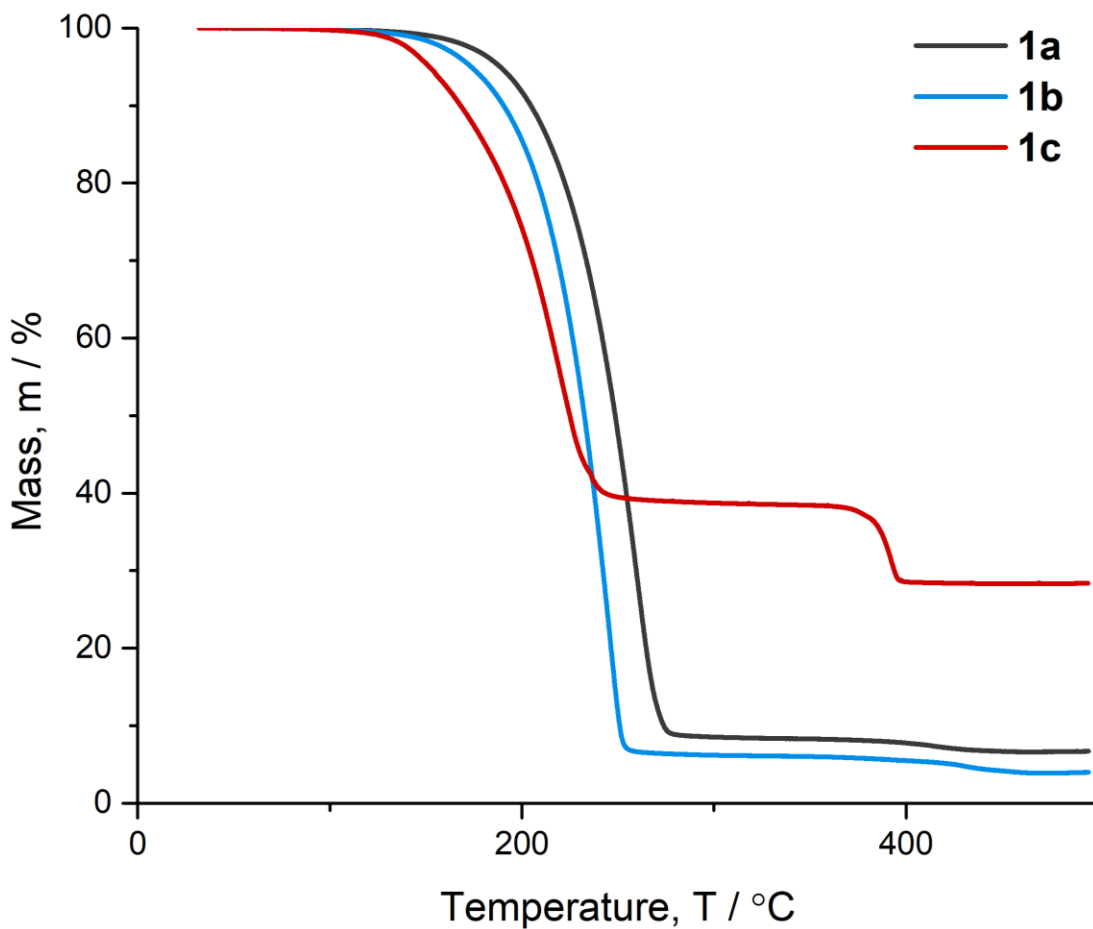
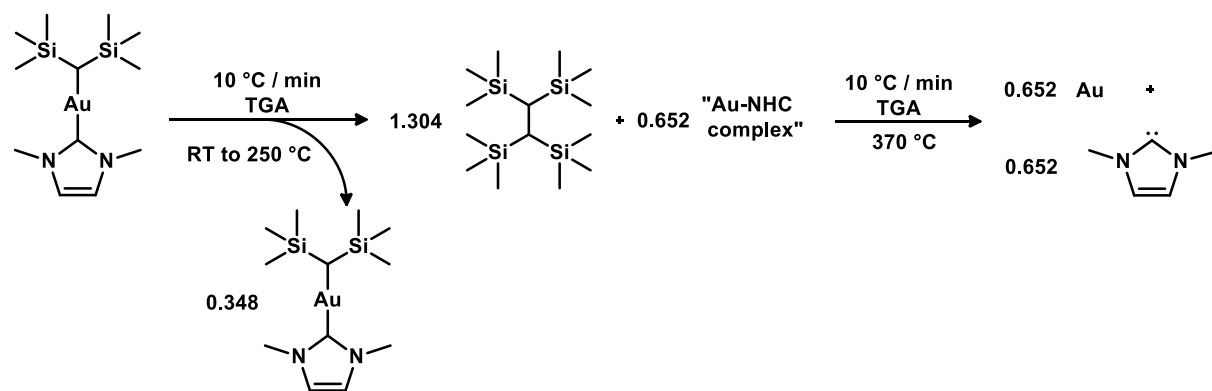


**Figure 7.1** TGA ramp experiments of **1a**, **1b**, and **1c** (ramp rate =  $10\text{ }^{\circ}\text{C min}^{-1}$ )

Inspection of the TGA pan at the end of the thermolysis of **1c** revealed a coating of bright gold metal. If we assume that the final residual mass ( $M_r = 28.3\%$ ) is composed entirely of gold metal, and note that the % mass of gold in the initial compound was 43.4%, then we can assume that 34.8 % of the initial sample evaporated without decomposing. If we further assume that this evaporation occurs in the first mass loss event, and if the remaining 65.2 % of the molecules decompose to lose only the bis-silyl ligand (MW = 159.39 g/mol, overall 22.9 %) in the first mass loss event, then the combined theoretical mass loss we should observe in the first thermolysis event would be the sum of evaporation and ligand loss (57.7 %), which would be observed as a remaining mass loading of 42.3 % (See Scheme 7.4). This is in fact very close to the % mass of the first

plateau of the thermolysis curve (~39%). The NHC ligand appears to remain in the system before evaporating at 375 °C, resulting in an observed mass loss of 11.7 % (theoretical = 13.8 %). This decomposition pathway appears to occur for **1a** and **1b** to a lesser degree as indicated by the slight mass loss near 400 °C. The analogous phosphine precursors to **1a**, **1b**, and **1c** all behave very well by TGA (Chapter 6) and the instability of **1c** was unexpected. The nature of the “Au-NHC intermediate” remains unknown but does allude to the potential of these carbene ligands to persist as self-limiting surface ligands.

**Scheme 7.4** Proposed thermolysis reaction for **1c** during the TGA experiment (mass loading of **1c** = 10.60 mg). Note that at the same temperature ramp rate, a different mass loading of **1c** will change the stoichiometric quantities of the various compounds.



The precursor figures of merit ( $\sigma$ )<sup>123</sup> for **1a**, **1b**, and **1c** were found to be -21, 47, and 25 respectively. By examining the TGA trace only, consensus in the field of precursor design might place compound **1c** as the least desirable due to its stark two-step thermolysis and high residual mass. Using the figure of merit is beneficial in this case because it highlights the useful range where **1c** is more desirable than **1a**, however in this series **1b** is still the best-candidate.

TGA ramp analyses of compounds **2a** and **2b** are shown in Figure 7.2. By saturating the carbene backbone,  $T_v$  of **2a** and **2b** is essentially unchanged by comparison to their unsaturated analogues (Table 7.1). Interestingly, the thermal stability ( $T_D$ ) gained by adding  $R = \text{CH}_2(\text{SiMe}_3)$  from **1a** to **1b** is not mirrored from **2a** to **2b**. In general, the  $\text{CH}_2(\text{SiMe}_3)$  ligand only increased thermal stability in the case of **1a** to **1b** and has little effect when using the other NHCs. However, compounds bearing  $R = \text{CH}_2(\text{SiMe}_3)$  were always more volatile than their methyl counterparts.

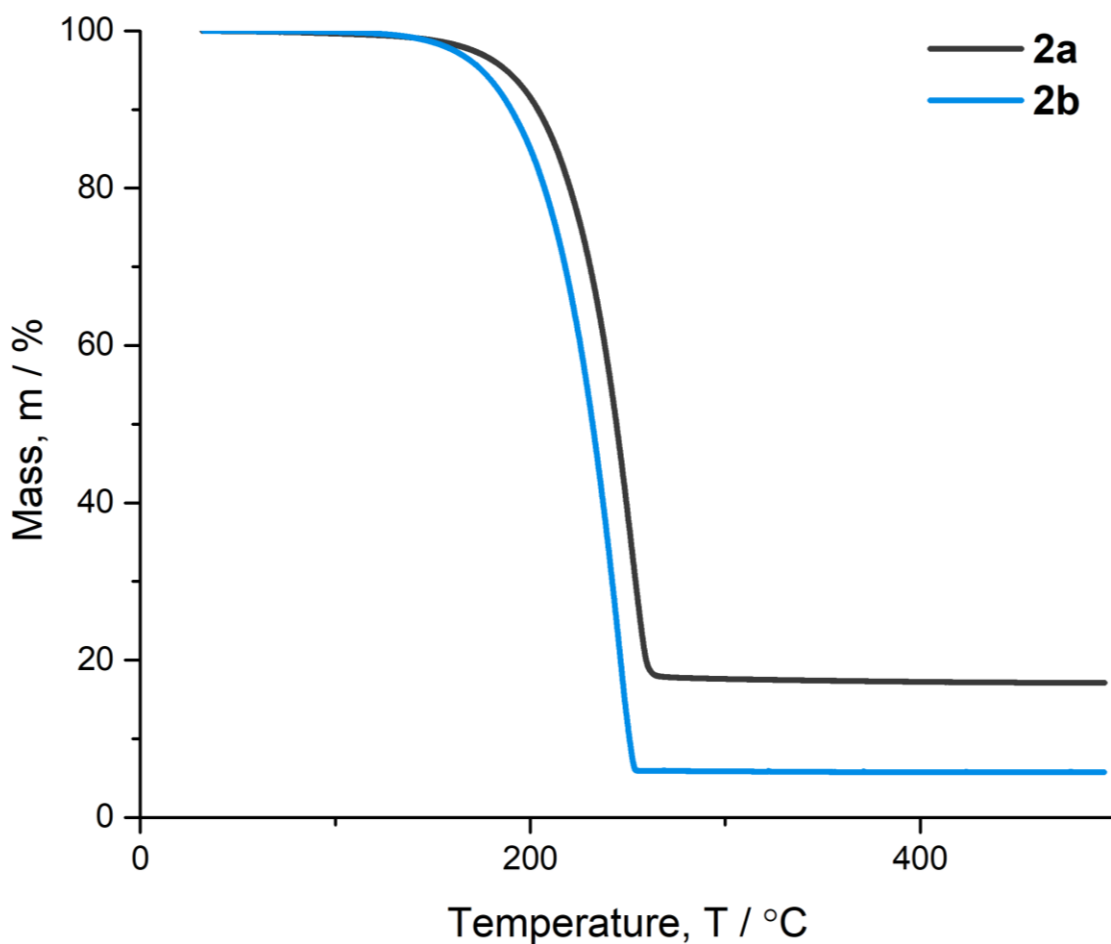


**Figure 7.2** TGA ramp experiments of **2a**, and **2b** (ramp rate = 10 °C min<sup>-1</sup>)

The effect of saturation on thermal stability and volatility was further studied by changing R' (on the NHC nitrogen) to an isopropyl group. TGA ramp experiments of **3a**, **3b**, **4a**, **4b**, and **4c** are shown in Figure 7.3. In this series,  $T_V$  increases when the NHC backbone is saturated. In combination with their lower residual masses from TGA ramp experiments, this gives **3a** and **3b** higher figures of merit. Thermal stability once again decreases from **3a** to **3b** as Me is exchanged for CH<sub>2</sub>(SiMe<sub>3</sub>), but this is counteracted by a significant decrease in  $T_V$  for **3b** by ~10 °C (Table 7.1). Interestingly, the useful thermal range is essentially the same between **3a** and **3b** and in fact **3b** exhibits the lowest  $T_V$  of all the compounds analyzed in this study.

In further discussion of the effect of fluorination and saturation of the NHC backbone on volatility and thermal stability, we compared compounds **4a**, **4b**, and **4c** (Figure 7.3).

Compounds **4a** and **4b** exhibit the same trend of increasing volatility with the substitution of Me for  $\text{CH}_2(\text{SiMe}_3)$ , but similar to compounds **2a,b**, and **3a,b**,  $\text{CH}_2(\text{SiMe}_3)$  causes a slight reduction in thermal stability. Interestingly, **4b** decomposes at the same temperature that it exhibits its one Torr temperature ( $T_D = 150.9\text{ }^\circ\text{C}$ ) limiting the useful thermal range to  $1.9\text{ }^\circ\text{C}$ . This carbene is a unique case where the  $\text{CH}_2(\text{SiMe}_3)$  substitution decreases the temperature range drastically. The other instance where a decrease of the temperature range with the substitution of  $\text{CH}_2(\text{SiMe}_3)$  was observed from **2a** to **2b**. This appears to be a trend for the saturated counterparts of the corresponding carbenes.

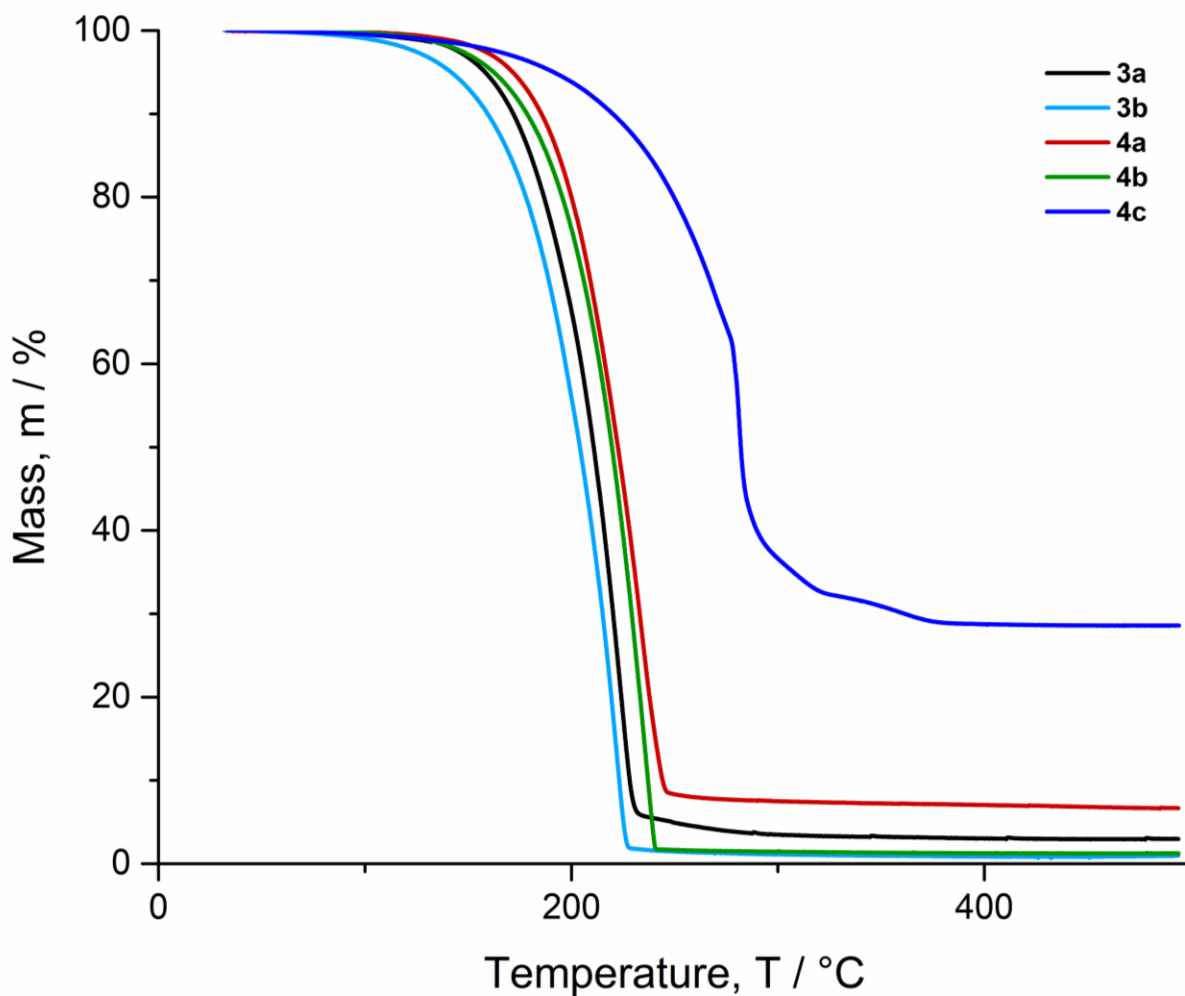


**Figure 7.3** TGA ramp experiments of **3a**, **3b**, **4a**, **4b**, and **4c** (ramp rate =  $10\text{ }^\circ\text{C min}^{-1}$ )

**Table 7.1** Thermal characteristics of the synthesized precursors.

	<i>MW (g/mol)</i>	<i>T<sub>V</sub></i> (°C)	<i>T<sub>D</sub></i> (°C)	<i>Useful temperature range</i> (°C) <sup>a</sup>	<i>Residual mass (M, %)</i>	<i>Fractional Gold remaining</i> (% <sub>Au</sub> )	<i>Figure of Merit</i> (σ) <sup>b</sup>	<i>Melting Point</i> (°C) <sup>c</sup>
<b>1a</b>	308.13	169.1	145.4	-23.7	6.7	10.5	-21.2	62
<b>1b</b>	381.32	152.5	202.5	50.0	3.12	6.0	47.0	78
<b>1c</b>	452.5	142.8	214.4	71.6	28.37	65.2	24.9	61
<b>2a</b>	310.15	169.1	179.7	10.6	19.6	30.9	7.3	121
<b>2b</b>	328.34	157.7	167	9.3	5.78	9.6	8.4	80
<b>3a</b>	364.25	141.1	164.5	23.4	2.98	5.5	22.1	140
<b>3b</b>	436.43	131.3	154.9	23.6	0.962	2.1	23.1	63
<b>4a</b>	366.26	157	167.6	10.6	6.67	12.4	9.3	142
<b>4b</b>	438.43	149	150.9	1.9	1.23	2.7	1.8	75
<b>4c</b>	420.23	189	207	18.0	28.58	61.0	7.0	-
<b>5a</b>	392.30	167.7	203.8	36.1	0	0.0	36.1	137
<b>5b</b>	464.48	164.4	215.5	51.1	0	0.0	51.1	86

<sup>a</sup>Difference between T<sub>V</sub> and T<sub>D</sub>. <sup>b</sup>See Equation 1. <sup>c</sup>Melting point determined by DSC.

The fluorinated methyl analogue, **4c**, performed far worse under thermolysis, exhibiting a TGA trace indicative of much higher T<sub>V</sub> which occurred concomitantly with decomposition. Based on its complicated mass loss curve, there appear to be at least 3 different thermal events that occur before leaving a residual mass of 28.6 %. Based on the onset of decomposition (T<sub>D</sub> = 207 °C), the mass loss at this temperature (92.7 %) indicates that

only 7.3% of **4c** volatilized prior to the onset of decomposition. Likely evaporation of a thermal decomposition product continues past the decomposition temperature, with 61 % of the gold remaining in the sample pan post-analysis.

We then compared **3a** and **3b** to compounds with the variation  $R'' = \text{Me}$  (i.e., backbone substitution; compounds **5a** and **5b**, (Figure 7.4). A few noticeable differences result from the addition of a backbone methyl substitution. A significant increase in thermal stability is observed, where  $T_D$  increases by 39.3 °C and 60.6 °C for **5a** and **5b** respectively, but this was accompanied by decreased volatility in both cases (Table 7.1). Most importantly, neither **5a** nor **5b** left any measurable residual mass in the sample pan which is a testament to their high thermal stability. Provided the large useful temperature range, this greatly increases their figures of merit (36.1, and 51.1, respectively). It is important to note here that backbone NHC substitution appears to have a much larger influence over the precursor properties than wingtip substitution.

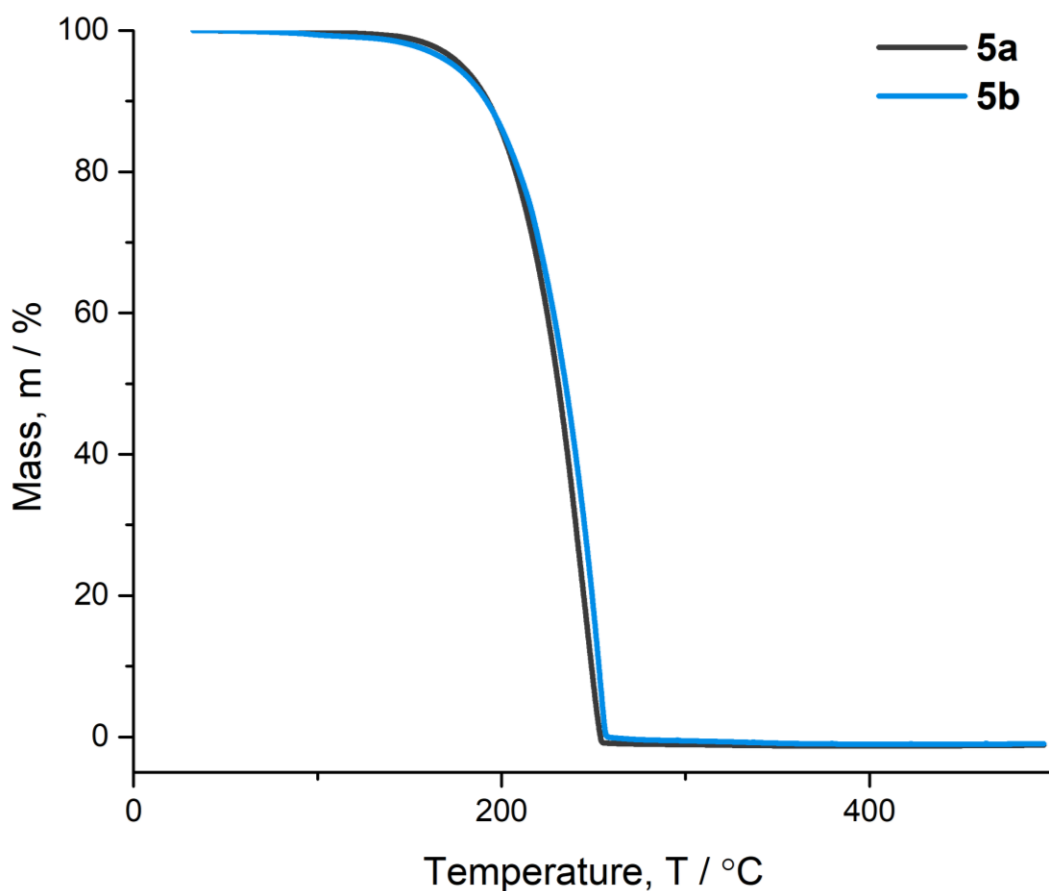


**Figure 7.4** TGA ramp experiments of **5a**, and **5b** (ramp rate = 10 °C min<sup>-1</sup>)

The high volatilization temperature is indeed disadvantageous, but it is not detrimental for an ALD process, provided high enough source temperatures are accessible. Previously while developing an ALD process for Cu metal, our group found that the same NHC found in **5a** and **5b** (*N,N'*-diisopropyl-4,5-dimethylimidazole-2-ylidene) produced non-metallic films when used as a ligand for the Cu precursor of interest.<sup>305</sup> However, when *N,N'*-diisopropylimidazolidin-2-ylidene (as in **4a-c**) was used, the desired metallic Cu films could be deposited. Thus, even though **5a** and **5b** exhibit excellent precursor qualities, it is possible that they are not the ideal candidates for ALD based on our prior knowledge of the Cu studies. In a separate study our group also found that the thermal stability of NHC-Cu-N(SiMe<sub>3</sub>)<sub>2</sub> compounds is heavily dependent on the backbone substitution of the NHC. However, in that study saturated NHCs outperformed their aromatic analogues.<sup>306</sup> It's interesting that for Au(I) the trend is not the same, but this is likely due to the difference in R ligands between the two studies as the N(SiMe<sub>3</sub>)<sub>2</sub><sup>-</sup> ligand was proposed to participate in the decomposition of aromatic NHC-Cu-N(SiMe<sub>3</sub>)<sub>2</sub> precursors by deprotonating the H atoms from the backbone of the NHC.

### 7.3.2 *In-situ* self-limiting chemisorption behavior of **1a** and **1b**

To assess these NHC-containing precursors for self-limiting behavior we used a home-built ALD reactor (Chapter 5) to monitor the chemisorption of **1a** on a gold surface using a gold-coated quartz-crystal microbalance (QCM). We were also able to simultaneously monitor the gas-phase species using a downstream quadrupole mass spectrometer (QMS). We chose **1a** for this test because, despite its low figure of merit, it provided the closest comparison to literature with respect to the autocatalytic surface decomposition of (PMe<sub>3</sub>)AuMe.<sup>307</sup>

Using a substrate temperature of 150 °C, we monitored an experiment consisting of 5 x [6s **1a** | 180 s N<sub>2</sub> purge] followed by 3 x [10 min **1a** | 5 min N<sub>2</sub> purge] to assess the saturation of the surface (Figure 7.5). We observed a mass gain during dosing with **1a** for 6 s followed by a plateau (during each purge), with a cumulative mass gain over all 6 s

doses. For the first 10 min dose, the QCM mass loading rate initially increased rapidly, but then plateaued. In the subsequent 2 x 10 min doses, very little mass gain was observed at all. Overall, it appeared that the QCM surface had been saturated midway through the first 10-minute long dose, and that further chemisorption of **1a** was prevented.

The saturated mass loading value after the first long pulse of **1a** was 441 ng cm<sup>-2</sup>, which translates to an equivalent thickness of 0.23 nm of close-packed Au on the surface (neglecting the mass of the NHC). This value is around half of the lattice constant for FCC gold metal. While it is quite high for a growth per cycle value in ALD literature, we believe that this corroborates our original growth model (Scheme 7.1) as more than a single monolayer of Au has been deposited in a single dose.

During each dose, a signal for *m/z* = 16 was observed (for the methyl on **1a**), which correlates exactly with the dose. By monitoring *m/z* = 30, we were able to observe the production of ethane in the first 5 x 6 s doses, as well as the beginning of the first 10 min dose, but only a very small signal was observed in the subsequent two 10 min doses. This demonstrates that the reduction occurring at the surface is indeed bimolecular reductive elimination, corroborating our original hypothesis.

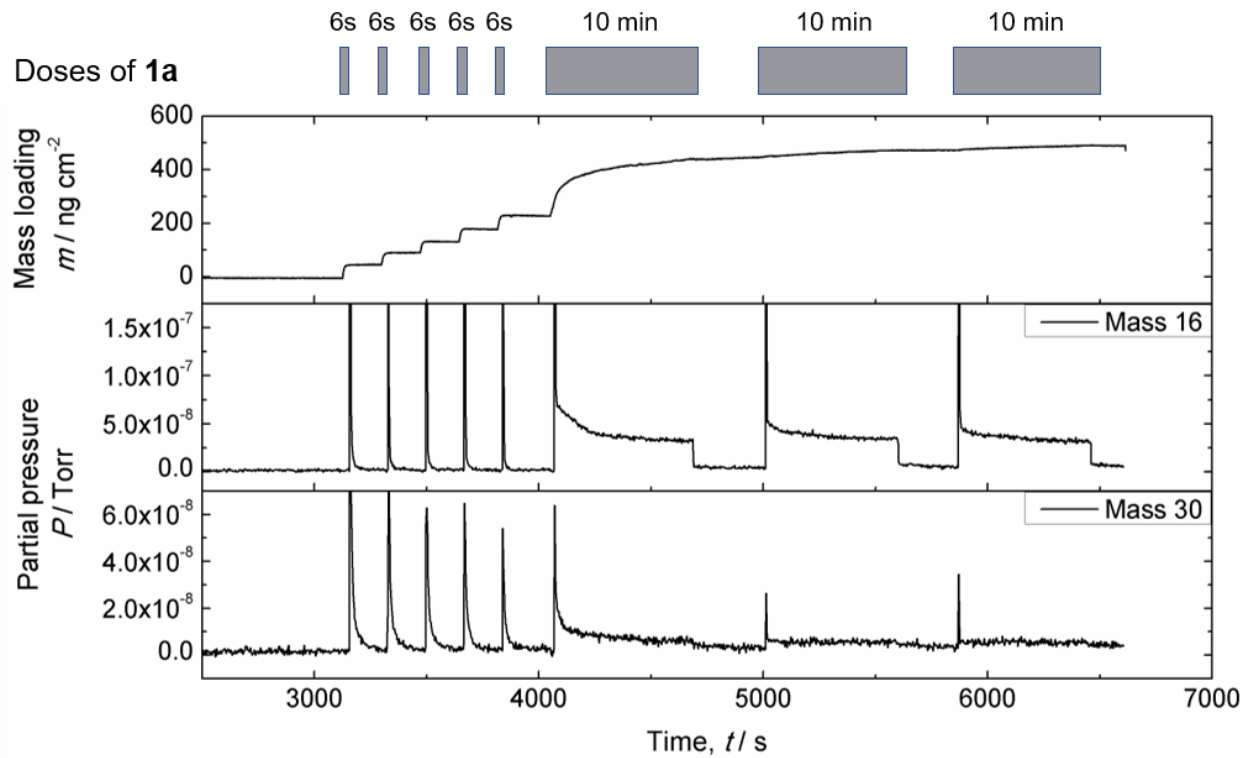


**Figure 7.5** Dual QCM / QMS *in situ* monitoring of **1a**. The pulse sequence was [6s **1a** | 3 min N<sub>2</sub> purge] x 5 then [10 min **1a** | 5 min purge] x 3 and is depicted graphically above the top frame. The top frame displays the QCM data where a mass gain is observed for the 5 x 6s pulses as well as the first of the 10 min pulses, but not the following two 10 min pulses. The middle and bottom frame display QMS data for m/z = 16 and m/z = 30. High m/z = 16 and m/z = 30 partial pressure correlates to precursor residing in the system and surface reaction occurring, respectively

We observed that ethane was only produced when a mass gain was also observed. By closely examining the second and third 10 min doses, we found that the QCM mass loading does in fact increase slightly, and we attributed this to a very slow thermal decomposition of **1a** at the QCM temperature of 150 °C (similar to its T<sub>D</sub> of 145.4 °C). This is likely the origin of the small m/z = 30 peak observed in the second and third 10 min doses.

Having observed the self-limiting ability of this small NHC, we wanted to find a co-reagent which could be used to remove the NHC from the surface. We attempted to use H<sub>2</sub>O but observed no mass change upon dosing H<sub>2</sub>O onto a **1a**-saturated surface using *in-situ* QCM monitoring. Upon inspection of the precursor source, we observed that **1a** had

significantly discolored, which indicated that it was moderately unstable under our delivery conditions.

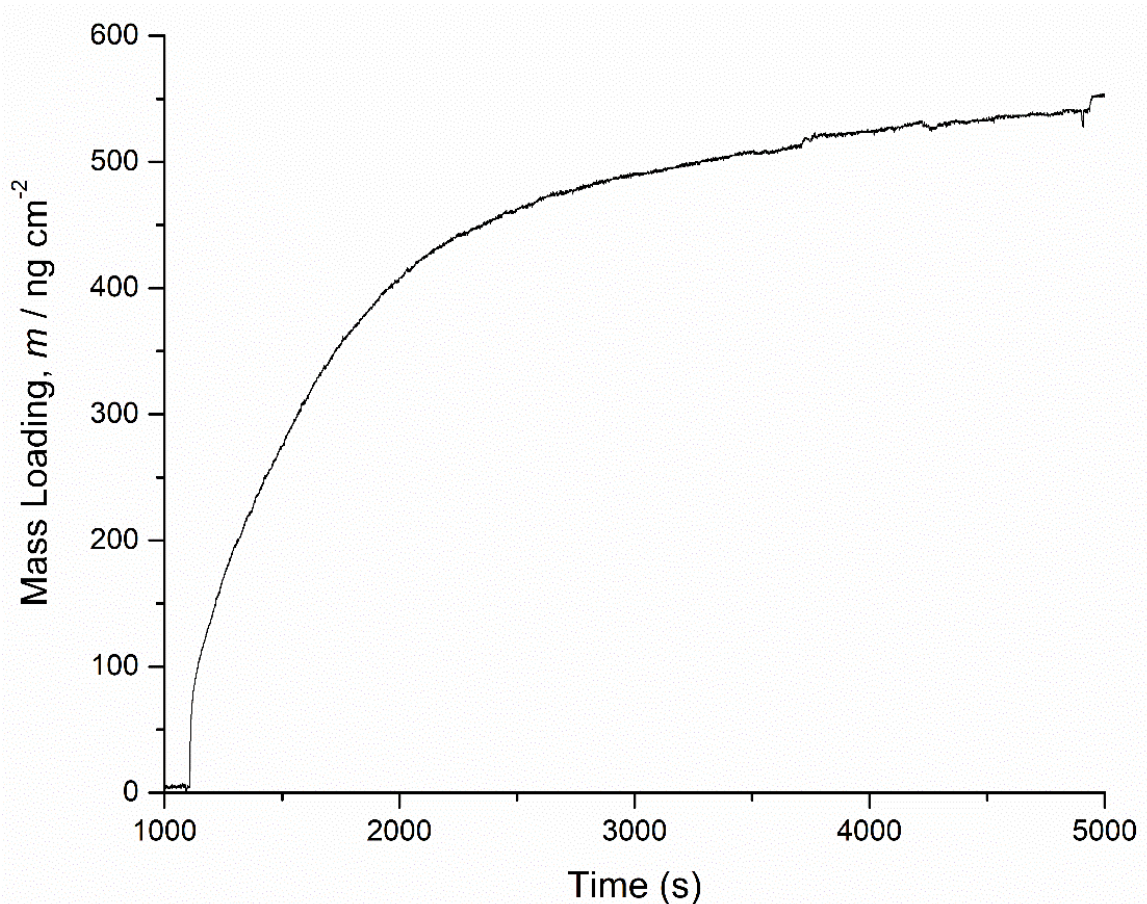


**Figure 7.6** QCM micrograph of a single hour-long dose of compound **1b** at 150 °C.

We then subjected **1b** to a similar surface saturation experiment where we performed a single hour-long dose where we observed that the QCM mass loading also saturated with a prolonged dose of **1b** (Figure 7.6). The saturated value was found to be 545  $\text{ng cm}^{-2}$  which is 19 % higher than the saturated mass loading observed for **1a**. This discrepancy could come from a difference in surface roughness of the two QCM crystals used, as well as the increased volatility and higher exposure of **1b** allowing more backside deposition onto the QCM during a prolonged experiment.

### 7.3.4 Deposition behavior of **1a** and **1b** using oxygen plasma

We then attempted to deposit gold films using **1a** and **1b** using an ALD-like experiment. We first attempted to use hydrogen plasma ( $\text{H}_2^*$ ) and otherwise identical conditions to the homemade tool: 1000 cycles of [ 6s Au | 15 s  $\text{N}_2$  purge | 14 s  $\text{H}_2^*$  (2800 W) | 15 s purge] at 150 °C substrate temperature using a Picosun R200 PE-ALD reactor. We were surprised that neither **1a** nor **1b** produced a film whatsoever on Si, glass, and Pt even when analyzed by energy-dispersive X-ray spectroscopy (EDX). The lack of film growth that we observe could be caused by the strong adherence of the methyl-wingtip NHCs on the surface, as reported by Crudden *et al.*<sup>304</sup> They observed that Me and Et-wingtip benzimidazole-2-ylidene NHCs chemisorbed parallel to the surface. Conversely, iPr wingtip NHCs were found to bind to the surface in an upright orientation, and these could be completely removed by thermal annealing, inferring that NHCs with small wingtip groups undergo some form of decomposition on the surface. Should a similar surface-fouling reaction be happening in this system, it could explain why  $\text{H}_2$  plasma was ineffective at removing surface-bound NHCs. We also attempted  $\text{N}_2$  plasma and a plasma mixture of  $\text{H}_2$  (5%) +  $\text{N}_2$  (95%) with **1a** and could not detect gold on any of our substrates using scanning electron microscopy (SEM) or EDX.

We then turned to  $\text{O}_2$  plasma ( $\text{O}_2^*$ ) and performed 1000 cycles of [ 6s Au | 15 s  $\text{N}_2$  purge | 14 s  $\text{O}_2^*$  (2800 W) | 15 s purge]. This time, **1a** produced a bright golden film which completely covered the 200 mm wafer substrate holder (Figure S-7.21). We analyzed the film deposited on the Si substrate by EDX and using GMR film<sup>308</sup> and found that they had an average thickness of  $54.9 \pm 2.4$  nm, corresponding to a growth per cycle of 0.55 Å. While this was by no means proven to be an ALD process, the growth rate was similar to previously reported gold metal processes. We also performed a 500-cycle experiment which again deposited mirror-like gold films on all three substrates. In this case the Si substrate was coated in  $30.1 \pm 1.7$  nm film, giving a growth per cycle of 0.60 Å.

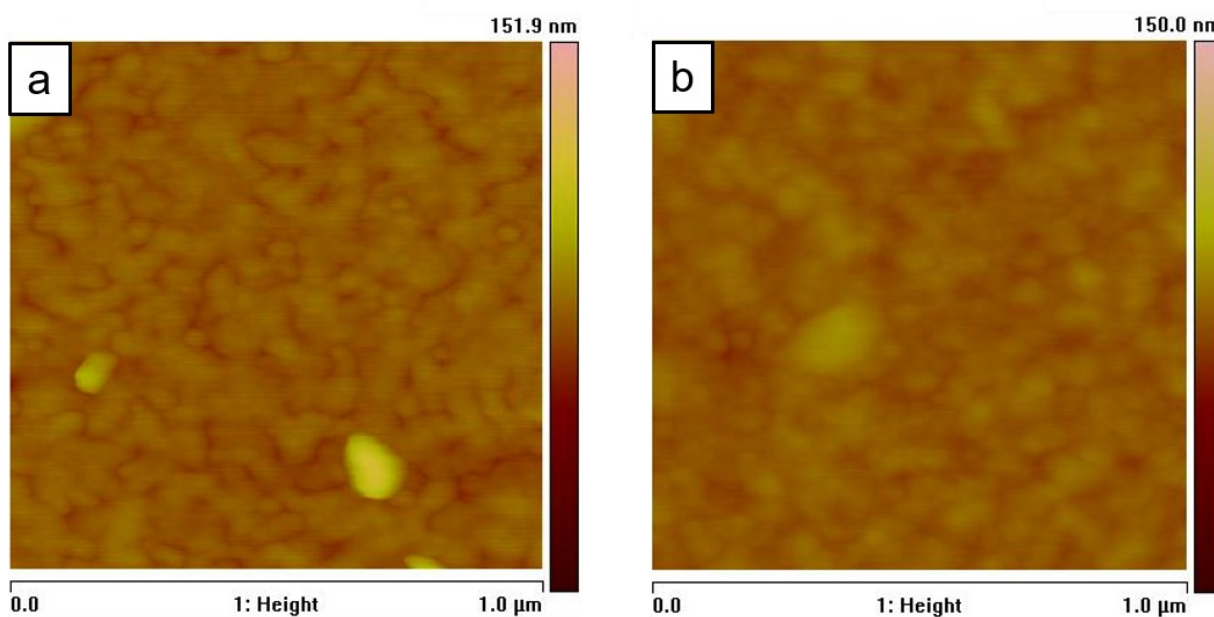


**Figure 7.7** AFM images of the 500-cycle film (~30.1 nm thickness) (a) and the 1000-cycle film (~54.9 nm thickness) (b) deposited on glass. The RMS roughness values of the 500-cycle and 1000-cycle films were 4.6 nm and 3.3 nm respectively.

We analyzed the films deposited on glass substrates by atomic force microscopy (AFM) to assess their morphology and connectivity (Figure 7.7). The 500-cycle film appears to be approaching a continuous film that likely initiated as islands, some of which are still visible at this thickness. The four-point probe measurements gave a resistivity of  $7.1 \mu\Omega \text{ cm}$ , which is close to the value for bulk gold ( $2.44 \mu\Omega \text{ cm}$ ). The 1000-cycle film still shows evidence of island-like initiation, but at this thickness was completely coalesced into a uniform film. It also displays a lower RMS roughness than the thinner film owing to the near-complete coalescence of the film. The resistivity measurements supported this coalescence ( $4.2 \mu\Omega \text{ cm}$ ), giving a resistivity lower than the best reported resistivity for a gold film deposited by ALD ( $4.5 \mu\Omega \text{ cm}$ ). By comparison, similarly thick films grown by the  $(\text{PMe}_3)\text{AuMe}_3 + \text{O}_2^* + \text{H}_2\text{O}$  process (Chapter 3) on the same apparatus at  $120^\circ\text{C}$  were non-conductive.

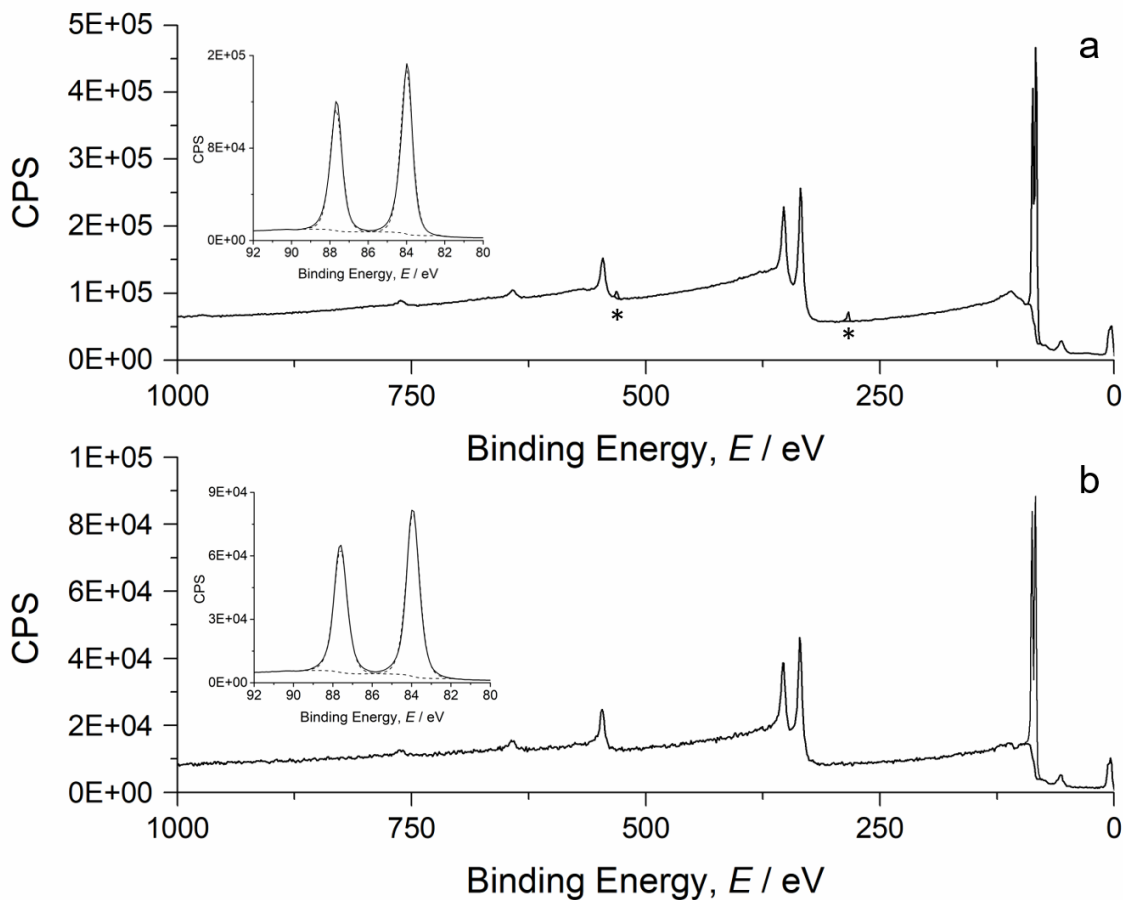


**Figure 7.8** XPS spectra the as-deposited (a) and Ar<sup>+</sup> sputtered (b) gold film (54.9 nm thickness) deposited from 1000 cycles of **1a** and O<sub>2</sub><sup>+</sup> on a silicon substrate which was terminated in its native oxide. The asterisks (\*) in panel a denote the O 1s (530.7 eV) and C 1s (283.7 eV) peak envelopes.

Using X-ray photoelectron spectroscopy (XPS) analysis, we found that the as-deposited 54.9 nm film contained metallic Au (57.9 at.%, Au 4f<sub>7/2</sub> = 84.00 eV, Au 4f<sub>5/2</sub> = 87.68 eV) as well as a large amount of C (31.2 at.%) and a small amount of O (8.8 at.%) (Figure 6.8). The Au 4f<sub>7/2</sub> peak was used to calibrate the spectrum since it is possible that some carbonaceous fragments remaining from the NHC surface species would complicate calibration using adventitious carbon. However, the lowest binding energy C 1s (for sp<sup>3</sup> adventitious carbon) is centered at 284.3 eV (Figure S-7.22) which is 0.5 eV off from the standard calibration value for adventitious carbon (284.8 eV). If we calibrate to what we suspect to be adventitious carbon, then the Au 4f<sub>7/2</sub> peak would be centered at 84.5 eV

which is close to what has been previously observed for nanoparticulate gold.<sup>99</sup> High-resolution analysis of the N 1s region showed some evidence of the NHC being present on the surface: a signal centered at 407.2 eV (Figure S-7.23) consisting of 2.1 at.% of the total surface (Au, C, O, and N). Typically, NHCs that bear no electron withdrawing groups like these ones show a N 1s signal around 400.5 eV when bound to gold as a self-assembled monolayer. Therefore we attribute this N 1s signal to an oxidized or hydrolyzed product of the original NHC monolayer which is not unreasonable considering the oxygen plasma used in the process as well as the handling of the substrate in ambient conditions. That being said, this impurity content clearly has little effect on the conductive properties of the films.

After argon ion etching the sample to remove the surface species, C, O, and N were undetectable by XPS, and the only element detected was Au in the metallic state. Compared to other known gold ALD processes, these gold films are of the highest purity that have been observed to date. We believe that the higher purity is partially because the precursor contains no oxygen-getting heteroatoms such as P or S and thus no oxygen is incorporated when using reactive oxygen-based co-reagents. It is possible that the C and O containing species are preferentially removed during the sputtering process, and an *operando* sputtering technique such as time-of-flight secondary-ion mass spectrometry (TOF-SIMS), time-of-flight elastic recoil detection analysis (TOF-ERDA), or Rutherford backscattering spectrometry (RBS) is necessary to determine the true purity of the film.

When we attempted the analogous O<sub>2</sub>\* experiment using **1b** we found what appeared to be a transparent film was deposited on all substrates, each of which displayed a different interference colour (Figure S-7.24). EDX analysis of an aluminum substrate showed a significant amount of Si, C, and O in the deposited film (Figure S-7.25), indicating that the CH<sub>2</sub>(SiMe<sub>3</sub>) ligand was being incorporated into the growing film and was getting oxidized from the plasma. While this contrasts our original hypothesis that the anionic ligand should dissociate from the surface during chemisorption, when O<sub>2</sub> plasma is used as the co-reagent in ALD the gold surface can itself become oxidized and participate in further surface chemistry with the incoming precursor (See Chapter 4). We believe that the origin of Si and O incorporation into the growing film comes from the chemisorption of **1b** onto

a partially oxidized Au surface, where the Si atom of the ligand then undergoes a decomposition reaction and becomes incorporated into the film.

## 7.4 Future work

Having discovered that **1a** and **1b** have desirable ALD characteristics, but that the NHC from **1a** cannot be removed without the use of strong oxidant, and that  $\text{CH}_2(\text{SiMe}_3)^-$  is unsuitable with strong oxidizing reagents like  $\text{O}_2$  plasma, we returned to our figure of merit table and chose **3a** as the most suitable candidate for further ALD studies. Not only does it have a high figure of merit, but it does not utilize the  $\text{CH}_2(\text{SiMe}_3)^-$  ligand. As well, it bears  $\text{iPr}$  wingtip groups, which should help the NHC monolayer remain chemically intact and thus facilitate removal by milder co-reactants. Compound **3a** has a lower figure of merit than **5a** (for example) but **3a** is substantially more volatile, which would facilitate its use in both our homemade ALD tool and our Picosun R200 PE-ALD tool. Furthermore, its decomposition temperature ( $T_D = 164.5 \text{ } ^\circ\text{C}$ ) is higher than our current substrate temperature ( $T = 150 \text{ } ^\circ\text{C}$ ) and so very little CVD-like behavior is expected. Although compound **6b** has a higher figure of merit than **3a**, in Chapter 5 we showed that **6b** rapidly decomposes at a substrate temperature of  $150 \text{ } ^\circ\text{C}$ , likely due to the  $\text{'Bu}$  wingtips being too sterically bulky to allow strong binding of the NHC to the growing surface.

## 7.5 Conclusions

A new family of organometallic Au(I) compounds of the type  $(\text{NHC})\text{AuR}$  was synthesized and thermally characterized by TGA, and DSC. From this data we were able to extract meaningful trends with respect to how specific NHC and R ligand choices affected the thermal stability and volatility of these compounds. The use of  $R = \text{CH}_2\text{SiMe}_3^-$  ligand invariably results in a more volatile compound than when  $R = \text{Me}^-$ . However, there is no clear trend for which of these ligands lends more thermal stability to a compound. We did observe that  $R = \text{CH}(\text{SiMe}_3)_2^-$  produces an even more volatile compound, but this species (**1c**) suffers a rapid kinetic decomposition on the TGA experiment timescale which suggests a different decomposition mechanism. With  $\text{CF}_3^-$  (as in compound **4c**) the

species is substantially more thermally stable than its aliphatic congeners **4a** and **4b**, but it is much less volatile, a trend which we have previously observed with the  $R = C_6F_5^-$  in Au(I) systems. Using our figure of merit ( $\sigma$ ), we found that for Au(I), unsaturated NHCs in general produced precursors with higher precursor merit than the saturated NHC analogues, and that substituting the backbone of the unsaturated NHC with Me groups produced a very significant increase in  $\sigma$  than any change in the NHC wingtip groups.

It is clear from our *in-situ* QCM and QMS measurements that **1a** and **1b** undergo self-limiting chemisorption on a gold surface. The accompanying QMS data supported our original hypothesis for chemisorption of **1a** since an excess of **1a** does not produce a further signal for ethane. Preliminary deposition experiments using **1a** produced pure gold films as shown by XPS analysis, and in fact these gold thin films were of higher purity than previously reported gold ALD processes. The purity of these films was corroborated by the low resistivity values obtained for both the 500-cycle and 1000-cycle films. Interestingly, we found that the Si from the  $CH_2SiMe_3^-$  ligand of **1b** becomes incorporated into the growing film when a similar experiment is performed using **1b** and  $O_2^*$ . While this unfortunately excludes the  $CH_2SiMe_3^-$  ligand from use in an Au ALD process that uses  $O_2^*$ , it does not exclude it from being used with other co-reagents. Future projects in our group will further explore Au ALD deposition using **1a** and  $O_2^*$  in the hopes of producing a process with a very large GPC, a phenomenon that should be possible given both our original hypothesis and the large saturative mass gain values observed in our QCM experiments.

## 7.6 Experimental Details

### In-situ surface saturation experiments

The apparatus for the *in-situ* monitoring experiments was our homemade ALD tool which is described in Chapter 6 of this thesis. Mechanical grade silicon was purchased from University Wafer and was cleaned using the RCA cleaning procedure before use. A quartz-crystal microbalance was purchased from Colnatech and used as received. Polished, gold-coated, RC-cut quartz crystals were purchased from Philip Tech and came

packaged in clean-room compatible, dust-free carousels in which they were stored until use. The gold-coated crystals were used as received, and the system was allowed to equilibrate to the desired temperature overnight under vacuum.

Prior to deposition, the delivery lines through which the precursors travel towards the furnace were allowed to pre-heat under vacuum overnight to their desired temperatures. The delivery lines were always heated such that a temperature gradient of at least + 10 °C was established between the gold bubbler (lower temp) and the entrance to the furnace (higher temp) in order to prevent precursor condensation in the delivery lines. On the day of the experiment, precursors were loaded into the gold precursor bubbler in an N<sub>2</sub>-filled glovebox, sealed, and then attached to the apparatus where they were evacuated to the operating pressure of the system. The bubbler was then allowed to heat to the desired delivery temperature and was held at temperature for 30 minutes before beginning the experiment.

## TGA and DSC

TGA was performed on a TA Instruments Q500 instrument which was housed in a nitrogen-filled glovebox. The purge gas during TGA and DSC experiments was nitrogen gas of (99.999 %, 5.0) and (99.998 %, 4.8) respectively. In a typical TGA experiment 10.000 ± 2 mg of analyte was placed in a platinum pan whose mass was monitored by the instrument during the analysis. For DSC experiments, due to the volatile nature of the analytes and their decomposition products, mass loadings greater than 1.000 mg often lead to a rupturing of the hermetically sealed aluminum pans. Thus, small mass loadings of 0.300 ± 0.200 mg were used for typical DSC experiment. DSC samples were hermetically sealed in aluminum pans inside the glovebox before analysis. Both TGA and DSC temperature ramp rates were 10.0 °C / min. Langmuir vapour pressure data were derived from TGA data using a previously reported method with Cu(tmhd)<sub>2</sub> as the calibrant.<sup>70,278</sup>

## Synthetic Details

All manipulations were performed under an inert atmosphere of dry nitrogen gas using an MBraun Labmaster 130 glovebox or standard Schlenk techniques unless otherwise stated. All synthesized compounds were treated as light sensitive materials during synthetic procedures and were stored at 5 °C in a refrigerator. NMR spectra were collected at room temperature on a Bruker 300 MHz or a Jeol 400 MHz spectrometer and were referenced to an internal standard of tetramethylsilane (TMS) in the case of CDCl<sub>3</sub> or residual protio solvent signal in the case of C<sub>6</sub>D<sub>6</sub> (7.16 ppm relative to TMS). C<sub>6</sub>D<sub>6</sub> was purchased from Aldrich and was degassed using freeze-pump-thaw cycles and subsequently stored over activated 4 Å molecular sieves under inert gas. Methylolithium (1.6 M in diethyl ether), (trimethylsilyl)methylolithium (1.0 M in pentane), *n*-butyllithium (1.6 M in hexanes), potassium hydride (30 weight % dispersion in mineral oil), sodium *tert*-butoxide, tetrahydrofuran (anhydrous), pentane (anhydrous), and dichloromethane (anhydrous) were purchased from Aldrich and used as received. Diethyl ether, hexanes, and toluene were purchased from VWR chemicals and purified using an MBraun solvent purification system prior to use. *N,N'*-dimethylimidazolium iodide,<sup>309</sup> *N,N'*-dimethylimidazolidinium tetrafluoroborate,<sup>310</sup> *N,N'*-diisopropylimidazolium chloride,<sup>311</sup> *N,N'*-diisopropylimidazolidinium tetrafluoroborate,<sup>310</sup> and *N,N'*-diisopropyl-4,5-dimethylimidazol-2-ylidene<sup>312</sup> were synthesized and purified according to literature procedures. (PMe<sub>3</sub>)AuMe,<sup>123</sup> (PMe<sub>3</sub>)AuCH<sub>2</sub>(SiMe<sub>3</sub>),<sup>123</sup> (PMe<sub>3</sub>)AuCH(SiMe<sub>3</sub>)<sub>2</sub>, and (PMe<sub>3</sub>)AuCF<sub>3</sub> were synthesized as previously described by methods in this thesis and elsewhere. All NHC-Au compounds reported here are novel.

### *N,N'*-dimethylimidazol-2-ylidene methylgold(I), (**1a**)

In a glovebox, 2.000 g (6.94 mmol, 1 eq.) of (PMe<sub>3</sub>)AuMe and 2.022 g (9.03 mmol, 1.3 eq.) of *N,N'*-dimethylimidazolium iodide were combined in 30 mL of tetrahydrofuran in a round-bottomed flask. To this flask were added 0.433 g (18.82 mmol, 2.7 eq.) of sodium hydride and 0.090 g (0.94 mmol, 5 mol % vs. sodium hydride) of sodium *tert*-butoxide. The flask was lightly stoppered, and the mixture was stirred overnight. The next day, the mixture was filtered through a short plug of celite, the plug was rinsed with 3 x 5 mL of tetrahydrofuran, and then the combined filtrates were evaporated to dryness. The residue

was dissolved in dichloromethane (30 mL), brought out of the glovebox, and transferred to a separatory funnel where it was washed with 3 x 10 mL portions of distilled water. The organic layer was then dried over MgSO<sub>4</sub>, filtered, and the solvent was removed using a rotary evaporator giving a white solid. This solid appeared to be air-stable and was purified by vacuum sublimation onto a water-cooled cold finger which gave a white solid (130 - 140 °C, 5 mTorr). Yield = 1.542 g (72 %)

T<sub>m</sub> = 62 °C (DSC)

**<sup>1</sup>H NMR** (300 MHz, C<sub>6</sub>D<sub>6</sub>): δ 1.37 (s, 3H, Au-CH<sub>3</sub>), 3.02 (s, 6H, N-CH<sub>3</sub>), 5.60 (s, 2H, CH-CH)

*N,N'-dimethylimidazol-2-ylidene (trimethylsilyl)methylgold(I), (1b)*

In a glovebox, 0.596 g (1.65 mmol, 1 eq.) of (PMe<sub>3</sub>)AuCH<sub>2</sub>(SiMe<sub>3</sub>) and 0.481 g (2.15 mmol, 1.3 eq.) of *N,N'*-dimethylimidazolium iodide were combined in 10 mL of tetrahydrofuran in a round-bottomed flask. To this flask were added 0.103 g (4.48 mmol, 2.7 eq.) of sodium hydride and 0.021 g (0.22 mmol, 5 mol % vs. sodium hydride) of sodium *tert*-butoxide. The flask was lightly stoppered, and the mixture was stirred overnight. The next day, the mixture was filtered through a short plug of celite, the plug was rinsed with 3 x 2 mL of tetrahydrofuran, and then the combined filtrates were evaporated to dryness. The residue was dissolved in dichloromethane (20 mL), brought out of the glovebox, and transferred to a separatory funnel where it was washed with 3 x 4 mL portions of distilled water. The organic layer was then dried over MgSO<sub>4</sub>, filtered, and the solvent was removed using a rotary evaporator giving a light brown solid. This solid appeared to be air-stable and was purified by vacuum sublimation onto a water-cooled cold finger which gave a white solid (120 - 130 °C, 5 mTorr). Yield = 0.259 g (41.3 %)

T<sub>m</sub> = 78 °C (DSC)

**<sup>1</sup>H NMR** (300 MHz, C<sub>6</sub>D<sub>6</sub>): δ 0.61 (s, 9H, Si-(CH<sub>3</sub>)<sub>3</sub>), 0.88 (s, 2H, Si-CH<sub>2</sub>), 6.25 (s, 6H, N-CH<sub>3</sub>), 5.57 (s, 2H, CH-CH)

*N,N'-dimethylimidazol-2-ylidene bis(trimethylsilyl)methylgold(I), (1c)*

In a glovebox, 0.500 g (1.16 mmol, 1 eq.) of  $(\text{PMe}_3)\text{AuCH}(\text{SiMe}_3)_2$  and 0.335 g (1.50 mmol, 1.3 eq.) of *N,N'*-dimethylimidazolium iodide were combined in 10 mL of tetrahydrofuran in a round-bottomed flask. To this flask were added 0.072 g (3.13 mmol, 2.7 eq.) of sodium hydride and 0.015 g (0.16 mmol, 5 mol % vs. sodium hydride) of sodium *tert*-butoxide. The flask was lightly stoppered, and the mixture was stirred overnight. The next day, the mixture was filtered through a short plug of celite, the plug was rinsed with 3 x 2 mL of tetrahydrofuran, and then the combined filtrates were evaporated to dryness. The residue was dissolved in dichloromethane (20 mL), brought out of the glovebox, and transferred to a separatory funnel where it was washed with 3 x 4 mL portions of distilled water. The organic layer was then dried over  $\text{MgSO}_4$ , filtered, and the solvent was removed using a rotary evaporator giving a light yellow solid. This solid appeared to be air-stable and was purified by vacuum sublimation onto a water-cooled cold finger which gave a white solid (120 - 130 °C, 5 mTorr). Yield = 0.450 g (87 %)

$T_m$  = 61 °C (DSC)

**$^1\text{H NMR}$**  (300 MHz,  $\text{C}_6\text{D}_6$ ):  $\delta$  0.30 (s, 1H, Au-CH), 0.51 (s, 18H, Si-(CH<sub>3</sub>)<sub>3</sub>), 2.86 (s, 6H, N-CH<sub>3</sub>) 5.53 (s, 2H, CH-CH)

### *N,N'-dimethylimidazolidin-2-ylidene methylgold(I), (2a)*

In a glovebox, 0.300 g (1.04 mmol, 1 eq.) of  $(\text{PMe}_3)\text{AuMe}$  and 0.233 g (1.20 mmol, 1.2 eq.) of *N,N'*-dimethylimidazolidinium tetrafluoroborate were combined in 5 mL of tetrahydrofuran in a round-bottomed flask. To this flask were added 0.057 g (2.48 mmol, 2.4 eq.) of sodium hydride and 0.011 g (0.12 mmol, 5 mol % vs. sodium hydride) of sodium *tert*-butoxide. The flask was lightly stoppered, and the mixture was stirred overnight. The next day, the mixture was filtered through a short plug of celite, the plug was rinsed with 3 x 2 mL of tetrahydrofuran, and then the combined filtrates were evaporated to dryness. The residue was dissolved in dichloromethane (20 mL), brought out of the glovebox, and transferred to a separatory funnel where it was washed with 3 x 4 mL portions of distilled water. The organic layer was then dried over  $\text{MgSO}_4$ , filtered, and the solvent was removed using a rotary evaporator giving a light purple solid. This solid appeared to be

air-stable and was purified by vacuum sublimation onto a water-cooled cold finger which gave a white solid (130 - 140 °C, 5 mTorr). Yield = 0.154 g (48 %)

T<sub>m</sub> = 121 °C (DSC)

**<sup>1</sup>H NMR** (300 MHz, CDCl<sub>3</sub>): δ 0.24 (s, 3H, Au-CH<sub>3</sub>), 3.22 (s, 6H, N-CH<sub>3</sub>), 3.48 (s, 4H, CH<sub>2</sub>-CH<sub>2</sub>)

*N,N'-dimethylimidazolidin-2-ylidene (trimethylsilyl)methylgold(I), (2b)*

In a glovebox, 0.300 g (0.83 mmol, 1 eq.) of (PMe<sub>3</sub>)AuCH<sub>2</sub>(SiMe)<sub>3</sub> and 0.465 g (2.50 mmol, 3 eq.) of *N,N'*-dimethylimidazolidinium tetrafluoroborate were combined in 10 mL of tetrahydrofuran in a round-bottomed flask. To this flask were added 0.120 g (5.22 mmol, 3 eq.) of sodium hydride and 0.025 g (0.26 mmol, 5 mol % vs. sodium hydride) of sodium *tert*-butoxide. The flask was lightly stoppered, and the mixture was stirred overnight. The next day, the mixture was filtered through a short plug of celite, the plug was rinsed with 3 x 2 mL of tetrahydrofuran, and then the combined filtrates were evaporated to dryness. The residue was dissolved in dichloromethane (20 mL), brought out of the glovebox, and transferred to a separatory funnel where it was washed with 3 x 4 mL portions of distilled water. The organic layer was then dried over MgSO<sub>4</sub>, filtered, and the solvent was removed using a rotary evaporator giving a white solid. This solid appeared to be air-stable and was purified by vacuum sublimation onto a water-cooled cold finger which gave a white solid (120 - 130 °C, 5 mTorr). Yield = 0.130 g (41 %)

T<sub>m</sub> = 80 °C (DSC)

**<sup>1</sup>H NMR** (300 MHz, C<sub>6</sub>D<sub>6</sub>): δ 0.59 (s, 6H, Si-(CH<sub>3</sub>)<sub>3</sub>), 0.83 (s, 2H, Au-CH<sub>2</sub>), 2.13 (s, 4H, CH-CH), 2.64 (s, 6H, N-CH<sub>3</sub>)

**<sup>13</sup>C NMR** (75.5 MHz, C<sub>6</sub>D<sub>6</sub>): δ 4.35 (s, Si-(CH<sub>3</sub>)<sub>3</sub>), 8.07 (s, Au-CH<sub>2</sub>), 35.59 (s, N-CH<sub>3</sub>), 50.33 (s, CH<sub>2</sub>-CH<sub>2</sub>), 216.91 (s, NCN)

*N,N'-diisopropylimidazol-2-ylidene methylgold(I), (3a)*

In a glovebox, 0.200 g (0.69 mmol, 1 eq.) of ( $\text{PMe}_3$ ) $\text{AuMe}$  and 0.170 g (0.90 mmol, 1.3 eq.) of  $N,N'$ -diisopropylimidazolium chloride were combined in 5 mL of tetrahydrofuran in a round-bottomed flask. To this flask were added 0.066 g (2.86 mmol, 4.1 eq.) of sodium hydride and 0.014 g (0.14 mmol, 5 mol % vs. sodium hydride) of sodium *tert*-butoxide. The flask was lightly stoppered, and the mixture was stirred for three hours. The mixture was then filtered through a short plug of celite, the plug was rinsed with 3 x 2 mL of tetrahydrofuran, and then the combined filtrates were evaporated to dryness. The residue was dissolved in dichloromethane (15 mL), brought out of the glovebox, and transferred to a separatory funnel where it was washed with 3 x 4 mL portions of distilled water. The organic layer was then dried over  $\text{MgSO}_4$ , filtered, and the solvent was removed using a rotary evaporator giving a light grey solid. This solid appeared to be air-stable and was purified by vacuum sublimation onto a water-cooled cold finger which gave a light yellow solid (120 - 130 °C, 5 mTorr). Yield = 0.173 g (68 %)

$T_m$  = 140 °C (DSC)

**$^1\text{H NMR}$**  (400 MHz,  $\text{C}_6\text{D}_6$ ):  $\delta$  0.93 (d,  $^3J_{\text{H-H}} = 6.8$  Hz, 12H,  $\text{CH}_2\text{-CH}_3$ ), 1.42 (s, 3H,  $\text{Au-CH}_3$ ), 5.07 (septet,  $^3J_{\text{H-H}} = 6.8$  Hz, 2H,  $\text{CH}_3\text{-CH}_2$ ), 6.10 (s, 2H,  $\text{CH-CH}$ )

**$^{13}\text{C NMR}$**  (100 MHz,  $\text{C}_6\text{D}_6$ ):  $\delta$  1.32 ( $\text{Au-CH}_3$ ), 22.70 (s,  $\text{CH}_2\text{-CH}_3$ ), 51.81 (s,  $\text{CH}_2\text{-CH}_3$ ), 151.16 (s,  $\text{CH-CH}$ ), 197.30 (s, NCN)

### *N,N'-diisopropylimidazol-2-ylidene (trimethylsilyl)methylgold(I), (3b)*

In a glovebox, 0.196 g (0.54 mmol, 1 eq.) of ( $\text{PMe}_3$ ) $\text{AuCH}_2(\text{SiMe}_3)$  and 0.132 g (0.70 mmol, 1.3 eq.) of  $N,N'$ -diisopropylimidazolium chloride were combined in 5 mL of tetrahydrofuran in a round-bottomed flask. To this flask were added 0.052 g (2.26 mmol, 4.2 eq.) of sodium hydride and 0.011 g (0.11 mmol, 5 mol % vs. sodium hydride) of sodium *tert*-butoxide. The flask was lightly stoppered, and the mixture was stirred for three hours. The mixture was then filtered through a short plug of celite, the plug was rinsed with 3 x 2 mL of tetrahydrofuran, and then the combined filtrates were evaporated to dryness. The residue was dissolved in dichloromethane (15 mL), brought out of the glovebox, and transferred to a separatory funnel where it was washed with 3 x 4 mL portions of distilled

water. The organic layer was then dried over MgSO<sub>4</sub>, filtered, and the solvent was removed using a rotary evaporator giving an off-white solid. This solid appeared to be air-stable and was purified by vacuum sublimation onto a water-cooled cold finger which gave a light yellow solid (110 - 120 °C, 5 mTorr). Yield = 0.208 g (88 %)

T<sub>m</sub> = 63 °C (DSC)

**<sup>1</sup>H NMR** (400 MHz, C<sub>6</sub>D<sub>6</sub>): δ 0.60 (s, 9H, Si-(CH<sub>3</sub>)<sub>3</sub>), 0.883 (s, 2H, Si-CH<sub>2</sub>), 0.961 (d, <sup>3</sup>J<sub>H-H</sub> = 6.8 Hz 12H, CH<sub>2</sub>-CH<sub>3</sub>), 5.00 (septet, <sup>3</sup>J<sub>H-H</sub> = 6.8 Hz, 2H, CH<sub>3</sub>-CH<sub>2</sub>), 6.08 (s, 2H, CH-CH)

**<sup>13</sup>C NMR** (100 MHz, C<sub>6</sub>D<sub>6</sub>): δ 4.20 (s, Si-(CH<sub>3</sub>)<sub>3</sub>), 7.20 (s, Au-CH<sub>2</sub>) 22.66 (s, CH<sub>2</sub>-CH<sub>3</sub>), 51.92 (s, CH<sub>2</sub>-CH<sub>3</sub>), 115.16 (s, CH-CH), 195.7 (s, NCN)

*N,N'-diisopropylimidazolidin-2-ylidene methylgold(I), (4a)*

In a glovebox, 0.420 g (2.20 mmol, 1.25 eq.) of *N,N'*-diisopropylimidazolidinium chloride was suspended in 10 mL of tetrahydrofuran in a Schlenk flask. Separately, 0.368 g (2.20 mmol, 1.25 eq.) of lithium bis(trimethylsilyl)amide was dissolved in 8 mL of tetrahydrofuran, and this was added dropwise to the stirred suspension of the imidazolidinium salt. The resulting mixture was allowed to stir at room temperature for 1 hour. The flask was then brought out of the glovebox to a Schlenk line and cooled to -78 °C. Once cold, 0.500 g (1.74 mmol, 1 eq.) of (PMe<sub>3</sub>)AuMe was added as a solid in 5 portions over 25 minutes. The solution was stirred at -78 °C for a further four hours and was then allowed to warm to room temperature. Once warm, the volatiles were removed under high vacuum giving a pale purple solid which was dissolved in 15 mL of dichloromethane. The solution was transferred to a separatory funnel and washed with 3 x 4 mL of distilled water. The organic fraction was kept, dried over MgSO<sub>4</sub>, filtered, and evaporated to dryness using a rotary evaporator giving a light purple solid. This solid was assumed to be air-stable and was purified by vacuum sublimation (120 – 130 °C, 5 mTorr). Yield 0.327 g (53 %).

T<sub>m</sub> = 142 °C (DSC)

**<sup>1</sup>H NMR** (400 MHz, C<sub>6</sub>D<sub>6</sub>): δ 0.72 (d, <sup>3</sup>J<sub>H-H</sub> = 6.8 Hz, 12H, CH<sub>2</sub>-CH<sub>3</sub>), 1.27 (s, 3H, Au-CH<sub>3</sub>), 2.4 (s, 4H, CH<sub>2</sub>-CH<sub>2</sub>), 4.87 (septet, <sup>3</sup>J<sub>H-H</sub> = 6.8 Hz, 2H, CH<sub>3</sub>-CH<sub>2</sub>)

**<sup>13</sup>C NMR** (100 MHz, C<sub>6</sub>D<sub>6</sub>): δ 1.84 (Au-CH<sub>3</sub>), 20.02 (s, CH<sub>2</sub>-CH<sub>3</sub>), 41.82 (s, CH<sub>2</sub>-CH<sub>3</sub>), 50.3 (s, CH<sub>2</sub>-CH<sub>2</sub>), 217.1 (s, NCN)

*N,N'-diisopropylimidazolidin-2-ylidene methylgold(I), (4b)*

In a glovebox, 0.116 g (0.61 mmol, 1.25 eq.) of *N,N'*-diisopropylimidazolidinium chloride was suspended in 10 mL of tetrahydrofuran in a Schlenk flask. Separately, 0.102 g (0.61 mmol, 1.25 eq.) of lithium bis(trimethylsilyl)amide was dissolved in 5 mL of tetrahydrofuran, and this was added dropwise to the stirred suspension of the imidazolidinium salt. The resulting mixture was allowed to stir at room temperature for 1 hour. The flask was then brought out of the glovebox to a Schlenk line and cooled to -78 °C. Once cold, 0.200 g (0.49 mmol, 1 eq.) of (PMe<sub>3</sub>)AuCH<sub>2</sub>(SiMe<sub>3</sub>) was added dropwise over 5 minutes. The solution was stirred at -78 °C for a further four hours and was then allowed to warm to room temperature. Once warm, the volatiles were removed under high vacuum giving a pale purple solid which was dissolved in 15 mL of dichloromethane. The solution was transferred to a separatory funnel and washed with 3 x 4 mL of distilled water. The organic fraction was kept, dried over MgSO<sub>4</sub>, filtered, and evaporated to dryness using a rotary evaporator giving a light purple solid. This solid was assumed to be air-stable and was purified by vacuum sublimation (120 - 130 °C, 5 mTorr). Yield 0.138 g (56 %).

T<sub>m</sub> = 75 °C (DSC)

**<sup>1</sup>H NMR** (400 MHz, C<sub>6</sub>D<sub>6</sub>): δ 0.56 (s, 9H, Si-(CH<sub>3</sub>)<sub>3</sub>), 0.811 (s, 2H, Si-CH<sub>2</sub>), 0.808 (d, <sup>3</sup>J<sub>H-H</sub> = 6.8 Hz 12H, CH<sub>2</sub>-CH<sub>3</sub>), 2.44 (s, 4H, CH<sub>2</sub>-CH<sub>2</sub>) 4.87 (septet, <sup>3</sup>J<sub>H-H</sub> = 6.8 Hz, 2H, CH<sub>3</sub>-CH<sub>2</sub>)

**<sup>13</sup>C NMR** (100 MHz, C<sub>6</sub>D<sub>6</sub>): δ 4.20 (s, Si-(CH<sub>3</sub>)<sub>3</sub>), 7.59 (s, Au-CH<sub>2</sub>) 20.02 (s, CH<sub>2</sub>-CH<sub>3</sub>), 41.63 (s, CH<sub>2</sub>-CH<sub>3</sub>), 49.9 (s, CH<sub>2</sub>-CH<sub>2</sub>), 215.0 (s, NCN)

*N,N'-diisopropylimidazolidin-2-ylidene trifluoromethylgold(I), (4c)*

In a glovebox, 0.354 g of *N,N'*-diisopropylimidazolidinium tetrafluoroborate was dissolved in 10 mL of tetrahydrofuran in a Schlenk flask. Separately, a solution of 0.245 g of lithium bis(trimethylsilyl) amide was prepared in 8 mL of diethyl ether. This solution was added dropwise to the solution of the NHC salt, and the mixture was allowed to stir at room temperature for one hour. The free carbene is not isolated and is used immediately for further reactions. The solution containing the free carbene was brought out of the glovebox and was cooled to -78 °C. Once cooled, 0.500 g of (PMe<sub>3</sub>)AuCF<sub>3</sub> were added in five portions, five minutes apart each. The solution was allowed to stir for four hours at -78 °C temperature and was then allowed to warm to room temperature. The volatiles were stripped under vacuum, the resulting light purple solid was dissolved in 15 mL of dichloromethane, transferred to a separatory funnel, and washed with 3 x 4 mL of distilled water. The dichloromethane layer was dried over MgSO<sub>4</sub>, filtered, and concentrated using a rotary evaporator. The resulting liquid was then placed under high vacuum to yield a light yellow solid which was purified by recrystallization. Yield 0.327 g (53 %).

**<sup>1</sup>H NMR** (400 MHz, C<sub>6</sub>D<sub>6</sub>): δ 0.56 (d, <sup>3</sup>J<sub>H-H</sub> = 6.4 Hz, 12H, CH<sub>2</sub>-CH<sub>3</sub>), 2.3 (s, 4H, CH<sub>2</sub>-CH<sub>2</sub>), 4.31 (septet, <sup>3</sup>J<sub>H-H</sub> = 6.4 Hz, 2H, CH<sub>3</sub>-CH<sub>2</sub>)

**<sup>19</sup>F NMR** (376 MHz, C<sub>6</sub>D<sub>6</sub>): δ -27.42 (s, CF<sub>3</sub>)

*N,N'-diisopropyl-4,5-dimethyl-imidazol-2-ylidene methylgold(I), (5a)*

In a glovebox, 0.200 g (0.69 mmol, 1 eq) of (PMe<sub>3</sub>)AuMe was dissolved in 5 mL of tetrahydrofuran in a round-bottomed flask. To this solution was added 0.163 g (0.90 mmol, 1.3 eq) of *N,N'*-diisopropyl-4,5-dimethyl-imidazol-2-ylidene and the solution was stirred for 3 hours. The solvent was then removed under vacuum and the resulting solid was dissolved in 10 mL of dichloromethane. This solution was brought out of the glovebox, transferred to a separatory funnel and washed with 3 x 3 mL of distilled water. The organic layer was kept, dried over MgSO<sub>4</sub>, filtered, and then the filtrate was evaporated to dryness using a rotary evaporator which gave an off-white solid that

appeared to be air-stable. This solid was purified by vacuum sublimation which gave a white solid (130 °C, 5 mTorr). Yield = 0.186 g (68 %).

T<sub>m</sub> = 137 °C (DSC)

**<sup>1</sup>H NMR** (300 MHz, C<sub>6</sub>D<sub>6</sub>): δ 1.38 (d, <sup>3</sup>J<sub>H-H</sub> = 6.9 Hz, 12H, CH-CH<sub>3</sub>), 1.41 (s, 3H, Au-CH<sub>3</sub>), 1.43 (s, 6H, C-CH<sub>3</sub>), 4.77 (septet, <sup>3</sup>J<sub>H-H</sub> = 6.9 Hz, 2H, CH-CH<sub>3</sub>)

*N,N'-diisopropyl-4,5-dimethyl-imidazol-2-ylidene (trimethylsilyl)methylgold(I), (5b)*

In a glovebox, 0.200 g (0.56 mmol, 1 eq) of (PMe<sub>3</sub>)AuCH<sub>2</sub>(SiMe<sub>3</sub>) was dissolved in 5 mL of tetrahydrofuran in a round-bottomed flask. To this solution was added 0.130 g (0.72 mmol, 1.3 eq) of *N,N'*-diisopropyl-4,5-dimethyl-imidazol-2-ylidene and the solution was stirred for 3 hours. The solvent was then removed under vacuum and the resulting solid was dissolved in 10 mL of dichloromethane. This solution was brought out of the glovebox, transferred to a separatory funnel and washed with 3 x 3 mL of distilled water. The organic layer was kept, dried over MgSO<sub>4</sub>, filtered, and then the filtrate was evaporated to dryness using a rotary evaporator which gave an off-white solid that appeared to be air-stable. This solid was purified by vacuum sublimation which gave a white solid (130 °C, 5 mTorr). Yield = 0.180 g (70 %).

T<sub>m</sub> = 86 °C (DSC)

**<sup>1</sup>H NMR** (300 MHz, C<sub>6</sub>D<sub>6</sub>): δ 0.51 (s, 9H, Si-(CH<sub>3</sub>)<sub>3</sub>), 0.88 (s, 2H, Au-CH<sub>2</sub>), 1.41 (d, <sup>3</sup>J<sub>H-H</sub> = 6.9 Hz, 12H, CH-CH<sub>3</sub>), 1.42 (s, 6H, C-CH<sub>3</sub>), 4.63 (septet, <sup>3</sup>J<sub>H-H</sub> = 6.9 Hz, 2H, CH-CH<sub>3</sub>)

**<sup>13</sup>C NMR** (75.5 MHz, C<sub>6</sub>D<sub>6</sub>): δ 4.08 (s, Si-(CH<sub>3</sub>)<sub>3</sub>), 5.22 (s, Au-CH<sub>2</sub>), 9.02 (s, N-CH), 22.72 (s, CH-CH<sub>3</sub>), 51.07 (s, C-CH<sub>3</sub>), 122.59 (s, C-C), 194.46 (s, NCN)

## 7.7 Supporting Information

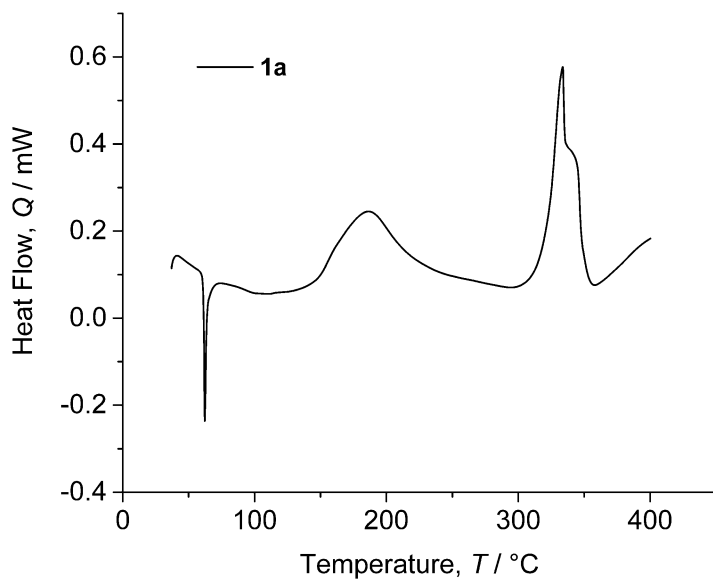


**Figure S-7.9** DSC of compound **1a**. Ramp rate =  $10\text{ }^{\circ}\text{C min}^{-1}$ .  $T_m = 62\text{ }^{\circ}\text{C}$ ,  $T_D = 145.4\text{ }^{\circ}\text{C}$

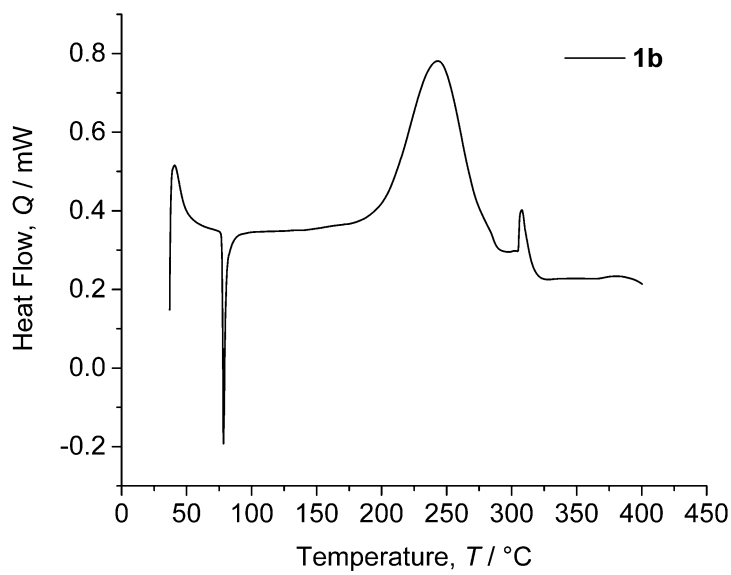


**Figure S-7.10** DSC of compound **1b**. Ramp rate =  $10\text{ }^{\circ}\text{C min}^{-1}$ .  $T_m = 78\text{ }^{\circ}\text{C}$ ,  $T_D = 202.5\text{ }^{\circ}\text{C}$

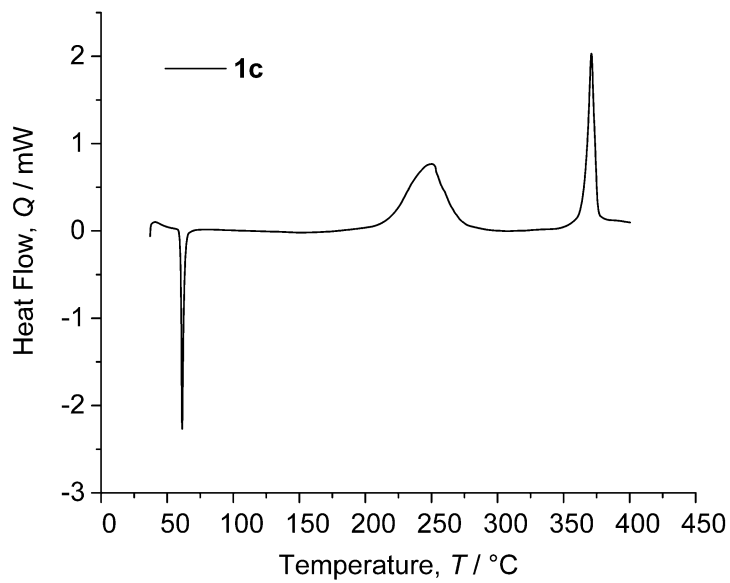


**Figure S-7.11** DSC of compound **1c**. Ramp rate =  $10 \text{ } ^\circ\text{C min}^{-1}$ .  $T_m = 61 \text{ } ^\circ\text{C}$ ,  $T_D = 214.4 \text{ } ^\circ\text{C}$

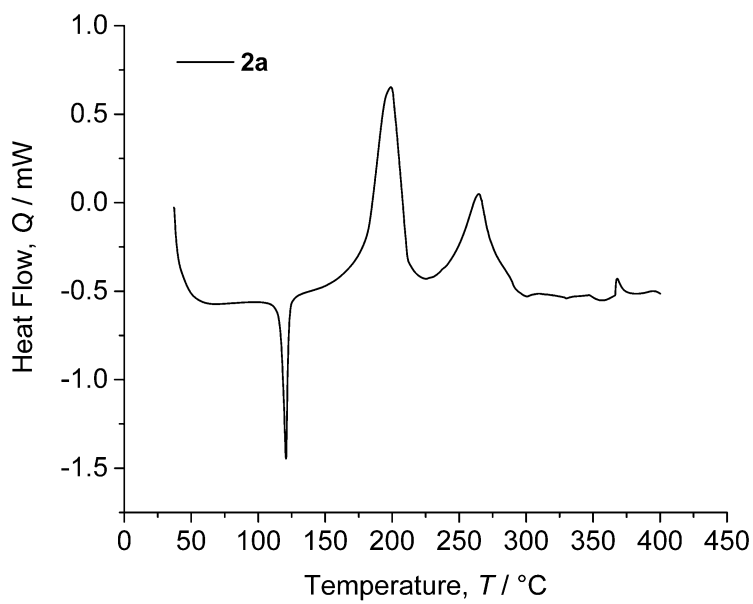


**Figure S-7.12** DSC of compound **2a**. Ramp rate =  $10 \text{ } ^\circ\text{C min}^{-1}$ .  $T_m = 121 \text{ } ^\circ\text{C}$ ,  $T_D = 179.7 \text{ } ^\circ\text{C}$

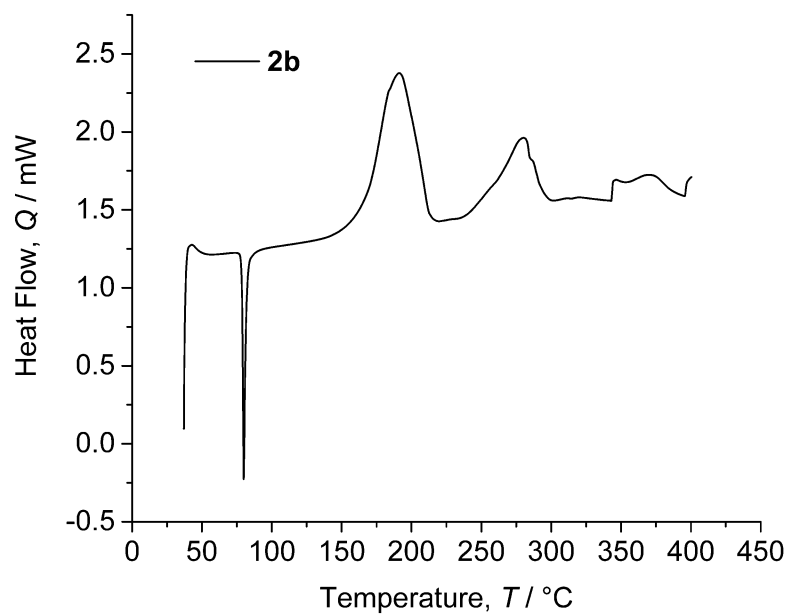


**Figure S-7.13** DSC of compound **2b**. Ramp rate =  $10\text{ }^{\circ}\text{C min}^{-1}$ .  $T_m = 80\text{ }^{\circ}\text{C}$ ,  $T_D = 167.0\text{ }^{\circ}\text{C}$

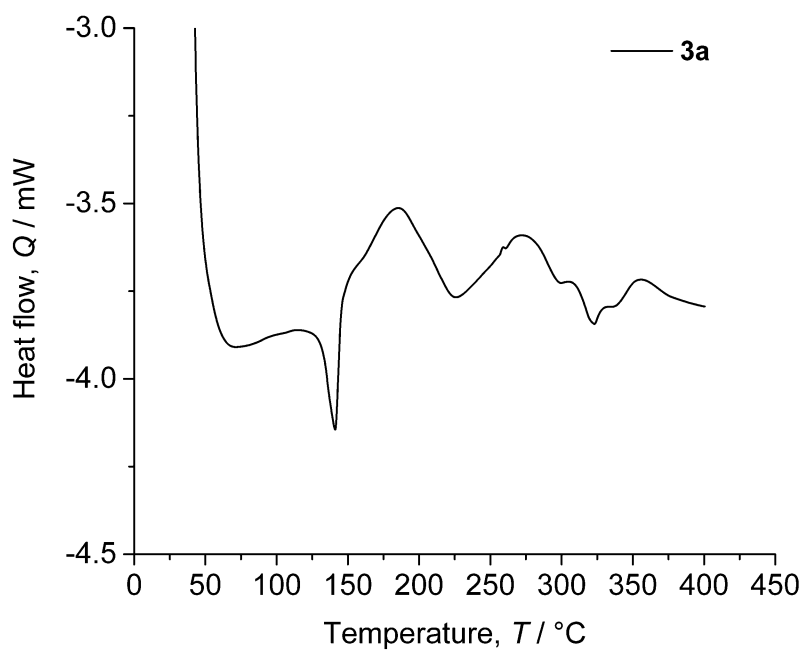


**Figure S-7.14** DSC of compound **3a**. Ramp rate =  $10\text{ }^{\circ}\text{C min}^{-1}$ .  $T_m = 140\text{ }^{\circ}\text{C}$ ,  $T_D = 164.5\text{ }^{\circ}\text{C}$

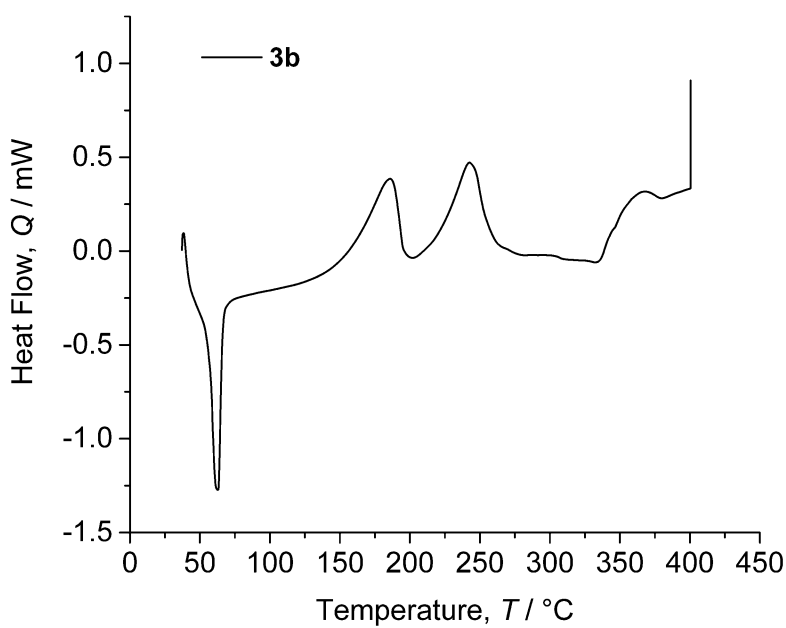


**Figure S-7.15** DSC of compound **3b**. Ramp rate =  $10\text{ °C min}^{-1}$ .  $T_m = 63\text{ °C}$ ,  $T_D = 154.9\text{ °C}$

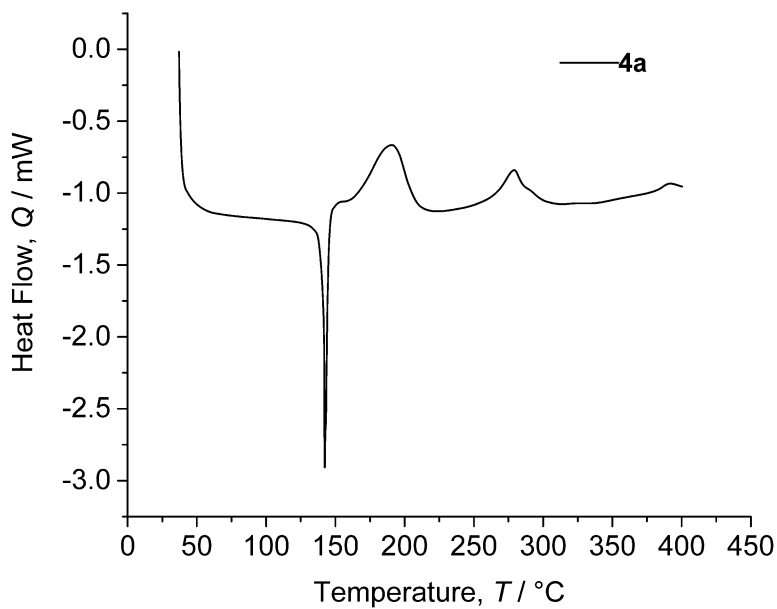


**Figure S-7.16** DSC of compound **4a**. Ramp rate =  $10\text{ °C min}^{-1}$ .  $T_m = 142\text{ °C}$ ,  $T_D = 167.6\text{ °C}$

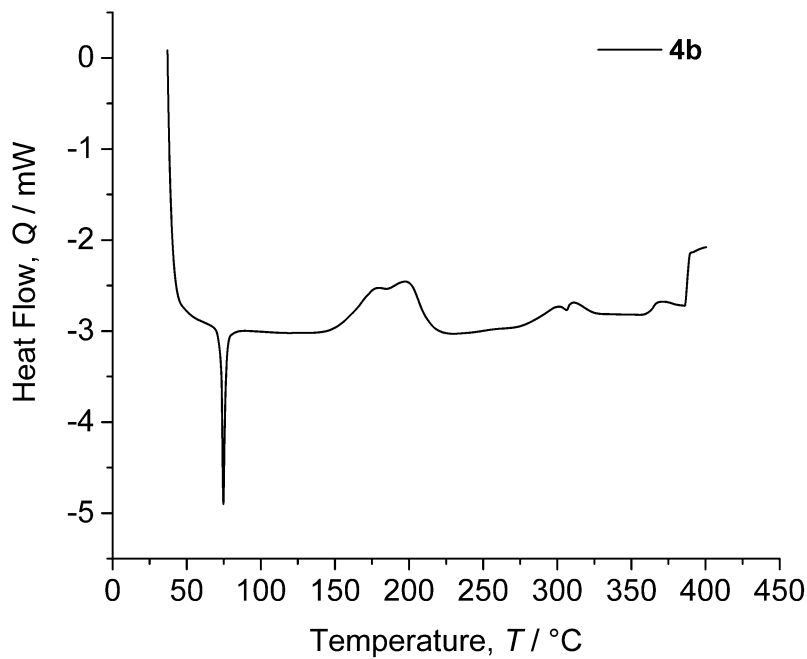


**Figure S-7.17** DSC of compound **4b**. Ramp rate =  $10\text{ }^{\circ}\text{C min}^{-1}$ .  $T_m = 75\text{ }^{\circ}\text{C}$ ,  $T_D = 150.9\text{ }^{\circ}\text{C}$

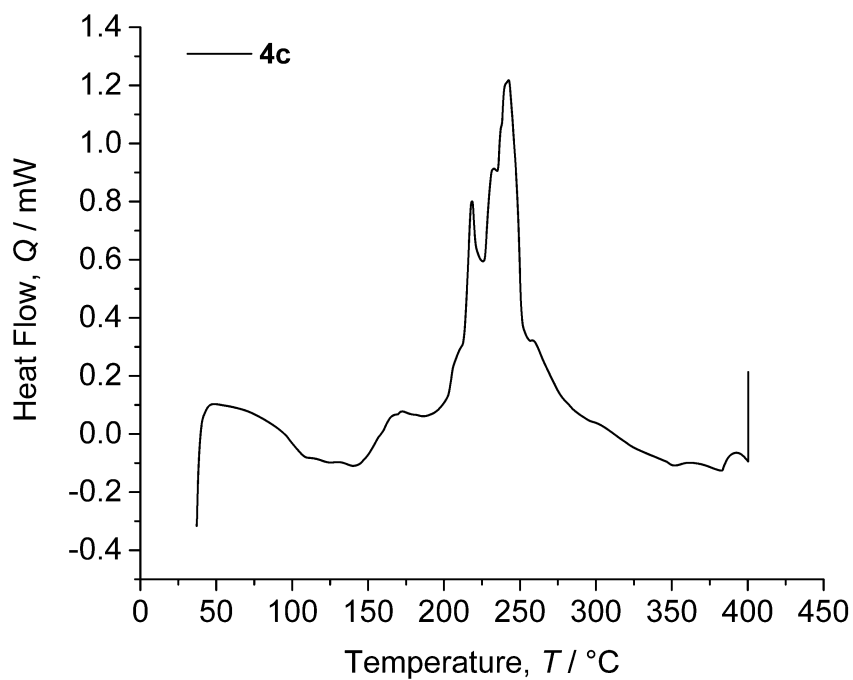


**Figure S-7.18** DSC of compound **4c**. Ramp rate =  $10\text{ }^{\circ}\text{C min}^{-1}$ .  $T_D = 207.0\text{ }^{\circ}\text{C}$

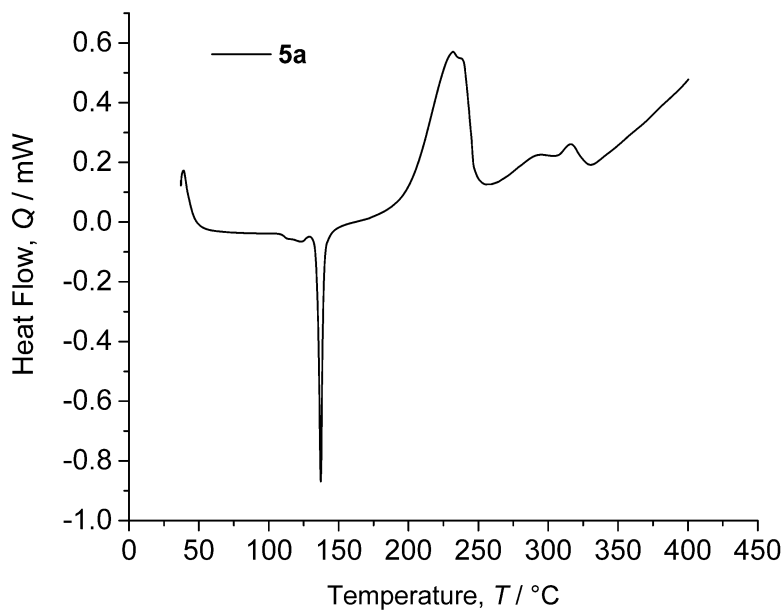


**Figure S-7.19** DSC of compound **4c**. Ramp rate = 10 °C min<sup>-1</sup>. T<sub>m</sub> = 137 °C, T<sub>D</sub> = 189.0 °C

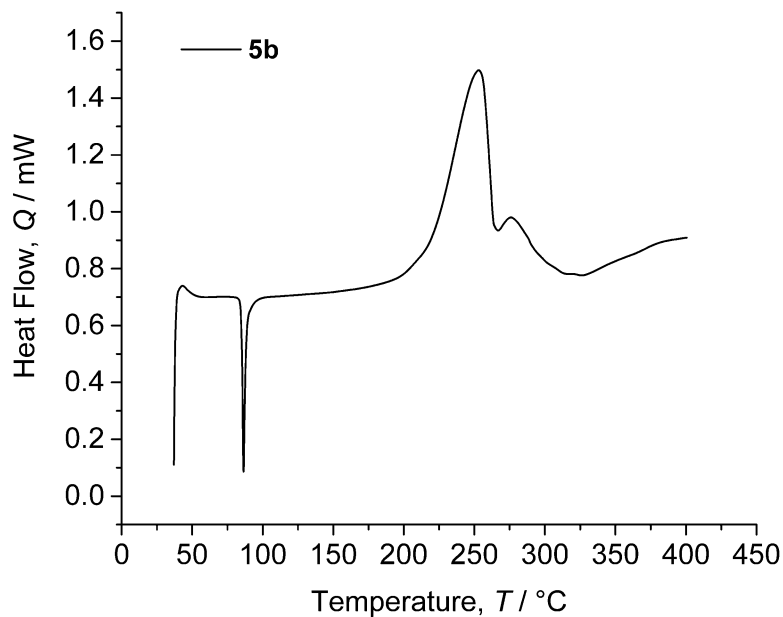


**Figure S-7.20** DSC of compound **4c**. Ramp rate = 10 °C min<sup>-1</sup>. T<sub>m</sub> = 86 °C, T<sub>D</sub> = 189.0 °C

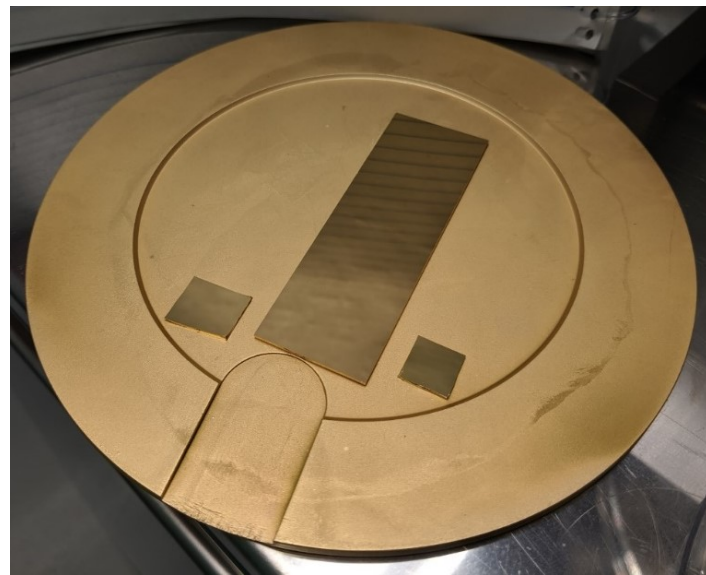


**Figure S-7.21** Picosun R200 PE-ALD apparatus substrate holder carrying (left to right) silicon, glass and Pt-coated Si substrates immediately after the 1000-cycle experiment using **1a** + O<sub>2</sub>\*. Both the substrates and the holder were completely covered in a bright golden film.

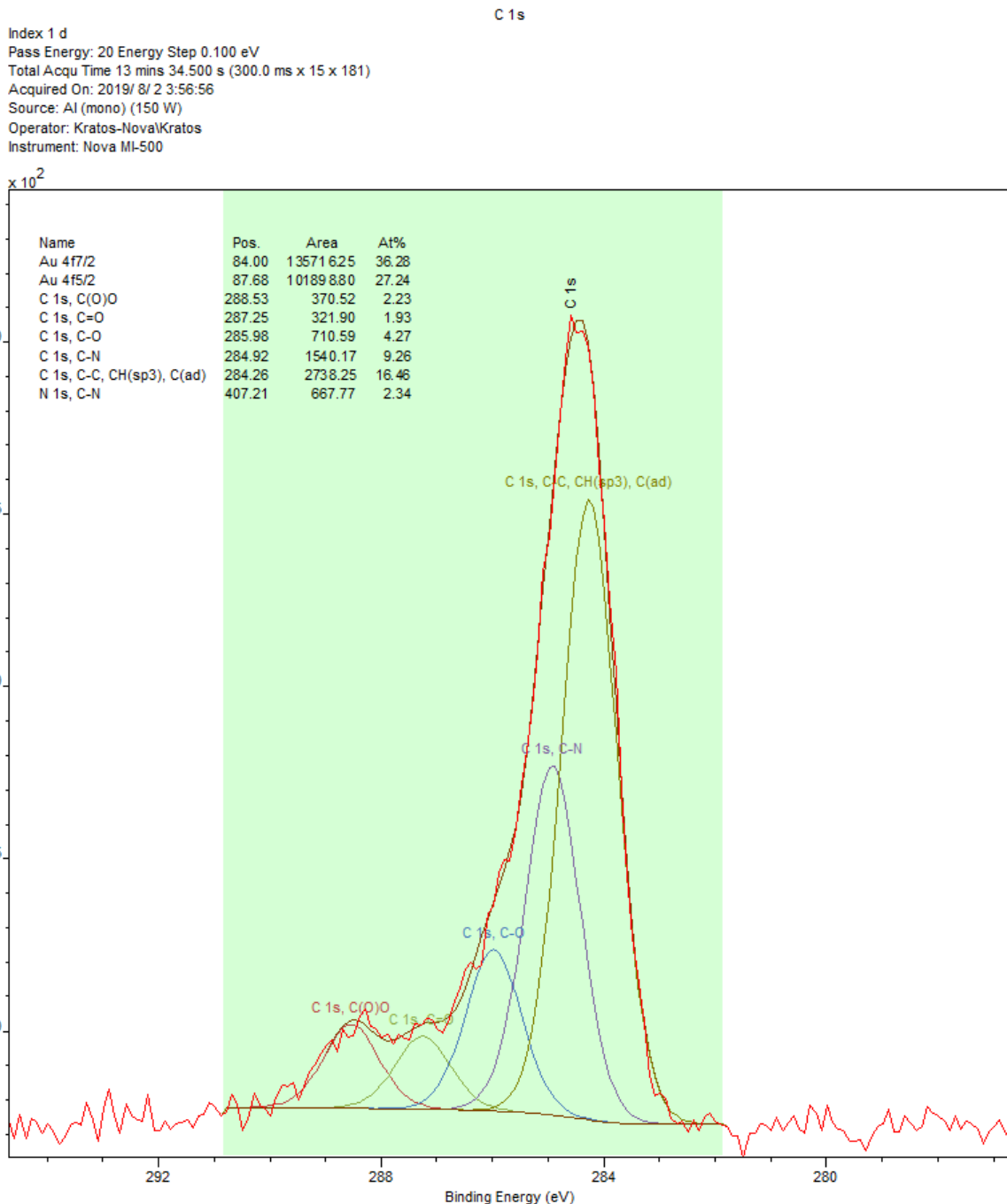


**Figure S-7.22** High-resolution XPS spectrum of the C 1s peak envelope on the as-deposited film produced by 1000 cycles of **1a** + O<sub>2</sub>\* (full spectrum shown in Figure 6.8a).

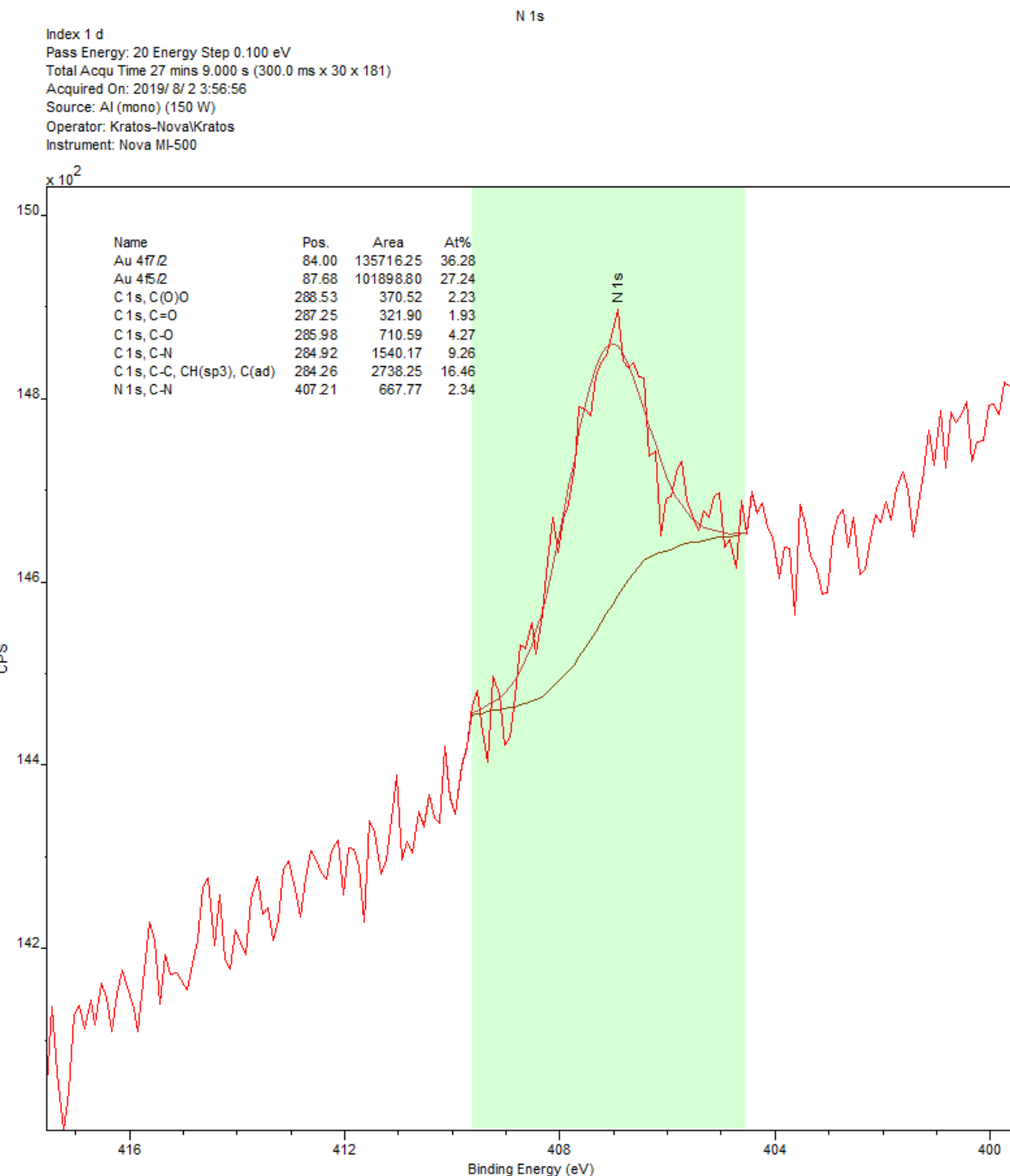


**Figure S-7.23** High-resolution XPS spectrum of the N 1s peak envelope on the as-deposited film produced by 1000 cycles of **1a** + O<sub>2</sub>\* (full spectrum shown in Figure 6.8a).

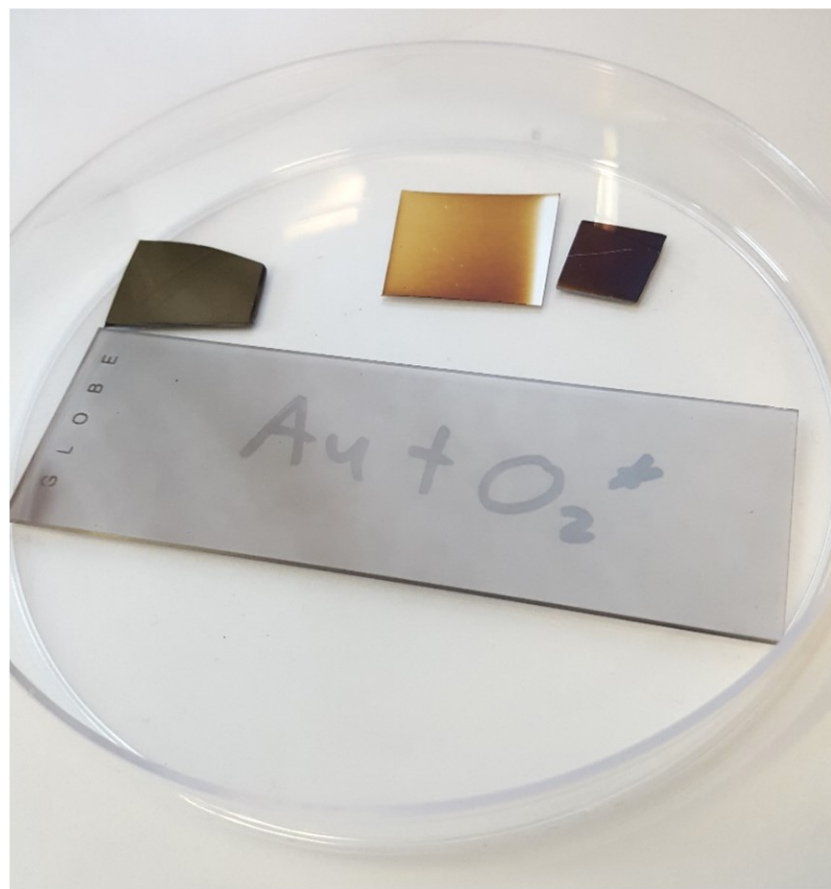


**Figure S-7.24** Substrates coated using the 1000-cycle experiment of **1b** + O<sub>2</sub>\* (clockwise from top left) silicon, aluminum, Pt-coated Si, and glass microscope slide. The Au + O<sub>2</sub>\* writing is visible through the purple nanoparticulate gold film deposited on the microscope slide.

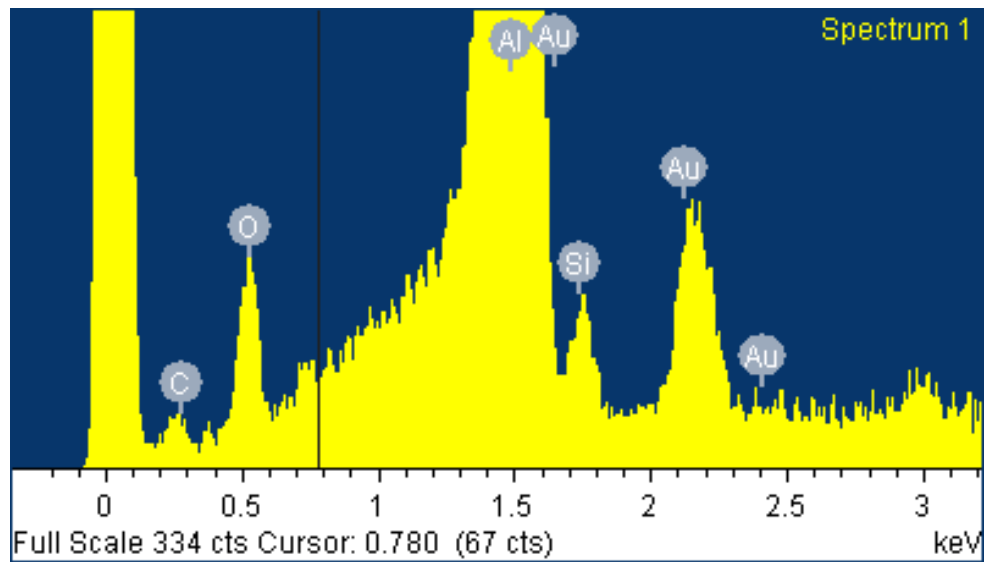


**Figure S-7.25** EDX spectrum of the as-deposited film produced by 1000 cycles of **1b** + O<sub>2</sub>\* on an aluminum substrate.

## Chapter 8 Conclusions

This thesis describes multiple studies of how precursor design can have a profound effect on CVD and ALD processes. In Chapter 3, the synthesis, thermolysis, and deposition behavior of both an NHC- and a phosphine- stabilized gold(I) amide CVD precursors were studied. The coordinative ligand of the precursors was found to play a role in directing the morphology of the gold nanoparticles deposited by each precursor. Large plates with nanoscale thicknesses grow only between 370 and 460 °C, with nanoparticle growth occurring outside of this intermediate temperature range. The desorption rate of the NHC and phosphine ligands from gold surfaces is thought to be slow enough in the intermediate temperature range to hinder CVD growth at different crystal facets. Each precursor displayed a different rate of nanobud formation due to the different rates of desorption of their respective coordinative ligands from metallic gold surfaces. Below 460 °C, the coordinative ligands effectively slow secondary nucleation on gold surfaces, promoting the growth of large nanocrystals from single seeds. The strongest evidence for this is the observation that secondary nucleation occurs most prominently under conditions of low precursor flux. This was one of the first Au CVD studies to use a precursor that was rationally designed to deposit anisotropic gold nanoparticles and microparticles.

The gold ALD precursor,  $(\text{PMe}_3)\text{AuMe}_3$ , possesses the excellent precursor characteristics of air-stability, liquid state during delivery to the ALD reaction chamber, and high volatility. The PE-ALD process using it in combination with  $\text{O}_2^*$  and  $\text{H}_2\text{O}$  was robust, with a steady-state GPC of 0.05 nm, and allowed for Ångström-level control over the deposition of gold metal nanostructures. This process was the first Au ALD process discovered and was a significant improvement over typical chemical vapor deposition processes in terms of thickness control and conformality of deposition. To date, this is the most popular gold ALD precursor and represents the beginning of a new field of study in ALD.

Growth of pure metallic gold films at the lowest reported temperature to date (50 °C) was demonstrated with a PE-ALD process, using  $(\text{PMe}_3)\text{AuMe}_3$  as the precursor and  $\text{H}_2^*$  as the co-reactant. The low temperature deposition enabled deposition of Au on tissue paper by PE-ALD which serves as an important first example of Au ALD on delicate substrates

which could be further extended to plastics or textiles. This process exhibits self-limiting chemisorption of both the precursor and reactant half cycles on gold surfaces with a steady growth rate of  $0.030 \pm 0.002$  nm cycle $^{-1}$ . A similar steady growth rate was obtained on bare SiO<sub>2</sub> surfaces after a sufficient number of cycles. A resistivity value of  $5.9 \pm 0.3$   $\mu\Omega$  cm was obtained for the thickest films, close to the bulk resistivity value of gold ( $2.44$   $\mu\Omega$  cm). The deposited films are pure gold with <1 at. % carbon and oxygen impurities in the film. During the main reaction mechanism of the (PMe<sub>3</sub>)AuMe<sub>3</sub> + H<sub>2</sub>\* process, the PMe<sub>3</sub> and CH<sub>3</sub> ligands of the precursor remain on the gold surface after chemisorption of **1**, causing self-saturating behaviour during the precursor exposure. The CH<sub>3</sub> ligands desorb rapidly, and ultimately the PMe<sub>3</sub> is the predominant self-limiting ligand. Both ligands are removed by the H<sub>2</sub>\* exposure, resulting in the formation of methane and PH<sub>x</sub>Me<sub>(3-x)</sub> species. At 120 °C, a minor amount of CVD could be observed due to the desorption of the PMe<sub>3</sub> ligands from the surface, as this effect creates additional adsorption sites for the next precursor exposure in a decomposition experiment. For substrate temperatures above 100 °C the amount of precursor decomposition increases with substrate temperature and at 120 °C the decomposition appears to be unsaturated, and becomes larger than the GPC of the ALD process at 100 °C. At all substrate temperatures the CH<sub>3</sub> groups desorb from the surface over time, occurring faster at higher substrate temperatures. The desorption of the PMe<sub>3</sub> groups from the surface, which increases with temperature, seems to be the main factor that determines the amount of parasitic CVD that occurs. This mechanistic study reveals the complex ligand desorption kinetics that occur upon chemisorption of (PMe<sub>3</sub>)AuMe<sub>3</sub> on Au surfaces.

In an attempt to advance our understanding of what design factors make the best gold(I) precursor, and motivated by the fact that no gold(I) ALD precursors have yet been identified, a family of 12 gold(I) compounds were synthesized and analyzed for their use as potential precursors for gold metal vapor deposition applications. Single crystal x-ray diffraction was used to structurally characterize 8 of these compounds to assess the effect of the anionic and coordinative ligands on intermolecular interactions. Compounds with Me and CH<sub>2</sub>(SiMe<sub>3</sub>) ligands displayed fewer intermolecular interactions than those with C<sub>6</sub>F<sub>5</sub> ligands due to the ability of the latter to undergo π-stacking and p-π interactions. These strong intermolecular interactions resulted in a substantial decrease in the volatility

of C<sub>6</sub>F<sub>5</sub>-containing compounds. TMS-ylide coordinative ligands produced compounds with fewer intermolecular interactions than bare ylide-containing compounds, which resulted in a higher volatility of the former type of precursor. Using TGA and DSC, we found that CH<sub>2</sub>(SiMe<sub>3</sub>) provides higher kinetic stability than Me as an anionic ligand for Au(I). NHC and C<sub>6</sub>F<sub>5</sub> ligands provide substantially higher thermodynamic stability to the gold(I) center, but adversely affected volatility. To deconvolute these effects we derived a figure of merit with which the viability of all gold(I) compounds may be compared for vapor deposition. Using DFT we found a linear correlation between the calculated Au-L bond strength and the measured onset of self-decomposition as measured by DSC which has allowed the possibility of predicting how thermally stable novel, not-yet-synthesized gold(I) precursors could be.

We then developed an *in-situ* monitoring methodology for testing the self-limiting capabilities of various gold CVD and ALD precursors. Bulky NHC-Au(I) compounds where the NHC bears <sup>t</sup>Bu wingtips were found to be likely inadequate as ALD precursors. CVD-like growth was observed at a GPC of 5.9 Å pulse<sup>-1</sup> and this phenomenon was attributed to the high steric bulk of the NHC preventing it from binding to the gold surface. The compound (PMe<sub>3</sub>)AuCH<sub>2</sub>(SiMe<sub>3</sub>) was observed to undergo very slow CVD on Al<sub>2</sub>O<sub>3</sub> surfaces, but the presence of formic acid causes an acceleration of growth through formation of Au<sup>0</sup> on Al<sub>2</sub>O<sub>3</sub> surfaces. Once formed, Au<sup>0</sup> catalyzes the CVD of (PMe<sub>3</sub>)AuCH<sub>2</sub>(SiMe<sub>3</sub>) and precludes its use as an ALD precursor for gold. In an attempt to circumvent this CVD mechanism, we synthesized a series of sterically bulky analogues to this precursor which were envisioned to increase the activation energy towards the CVD pathway. While (PMe<sub>3</sub>)AuMe undergoes rapid CVD, we can qualitatively say from *in situ* QCM and QMS analysis that CVD of the bulky (PMe<sub>3</sub>)AuCH(SiMe<sub>3</sub>)<sub>2</sub> has a much higher activation energy. If the increase in activation energy is due to a mechanistic change of the rate-limiting step of the CVD reaction, then (PMe<sub>3</sub>)AuCH(SiMe<sub>3</sub>)<sub>2</sub> and likely (PMe<sub>3</sub>)AuC(SiMe<sub>3</sub>)<sub>3</sub> should behave as kinetically-limited ALD precursors for gold metal which is a new concept in the field that has only been demonstrated in a few examples.

Based off of the growing body of literature of NHCs acting as thermally robust SAMs, a new family of potential Au(I) precursors of the type (NHC)AuR were synthesized and

thermally characterized by TGA, and DSC. The use of  $R = CH_2SiMe_3^-$  ligand invariably results in a more volatile compound than when  $R = Me^-$ . However, there was no clear trend for which of these ligands produced more thermal stability to a compound.  $R = CF_3^-$  produces a more stable but less volatile, and ultimately the  $CF_3^-$  ligand does not produce a useful precursor for (NHC)AuR type compounds. Using our precursor figure of merit ( $\sigma$ ), we found that unsaturated NHCs produced precursors with higher precursor merit than the saturated NHC analogues, and that substituting the backbone of the unsaturated NHC with Me groups gave a much higher  $\sigma$  precursor compared to a substitution of the wingtip group.

Using *in situ* QCM and QMS, we found that Me wingtip NHC precursors with  $R = Me^-$  and  $CH_2(SiMe_3)^-$  undergo self-limiting chemisorption on gold surfaces. Preliminary deposition experiments with the  $R = Me^-$  precursor produced pure gold films as shown by XPS analysis, and in fact these gold thin films were of higher purity than previously reported gold ALD processes. The purity of these films was corroborated by the excellent resistivity values obtained for both the 500-cycle and 1000-cycle films. When  $R = CH_2(SiMe_3)^-$  silicon-containing impurities become incorporated into the growing film when  $O_2^*$  is used as a co-reagent. While this unfortunately excludes the  $CH_2SiMe_3^-$  ligand from use in an Au ALD process that uses  $O_2^*$ , it does not exclude it from being used with other co-reagents. Future projects in our group will further explore Au ALD deposition using these precursors in the hopes of producing a process with a very large GPC, a phenomenon that should be possible given both our original hypothesis and the large saturative mass gain values observed in our QCM experiments. It highlights the ability of our *in-situ* monitoring method to rapidly screen and identify potential candidates for ALD and this study represents the first identification of a self-limiting Au(I) ALD precursor which was developed without a traditional ALD study.

## Chapter 9 References

- (1) Freestone, I.; Meeks, N.; Sax, M.; Higgitt, C. The Lycurgus Cup — A Roman Nanotechnology.

*Gold Bull.* **2007**, *40* (4), 270–277.

- (2) Eustis, S.; El-Sayed, M. A. Why Gold Nanoparticles Are More Precious than Pretty Gold: Noble Metal Surface Plasmon Resonance and Its Enhancement of the Radiative and Nonradiative Properties of Nanocrystals of Different Shapes. *Chem. Soc. Rev.* **2006**, *35* (3), 209–217.
- (3) Campbell, Dean J.; Xia, Y. J. Advanced Chemistry Classroom and Laboratory Plasmons : Why Should We Care ? *J. Chem. Educ.* **2007**, *84* (1), 91–96.
- (4) Gaspera, E. Della; Buso, D.; Martucci, A. Gold Nanoparticles to Boost the Gas Sensing Performance of Porous Sol-Gel Thin Films. *J. Sol-Gel Sci. Technol.* **2011**, *60* (3), 366–377.
- (5) Saha, K.; Agasti, S. S.; Kim, C.; Li, X.; Rotello, V. M. Gold Nanoparticles in Chemical and Biological Sensing. *Chem. Rev.* **2012**, *112* (5), 2739–2779.
- (6) Zhou, W.; Mandia, D. J.; Griffiths, M. B. E.; Bialiayeu, A.; Zhang, Y.; Gordon, P. G.; Barry, S. T.; Albert, J. Polarization-Dependent Properties of the Cladding Modes of a Single Mode Fiber Covered with Gold Nanoparticles. *Opt. Express* **2013**, *21* (1), 245.
- (7) Mandia, D. J.; Griffiths, M. B. E.; Zhou, W.; Gordon, P. G.; Albert, J.; Barry, S. T. In Situ Deposition Monitoring by a Tilted Fiber Bragg Grating Optical Probe: Probing Nucleation in Chemical Vapour Deposition of Gold. *Phys. Procedia* **2013**, *46* (Eurocvd 19), 12–20.
- (8) Zhou, W.; Mandia, D. J.; Griffiths, M. B. E.; Barry, S. T.; Albert, J. Effective Permittivity of Ultrathin Chemical Vapor Deposited Gold Films on Optical Fibers at Infrared Wavelengths. *J. Phys. Chem. C* **2014**, *118* (1), 670–678.
- (9) Zhou, W.; Mandia, D. J.; Barry, S. T.; Albert, J. Anisotropic Effective Permittivity of an Ultrathin Gold Coating on Optical Fiber in Air, Water and Saline Solutions. *Opt. Express* **2014**, *22* (26), 31665.
- (10) Mandia, D. J.; Zhou, W.; Albert, J.; Barry, S. T. CVD on Optical Fibers: Tilted Fiber Bragg Gratings as Real-Time Sensing Platforms. *Chem. Vap. Depos.* **2015**, *21* (1–3), 4–20.
- (11) Zhou, W.; Mandia, D. J.; Barry, S. T.; Albert, J. Absolute Near-Infrared Refractometry with a Calibrated Tilted Fiber Bragg Grating. *Opt. Lett.* **2015**, *40* (8), 1713.
- (12) Sabela, M.; Balme, S.; Bechelany, M.; Janot, J. M.; Bisetty, K. A Review of Gold and Silver Nanoparticle-Based Colorimetric Sensing Assays. *Adv. Eng. Mater.* **2017**, *19* (12), 1–24.
- (13) Tabasi, O.; Falamaki, C. Recent Advancements in the Methodologies Applied for the Sensitivity Enhancement of Surface Plasmon Resonance Sensors. *Anal. Methods* **2018**, *10* (32), 3906–3925.
- (14) Du, L.; Furube, A.; Hara, K.; Katoh, R.; Tachiya, M. Ultrafast Plasmon Induced Electron Injection Mechanism in Gold-TiO<sub>2</sub> Nanoparticle System. *J. Photochem. Photobiol. C Photochem. Rev.* **2013**, *15* (1), 21–30.
- (15) Zhang, X.; Liu, Y.; Lee, S. T.; Yang, S.; Kang, Z. Coupling Surface Plasmon Resonance of Gold Nanoparticles with Slow-Photon-Effect of TiO<sub>2</sub> Photonic Crystals for Synergistically Enhanced Photoelectrochemical Water Splitting. *Energy Environ. Sci.* **2014**, *7* (4), 1409–1419.
- (16) Notarianni, M.; Vernon, K.; Chou, A.; Aljada, M.; Liu, J.; Motta, N. Plasmonic Effect of Gold Nanoparticles in Organic Solar Cells. *Sol. Energy* **2014**, *106*, 23–37.
- (17) Robatjazi, H.; Bahauddin, S. M.; Doiron, C.; Thomann, I. Direct Plasmon-Driven Photoelectrocatalysis. *Nano Lett.* **2015**, *15* (9), 6155–6161.
- (18) Fan, W.; Leung, M. K. H.; Yu, J. C.; Ho, W. K. Recent Development of Plasmonic Resonance-Based Photocatalysis and Photovoltaics for Solar Utilization. *Molecules* **2016**, *21* (2).
- (19) Royanian, S.; Abdolahzadeh Ziabari, A.; Yousefi, R. Efficiency Enhancement of Ultra-Thin CIGS

- Solar Cells Using Bandgap Grading and Embedding Au Plasmonic Nanoparticles. *Plasmonics* **2020**, 1173–1182.
- (20) Zhang, Y.; Cui, X.; Shi, F.; Deng, Y. Nano-Gold Catalysis in Fine Chemical Synthesis. *Chem. Rev.* **2012**, 112 (4), 2467–2505.
- (21) Hashmi, A. S. K.; Hutchings, G. J. Gold Catalysis. *Angew. Chemie - Int. Ed.* **2006**, 45 (47), 7896–7936.
- (22) Tian, B.; Lei, Q.; Zhang, W.; Cui, Y.; Tian, Y.; Tian, B. UV-Driven Overall Water Splitting Using Unsupported Gold Nanoparticles as Photocatalysts. *Chem. Commun.* **2018**, 54 (15), 1845–1848.
- (23) Daniel, M. C.; Astruc, D. Gold Nanoparticles: Assembly, Supramolecular Chemistry, Quantum-Size-Related Properties, and Applications Toward Biology, Catalysis, and Nanotechnology. *Chem. Rev.* **2004**, 104 (1), 293–346.
- (24) Tada, H. Overall Water Splitting and Hydrogen Peroxide Synthesis by Gold Nanoparticle-Based Plasmonic Photocatalysts. *Nanoscale Adv.* **2019**, 1 (11), 4238–4245.
- (25) Hashemi, F. S. M.; Grillo, F.; Ravikumar, V. R.; Benz, D.; Shekhar, A.; Griffiths, M. B. E.; Barry, S. T.; Van Ommen, J. R. Thermal Atomic Layer Deposition of Gold Nanoparticles: Controlled Growth and Size Selection for Photocatalysis. *Nanoscale* **2020**, 12 (16), 9005–9013.
- (26) Morales-Guio, C. G.; Cave, E. R.; Nitopi, S. A.; Feaster, J. T.; Wang, L.; Kuhl, K. P.; Jackson, A.; Johnson, N. C.; Abram, D. N.; Hatsukade, T.; et al. Improved CO<sub>2</sub> Reduction Activity towards C<sub>2+</sub> Alcohols on a Tandem Gold on Copper Electrocatalyst. *Nat. Catal.* **2018**, 1 (10), 764–771.
- (27) Woldu, A. R. From Low to High-Index Facets of Noble Metal Nanocrystals: A Way Forward to Enhance the Performance of Electrochemical CO<sub>2</sub> Reduction. *Nanoscale* **2020**, 12 (16), 8626–8635.
- (28) Zhao, S.; Jin, R.; Jin, R. Opportunities and Challenges in CO<sub>2</sub> Reduction by Gold- and Silver-Based Electrocatalysts: From Bulk Metals to Nanoparticles and Atomically Precise Nanoclusters. *ACS Energy Lett.* **2018**, 3 (2), 452–462.
- (29) Kas, R.; Yang, K.; Bohra, D.; Kortlever, R.; Burdyny, T.; Smith, W. A. Electrochemical Co<sub>2</sub> Reduction on Nanostructured Metal Electrodes: Fact or Defect? *Chem. Sci.* **2020**, 11 (7), 1738–1749.
- (30) Liu, M.; Pang, Y.; Zhang, B.; De Luna, P.; Voznyy, O.; Xu, J.; Zheng, X.; Dinh, C. T.; Fan, F.; Cao, C.; et al. Enhanced Electrocatalytic CO<sub>2</sub> Reduction via Field-Induced Reagent Concentration. *Nature* **2016**, 537 (7620), 382–386.
- (31) Baum, T. H.; Comita, P. B. Chemical Vapor Deposition of Gold and Silver. In *The Chemistry of Metal CVD*; Kodas, T. T., Hampden-Smith, M. J., Eds.; Wiley-VCH Verlag GmbH: Weinheim, Germany, 1994; pp 303–327.
- (32) Kern, W.; Jensen, K. F. Thin Film Processes II. In *Thin Film Processes II*; Vossen, J. L., Kern, W., Eds.; Academic Press Inc.: San Diego, 1991; pp 283–312.
- (33) Feng, J.; Gong, X.; Lou, X.; Gordon, R. G. Direct-Liquid-Evaporation Chemical Vapor Deposition of Nanocrystalline Cobalt Metal for Nanoscale Copper Interconnect Encapsulation. *ACS Appl. Mater. Interfaces* **2017**, 9 (12), 10914–10920.
- (34) Han, J. H.; Lee, S. W.; Choi, G. J.; Lee, S. Y.; Hwang, C. S.; Dussarrat, C.; Gatineau, J. Chemical Vapor Deposition of Ru Thin Films with an Enhanced Morphology, Thermal Stability, and Electrical Properties Using a RuO<sub>4</sub> Precursor. *Chem. Mater.* **2009**, 21 (2), 207–209.
- (35) Huang, H.; McLaughlin, P. S.; Kelly, J. J.; Yang, C. C.; Southwick, R. G.; Wang, M.; Bonilla, G.; Karve, G. Time Dependent Dielectric Breakdown of Cobalt and Ruthenium Interconnects at 36nm Pitch. *IEEE Int. Reliab. Phys. Symp. Proc.* **2019**, 2019-March, 3–7.

- (36) He, M.; Zhang, X.; Nogami, T.; Lin, X.; Kelly, J.; Kim, H.; Spooner, T.; Edelstein, D.; Zhao, L. Mechanism of Co Liner as Enhancement Layer for Cu Interconnect Gap-Fill. *J. Electrochem. Soc.* **2013**, *160* (12), D3040–D3044.
- (37) Kwon, O.-K.; Kim, J.-H.; Park, H.-S.; Kang, S.-W. Atomic Layer Deposition of Ruthenium Thin Films for Copper Glue Layer. *J. Electrochem. Soc.* **2004**, *151* (2), G109.
- (38) Misra, V.; Lucovsky, G.; Parsons, G. Issues in High-k Gate Stack Interfaces. *MRS Bull.* **2002**, *27* (3), 212–216.
- (39) Bekiaris, N.; Wu, Z.; Ren, H.; Naik, M.; Park, J. H.; Lee, M.; Ha, T. H.; Hou, W.; Bakke, J. R.; Gage, M.; et al. Cobalt Fill for Advanced Interconnects. *IITC 2017 - 2017 IEEE Int. Interconnect Technol. Conf.* **2017**, 10–12.
- (40) Talukdar, T. K.; Girolami, G. S.; Abelson, J. R. Seamless Fill of Deep Trenches by Chemical Vapor Deposition: Use of a Molecular Growth Inhibitor to Eliminate Pinch-Off. *J. Vac. Sci. Technol. A* **2019**, *37* (2), 021509.
- (41) Vos, M. F. J.; Van Straaten, G.; Kessels, W. M. M. E.; Mackus, A. J. M. Atomic Layer Deposition of Cobalt Using H<sub>2</sub>-, N<sub>2</sub>-, and NH<sub>3</sub>-Based Plasmas: On the Role of the Co-Reactant. *J. Phys. Chem. C* **2018**, *122* (39), 22519–22529.
- (42) Van Daele, M.; Detavernier, C.; Dendooven, J. Surface Species during ALD of Platinum Observed with: In Situ Reflection IR Spectroscopy. *Phys. Chem. Chem. Phys.* **2018**, *20* (39), 25343–25356.
- (43) de Rouffignac, P.; Yousef, A. P.; Kim, K. H.; Gordon, R. G. ALD of Scandium Oxide from Scandium Tris(N,N'-Diisopropylacetamidinate) and Water. *Electrochem. Solid-State Lett.* **2006**, *9* (6), F45.
- (44) Vos, M. F. J.; Mackus, A. J. M.; Kessels, W. M. M. Atomic Layer Process Development - 10 steps to successfully develop, optimize and characterize ALD recipes  
<https://www.atomiclimits.com/2019/02/12/atomic-layer-deposition-process-development-10-steps-to-successfully-develop-optimize-and-characterize-ald-recipes/> (accessed Jul 10, 2020).
- (45) Miikkulainen, V.; Leskelä, M.; Ritala, M.; Puurunen, R. L. Crystallinity of Inorganic Films Grown by Atomic Layer Deposition: Overview and General Trends. *J. Appl. Phys.* **2013**, *113* (2).
- (46) Van Delft, J. A.; Garcia-Alonso, D.; Kessels, W. M. M. Atomic Layer Deposition for Photovoltaics: Applications and Prospects for Solar Cell Manufacturing. *Semicond. Sci. Technol.* **2012**, *27* (7).
- (47) Knez, M.; Nielsch, K.; Niinistö, L. Synthesis and Surface Engineering of Complex Nanostructures by Atomic Layer Deposition. *Adv. Mater.* **2007**, *19* (21), 3425–3438.
- (48) George, S. M. Atomic Layer Deposition: An Overview. *Chem. Rev.* **2010**, *110* (1), 111–131.
- (49) Johnson, R. W.; Hultqvist, A.; Bent, S. F. A Brief Review of Atomic Layer Deposition: From Fundamentals to Applications. *Mater. Today* **2014**, *17* (5), 236–246.
- (50) Wu, Y.; Potts, S. E.; Hermkens, P. M.; Knoops, H. C. M.; Roozeboom, F.; Kessels, W. M. M. Enhanced Doping Efficiency of Al-Doped ZnO by Atomic Layer Deposition Using Dimethylaluminum Isopropoxide as an Alternative Aluminum Precursor. *Chem. Mater.* **2013**, *25* (22), 4619–4622.
- (51) Kalanyan, B.; Lemaire, P. C.; Atanasov, S. E.; Ritz, M. J.; Parsons, G. N. Using Hydrogen to Expand the Inherent Substrate Selectivity Window during Tungsten Atomic Layer Deposition. *Chem. Mater.* **2016**, *28* (1), 117–126.
- (52) Dasgupta, N. P.; Lee, W.; Prinz, F. B. Atomic Layer Deposition of Lead Sulfide Thin Films for Quantum Confinement. *Chem. Mater.* **2009**, *21* (17), 3973–3978.
- (53) Dasgupta, N. P.; MacK, J. F.; Langston, M. C.; Bousetta, A.; Prinz, F. B. Design of an Atomic

Layer Deposition Reactor for Hydrogen Sulfide Compatibility. *Rev. Sci. Instrum.* **2010**, *81* (4).

- (54) Homma, T.; Takasaki, A.; Yamaguchi, M.; Kokubun, H.; Machida, H. A Process for Copper Film Deposition by Pyrolysis of Organic Copper Materials. *J. Electrochem. Soc.* **2000**, *147* (2), 580.
- (55) Choi, K.; Rhee, S. Chemical Vapor Deposition of Copper Film from Hexafluoroacetyl-AcetonateCu(I)Vinylcyclohexane. *Thin Solid Films* **2001**, *397* (1–2), 70–77.
- (56) Mohimi, E.; Chu, X. I.; Trinh, B. B.; Babar, S.; Girolami, G. S.; Abelson, J. R. Thermal Atomic Layer Etching of Copper by Sequential Steps Involving Oxidation and Exposure to Hexafluoroacetylacetone. *ECS J. Solid State Sci. Technol.* **2018**, *7* (9), P491–P495.
- (57) Konh, M.; He, C.; Lin, X.; Guo, X.; Pallem, V.; Opila, R. L.; Teplyakov, A. V.; Wang, Z.; Yuan, B. Molecular Mechanisms of Atomic Layer Etching of Cobalt with Sequential Exposure to Molecular Chlorine and Diketones. *J. Vac. Sci. Technol. A* **2019**, *37* (2), 021004.
- (58) Wexler, D.; Zink, J. I.; Tutt, L. W.; Lunt, S. R. Laser-Assisted Deposition of Pure Gold from (Hexafluoroacetylacetone)Dimethylgold(III) and Gas-Phase Luminescence Identification of Photofragments. *J. Phys. Chem.* **1993**, *97* (51), 13563–13567.
- (59) Cotton, A. F.; Wilkinson, S. G.; Murillo, C. A.; Bochmann, M. *Advanced Inorganic Chemistry*, 2nd ed.; Interscience Publishers (a division of John Wiley and Sons, Inc.), New York, 1966.
- (60) Physical Constants of Inorganic Compounds. In *CRC Handbook of Chemistry and Physics, 101st Edition (internet Version 2020)*; Rumble, J. R., Ed.; CRC Press/Taylor & Francis, Boca Raton, FL, 2020; pp 1–162.
- (61) Schmidbaur, H.; Schier, A. A Briefing on Auophilicity. *Chem. Soc. Rev.* **2008**, *37* (9), 1931–1951.
- (62) Lima, J. C.; Rodríguez, L. Applications of Gold(i) Alkynyl Systems: A Growing Field to Explore. *Chem. Soc. Rev.* **2011**, *40* (11), 5442–5456.
- (63) Wuttke, A.; Feldt, M.; Mata, R. A. All That Binds Is Not Gold-The Relative Weight of Auophilic Interactions in Complex Formation. *J. Phys. Chem. A* **2018**, *122* (34), 6918–6925.
- (64) Coyle, J. P.; Kurek, A.; Pallister, P. J.; Sirianni, E. R.; Yap, G. P. A.; Barry, S. T.; Sun, Z. M. Preventing Thermolysis: Precursor Design for Volatile Copper Compounds. *Chem. Commun.* **2012**, *48* (84), 10440–10442.
- (65) Wilkinson, G. The Long Search for Stable Transition Metal Alkyls. *Science (80-.)* **1974**, *185* (4146), 109–112.
- (66) Wozniak, B.; Ruddick, J. D.; Wilkinson, G. Trimethylsilylmethyl Complexes of Transition Metals with π-Bonding Ligands. *J. Chem. Soc. A* **1971**, No. 31, 3116–3120.
- (67) Mowat, W.; Shortland, A.; Yagupsky, G.; Hill, N. J.; Yagupsky, M.; Wilkinson, G. Elimination Stabilized Alkyls. Part I. Chromium, Molybdenum, Tungsten, and Vanadium. *J. Chem. Soc. Dalton Trans.* **1972**, No. 4, 533.
- (68) Fawcett, F. S. Bredt's Rule of Double Bonds in Atomic-Bridged-Ring Structures. *Chem. Rev.* **1950**, *47* (2), 219–274.
- (69) Bower, B. K.; Tennent, H. G. Transition Metal Bicyclo[2.2.1]Hept-1-Yls. *J. Am. Chem. Soc.* **1972**, *94* (7), 2512–2514.
- (70) Kunte, G. V.; Shivashankar, S. A.; Umarji, A. M. Thermogravimetric Evaluation of the Suitability of Precursors for MOCVD. *Meas. Sci. Technol.* **2008**, *19* (2), 025704.
- (71) TA Instruments. Universal Analysis 2000 Operator's Manual. **2002**, No. September, 183–183.
- (72) Basova, T. V.; Hassan, A.; Morozova, N. B. Chemistry of Gold(I, III) Complexes with Organic Ligands as Potential MOCVD Precursors for Fabrication of Thin Metallic Films and Nanoparticles.

*Coord. Chem. Rev.* **2019**, *380*, 58–82.

- (73) Chemcraft - graphical software for visualization of quantum chemistry computations. <https://www.chemcraftprog.com>.
- (74) Turgambaeva, A. E.; Zharkova, G.; Semyannikov, P.; Krisyuk, V. V.; Koretskaya, T.; Trubin, S.; Kuchumov, B.; Igumenov, I. Oxygen-Free Precursor for Chemical Vapor Deposition of Gold Films: Thermal Properties and Decomposition Mechanism. *Gold Bull.* **2011**, *44* (3), 177–184.
- (75) Uchida, H.; Saitou, N.; Satou, M.; Tebakari, M.; Ogi, K. Properties of A New Liquid Organo Gold Compound for MOCVD. *MRS Proc.* **1993**, *334*, 293.
- (76) Land, M. A.; Robertson, K. N.; Barry, S. T. Ligand-Assisted Volatilization and Thermal Stability of Bis(Imido)Dichloromolybdenum(VI) ( $[(t\text{-BuN}=\text{})_2\text{MoCl}_2]_2$ ) and Its Adducts. *Organometallics* **2020**, *39* (7), 916–927.
- (77) Nikitenko, N. G.; Shestakov, A. F. Thermal Decomposition Mechanism of Dimethyl(Acetylacetonato)Gold(III): Quantum Chemical Modeling. *Kinet. Catal.* **2014**, *55* (4), 401–408.
- (78) Baum, T. H. Laser Chemical Vapor Deposition of Gold. *J. Electrochem. Soc.* **1987**, *134* (10), 2616.
- (79) Parkhomenko, R. G.; Plekhanov, A. I.; Kuchyanov, A. S.; Trubin, S. V.; Kuchumov, B. M.; Igumenov, I. K. Gold Nanostructure Formation in the Photonic Crystal Matrix by Means of MOCVD Technique. *Surf. Coatings Technol.* **2013**, *230*, 279–283.
- (80) Uchida, H.; Saitou, N.; Sato, M.; Take, M.; Ogi, K. Dimethyl Gold Beta-Iminoketone for CVD. JPH06100570 (A), 1994.
- (81) Saitou, N.; Uchida, H.; Ogi, K. Preparation of Organogold Complexes as Materials for Gold Film. JPH06157546 (A), 1994.
- (82) Schmidbaur, H.; Gasser, O.; Krüger, C.; Sekutowski, J. C. Doppelylide, II. Synthese, Eigenschaften Und Eine Kristallstrukturbestimmung Einiger [Methanidobis(Dimethylphosphonium-Methylid)]-Komplexe von Haupt- Und Nebengruppenmetallen (Al, Ga, Ni, Pd, Pt, Au, Zn, Cd). *Chem. Ber.* **1977**, *110* (11), 3517–3527.
- (83) Uchida, H.; Saitou, N.; Sato, M.; Take, M.; Ogi, K. Dimethyl Gold Phosphonium Complex for Laser CVD. JPH06158322 (A), 1994.
- (84) Schmidbaur, H.; Füller, H. -J.; Bejenke, V.; Franck, A.; Huttner, G. Doppelylide, IV. Synthese, Eigenschaften Und Eine Röntgenstrukturanalyse von Nitridobis(Dimethylphosphonium-methylid)-Komplexen Einiger D8- Und D10-Übergangsmetalle (Ni, Pt, Au, Zn, Cd). *Chem. Ber.* **1977**, *110* (11), 3536–3543.
- (85) Baum, T. H.; Brock, P. J.; Dawson, D. J. Simplified Synthesis of Dialkylgold(III) Beta-Diketonates. US5023360 (A), 1991.
- (86) Turgambaeva, A. E.; Parkhomenko, R. G.; Krisyuk, V. V.; Igumenov, I. K. Volatile Dimethylgold(III) Complex with Di- Iso -Butyldithiophosphinate Ligand: Synthesis, Structure, and Thermal Behavior in Condensed and Gas Phase. *J. Coord. Chem.* **2015**, *68* (11), 1878–1889.
- (87) Parkhomenko, R. G.; Trubin, S. V.; Turgambaeva, A. E.; Igumenov, I. K. Deposition of Pure Gold Thin Films from Organometallic Precursors. *J. Cryst. Growth* **2015**, *414*, 143–150.
- (88) Parkhomenko, R.; Alexeyev, A.; Morozova, N.; Igumenov, I. Syntheses, Structures, and Thermal Properties of New Au(III) Organometallic Compounds with Ancillary S-, O-, and/or N-Donor Ligands. *J. Coord. Chem.* **2012**, *65* (18), 3227–3237.
- (89) Mäkelä, M.; Hatanpää, T.; Mizohata, K.; Räisänen, J.; Ritala, M.; Leskelä, M. Thermal Atomic Layer Deposition of Continuous and Highly Conducting Gold Thin Films. *Chem. Mater.* **2017**, *29*

(14), 6130–6136.

- (90) Bessonov, A. a.; Morozova, N. B.; Gelfond, N. V.; Semyannikov, P. P.; Baidina, I. a.; Trubin, S. V.; Shevtsov, Y. V.; Igumenov, I. K. Synthesis, Crystal Structure and Thermal Behavior of Dimethylgold(III) Derivatives of Salicylaldimine Schiff Bases – Novel Precursors for Gold MOCVD Applications. *J. Organomet. Chem.* **2008**, 693 (15), 2572–2578.
- (91) Bessonov, A. A.; Morozova, N. B.; Semyannikov, P. P.; Trubin, S. V.; Gel'fond, N. V.; Igumenov, I. K. Thermal Properties of Dimethylgold(III) 8-Hydroxyquinolinate and 8-Mercaptoquinolinate. *Russ. J. Coord. Chem.* **2008**, 34 (3), 186–189.
- (92) Blaauw, H. J. A.; Nivard, R. J. F.; Van Der Kerk, G. J. M. Chemistry of Organogold Compounds. *J. Organomet. Chem.* **1964**, 2 (3), 236–244.
- (93) Heinrich, D. D.; Wang, J. C.; Fackler Jnr, J. P. Structure of Au<sub>2</sub>[S<sub>2</sub>CN(C<sub>2</sub>H<sub>5</sub>)<sub>2</sub>]<sub>2</sub>, Bis(Diethyldithiocarbamato)Digold(I). *Acta Crystallogr. Sect. C Cryst. Struct. Commun.* **1990**, 46 (8), 1444–1447.
- (94) Bessonov, A. A.; Morozova, N. B.; Gelfond, N. V.; Semyannikov, P. P.; Trubin, S. V.; Shevtsov, Y. V.; Shubin, Y. V.; Igumenov, I. K. Dimethylgold(III) Carboxylates as New Precursors for Gold CVD. *Surf. Coatings Technol.* **2007**, 201 (22–23), 9099–9103.
- (95) Parkhomenko, R. G.; Morozova, N. B.; Zharkova, G. I.; Shubin, Y. V.; Trubin, S. V.; Kriventsov, V. V.; Kuchumov, B. M.; Koretskaya, T. P.; Igumenov, I. K. Deposition of Au Thin Films and Nanoparticles by MOCVD. *Chem. Vap. Depos.* **2012**, 18 (10–12), 336–342.
- (96) Schmidbaur, H.; Bergfeld, M. Trimethylsiloxydimethylgold. *Inorg. Chem.* **1966**, 5 (11), 2069–2070.
- (97) Uchida, H.; Saitou, N.; Sato, M.; Take, M.; Ogi, K. Formation of Thin Film Gold. JPH06101046 (A), 1994.
- (98) Messelhäuser, J.; Flint, E. B.; Suhr, H. Laser Induced CVD of Gold Using New Precursors. *Appl. Surf. Sci.* **1992**, 54, 64–68.
- (99) Griffiths, M. B. E.; Pallister, P. J.; Mandia, D. J.; Barry, S. T. Atomic Layer Deposition of Gold Metal. *Chem. Mater.* **2016**, 28 (1), 44–46.
- (100) Van Daele, M.; Griffiths, M. B. E.; Raza, A.; Minjauw, M. M.; Solano, E.; Feng, J. Y.; Ramachandran, R. K.; Clemmen, S.; Baets, R.; Barry, S. T.; et al. Plasma-Enhanced Atomic Layer Deposition of Nanostructured Gold near Room Temperature. *ACS Appl. Mater. Interfaces* **2019**, 11 (40), 36824–36830.
- (101) Hashemi, F. S. M.; Grillo, F.; Ravikumar, V. R.; Benz, D.; Shekhar, A.; Griffiths, M. B. E.; Barry, S. T.; van Ommen, J. R. Thermal Atomic Layer Deposition of Gold Nanoparticles: Controlled Growth and Size Selection for Photocatalysis. *Nanoscale* **2020**, 12 (16), 9005–9013.
- (102) Van Daele, M.; Griffiths, M. B. E.; Minjauw, M. M.; Barry, S. T.; Detavernier, C.; Dendooven, J. Reaction Mechanism of the Me<sub>3</sub>AuPMe<sub>3</sub>–H<sub>2</sub> Plasma-Enhanced ALD Process. *Phys. Chem. Chem. Phys.* **2020**, 22 (21), 11903–11914.
- (103) Whitehorne, T. J. J. Synthesis, Structure and Thermochemistry of Selected Group 11 and 12 Metals, Carleton University, 2009.
- (104) Whitehorne, T. J. J.; Coyle, J. P.; Mahmood, A.; Monillas, W. H.; Yap, G. P. a.; Barry, S. T. Group 11 Amidinates and Guanidinates: Potential Precursors for Vapour Deposition. *Eur. J. Inorg. Chem.* **2011**, 2011 (21), 3240–3247.
- (105) Zhou, W.; Mandia, D. J.; Griffiths, M. B. E.; Bialiayeu, A.; Zhang, Y.; Gordon, P. G.; Barry, S. T.; Albert, J. Polarization-Dependent Properties of the Cladding Modes of a Single Mode Fiber Covered with Gold Nanoparticles. *Opt. Express* **2013**, 21 (1), 245.

- (106) Coyle, J. P.; Gordon, P. G.; Wells, A. P.; Mandia, D. J.; Sirianni, E. R.; Yap, G. P. a.; Barry, S. T. Thermally Robust Gold and Silver Iminopyrrolidinates for Chemical Vapor Deposition of Metal Films. *Chem. Mater.* **2013**, *25* (22), 4566–4573.
- (107) Zhou, W.; Mandia, D. J.; Griffiths, M. B. E.; Barry, S. T.; Albert, J. Effective Permittivity of Ultrathin Chemical Vapor Deposited Gold Films on Optical Fibers at Infrared Wavelengths. *J. Phys. Chem. C* **2014**, *118* (1), 670–678.
- (108) Tong, L.; Davis, L. M.; Gong, X.; Feng, J.; Beh, E. S.; Gordon, R. G. Synthesis of Volatile, Reactive Coinage Metal 5,5-Bicyclic Amidinates with Enhanced Thermal Stability for Chemical Vapor Deposition. *Dalt. Trans.* **2019**, *48* (20), 6709–6713.
- (109) Schmidbaur, H.; Shiotani, A. Organosilicon Compounds Containing Monovalent Gold. *J. Am. Chem. Soc.* **1970**, *92* (23), 7003–7004.
- (110) Griffiths, M. B. E.; Koponen, S. E.; Mandia, D. J.; McLeod, J. F.; Coyle, J. P.; Sims, J. J.; Giorgi, J. B.; Sirianni, E. R.; Yap, G. P. A.; Barry, S. T. Surfactant Directed Growth of Gold Metal Nanoplates by Chemical Vapor Deposition. *Chem. Mater.* **2015**, *27* (17), 6116–6124.
- (111) Mäkelä, M.; Hatanpää, T.; Ritala, M.; Leskelä, M.; Mizohata, K.; Meinander, K.; Räisänen, J. Potential Gold(I) Precursors Evaluated for Atomic Layer Deposition. *J. Vac. Sci. Technol. A Vacuum, Surfaces, Film.* **2017**, *35* (1), 01B112.
- (112) Weidner, T.; Baio, J. E.; Mundstock, A.; Große, C.; Karthäuser, S.; Bruhn, C.; Siemeling, U. NHC-Based Self-Assembled Monolayers on Solid Gold Substrates. *Aust. J. Chem.* **2011**, *64* (8), 1177.
- (113) Crudden, C. M.; Horton, J. H.; Ebralidze, I. I.; Zenkina, O. V.; McLean, A. B.; Drevniok, B.; She, Z.; Kraatz, H. B.; Mosey, N. J.; Seki, T.; et al. Ultra Stable Self-Assembled Monolayers of N-Heterocyclic Carbenes on Gold. *Nat. Chem.* **2014**, *6* (5), 409–414.
- (114) Ahvenniemi, E.; Akbashev, A. R.; Ali, S.; Bechelany, M.; Berdova, M.; Boyadjiev, S.; Cameron, D. C.; Chen, R.; Chubarov, M.; Cremers, V.; et al. Review Article: Recommended Reading List of Early Publications on Atomic Layer Deposition—Outcome of the “Virtual Project on the History of ALD.” *J. Vac. Sci. Technol. A Vacuum, Surfaces, Film.* **2017**, *35* (1), 010801.
- (115) Man, R. W. Y.; Li, C. H.; MacLean, M. W. A.; Zenkina, O. V.; Zamora, M. T.; Saunders, L. N.; Rousina-Webb, A.; Nambo, M.; Crudden, C. M. Ultrastable Gold Nanoparticles Modified by Bidentate N-Heterocyclic Carbene Ligands. *J. Am. Chem. Soc.* **2018**, *140* (5), 1576–1579.
- (116) Colgate, S. O.; Palenik, G. J.; House, V. E.; Schoenfeld, D. W. Area Selective Metalorganic Chemical Vapor Deposition of Gold on Tungsten Patterned on Silicon. *J. Vac. Sci. Technol. A Vacuum, Surfaces, Film.* **1990**, *8* (3), 1411–1412.
- (117) Fuß, W.; Rühe, M. Chlor(Trifluorophosphoran)Gold(I), Eine Einfache Flüchtige Notizen: Goldverbindung/Chloro(Trifluorophosphane)Gold(I), a Simple Volatile Gold Compound. *Zeitschrift für Naturforsch. B* **1992**, *47* (4), 591–593.
- (118) Jansen, F.; Kruck, T. Promising New Precursors for the CVD of Gold. *Adv. Mater.* **1995**, *7* (3), 297–300.
- (119) Schmidbaur, H.; Franke, R. Methylgold(I) Und Gold(I)Halogenide Als Komplexbildende Zentren Fuer Trimethylphosphin Unf Trimethylphophit. *Chem. Ber.* **1972**, *105*, 2985–2997.
- (120) Blessmann, D.; Gräfe, A.; Heinen, R.; Jansen, F.; Kruck, T.; Terfloth, C. Organometallic Compounds: The Chemist’s Contribution to New Electronic Materials. *Mater. Sci. Eng. B* **1993**, *17* (1–3), 104–107.
- (121) Banaszak Holl, M. M.; Seidler, P. F.; Kowalczyk, S. P.; McFeely, F. R. Surface Reactivity of Alkylgold(I) Complexes: Substrate-Selective Chemical Vapor Deposition of Gold from RAuP(CH<sub>3</sub>)<sub>3</sub> (R = CH<sub>2</sub>CH<sub>3</sub>, CH<sub>3</sub>) at Remarkably Low Temperatures. *Inorg. Chem.* **1994**, *33* (3),

510–517.

- (122) Kandeepan, S.; Paquette, J. A.; Gilroy, J. B.; Mittler, S. OMCVD Gold Nanoparticles Covalently Attached to Polystyrene for Biosensing Applications. *Chem. Vap. Depos.* **2015**, 21 (10), 275–280.
- (123) Griffiths, M. B. E.; Dubrawski, Z. S.; Baćić, G.; Japahuge, A.; Masuda, J. D.; Zeng, T.; Barry, S. T. Controlling the Thermal Stability and Volatility of Organogold(I) Compounds for Vapor Deposition with Complementary Ligand Design. *Eur. J. Inorg. Chem.* **2019**, 2019 (46), 4927–4938.
- (124) Allen, D. W.; Haigh, J. The Structure of Very Thin Gold Layers Produced by Metalorganic Chemical Vapour Deposition. *Appl. Organomet. Chem.* **1995**, 9 (1), 83–88.
- (125) Banaszak Holl, M. M.; Seidler, P. F.; Kowalczyk, S. P.; McFeely, F. R. Low-temperature Selective-area Deposition of Metals: Chemical Vapor Deposition of Gold from Ethyl(Trimethylphosphine)Gold(I). *Appl. Phys. Lett.* **1993**, 62 (13), 1475–1477.
- (126) Kouvetsakis, J.; SharmA, R.; Ramakrisna, B. L.; Drucker, J.; Seidler, P. Electron Beam Assisted Chemical Vapor Deposition of Gold in an Environmental Tem. *MRS Proc.* **1995**, 388, 323.
- (127) Puddephatt, R. J.; Treurnicht, I. Volatile Organogold Compounds [AuR(CNR1)]: Their Potential for Chemical Vapour Deposition of Gold. *J. Organomet. Chem.* **1987**, 319 (1), 129–137.
- (128) Puddephatt, R. J.; Treurnicht, I. Method of Gold Deposition Using Volatile Organogold Complexes. 4,714,627, 1987.
- (129) Dryden, N. H.; Shapter, J. G.; Coatsworth, L. L.; Norton, P. R.; Puddephatt, R. J. [CF<sub>3</sub>Au(C.Tpbond.NMe)] as a Precursor for CVD of Gold. *Chem. Mater.* **1992**, 4 (5), 979–981.
- (130) Kadri, A. Fluorination Stability and Potential Carbene Surface Passivation of Gold Precursors for Atomic Layer Deposition, Carleton University, 2020.
- (131) Blaya, M.; Bautista, D.; Gil-Rubio, J.; Vicente, J. Synthesis of Au(I) Trifluoromethyl Complexes. Oxidation to Au(III) and Reductive Elimination of Halotrifluoromethanes. *Organometallics* **2014**, 33 (22), 6358–6368.
- (132) Menjón, A. B.; Pérez-bitrián, A.; Baya, M.; María, J.; Falvello, L. R.; Martín, A.; Pérez-bitrián, A.; Baya, M.; Casas, J. M.; Falvello, L. R.; et al. ( CF 3 ) 3 Au as a Highly Acidic Organogold ( III ) Fragment. No. iii.
- (133) Sosnovskikh, V. Y.; Mel'nikov, M. Y.; Zaitsev, A. V.; Bogdanov, E. A. Synthesis and Reactions of 2-Hydroxy-5,5-Dimethyl- and 2-Hydroxy-5,5-Pentamethylene-2-Trifluoromethyltetrahydro-4-Pyanones WithN-Nucleophiles. *Russ. Chem. Bull.* **1998**, 47 (6), 1170–1174.
- (134) King, S.; Massicot, J.; McDonagh, A. A Straightforward Route to Tetrachloroauric Acid from Gold Metal and Molecular Chlorine for Nanoparticle Synthesis. *Metals (Basel)*. **2015**, 5 (3), 1454–1461.
- (135) Blaya, M.; Bautista, D.; Gil-Rubio, J.; Vicente, J. Synthesis of Au(I) Trifluoromethyl Complexes. Oxidation to Au(III) and Reductive Elimination of Halotrifluoromethanes. *Organometallics* **2014**, 33 (22), 6358–6368.
- (136) Sun, T.; Zhang, Y. S.; Pang, B.; Hyun, D. C.; Yang, M.; Xia, Y. Engineered Nanoparticles for Drug Delivery in Cancer Therapy. *Angew. Chemie, Int. Ed.* **2014**, 53 (46), 12320–12364.
- (137) Dykman, L.; Khlebtsov, N. Gold Nanoparticles in Biomedical Applications: Recent Advances and Perspectives. *Chem. Soc. Rev.* **2012**, 41 (6), 2256–2282.
- (138) Chen, L.; Wu, B.; Guo, L.; Tey, R.; Huang, Y.; Kim, D.-H. A Single-Nanoparticle NO 2 Gas Sensor Constructed Using Active Molecular Plasmonics. *Chem. Commun.* **2015**, 51 (7), 1326–1329.
- (139) Liu, N.; Tang, M. L.; Hentschel, M.; Giessen, H.; Alivisatos, A. P. Nanoantenna-Enhanced Gas Sensing in a Single Tailored Nanofocus. *Nat. Mater.* **2011**, 10 (8), 631–636.

- (140) Peeters, D.; Barreca, D.; Carraro, G.; Comini, E.; Gasparotto, A.; Maccato, C.; Sada, C.; Sberveglieri, G. Au/ $\epsilon$ -Fe 2 O 3 Nanocomposites as Selective NO 2 Gas Sensors. *J. Phys. Chem. C* **2014**, *118* (22), 11813–11819.
- (141) Korotcenkov, G.; Brinzari, V.; Cho, B. K. What Restricts Gold Clusters Reactivity in Catalysis and Gas Sensing Effects: A Focused Review. *Mater. Lett.* **2015**, *147*, 101–104.
- (142) Corma, A.; Garcia, H. Supported Gold Nanoparticles as Catalysts for Organic Reactions. *Chem. Soc. Rev.* **2008**, *37* (9), 2096–2126.
- (143) Haruta, M. Size- and Support-Dependency in the Catalysis of Gold. *Catal. Today* **1997**, *36* (1), 153–166.
- (144) Novo, C.; Funston, A. M.; Mulvaney, P. Direct Observation of Chemical Reactions on Single Gold Nanocrystals Using Surface Plasmon Spectroscopy. *Nat. Nanotechnol.* **2008**, *3* (10), 598–602.
- (145) Wang, P.; Huang, B.; Dai, Y.; Whangbo, M.-H. Plasmonic Photocatalysts: Harvesting Visible Light with Noble Metal Nanoparticles. *Phys. Chem. Chem. Phys.* **2012**, *14* (28), 9813–9825.
- (146) Hou, W.; Cronin, S. B. A Review of Surface Plasmon Resonance-Enhanced Photocatalysis. *Adv. Funct. Mater.* **2013**, *23* (13), 1612–1619.
- (147) Zhang, X.; Liu, Y.; Lee, S.-T.; Yang, S.; Kang, Z. Coupling Surface Plasmon Resonance of Gold Nanoparticles with Slow-Photon-Effect of TiO<sub>2</sub> Photonic Crystals for Synergistically Enhanced Photoelectrochemical Water Splitting. *Energy Environ. Sci.* **2014**, *7* (4), 1409.
- (148) Sau, T. K.; Rogach, A. L.; Jaeckel, F.; Klar, T. A.; Feldmann, J. Properties and Applications of Colloidal Nonspherical Noble Metal Nanoparticles. *Adv. Mater. (Weinheim, Ger.)* **2010**, *22* (16), 1805–1825.
- (149) Sau, T. K.; Rogach, A. L. Nonspherical Noble Metal Nanoparticles: Colloid-Chemical Synthesis and Morphology Control. *Adv. Mater. (Weinheim, Ger.)* **2010**, *22* (16), 1781–1804.
- (150) Xia, Y.; Xiong, Y.; Lim, B.; Skrabalak, S. E. Shape-Controlled Synthesis of Metal Nanocrystals: Simple Chemistry Meets Complex Physics?. *Angew. Chemie, Int. Ed.* **2009**, *48* (1), 60–103.
- (151) Chiu, C.-Y.; Chung, P.-J.; Lao, K.-U.; Liao, C.-W.; Huang, M. H. Facet-Dependent Catalytic Activity of Gold Nanocubes, Octahedra, and Rhombic Dodecahedra toward 4-Nitroaniline Reduction. *J. Phys. Chem. C* **2012**, *116* (44), 23757–23763.
- (152) Halperin, W. P. Quantum Size Effects in Metal Particles. *Rev. Mod. Phys.* **1986**, *58* (3), 533–606.
- (153) Vigderman, L.; Khanal, B. P.; Zubarev, E. R. Functional Gold Nanorods: Synthesis, Self-Assembly, and Sensing Applications. *Adv. Mater. (Weinheim, Ger.)* **2012**, *24* (36), 4811–4841.
- (154) Xia, X.; Rycenga, M.; Qin, D.; Xia, Y. A Silver Nanocube on a Gold Microplate as a Well-Defined and Highly Active Substrate for SERS Detection. *J. Mater. Chem. C Mater. Opt. Electron. Devices* **2013**, *1* (38), 6145–6150.
- (155) Ren, B.; Picardi, G.; Pettinger, B.; Schuster, R.; Ertl, G. Tip-Enhanced Raman Spectroscopy of Benzenethiol Adsorbed on Au and Pt Single-Crystal Surfaces. *Angew. Chemie, Int. Ed.* **2005**, *44* (1), 139–142.
- (156) Hampden-Smith, M. J.; Kodas, T. T. Chemical Vapor Deposition of Metals. Part 1. An Overview of CVD Processes. *Chem. Vap. Depos.* **1995**, *1* (1), 8–23.
- (157) Kang, K.; Kim, C.-J.; Jo, M.-H. Unconventional Roles of Metal Catalysts in Chemical-Vapor Syntheses of Single-Crystalline Nanowires. *J. Appl. Phys.* **2009**, *105* (12), 122407/1–122407/5.
- (158) Benson, J.; Boukhalfa, S.; Magasinski, A.; Kvit, A.; Yushin, G. Chemical Vapor Deposition of Aluminum Nanowires on Metal Substrates for Electrical Energy Storage Applications. *ACS Nano*

2012, 6 (1), 118–125.

- (159) Kodambaka, S.; Tersoff, J.; Reuter, M. C.; Ross, F. M. Germanium Nanowire Growth below the Eutectic Temperature. *Science* **2007**, 316 (5825), 729–732.
- (160) Chen, Y.; Zhang, Y.; Hu, Y.; Kang, L.; Zhang, S.; Xie, H.; Liu, D.; Zhao, Q.; Li, Q.; Zhang, J. State of the Art of Single-Walled Carbon Nanotube Synthesis on Surfaces. *Adv. Mater. (Weinheim, Ger.)* **2014**, 26 (34), 5898–5922.
- (161) Zhou, W.; Han, Z.; Wang, J.; Zhang, Y.; Jin, Z.; Sun, X.; Zhang, Y.; Yan, C.; Li, Y. Copper Catalyzing Growth of Single-Walled Carbon Nanotubes on Substrates. *Nano Lett.* **2006**, 6 (12), 2987–2990.
- (162) Ding, Y.; Gao, P. X.; Wang, Z. L. Catalyst-Nanostructure Interfacial Lattice Mismatch in Determining the Shape of VLS Grown Nanowires and Nanobelts: A Case of Sn/ZnO. *J. Am. Chem. Soc.* **2004**, 126 (7), 2066–2072.
- (163) Woo, R. L.; Gao, L.; Goel, N.; Hudait, M. K.; Wang, K. L.; Kodambaka, S.; Hicks, R. F. Kinetic Control of Self-Catalyzed Indium Phosphide Nanowires, Nanocones, and Nanopillars. *Nano Lett.* **2009**, 9 (6), 2207–2211.
- (164) Yan, C.; Singh, N.; Lee, P. S. Kinking-Induced Structural Evolution of Metal Oxide Nanowires into Single-Crystalline Nanorings. *ACS Nano* **2010**, 4 (9), 5350–5356.
- (165) Kim, J. W.; Manna, S.; Dietze, S. H.; Ulvestad, A.; Harder, R.; Fohtung, E.; Fullerton, E. E.; Shpyrko, O. G. Curvature-Induced and Thermal Strain in Polyhedral Gold Nanocrystals. *Appl. Phys. Lett.* **2014**, 105 (17), 1–6.
- (166) Chen, Y.; Tian, X.; Zeng, W.; Zhu, X.; Hu, H.; Duan, H. Vapor-Phase Preparation of Gold Nanocrystals by Chloroauric Acid Pyrolysis. *J. Colloid Interface Sci.* **2015**, 439, 21–27.
- (167) Ertorer, E.; Avery, J. C.; Pavelka, L. C.; Mittler, S. Surface-Immobilized Gold Nanoparticles by Organometallic CVD on Amine-Terminated Glass Surfaces. *Chem. Vap. Depos.* **2013**, 19 (10-11-12), 338–346.
- (168) Jen Cho, S.; Suri, A.; Mei, X.; Ouyang, J. In Situ Deposition of Gold Nanostructures with Well-Defined Shapes on Unfunctionalized Reduced Graphene Oxide through Chemical Reduction of a Dry Gold Precursor with Ethylene Glycol Vapor. *RSC Adv.* **2013**, 3 (4), 1201–1209.
- (169) Miikkulainen, V.; Leskela, M.; Ritala, M.; Puurunen, R. L. Crystallinity of Inorganic Films Grown by Atomic Layer Deposition: Overview and General Trends. *J. Appl. Phys. (Melville, NY, United States)* **2013**, 113 (2), 021301/1–021301/101.
- (170) Zhukhovitskiy, A. V.; Mavros, M. G.; Van Voorhis, T.; Johnson, J. A. Addressable Carbene Anchors for Gold Surfaces. *J. Am. Chem. Soc.* **2013**, 135 (20), 7418–7421.
- (171) Hopkinson, M. N.; Richter, C.; Schedler, M.; Glorius, F. An Overview of N-Heterocyclic Carbenes. *Nat. (London, United Kingdom)* **2014**, 510 (7506), 485–496.
- (172) Ling, X.; Roland, S.; Pilani, M.-P. Supracrystals of N-Heterocyclic Carbene-Coated Au Nanocrystals. *Chem. Mater.* **2015**, 27 (2), 414–423.
- (173) Jewell, A. D.; Sykes, E. C. H.; Kyriakou, G. Molecular-Scale Surface Chemistry of a Common Metal Nanoparticle Capping Agent: Triphenylphosphine on Au(111). *ACS Nano* **2012**, 6 (4), 3545–3552.
- (174) Schmid, G. The Relevance of Shape and Size of Au55 Clusters. *Chem. Soc. Rev.* **2008**, 37 (9), 1909–1930.
- (175) Woehrle, G. H.; Brown, L. O.; Hutchison, J. E. Thiol-Functionalized, 1.5-Nm Gold Nanoparticles through Ligand Exchange Reactions: Scope and Mechanism of Ligand Exchange. *J. Am. Chem.*

*Soc.* **2005**, *127* (7), 2172–2183.

- (176) Coates, G. E.; Parkin, C. Tertiary Phosphine Complexes of Trimethylgold: Infrared Spectra of Complexes of Gold and Some Other Metals. *J. Chem. Soc.* **1963**, 421–429.
- (177) Banaszak Holl, M. M.; Seidler, P. F.; Kowalczyk, S. P.; McFeely, F. R. Surface Reactivity of Alkylgold(I) Complexes: Substrate-Selective Chemical Vapor Deposition of Gold from RAuP(CH<sub>3</sub>)<sub>3</sub> (R = CH<sub>2</sub>CH<sub>3</sub>, CH<sub>3</sub>) at Remarkably Low Temperatures. *Inorg. Chem.* **1994**, *33* (3), 510–517.
- (178) Marion, N.; Nolan, S. P. N-Heterocyclic Carbenes in Gold Catalysis. *Chem. Soc. Rev.* **2008**, *37* (9), 1776–1782.
- (179) Cradden, C. M.; Horton, J. H.; Ebralidze, I. I.; Zenkina, O. V.; McLean, A. B.; Drevniok, B.; She, Z.; Kraatz, H.-B.; Mosey, N. J.; Seki, T.; et al. Ultra Stable Self-Assembled Monolayers of N-Heterocyclic Carbenes on Gold. *Nat. Chem.* **2014**, *6* (5), 409–414.
- (180) Schmidbaur, H.; Shiotani, A. Organosilicon Compounds Containing Monovalent Gold. *J. Am. Chem. Soc.* **1970**, *92* (23), 7003–7004.
- (181) Coyle, J. P.; Dey, G.; Sirianni, E. R.; Kemell, M. L.; Yap, G. P. A.; Ritala, M.; Leskela, M.; Elliott, S. D.; Barry, S. T. Deposition of Copper by Plasma-Enhanced Atomic Layer Deposition Using a Novel N-Heterocyclic Carbene Precursor. *Chem. Mater.* **2013**, *25* (7), 1132–1138.
- (182) Bunge, S. D.; Just, O.; Rees Jr., W. S. [{Au[μ-N(SiMe<sub>3</sub>)<sub>2</sub>]})<sub>4</sub>]: The First Base-Free Gold Amide. *Angew. Chemie, Int. Ed.* **2000**, *39* (17), 3082–3084.
- (183) Kunte, G. V.; Shivashankar, S. A.; Umarji, A. M. Thermogravimetric Evaluation of the Suitability of Precursors for MOCVD. *Meas. Sci. Technol.* **2008**, *19* (2), 025704/1–025704/7.
- (184) Coyle, J. P.; Gordon, P. G.; Wells, A. P.; Mandia, D. J.; Sirianni, E. R.; Yap, G. P. A.; Barry, S. T. Thermally Robust Gold and Silver Iminopyrrolidinates for Chemical Vapor Deposition of Metal Films. *Chem. Mater.* **2013**, *25* (22), 4566–4573.
- (185) Colominas, C.; Lau, K. H.; Hildenbrand, D. L.; Crouch-Baker, S.; Sanjurjo, A. Vapor Pressures of the Copper and Yttrium β-Diketonate MOCVD Precursors. *J. Chem. Eng. Data* **2001**, *46* (2), 446–450.
- (186) Zhou, W.; Mandia, D. J.; Griffiths, M. B. E.; Bialiayeu, A.; Zhang, Y.; Gordon, P. G.; Barry, S. T.; Albert, J. Polarization-Dependent Properties of the Cladding Modes of a Single Mode Fiber Covered with Gold Nanoparticles. *Opt. Express* **2013**, *21* (1), 245–255.
- (187) Lofton, C.; Sigmund, W. Mechanisms Controlling Crystal Habits of Gold and Silver Colloids. *Adv. Funct. Mater.* **2005**, *15* (7), 1197–1208.
- (188) Li, C.; Cai, W.; Cao, B.; Sun, F.; Li, Y.; Kan, C.; Zhang, L. Mass Synthesis of Large, Single-Crystal Au Nanosheets Based on a Polyol Process. *Adv. Funct. Mater.* **2006**, *16* (1), 83–90.
- (189) Kim, C.; Gu, W.; Briceno, M.; Robertson, I. M.; Choi, H.; Kim, K. Copper Nanowires with a Five-Twinned Structure Grown by Chemical Vapor Deposition. *Adv. Mater. (Weinheim, Ger.)* **2008**, *20* (10), 1859–1863.
- (190) Haukka, S.; Root, A. The Reaction of Hexamethyldisilazane and Subsequent Oxidation of Trimethylsilyl Groups on Silica Studied by Solid-State NMR and FTIR. *J. Phys. Chem.* **1994**, *98* (6), 1695–1703.
- (191) Gajan, D.; Guillois, K.; Delichere, P.; Basset, J.-M.; Candy, J.-P.; Caps, V.; Coperet, C.; Lesage, A.; Emsley, L. Gold Nanoparticles Supported on Passivated Silica: Access to an Efficient Aerobic Epoxidation Catalyst and the Intrinsic Oxidation Activity of Gold. *J. Am. Chem. Soc.* **2009**, *131* (41), 14667–14669.

- (192) Choi, H.; Kim, K. Metallic Nanostructures. US20080206555A1, August 28, 2008.
- (193) Bittermann, A.; Baskakov, D.; Herrmann, W. A. Carbene Complexes Made Easily: Decomposition of Reissert Compounds and Further Synthetic Approaches. *Organometallics* **2009**, *28* (17), 5107–5111.
- (194) Uson, R.; Laguna, A.; Laguna, M. (Tetrahydrothiophene)Gold(I) or Gold(III) Complexes. *Inorg. Synth.* **1989**, *26*, 85–91.
- (195) Lappert, M. F.; Slade, M. J.; Singh, A.; Atwood, J. L.; Rogers, R. D.; Shakir, R. Structure and Reactivity of Sterically Hindered Lithium Amides and Their Diethyl Etherates: Crystal and Molecular Structures of  $[\text{Li}\{\text{N}(\text{SiMe}_3)_2\}\{\text{OEt}_2\}]_2$  and Tetrakis(2,2,6,6-Tetramethylpiperidinololithium). *J. Am. Chem. Soc.* **1983**, *105* (2), 302–304.
- (196) Stratakis, M.; Garcia, H. Catalysis by Supported Gold Nanoparticles: Beyond Aerobic Oxidative Processes. *Chem. Rev.* **2012**, *112* (8), 4469–4506.
- (197) M. George, S. Atomic Layer Deposition: An Overview. *Chem. Rev.* **2009**, *110* (1), 111–131.
- (198) Louis, C.; Pluchery, O. *Gold Nanoparticles for Physics, Chemistry and Biology*; IMPERIAL COLLEGE PRESS, 2012.
- (199) Miikkulainen, V.; Leskelä, M.; Ritala, M.; Puurunen, R. L. Crystallinity of Inorganic Films Grown by Atomic Layer Deposition: Overview and General Trends. *J. Appl. Phys.* **2013**, *113* (2), 021301.
- (200) Gordon, P. G.; Kurek, A.; Barry, S. T. Trends in Copper Precursor Development for CVD and ALD Applications. *ECS J. Solid State Sci. Technol.* **2015**, *4* (1), N3188–N3197.
- (201) Niskanen, A.; Hatanpää, T.; Arstila, K.; Leskelä, M.; Ritala, M. Radical-Enhanced Atomic Layer Deposition of Silver Thin Films Using Phosphine-Adducted Silver Carboxylates. *Chem. Vap. Depos.* **2007**, *13* (8), 408–413.
- (202) Chalker, P. R.; Romani, S.; Marshall, P. A.; Rosseinsky, M. J.; Rushworth, S.; Williams, P. A. Liquid Injection Atomic Layer Deposition of Silver Nanoparticles. *Nanotechnology* **2010**, *21* (40), 405602.
- (203) Kariniemi, M.; Niinistö, J.; Hatanpää, T.; Kemell, M.; Sajavaara, T.; Ritala, M.; Leskelä, M. Plasma-Enhanced Atomic Layer Deposition of Silver Thin Films. *Chem. Mater.* **2011**, *23* (11), 2901–2907.
- (204) Messelhäuser, J.; Flint, E. B.; Suhr, H. Direct Writing of Gold Lines by Laser-Induced Chemical Vapor Deposition. *Appl. Phys. A Solids Surfaces* **1992**, *55* (2), 196–202.
- (205) Kunte, G. V; Shivashankar, S. A.; Umarji, A. M. Thermogravimetric Evaluation of the Suitability of Precursors for MOCVD. *Meas. Sci. Technol.* **2008**, *19* (2), 025704.
- (206) Hämäläinen, J.; Ritala, M.; Leskelä, M. Atomic Layer Deposition of Noble Metals and Their Oxides. *Chem. Mater.* **2014**, *26* (1), 786–801.
- (207) Krozer, A.; Rodahl, M. X-Ray Photoemission Spectroscopy Study of UV/Ozone Oxidation of Au under Ultrahigh Vacuum Conditions. *J. Vac. Sci. Technol. A Vacuum, Surfaces, Film.* **1997**, *15* (3), 1704–1709.
- (208) Waldo, R. A. *Microbeam Analysis*; Newbury, D. E., Ed.; San Francisco Press: San Francisco, CA, 1988.
- (209) Wyckoff, R. W. G. *Crystal Structures*; Interscience Publishers: New York, NY, 1963.
- (210) Wang, X.; Andrews, L. Infrared Spectra and Structures of the Coinage Metal Dihydroxide Molecules. *Inorg. Chem.* **2005**, *44* (24), 9076–9083.
- (211) Van Daele, M.; Detavernier, C.; Dendooven, J. Surface Species during ALD of Platinum Observed with in Situ Reflection IR Spectroscopy. *Phys. Chem. Chem. Phys.* **2018**, *20* (39), 25343–25356.

- (212) Shaw, C. F.; Tobias, R. S. Bonding in Methygold(I) and Trimethygold(III) Compounds. Nuclear Magnetic Resonance, Raman, and Infrared Spectra and Normal Coordinates. *Inorg. Chem.* **1973**, *12* (5), 965–978.
- (213) McKean, D. C.; McQuillan, G. P.; Murphy, W. F.; Zerbetto, F. Vibrational Spectrum and Harmonic Force Field of Trimethylphosphine. *J. Phys. Chem.* **1990**, *94* (12), 4820–4831.
- (214) Cho, H.-G.; Andrews, L. Infrared Spectra of CH<sub>3</sub>–MX and CH<sub>2</sub>X–MH Prepared in Reactions of Laser-Ablated Gold, Platinum, Palladium, and Nickel Atoms with CH<sub>3</sub>Cl and CH<sub>3</sub>Br. *Organometallics* **2013**, *32* (9), 2753–2759.
- (215) Daasch, L. W.; Smith, D. C. The Infrared and Raman Spectra of Trimethylphosphine Oxide. *J. Chem. Phys.* **1951**, *19* (1), 22–25.
- (216) Jensen, J. O.; Banerjee, A.; Zeroka, D.; Merrow, C. N.; Gilliam, S. J.; Kirkby, S. J. A Theoretical Study of P<sub>4</sub>O<sub>10</sub>: Vibrational Analysis, Infrared and Raman Spectra. *Spectrochim. Acta Part A Mol. Biomol. Spectrosc.* **2004**, *60* (8–9), 1947–1955.
- (217) Mielke, Z.; Andrews, L. Infrared Spectra of Phosphorus Oxides (P<sub>4</sub>O<sub>6</sub>, P<sub>4</sub>O<sub>7</sub>, P<sub>4</sub>O<sub>8</sub>, P<sub>4</sub>O<sub>9</sub> and P<sub>4</sub>O<sub>10</sub>) in Solid Argon. *J. Phys. Chem.* **1989**, *93* (8), 2971–2976.
- (218) Hashmi, A. S. K.; Hutchings, G. J. Gold Catalysis. *Angew. Chemie Int. Ed.* **2006**, *45* (47), 7896–7936.
- (219) Willets, K. A.; Van Duyne, R. P. Localized Surface Plasmon Resonance Spectroscopy and Sensing. *Annu. Rev. Phys. Chem.* **2007**, *58* (1), 267–297.
- (220) Mayer, K. M.; Hafner, J. H. Localized Surface Plasmon Resonance Sensors. *Chem. Rev.* **2011**, *111* (6), 3828–3857.
- (221) Hampden-Smith, M. J.; Kodas, T. T. Chemical Vapor Deposition of Metals: Part 1. An Overview of CVD Processes. *Chem. Vap. Depos.* **1995**, *1* (1), 8–23.
- (222) Baum, T. H.; Jones, C. R. Laser Chemical Vapor Deposition of Gold. *Appl. Phys. Lett.* **1985**, *47* (5), 538–540.
- (223) Mäkelä, M.; Hatanpää, T.; Ritala, M.; Leskelä, M.; Mizohata, K.; Meinander, K.; Räisänen, J. Potential Gold(I) Precursors Evaluated for Atomic Layer Deposition. *J. Vac. Sci. Technol. A Vacuum, Surfaces, Film.* **2017**, *35* (1), 01B112.
- (224) Mäkelä, M.; Hatanpää, T.; Mizohata, K.; Räisänen, J.; Ritala, M.; Leskelä, M. Thermal Atomic Layer Deposition of Continuous and Highly Conducting Gold Thin Films. *Chem. Mater.* **2017**, *29* (14), 6130–6136.
- (225) Banaszak Holl, M. M.; Seidler, P. F.; Kowalczyk, S. P.; McFeely, F. R. Surface Reactivity of Alkylgold(I) Complexes: Substrate-Selective Chemical Vapor Deposition of Gold from RAuP(CH<sub>3</sub>)<sub>3</sub> (R = CH<sub>2</sub>CH<sub>3</sub>, CH<sub>3</sub>) at Remarkably Low Temperatures. *Inorg. Chem.* **1994**, *33* (3), 510–517.
- (226) Komiya, S.; Albright, T. A.; Hoffmann, R.; Kochi, J. K. Reductive Elimination and Isomerization of Organogold Complexes. Theoretical Studies of Trialkylgold Species as Reactive Intermediates. *J. Am. Chem. Soc.* **1976**, *98* (23), 7255–7265.
- (227) Komiya, S.; Kochi, J. K. Electrophilic Cleavage of Organogold Complexes with Acids. The Mechanism of the Reductive Elimination of Dialkyl(Aniono)Gold(III) Species. *J. Am. Chem. Soc.* **1976**, *98* (24), 7599–7607.
- (228) Tamaki, A.; Kochi, J. K. Formation and Decomposition of Alkyl-Gold(I) Complexes. *J. Organomet. Chem.* **1973**, *61*, 441–450.
- (229) Jubber, M.; Wilson, J. I. B.; Davidson, J. L.; Fernie, P. A.; John, P. Laser Writing of High-purity

Gold Lines. *Appl. Phys. Lett.* **1989**, *55* (14), 1477–1479.

- (230) Gong, S.; Schwalb, W.; Wang, Y.; Chen, Y.; Tang, Y.; Si, J.; Shirinzadeh, B.; Cheng, W. A Wearable and Highly Sensitive Pressure Sensor with Ultrathin Gold Nanowires. *Nat. Commun.* **2014**, *5* (1), 3132.
- (231) Fateixa, S.; Pinheiro, P. C.; Nogueira, H. I. S.; Trindade, T. Gold Loaded Textile Fibres as Substrates for SERS Detection. *J. Mol. Struct.* **2019**, *1185*, 333–340.
- (232) Wang, X.; Andrews, L. Infrared Spectra and DFT Calculations for the Gold Hydrides AuH, (H<sub>2</sub>)AuH, and the AuH<sub>3</sub> Transition State Stabilized in (H<sub>2</sub>)AuH 3. *J. Phys. Chem. A* **2002**, *106* (15), 3744–3748.
- (233) Stobiński, L.; Duś, R. Molecular Hydrogen Chemisorption on Thin Unsintered Gold Films Deposited at Low Temperature. *Surf. Sci.* **1993**, *298* (1), 101–106.
- (234) Paul, A. M.; Bent, B. E. Alkyl Coupling on Copper, Silver, and Gold: Correlation Between the Coupling Rate and the Metal-Alkyl Bond Strength. *J. Catal.* **1994**, *147* (1), 264–271.
- (235) Paul, A.; Yang, M. X.; Bent, B. E. Disproportionation and Coupling Reactions of Alkyl Iodides on a Au(111) Surface. *Surf. Sci.* **1993**, *297* (3), 327–344.
- (236) Kariis, H.; Westermark, G.; Persson, I.; Liedberg, B. Infrared Spectroscopic and Temperature-Programmed Desorption Studies of Dimethylphenylphosphine Adsorbed on the Coinage Metals. *Langmuir* **1998**, *14* (10), 2736–2743.
- (237) Jewell, A. D.; Tierney, H. L.; Sykes, E. C. H. Gently Lifting Gold's Herringbone Reconstruction: Trimethylphosphine on Au(111). *Phys. Rev. B* **2010**, *82* (20), 205401.
- (238) Westermark, G.; Kariis, H.; Persson, I.; Liedberg, B. An Infrared Study on the Chemisorption of Tertiary Phosphines on Coinage and Platinum Group Metal Surfaces. *Colloids Surfaces A Physicochem. Eng. Asp.* **1999**, *150* (1–3), 31–43.
- (239) Onyiriuka, E. C. Zinc Phosphate Glass Surfaces Studied by XPS. *J. Non. Cryst. Solids* **1993**, *163* (3), 268–273.
- (240) Edmonds, M. T.; Tadich, A.; Carvalho, A.; Ziletti, A.; O'Donnell, K. M.; Koenig, S. P.; Coker, D. F.; Özyilmaz, B.; Neto, A. H. C.; Fuhrer, M. S. Creating a Stable Oxide at the Surface of Black Phosphorus. *ACS Appl. Mater. Interfaces* **2015**, *7* (27), 14557–14562.
- (241) Levrau, E.; Van de Kerckhove, K.; Devloo-Casier, K.; Pulinthanathu Sree, S.; Martens, J. A.; Detavernier, C.; Dendooven, J. In Situ IR Spectroscopic Investigation of Alumina ALD on Porous Silica Films: Thermal versus Plasma-Enhanced ALD. *J. Phys. Chem. C* **2014**, *118* (51), 29854–29859.
- (242) Minjauw, M. M.; Rijckaert, H.; Driessche, I. Van; Detavernier, C.; Dendooven, J. Nucleation Enhancement and Area-Selective Atomic Layer Deposition of Ruthenium Using RuO<sub>4</sub> and H<sub>2</sub> Gas. *Chem. Mater.* **2019**, *31* (5), 1491–1499.
- (243) Griffiths, M. B. E.; Pallister, P. J.; Mandia, D. J.; Barry, S. T. Atomic Layer Deposition of Gold Metal. *Chem. Mater.* **2016**, *28* (1), 44–46.
- (244) Profijt, H. B.; Potts, S. E.; van de Sanden, M. C. M.; Kessels, W. M. M. Plasma-Assisted Atomic Layer Deposition: Basics, Opportunities, and Challenges. *J. Vac. Sci. Technol. A Vacuum, Surfaces, Film.* **2011**, *29* (5), 050801.
- (245) Knoops, H. C. M.; Elam, J. W.; Libera, J. A.; Kessels, W. M. M. Surface Loss in Ozone-Based Atomic Layer Deposition Processes. *Chem. Mater.* **2011**, *23* (9), 2381–2387.
- (246) Messelhäuser, J.; Flint, E. B.; Suhr, H. Laser Induced CVD of Gold Using New Precursors. *Appl. Surf. Sci.* **1992**, *54*, 64–68.

- (247) Bernal Ramos, K.; Saly, M. J.; Chabal, Y. J. Precursor Design and Reaction Mechanisms for the Atomic Layer Deposition of Metal Films. *Coord. Chem. Rev.* **2013**, *257* (23–24), 3271–3281.
- (248) Gordon, P. G.; Kurek, A.; Barry, S. T. Trends in Copper Precursor Development for CVD and ALD Applications. *ECS J. Solid State Sci. Technol.* **2014**, *4* (1), N3188–N3197.
- (249) Tamaki, A.; Kochi, J. K. Formation and Decomposition of Alkyl-Gold(I) Complexes. *J. Organomet. Chem.* **1973**, *61*, 441–450.
- (250) Jansen, F.; Kruck, T. Promising New Precursors for the CVD of Gold. *Adv. Mater.* **1995**, *7* (3), 297–300.
- (251) Price, J. S.; Chadha, P.; Emslie, D. J. H. Base-Free and Bisphosphine Ligand Dialkylmanganese(II) Complexes as Precursors for Manganese Metal Deposition. *Organometallics* **2016**, *35* (2), 168–180.
- (252) Vaughan, L. G.; Sheppard, W. A. Organogold Chemistry II. Tris(Pentafluorophenyl)Gold(III). *J. Organomet. Chem.* **1970**, *22* (3), 739–742.
- (253) Usón, R.; Laguna, A.; Laguna, M.; Usón, A. A New Route for the Synthesis of Gold(I) and Gold(II) Pentafluorophenyl(Ylide) Complexes. *Inorganica Chim. Acta* **1983**, *73* (C), 63–66.
- (254) Schmidbaur, H.; Franke, R. Organogold-Chemie, XV. Gold(I)-Verbindungen Einfacher Phosphor-Ylide. *Chem. Ber.* **1975**, *108* (4), 1321–1328.
- (255) Coyle, J. P.; Dey, G.; Sirianni, E. R.; Kemell, M. L.; Yap, G. P. A.; Ritala, M.; Leskelä, M.; Elliott, S. D.; Barry, S. T. Deposition of Copper by Plasma-Enhanced Atomic Layer Deposition Using a Novel N-Heterocyclic Carbene Precursor. *Chem. Mater.* **2013**, *25* (7), 1132–1138.
- (256) Coyle, J. P.; Sirianni, E. R.; Korobkov, I.; Yap, G. P. A.; Dey, G.; Barry, S. T. Study of Monomeric Copper Complexes Supported by N - Heterocyclic and Acyclic Diamino Carbenes. *Organometallics* **2017**, *35*, 2800–2810.
- (257) Griffiths, M. B. E.; Koponen, S. E.; Mandia, D. J.; McLeod, J. F.; Coyle, J. P.; Sims, J. J.; Giorgi, J. B.; Sirianni, E. R.; Yap, G. P. A.; Barry, S. T. Surfactant Directed Growth of Gold Metal Nanoplates by Chemical Vapor Deposition. *Chem. Mater.* **2015**, *27* (17), 6116–6124.
- (258) Boysen, N.; Hasselmann, T.; Karle, S.; Rogalla, D.; Theirich, D.; Winter, M.; Riedl, T.; Devi, A. An N-Heterocyclic Carbene Based Silver Precursor for Plasma-Enhanced Spatial Atomic Layer Deposition of Silver Thin Films at Atmospheric Pressure. *Angew. Chemie Int. Ed.* **2018**, *57* (49), 16224–16227.
- (259) Denk, M. K.; Thadani, A.; Hatano, K.; Lough, A. J. Steric Stabilization of Nucleophilic Carbenes. *Angew. Chemie Int. Ed. English* **1997**, *36* (23), 2607–2609.
- (260) Schmidbaur, H.; Franke, R. Phosphor-Ylide Als Bauelemente von Organogoldverbindungen. *Angew. Chemie* **1973**, *85* (10), 449–450.
- (261) Gaillard, S.; Nun, P.; Slawin, A. M. Z.; Nolan, S. P. Expedited Synthesis of [Au(NHC)(L)] + (NHC = N-Heterocyclic Carbene; L = Phosphine or NHC) Complexes. *Organometallics* **2010**, *29* (21), 5402–5408.
- (262) Battisti, A.; Bellina, O.; Diversi, P.; Losi, S.; Marchetti, F.; Zanello, P. Preparation, Structure and Reactivity of Polynuclear Gold(I) Phosphanyl Alkanethiolates. *Eur. J. Inorg. Chem.* **2007**, No. 6, 865–875.
- (263) Schmidbaur, H.; Raethlein, K. H. *Inorganic Syntheses, Volume 18*; 1978; Vol. 18.
- (264) Schmidbaur, H.; Franke, R. Organogold-Chemie, XV. Gold(I)-Verbindungen Einfacher Phosphor-Ylide. *Chem. Ber.* **1975**, *108* (4), 1321–1328.

- (265) Schmidbaur, H.; Franke, R. Phosphor-Ylide Als Bauelemente von Organogoldverbindungen. *Angew. Chemie* **1973**, *85* (10), 449–450.
- (266) López-de-Luzuriaga, J. M.; Monge, M.; Olmos, M. E.; Pascual, D.; Lasanta, T. Amalgamating at the Molecular Level. A Study of the Strong Closed-Shell Au(I)…Hg(II) Interaction. *Chem. Commun.* **2011**, *47* (24), 6795.
- (267) Arentsen, K.; Caddick, S.; Cloke, F. G. N. On the Efficiency of Two-Coordinate Palladium(0) N-Heterocyclic Carbene Complexes in Amination and Suzuki–Miyaura Reactions of Aryl Chlorides. *Tetrahedron* **2005**, *61* (41), 9710–9715.
- (268) Kooijman, H. *Interpretation of Crystal Structure Determinations*; 2005.
- (269) Ebsworth, E. A. V.; Fraser, T. E.; Rankin, D. W. H. The Molecular Structure of Trimethyl(Methylene)Phosphorane in the Gas Phase, Determined by Electron Diffraction. *Chem. Ber.* **1977**, *110* (11), 3494–3500.
- (270) Schmidbaur, H.; Schier, A. Auophilic Interactions as a Subject of Current Research: An up-Date. *Chem. Soc. Rev.* **2012**, *41* (1), 370–412.
- (271) Baker, R. W.; Pauling, P. J. Crystal Structure of (Pentafluorophenyl)(Triphenylphosphine)Gold(I). *J. Chem. Soc. Dalt. Trans.* **1972**, No. 20, 2264.
- (272) Carden, W. G.; Pedziwiatr, J.; Abboud, K. A.; McElwee-White, L. Halide Effects on the Sublimation Temperature of X-Au-L Complexes: Implications for Their Use as Precursors in Vapor Phase Deposition Methods. *ACS Appl. Mater. Interfaces* **2017**, *9* (46), 40998–41005.
- (273) Carden, W. G.; Thorman, R. M.; Unlu, I.; Abboud, K. A.; Fairbrother, D. H.; McElwee-White, L. Design, Synthesis, and Evaluation of CF<sub>3</sub> AuCNR Precursors for Focused Electron Beam-Induced Deposition of Gold. *ACS Appl. Mater. Interfaces* **2019**, *11*, 11976–11987.
- (274) Chai, J.-D.; Head-Gordon, M. Systematic Optimization of Long-Range Corrected Hybrid Density Functionals. *J. Chem. Phys.* **2008**, *128* (8), 084106.
- (275) Chai, J.-D.; Head-Gordon, M. Long-Range Corrected Hybrid Density Functionals with Damped Atom–Atom Dispersion Corrections. *Phys. Chem. Chem. Phys.* **2008**, *10* (44), 6615.
- (276) Lovallo, C. C.; Klobukowski, M. Development of New Pseudopotential Methods: Improved Model Core Potentials for the First-Row Transition Metals. *J. Comput. Chem.* **2003**, *24* (9), 1009–1015.
- (277) Zeng, T.; Klobukowski, M. New Model Core Potentials for Gold. *J. Chem. Phys.* **2009**, *130* (20), 204107.
- (278) Colominas, C.; Lau, K. H.; Hildenbrand, D. L.; Crouch-Baker, S.; Sanjurjo, A. Vapor Pressures of the Copper and Yttrium β-Diketonate MOCVD Precursors. *J. Chem. Eng. Data* **2001**, *46* (2), 446–450.
- (279) Uson, R.; Laguna, A.; Laguna, M.; Briggs, D. A.; Murray, H. H.; Fackler, J. P. (Tetrahydrothiophene)Gold(I) or Gold(III) Complexes. *Inorg. Synth.* **2007**, *26*, 85–91.
- (280) Schmidbaur, H. A Phosphorus Ylide and Some of Its Metal Complexes. Trimethylphosphonium Methylide (Trimethylmethylenephosphorane). *Inorg. Synth.* **1978**, *18*, 135–140.
- (281) Griffiths, M. B. E.; Pallister, P. J.; Mandia, D. J.; Barry, S. T. Atomic Layer Deposition of Gold Metal. *Chem. Mater.* **2016**, *28* (1), 44–46.
- (282) Barry, S.; Coyle, J. P.; Clark, T. J.; Hastie, J. J. M. Group 11 Mono-Metallic Precursor Compounds and Use Thereof in Metal Deposition. WO2012155264, 2011.
- (283) Leutkens, M. L. J.; Sattelberger, A. P.; Murray, H. H.; Basil, J. D.; Fackler, J. P. J. Trimethylphosphine. *Inorg. Synth.* **1990**, *28*, 305.

- (284) Miikkulainen, V.; Leskelä, M.; Ritala, M.; Puurunen, R. L. Crystallinity of Inorganic Films Grown by Atomic Layer Deposition: Overview and General Trends. *J. Appl. Phys.* **2013**, *113* (2).
- (285) Kolasinski, K. W. *Surface Science*; John Wiley & Sons, Ltd: Chichester, UK, 2012.
- (286) Riha, S. C.; Libera, J. A.; Elam, J. W.; Martinson, A. B. F. Design and Implementation of an Integral Wall-Mounted Quartz Crystal Microbalance for Atomic Layer Deposition. *Rev. Sci. Instrum.* **2012**, *83* (9).
- (287) Blanquart, T.; Niinistö, J.; Aslam, N.; Banerjee, M.; Tomczak, Y.; Gavagnin, M.; Longo, V.; Puukilainen, E.; Wanzenboeck, H. D.; Kessels, W. M. M.; et al. Zr(NEtMe<sub>2</sub>)<sub>2</sub>(Guan-NEtMe<sub>2</sub>)<sub>2</sub>] as a Novel Atomic Layer Deposition Precursor: ZrO<sub>2</sub> Film Growth and Mechanistic Studies. *Chem. Mater.* **2013**, *25* (15), 3088–3095.
- (288) Meng, X.; Libera, J. A.; Fister, T. T.; Zhou, H.; Hedlund, J. K.; Fenter, P.; Elam, J. W. Atomic Layer Deposition of Gallium Sulfide Films Using Hexakis(Dimethylamido)Digallium and Hydrogen Sulfide. *Chem. Mater.* **2014**, *26* (2), 1029–1039.
- (289) Gertsch, J. C.; Cano, A. M.; Bright, V. M.; George, S. M. SF<sub>4</sub> as the Fluorination Reactant for Al<sub>2</sub>O<sub>3</sub> and VO<sub>2</sub> Thermal Atomic Layer Etching. *Chem. Mater.* **2019**.
- (290) Gebhard, M.; Letourneau, S.; Mandia, D. J.; Choudhury, D.; Yanguas-Gil, A.; Mane, A.; Sattelberger, A. P.; Elam, J. W. Formation of Unsaturated Hydrocarbons and Hydrogen: Surface Chemistry of Methyltrioxorhenium(VII) in ALD of Mixed-Metal Oxide Structures Comprising Re(III) Units. *Chem. Mater.* **2019**, *31* (19), 7821–7832.
- (291) Puurunen, R. L. Correlation between the Growth-per-Cycle and the Surface Hydroxyl Group Concentration in the Atomic Layer Deposition of Aluminum Oxide from Trimethylaluminum and Water. *Appl. Surf. Sci.* **2005**, *245* (1–4), 6–10.
- (292) Puurunen, R. L. Surface Chemistry of Atomic Layer Deposition: A Case Study for the Trimethylaluminum/Water Process. *J. Appl. Phys.* **2005**, *97* (12).
- (293) Groner, M. D.; Fabreguette, F. H.; Elam, J. W.; George, S. M. Low-Temperature Al<sub>2</sub>O<sub>3</sub> Atomic Layer Deposition. *Chem. Mater.* **2004**, *16* (4), 639–645.
- (294) Sugahara, S.; Kitamura, T.; Imai, S.; Matsumura, M. Atomic Layer Epitaxy of Germanium. *Appl. Surf. Sci.* **1994**, *82–83* (C), 380–386.
- (295) Pedersen, H. Time as the Fourth Dimension: Opening up New Possibilities in Chemical Vapor Deposition. *Chem. Mater.* **2016**, *28* (3), 691–699.
- (296) Cook, M. A.; Eaborn, C.; Jukes, A. E.; Walton, D. R. M. [Tris(Trimethylsilyl)Methyl]Lithium: An Alkyllithium Compound of Unusual Stability. *J. Organomet. Chem.* **1970**, *24* (3), 529–535.
- (297) Li, H.; Aquino, A. J. A.; Cordes, D. B.; Hung-Low, F.; Hase, W. L.; Krempner, C. A. Zwitterionic Carbanion Frustrated by Boranes - Dihydrogen Cleavage with Weak Lewis Acids via an “Inverse” Frustrated Lewis Pair Approach. *J. Am. Chem. Soc.* **2013**, *135* (43), 16066–16069.
- (298) Eaborn, C.; Hitchcock, P. B.; Smith, J. D.; Sullivan, A. C. Crystal Structure of the Tetrahydrofuran Adduct of Tris(Trimethylsilyl)-Methyl-Lithium, [Li(Thf)<sub>4</sub>][Li{C(SiMe<sub>3</sub>)<sub>3</sub>}<sub>2</sub>], an Ate Derivative of Lithium. *J. Chem. Soc. Chem. Commun.* **1983**, No. 15, 827.
- (299) Van Daele, M.; Griffiths, M. B. E.; Minjauw, M. M.; Barry, S. T.; Detavernier, C.; Dendooven, J. Reaction Mechanism of the Me<sub>3</sub>AuPMe<sub>3</sub>-H<sub>2</sub>plasma-Enhanced ALD Process. *Phys. Chem. Chem. Phys.* **2020**, *22* (21), 11903–11914.
- (300) Jiang, L.; Zhang, B.; Médard, G.; Seitsonen, A. P.; Haag, F.; Allegretti, F.; Reichert, J.; Kuster, B.; Barth, J. V.; Papageorgiou, A. C. N -Heterocyclic Carbenes on Close-Packed Coinage Metal Surfaces: Bis-Carbene Metal Adatom Bonding Scheme of Monolayer Films on Au, Ag and Cu. *Chem. Sci.* **2017**, *8* (12), 8301–8308.

- (301) Wang, G.; Rühling, A.; Amirjalayer, S.; Knor, M.; Ernst, J. B.; Richter, C.; Gao, H. J.; Timmer, A.; Gao, H. Y.; Doltsinis, N. L.; et al. Ballbot-Type Motion of N-Heterocyclic Carbene on Gold Surfaces. *Nat. Chem.* **2017**, *9* (2), 152–156.
- (302) Smith, C. A.; Narouz, M. R.; Lummis, P. A.; Singh, I.; Nazemi, A.; Li, C. H.; Crudden, C. M. N-Heterocyclic Carbene in Materials Chemistry. *Chem. Rev.* **2019**, *119* (8), 4986–5056.
- (303) Ren, J.; Freitag, M.; Schwermann, C.; Bakker, A.; Amirjalayer, S.; Rühling, A.; Gao, H.-Y.; Doltsinis, N. L.; Glorius, F.; Fuchs, H. A Unidirectional Surface-Anchored N-Heterocyclic Carbene Rotor. *Nano Lett.* **2020**.
- (304) Larrea, C. R.; Baddeley, C. J.; Narouz, M. R.; Mosey, N. J.; Horton, J. H.; Crudden, C. M. N-Heterocyclic Carbene Self-Assembled Monolayers on Copper and Gold: Dramatic Effect of Wingtip Groups on Binding, Orientation and Assembly. *ChemPhysChem* **2017**, *18* (24), 3536–3539.
- (305) Coyle, J. P.; Dey, G.; Sirianni, E. R.; Kemell, M. L.; Yap, G. P. A.; Ritala, M.; Leskelä, M.; Elliott, S. D.; Barry, S. T. Deposition of Copper by Plasma-Enhanced Atomic Layer Deposition Using a Novel n-Heterocyclic Carbene Precursor. *Chem. Mater.* **2013**, *25* (7), 1132–1138.
- (306) Coyle, J. P.; Sirianni, E. R.; Korobkov, I.; Yap, G. P. A.; Dey, G.; Barry, S. T. Study of Monomeric Copper Complexes Supported by N-Heterocyclic and Acyclic Diamino Carbene. *Organometallics* **2017**, *36* (15), 2800–2810.
- (307) Banaszak Holl, M. M.; Seidler, P. F.; Kowalczyk, S. P.; McFeely, F. R. Surface Reactivity of Alkylgold(I) Complexes: Substrate-Selective Chemical Vapor Deposition of Gold from RAuP(CH<sub>3</sub>)<sub>3</sub> (R = CH<sub>2</sub>CH<sub>3</sub>, CH<sub>3</sub>) at Remarkably Low Temperatures. *Inorg. Chem.* **1994**, *33* (3), 510–517.
- (308) Waldo, R. A. Microbeam Analysis. In *Microbeam Analysis*; Newbury, D. E., Ed.; San Francisco Press: San Fransicso, CA, 1988; pp 310–314.
- (309) Oertel, A. M.; Ritteng, V.; Burr, L.; Chetcuti, M. J. Synthesis and Structural Characterization of Half-Sandwich Nickel Complexes Bearing Two Different n-Heterocyclic Carbene Ligands. *Organometallics* **2011**, *30* (24), 6685–6691.
- (310) Saba, S.; Brescia, A. M.; Kaloustian, M. K. One-Pot Synthesis of Cyclic Amidinium Tetrafluoroborates and Hexafluorophosphates; the Simplest Models of N<sub>5</sub>,N<sup>100</sup>methyltetrahydrofolate Coenzyme. *Tetrahedron Lett.* **1991**, *32* (38), 5031–5034.
- (311) Schaub, T.; Backes, M.; Radius, U. Nickel(O) Complexes of N-Alkyl-Substituted N-Heterocyclic Carbene and Their Use in the Catalytic Carbon-Carbon Bond Activation of Biphenylene. *Organometallics* **2006**, *25* (17), 4196–4206.
- (312) Kuhn, N.; Kratz, T. Synthesis of Imidazol-2-Ylidenes by Reduction of Imidazole-2(3H)-Thiones. *Synthesis (Stuttg.)* **1993**, No. 6, 561–562.